Predicting the Rheological Properties of Dilute Polymer Solutions using Bead-Spring Models: Brownian Dynamics Simulations and Closure Approximations

A THESIS

SUBMITTED FOR THE DEGREE OF DOCTOR OF PHILOSOPHY

by

Prabhakar Ranganathan

B. Tech., M.S. (I.I.T. Madras)

Department of Chemical Engineering

Monash University

Clayton, Australia

July 5, 2005

This thesis, contains no material which has been accepted for the award of any other degree or diploma in any university or other institution. I affirm that, to the best of my knowledge, the thesis contains no material previously published or written by another person, except where due reference is made in the text of the thesis.

_____

Prabhakar Ranganathan

To Anu, and my parents

Acknowledgements

The work presented in this thesis was carried out under the supervision of Dr. J. Ravi Prakash. I shall forever owe Ravi a debt of gratitude for sharing his deep knowledge and insight, and for inspiring me with his boundless enthusiasm for molecular rheology. I have also benefited greatly from his measured criticism of my often wild ideas. I thank him further for his guidance in writing this thesis. I am grateful to Prof. T. Sridhar for his guidance, and for helping put things into perspective while writing our papers.

I thank Prof. E. S. G. Shaqfeh, Dr. Matteo Pasquali, Prof. H. C. Öttinger and Prof. G. H. McKinley for their helpful comments and suggestions. It is a pleasure to thank my colleagues Sunthar, Mohit Bajaj, Duc At Nguyen, Pradipto Bhattacharjee, Xiangnan Ye, Tri Pham, Mohini Acharya, Satheesh Kumar, and Rudolf Dubbelboer for the several complicated but fascinating technical discussions, and for all the fun. I am grateful to the staff at the Department of Chemical Engineering, in particular Lilyanne Price and Stelios Konstantinidis, for their help and advice on administrative matters.

My work would not have been possible without the scholarships from the Monash Research Graduate School (MRGS), and the Department of Chemical Engineering at Monash University. Travel grants provided by the MRGS also enabled me to present at conferences in New Zealand and Korea.

I thank the Australian Partnership for Advanced Computing (APAC) and the Victorian Partnership for Advanced Computing (VPAC) for allocations of CPU-time on their supercomputers.

Abstract

In this study, a coarse-grained bead-spring model of dilute solutions of long, flexible polymers is used to obtain a detailed predictive understanding of the influence of the nonlinear phenomena of intramolecular hydrodynamic interactions (HI), and to a lesser extent, intramolecular excluded volume (EV) interactions in strong homogeneous flows. In such conditions, the finite extensibility (FE) of polymer chains plays an important role in determining the macroscopic rheological behaviour of dilute polymer solutions. Predictions for the nonlinear viscoelastic and other related properties are obtained with Brownian dynamics simulations of finitely extensible bead-spring chains with EV and HI.

An unconditionally stable semi-implicit, predictor-corrector simulation algorithm with adaptive time-stepping is developed for the integration of the nonlinear stochastic differential equations governing the behaviour of individual chains with FENE springs and with EV and HI. Simulations of 20-bead chains are used to explore the coupling of the nonlinear phenomena in the model, and it is shown that most of the rheological properties of interest in shear and extensional flows can be approximately resolved as the product of independent contributions from each of the nonlinear effects of FE, EV and HI.

It is further shown that when a bead-spring chain with N_{S} springs is used to model a long but finite macromolecule of N_{K} Kuhn segments, the predictions obtained depend strongly on the degree of coarse-graining $N_{\mathrm{K,\,S}} = N_{\mathrm{K}}/N_{\mathrm{S}}$ in conditions where chains experience significant stretching. To reduce this dependence, the Successive Fine-Graining (SFG) procedure is introduced wherein predictions accumulated for several values of N_{S} are extrapolated to the $N_{\mathrm{S}} \to N_{\mathrm{K}}$ limit. The extrapolated results obtained with simulations without EV effects for the growth of the extensional

viscosity during start-up of strong extensional flows are found to be in good agreement with the experimental data of Gupta *et al.* [2000] for polystyrene solutions in theta solvents. This quantitative agreement with experimental data underlines the importance of the phenomenon of hydrodynamic interactions even well away from equilibrium. The results of the simulations are also able to explain the anomalous molecular weight scaling of the transient extensional viscosity observed by Gupta *et al.*.

Besides Brownian dynamics simulations, closure approximations are also used in this study to obtain predictions in strong shear and extensional flows. The Gaussian approximation, studied previously for Rouse chains with HI [Öttinger, 1989a] and EV [Prakash, 2001b], is used to derive a new closure approximation for the FENE nonlinearity—the "FENE-PG" approximation. This approximation improves upon the well known FENE-P approximation by accounting for fluctuations in the spring force.

Several closure approximations for FENE chains with HI are tested for their accuracy by comparing their predictions with the results of Brownian dynamics simulations of 20-bead chains. The method of combining the Gaussian approximation for HI with the FENE-PG approximation for the FENE nonlinearity suggested in this study leads to predictions that compare well with the results of simulations in steady and unsteady shear and extensional flows, thus confirming the importance of fluctuations in HI and spring forces.

Closure approximations for FENE chains with HI predict multiple steady-states in the steady-state extensional viscosity in a range of extension-rates immediately below the critical strain rate for the coil-to-stretch transition. A one-dimensional dumbbell model with configuration dependent drag is used to understand the origins of the phenomenon of coil-stretch hysteresis. It is shown that the unique, multi-modal probability distribution obtained with the exact model in the range of extension-rates where coil-stretch hysteresis is observed, is substituted with multiple, uni-modal distributions when mean-field closure approximations are used to handle the nonlinearities due to HI and FE.

Contents

List of Tables

List of Figures

Chapter 1

Introduction

Dilute solutions of polymer molecules are used extensively in the routine structural characterization of polymer molecules. This most common application of dilute polymer solutions is based on the tremendous success of theories that describe their properties at and near equilibrium. The fact that the addition of a small amount of polymeric material to a Newtonian solvent can cause a dramatic change in its behaviour in flow, has led to dilute polymer solutions finding use in a variety of other areas, such as turbulent drag reduction, ink-jet printing, roll coating etc. In most of these applications, the fluid is subjected to conditions that take it well away from equilibrium. However, molecular theories of the behaviour of dilute polymer solutions beyond equilibrium have not been widely tested against experiments. This study takes a step towards developing a fuller understanding of the non-equilibrium behaviour of dilute solutions of long, flexible linear macromolecules in non-polar solvents.

At first glance, it would seem that it is the nature of the polymer molecule itself that must be responsible for the macroscopically observed viscoelastic behaviour of a dilute polymer solution. This, however, is only partially true. Since the polymer molecule is suspended in the solvent, its motion is considerably influenced by that of the surrounding solvent medium. As the solvent medium moves under the influence of an externally imposed velocity field, it exerts hydrodynamic drag forces on the different parts of the polymer chain, which cause the chain to orient, unravel, and stretch in strong flows. In addition to these, the segments of chain also experience

Brownian forces due to the random thermal motion of the solvent molecules.

The role of the solvent does not end there. There are two more subtle mechanisms through which the solvent influences the dynamics of the dissolved polymer. The first of these effects stems from the fact no two parts of a polymer chain can occupy the same position in space at the same time. Two segments far apart from each other along the chain tend to strongly repel each other when they approach closely. At larger separations, however, the force between the segments depends significantly on polymer-solvent interactions. The effect of these complicated interactions is further modified by the temperature of the solvent. Usually, at temperatures below a temperature known as the "theta" temperature, unfavourable polymer-solvent interactions cause the polymer chain to assume the form of a dense coil, in spite of the repulsive forces between segments. This results in phase separation, and it is not possible to form a uniform solution. At the theta temperature itself, the outward expansion caused by the excluded volume interactions is exactly balanced by the energetics of the polymer-solvent interactions. Thus, at this temperature the *net* result is that the polymer molecule behaves as though it feels *neither* effect. With increasing temperature, the influence of the polymer-solvent interactions weakens, effectively leading to an improvement in the *solvent quality*. Therefore, at higher temperatures, the average sizes of polymer coils are larger than at the theta state.

The solvent also plays a vital role in another phenomenon wherein it acts as the medium through which the motion of any part of the polymer chain is communicated to all others. The net perturbation in the solvent's velocity field in the neighbourhood of a segment, caused by the motion of all the other segments in the chain, modifies the drag force experienced by that segment, and thereby affecting its motion. This *hydrodynamic interaction* results in a strong coupling of the motions of even segments that are far apart along the chain's contour. In this sense, the phenomenon of hydrodynamic interactions, like the excluded volume effect, is a "long range" effect.

Confirmation of excluded volume and hydrodynamic interactions as the dominant phenomena governing the dynamics of isolated polymer molecules in solution is based on the excellent agreement between theories that account for these phenomena and experiments at and near equilibrium, and is widely recognized as a major

achievement in polymer physics. However, until about the time the present work commenced, such theories remained relatively untested well away from equilibrium.

That situation has changed considerably during the course of the present study. In the past few years, several researchers have used Brownian dynamics simulations of models of dilute polymer solutions to obtain predictions that are in good agreement with experimental data in strong shear and extensional flows [Doyle *et al.*, 1998; Hsieh and Larson, 2004; Hsieh *et al.*, 2003; Jendrejack *et al.*, 2002; Larson *et al.*, 1999; Li and Larson, 2000a,b; Li *et al.*, 2000; Pamies *et al.*, 2005; Schroeder *et al.*, 2003, 2004]. The key to such successful prediction of properties of dilute polymer solutions in strong flows has been the understanding of the roles of excluded volume and hydrodynamic interactions in strong shear and extensional flows where polymer molecules are significantly stretched, and the finiteness of their contour lengths plays an important part in determining their overall behaviour.

Although the results of the simulations in the studies cited above agree well with experimental data, there is still some ambiguity regarding the estimation of model parameters in these simulations. The reason for this ambiguity is that model parameters in coarse-grained descriptions of polymer solutions— such as the bead-spring chain model used in the present study and those cited above—are often chosen such that model predictions match experiment at and near equilibrium, where polymer molecules are not stretched. However, when the same set of parameters are used to predict behaviour in strong flows where molecules are highly stretched, predictions are observed to deviate from experimental data. Adjusting the parameters to bring theoretical predictions in alignment with experiments in strong flows on the other hand leads to deterioration of the near equilibrium predictions.

The reason for this behaviour lies in the coarse-grained nature of the bead-spring model. In this study, an alternative approach—dubbed here as the "Successive Fine Graining" approach—is proposed to correct for the influence of coarse-graining on the predictions obtained with bead-spring chains. The Successive Fine-Graining approach is used in this study to obtain theoretical predictions for finitely extensible chains with hydrodynamic interactions in a manner that is also consistent with the current paradigm for comparing theory with experiments near equilibrium.

The results in this study clearly show that a proper description of hydrodynamic

interactions is crucial for a quantitative description of the rheological properties of dilute solutions of polymers in theta solvents well away from equilibrium. A highlight of this work is the remarkable agreement of the theoretical predictions with experimental data on dilute solutions of polystyrene obtained across a range of extension-rates in strong extensional flows by Gupta *et al.* [2000]. Along with the recent successful prediction by Sunthar and Prakash [2005] of the behaviour of DNA molecules in good solvents, the present work confirms the importance of the phenomena of excluded volume and hydrodynamic interactions well beyond equilibrium.

Although the bead-spring model used in this study is well known, until about the time the present work was begun, prevalent algorithms for performing Brownian dynamics simulations of finitely extensible bead-spring chains with hydrodynamic and excluded volume interactions were not computationally efficient. The unconditionally stable semi-implicit, predictor-corrector algorithm developed in this study is an important breakthrough using which the exact predictions of the bead-spring model can be efficiently obtained for strong shear and extensional flows. Although the influence of excluded volume interactions has not been studied in detail in this study, the nature of the coupling between excluded volume, hydrodynamic interactions and finite chain extensibility is explored using Brownian dynamics simulations. It is observed that, despite their highly nonlinear nature, the coupling between these phenomena appears to follow some very simple rules.

While Brownian dynamics simulations of bead-spring models are attractive because they permit exact solutions to the theoretical equations for macroscopic properties, such simulations are computationally very expensive. In addition, the nonlinear spring-force laws used typically to model finitely extensible chains cause the stochastic differential equations underlying Brownian simulations of polymer chains to become stiff in situations where chains can be stretched close to their maximum allowed extension. On the other hand, it is difficult to obtain closed-form analytical solutions of the model equations, as a result of the nonlinearities due to finite chain extensibility and intra-chain interactions.

Before the advent of the high-performance computing that has made possible the Brownian dynamics simulations of large bead-spring chains in this and other recent

studies, approximate methods were for long the only way forward in the study of dilute polymer solutions. In fact, much of what we know and understand today of the behaviour near equilibrium comes undeniably from the pioneering work of Flory, Kirkwood, Zimm, Fixman, Edwards, De Gennes and others, who have brought to bear methods of ever-increasing sophistication on the scientific and technical challenge posed by excluded volume and hydrodynamic interactions. The problem with any approximate method is that when theoretical predictions obtained with its use are at variance with experiment, it is not possible in general to wisely apportion blame between the incorrectness of the physics and the inaccuracy of the approximation.

While some have seized on Brownian dynamics simulations as a way out of such ambiguity, other have preferred to employ simulations to provide benchmarks with which the accuracy of approximations can be gauged. The reason for the continued interest in approximate solutions is essentially three fold. Firstly, calculations with approximate models are much faster and the resulting prediction are free of the noise that is inevitable in Brownian dynamics simulations. As a result, approximate models can be used to explore much larger domains in parameter space, even if they are only moderately accurate. Secondly, as pointed out at the outset, dilute polymer solutions are frequently used in complex industrial flows. Numerical prediction of these flows using computational fluid dynamics requires constitutive equations for the polymer's contribution to the total fluid stress field. Expressions derived from continuum mechanics have for long been the mainstay of numerical simulations of complex flows of polymeric fluids. Approximate equations for the polymer stress derived from a more fundamental molecular picture of the polymeric fluid have the added advantage that these models have a direct physical interpretation. The third reason for studying approximate models is that they are invaluable in gaining insight into the inner workings of the physical phenomena that are represented in the model.

Closure approximations for bead-spring models of dilute polymer solutions have a long and rich history, starting from the well known Zimm model [Zimm, 1956] for treating hydrodynamic interactions. Fixman [1966a; 1966b] improved upon Zimm's treatment, and also incorporated an equivalent description of excluded volume interactions to obtain the first predictions of the influence of these phenomena on the

nonlinear viscoelastic behaviour of dilute polymer solutions. The complexities of the boson-operator formalism used by Fixman were avoided by Öttinger [1987a; 1989a] in his consistent-averaging and Gaussian approximations for hydrodynamic interactions. The Gaussian approximation approach was examined in detail for bead-spring chains with excluded volume, but no hydrodynamic interactions, by Prakash [2001b]. Peterlin [1966b] introduced an approximation for handling the nonlinearity due to finite extensibility, which was later used by Bird *et al.* [1980] to formulate their well known FENE-P model.

In this study, a closure approximation is derived for the bead-spring model combining the nonlinear phenomena of finite extensibility, excluded volume and hydrodynamic interactions. The predictions of this approximate model for the theta state are shown to be reasonably accurate in comparison with the exact results of Brownian dynamics simulations. Analysis of the predictions of this closure approximation and others reveals the important role that fluctuations in hydrodynamic interactions and spring forces play in determining the overall behaviour of dilute polymer solutions in steady and unsteady shear and extensional flows. When combined with the Successive Fine-Graining procedure, the results obtained with closure approximations are found to in good agreement with experimental data in strong extensional flows.

In a seminal paper, De Gennes [1974] used an approximate model to show that the existence of hydrodynamic interactions leads to the emergence of large barriers in the effective steady-state free-energy landscape in flows with a dominant extensional component, and predicted that these ergodicity breaking barriers would result in the phenomenon of coil-stretch hysteresis in extensional flows. Since Fan *et al.*'s analysis of De Gennes' model, it has been a long standing question whether the prediction of coil-stretch hysteresis is just an artifact of the approximation used by De Gennes. Schroeder *et al.* [2004] have demonstrated conclusively the existence of such a phenomenon with both experiments and Brownian dynamics simulations. In this study, the manner in which closure approximations replicate such ergodicity breaking phenomena is explored further.

The present thesis is organized as follows. A more detailed description of the bead-spring model and the equations governing its behaviour are given in Chapter 2.

The numerical schemes for the Brownian dynamics simulations of dumbbells and bead-spring chains with excluded volume and hydrodynamic interactions are presented in Chapter 3. This is followed by a qualitative examination of the coupling between the nonlinear phenomena in the model in Chapter 4. The equations for the closure approximations considered in this study are discussed next in Chapter 5, and the accuracy and qualitative features of the predictions of the approximations are explored in Chapter 6. Chapter 7 reviews the current paradigm for comparing theory with experiment near equilibrium, which forms the basis of the argument used to derive the Successive Fine-Graining procedure in Chapter 8. Chapter 8 also compares the results of simulations and approximations with experiments. The major conclusions of this work are finally summarized in Chapter 9.

Chapter 2

Basic equations for the bead-spring model of dilute polymer solutions

Recognizing that macroscopic material behaviour away from equilibrium stems from the dynamics at the molecular level, rheology uses observations of the stress-deformation relationship exhibited by materials to understand the dynamics of their microstructures. A rheological analysis of dilute polymer solutions can thus be used to probe the physics that governs the motion of isolated polymer molecules in solution. As in any other field of scientific endeavour, this understanding is achieved through the cyclic process of making intelligent guesses about the physical processes involved, expressing these ideas in a mathematical form and comparing the predictions of the mathematical models with experimental measurements. In polymer solution rheology, mathematical models of the physical phenomena influencing the behaviour of macromolecules are used to relate the stresses developed in a dilute polymer solution to the strength and the kind of flow imposed on it.

Since inter- and intra-molecular interactions are ultimately responsible for the behaviour of any material observed at macroscopic scales, one would expect that accurate prediction of properties of polymer solutions would require computer simulations of detailed molecular models of these systems. Such simulations are enormously expensive to perform. Furthermore, the tremendous variety in polymer

molecules and their solvents makes it impossible to calculate properties for each polymer solution individually using molecular simulations. In spite of their diversity, the macroscopic properties of large classes of polymeric materials share common features, and appear to in fact depend only on a small set of parameters. It is further found that the experimental data for different polymer-solvent systems can be collapsed on to universal master plots. In the words of Doi and Edwards [1986], "the ability of such superposition indicates the existence of an inherent simplicity hidden behind the apparent complexity of the polymer systems." The universal features of macroscopic behaviour that are shared by different polymer systems within any single class of polymeric materials must therefore be independent of the details of polymer/solvent chemistry. Furthermore, the fact that master plots can be obtained by rescaling raw experimental data with a few well defined parameters means that all chemistry dependence resides in those few parameters alone.

Since local chemical details influence only a small set of parameters, it must be possible to construct models of polymer systems by representing only a few essential elements of polymeric systems. Once the accuracy of a model in describing the universal features of experimentally observed macroscopic behaviour is proven, the relevant parameters in the model may, in principle, be subsequently related to the chemistry of the polymer system using a more detailed molecular model. This essentially phenomenological approach has been remarkably successful. The reptation theory of Doi and Edwards for concentrated solutions and melts of polymers is a prime example of this approach.

Phenomenological models of dilute polymer solutions must attempt to capture the key features of the physics that governs the behaviour of isolated polymer molecules when suspended in a sea of much smaller solvent molecules. A real linear polymer molecule typically consists of several repeating chemical units connected together as a chain. In a large polymer molecule, there exists a wide separation of length scales, ranging from the length of a single bond on the chain's backbone to the mean radius of the polymeric coil while in solution. Most macroscopic properties of interest in polymer solutions are however related to the gross dynamics of the polymer chain as a whole.

For the successful prediction of such properties therefore, a structural model of

the polymer-solvent system that replicates the gross features of the system may be sufficient. To this end, it is found that an adequate description of the gross physical structure of a polymer-solvent system for solutions of long and highly flexible polymer molecules can be achieved as follows [Bird *et al.*, 1987b; Yamakawa, 1971]. The solvent molecules are replaced by a featureless continuum, and the polymer solution consists of n_{p} polymer molecules per unit volume suspended in this continuum. A single polymer molecule is represented as a linear chain of rigid massless rods of uniform length, in which every rod is permitted to rotate unhindered in any direction. This "freely jointed chain", or "Kramer's chain" equivalent of a real polymer molecule captures all the gross features of the molecule such as its topological connectivity and its flexibility, that is, its ability to take on a large number of configurations. In this model, the structure of each polymer molecule is characterized by the specification of only two parameters: the length of each rod, b_{K}, and the number of rods in the chain N_{K}. The combined effect of the local chemical details at the monomeric level—such as bond lengths, bond angles, steric hindrances, etc.—on the overall polymer structure is bundled into a single number, b_{K}. The Kuhn segment length serves as a measure of the local stiffness of a polymer chain.

The structural simplification effected by the use of coarse-grained models, however, comes at a price. In a truly molecular description of the polymer-solvent system, the dynamic evolution of the ensemble of polymer and solvent molecules under the influence of inter- and intra-molecular interactions is governed solely by Newton's laws of motion. To reproduce the gross features of the dynamics of the original system consisting of solvent and polymer molecules, with a coarse-grained model consisting of a continuum solvent and Kramer's chains, it becomes necessary to introduce phenomenological interactions in the coarse-grained model. The number and the mathematical nature of such interactions is *a priori* unknown, and one is guided by intuition and experience in formulating them.

For instance, in the model described originally by Kramer [1944], the total force exerted by solvent molecules on a segment of a real polymer molecule represented by a single Kuhn segment in the model, is treated as the sum of a smooth "hydrodynamic drag" component and a noisy "Brownian" component. Drawing inspiration from classical hydrodynamics, the smooth hydrodynamic force on a Kuhn segment

is modeled as being proportional to the velocity of the segment relative to $\boldsymbol{v}$, the velocity of the solvent continuum at its position, and acting in a direction opposing the relative motion. Applying this "Stokes' law empiricism" [Bird *et al.*, 1987b] to give mathematical form to the hydrodynamic force necessitates the introduction of a new parameter in the model: the drag coefficient of a Kuhn segment, ζ_{K}. The drag coefficient ζ_{K} is a phenomenological constant that depends solely on the chemical nature of the polymer-solvent system. In fact, the individual influences of the chemical nature of the solvent and polymer on ζ_{K} may be further separated by using the Stokes' equation $\zeta_{\mathrm{K}} = 6\pi\eta_{\mathrm{s}}a_{\mathrm{K}}$, where η_{s} is the viscosity of the Newtonian solvent and a_{K} is the hydrodynamic radius of the Kuhn segment. The hydrodynamic radius a_{K} can be regarded as a fundamental characteristic of the polymer molecule, on par with the Kuhn segment length b_{K}. Thus, an individual polymer molecule may be conveniently pictured as a linear chain of N_{K} rods of length b_{K} with spherical "beads" of radius a_{K} located between adjacent rods. An expression for the Brownian force is obtained by making additional assumptions on the nature of the distribution of the velocities of the Kuhn segments [Bird *et al.*, 1987b]. The final expression for the Brownian force is proportional to $k_{\mathrm{B}}T$, where k_{B} is the Boltzmann constant and T is the temperature of the solvent.

In this basic coarse-grained model of a polymer solution, known as the "bead-rod" model, the (monodisperse) polymer-solvent system is characterized by a handful of parameters *viz.* n_{p}, b_{K}, N_{K}, a_{K}, η_{s} and T. Out of these, b_{K}, N_{K}, and a_{K} are considered to depend uniquely on the polymer molecule's chemical nature. Further, the parameters b_{K} and a_{K} are properties of an individual Kuhn segment, and must therefore be independent of N_{K}.

This model, however, is far from being complete in the sense that the incorporation of hydrodynamic and Brownian forces alone are inadequate in fully predicting the observed behaviour in experiment. The developments in the kinetic theory of dilute polymer solutions over the past few decades clearly show that it is essential to incorporate at least two other important phenomenological interactions.

The first of these, known as the *excluded volume effect* has been reviewed in great detail by Yamakawa [1971] and Schäfer [1999]. This effect essentially stems from the fact that a polymer chain cannot cross itself in space. Therefore, when any two

segments of a real molecule approach each other closely, they experience a strong mutual repulsion. At larger separations, the force experienced by non-adjacent monomers is in general weakly attractive. This weak van der Waals type attraction is the result of the interactions between a monomer and the solvent molecules, and is controlled by the thermodynamics of such interactions, and therefore by the temperature [Schäfer, 1999]. The excluded volume repulsion between monomers tends to increase the average size of a polymer molecule. The solvent-mediated attraction opposes this tendency of the polymer chain to swell.

At low temperatures, interactions between monomers and the solvent molecules are energetically unfavourable. In such "poor solvent" conditions, the monomer-monomer attraction is strong enough to overcome the entropic tendency of the coil to assume random configurations, and the polymer molecule collapses as a tightly wound globule. As temperature increases, the monomer-monomer attraction is progressively weakened, and the mean coil size increases. At a particular value of the temperature, which is unique for a given polymer-solvent system, the coil size is the same as that of an idealized polymer coil in which neither the short-range repulsion nor the attraction at larger inter-monomer separations, is present. At temperatures higher than this "theta temperature", the short-range repulsion dominates, and the coil is swollen relative to its size at the theta temperature. Thus, T_θ divides the poor solvent and good solvent regimes in temperature.

The description of the excluded volume effect so far is based on a molecular picture. A phenomenological interpretation of the behaviour in the good solvent regime is achieved in the context of the bead-rod model by incorporating an effective inter-segmental excluded volume potential. Although the potential of mean excluded volume force between any two segments is expected to be a complicated function of the inter-segmental distance, this is dominated by its short-range repulsive nature [Yamakawa, 1971], which is parameterized by the excluded volume of a Kuhn segment, v_{K}. The temperature dependence of the excluded volume effect for $T > T_\theta$ is typically taken into account by treating v_{K} a function of temperature. For moderate deviations from T_θ, a function of the form $v_{\mathrm{K}}(T) = v_{\mathrm{K},0}(1 - T_\theta/T)$ is typically used, in which all the influence of the chemistry of the polymer-solvent combination is absorbed into the constants $v_{\mathrm{K},0}$ and T_θ. At $T = T_\theta$, $v_{\mathrm{K}} = 0$, the

effect of excluded volume interactions vanish, and the chains in the coarse-grained model behave as "phantom" chains capable of self-intersection.

At the theta temperature, the phantom Kramer's chains take on random configurations at equilibrium, under the influence of the Brownian forces exerted by the solvent. The statistical properties of such random configurations have long been studied in the form of ideal three-dimensional random walks. The mean radius of gyration of phantom Kramer's chains at equilibrium is calculated as

$$R^{\theta}_{\mathrm{G,eq}} = \frac{1}{\sqrt{6}} b_{\mathrm{K}} N_{\mathrm{K}}^{1/2}. \tag{2.1}$$

Since N_{K} is proportional to the contour length $L = b_{\mathrm{K}} N_{\mathrm{K}}$ of a polymer molecule, which in turn is proportional to its molecular weight M, the equation above suggests that for long, flexible polymer molecules, $R^{\theta}_{\mathrm{G,eq}} \sim M^{1/2}$, a fact that has been known since the times of Flory [1953]. In fact, this well established equation can be used to empirically extract the parameters b_{K} and N_{K}, since

$$b_{\mathrm{K}} = \frac{6 R^{\theta\,2}_{\mathrm{G,eq}}}{L}; \quad N_{\mathrm{K}} = \frac{L^2}{6 R^{\theta\,2}_{\mathrm{G,eq}}}, \tag{2.2}$$

with the contour length L being calculated from the known chemical structure of the polymer molecule in question.

Excluded volume interactions characterized by v_{K} are fundamentally different from the local interactions between neighbouring monomers on the chain backbone which determine the chain's stiffness, and are accounted for through the length of the Kuhn segment, b_{K}. Excluded volume interactions can occur between segments that are far apart along the chain backbone. In this sense, therefore, these interactions have a "long range", leading to an intimate coupling of the behaviour of all the different segments in the chain, and thus giving rise to the non-Markovian nature of chain configurational statistics [Yamakawa, 1971].

Predictions of static properties at equilibrium are independent of the drag coefficient ζ_{K} introduced earlier. However, the dynamics of polymer solutions at and beyond equilibrium can be expected to depend on this parameter. Kirkwood and Riseman [1948] pointed out that for a proper description of the dynamical behaviour of polymer molecules in solutions with a bead-rod model, it is necessary to

incorporate another "long-range" interaction between non-adjacent segments in the chain. The phenomenon of hydrodynamic interaction, accounts for the fact that the motion of a segment is propagated to all the other segments in the chain by the solvent molecules. Kirkwood and Riseman thus introduced the idea of hydrodynamic interaction whereby the hydrodynamic force exerted by a bead in the bead-rod chain as it moves through the solvent perturbs the solvent's velocity field at the locations of all the other beads in the chain. The total modification of the solvent's velocity field around a Kuhn segment due to the motion of all the other beads in the chain modifies the net drag force it experiences. The mathematical treatment of this effect however introduces no new parameters, the strength of hydrodynamic interaction between any two Kuhn segments being proportional to ζ_{K}.

The incorporation of the phenomena of excluded volume and hydrodynamic interactions in coarse-grained models of dilute polymer solutions leads to highly accurate predictions of the universal features of static properties and transport coefficients of dilute polymer solutions close to equilibrium, in theta and good solvents [Freed *et al.*, 1988; Prakash, 1999; Schäfer, 1999; Yamakawa, 1971]. This success is based on the recognition that the origin of universal behaviour lies in the large separation of length scales that exists in long, flexible polymer molecules. The resulting scale invariance in the structure of long polymer coils near equilibrium leads to an insensitivity of the gross behavior of the chains to the chemical structure of the monomers or the solvents. In fact, the theoretical results referred to above are typically obtained by keeping $R^{\theta}_{\mathrm{G,\,eq}}$ fixed, and taking the limit $L \to \infty$, which results in an ideal self-similar fractal object. Experimental data are of course obtained with long, but finite molecules. However, calculations of the corrections to the infinite chain results due to chain finiteness show that these corrections decrease with increasing chain length, thus making it possible to compare directly the asymptotic results of the theory with experiment near equilibrium.

It is also well known, however, that the behaviour of finite chains well away from equilibrium is qualitatively different from that predicted in the limit of infinite chains. For example, theoretical predictions for infinite chains show that the contribution of polymers to the steady-state viscosity of dilute solutions increases

without bound when the shear-rate is increased, in complete contrast to the behaviour predicted for finite chains, for which the polymer viscosity is observed to become vanishingly small. Thus, in order to test whether the phenomena of excluded volume and hydrodynamic interactions are sufficient in describing experimental observations in strong flows, it is necessary obtain predictions for chains of finite $R^{\theta}_{\mathrm{G,\,eq}}$ and L. *The primary objective of this study is to understand the roles of excluded volume and hydrodynamic interactions in long, flexible polymer molecules in those situations where the finiteness of their contour length plays an important part in determining their overall behaviour.*

Another important feature of theoretical calculations close to equilibrium is that many of the results have been obtained through the use of analytical approximations, since the inclusion of excluded volume and hydrodynamic interactions into the model makes the task of obtaining exact results for most average macroscopic properties of interest extremely difficult. It is in principle possible to achieve exact results through the use of computer simulations of ensembles of large ($N_{\mathrm{K}} \sim 10^3$) bead-rod chains acting under the combined influence of random Brownian forces, hydrodynamic drag, and excluded volume and hydrodynamic interactions. However, routine simulations of large bead-rod chains are currently beyond the reach of most research groups working in this field. It is more advantageous to use a coarser description of the polymer molecule introduced first by Rouse [1953]. This bead-spring model of a polymer molecule consists of replacing large, equal-sized segments of the bead-rod chain with flexible springs connecting larger beads representing the drag characteristics of the segments. As in the case of the bead-rod model, it is possible to introduce excluded volume and hydrodynamic interactions into the more coarse-grained bead-spring version as well. The finite contour length of a molecule is modeled in the bead-spring model through the use of finitely extensible springs.

The equations for finitely extensible bead-spring models with excluded volume and hydrodynamic interactions are quite well known, and are briefly reviewed here primarily to introduce the notation that will be used in the rest of the thesis.

2.1 The Fokker-Planck equation

In the bead-spring model of polymer solutions, the incompressible Newtonian solvent is treated as a continuum. For homogeneous flows, the velocity field of the continuum solvent can be expressed as $\boldsymbol{v}(\boldsymbol{r},t) = \boldsymbol{v}_0 + \boldsymbol{\kappa}(t)\cdot\boldsymbol{r}$, where $\boldsymbol{v}_0$ is the constant velocity of the frame of reference, $\boldsymbol{\kappa}$ is the transpose of the position-independent traceless velocity gradient $\nabla\boldsymbol{v}$, and $\boldsymbol{r}$ is the position vector of any point in the solution with respect to the frame of reference.

In the conventional bead-spring model of a polymer solution, a polymer molecule is discretized into N_s sub-molecules of equal contour length, and each sub-molecule is represented as a massless "spring". This mechanical analogue is based on the fact that any sub-molecule resists separation of its ends due to entropic considerations. The overall drag coefficient of each sub-molecule is taken to be a constant, ζ. The insertion of $N = N_\mathrm{s} + 1$ spherical beads of radius $a = \zeta/(6\pi\eta_\mathrm{s})$ between adjacent springs (including beads at the chain ends) then completes the mechanical representation of the molecule as a bead-spring chain. The polymer solution consists of n_p bead-spring chains per unit volume suspended in the solvent continuum. In modeling a dilute solution, explicit interactions between polymer chains are excluded from the model formulation.

The instantaneous configurational state of any arbitrary bead-spring chain is specified by the set of position vectors $\{\boldsymbol{r}_\nu \,|\, \nu = 1,\ldots,N\}$ of the N beads. Using kinetic theory, the following Fokker-Planck equation for the evolution of the configurational probability distribution $\Psi(\boldsymbol{r}_1,\ldots,\boldsymbol{r}_N)$ can be derived starting from a very general phase-space description of the polymer-solvent system after making several well-tested assumptions [Bird *et al.*, 1987b, Chapters 17 & 18]:

$$\frac{\partial\Psi}{\partial t} = -\sum_{\nu=1}^{N}\frac{\partial}{\partial\boldsymbol{r}_\nu}\cdot\left\{\boldsymbol{\kappa}\cdot\boldsymbol{r}_\nu + \frac{1}{\zeta}\sum_{\mu=1}^{N}\boldsymbol{\Upsilon}_{\nu\mu}\cdot\boldsymbol{F}_\mu^\phi\right\}\Psi + \frac{k_\mathrm{B}T}{\zeta}\sum_{\nu,\mu=1}^{N}\frac{\partial}{\partial\boldsymbol{r}_\nu}\cdot\boldsymbol{\Upsilon}_{\nu\mu}\cdot\frac{\partial\Psi}{\partial\boldsymbol{r}_\mu}\,, \tag{2.3}$$

where k_B is Boltzmann''s constant, and T is the absolute temperature of the solution. In the equation above, $\boldsymbol{\Upsilon}_{\nu\mu}$ are dimensionless diffusion tensors that are related to

the hydrodynamic interaction tensors $\boldsymbol{\Omega}_{\nu\mu}$ through the definition

$$\boldsymbol{\Upsilon}_{\nu\mu} \equiv \boldsymbol{\delta} - \zeta\boldsymbol{\Omega}_{\nu\mu}\,, \tag{2.4}$$

where $\boldsymbol{\delta}$ is the unit tensor. The tensors $\boldsymbol{\Omega}_{\nu\mu}$ are discussed in greater detail in Section 2.3. The total force on the ν-th bead due to non-hydrodynamic conservative intramolecular interactions, $\boldsymbol{F}_{\nu}^{\phi}$, is expressed in terms of the intramolecular potential energy ϕ as

$$\boldsymbol{F}_{\nu}^{\phi} = -\frac{\partial\phi}{\partial\boldsymbol{r}_{\nu}}\,. \tag{2.5}$$

Under homogeneous conditions, $\Psi(\boldsymbol{r}_1,\ldots,\boldsymbol{r}_N) = V_{\mathrm{sol}}^{-1}\psi(\boldsymbol{Q}_1,\ldots,\boldsymbol{Q}_{N_\mathrm{s}})$, where V_{sol} is the total volume of the solution and ψ is the probability distribution for the set of vectors, $\{\boldsymbol{Q}_i\,|\,i=1,\ldots,N_\mathrm{s}\}$. The connector vector $\boldsymbol{Q}_i = \boldsymbol{r}_{i+1} - \boldsymbol{r}_i$ defines the configurational state of the i-th spring in the chain. Equation (2.3) can be transformed to obtain a Fokker-Planck equation for ψ:

$$\frac{\partial\psi}{\partial t} = -\sum_{i=1}^{N_\mathrm{s}}\frac{\partial}{\partial\boldsymbol{Q}_i}\cdot\left\{\boldsymbol{\kappa}\cdot\boldsymbol{Q}_i - \frac{1}{\zeta}\sum_{j=1}^{N_\mathrm{s}}\widetilde{\boldsymbol{A}}_{ij}\cdot\boldsymbol{F}_j^{\phi,\,c}\right\}\psi + \frac{k_\mathrm{B}T}{\zeta}\sum_{i,\,j=1}^{N_\mathrm{s}}\frac{\partial}{\partial\boldsymbol{Q}_i}\cdot\widetilde{\boldsymbol{A}}_{ij}\cdot\frac{\partial\psi}{\partial\boldsymbol{Q}_j}\,. \tag{2.6}$$

The total connector force $\boldsymbol{F}_j^{\phi,\,c}$ in Eq. (2.6) is given by

$$\boldsymbol{F}_j^{\phi,\,c} = \frac{\partial\phi}{\partial\boldsymbol{Q}_j}\,. \tag{2.7}$$

The diffusion tensors $\widetilde{\boldsymbol{A}}_{ij}$ in Eq. (2.6) are related to the hydrodynamic tensors through

$$\widetilde{\boldsymbol{A}}_{ij} = A_{ij}\boldsymbol{\delta} + \zeta\left(\boldsymbol{\Omega}_{ij} + \boldsymbol{\Omega}_{i+1,\,j+1} - \boldsymbol{\Omega}_{i,\,j+1} - \boldsymbol{\Omega}_{i+1,\,j}\right)\,, \tag{2.8}$$

where $A_{ij} = \delta_{ij} + \delta_{i+1,\,j+1} - \delta_{i,\,j+1} - \delta_{i+1,\,j} = 2\delta_{ij} - \delta_{|i-j|,1}$ is an element of the $N_\mathrm{s}\times N_\mathrm{s}$ Rouse matrix.

In this thesis, the bead position-vector form of the Fokker-Planck, Eq. (2.3), is used primarily in the exposition of the algorithm for Brownian dynamics simulations

in the next Chapter. In the construction of approximation schemes, the connector-vector form in Eq. (2.6) above is found to be more useful, and unless specified otherwise, general references to the Fokker-Planck equation will henceforth mean the connector-vector form.

Although hydrodynamic interactions play an important role in determining the dynamic behaviour of polymer solutions near and beyond equilibrium, the static properties of the solutions at equilibrium do not depend on hydrodynamic interactions. At equilibrium, ($\boldsymbol{\kappa} = 0$; $t \to \infty$), the solution of the Fokker-Planck equation is given by the Boltzmann distribution

$$\psi_{\text{eq}} = \frac{\exp\left[-\phi/k_{\text{B}}T\right]}{\int \ldots \int \exp\left[-\phi/k_{\text{B}}T\right] d\boldsymbol{Q}_1 \ \ldots \ d\boldsymbol{Q}_{N_{\text{s}}}} \,. \tag{2.9}$$

The statistical properties of the equilibrium state are thus completely specified by the intramolecular potential energy ϕ which is discussed in greater detail below.

2.2 Conservative intramolecular interactions

In the bead-spring model, the total intramolecular potential energy in the molecule ϕ is written as the sum of two independent contributions,

$$\phi = \phi^{\text{S}} + \phi^{\text{E}} \,, \tag{2.10}$$

where, ϕ^{S} is the total free-energy potential contained in the springs, while ϕ^{E} is the total potential energy due to excluded volume repulsions between different parts of the chain.

2.2.1 Spring forces

In his seminal work, Rouse [1953] introduced the concept of an "entropic spring" based on the well known observation that as the ends of any polymer molecule (or sub-molecule) are separated by any length, the number of molecular configurations available that are consistent with that extension of the ends, decreases. This leads to a decrease in the entropy, and consequently work has to be done by the external

agency seeking to stretch the molecule in order to achieve the necessary increase in free energy. The external agency thus experiences a resistive force opposing the separation of the molecules ends: the molecule acts as an entropic "spring". While representing a polymer molecule as a coarse-grained chain of N_{S} sub-molecules, the total entropic resistance to changes in the overall configuration of the coarse-grained chain is modeled through the total spring potential ϕ^{S} which is the sum of the potentials of the individual springs:

$$\phi^{\mathrm{S}} = \sum_{k=1}^{N_{\mathrm{S}}} S(Q_k) = \sum_{k=1}^{N_{\mathrm{S}}} S_k \,. \tag{2.11}$$

The spring contribution to the total connector force, $\boldsymbol{F}_j^{\phi,\,c}$ defined in Eq. (2.7) is

$$\boldsymbol{F}_j^{\mathrm{S},\,c} = \frac{\partial S_j}{\partial \boldsymbol{Q}_j} \,. \tag{2.12}$$

If the characteristic time scale of the external agency—such as solvent's velocity field—forcing a change in the chain's configuration is much larger than the time scale required by the sub-molecules to ergodically sample their configuration spaces consistent with the set of their end-to-end vectors $\{\boldsymbol{Q}_j | j = 1, \ldots, N_{\mathrm{S}}\}$, it is possible to use standard results from equilibrium statistical mechanics to obtain

$$\boldsymbol{F}_j^{\mathrm{S},\,c} = -\frac{\partial \ln P_{\mathrm{eq}}(\boldsymbol{Q}_j)}{\partial \boldsymbol{Q}_j} \,, \tag{2.13}$$

where $P_{\mathrm{eq}}(\boldsymbol{Q})$ is the probability that the end-to-end vector of a sub-molecule is equal to $\boldsymbol{Q}$ at equilibrium. In order to obtain an analytical expression (as opposed to an empirical equation determined from experimental measurements) for $P_{\mathrm{eq}}(\boldsymbol{Q})$, it is necessary to invoke a more detailed model of the sub-molecule.

As discussed before in this Chapter, the gross structural features of a real long, linear, highly flexible polymer molecule suspended in the solvent continuum are generally believed to be well characterized by the specification of two key parameters, the Kuhn segment length b_{K} and the number of Kuhn segments $N_{\mathrm{K}} \gg 1$. Since the

total contour length of a real molecule is

$$L = b_{\mathrm{K}} N_{\mathrm{K}} \,, \tag{2.14}$$

on discretizing the molecule into N_{S} springs, each sub-molecule "contained" in a spring consists of $N_{\mathrm{K,\,S}} = N_{\mathrm{K}}/N_{\mathrm{S}}$ Kuhn segments. The ratio $N_{\mathrm{K,\,S}}$ serves as a convenient measure of the degree of coarse-graining that a certain choice of N_{S} implies when seeking to model a molecule of N_{K} Kuhn segments.

When modeling highly flexible molecules, analytical results for the probability $P_{\mathrm{eq}}(\boldsymbol{Q})$ can then be obtained by representing each sub-molecule as a Kramer's chain of $N_{\mathrm{K,\,S}}$ freely-jointed Kuhn segments [Yamakawa, 1971], from which expressions for the entropic spring force can be derived using Eq. (2.13) for different degrees of coarse-graining. For $N_{\mathrm{K,\,S}} \gtrsim 10$, the exact expression for the magnitude of the spring force approaches the inverse-Langevin function, which however is not easy to implement in numerical routines. Instead, the following FENE (or Warner) expression for the spring force law is used in this study, as it is known to be a good approximation to the inverse-Langevin expression [Warner, 1972]:

$$\boldsymbol{F}_j^{\mathrm{S},\,c} \;=\; H \left(\frac{1}{1 - \boldsymbol{Q}_j^2/Q_0^2} \right) \boldsymbol{Q}_j \;=\; H\,\xi(Q_j)\,\boldsymbol{Q}_j \,. \tag{2.15}$$

Here, H is the spring constant, $Q_j = |\,\boldsymbol{Q}_j\,|$, Q_0 is the contour length of the sub-molecule underlying a single spring, and ξ is the nonlinearity in the FENE spring force law. Moreover, the equation above is also easier to work with while developing approximations. Although the function ξ will be used to refer to the FENE nonlinearity, on occasion the same notation will be used for the nonlinearity in any general spring force expression of the form $\boldsymbol{F}^{\mathrm{S},\,c} = H\xi\,\boldsymbol{Q}$.

The simple expression in Eq. (2.15) above captures the essential features of the exact inverse-Langevin expression. As $Q = |\boldsymbol{Q}| \to 0$, the magnitude of the spring force approaches 0. For small extensions, when $Q \ll Q_0$, $\xi \approx 1$ and the force grows linearly with Q. As $Q \to Q_0$, the singularity in the nonlinearity ξ causes the force to diverge as $[1 - (Q/Q_0)]^{-1}$, which is also the rate at which the inverse-Langevin force diverges. The divergence of the force at a finite value of Q ensures that the spring is finitely extensible, and cannot be stretched beyond the true contour length

of the sub-molecule that a spring represents.

The parameters in the FENE spring-force law, H and Q_0, can be related to the two parameters characterizing the equilibrium structure of the sub-molecule underlying the spring, b_{K} and $N_{\mathrm{K,\,S}}$. Firstly, the contour length of the sub-molecule is $b_{\mathrm{K}}N_{\mathrm{K,\,S}}$ and therefore, $Q_0 = b_{\mathrm{K}}N_{\mathrm{K,\,S}}$. Secondly, at the theta temperature, it is well known that the mean square end-to-end distance of flexible polymer molecules at equilibrium is given by

$$R^2_{\mathrm{e,\,eq}} = b^2_{\mathrm{K}}N_{\mathrm{K}}\,. \tag{2.16}$$

Further, the equilibrium mean square end-to-end distance of a sub-molecule modeled as a Kramer's chain, in the absence of excluded volume forces, is

$$R^2_{\mathrm{S}} = b^2_{\mathrm{K}}N_{\mathrm{K,\,S}}\,. \tag{2.17}$$

On the other hand, using the equilibrium Boltzmann distribution $\psi_{\mathrm{eq}} \sim \exp(-\phi^{\mathrm{S}}/k_{\mathrm{B}}T)$ for a single spring governed by any spring force law, for which the spring potential

$$\phi^{\mathrm{S}}(Q) = \int F^{\mathrm{S},c}dQ' = H\int \xi(Q')Q'dQ'\,, \tag{2.18}$$

the analytical expression for the mean-squared end-to-end distance can be written in the following form [Sunthar and Prakash, 2005]:

$$R^2_{\mathrm{S}} = \frac{3k_{\mathrm{B}}T}{H}\chi^2(H, Q_0) \tag{2.19}$$

Here,

$$\chi^2 = \frac{H}{3k_{\mathrm{B}}T}\frac{\int_0^\infty Q^4 \exp[-(H/k_{\mathrm{B}}T)\int_0^Q \xi(Q')Q'\,dQ']\,dQ}{\int_0^\infty Q^2 \exp[-(H/k_{\mathrm{B}}T)\int_0^Q \xi(Q')Q'\,dQ']\,dQ}\,. \tag{2.20}$$

Thus, the dimensionless function χ in general depends on both H and Q_0 in a manner determined by the spring-force nonlinearity, ξ. For FENE springs [Bird

et al., 1987b],

$$\chi^2 = \frac{Q_0^2\, H/k_{\mathrm{B}}T}{Q_0^2\, H/k_{\mathrm{B}}T + 5}\,, \tag{2.21}$$

using which it can be shown that

$$\frac{H}{k_{\mathrm{B}}T} = \frac{3}{R_{\mathrm{S}}^2} - \frac{5}{Q_0^2}\,. \tag{2.22}$$

Substituting for R_{S}^2 and Q_0^2 in terms of b_{K} and $N_{\mathrm{K,\,S}}$ gives

$$\frac{H}{k_{\mathrm{B}}T} = \frac{1}{b_{\mathrm{K}}^2}\,\frac{3N_{\mathrm{K,\,S}} - 5}{N_{\mathrm{K,\,S}}^2}\,. \tag{2.23}$$

The equations above indicate that taking the limit $Q_0 \to \infty$ while keeping R_{S}^2 constant, leads to $\chi \to 1$. In this limit, $R_{\mathrm{S}}^2 = 3k_{\mathrm{B}}T/H$, and the FENE spring-force expression reduces to the Hookean spring force law, $\boldsymbol{F}^{\mathrm{S},\,c} = H\boldsymbol{Q}$. In other words, as the contour length of the sub-molecule becomes infinitely large, while the R_{S}^2 is kept constant and finite, the "Hookean limit" is approached. The linear Hookean spring can hence be regarded as the coarse-grained representation of an idealized (fractal) chain with infinite contour length, but finite R_{S}^2. In this study, chains with Hookean springs will be referred to as "Rouse" chains, while finitely-extensible bead-spring chains will be denoted as "FEBS" chains.

2.2.2 Excluded volume interactions

The excluded volume (EV) effect is typically modeled by incorporating a potential of mean force between any pair of beads of a bead-spring chain, representing the net solvent-modified EV interaction between a pair of sub-molecular segments. It is further assumed that the total potential energy in the chain due to EV interactions can be modeled as the sum of pair-wise interactions, and

$$\phi^{\mathrm{E}} = \frac{1}{2}\sum_{\substack{\nu,\,\mu=1\\ \nu\neq\mu}}^{N} E(r_{\mu\nu}) = \frac{1}{2}\sum_{\substack{\mu,\,\nu=1\\ \mu\neq\nu}}^{N} E_{\mu\nu}\,, \tag{2.24}$$

where $\boldsymbol{r}_{\mu\nu}$ is the inter-bead displacement $\boldsymbol{r}_\nu - \boldsymbol{r}_\mu$, and $r_{\mu\nu} = |\boldsymbol{r}_{\mu\nu}|$. At this point, it is necessary to digress briefly to introduce some useful notation.

The displacement $\boldsymbol{r}_{\mu\nu}$ is expressible as a linear combination of the connector vectors using

$$\boldsymbol{r}_{\mu\nu} = \mathrm{sgn}(\nu - \mu) \sum_{i\,=\,\min(\nu,\mu)}^{\max(\nu,\mu)-1} \boldsymbol{Q}_i \,, \tag{2.25}$$

$$= \sum_{i=1}^{N_\mathrm{s}} \Delta\Theta^i_{\mu\nu} \boldsymbol{Q}_i \,, \tag{2.26}$$

for all $1 \leq \mu, \nu \leq N$ and $1 \leq i \leq N_\mathrm{s}$. Here,

$$\Delta\Theta^i_{\mu\nu} = \begin{cases} 1, & \text{if } \mu \leq i < \nu \,, \\ -1, & \text{if } \nu \leq i < \mu \,, \\ 0 \,, & \text{otherwise,} \end{cases} \tag{2.27}$$

is the one-dimensional "box" function. This function can be succinctly expressed in terms of the Heaviside step function,

$$\Theta(m,n) = \begin{cases} 1, & \text{if } n \geq m \\ 0 & \text{otherwise} \,, \end{cases} \tag{2.28}$$

as $\Delta\Theta^i_{\mu\nu} = \Theta(\mu, i) - \Theta(\nu, i) = -\Delta\Theta^i_{\nu\mu}$. Further, the dyad

$$\boldsymbol{r}_{\mu\nu}\boldsymbol{r}_{\mu\nu} = \sum_{i,j\,=\min(\nu,\mu)}^{\max(\nu,\mu)-1} \boldsymbol{Q}_i\boldsymbol{Q}_i = \sum_{i,j\,=1}^{N_\mathrm{s}} \Delta\Theta^{ij}_{\mu\nu} \boldsymbol{Q}_i\boldsymbol{Q}_j \,, \tag{2.29}$$

where the two-dimensional box function

$$\Delta\Theta^{ij}_{\mu\nu} = \Delta\Theta^i_{\mu\nu}\Delta\Theta^j_{\mu\nu} \,. \tag{2.30}$$

This function is symmetric with respect to an exchange of the indices μ and ν, and/or i and j.

The EV connector force

$$\boldsymbol{F}_j^{\mathrm{E},\,c} = \frac{\partial \phi^{\mathrm{E}}}{\partial \boldsymbol{Q}_j}\,, \tag{2.31}$$

is related to the pair-wise EV potential E using Eq. (2.24):

$$\boldsymbol{F}_j^{\mathrm{E},\,c} = \frac{1}{2}\sum_{\substack{\mu,\,\nu=1\\ \mu\neq\nu}}^{N} \frac{\partial E_{\mu\nu}}{\partial \boldsymbol{Q}_j}\,, \tag{2.32}$$

$$= \frac{1}{2}\sum_{\substack{\mu,\,\nu=1\\ \mu\neq\nu}}^{N} \frac{\partial E_{\mu\nu}}{\partial \boldsymbol{r}_{\mu\nu}} \cdot \frac{\partial \boldsymbol{r}_{\mu\nu}}{\partial \boldsymbol{Q}_j}\,. \tag{2.33}$$

From Eq. (2.26),

$$\boldsymbol{F}_j^{\mathrm{E},\,c} = \frac{1}{2}\sum_{\substack{\mu,\,\nu=1\\ \mu\neq\nu}}^{N} \frac{\partial E_{\nu\mu}}{\partial \boldsymbol{r}_{\nu\mu}} \Delta\Theta_{\mu\nu}^{j}\,. \tag{2.34}$$

The EV force exerted on the ν-th bead by the μ-th bead in the chain is given by

$$\boldsymbol{F}_{\mu\nu}^{\mathrm{E}} = -\frac{\partial E_{\mu\nu}}{\partial \boldsymbol{r}_{\mu\nu}} = 2\varrho_{\mu\nu}\boldsymbol{r}_{\mu\nu}\,, \tag{2.35}$$

where the function $\varrho_{\mu\nu}$ introduced above represents the nonlinearity in the EV force, and is related to $E_{\mu\nu}$ through

$$\varrho_{\mu\nu} \equiv -\frac{1}{2r_{\mu\nu}}\frac{\partial E_{\mu\nu}}{\partial r_{\mu\nu}}\,, \tag{2.36}$$

$$= -\frac{\partial E_{\mu\nu}}{\partial (r_{\mu\nu}^2)}\,. \tag{2.37}$$

The EV connector force can then be formally expressed as

$$\begin{aligned}
\boldsymbol{F}_j^{\mathrm{E},c} &= -\frac{1}{2}\sum_{\substack{\mu,\nu=1\\ \mu\neq\nu}}^{N} \boldsymbol{F}_{\mu\nu}^{\mathrm{E}}\Delta\Theta_{\mu\nu}^{j}\,, \\
&= -\sum_{\substack{\mu,\nu=1\\ \mu\neq\nu}}^{N} \varrho_{\mu\nu}\boldsymbol{r}_{\mu\nu}\Delta\Theta_{\mu\nu}^{j}\,, \\
&= -\sum_{\substack{\mu,\nu=1\\ \mu\neq\nu}}^{N}\sum_{k=1}^{N_{\mathrm{S}}} \varrho_{\mu\nu}\Delta\Theta_{\mu\nu}^{jk}\boldsymbol{Q}_k\,, \\
&= -\sum_{k=1}^{N_{\mathrm{S}}} w_{jk}\,\boldsymbol{Q}_k\,,
\end{aligned} \tag{2.38}$$

where the nonlinear function

$$w_{jk} = w_{kj} \equiv \sum_{\substack{\mu,\nu=1\\ \mu\neq\nu}}^{N} \Delta\Theta_{\mu\nu}^{jk}\varrho_{\mu\nu}\,, \tag{2.39}$$

is the counterpart of the EV nonlinearity $\varrho_{\mu\nu}$ in connector vector coordinates.

Turning now to the mathematical form of the pair-wise EV potential E, the true EV potential in a polymer solution has a complicated dependence on the separation between any two parts of the chain [Yamakawa, 1971]. But this spatial dependence is dominated by the strong repulsion at short (spatial) range. In comparison with the overall dimensions of a long polymer coil, the short range of the potential is negligible. Based on this observation, several profound results on the excluded volume problem have been obtained by representing a macromolecule as a continuous chain, and using a δ-function repulsive potential between any pair of points on the polymer chains [des Cloizeaux and Jannink, 1990; Doi and Edwards, 1986; Schäfer, 1999; Yamakawa, 1971]. In computer simulations of discrete chain models, however, singular functions such as the δ-function cannot be directly implemented, and it is customary to use a "soft" potential with a strongly repulsive core. In previous efforts, several expressions for the excluded volume potential, such as the Lennard-Jones [Graessley *et al.*, 1999; Li and Larson, 2000b], Morse [Andrews *et al.*, 1998]

and exponential potentials [Hernandez Cifre and Garcia de la Torre, 1999], have been used in bead-spring models, with the justification that any soft EV potential will lead to the same predictions for long chain molecules as the δ-function potential, as long as it retains the short range repulsive nature of the δ-function.

Prakash and Öttinger [1999] used the repulsive "Narrow Gaussian" excluded volume (NGEV) potential,

$$E_{\mu\nu} = \frac{v k_{\mathrm{B}} T}{(2\pi)^{3/2} \widetilde{d}^3} \exp\left(- \frac{r_{\mu\nu}^2}{2\,\widetilde{d}^2} \right) , \tag{2.40}$$

between any pair of beads in a bead-spring chain as a regularization of the δ-function potential, noting that in the limit $\widetilde{d} \to 0$, the δ-function is recovered. Here, the EV parameter v quantifies the strength of the potential while $\widetilde{d}$ is the spatial range of the potential. Using the definition in Eq. (2.37), one obtains for the NGEV potential above,

$$\varrho_{\mu\nu} = \frac{v k_{\mathrm{B}} T}{2(2\pi)^{3/2} \widetilde{d}^5} \exp\left(- \frac{r_{\mu\nu}^2}{2\,\widetilde{d}^2} \right) = \frac{E_{\mu\nu}}{2\widetilde{d}^2} . \tag{2.41}$$

This potential has been used to obtain predictions that are in excellent agreement with experimental data for properties of dilute polymer solutions at equilibrium [Kumar and Prakash, 2004] and beyond [Sunthar and Prakash, 2005], showing that the NGEV potential possesses all the desirable properties that a more realistic potential would. Furthermore, the Gaussian form of the potential is an advantage in the development of approximations for the bead-spring model with EV presented above [Prabhakar and Prakash, 2002; Prakash, 2001a,b, 2002; Prakash and Öttinger, 1999].

The following section briefly reviews the standard method of incorporating the influence of hydrodynamic interactions (HI) into the bead-spring model.

2.3 Hydrodynamic interactions

In the derivation of Eqs. (2.3) and (2.6), the total hydrodynamic force exerted by the solvent on the ν-th bead in the bead-spring chain is assumed to be

$$\boldsymbol{F}_{\nu}^{\mathrm{h}} = -\zeta \left[[\![\, \dot{\boldsymbol{r}}_{\nu} \,]\!] - (\boldsymbol{v}_{\nu} + \Delta \boldsymbol{v}_{\nu}) \right] . \tag{2.42}$$

In this "Stokes law empiricism" [Bird *et al.*, 1987b], $[\![\, \dot{\boldsymbol{r}}_{\nu} \,]\!]$ is the momentum-space averaged velocity of the ν-th bead, and $(\boldsymbol{v}_{\nu} + \Delta \boldsymbol{v}_{\nu})$ is the total velocity of the solvent at the ν-th bead's position, $\boldsymbol{r}_{\nu}$. This total solvent velocity comprises the imposed velocity of the continuum $\boldsymbol{v}_{\nu} = \boldsymbol{v}_0 + \boldsymbol{\kappa} \cdot \boldsymbol{r}_{\nu}$ and $\Delta \boldsymbol{v}_{\nu}$, the total perturbation in the velocity field at $\boldsymbol{r}_{\nu}$ caused by the hydrodynamic forces exerted *on* the solvent by all the other beads in the chain. The total velocity perturbation at $\boldsymbol{r}_{\nu}$ is assumed to be the sum of individual perturbations caused by each of the other beads in the chain and,

$$\Delta \boldsymbol{v}_{\nu} = \sum_{\substack{\mu=1 \\ \nu \neq \mu}}^{N} \Delta \boldsymbol{v}_{\nu\mu} \, . \tag{2.43}$$

The velocity perturbation $\Delta \boldsymbol{v}_{\nu\mu}$ at the ν-th bead's position caused by $-\boldsymbol{F}_{\mu}^{\mathrm{h}}$, the hydrodynamic force exerted by the μ-th bead on the solvent, is

$$\Delta \boldsymbol{v}_{\nu\mu} = \boldsymbol{\Omega}(\boldsymbol{r}_{\nu\mu}) \cdot (-\boldsymbol{F}_{\mu}^{\mathrm{h}}) \, , \tag{2.44}$$

where the HI tensor $\boldsymbol{\Omega}$ is a tensorial function of the inter-bead displacement $\boldsymbol{r}_{\mu\nu}$. Following from classical hydrodynamics, expressions of the following form are used typically to relate the HI tensor $\boldsymbol{\Omega}_{\nu\mu} = \boldsymbol{\Omega}(\boldsymbol{r}_{\mu\nu})$ to the inter-bead displacement:

$$\boldsymbol{\Omega}_{\nu\mu} = \frac{1}{8\pi\eta_{\mathrm{s}} \, r_{\mu\nu}} \boldsymbol{C}(\boldsymbol{r}_{\mu\nu}) \, . \tag{2.45}$$

In this context, models which neglect the influence of HI—such as the original bead-spring model of Rouse [Rouse, 1953]—can be interpreted as ones in which the tensor $\boldsymbol{C}$ is set to zero. The earliest models incorporating HI [Kirkwood and

Riseman, 1948; Zimm, 1956] used the Oseen-Burgers form of the HI tensor, in which

$$\boldsymbol{C} = \boldsymbol{\delta} + \frac{\boldsymbol{r}_{\mu\nu}\boldsymbol{r}_{\mu\nu}}{r_{\mu\nu}^2}. \tag{2.46}$$

This simple form is useful in the construction of analytical approximations, and is used in that context in this study. In numerical simulations of individual chains, however, the simple expression above becomes problematic when bead overlap occurs, and $r_{\nu\mu} \leq a$. In such a case, the $3N \times 3N$ diffusion block-matrix comprising the $\boldsymbol{\Upsilon}_{\nu\mu}$ tensors as its constituent blocks, becomes non-positive definite, which is unphysical [Rotne and Prager, 1969]. Instead, the Rotne-Prager-Yamakawa (RPY) modification [Rotne and Prager, 1969; Yamakawa, 1970] of the Oseen-Burgers tensor, which ensures that the diffusion block-matrix remains positive-definite always, is used in this study. In this case,

$$\boldsymbol{C} = \begin{cases} \left(1 + \dfrac{2}{3}\dfrac{a^2}{r_{\mu\nu}^2}\right)\boldsymbol{\delta} + \left(1 - \dfrac{2a^2}{r_{\mu\nu}^2}\right)\dfrac{\boldsymbol{r}_{\mu\nu}\boldsymbol{r}_{\mu\nu}}{r_{\mu\nu}^2}\,, & \text{if } r_{\mu\nu} \geq 2a, \\ \dfrac{r_{\mu\nu}}{2a}\left[\left(\dfrac{8}{3} - \dfrac{3r_{\mu\nu}}{4a}\right)\boldsymbol{\delta} + \left(\dfrac{r_{\mu\nu}}{4a}\right)\dfrac{\boldsymbol{r}_{\mu\nu}\boldsymbol{r}_{\mu\nu}}{r_{\mu\nu}^2}\right], & \text{if } r_{\mu\nu} < 2a. \end{cases} \tag{2.47}$$

The Sections above have summarized the key features of the bead-spring model of dilute polymer solutions incorporating the FE, HI and EV. It is frequently useful to analyze predictions of the model in dimensionless terms. The following Section discusses the conversion of the model's equations into dimensionless form.

2.4 Dimensionless equations

The Fokker-Planck equation for ψ can be written after explicitly including the contributions from the spring and EV forces:

$$\frac{\partial \psi}{\partial t} = -\sum_{i=1}^{N_S} \frac{\partial}{\partial \boldsymbol{Q}_i} \cdot \left\{ \boldsymbol{\kappa} \cdot \boldsymbol{Q}_i - \frac{H}{\zeta} \sum_{j=1}^{N_S} \widetilde{\boldsymbol{A}}_{ij} \cdot \xi_j \boldsymbol{Q}_j + \frac{1}{\zeta} \sum_{j,k=1}^{N_S} \widetilde{\boldsymbol{A}}_{ij} \cdot w_{jk} \boldsymbol{Q}_k \right\} \psi + \frac{k_B T}{\zeta} \sum_{i,j=1}^{N_S} \frac{\partial}{\partial \boldsymbol{Q}_i} \cdot \widetilde{\boldsymbol{A}}_{ij} \cdot \frac{\partial \psi}{\partial \boldsymbol{Q}_j}. \tag{2.48}$$

To express this equation in a dimensionless form, it is necessary to first decide on the basic length and time scales in the model. In most studies where results are expressed in dimensionless form, it has been customary to choose the length scale $\ell_H = \sqrt{k_B T / H}$ and the associated time scale $\lambda_H = \zeta / 4H = \zeta\, \ell_H^2 / 4 k_B T$. The quantity $3\,\ell_H$ is the equilibrium root mean square end-to-end length of a single Hookean spring in the absence of EV interactions, while λ_H is a measure of the time scale for a submolecule represented as a Hookean spring to ergodically sample its configuration space in a theta solvent at equilibrium. This choice is justifiable even in studies using finitely extensible chains, when the objective is to explore the influence of finite extensibility (FE) by comparing predictions against those obtained with Rouse chains.

In the present study, however, the emphasis is largely on studying the influence of HI and EV on the behaviour of FEBS chains. Moreover, a significant portion of this work is devoted to understanding the influence of the degree of coarse-graining $N_{K,\,S}$ in predicting the behaviour of molecules with fixed N_K. In these situations, the recent investigations of Sunthar and Prakash [2005] show that

$$\ell_S \equiv \frac{R_S}{\sqrt{3}} = \ell_H \chi\,, \tag{2.49}$$

is the appropriate basic length scale. As in the conventional scheme, the associated time scale

$$\lambda_S \equiv \frac{\zeta\, \ell_S^2}{4 k_B T}\,. \tag{2.50}$$

In the Hookean limit, the length and time scales reduce to $\ell_{\rm H}$ and $\lambda_{\rm H}$, respectively. Dimensionless quantities formed using these length and time-scales are identified with a "$*$" in superscript.

With $t^* \equiv t/\lambda_{\rm S}$, $\boldsymbol{Q}_i^* \equiv \boldsymbol{Q}_i/\,\ell_{\rm S}$, $\boldsymbol{\kappa}^* \equiv \lambda_{\rm S}\boldsymbol{\kappa}$, the Fokker-Planck equation can be recast in dimensionless terms as

$$\begin{aligned}\frac{\partial \psi}{\partial t^*} = &-\sum_{i=1}^{N_{\rm S}} \frac{\partial}{\partial \boldsymbol{Q}_i^*} \cdot \left\{ \boldsymbol{\kappa}^* \cdot \boldsymbol{Q}_i^* - \frac{H^*}{4} \sum_{j=1}^{N_{\rm S}} \widetilde{\boldsymbol{A}}_{ij} \cdot \xi_j \boldsymbol{Q}_j^* + \frac{1}{4} \sum_{j,k=1}^{N_{\rm S}} \widetilde{\boldsymbol{A}}_{ij} \cdot w_{jk}^* \boldsymbol{Q}_k^* \right\} \psi \\ &+ \frac{1}{4} \sum_{i,\,j=1}^{N_{\rm S}} \frac{\partial}{\partial \boldsymbol{Q}_i^*} \cdot \widetilde{\boldsymbol{A}}_{ij} \cdot \frac{\partial \psi}{\partial \boldsymbol{Q}_j^*}\,,\end{aligned} \tag{2.51}$$

where

$$H^* \equiv \frac{H\,\ell_{\rm S}^2}{k_{\rm B}T} = \frac{\ell_{\rm S}^2}{\ell_{\rm H}^2} = \chi^2\,, \tag{2.52}$$

is the dimensionless spring constant, and

$$w_{jk}^* \equiv \frac{w_{jk}\,\ell_{\rm S}^2}{k_{\rm B}T}\,, \tag{2.53}$$

is the dimensionless EV force nonlinearity. It is to be noted here that the tensors $\widetilde{\boldsymbol{A}}_{ij}$ are already dimensionless. For the special case of a dumbbell model ($N = 2$), the dimensionless Fokker-Planck equation above reduces to

$$\frac{\partial \psi}{\partial t^*} = -\frac{\partial}{\partial \boldsymbol{Q}^*} \cdot \left\{ \boldsymbol{\kappa}^* \cdot \boldsymbol{Q}^* - \frac{1}{4} \widetilde{\boldsymbol{A}} \cdot H_{\rm eff}^* \boldsymbol{Q}^* \right\} \psi + \frac{1}{4} \frac{\partial}{\partial \boldsymbol{Q}^*} \cdot \widetilde{\boldsymbol{A}} \cdot \frac{\partial \psi}{\partial \boldsymbol{Q}^*}\,, \tag{2.54}$$

where $H_{\rm eff}^* \equiv H^*\xi - w^* = H^*\xi - (z^*/d^{*5})\exp(-Q^{*2}/2d^{*2})$ and $\widetilde{\boldsymbol{A}} = 2(\boldsymbol{\delta} - \zeta\boldsymbol{\Omega})$.

It is useful to relate the dimensionless parameters in the bead-spring model to the basic structural parameters of the sub-molecule underlying each spring. From the definition of $\ell_{\rm S}$ in Eq. (2.49) and using $R_{\rm S}^2 = b_{\rm K}^2 N_{\rm K,\,S}$, one obtains

$$\ell_{\rm S}^2 = \frac{b_{\rm K}^2 N_{\rm K,\,S}}{3}\,. \tag{2.55}$$

In studies using ℓ_{H} as the basic length scale, the parameter Q_0 is represented in dimensionless terms by the well known finite extensibility parameter, $b \equiv Q_0^2/\,\ell_{\text{H}}^2$ [Bird *et al.*, 1987b]. The counterpart of this FE parameter in the non-dimensionalization scheme adopted in this study is

$$b^* \equiv \frac{Q_0^2}{\ell_{\text{S}}^2}\,. \tag{2.56}$$

Since $Q_0 = b_{\text{K}} N_{\text{K, S}}$, using Eq. (2.56) above, it is seen that

$$b^* = 3N_{\text{K, S}}\,. \tag{2.57}$$

Because of this direct relation of b^* to the degree of coarse-graining $N_{\text{K, S}}$, the latter is often reported in this study instead of b^* when results are presented. Using this definition, the dimensionless FENE nonlinearity

$$\xi(Q_j^*) = \frac{1}{1 - Q_j^{*\,2}/b^*}\,. \tag{2.58}$$

Similarly, combining the definition of H^* in Eq. (2.52) with Eq. (2.23) earlier, one obtains

$$H^* = \frac{3N_{\text{K, S}} - 5}{3N_{\text{K, S}}} = \frac{b^* - 5}{b^*}\,. \tag{2.59}$$

Interestingly, Eq. (2.59) above shows that when $b^* = 5$ or $N_{\text{K, S}} = 5/3$, $H^* = 0$, and the spring force responsible for maintaining the connectivity of the chain, vanishes. This is an artifice of the FENE expression used to model the spring force, and $N_{\text{K, S}} = 5/3$ is a "hard" lower limit on $N_{\text{K, S}}$ below which the FENE spring-force law will lead to non-physical results. However, since the FENE expression is only an approximation for the inverse-Langevin force law, which is itself only valid when $N_{\text{K, S}} \gtrsim 10$, for smaller values of $N_{\text{K, S}}$, it may be necessary to use exact expressions for the spring force derived from equilibrium statistical mechanics [Yamakawa, 1971]. Values of $N_{\text{K, S}} > 10$ are used in most situations examined in this study.

Corresponding dimensionless versions of the other parameters in the bead-spring model, *viz.*, a, v, $\widetilde{d}$ can be defined such that the standard definitions for models with

Rouse chains are recovered in the Hookean limit.

The hydrodynamic interaction parameter, h^*, is defined as

$$h^* = \frac{a}{\sqrt{\pi}\,\ell_{\mathrm{s}}}\,. \tag{2.60}$$

With this definition, the dimensionless tensor $\zeta\boldsymbol{\Omega}_{\nu\mu}$ occurring in the definitions of the diffusion tensors [Eqs. (2.4) and (2.8)] can be written as

$$\zeta\boldsymbol{\Omega}_{\nu\mu} = \frac{3\sqrt{\pi}h^*}{4\,r^*_{\mu\nu}}\,\boldsymbol{C}(\boldsymbol{r}^*_{\mu\nu})\,, \tag{2.61}$$

where $\boldsymbol{r}^*_{\mu\nu} = (1/\,\ell_{\mathrm{s}})\boldsymbol{r}_{\mu\nu}$. Since $\zeta = 6\pi\eta_{\mathrm{s}}a = 6\pi^{3/2}\eta_{\mathrm{s}}\,\ell_{\mathrm{s}}h^*$, Eq. (2.50) defining the basic time-scale λ_{s} can also be written as

$$\lambda_{\mathrm{s}} = \frac{3\pi^{3/2}}{2}\frac{\eta_{\mathrm{s}}}{k_{\mathrm{B}}T}h^*\,\ell_{\mathrm{s}}^3\,. \tag{2.62}$$

Thus, the time-scale used for rendering the mathematical model dimensionless is itself dependent on a phenomenological constant in the model. This has implications while comparing dimensionless model predictions with experiment, and is discussed later in Chapter 8.

The dimensionless version of the strength of the NGEV potential v,

$$z^* \equiv \frac{v}{(2\pi)^{3/2}\,\ell_{\mathrm{s}}^3}\,, \tag{2.63}$$

is referred to as the excluded volume parameter, while the dimensionless range of the potential

$$d^* \equiv \frac{\widetilde{d}}{\ell_{\mathrm{s}}}\,. \tag{2.64}$$

Therefore, the NGEV potential defined in Eq. (2.40) can be expressed in dimensionless terms as

$$E^*_{\mu\nu} = \frac{E_{\mu\nu}}{k_{\mathrm{B}}T} = \frac{z^*}{d^{*\,3}}\exp\left[-\frac{r^{*\,2}_{\mu\nu}}{2d^{*\,2}}\right]\,, \tag{2.65}$$

and $\varrho^*_{\mu\nu} = \varrho_{\mu\nu}\,\ell_{\rm S}^2/k_{\rm B}T = E^*_{\mu\nu}/d^{*\,2}$.

In summary, for any given number of beads N, the chief dimensionless parameters of the bead-spring model described above are H^*, b^*, h^*, z^* and d^*. Out of these, H^* and b^* depend solely on the degree of coarse-graining $N_{\rm K,\,S}$, and are immediately calculated once the $N_{\rm K}$ for the polymer molecule to be modeled is specified, and a choice of $N_{\rm S}$ is made. Using the FENE spring force expression places an upper limit on the choice of $N_{\rm S}$ while modeling a molecule of known $N_{\rm K}$. As will be shown shortly, the use of a spring-force expression based on equilibrium statistical mechanics also places a lower limit on the values of $N_{\rm S}$ that can be chosen while modeling the behaviour of polymer solutions in homogeneous flows. To compare the predictions of the rheological properties of the FEBS model with experiment at some time t and for a given homogeneous flow field $\boldsymbol{\kappa}$, the values of the length and time scales, $\ell_{\rm S}$ and $\lambda_{\rm S}$, need to be calculated, for which one requires besides $b_{\rm K}$ and $N_{\rm K}$, the solvent viscosity $\eta_{\rm s}$, the solution temperature T, and, as will be shown below, the number density of the polymer in solution $n_{\rm p}$.

The significance of the HI parameter h^*, and the values used for these parameters is discussed later in Chapters 4, 7 and 8. In the current study, a detailed analysis of the influence of the parameters of the NGEV potential is not performed. Attention is restricted to examining a few interesting qualitative features of the predictions with the NGEV potential in Chapter 4, where the significance of the parameters z^* and d^* is discussed briefly. An approximate treatment of this potential in the presence of HI is described in Chapter 5.

It is noted that as $N_{\rm K,\,S} \to 1,\ \ell_{\rm S} \to b_{\rm K}/\sqrt{3}$. In this limit, the drag coefficient ζ of a sub-molecule represented by a spring, and its excluded volume v, must respectively approach $\zeta_{\rm K}$ and $v_{\rm K}$, the phenomenological parameters introduced previously in this Chapter characterizing a single Kuhn segment . The dimensionless versions of these parameters characterizing the Kuhn segment are

$$h^*_{\rm K} \equiv \sqrt{\frac{3}{\pi}}\frac{a_{\rm K}}{b_{\rm K}}\,, \tag{2.66}$$

and

$$z_{\mathrm{K}}^{*} \equiv \left(\frac{3}{2\pi}\right)^{3/2} \frac{v_{\mathrm{K}}}{b_{\mathrm{K}}^{3}} \,. \tag{2.67}$$

Further, using Eq. (2.62), the time scale of a single Kuhn step is equivalently defined:

$$\lambda_{\mathrm{K}} \equiv \frac{3\pi^{3/2}}{2} \frac{\eta_{\mathrm{s}}}{k_{\mathrm{B}}T} h_{\mathrm{K}}^{*} \frac{b_{\mathrm{K}}^{3}}{3^{3/2}} = \frac{\pi^{3/2}}{\sqrt{12}} \frac{\eta_{\mathrm{s}}}{k_{\mathrm{B}}T} h_{\mathrm{K}}^{*} b_{\mathrm{K}}^{3} \,. \tag{2.68}$$

The following Section defines the two types of rheometric flows studied in this work and the macroscopic properties of interest in these flows.

2.5 Macroscopic properties

The macroscopically observed properties of dilute polymer solutions are predicted using the bead-spring model by first relating these properties to expectations of functions of the polymer configuration. The expectations can then, in principle, be evaluated using the solution of the Fokker-Planck equation for ψ. The macroscopic solution properties of interest in this work, and expressions for these in terms of configurational expectations are discussed in this Section. Since the primary focus of this work is on the modeling of the rheological properties of dilute polymer solutions, the main flow patterns of interest are first described below.

2.5.1 Shear and uniaxial extensional flows

In this study, attention is restricted to simple shear and uniaxial extensional flows. For a simple homogeneous shear flow characterized by the shear-rate $\dot{\gamma}$, the continuum solvent's velocity components in Cartesian coordinates are given by $v_x = \dot{\gamma}(t)\, y$, $v_y = 0$ and $v_z = 0$. The tensor $\boldsymbol{\kappa}^{*} = \lambda_{\mathrm{s}} \boldsymbol{\nabla v}$ is

$$\boldsymbol{\kappa}^{*}(t^{*}) = \dot{\gamma}^{*}(t^{*}) \widetilde{\boldsymbol{\kappa}} \,, \tag{2.69a}$$

where $\dot{\gamma}^* = \dot{\gamma}\lambda_s$ is the time dependent dimensionless shear-rate, and

$$\widetilde{\boldsymbol{\kappa}} = \begin{pmatrix} 0 & 1 & 0 \\ 0 & 0 & 0 \\ 0 & 0 & 0 \end{pmatrix} , \tag{2.69b}$$

defines the structure of the homogeneous shear flow in Cartesian coordinates. In a uniaxial extensional flow with an extension-rate $\dot{\varepsilon}$, the velocity field is specified by $v_x = \dot{\varepsilon}(t)x$, $v_y = -(\dot{\varepsilon}(t)/2)y$ and $v_z = -(\dot{\varepsilon}(t)/2)z$. Therefore,

$$\boldsymbol{\kappa}^*(t^*) = \dot{\varepsilon}^*(t^*)\widetilde{\boldsymbol{\kappa}} , \tag{2.70a}$$

where $\dot{\varepsilon}^* = \dot{\varepsilon}\lambda_s$ is the time dependent dimensionless extension-rate, and the flow structure tensor

$$\widetilde{\boldsymbol{\kappa}} = \begin{pmatrix} 1 & 0 & 0 \\ 0 & -\frac{1}{2} & 0 \\ 0 & 0 & -\frac{1}{2} \end{pmatrix} . \tag{2.70b}$$

In this work the convention suggested by Bird *et al.* [1987a] is followed wherein $\dot{\gamma}$ is also used to denote the strain rate for a general homogenous flow whose velocity gradient is expressed as $\boldsymbol{\kappa}^* = \dot{\gamma}^*\widetilde{\boldsymbol{\kappa}}$ where $\widetilde{\boldsymbol{\kappa}}$ represents the flow structure,

$$\dot{\gamma}^* = \sqrt{\frac{1}{2}\,\dot{\boldsymbol{\gamma}}^* : \dot{\boldsymbol{\gamma}}^*} , \tag{2.71}$$

and,

$$\dot{\boldsymbol{\gamma}}^* = \boldsymbol{\kappa}^* + \boldsymbol{\kappa}^{*\mathrm{T}} , \tag{2.72}$$

is the rate-of-strain tensor.

The dimensionless shear-rate $\dot{\gamma}^* = \dot{\gamma}\lambda_s$ and extension-rate $\dot{\varepsilon}^* = \dot{\epsilon}\lambda_s$ are in fact ratios of the local characteristic diffusive time-scale of a single spring λ_s to the time-scales $\dot{\gamma}^{-1}$ and $\dot{\epsilon}^{-1}$ of the imposed flows, respectively, and are Peclet numbers for any sub-molecule represented as a spring. The use of the bead-spring model

described in the earlier Sections is restricted to flows where the bead Peclet number $\dot{\gamma}^*$ or $\dot{\varepsilon}^*$ is not significantly larger than unity. This constraint stems from the central assumption in deriving the spring force law that the sub-molecule represented by a single spring always has enough time to ergodically sample all the configurations consistent with its end-to-end vector. This restricts the use of such spring force laws to experiments whose time-scales are larger than the time-scale of diffusive processes at the level of the sub-molecule. Ghosh *et al.* [2001] have shown that when bead Peclet numbers are much larger than unity, the predictions of a FENE dumbbell model differ considerably from those obtained with a bead-rod model with the same number of Kuhn segments.

The dimensionless strain rates $\dot{\gamma}^*$ and $\dot{\varepsilon}^*$ are in general functions of time. In this study, the time dependence of solution properties is examined for the following kinds of unsteady flows.

Sudden imposition of steady shear or uniaxial extensional flow:

$$\dot{\gamma}^*(t^*)\,, \dot{\varepsilon}^*(t^*) = \begin{cases} 0\,, & t^* < 0\,, \\ \dot{\gamma}_0^*\,, \dot{\varepsilon}_0^*\,, & t^* \geq 0\,. \end{cases} \tag{2.73}$$

Sudden imposition followed by cessation of steady uniaxial extensional flow:

$$\dot{\varepsilon}^*(t^*) = \begin{cases} 0\,, & t^* < 0\,, \\ \dot{\varepsilon}_0^*\,, & 0 \leq t^* \leq t^*_{\max} \text{ (the stress-growth phase)}\,, \\ 0\,, & t^* > t^*_{\max} \text{ (the stress-relaxation phase)}\,. \end{cases} \tag{2.74}$$

The word "steady" used in the description of these flows refers to the fact that the imposed strain rates $\dot{\gamma}_0^*$ and $\dot{\varepsilon}_0^*$ are constant. However, the solution as a whole is in an unsteady state since the properties of the solution change in response to the imposition (or cessation) of the flow. steady-state is reached when all properties reach time-independent values which are functions solely of the imposed steady strain rate and the other physical parameters characterizing the solution. For the sake of notational simplicity, the subscript 0 will be dropped in the discussions on unsteady flow, and references to $\dot{\gamma}^*$ and $\dot{\varepsilon}^*$ made in this context should be understood

to mean the constants $\dot{\gamma}_0^*$ and $\dot{\varepsilon}_0^*$, respectively.

The time-dependence of properties in an unsteady state is often expressed in terms $\gamma = \dot{\gamma}_0 t = \dot{\gamma}_0^* t^*$ or $\varepsilon = \dot{\varepsilon}_0 t = \dot{\varepsilon}_0^* t^*$ for shear and extensional flows, respectively. These quantities take on the meaning of strain measures during the period in which the imposed strain-rate is non-zero. For a flow described by Eq. (2.74), however, although the Hencky strain is constant ($\varepsilon_{\max} = \dot{\varepsilon}_0^* t_{\max}^*$) for all times after $t_{\max}^*$ when flow stops, the time variation of properties in both stress-growth and relaxation phases is presented in the same graph by plotting them against $\dot{\varepsilon}_0^* t^*$.

2.5.2 The stress tensor and material functions

In a polymer solution, the stress tensor [1] $\boldsymbol{\tau} = \boldsymbol{\pi} - p\boldsymbol{\delta}$, where $\boldsymbol{\pi}$ is the total Cauchy stress tensor and p is the pressure, is separated into a contribution arising from the continuum Newtonian solvent given by $-\eta_s(\boldsymbol{\kappa} + \boldsymbol{\kappa}^T)$ and that due to the presence of the polymer molecules denoted as $\boldsymbol{\tau}_p$. That is, $\boldsymbol{\tau} = -\eta_s(\boldsymbol{\kappa} + \boldsymbol{\kappa}^T) + \boldsymbol{\tau}_p$, where the polymer contribution $\boldsymbol{\tau}_p$ for a general polymer solution is a function of the concentration n_p. The dimensionless version of the polymer stress contribution is defined as

$$\boldsymbol{\tau}_p^* = \frac{1}{n_p k_B T} \boldsymbol{\tau}_p \,. \tag{2.75}$$

The present model for dilute polymer solutions is only strictly valid in the dilute solution limit $n_p \to 0$, in which case $\boldsymbol{\tau}_p \to 0$, by definition. However, the ratio $(1/n_p)\boldsymbol{\tau}_p$ and therefore $\boldsymbol{\tau}_p^*$, remains non-zero in this limit, and can be estimated in experiments with non-zero n_p, as long as the data are collected in a regime where the stress varies linearly with the concentration. Although theories for dilute solutions essentially predict properties in the limit, $\lim_{n_p \to 0} \boldsymbol{\tau}_p^*$, this value can still be used to predict the stresses for small concentrations where $\boldsymbol{\tau}_p$ varies linearly with n_p, since $\boldsymbol{\tau}_p = n_p k_B T(\lim_{n_p \to 0} \boldsymbol{\tau}_p^*) + \ldots$ In experimental conditions where terms proportional to n_p^2 or higher are observed to dominate, a dilute solution theory which does not account explicitly for intermolecular interactions can no longer be used to model

[1] The sign convention suggested by Bird *et al.* [1987a] for the stress tensor is used in this study, wherein tensile stresses are negative and compressive stresses are positive.

the polymer solution, since the dependence on n_{p}^2 signals the onset of interactions between pairs of molecules. The critical concentration below which it is permitted to validly compare the predictions the bead-spring model used herein with experiment is not known *a priori*, and can be anticipated to be dependent on flow conditions, since molecules may be forced closer together by the flow. In Chapter 8, this aspect is explored further using the predictions of the bead-spring model.

The polymer contribution to the stress tensor, which is a macroscopic observable, is connected to the microscopic dynamics prescribed by the Fokker-Planck equation of the bead-spring model through the Kramer's expression for the polymer contribution to the total extra stress $\boldsymbol{\tau}$ [Bird *et al.*, 1987b]:

$$\boldsymbol{\tau}_{\mathrm{p}} = n_{\mathrm{p}} k_{\mathrm{B}} T N_{\mathrm{s}} \boldsymbol{\delta} - n_{\mathrm{p}} \sum_{i=1}^{N_{\mathrm{s}}} \langle \boldsymbol{Q}_i \boldsymbol{F}_i^{\phi,c} \rangle \,, \tag{2.76}$$

where the angular brackets around any function of the configuration denote an expectation of that function:

$$\langle f(\{\boldsymbol{Q}_i^*\}) \rangle = \int f(\{\boldsymbol{Q}_i^*\}) \psi(\{\boldsymbol{Q}_i^*\}) d\boldsymbol{Q}_1^* \ldots d\boldsymbol{Q}_{N_{\mathrm{s}}}^* \,. \tag{2.77}$$

After resolving the total spring and EV contributions to the connector force in the equation above, Eq. (2.76) above can be written in dimensionless terms as

$$\boldsymbol{\tau}_{\mathrm{p}}^* = N_{\mathrm{s}} \boldsymbol{\delta} - H^* \sum_{i=1}^{N_{\mathrm{s}}} \langle \xi_i \boldsymbol{Q}_i^* \boldsymbol{Q}_i^* \rangle + \sum_{i,j=1}^{N_{\mathrm{s}}} \langle w_{ij}^* \boldsymbol{Q}_i^* \boldsymbol{Q}_j^* \rangle \,. \tag{2.78}$$

Using the definition of w_{ij} in Eq. (2.39), the equation above can also be written as

$$\boldsymbol{\tau}_{\mathrm{p}}^* = N_{\mathrm{s}} \boldsymbol{\delta} - H^* \sum_{i=1}^{N_{\mathrm{s}}} \langle \xi_i \boldsymbol{Q}_i^* \boldsymbol{Q}_i^* \rangle + \sum_{\substack{\mu,\,\nu=1 \\ \mu \neq \nu}}^{N} \langle \varrho_{\mu\nu}^* \boldsymbol{r}_{\mu\nu}^* \boldsymbol{r}_{\mu\nu}^* \rangle \,. \tag{2.79}$$

The last term on the right-hand side in the equations above represent the direct contribution of EV interactions to the polymer stress. Doi and Edwards [1986] show that for a polymer molecule modeled as an infinite continuous chain with δ-function EV interactions between any pair of points on the chain, the direct EV

contribution is isotropic, and therefore rheologically unimportant. This argument has been cited to justify neglecting this term in many studies, although they are based on simulations that employ finite, discrete chains using soft EV potentials, in contrast to the model used by Doi and Edwards [Cascales and Garcia de la Torre, 1991; Hernandez Cifre and Garcia de la Torre, 1999; Knudsen *et al.*, 1996; Li and Larson, 2000b]. In simulations of dumbbells with the NGEV potential, the contribution of this term to the rheological properties is found to be non-trivial, its relative size depending strongly on the values of the parameters used in the model [Prabhakar and Prakash, 2002]. On the other hand, since the predictions of finite chains with the NGEV potential are found to approach those of continuous chains with δ-function EV interactions in the limit of infinitely long chains [Kumar and Prakash, 2003], it is anticipated that the significance of the direct EV contribution will diminish for long chains. Nevertheless, for the sake of completeness, this term is retained while evaluating $\boldsymbol{\tau}_{\mathrm{p}}^{*}$ in the simulations performed in this study.

For a simple shear flow defined in Eq. (2.73) characterized by the imposed steady shear-rate $\dot{\gamma}_0^*$, the rheological properties of interest are the polymer's contribution to the (dimensional) viscosity η_{p}, the dimensionless first normal-stress difference coefficient Ψ_1, and the dimensionless second normal-stress difference coefficient Ψ_2, which are respectively defined by the following relations:

$$\eta_{\mathrm{p}} \equiv -\frac{\tau_{\mathrm{p},\,yx}}{\dot{\gamma}_0}, \tag{2.80}$$

$$\Psi_1 \equiv -\frac{\tau_{\mathrm{p},\,xx} - \tau_{\mathrm{p},\,yy}}{\dot{\gamma}_0^2}, \tag{2.81}$$

$$\Psi_2 \equiv -\frac{\tau_{\mathrm{p},\,yy} - \tau_{\mathrm{p},\,zz}}{\dot{\gamma}_0^2}\,. \tag{2.82}$$

In the case of a uniaxial extensional flow specified by Eq. (2.73), the polymer contribution to the dimensionless extensional viscosity, denoted as $\overline{\eta}_{\mathrm{p}}^{*}$, is given by

$$\overline{\eta}_{\mathrm{p}} \equiv -\frac{\tau_{\mathrm{p},\,xx} - \tau_{\mathrm{p},\,yy}}{\dot{\varepsilon}_0}\,. \tag{2.83}$$

The dimensionless versions of these properties are

$$\eta_{\mathrm{p}}^{*} \equiv \frac{\eta_{\mathrm{p}}}{n_{\mathrm{p}} k_{\mathrm{B}} T \lambda_{\mathrm{s}}}\,, \tag{2.84}$$

$$\Psi_{1}^{*} \equiv \frac{\Psi_{1}}{n_{\mathrm{p}} k_{\mathrm{B}} T \lambda_{\mathrm{s}}^{2}}\,, \tag{2.85}$$

$$\Psi_{2}^{*} \equiv \frac{\Psi_{2}}{n_{\mathrm{p}} k_{\mathrm{B}} T \lambda_{\mathrm{s}}^{2}}\,, \tag{2.86}$$

and,

$$\overline{\eta}_{\mathrm{p}}^{*} \equiv \frac{\overline{\eta}_{\mathrm{p}}}{n_{\mathrm{p}} k_{\mathrm{B}} T \lambda_{\mathrm{s}}}\,, \tag{2.87}$$

$$\tag{2.88}$$

It must be noted here that the dependence of λ_{s} on the model parameter h^{*}, implies that expression of experimental data for these rheological properties in the same dimensionless form as above, requires the use of a model parameter. This dependence is undesirable while studying the influence of the parameter h^{*} on the comparison of theory with experiment. A solution to this problem is proposed in Chapter 8.

For the flow pattern described in Eq. (2.74), rheological data is presented in this thesis in terms of N_{1}^{*}, the magnitude of the polymer's contribution to the dimensionless first normal stress difference:

$$N_{1,\mathrm{p}}^{*} = \left|\tau_{\mathrm{p},\,xx}^{*} - \tau_{\mathrm{p},\,yy}^{*}\right|. \tag{2.89}$$

Although Bird *et al.* [1987a] recommend distinguishing these time dependent material functions from their time-independent values at steady-state by using a "+" or "−" in superscript, this notation is not followed in this thesis, as the nature of the time-dependence will be clear from the context, or will be explicitly stated.

In much of the experimental literature on dilute polymer solutions, the shear viscosity is expressed in terms of an "intrinsic viscosity"

$$[\eta] \equiv \lim_{c \to 0} \frac{\eta_{\mathrm{p}}}{c\,\eta_{\mathrm{s}}}\,, \tag{2.90}$$

where $c = n_{\mathrm{p}} M / N_{\mathrm{A}}$ is the mass concentration of the polymer, M is the molecular weight of the polymer and N_{A} is the Avogadro number. As mentioned earlier, in the dilute solution limit, ratios such as η_{p}/c have a non-vanishing value, although η_{p} itself approaches 0. In the dilute regime, $\eta_{\mathrm{p}} = [\eta] c \eta_{\mathrm{s}}$, and therefore

$$\frac{[\eta] M}{N_{\mathrm{A}}} = \frac{3\pi^{3/2}}{2} \eta_{\mathrm{p}}^{*} h^{*}. \tag{2.91}$$

A similar quantity can also be defined for extensional flows, in which case the intrinsic viscosity is denoted as $[\overline{\eta}]$.

2.5.2.1 Linear viscoelastic properties

In analogy with the dilute solution limit, a zero-shear-rate limit exists in which material functions such as the viscosity and first and second normal-stress difference coefficients are non-zero although the stress itself becomes vanishingly small as the shear-rate approach zero. Zero-shear-rate properties are identified with a "0" in subscript *e.g.* $\eta^{*}_{\mathrm{p},\,0}$, $\Psi^{*}_{1,\,0}$ and $\Psi^{*}_{2,\,0}$, where for instance

$$\eta^{*}_{\mathrm{p},\,0} \equiv \lim_{\dot{\gamma}^{*} \to 0} \eta^{*}_{\mathrm{p}} \,. \tag{2.92}$$

Theoretical predictions for these properties can be obtained by extrapolating the results obtained at several low values of shear-rate to the zero shear-rate limit. It is also possible to calculate the zero-shear-rate viscosity as

$$\eta^{*}_{\mathrm{p},\,0} = \int_{0}^{\infty} G^{*}_{\mathrm{p}}(t^{*}) dt^{*} \,, \tag{2.93}$$

where G^{*}_{p} is the near-equilibrium stress relaxation modulus. The relaxation modulus G^{*}_{p} is the limiting function defined as

$$G^{*}_{\mathrm{p}}(t^{*}) \equiv - \lim_{\gamma_0 \to 0} \frac{\tau^{*}_{\mathrm{p},\,yx}(t^{*})}{\gamma_0} \,, \tag{2.94}$$

where $\tau^{*}_{\mathrm{p},yx}(t^{*})$ is the variation in the shear stress measured after imposing a sudden shearing displacement whose shear-rate is given by $\dot{\gamma}^{*} = \gamma_0 \delta(t^{*})$. The relaxation modulus can be shown to be equal to the following equilibrium autocorrelation

(defined in Appendix A):

$$G^*_{\rm p}(t^*) = \langle I^*_{yx}(t^*) I^*_{yx}(0) \rangle_{\rm eq} \,, \tag{2.95}$$

where the tensor $\boldsymbol{I}^*$ is defined as

$$\boldsymbol{I}^* = H^* \sum_{i=1}^{N_{\rm s}} \xi_i \boldsymbol{Q}^*_i \boldsymbol{Q}^*_i - \sum_{i,j=1}^{N_{\rm s}} w^*_{ij} \boldsymbol{Q}^*_i \boldsymbol{Q}^*_j . \tag{2.96}$$

The Green-Kubo relation shown above is derived in Appendix A.

2.5.3 Other macroscopic properties

Besides the rheological properties listed above, it is necessary to also obtain information related to the average gross physical size and shape of polymer molecules as they stretch and orient in response to the imposition of a flow on the solution. A useful measure of the average dimensions of polymer molecules in solution is given by the gyration tensor,

$$\boldsymbol{G} \equiv \frac{1}{N} \sum_{\nu=1}^{N} \langle \boldsymbol{R}_\nu \boldsymbol{R}_\nu \rangle \,, \tag{2.97}$$

where $\boldsymbol{R}_\nu$ is the displacement vector of the ν-th bead from the centre-of-mass of the polymer chain, $\boldsymbol{R}_\nu = \boldsymbol{r}_\nu - (1/N) \sum_{\mu=1}^{N} \boldsymbol{r}_\mu$. Using standard relations for bead-spring chains [Bird *et al.*, 1987b] it can be shown that the dimensionless gyration tensor $\boldsymbol{G}^* = (1/\ell_{\rm s}^2)\boldsymbol{G}$ is expressible in terms of the dimensionless second moments of the probability distribution ψ:

$$\boldsymbol{G}^* = \frac{1}{N} \sum_{i,j=1}^{N_{\rm s}} C_{ij} \langle \, \boldsymbol{Q}^*_i \boldsymbol{Q}^*_j \, \rangle \,, \tag{2.98}$$

where

$$C_{ij} = \frac{1}{2} \left\{ i + j - |i - j| - \frac{2ij}{N} \right\}, \quad i, j = 1, \ldots, N_{\rm s} \,, \tag{2.99}$$

are the elements of the Kramer's matrix [Bird *et al.*, 1987b; Öttinger, 1987a]. The quantity,

$$R_{\mathrm{G}}^{*} \equiv \sqrt{\operatorname{tr} \boldsymbol{G}^{*}}\,, \tag{2.100}$$

is commonly referred to as the radius of gyration. The value of the radius of gyration at equilibrium, $R_{\mathrm{G,eq}}^{*}$, when $\boldsymbol{G}^{*}$ is isotropic, serves as a useful estimate of the average radius of polymer coils.

Another measure of the average size of a polymer chain is the mean square end-to-end distance,

$$R_{\mathrm{e}}^{2} \equiv \langle \boldsymbol{r}_{1,\,N}^{2} \rangle\,, \tag{2.101}$$

whose dimensionless version $R_{\mathrm{e}}^{*\,2} = R_{\mathrm{e}}^{2} / \ell_{\mathrm{s}}^{2}$ is also related to the second moments of the probability distribution through

$$R_{\mathrm{e}}^{*\,2} = \sum_{i,j=1}^{N_{\mathrm{s}}} \operatorname{tr} \langle\, \boldsymbol{Q}_{i}^{*} \boldsymbol{Q}_{j}^{*} \,\rangle\,. \tag{2.102}$$

Unlike the radius of gyration, which can be measured using static and dynamic light scattering techniques [Ströbl, 1996], $R_{\mathrm{e}}^{*\,2}$ is not experimentally accessible. However, prediction of $R_{\mathrm{e}}^{*\,2}$ is useful since it is a good indicator of the extent to which the model chain is stretched.

2.5.4 Evolution equation for second moments

The discussion above shows that all the macroscopic properties of interest in dilute polymer solution can be described in terms expectations of configuration dependent functions. It is possible to obtain formally the equation for the time evolution of a configuration dependent function B, by multiplying the Fokker-Planck equation with the function and then integrating over all possible configurations. In terms of the dimensionless connector vectors, the equation thus obtained for homogeneous

flows is

$$\frac{d\langle B\rangle}{dt^*} = \sum_{i,j=1}^{N_s}\left[\boldsymbol{\kappa}^*\colon\langle \boldsymbol{Q}_j^*\frac{\partial B}{\partial \boldsymbol{Q}_i^*}\rangle - \frac{H^*}{4}\langle\widetilde{\boldsymbol{A}}_{ij}\colon \xi_j\boldsymbol{Q}_j^*\frac{\partial B}{\partial \boldsymbol{Q}_i^*}\rangle + \frac{1}{4}\sum_{k=1}^{N_s}\langle\widetilde{\boldsymbol{A}}_{ij}\colon w_{jk}^*\boldsymbol{Q}_k^*\frac{\partial B}{\partial \boldsymbol{Q}_i^*}\rangle\right] + \frac{1}{4}\sum_{i,j=1}^{N_s}\langle\widetilde{\boldsymbol{A}}_{ij}\colon\frac{\partial^2 B}{\partial \boldsymbol{Q}_j^*\partial \boldsymbol{Q}_i^*}\rangle. \tag{2.103}$$

The general equation above can be used to generate the time evolution equations for any of the macroscopic properties described earlier. However, as a direct consequence of the nonlinearities in the model arising from FE, HI, and EV, the resulting equations are not closed with respect to the expectations whose evolution equations are desired. For such nonlinear models, Brownian dynamics simulations are usually the only viable way of obtaining exact predictions of properties away from equilibrium. Nevertheless, it is possible to obtain approximate predictions by making assumptions which lead to sets of closed equations. The starting point for most such closure approximations is the following set of evolution equations for the second moments of the probability distribution ψ:

$$\begin{aligned}\langle\, \boldsymbol{Q}_i^*\boldsymbol{Q}_j^*\,\rangle_{(1)} &\equiv \frac{d\langle\, \boldsymbol{Q}_i^*\boldsymbol{Q}_j^*\,\rangle}{dt^*} - \boldsymbol{\kappa}^*\cdot\langle\, \boldsymbol{Q}_i^*\boldsymbol{Q}_j^*\,\rangle - \langle\, \boldsymbol{Q}_i^*\boldsymbol{Q}_j^*\,\rangle\cdot\boldsymbol{\kappa}^{*\mathrm{T}}\\ &= -\frac{H^*}{4}\sum_{m=1}^{N_s}\langle\boldsymbol{Q}_i^*\boldsymbol{Q}_m^*\xi_m\cdot\widetilde{\boldsymbol{A}}_{mj} + \widetilde{\boldsymbol{A}}_{im}\cdot\xi_m\boldsymbol{Q}_m^*\boldsymbol{Q}_j^*\rangle\\ &\quad + \frac{1}{4}\sum_{m,n=1}^{N_s}\langle\boldsymbol{Q}_i^*\boldsymbol{Q}_n^*w_{nm}^*\cdot\widetilde{\boldsymbol{A}}_{mj} + \widetilde{\boldsymbol{A}}_{im}\cdot w_{mn}^*\boldsymbol{Q}_n^*\boldsymbol{Q}_j^*\rangle + \frac{1}{2}\langle\widetilde{\boldsymbol{A}}_{ij}\rangle,\end{aligned} \tag{2.104}$$

where the subscript "(1)" denotes the contravariant convected time derivative of a tensor [Bird *et al.*, 1987a].

2.5.5 Characteristic large-scale relaxation times at equilibrium

Dynamic properties measured or predicted near equilibrium can be used to estimate the time scale in which the overall configuration of a polymer coil at equilibrium will

change in response to a imposed force. This characteristic large-scale response or "relaxation" time—temporarily denoted as Λ—is important in rheological measurements since it provides an unambiguous way in which the strength of the flow can be measured. For any general homogeneous flow, the reciprocal of the strain-rate $\dot{\gamma}$ can be taken to be the characteristic time scale of the imposed flow which forces a polymer coil to change its configuration. As $\dot{\gamma} \to 0$, the time scale of the experiment approaches infinity, and for very weak flows the polymer solution is only marginally perturbed from it equilibrium state. For such low strain rates, the rheological properties correspond to the linear viscoelastic properties described earlier. If, on the other hand, $\dot{\gamma}$ is so large that the experimental time scale is much smaller than Λ, then the system can no longer be regarded as being only marginally perturbed from its equilibrium state. For such flows, properties depend in a nonlinear fashion on the imposed strain rate. The Weissenberg number, which is ratio of Λ to the experimental time scale $\dot{\gamma}^{-1}$, can therefore be used to judge whether a flow is "weak" or "strong".

There are several measures of the characteristic equilibrium relaxation time of a polymer coil, and a Weissenberg number can be defined with each of these. For instance, it is possible to define the following relaxation time using the zero-shear-rate viscosity:

$$\Lambda_{\eta,0} \equiv \frac{\eta_{\mathrm{p},0}}{n_{\mathrm{p}} k_{\mathrm{B}} T} = \frac{[\eta]_0 M \eta_{\mathrm{s}}}{N_{\mathrm{A}} k_{\mathrm{B}} T} \,. \tag{2.105}$$

where $[\eta]_0$ is the zero-shear-rate intrinsic viscosity of the solution. In dimensionless terms, the definition above reduces to

$$\Lambda^*_{\eta,0} \equiv \frac{\Lambda_{\eta,0}}{\lambda_{\mathrm{S}}} = \eta^*_{\mathrm{p},\,0} \,. \tag{2.106}$$

The Weissenberg number defined with this time constant,

$$\beta \equiv \Lambda_{\eta,0} \dot{\gamma} = \eta^*_{\mathrm{p},\,0} \dot{\gamma}^* \,, \tag{2.107}$$

is frequently used in reporting data in shear flows, and is referred to as the shear Weissenberg number in this study. In studies on extensional flows, a different time

constant is typically used to define a Weissenberg number. This time constant is known as the "longest" relaxation time, denoted in this work as $\Lambda_{1,0}$, and the corresponding Weissenberg number is

$$Wi \equiv \Lambda_{1,0}\dot{\varepsilon} = \Lambda^*_{1,0}\dot{\varepsilon}^* \,. \tag{2.108}$$

The estimation of $\Lambda_{1,0}$ is described in Chapter 8. It is useful to also define a Weissenberg number in an extensional flow using $\Lambda_{\eta,0}$, wherein $Wi_\eta = \Lambda_{\eta,0}\dot{\varepsilon}$.

Chapter 3

Brownian Dynamics Simulations

In the previous Chapter, the master equations for FEBS chains for the configurational probability distribution functions were presented. It was shown that predictions of macroscopic observables are related to expectations of functions of the chain configuration. While in principle, these expectations can be calculated once the Fokker-Planck equations are solved for the probability densities, analytical closed-form solutions are in general unavailable for Fokker-Planck equations that are non-linear in the independent variables, and direct numerical solutions are not easy. However, in most cases one is not interested in the probability distribution *per se*, but in the expectations. The technique of Brownian Dynamics (BD) simulations allows the calculation of the desired expectations without actually evaluating the probability density. This technique is based on the formal equivalence of a Fokker-Planck equation for the probability density of random variables, to Itô stochastic differential equations (SDE) for the random variables. The mathematical foundation for this equivalence, and its application to the solution of problems in polymer kinetic theory has been reviewed by Öttinger [1996a].

This Chapter presents the details of the numerical integration schemes used in the BD simulations performed in this study. One of the significant outcomes of this work has been the development of an unconditionally stable and highly efficient numerical algorithm for simulations of FEBS chains with EV and HI in strong flows [Prabhakar and Prakash, 2004]. This numerical scheme is described in Section 3.2. Before that however, a simulation algorithm for Hookean dumbbells with EV and

HI is first presented in the following Section. The dumbbell model was used early in this study to obtain qualitative insight into the coupling between EV and HI, and the influence of these phenomena in steady shear flows [Prabhakar and Prakash, 2002].

3.1 Numerical integration scheme for Hookean dumbbells with EV and HI

The connector vector form of the Fokker-Planck equation in Eq. (2.54) for a general dumbbell model with nonlinear springs and EV and HI, reduces to the following for Hookean springs ($\xi = 1; H^* = 1$):

$$\frac{\partial \psi}{\partial t^*} = -\frac{\partial}{\partial \boldsymbol{Q}^*} \cdot \left\{ \boldsymbol{\kappa}^* \cdot \boldsymbol{Q}^* - \frac{1}{4} \widetilde{\boldsymbol{A}} \cdot H^*_{\text{eff}} \boldsymbol{Q}^* \right\} \psi + \frac{1}{4} \frac{\partial}{\partial \boldsymbol{Q}^*} \cdot \widetilde{\boldsymbol{A}} \cdot \frac{\partial \psi}{\partial \boldsymbol{Q}^*} \,, \tag{2.54}$$

where $\widetilde{\boldsymbol{A}} = 2(\boldsymbol{\delta} - \zeta \boldsymbol{\Omega})$ as before, but $H^*_{\text{eff}} = 1 - w^* = 1 - (z^*/d^{*5}) \exp(-Q^{*2}/2d^{*2})$.

For the simulations of the dumbbell model in this study, a regularization of the Oseen-Burgers tensor suggested by Zylka and Öttinger [1989] is used instead of the RPY form of the HI tensor shown in Eq. (2.47) of Chapter 2. In this case,

$$\zeta \boldsymbol{\Omega} = \frac{3\sqrt{\pi} h^*}{4\zeta Q^* \left(Q^{*2} + c^2\right)^3} \left(f\, \boldsymbol{\delta} + g\, \frac{\boldsymbol{Q}^* \boldsymbol{Q}^*}{Q^{*2}} \right) , \tag{3.1}$$

where $c = 2\sqrt{\pi} h^* / \sqrt{3}$,

$$f = Q^{*6} + \frac{7}{2} c^2 Q^{*4} + \frac{9}{2} c^4 Q^{*2}, \tag{3.2}$$

and,

$$g = Q^{*6} + \frac{3}{2} c^2 Q^{*4} - \frac{3}{2} c^4 Q^{*2} \,. \tag{3.3}$$

As a result of this regularization, the singularity in the Oseen-Burgers tensor at $\boldsymbol{Q}^* = \boldsymbol{0}$ is removed and the tensor $\widetilde{\boldsymbol{A}}$ is positive-definite for any $\boldsymbol{Q}^*$. The merits and demerits of the regularized Oseen tensor defined above have been discussed elsewhere

[Öttinger, 1996a; Zylka and Öttinger, 1989]. Briefly, the regularized Oseen tensor has a smooth dependence on the distance between the beads Q^*, whereas the RPY tensor has two branches depending on the magnitude of Q^* relative to $2(a/\ell_s) = 2\sqrt{\pi}h^*$. Besides making the implementation of the numerical scheme marginally easier, an important motivation for proposing this continuous alternative of the Oseen-Burgers tensor is its use in the development of higher-order integration schemes, which may involve derivatives of the diffusion matrix. Further, for $Q^* \geq 2\sqrt{\pi}h^*$, the regularized Oseen tensor agrees with the RPY tensor to order Q^{*-3}, and is an equally accurate representation of the effect of finite bead size (to order Q^{*-5}). On the other hand, use of the regularized Oseen-Burgers tensor does not lead to a positive-definite diffusion matrix for bead-spring chains, which is why the RPY tensor is generally preferred for BD simulations of chains with HI.

From the theory of stochastic processes [Öttinger, 1996a], the following Itô stochastic differential equation corresponding to the Fokker-Planck equation for the dumbbell model is written by inspecting Eq. (2.54):

$$d\boldsymbol{Q}^* = \left\{ \boldsymbol{\kappa}^* \cdot \boldsymbol{Q}^* - \frac{1}{4}\widetilde{\boldsymbol{A}}(\boldsymbol{Q}^*) \cdot H^*_{\text{eff}}(\boldsymbol{Q}^*)\boldsymbol{Q}^* \right\} dt^* + \frac{1}{\sqrt{2}}\boldsymbol{B}(\boldsymbol{Q}^*) \cdot d\boldsymbol{W} \,. \tag{3.4}$$

Here, $\boldsymbol{W}$ is a 3-dimensional vector each of whose components is an independent (dimensionless) Wiener process, and $\boldsymbol{B}(\boldsymbol{Q}^*)$ is a 3×3 matrix function whose components need to be chosen such that they satisfy

$$\boldsymbol{B} \cdot \boldsymbol{B}^{\mathrm{T}} = \widetilde{\boldsymbol{A}} \,. \tag{3.5}$$

Since the equation above is used to calculate the values of the components of $\boldsymbol{B}$ once the components of $\widetilde{\boldsymbol{A}}$ are given, this equation is referred to as the "decomposition" of the diffusion matrix $\widetilde{\boldsymbol{A}}$. This relation is also described as the "fluctuation-dissipation" equation, since it relates $\boldsymbol{B}$, a quantity controlling the strength of the fluctuations in the system to the diffusion matrix $\widetilde{\boldsymbol{A}}$, which characterizes the dissipative processes in the system. The calculation of the $\boldsymbol{B}$ tensor is taken up after the following description of the scheme used to integrate the SDE in Eq. (3.4).

To numerically integrate Eq. (3.4), a Runge-Kutta-like derivative-free algorithm is used. This scheme has been shown by Öttinger [1996a] to be well-suited for

simulation of dumbbells with HI, since it is better than other methods both in terms of computational intensity and the order of convergence. For an integration starting from $t^* = 0$ and ending at $t^* = t^*_{\max}$, the time interval $[0, t^*_{\max}]$ is divided into $n_{\max}$ discrete time-steps of equal size $\Delta t^* = t^*_{\max}/n_{\max}$. To calculate the dumbbell configuration at the end of the n-th time step $\boldsymbol{Q}^*_{n+1}$, an estimate, $\widetilde{\boldsymbol{Q}}^*_{n+1}$, is first obtained using an Euler-Maruyama discretization of Eq. (3.4) as a predictor step:

$$\widetilde{\boldsymbol{Q}}^*_{n+1}, = \boldsymbol{Q}^*_n + \boldsymbol{\mathcal{J}}(\boldsymbol{Q}^*_n)\Delta t^* + \boldsymbol{B}(\boldsymbol{Q}^*_n) \cdot \Delta \boldsymbol{W}_n \,, \tag{3.6}$$

where $\boldsymbol{Q}^*_n$ is the value of the vector $\boldsymbol{Q}^*$ at the previous completed time-step, $\boldsymbol{\mathcal{J}}(\boldsymbol{Q}^*) = \left\{ \boldsymbol{\kappa}^* \cdot \boldsymbol{Q}^* - \frac{1}{4}\widetilde{\boldsymbol{A}}(\boldsymbol{Q}^*) \cdot H^*_{\text{eff}}(\boldsymbol{Q}^*)\boldsymbol{Q}^* \right\}$ denotes the drift term in Eq. (3.4) and $\Delta \boldsymbol{W}_n$ is a Wiener increment, whose estimation is discussed shortly. In addition, the following supporting vectors are also calculated:

$$\boldsymbol{\Gamma}^\alpha_n = \boldsymbol{Q}^*_n + \frac{1}{3}\boldsymbol{\mathcal{J}}(\boldsymbol{Q}^*_n)\Delta t^* + \frac{1}{\sqrt{2}}\boldsymbol{b}_\alpha(\boldsymbol{Q}^*_n)\Delta t^* \tag{3.7}$$

$$\widetilde{\boldsymbol{\Gamma}}^\alpha_n = \boldsymbol{Q}^*_n + \frac{1}{3}\boldsymbol{\mathcal{J}}(\boldsymbol{Q}^*_n)\Delta t^* - \frac{1}{\sqrt{2}}\boldsymbol{b}_\alpha(\boldsymbol{Q}^*_n)\Delta t^* \,, \tag{3.8}$$

where $\alpha = 1, 2, 3$ and $\boldsymbol{b}_\alpha$ is the α-th column vector of the matrix $\boldsymbol{B}(\boldsymbol{Q}^*_n)$. The value of $\boldsymbol{Q}^*_{n+1}$ is then calculated using the corrector step:

$$\begin{aligned} \boldsymbol{Q}^*_{n+1} = \boldsymbol{Q}^*_n &+ \frac{1}{2}\left[\boldsymbol{\mathcal{J}}(\widetilde{\boldsymbol{Q}}^*_{n+1}) + \boldsymbol{\mathcal{J}}(\boldsymbol{Q}^*_n)\right]\Delta t^* - \frac{1}{2\sqrt{2}}\boldsymbol{B}(\boldsymbol{Q}^*_n) \cdot \Delta \boldsymbol{W}_n \\ &+ \frac{1}{4\sqrt{2}}\sum_{\alpha=1}^{3}\left[\boldsymbol{B}(\boldsymbol{\Gamma}^\alpha_n) + \boldsymbol{B}(\widetilde{\boldsymbol{\Gamma}}^\alpha_n)\right] \cdot \Delta \boldsymbol{W}_n + \boldsymbol{\Lambda}_n \,, \end{aligned} \tag{3.9}$$

where the α-th component ($\alpha = 1, 2, 3$) of the 3-dimensional vector $\boldsymbol{\Lambda}_n$ is given by:

$$(\boldsymbol{\Lambda}_n)_\alpha = \frac{1}{4\sqrt{2\Delta t^*}} \sum_{\beta,\,\gamma=1}^{3} (\Delta \boldsymbol{W}_n \Delta \boldsymbol{W}_n \,-\, \Delta t^* \boldsymbol{\delta} \,+\, \Delta \boldsymbol{V}_n)_{\beta\gamma} \left[B_{\alpha\beta}(\boldsymbol{\Gamma}^\gamma_n) - B_{\alpha\beta}(\widetilde{\boldsymbol{\Gamma}}^\gamma_n)\right] . \tag{3.10}$$

Here, $\Delta \boldsymbol{V}_n$ is an anti-symmetric tensor, whose three components above the diagonal are generated in the same way that the components of $\boldsymbol{W}_n$ are generated, as described below.

From the definition of a Wiener process, it is shown that the Wiener increment $\Delta \boldsymbol{W}_n$ is a Gaussian random variable with mean $\langle \Delta \boldsymbol{W}_n \rangle = \mathbf{0}$ and variance $\langle \Delta \boldsymbol{W}_n^2 \rangle = \Delta t_n$ [Öttinger, 1996a]. Thus, Wiener increments required in the implementations of numerical integration schemes are best simulated by using computer-generated random numbers which obey a Gaussian distribution with the desired mean and variance. However, the generation of Gaussian random numbers is computationally expensive and it is desirable to approximate the Wiener increments using random numbers that are more efficient to generate. This is justified as follows. In simulations such as those employed in this study, the major goal is the evaluation of expectations, and the individual stochastic trajectories themselves are of little interest. In the language of the theory of stochastic processes, one is only interested in generating a weak solution to the SDE. For weak solutions and for sufficiently small Δt^*, the error in the expectation of any well-behaved function f estimated using a discretization of the SDE, varies with Δt as

$$|\langle f \rangle - \langle f \rangle_{\Delta t^*}| \leq c_f (\Delta t^*)^p. \tag{3.11}$$

Here, p is the order of weak convergence of the numerical scheme, and c_f is a positive constant which depends on the function f and time t^*, but is independent of Δt^*. Since the errors introduced due to the discretization itself scales as $(\Delta t^*)^p$, one can use a non-Gaussian random variable M to approximate a Gaussian Wiener increment, as long as all the first $2p$-th central moments of the distribution of M are identical to those of the Wiener increment. In the simulations performed in this study, the following random variable suggested by Öttinger [1996a] is used in place of a Wiener increment:

$$M = \sqrt{\Delta t^*} \left(U - \frac{1}{2} \right) \left[c_1 \left| U - \frac{1}{2} \right| + c_2 \right], \tag{3.12}$$

where U is a random variable that is uniformly distributed in [0, 1], and the constants c_1 and c_2 are 10.72458949 and -0.71691890 respectively. This choice of M and c_1 and c_2 ensures that the approximation of a Wiener increment by M is accurate to second order in Δt^*. In computer simulations in this study, each component of $\Delta \boldsymbol{W}_n$ and of the upper-diagonal part of $\Delta \boldsymbol{V}_n$ [Eqs. (3.6), (3.8) and (3.9)] is approximated at every

time step using the rule in Eq. (3.12) after generating a pseudorandom number U using an algorithm combining two linear congruential generators [Öttinger, 1996a; Press *et al.*, 1992].

The calculation of the tensor $\boldsymbol{B}$ in each time-step remains to be specified. As mentioned above, the decomposition rule in Eq. (3.5) is used to calculate $\boldsymbol{B}$ given the tensor $\widetilde{\boldsymbol{A}}$. Since the HI tensor is chosen such that the diffusion tensor $\widetilde{\boldsymbol{A}}$ is always positive-definite for all configurations $\boldsymbol{Q}^*$ of the dumbbell, this decomposition can be performed. However, since $\widetilde{\boldsymbol{A}}$ is also symmetric, the decomposition rule leads to only 6 independent equations for the 9 components of $\boldsymbol{B}$. As a result, there are infinitely many tensors $\boldsymbol{B}$ that can satisfy the decomposition rule. For simulations of Hookean dumbbells with EV and HI performed in this study, a scheme suggested by Öttinger [1996a] is implemented. Firstly, the tensor $\boldsymbol{B}$ is chosen to be symmetric, which means that $\boldsymbol{B}$ is the matrix square-root tensor of $\widetilde{\boldsymbol{A}}$. Taking advantage of the fact that the tensor $\widetilde{\boldsymbol{A}}$ has the form $g(Q^*)\boldsymbol{\delta} + \tilde{g}(Q^*)\,\boldsymbol{Q}^*\boldsymbol{Q}^*/Q^{*2}$, $\boldsymbol{B}$ is chosen to be

$$\boldsymbol{B}(\boldsymbol{Q}^*) \;=\; \sqrt{g(Q^*)}\boldsymbol{\delta} + \Big(\sqrt{g(Q^*) + \tilde{g}(Q^*)} \;-\; \sqrt{g(Q^*)} \Big) \frac{Q^*Q^*}{Q^{*2}} \,. \tag{3.13}$$

With this expression for $\boldsymbol{B}$, matrix inversion and other matrix manipulations are avoided.

For simulations in this study, the initial condition $\boldsymbol{Q}_0^*$ at $t^* = 0$ is chosen such that the distribution of $\boldsymbol{Q}_0^*$ across an ensemble of trajectories is the same as the equilibrium probability distribution ψ_{eq}. In the absence of EV interactions ($z^* = 0$), this is achieved by using three computer-generated Gaussian random numbers with zero mean and unit variance for the three components of $\boldsymbol{Q}_0^*$, since in this case $\psi_{\text{eq}} \sim \exp(-Q^{*2}/2)$. For dumbbells with EV interactions, the initial $\boldsymbol{Q}_0^*$ at $t^* = 0$ consistent with $\psi_{\text{eq}} \sim \exp(-H_{\text{eff}}^* Q^{*2}/2)$ is generated by starting with a Gaussian random vector, and integrating the SDE under no-flow conditions for the time period $-100 \le t^* \le 0$.

The estimation, at some time t_n^*, $n \in \{0, \ldots, n_{\max}\}$, of the expectation of some well-behaved function $f(\boldsymbol{Q}^*)$ for which $\langle f(\boldsymbol{Q}^*)\rangle$ exists for all $t^* \in [0, t_{\max}^*]$ is accomplished by calculating at t_n^*, $\overline{f}$, the arithmetic mean of f across an ensemble of N_{T}

trajectories:

$$\langle f \rangle \approx \overline{f} = \frac{1}{N_{\mathrm{T}}} \sum_{j=1}^{N_{\mathrm{T}}} f_{(j)} \,, \tag{3.14}$$

where $f_{(j)}$ is the value of f realized in the j-th trajectory at t_n^*. The standard error in this "ensemble average" estimate of the true expectation is calculated as $\sqrt{\mathrm{Var}(f)/N_{\mathrm{T}}}$ where $\mathrm{Var}(f)$ is the variance of f, whose value is in turn estimated by [Öttinger, 1996a]

$$\mathrm{Var}(f) \approx \frac{1}{N_{\mathrm{T}} - 1} \sum_{j=1}^{N_{\mathrm{T}}} f_{(j)}^2 - \frac{N_{\mathrm{T}}}{N_{\mathrm{T}} - 1} \overline{f}^{\,2} \,. \tag{3.15}$$

Static properties at equilibrium and steady-state properties at larger shear-rates ($\dot{\gamma}^* \geq 0.1$) are calculated by simulating a single long trajectory (after discarding the initial transients) and dividing the trajectory into N_{T} large blocks. The time average of f within the j-th block takes the place of $f_{(j)}$ in Eqs. (3.14) and (3.15) above. In addition, the ensemble averages estimated in this fashion carry the error due to discretization of the time-step. For all macroscopic properties calculated for the dumbbell model, results of simulations with successively smaller time steps were extrapolated to zero time-step size to obtain the predictions in the limit of vanishingly small time-step size [Öttinger, 1996a]. The dimensionless time-step width sizes ranged from 0.05 down to 0.005.

Predictions at lower shear-rates were generated using a large ensemble of 10^6 trajectories. In addition, a variance reduction scheme suggested by Wagner and Öttinger [1997] using equilibrium trajectories as control variates was also used to reduce the error in the simulations.

The algorithm described thus far relates to the simulations of Hookean dumbbells with EV and HI. The following Section elaborates the numerical scheme used to perform simulations of FEBS chains with EV and HI.

3.2 Numerical integration scheme for FEBS chains

For a clearer description of the numerical scheme for bead-spring chains, it is advantageous to start with the Fokker-Planck equation for the probability distribution Ψ of the bead position-vectors [Eq. (2.3)], which in dimensionless form is,

$$\frac{\partial \Psi}{\partial t^*} = -\sum_{\nu=1}^{N} \frac{\partial}{\partial \boldsymbol{r}_\nu^*} \cdot \left\{ \boldsymbol{\kappa}^* \cdot \boldsymbol{r}_\nu^* + \frac{1}{4} \sum_{\mu} \boldsymbol{\Upsilon}_{\nu\mu} \cdot (\boldsymbol{F}_\mu^{\mathrm{S}\,*} + \boldsymbol{F}_\mu^{\mathrm{E}\,*}) \right\} \Psi + \frac{1}{4} \sum_{\nu,\mu=1}^{N} \frac{\partial}{\partial \boldsymbol{r}_\nu^*} \cdot \boldsymbol{\Upsilon}_{\nu\mu} \cdot \frac{\partial \Psi}{\partial \boldsymbol{r}_\mu^*}, \tag{3.16}$$

where the spring and EV forces on the μ-th bead, $\boldsymbol{F}_\mu^{\mathrm{S}}$ and $\boldsymbol{F}_\mu^{\mathrm{E}}$, have been made dimensionless by dividing with $k_{\mathrm{B}}T/\,\ell_{\mathrm{S}}$. The Itô SDE corresponding to this Fokker-Planck equation is

$$d\boldsymbol{r}_\nu^* = \left\{ \boldsymbol{\kappa}^* \cdot \boldsymbol{r}_\nu^* + \frac{1}{4} \sum_{\mu} \boldsymbol{\Upsilon}_{\nu\mu} \cdot (\boldsymbol{F}_\mu^{\mathrm{S}\,*} + \boldsymbol{F}_\mu^{\mathrm{E}\,*}) \right\} \Delta t^* + \frac{1}{\sqrt{2}} \sum_{\mu=1}^{N} \boldsymbol{B}_{\nu\mu} \cdot d\boldsymbol{W}_\mu, \tag{3.17}$$

where for all $\mu = 1, \ldots, N$, $\boldsymbol{W}_\mu$ is a 3-dimensional vector whose components are independent Wiener processes, and

$$\sum_{\theta=1}^{N} \boldsymbol{B}_{\nu\theta} \cdot \boldsymbol{B}_{\mu\theta}^{\mathrm{T}} = \boldsymbol{\Upsilon}_{\nu\mu} \tag{3.18}$$

is the equivalent of Eq. (3.5) for bead-spring chains with HI.

Instead of $\boldsymbol{r}_\nu^*$, the SDE above in Eq. (3.17) can be written for $\mathbf{R}$, the chain configuration vector consisting of the $3N$ coordinates of the dimensionless position vectors of the N beads, with $R_i = r^{*\alpha}_{\nu}$, where $i = 3(\nu - 1) + \alpha$, $\nu = 1, \ldots, N$, and $\alpha = 1, 2, 3$. Similarly, the $3N$-dimensional chain spring-force and EV force vectors, $\mathbf{F}^{\mathrm{S}}$ and $\mathbf{F}^{\mathrm{E}}$ respectively, consist of the $3N$ components of the corresponding bead forces. The $3N \times 3N$ matrix $\mathbf{K}$ is a diagonal block-matrix, whose 3×3 diagonal-blocks are each equal to the tensor $\boldsymbol{\kappa}^*$, while all the off-diagonal 3×3 blocks are equal to $\mathbf{0}$. The diffusion matrix $\mathbf{D}$ and the matrix $\mathbf{B}$ are defined as block matrices, each consisting of $N \times N$ blocks having dimensions of 3×3, with the (ν, μ)-th block of $\mathbf{D}$ containing the components of the $\boldsymbol{\Upsilon}_{\nu\mu}$ tensor, and that of $\mathbf{B}$ being equal to $\boldsymbol{B}_{\nu\mu}$. Since $\boldsymbol{\Upsilon}_{\nu\mu} = \boldsymbol{\Upsilon}_{\nu\mu}^{\mathrm{T}} = \boldsymbol{\Upsilon}_{\mu\nu} = \boldsymbol{\Upsilon}_{\mu\nu}^{\mathrm{T}}$, and the HI tensor is defined using

the RPY formulation, the diffusion matrix $\mathbf{D}$ is symmetric positive-definite for all configurations of a chain. Then, the decomposition rule in Eq. (3.18) is expressed as

$$\mathbf{B} \cdot \mathbf{B}^{\mathrm{T}} = \mathbf{D}. \tag{3.19}$$

With these definitions, the Îto SDE for the chain configuration equivalent is

$$d\,\mathbf{R} = \left[\mathbf{K} \cdot \mathbf{R} + \frac{1}{4}\,\mathbf{D} \cdot (\mathbf{F}^{\mathrm{S}} + \mathbf{F}^{\mathrm{E}}) \right] dt^* + \frac{1}{\sqrt{2}}\,\mathbf{B} \cdot d\,\mathbf{W}, \tag{3.20}$$

where $\mathbf{W}$ is a $3N$-dimensional Wiener process.

3.2.1 Decomposition of the diffusion matrix

Unlike the situation in the dumbbell model described earlier, it is not in general possible to derive a simple analytical expression to evaluate $\mathbf{B}$ from $\mathbf{D}$ using the decomposition rule in Eq. (3.19). As before, there is no unique way to carry out the decomposition. Assuming that $\mathbf{B}$ is a lower (or upper) triangular matrix leads to its calculation using a Cholesky decomposition of $\mathbf{D}$. The computational intensity of such a decomposition is known to scale as N^3. In this study, a more efficient method of handling the stochastic term in the SDE proposed by Fixman [1986] is used, whose CPU-time requirement has been shown to scale roughly as $N^{2.25}$.

Fixman's method assumes that $\mathbf{B}$ is symmetric and can hence be regarded as the matrix square-root of the diffusion matrix $\mathbf{D}$, that is $\mathbf{B} = \sqrt{\mathbf{D}}$. The next step in this method is to introduce a Chebyshev polynomial approximation for the square root function. In the case of scalars, the Chebyshev polynomial approximation for the square-root of $x \in [x_{\min}, x_{\max}]$ is given by

$$\sqrt{x} \approx \sum_{p=0}^{N_{\mathrm{C}}-1} c_p T_p[y(x)] - \frac{c_0}{2}, \tag{3.21}$$

where N_{C} is the number of terms used in the Chebyshev polynomial approximation of the function on the left-hand side of the equation above, and $y(x)$ is an invertible mapping of the domain $[x_{\min}, x_{\max}]$ into the domain $[-1, 1]$. For instance, $y =$

$2(x-x_{\min})/(x_{\max}-x_{\min})-1$, in a linear mapping. The functions T_p are the Chebyshev polynomials which are calculated using the recurrence relation,

$$T_p(y) = 2yT_{p-1}(y) - T_{p-2}(y), \tag{3.22}$$

with $T_0(y) = 1$ and $T_1(y) = y$. The constant coefficients c_p are related to the zeroes of the Chebyshev polynomial T_{N_c}. The k-th zero of the Chebyshev polynomial T_{N_c} is

$$y_k = \cos\left(\frac{\pi\{k-1/2\}}{N_c}\right), \tag{3.23}$$

and the coefficients c_p are given by

$$c_p = \frac{2}{N_c}\sum_{k=1}^{N_c}\sqrt{x(y_k)}\cos(py_k), \tag{3.24}$$

where $x(y_k) = y^{-1}(y_k) = x_{\min} + (y_k + 1)/2(x_{\max} - x_{\min})$ for the linear mapping specified earlier. The determination of N_c, the number of terms in the Chebyshev approximation, is crucial to the efficient implementation of the approximation, and is discussed shortly.

The Chebyshev polynomial approximation for the matrix square root of the matrix $\mathbf{D}$ is constructed by writing Eq. (3.21) in a matrix form:

$$\sqrt{\mathbf{D}} \approx \sum_{p=0}^{N_c-1} c_p \mathbf{T}_p[\mathbf{Y}(\mathbf{D})] - \frac{c_0}{2}\mathbf{1}. \tag{3.25}$$

where $\mathbf{1}$ denotes the $3N \times 3N$-dimensional identity matrix. In this case, the linear mapping

$$\mathbf{Y}(\mathbf{D}) = \left(\frac{2}{d_{\max}-d_{\min}}\right)\mathbf{D} - \left(\frac{d_{\max}+d_{\min}}{d_{\max}-d_{\min}}\right)\mathbf{1}, \tag{3.26}$$

ensures that the eigenvalues of $\mathbf{Y}$ lie in the domain $[-1, 1]$ when the eigenvalues of $\mathbf{D}$

are within $[d_{\min}, d_{\max}]$. The matrix version of the recurrence relation in Eq. (3.22),

$$\mathbf{T}_p(\mathbf{Y}) = 2\mathbf{Y} \cdot \mathbf{T}_{p-1}(\mathbf{Y}) - \mathbf{T}_{p-2}(\mathbf{Y}) \,, \tag{3.27}$$

with $\mathbf{T}_0(\mathbf{Y}) = \mathbf{1}$ and $\mathbf{T}_1(\mathbf{Y}) = \mathbf{Y}$ is used to calculate $\mathbf{T}_p$. The coefficients c_p in Eq. (3.25) are calculated using Eqs. (3.24) and (3.23), but with d_{min} and d_{max} in place of x_{min} and x_{max} respectively to calculate $x(y_k)$.

In Eq. (3.27), the number of floating point operations involved in the matrix multiplication of $\mathbf{Y}$ with $\mathbf{T}_{p-1}$ scales as N^3. Therefore, for a fixed value of $N_{\rm C}$, the CPU-time required for each instance of calculating $\mathbf{B}$ scales as N^3, and the Chebyshev approximation by itself offers no significant gains over the Cholesky decomposition of $\mathbf{D}$. However, Fixman pointed out that in the numerical integration of an SDE one is interested in the product $\mathbf{B} \cdot d\mathbf{W}$, and the individual columns of the matrix $\mathbf{B}$ are in themselves not of much interest. Multiplying Eq. (3.27) by $d\mathbf{W}$ leads to

$$d\mathbf{V}_p(\mathbf{Y}) = \mathbf{T}_p(\mathbf{Y}) \cdot d\mathbf{W} = 2\mathbf{Y} \cdot d\mathbf{V}_{p-1}(\mathbf{Y}) - d\mathbf{V}_{p-2}(\mathbf{Y}), \tag{3.28}$$

with $d\mathbf{V}_0(\mathbf{Y}) = d\mathbf{W}$ and $d\mathbf{V}_1(\mathbf{Y}) = \mathbf{Y} \cdot d\mathbf{W}$. Therefore, one directly obtains

$$d\mathbf{S} = \sqrt{\mathbf{D}} \cdot d\mathbf{W} \approx \sum_{p=0}^{N_{\rm C}-1} c_p \, d\mathbf{V}_p \left[\mathbf{Y}(\mathbf{D})\right] - \frac{c_0}{2} \, d\mathbf{W} \; . \tag{3.29}$$

For a given $N_{\rm C}$, the cost of the direct calculation of the $3N$-dimensional vector $d\mathbf{S}$ without the intermediate calculation of $\mathbf{B}$ is proportional to $N_{\rm C}\, N^2$.

What remains to be specified are the bounds $d_{\min}$ and $d_{\max}$, and the order of the polynomial approximation $N_{\rm C}$. Although there are several standard methods for calculating exactly the maximum and minimum eigenvalues for any given diffusion matrix, these are computationally intensive. However, it is not necessary to calculate the largest and smallest eigenvalues exactly, but only obtain good estimates of upper and lower bounds for these values, respectively. Estimates based on suggestions by Fixman [1986] are used in this study. The following Rayleigh quotient is used for

the upper bound:

$$d_{\max} = \frac{2}{3N}\,\mathbf{D}\colon(\boldsymbol{u}^{+}\boldsymbol{u}^{+})\,, \tag{3.30}$$

where $\boldsymbol{u}^{+}$ is a $3N$-dimensional vector all of whose elements are equal to 1. For the lower bound,

$$d_{\min} = \frac{1}{6N}\,\mathbf{D}\colon(\boldsymbol{u}^{-}\boldsymbol{u}^{-})\,, \tag{3.31}$$

where $\boldsymbol{u}^{-}$ is a $3N$-dimensional vector with alternating 1's and -1's. The physical reasons for this choice have been elaborated by Kröger *et al.* [2000]. The choice of N_{C} is related to the accuracy of the polynomial approximation. One of the salient features of the Chebyshev polynomial approximation is that it achieves a practically uniform error across the entire domain $[d_{\min}, d_{\max}]$. Consequently, for a fixed value of N_{C}, the root-mean-squared deviation from the exact value of the square-root function grows as the size of the domain increases. Fixman showed that, close to equilibrium, the value of N_{C} required to keep the deviations below a fixed tolerance must be increased as $(d_{\max}/d_{\min})^{0.5}$. Therefore, at every time-step in the numerical integration, $d_{\max}$ and $d_{\min}$ are calculated and N_{C} is determined using the following rule suggested by Kröger *et al.* [2000]:

$$N_{\mathrm{C}} = \mathrm{nint}\left[\left(\frac{d_{\max}}{d_{\min}}\right)^{1/2}\right] + 1\,, \tag{3.32}$$

where nint is the nearest integer function. Near equilibrium, $d_{\max}/d_{\min} \sim N^{0.5}$ and therefore, $N_{\mathrm{C}} \sim N^{1/4}$. The CPU-time requirement for the calculation of $d\mathbf{S}$ in Fixman's method thus scales as $N_{\mathrm{C}}N^2 \sim N^{9/4}$.

In situations where chains can be highly stretched, the computational intensity is dominated by the stiffness of the SDE caused by the presence of the large spring forces. The numerical integration scheme developed during the course of this study handles these problems very efficiently, and is described next.

3.2.2 The semi-implicit, predictor-corrector scheme

To numerically integrate Eq. (3.20), a semi-implicit, predictor-corrector scheme was used in this work. In this scheme the numerical discretization of the SDE in Eq. (3.20) above treats the spring forces (*i.e* $\mathbf{F}^{\mathrm{S}}$) implicitly, but the excluded-volume forces ($\mathbf{F}^{\mathrm{E}}$) are handled using a predictor-corrector approach, while the terms related to HI (*i.e* the matrices $\mathbf{D}$ and $\mathbf{B}$) are treated explicitly. Such an algorithm has been implemented previously by Jendrejack *et al.* [2000]. However, these authors used an iterative Newton method to solve the implicit part of the equation (discussed in greater detail below), whereas the method discussed here uses a more efficient algorithm based on an idea originally suggested by Öttinger [1996a] for FENE dumbbells, and later adapted by Somasi *et al.* [2002] for FEBS chains. In both cases, the models did not incorporate HI or EV effects. The numerical scheme presented below [Prabhakar and Prakash, 2004] extends the ideas of Öttinger and Somasi *et al.* to chains with HI and EV. A similar extension has also been proposed by Hsieh *et al.* [2003]. Each time-step in this method proceeds in three major steps which are described below.

Step 1

Firstly, a predictor step is used to obtain $\tilde{\mathbf{R}}_{n+1}$, the first-estimate of the configuration vector after the n-th time step, by employing an Euler-Maruyama explicit discretization of Eq. (3.20),

$$\widetilde{\mathbf{R}}_{n+1} = \mathbf{R}_n + \left[\mathbf{K}\cdot\mathbf{R}_n + \frac{1}{4}\mathbf{D}_n\cdot\mathbf{F}_n^{\mathrm{S}} + \frac{1}{4}\mathbf{D}_n\cdot\mathbf{F}_n^{\mathrm{E}}\right]\Delta t^* + \frac{1}{\sqrt{2}}\Delta\mathbf{S}_n\,. \tag{3.33}$$

where $\Delta\mathbf{S}_n = \mathbf{B}_n\cdot\Delta\,\mathbf{W}_n$ and will be referred to as the diffusion term.

Since $\mathbf{R}_n$ is known from the previous time-step, the components of the configuration dependent diffusion matrix $\mathbf{D}_n$ and force vectors $\mathbf{F}_n^{\mathrm{S}}$ and $\mathbf{F}_n^{\mathrm{E}}$ can be determined in the above equation. The components of the Wiener increment vector $\Delta\mathbf{W}_n$ are calculated in the same way as described in Section 3.1, using Eq. (3.12). For BD simulations of chains, a fast uniform random number generator, combining a Marsaglia-shift and a linear congruential generator, is used to generate the random variable U in Eq. (3.12) [Press *et al.*, 1996].

Step 2

Using the estimate generated in the predictor step, the following corrector step is constructed:

$$\begin{aligned}\mathbf{R}_{n+1} =& \mathbf{R}_n + \left[\frac{1}{2} \left\{ \mathbf{K} \cdot \mathbf{R}_n + \mathbf{K} \cdot \widetilde{\mathbf{R}}_{n+1} \right\} \right. \\ & \left. + \frac{1}{8} \mathbf{D}_n \cdot \left\{ \mathbf{F}^{\mathrm{S}}_n + \mathbf{F}^{\mathrm{S}}_{n+1} \right\} + \frac{1}{8} \mathbf{D}_n \cdot \left\{ \mathbf{F}^{\mathrm{E}}_n + \widetilde{\mathbf{F}}^{\mathrm{E}}_{n+1} \right\} \right] \Delta t^* + \frac{1}{\sqrt{2}} \Delta \mathbf{S}_n \,.\end{aligned} \tag{3.34}$$

In the equation above, the vector $\widetilde{\mathbf{F}}^{\mathrm{E}}_{n+1}$ is the excluded volume force vector evaluated using the configuration estimate $\widetilde{\mathbf{R}}_{n+1}$ predicted by Eq. (3.33). Hence, the equation above shows that the EV contribution is handled through a predictor-corrector approach. The FENE force term, however, is treated *implicitly*, with the term $\mathbf{F}^{\mathrm{S}}_{n+1}$ formally being evaluated using the yet-to-be-determined $\mathbf{R}_{n+1}$. In this equation, the values of the diffusion matrix $\mathbf{D}_n$ and the related quantity, $\Delta \mathbf{S}_n$, are the same as those used in Eq. (3.33) before, and the contributions stemming from HI are thus treated explicitly in the numerical scheme. As discussed by Öttinger [1996a], explicit treatment of the diffusion matrix is necessary in order to retain the Îto interpretation (as opposed to the Stratonovich interpretation) of the diffusion term $\mathbf{B} \cdot d\mathbf{W}$.

Using the implicit formulation outlined above and solving for $\mathbf{R}_{n+1}$ leads to greater stability of the numerical algorithm [Öttinger, 1996a], which in turn permits the use of larger times steps leading to a reduction in the CPU-time required for the simulation of a bead-spring chain. Iterative methods for the numerical solution of the nonlinear set of equations for the components of $\mathbf{R}_{n+1}$, such as Newton's method, involve the calculation and inversion of large Jacobian matrices. Somasi *et al.* [2002] show that the computational overhead that this implies can outweigh the gains achieved by the increase in the time-step size. In addition, in the course of the iterations, it is possible that some springs have lengths greater than $\sqrt{b^*}$, which could lead to unphysical results. Such effects can be handled in an *ad hoc* manner by replacing the unnatural spring lengths obtained during the course of a Newton iteration by values slightly less than $\sqrt{b^*}$ [Jendrejack *et al.*, 2000]. However, Somasi *et al.* show that these problems are circumvented and considerable gains in computational efficiency over the Newton method are achieved by using a novel

technique, which forms the next step in the integration scheme.

Step 3

The corrector step above in Eq. (3.34) is written in an alternative form by introducing an operator $\mathcal{D}_j$, $j = 1, \ldots, N_\mathrm{s}$, which operates on any $3N \times M$ matrix to give a $3 \times M$ matrix formed by the subtraction of the three rows corresponding to the j-th block of rows—which is a $3 \times M$ matrix—from the $j+1$-th block of three rows. For instance, the operation $\mathcal{D}_j[\mathbf{R}]$ yields the 3-dimensional vector $\boldsymbol{r}^*_{j+1} - \boldsymbol{r}^*_j = \boldsymbol{Q}^*_j$,which is the connector vector from the j-th bead to the $j+1$-th bead. The following corrector step for the connector vector $\boldsymbol{Q}^*_j$ can then be derived, after some algebraic manipulations, by applying the operator $\mathcal{D}_j$ to the whole of Eq. (3.34):

$$\boldsymbol{Q}^*_{j,\,n+1} = \mathcal{D}_j\left[\mathbf{P}_{n+1}\right] + \frac{1}{8}\mathcal{D}_j\left[\mathbf{D}_n \cdot \mathbf{F}^{\mathrm{S}}_{n+1}\right]\Delta t^* \,. \tag{3.35}$$

Here, the term, $\mathbf{P}_{n+1}$ denotes

$$\begin{aligned}\mathbf{P}_{n+1} = \mathbf{R}_n + \big[\,\frac{1}{2}\left\{\mathbf{K}\cdot\mathbf{R}_n + \mathbf{K}\cdot\widetilde{\mathbf{R}}_{n+1}\right\} \\ + \frac{1}{8}\,\mathbf{D}_n\cdot\mathbf{F}^{\mathrm{S}}_n + \frac{1}{8}\,\mathbf{D}_n\cdot\left\{\mathbf{F}^{\mathrm{E}}_n + \widetilde{\mathbf{F}}^{\mathrm{E}}_{n+1}\right\}\big]\Delta t^* + \frac{1}{\sqrt{2}}\,\Delta\mathbf{S}_n\,.\end{aligned} \tag{3.36}$$

Thus, $\mathbf{P}_{n+1}$ contains no terms that depend implicitly on any component of $\mathbf{R}_{n+1}$.

After this rearrangement, an iterative scheme similar to a Gauss-Seidel iteration is applied to solve for the all the $\boldsymbol{Q}^*{}_{j,\,n+1}$, $j = 1, \ldots, N_\mathrm{s}$. In the following discussion, the time-step indices n and $n+1$ are dropped for the sake of clarity. It is to be noted that for any matrix-vector product of the form $\mathbf{M}\cdot\mathbf{V}$, $\mathcal{D}_j[\mathbf{M}\cdot\mathbf{V}] = \mathcal{D}_j[\mathbf{M}]\cdot\mathbf{V}$. The super-matrix $\mathbf{D}$ has the structure

$$\mathbf{D} = \begin{bmatrix} \boldsymbol{\delta} & \zeta\boldsymbol{\Omega}_{12} & \cdots & \cdots & \cdots \\ & & \vdots & & \\ \cdots & \boldsymbol{\delta} & \zeta\boldsymbol{\Omega}_{j,j+1} & \cdots & \cdots \\ \cdots & \zeta\boldsymbol{\Omega}_{j+1,j} & \boldsymbol{\delta} & \cdots & \cdots \\ & & \vdots & & \\ \cdots & \cdots & \cdots & \zeta\boldsymbol{\Omega}_{N-1,N} & \boldsymbol{\delta} \end{bmatrix}. \tag{3.37}$$

Therefore, dropping the superscript "S" and the "$*$" for clarity,

$$\mathcal{D}_j[\mathbf{D}]\cdot\mathbf{F} = \Big[\ldots \quad (\boldsymbol{\Omega}_{j+1,j}-\boldsymbol{\delta}) \quad (\boldsymbol{\delta}-\zeta\boldsymbol{\Omega}_{j,j+1}) \quad \ldots\Big]\cdot\mathbf{F} \tag{3.38}$$

$$= \ldots + (\zeta\boldsymbol{\Omega}_{j+1,j}\cdot\boldsymbol{F}_j - \boldsymbol{F}_j) + (\boldsymbol{F}_{j+1} - \zeta\boldsymbol{\Omega}_{j,j+1}\cdot\boldsymbol{F}_{j+1}) + \ldots\,, \tag{3.39}$$

$$= \ldots + \zeta\boldsymbol{\Omega}_{j+1,j}\cdot\boldsymbol{F}_j + \boldsymbol{F}^c_{j-1} - 2\boldsymbol{F}^c_j + \boldsymbol{F}^c_{j+1} - \zeta\boldsymbol{\Omega}_{j,j+1}\cdot\boldsymbol{F}_{j+1} + \ldots\,, \tag{3.40}$$

Thus, the full expansion of the matrix multiplication in the implicit second term on the right-hand side of Eq. (3.35) contains the term, $-(1/4)\boldsymbol{F}^c_j\Delta t^*$, which is the FENE force in the j-th *connector* and is a hence solely a function of $\boldsymbol{Q}_j$. Although there are other terms on the right-hand side of Eq. (3.35) that contain $\boldsymbol{Q}_j$, only $(1/4)\boldsymbol{F}^c_j\,\Delta t^*$ is transposed to the left-hand side. This transposition is formally indicated by adding $(1/4)\boldsymbol{F}^c_j$ to both sides of Eq. (3.35).

The resulting equation can be solved using a successive substitution algorithm in which the equation for the p-th iteration, $p = 1, 2, \ldots$, at a given j, is written as:

$$\boldsymbol{Q}^{(p)}_j + \frac{\Delta t^*}{4}\boldsymbol{F}^{c\,(p)}_j = \boldsymbol{\Gamma}^{(p-1)}_j\,. \tag{3.41}$$

Here,

$$\boldsymbol{\Gamma}^{(p-1)}_j = \mathcal{D}_j\left[\mathbf{P}\right] + \frac{1}{8}\mathcal{D}_j\left[\mathbf{D}\cdot\mathbf{F}^{\,(p-1)}\right]\,\Delta t^* + \frac{1}{4}\boldsymbol{F}^{c\,(p-1)}_j\,\Delta t^*\,. \tag{3.42}$$

The left-hand side of Eq. (3.41) above is a function of $\boldsymbol{Q}^{(p)}_j$ alone. On the right-hand side of Eq. (3.42) above, the quantities $\mathbf{P}$ and $\mathbf{D}$ do not change during the iterative solution. On the right-hand side of Eq. (3.42), the super-vector

$$\mathbf{F}^{\,(p-1)} = \begin{bmatrix} \boldsymbol{F}^{(p)}_1 \\ \vdots \\ \boldsymbol{F}^{(p)}_{j-1} \\ \boldsymbol{F}^{(p-1)}_j \\ \boldsymbol{F}^{(p-1)}_{j+1} \\ \vdots \\ \boldsymbol{F}^{(p-1)}_N \end{bmatrix} = \begin{bmatrix} \boldsymbol{F}^{c\,(p)}_1 \\ \vdots \\ \boldsymbol{F}^{c\,(p)}_{j-1} - \boldsymbol{F}^{c\,(p)}_{j-2} \\ \boldsymbol{F}^{c\,(p-1)}_j - \boldsymbol{F}^{c\,(p)}_{j-1} \\ \boldsymbol{F}^{c\,(p-1)}_{j+1} - \boldsymbol{F}^{c\,(p-1)}_j \\ \vdots \\ -\boldsymbol{F}^{c\,(p-1)}_{N-1} \end{bmatrix}\,. \tag{3.43}$$

The p-th iteration in this scheme consists of successively solving for $\boldsymbol{Q}_j^{(p)}$ using Eqs. (3.41) and (3.42), starting from $j = 1$ and proceeding until $j = N_{\rm s}$. The method for solving the equation for a given j is described shortly. After solving for each $\boldsymbol{Q}_j^{(p)}$, the configuration $\mathbf{R}$ and the force $\mathbf{F}^{\rm s}$ vectors are immediately updated by using the newly determined $\boldsymbol{Q}_j^{(p)}$, before proceeding to solve for $\boldsymbol{Q}_{j+1}^{(p)}$. After solving for $\boldsymbol{Q}_{N_{\rm s}}$, p-th iteration is complete, and the entire configuration vector $\mathbf{R}_{n+1}^{(p)}$ at the end of the p-th iteration is known (where n is the time-step index). If the relative error

$$E_{\rm iter} = \frac{|\,\mathbf{R}_{n+1}^{(p)} - \mathbf{R}_{n+1}^{(p-1)}\,|}{|\,\mathbf{R}_{n+1}^{(p)}|}\,, \tag{3.44}$$

is greater than a specified tolerance $E_{\rm tol}$, the process is repeated for the next value of p using Eq. (3.41) and starting from $j = 1$. The starting configurational guess for the $p = 1$ iteration is chosen as $\mathbf{R}_n$, and not the predictor $\widetilde{\mathbf{R}}_{n+1}$. This choice is observed to lead to a more stable algorithm, particularly at high elongational rates.

For FENE springs, the primary reason behind the efficiency of the algorithm described above lies in the method of solution of Eq. (3.41) for the unknown $\boldsymbol{Q}_j^{(p)}$. On substituting for $\boldsymbol{F}_j^{c\,(p)}$, one obtains for FENE springs

$$\left(1 + \frac{1}{4}\frac{\Delta t^*}{1 - |\boldsymbol{Q}_j^{(p)}|^{\,2}/b^*}\right)\boldsymbol{Q}_j^{(p)} = \boldsymbol{\Gamma}_j^{(p-1)}\,. \tag{3.45}$$

Öttinger [1996a] pointed out that the equation above can be quickly solved, since it shows that the direction of $\boldsymbol{Q}_j^{(p)}$ is given by the direction of the right-hand side, $\boldsymbol{\Gamma}_j^{(p-1)}$, which is known, and the equation for the magnitude, $x = |\boldsymbol{Q}_j^{(p)}\,|$ is a cubic equation in x,

$$x^3 - Gx^2 - b^*\left(1 + \frac{\Delta t^*}{4}\right)x + b^*\,G = 0\,, \tag{3.46}$$

where $G = |\,\boldsymbol{\Gamma}_j^{(p-1)}\,|$. Given the values of b^* and Δt^*, the roots of this equation are functions of the parameter G. It can be shown that this equation has exactly one root in the domain $(0, \sqrt{b^*})$ when $0 < G < \infty$, and this root can be obtained analytically using standard formulae for solutions of cubic equations [Öttinger, 1996a].

The advantage with this algorithm is two-fold. Firstly, it achieves unconditional stability by ensuring that the magnitudes of the connector vectors remain in the domain $(0, \sqrt{b^*})$ during the entire iterative procedure. Secondly, since the closed-form analytical solution avoids any further iterations. Further, since the value of the desired root is solely determined by the parameter G, further optimization is achieved by storing the values of the root for different predetermined values of G in a look-up table at the beginning of the simulation. During the numerical integration, the desired root corresponding to a value of G calculated for any $\mathbf{\Gamma}_j^{(p-1)}$, is quickly estimated by interpolating between entries in the look-up table [Somasi *et al.*, 2002].

While the iterative procedure described above can be carried out until the error E_{iter} is smaller than E_{tol}, in the simulations performed in this study, a different strategy is employed. The iteration loop for the chain configuration after the n-th time-step is continued until either convergence is achieved, or the number of iterations $p = N$, the number of beads in the chain. At this stage, the iteration loop is stopped and the relative change between the predictor and the iterated corrector

$$E_{\text{pc}} = \frac{|\,\mathbf{R}_{n+1} - \tilde{\mathbf{R}}_{n+1}\,|}{|\,\mathbf{R}_{n+1}|}\,, \tag{3.47}$$

is computed. If this error is greater than the tolerance E_{tol}, the time-step size Δt^* is reduced by half, and the calculations are repeated beginning from Eq. (3.33) with the smaller time-step size. Otherwise, the last calculated value of $\mathbf{R}_{n+1}$ in the iteration loop is accepted, and the integration proceeds to the next time-step. If E_{pc} is found to be smaller than the E_{tol} by more than an order of magnitude, the size of the next time-step is doubled before proceeding with the calculation for the next time-step.

This adaptive time-step scheme, suggested by Öttinger [1996a] for SDE's encountered in simulations of polymer solutions, attempts to keep the local truncation error (of which E_{pc} is an estimate) within an acceptable tolerance by varying the time-step. In a constant time-step scheme, the local truncation error on an average grows as the SDE becomes stiffer. This can be checked by storing the variation of E_{pc} with t^* for each trajectory, and then taking the ensemble average of the truncation error at each fixed t^*. Figure. 3.1 plots the variation in the ensemble average $\langle E_{\text{pc}} \rangle$ in a typical simulation using the constant time-step size scheme, for

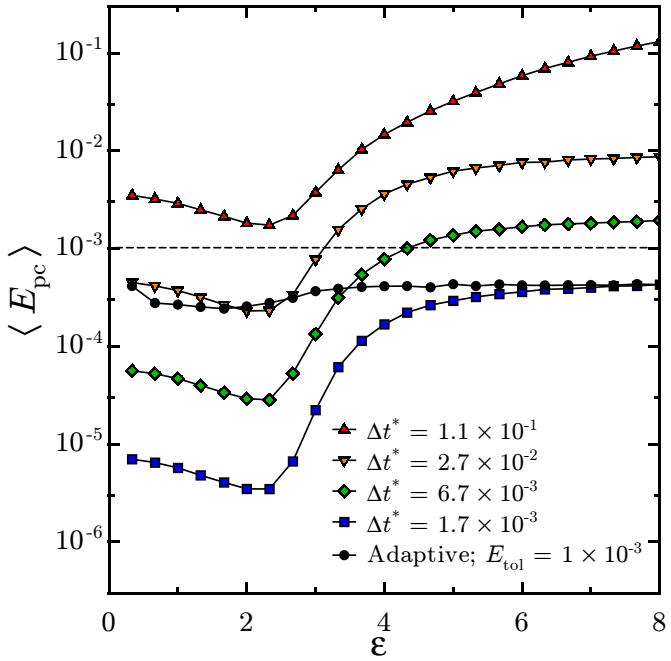

Figure 3.1: Variation of $\langle E_{pc} \rangle$ with respect to the Hencky strain ε, in a typical simulation of start-up of extensional flow. Errors in estimation of $\langle E_{pc} \rangle$ are smaller than the sizes of the symbols used. Values of the simulation parameters used are shown in the the following Figure.

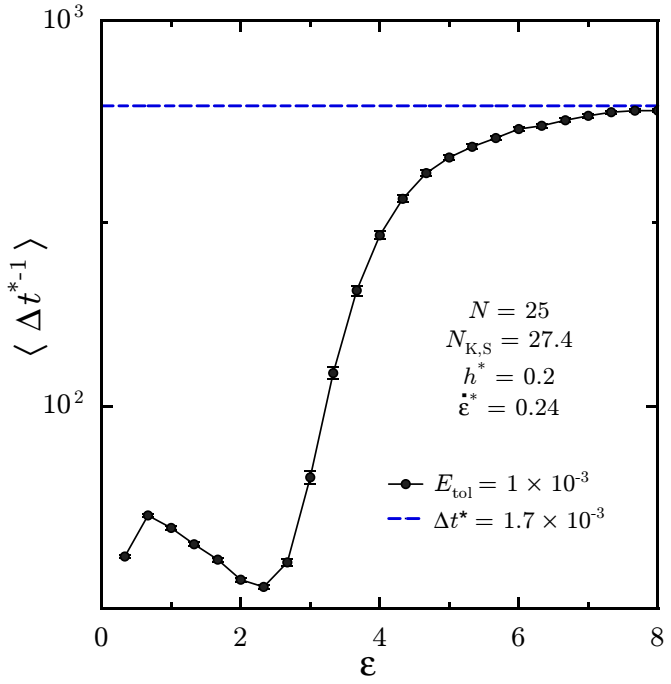

Figure 3.2: Variation in the mean reciprocal of time-step size in the adaptive time-step scheme (black circles). The blue dashed line shows the value of $1/\Delta t^*$ for a constant time-step scheme of comparable accuracy. The area under the curves is proportional to the CPU-time required for integration.

different values of the time-step size. Also plotted is the $\langle E_{\rm pc} \rangle$ for a simulation with an adaptive time-step scheme, with a fixed tolerance whose level is indicated by the horizontal line in Fig. 3.1.

The data shown were obtained with FEBS chains with $N = 25$ in an extensional flow simulation. In Fig. 3.2, the variation of the mean $1/\Delta t^*$ in the adaptive time-step scheme is shown. The mean total number of time-steps executed in a single trajectory simulated using the adaptive scheme can be estimated by $\int_0^{t^*_{\rm max}} \langle \Delta t^{*-1} \rangle dt^*$. From Fig. 3.2, it can be seen that significant savings can be achieved in comparison with a constant time-step scheme of similar accuracy. The gain in the efficiency of computation is of course highly dependent on the parameters of the model and the imposed flow conditions and cannot be quantified *a priori* in general. Nevertheless, it is observed that a reduction of as much as 1/2 to 1/3 of the CPU-time is achievable, particularly in simulations of strong extensional flow.

3.2.3 Generation of equilibrium configurations for FEBS chains

For simulations starting with equilibrium initial conditions, the initial configuration for each stochastic trajectory must be consistent with the equilibrium probability distribution for the bead-spring chain model. For chains with $N_{\rm s}$ FENE springs, the dimensionless length Q^* of each spring must satisfy the probability distribution

$$P_Q \, dQ^* = \mathcal{N} \left(1 - Q^{*\,2}/b^*\right)^{b^*/2} Q^{*\,2} \, dQ^* \tag{3.48}$$

where

$$\mathcal{N}^{-1} = \int_0^{\sqrt{b^*}} \left(1 - Q^{*\,2}/b^*\right)^{b^*/2} Q^{*\,2} \, dQ^* \tag{3.49}$$

while orientations of the connector vectors are completely random.

A random number X distributed uniformly in the interval $(0, 1)$ can be used to generate another random number satisfying the FENE distribution above, using a one-to-one transformation $Q^* = Q^*(X)$ such that $P_X dX = 1 dX = P_Q \, dQ^*$. Hence, the Jacobian of the transformation is $|dX/dQ^*| = \mathcal{N} (1 - Q^{*\,2}/b^*)^{b^*/2} Q^{*\,2}$. For

$X > 0$, $Q^* > 0$, the inverse transformation is obtained as

$$X(Q^*) = \mathcal{N} \int_0^{Q^*} \left(1 - t^2/b^*\right)^{b^*/2} t^2 dt. \tag{3.50}$$

Instead of inverting this equation analytically, a look-up table for X is calculated by numerically evaluating the integral above for different values of Q^* in the range $(0, \sqrt{b^*})$ at the start of the simulation.

"FENE random numbers" are then calculated by first generating a uniform random number X in $(0, 1)$ and then finding the corresponding Q^* by interpolating between the entries in the look-up table. The values of Q^* thus generated is used as the magnitude of the connector vector. The random orientation of the connector vector is calculated by generating uniform random numbers on the unit sphere.

Chapter 4

Multiplicative separation of the influences of excluded volume, hydrodynamic interactions and finite extensibility

In this Chapter, Brownian dynamics simulations are used to study an interesting qualitative feature of the predictions of bead-spring models. The phenomena of EV and HI both lead to a coupling of the dynamics of all the beads in a chain (or a dumbbell), even if those beads are far apart along the chain backbone. In this sense, therefore, these two nonlinear interactions are "long-range" effects, and will be referred together as "long-range interactions". In contrast, FE is the result of a "local" nonlinear effect. At the level of the Fokker-Planck equation for the model, a simplification leading to a decoupling of the nonlinear terms is not immediately obvious, and therefore one expects the nature of the coupling between these nonlinear phenomena to be quite complex. Nevertheless, the results presented in this Chapter show that, to a good approximation, the individual influences of EV, HI and FE on most rheological properties of interest can be separated into independent multiplicative factors.

Before proceeding further, it must be noted that in this Chapter, the basic length scale used for construction of dimensionless quantities is $\ell_{\text{H}} = \sqrt{k_{\text{B}}T/H}$, and the

corresponding time-scale is $\lambda_{\text{H}} = \zeta/4H = \zeta\,\ell_{\text{H}}^2/4k_{\text{B}}T$. The definitions of the key dimensionless parameters governing HI and EV are $h^* = a/\sqrt{\pi}\,\ell_{\text{H}}$, $z^* = v/(2\pi)^{3/2}\,\ell_{\text{H}}^3$ and $d^* = \widetilde{d}/\,\ell_{\text{H}}$, while the parameter controlling the strength of the FENE nonlinearity is the well known FE parameter, $b = Q_0/\,\ell_{\text{H}}$. The results presented in this Chapter were obtained during the initial part of this study, at which stage ℓ_{H} was chosen as the basic length scale firstly as a matter of convention, and also to ensure continuity with already published literature exploring the qualitative influence of HI, EV and FE in bead-spring chain models. Here, the choice of ℓ_{H} as the basic length scale is justified, since the emphasis is on understanding the qualitative differences stemming from the incorporation of HI, EV and/or FE. Therefore, the Rouse model with Hookean springs serves a standard reference model, for which ℓ_{H} is the natural choice for the length scale.

In the following Section, the equilibrium and non-equilibrium behaviour of dumbbell models with different combinations of the three nonlinear phenomena is examined. The results for bead-spring chains with $N = 20$ are then examined in Section 4.2 in the light of the insight gained from the dumbbell models.

4.1 Dumbbell models

As the simplest models of polymer molecules, dumbbell models serve as a useful starting point in understanding the consequences of including or neglecting different phenomena in the mathematical description of dilute polymer solutions. The small number of degrees of freedom in such models means that simulations can be quickly performed, and large regions in parameter space can be explored. In addition, exact values for static properties at equilibrium such as the mean-squared end-to-end distance $\langle Q^{*2}\rangle_{\text{eq}}$ can be easily evaluated by simple numerical quadrature, since the equilibrium Boltzmann distribution is known and the calculation of these properties can be typically reduced to evaluating integrals over a single variable. For instance, for Hookean springs with EV interactions between the beads, one has

$$\langle Q^{*2}\rangle_{\text{eq}} = \frac{\int_0^\infty Q^{*4}\exp[-(1/2)Q^{*2} - E^*]\,dQ^*}{\int_0^\infty Q^{*2}\exp[-(1/2)Q^{*2} - E^*]\,dQ^*}\,, \tag{4.1}$$

while for FENE springs with EV,

$$\langle Q^{*2}\rangle_{\rm eq} = \frac{\int_0^\infty Q^{*4}(1-Q^{*2}/b)^{b/2}\exp[-E^*]\,dQ^*}{\int_0^\infty Q^{*2}(1-Q^{*2}/b)^{b/2}\exp[-E^*]\,dQ^*}\,, \tag{4.2}$$

where, for an NGEV potential, $E^* = (z^*/d^{*3})\exp[-Q^{*2}/2d^{*2}]$. For the FENE dumbbell model with NGEV interactions, static properties are solely determined by the parameters z^*, d^* and b, and as $b \to \infty$, the results approach those obtained for Hookean dumbbells using Eq. (4.1) above. The influence of the parameters on the prediction of $\langle Q^{*2}\rangle_{\rm eq}$ is examined below.

4.1.1 Static properties at equilibrium

In the absence of EV interactions, $\langle Q^{*2}\rangle_{\rm eq}$ is related analytically to b by [Bird *et al.*, 1987b]

$$\langle Q^{*2}\rangle_{\rm eq} = 3\frac{b}{b+5}\,. \tag{4.3}$$

As $b \to \infty$, one recovers the Hookean dumbbell result,

$$\langle Q^{*2}\rangle_{\rm eq} = 3\,. \tag{4.4}$$

The effect of including EV on the static properties of the polymer chain is usually studied in terms of "swelling" ratios [Yamakawa, 1971]. The swelling ratio for $\langle Q^{*2}\rangle_{\rm eq}$ is defined as

$$\alpha^2_{\rm e,eq} = \frac{\langle Q^{*2}\rangle_{\rm eq}}{\langle Q^{*2}\rangle^\theta_{\rm eq}}\,, \tag{4.5}$$

where the "θ" in the denominator indicates the value of $\langle Q^{*2}\rangle_{\rm eq}$ predicted under theta conditions in the absence of interactions, by Eqs. (4.3) (for FENE springs) or (4.4) (for Hookean springs). Since, for $z^* \neq 0$, $\langle Q^{*2}\rangle_{\rm eq}$ depends on b, as well as z^* and d^*, in general, $\alpha^2_{\rm e,eq} = \alpha^2_{\rm e,eq}(z^*, d^*, b)$.

Figure 4.1, which plots $\alpha^2_{\rm e,eq}$ predicted for two different values of z^* and a range of b values, against the parameter d^*, reveals some characteristic features of predictions

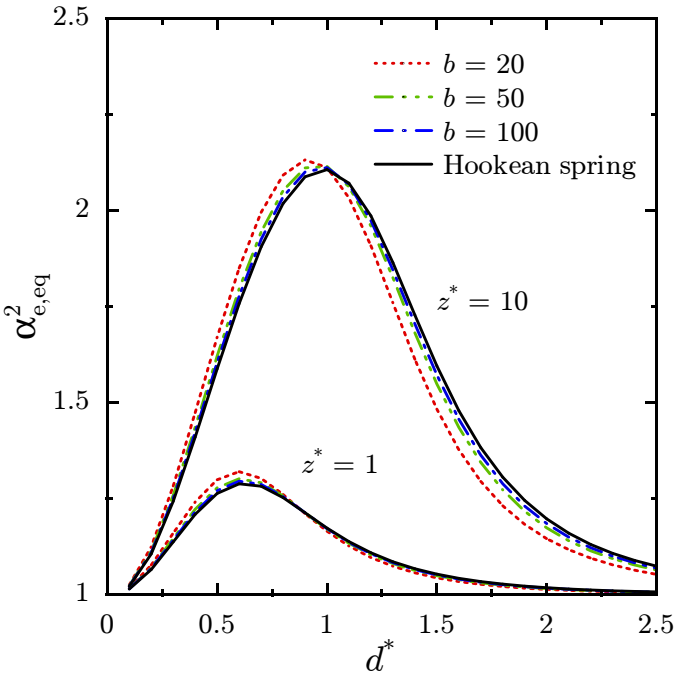

Figure 4.1: Equilibrium swelling ratio $\alpha^2_{e,eq}$ versus the range of the NGEV potential d^*, obtained using numerical quadrature and Eqs. (4.1) and (4.2).

obtained with finite chains using the NGEV potential, that are now well understood [Kumar and Prakash, 2003; Prakash and Öttinger, 1999]. Firstly, for all positive values of d^* and z^*, $\alpha^2_{e,eq}$ is greater than unity, since the presence of the EV repulsion causes chains to expand relative to their dimensions in a theta solution; a classic signature of the EV effect and pointed out long ago by Flory [1949]. Since z^* quantifies the strength of the repulsion between the beads, a larger value of z^* at any fixed value of d^* leads, on an average, to a greater expansion of the polymer coil, or the dumbbell in this case. In the NGEV potential, increasing d^* at a fixed z^*, increases the spatial range of the potential, but also decreases the maximum gradient in the potential, leading to a decrease in the average EV force between the beads [Prabhakar and Prakash, 2002]. Thus, as $d^* \to \infty$, the influence of the EV potential diminishes and $\alpha^2_{e,eq} \to 1$. However, this decrease in the EV effect as d^* increases is not monotonic.

As shown in Fig. 4.1, properties also approach their theta state values for any non-zero z^*, as $d^* \to 0$. At first sight, this appears problematic, since the original

motivation for using the NGEV potential was that it serves as a regularization of the δ-function. Several important results for universal behaviour in good solvents have been obtained in analytical treatments using δ-function EV interactions [Schäfer, 1999; Yamakawa, 1971]. However, even the most sophisticated of the analytical methods need to introduce approximations at some point. With BD simulations, it is possible to obtain the exact results which can then be used to discriminate between the different analytical approaches. To keep simulations and analysis on an equal footing, it is useful to attempt to obtain exact results for the same δ-function EV potential that is used in most analytical approaches. The NGEV potential was first used by [Prakash and Öttinger, 1999] in a dumbbell model with the intention of extrapolating results obtained for non-zero d^* values to the $d^* \to 0$ limit, since in this limit the NGEV approached a δ-function. However, Prakash and Öttinger observed that in the limit $d^* \to 0$, the value of $\langle {Q^*}^2 \rangle_{\text{eq}}$ is identical to that predicted for the theta state. This behaviour was also observed for all other static and dynamic properties.

These results show that a δ-function EV potential in a dumbbell model has no influence at all on any of the properties, no matter how large a value is chosen for z^*. This can be understood by noting that with δ-function repulsions between the beads, the probability distribution for any finite value of N and under any flow situation, differs from the theta state probability distribution only on a set of points of zero measure. Therefore, the expectations of smooth functions of chain configuration do not change if δ-function repulsions are used in finite, discrete chains.

However, as pointed out earlier, non-trivial analytical results are in fact obtained with δ-function EV repulsions. The key to resolving this apparent paradox is that analytical results are technically valid only in the $N \to \infty$ limit. While for any finite chain size, as $d^* \to 0$, exact results will approach those predicted for the theta state, the infinite chain limit is fundamentally different. As shown by Kumar and Prakash [2003] in the context of a bead-spring model with the NGEV potential, the limits $N \to \infty$ and $d^* \to 0$ do not commute. Non-trivial results can be obtained by taking the limit $N \to \infty$ first, with a fixed non-zero d^*. Remarkably, in this limit, the predictions of large scale properties such as the swelling ratios become independent of d^*, and thus actually carrying out the limit $d^* \to 0$ is not necessary.

Returning to the dumbbell model, the discussion above explains why $\alpha^2_{\mathrm{e,eq}}$ approaches the theta state value of unity as $d^* \to \infty$ and $d^* \to 0$ in Fig. 4.1. At some intermediate d^*, the influence of the EV potential on the swelling ratio reaches a maximum.

It is interesting to note in Fig. 4.1 that the parameter b has a much weaker effect on $\alpha^2_{\mathrm{e,eq}}$ in the range of b values examined. In other words, for any fixed value of d^*, $\alpha^2_{\mathrm{e,eq}}(z^*, b)$ is nearly the same as $\alpha^2_{\mathrm{e,eq}}(z^*, \infty)$, the latter denoting the result obtained with Hookean springs. Therefore, one obtains the following approximate result,

$$\langle Q^{*2}\rangle_{\mathrm{eq}}(z^*, b) \approx \langle Q^{*2}\rangle_{\mathrm{eq}}(0, b)\, \alpha^2_{\mathrm{e,eq}}(z^*, \infty), \tag{4.6}$$

$$\approx \langle Q^{*2}\rangle_{\mathrm{eq}}(0, b)\, \left[\frac{\langle Q^{*2}\rangle_{\mathrm{eq}}(z^*, \infty)}{\langle Q^{*2}\rangle_{\mathrm{eq}}(0, \infty)}\right], \tag{4.7}$$

which shows that the overall effect of EV and FE on $\langle Q^{*2}\rangle_{\mathrm{eq}}$ is approximately separable into a product of individual contributions stemming solely from FE and EV, respectively.

The influence of the model parameters on the steady-state shear viscosity is discussed below.

4.1.2 Steady-state shear viscosity

For dumbbell models without HI, and for any total spring potential ϕ^*, a retarded-motion expansion of the probability distribution in the velocity gradient can be used to derive the following expansion for stress tensor [Bird *et al.*, 1987b]:

$$\boldsymbol{\tau}^*_{\mathrm{p}} = \frac{1}{3}\langle Q^{*2}\rangle_{\mathrm{eq}}\dot{\boldsymbol{\gamma}}^* + \frac{1}{30}\langle Q^{*4}\rangle_{\mathrm{eq}}\{2\,\dot{\boldsymbol{\gamma}}^* \cdot \dot{\boldsymbol{\gamma}}^* - (\dot{\boldsymbol{\gamma}}^* \cdot \boldsymbol{\omega}^* - \boldsymbol{\omega}^* \cdot \dot{\boldsymbol{\gamma}}^*)\} + \dots, \tag{4.8}$$

where $\dot{\boldsymbol{\gamma}}^* = \boldsymbol{\kappa}^* + \boldsymbol{\kappa}^{*\mathrm{T}}$, and $\boldsymbol{\omega}^* = \boldsymbol{\kappa}^* - \boldsymbol{\kappa}^{*\mathrm{T}}$ is the vorticity tensor [Bird *et al.*, 1987a]. Using this result, the zero-shear-rate properties $\eta^*_{\mathrm{p},0}$ and $\Psi^*_{1,0}$ are related to the equilibrium moments:

$$\eta^*_{\mathrm{p},0} = \frac{1}{3}\langle Q^{*2}\rangle_{\mathrm{eq}}; \quad \Psi^*_{1,0} = \frac{2}{15}\langle Q^{*4}\rangle_{\mathrm{eq}}\,. \tag{4.9}$$

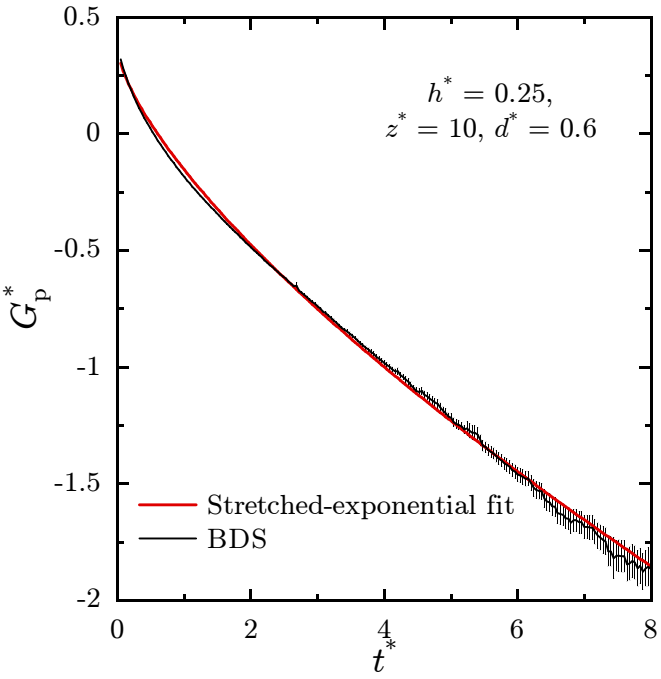

Figure 4.2: Exact BD simulations prediction of the time decay of the dimensionless relaxation modulus $G^*_{\rm p}$ (black line) for a typical set of parameter values for a Hookean dumbbell model with HI and EV. The dashed red curve is a stretched-exponential fit through the BD simulations data.

Hence, the variation of $\eta^*_{\rm p,\,0}$ in a dumbbell model without HI with respect to the parameters z^*, d^* and b is identical to that observed in Fig. 4.1.

For models with fluctuating (configuration-dependent) HI, a retarded motion expansion cannot be used to obtain closed-form results for the linear viscoelastic properties. Instead, the zero-shear-rate viscosity is obtained for dumbbell models with HI using Eq. (2.93) in Chapter 2, wherein the relaxation modulus $G^*_{\rm p}$ is evaluated with BD simulations under no-flow conditions using the Green-Kubo relation in Eq. (2.95).

Figure 4.2 shows the decay in time of the relaxation modulus $G^*_{\rm p}$ for a typical set of parameter values. At large t^*, the value of this function becomes of the same order as the errors in the simulations. Therefore, in the calculation of $\eta^*_{\rm p,\,0}$, the numerical integration of the BD simulations' data shown in Fig. 4.2 has to be terminated at some $t^* = t^*_{\rm c}$ where the value of $G^*_{\rm p}$ is larger by at least one order of magnitude than the error in its estimation. The value of $t^*_{\rm c}$ depends on the set of parameters

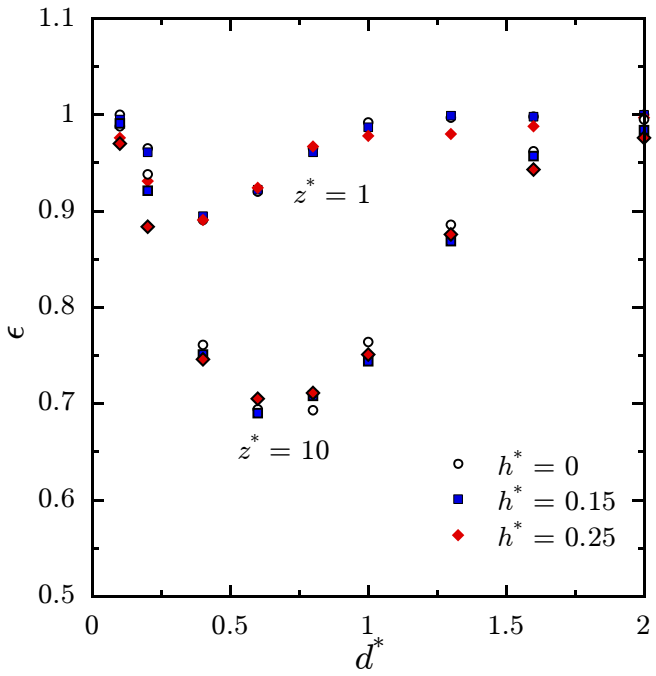

Figure 4.3: Dependence of the exponent ϵ in Eq. eqrefe:strexp on the model parameters d^*, z^* and h^*. The errors in the simulations' results are smaller than the symbols used. [2]

used. In order to obtain an estimate of uncertainty in the calculation of $\eta^*_{\mathrm{p},0}$ due to truncating the integral in Eq. (2.93) at t^*_{c}, a "stretched-exponential" function of the following form is fitted to the G^*_{p}-versus-t^* data for $t^* \leq t^*_{\mathrm{c}}$:

$$G^*_{\mathrm{p}}(t^*) = G^*_{\mathrm{p}}(0)\exp(-t^*/\mu)^{\epsilon}\,. \tag{4.10}$$

Here, $G^*_{\mathrm{p}}(0)$ is the value of G^*_{p} at $t^* = 0$ predicted by the simulations. The constants μ and ϵ are obtained using least-squares regression. It is observed that the data are well described by the stretched exponential decay, as demonstrated by Fig. 4.2. The error due to the truncation of the integral is then estimated as:

$$E_{\mathrm{trunc}} = G^*_{\mathrm{p}}(0)\int_{t^*_{\mathrm{c}}}^{\infty}\exp(-t^*/\mu)^{\epsilon}\,dt^*\,. \tag{4.11}$$

This integral can be numerically evaluated in terms of incomplete Gamma functions. For the simulations performed in this work, the values of E_{trunc} were small in

comparison with the error due to Brownian fluctuations [Prabhakar and Prakash, 2002].

Although it is known that the stretched exponential expression describes the relaxation behavior of many polymeric fluids well [De Gennes, 2002; Phillies and Peczak, 1988], the reason for using this expression here is purely empirical. The simulations' data for the relaxation modulus could have also been fitted by a superposition of two or more exponentials. However, one would need to obtain four or more parameters. In spite of its *ad hoc* use here, the parameters μ and ϵ of the stretched exponential are observed to vary quite systematically with the model parameters. As is well known, in the case of the Hookean dumbbell without EV or HI, the exponent ϵ and the dimensionless time constant μ are identically equal to unity. Figure 4.3 shows that the exponent ϵ is only weakly dependent on the HI parameter h^*, but depends strongly on z^*. The time constant μ on the other hand is found to strongly depend on all the parameters h^*, and/or z^* and d^* when HI and/or EV is included (not shown). These results show that HI influences the relaxation behaviour only through the time constant, whereas EV also exerts its influence through ϵ. This interesting dependence is however not explored further in this study.

The data for the zero-shear-rate viscosity can be expressed in terms of a length scale [Graessley *et al.*, 1999],

$$R_{\mathrm{V},0} \equiv \left(\frac{\eta_{\mathrm{p},0}}{n_{\mathrm{p}} \eta_{\mathrm{s}}} \right)^{1/3} . \tag{4.12}$$

Therefore, it is possible to identify a swelling ratio $\alpha_{\eta,0} \equiv R_{\mathrm{V},0}/R^{\theta}_{\mathrm{V},0}$ similar to $\alpha_{\mathrm{e,eq}}$ introduced earlier such that

$$\alpha^3_{\eta,0} = \frac{\eta_{\mathrm{p},0}}{\eta^{\theta}_{\mathrm{p},0}} = \frac{\eta^*_{\mathrm{p},0}}{\eta^{*\theta}_{\mathrm{p},0}} . \tag{4.13}$$

Here, for any fixed value of d^*, $\eta^*_{\mathrm{p},0} = \eta^*_{\mathrm{p},0}(h^*, z^*, b)$ for FENE dumbbells with EV and HI, whereas in the absence of EV interactions, $\eta^{*\theta}_{\mathrm{p},0} = \eta^{*\theta}_{\mathrm{p},0}(h^*, 0, b)$.

For Hookean dumbbells ($b = \infty$), it is observed in Fig. 4.4 that predictions of $\alpha^3_{\eta,0}$ obtained with $h^* = 0$ ("free-draining" dumbbells) are close to those obtained

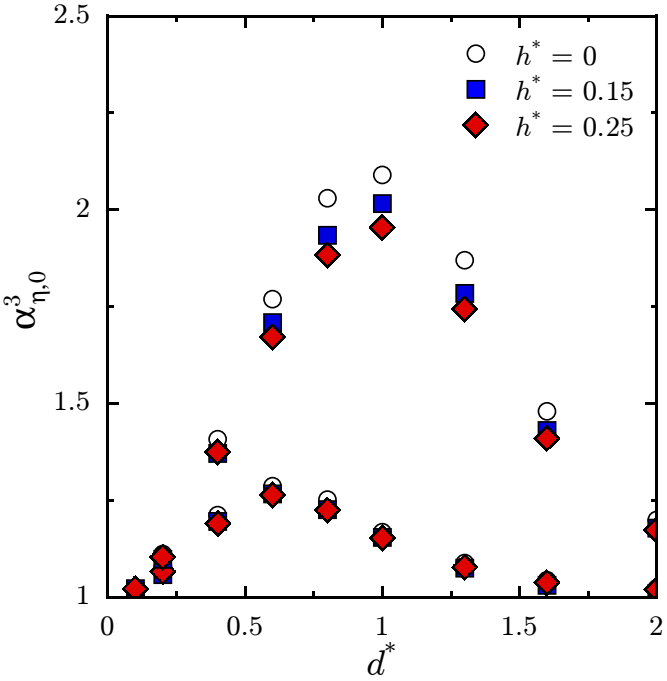

Figure 4.4: Exact predictions for $\alpha^3_{\eta,0}$ for a Hookean dumbbell model with excluded volume and hydrodynamic interactions, versus the range of the narrow Gaussian excluded volume potential d^*.

with non-zero h^*, for both the values of z^* studied. In other words, the sensitivity of $\alpha^3_{\eta,0}$ to h^* seems much weaker in Fig. 4.4 than to z^*. These results suggest that in the Hookean dumbbell model with HI and EV, for any value of d^*,

$$\frac{\eta^*_{\mathrm{p},0}(h^*, z^*, \infty)}{\eta^*_{\mathrm{p},0}(h^*, 0, \infty)} \approx \frac{\eta^*_{\mathrm{p},0}(0, z^*, \infty)}{\eta^*_{\mathrm{p},0}(0, 0, \infty)},$$

or,

$$\eta^*_{\mathrm{p},0}(h^*, z^*, \infty) \approx \eta^*_{\mathrm{p},0}(0, 0, \infty) \left[\frac{\eta^*_{\mathrm{p},0}(h^*, 0, \infty)}{\eta^*_{\mathrm{p},0}(0, 0, \infty)}\right] \left[\frac{\eta^*_{\mathrm{p},0}(0, z^*, \infty)}{\eta^*_{\mathrm{p},0}(0, 0, \infty)}\right]. \tag{4.14}$$

As before, the "∞" indicates that the results above are for Hookean springs, and $\eta_{\mathrm{p},0}(0, 0, \infty)$ is the prediction for a plain Hookean dumbbell without EV or HI. In this case, it is seen that the overall prediction for a model with EV *and* HI can be approximately separated as the product of independent multiplicative factors arising from each long-range nonlinearity. This result mirrors the nature of the coupling

between the nonlinearities in Eq. (4.7) between EV and FE in the absence of HI.

The shear-rate dependence of the steady-state viscosity can be studied in terms of a ratio α_η defined for higher shear-rates as in Eq. (4.13), that is $\alpha_\eta^3 = \eta_{\rm p}^*/\eta_{\rm p}^{*\theta}$. The variation of α_η^3 with respect to shear-rate for a fixed value of d^* is shown in Figure 4.5 for different dumbbell models. For both the values of z^* considered (1 and 10), it appears that the predictions of the models are less sensitive to either h^* or b for the range of parameter values examined. In other words, the data suggest that at fixed $\dot{\gamma}^*$ and d^*,

$$\frac{\eta_{\rm p}^*(h^*, z^*, b)}{\eta_{\rm p}^*(h^*, 0, b)} \approx \frac{\eta_{\rm p}^*(0, z^*, \infty)}{\eta_{\rm p}^*(0, 0, \infty)},$$

or,

$$\eta_{\rm p}^*(h^*, z^*, b) \approx \eta_{\rm p}^*(h^*, 0, b) \left[\frac{\eta_{\rm p}^*(0, z^*, \infty)}{\eta_{\rm p}^*(0, 0, \infty)}\right]. \tag{4.15}$$

The right-hand side of the equation above contains $\eta_{\rm p}^*(h^*, 0, b)$, the prediction of a dumbbell model with FE and HI, but no EV. To analyze the nature of the coupling between FE and HI in the absence of EV, the following ratio is defined:

$$\chi_\eta \equiv \frac{\eta_{\rm p}^*(h^*, 0, b)}{\eta_{\rm p}^*(0, 0, b)}. \tag{4.16}$$

Figure 4.6 plots this ratio as a function of the strain rate for different dumbbell models without EV interactions. It is observed that χ_η is more sensitive to h^* than to b, and therefore

$$\frac{\eta_{\rm p}^*(h^*, 0, b)}{\eta_{\rm p}^*(0, 0, b)} \approx \frac{\eta_{\rm p}^*(h^*, 0, \infty)}{\eta_{\rm p}^*(0, 0, \infty)},$$

or,

$$\eta_{\rm p}^*(h^*, 0, b) \approx \eta_{\rm p}^*(0, 0, b) \left[\frac{\eta_{\rm p}^*(h^*, 0, \infty)}{\eta_{\rm p}^*(0, 0, \infty)}\right]. \tag{4.17}$$

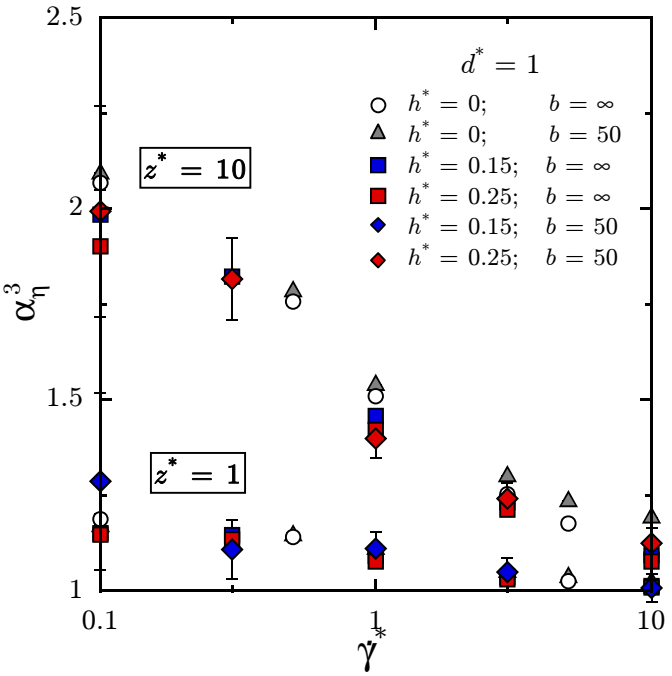

Figure 4.5: Exact predictions for the variation of the swelling ratio α_η^3 with respect to the dimensionless shear-rate $\dot{\gamma}^*$ at a fixed value of $d^* = 1$, for different dumbbell models including FE and/or HI.

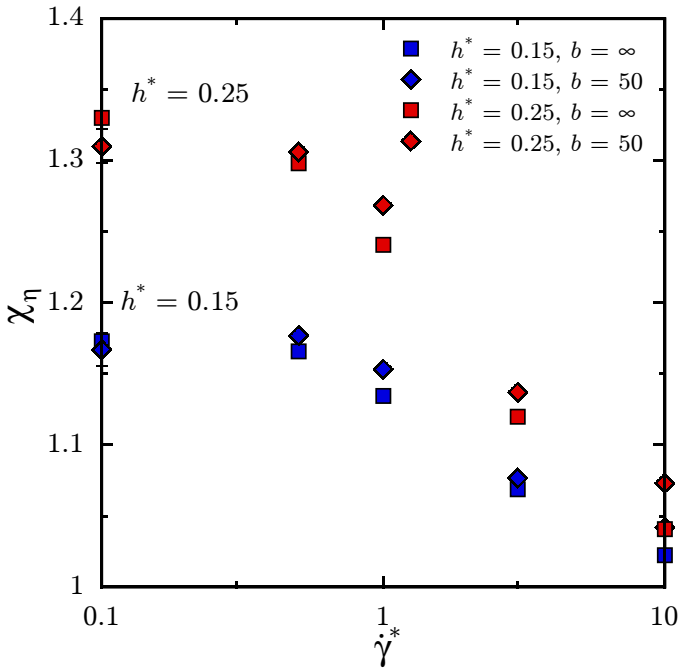

Figure 4.6: Exact predictions for the variation of the ratio χ_η with respect to the dimensionless shear-rate $\dot{\gamma}^*$ at a fixed value of $d^* = 1$, for dumbbell models without EV interactions, but including FE and/or HI.

Combining this approximate result with that in Eq. (4.15), one obtains

$$\eta_{\mathrm{p}}^{*}(h^{*}, z^{*}, b) \approx \eta_{\mathrm{p}}^{*}(0, 0, b) \left[\frac{\eta_{\mathrm{p}}^{*}(h^{*}, 0, \infty)}{\eta_{\mathrm{p}}^{*}(0, 0, \infty)}\right] \left[\frac{\eta_{\mathrm{p}}^{*}(0, z^{*}, \infty)}{\eta_{\mathrm{p}}^{*}(0, 0, \infty)}\right] . \tag{4.18}$$

Therefore, the predictions of model combining all the three nonlinear effects of FE, HI and EV seem to be well approximated as the product of three independent factors, each of which can be predicted using simpler models which incorporate the nonlinearities in isolation. The following section examines whether this approximate decoupling is also observed in bead-spring chains.

4.2 Chain models

4.2.1 Choice of parameter values

Rather thanexploring the nature of the coupling between the nonlinear phenomena in detail across a large domain in parameter space, the simulations whose results are presented in this section are performed for a small set of parameter values typically encountered in the literature on bead-spring chain models. Besides the number of beads N, and the dimensionless velocity gradient tensor $\boldsymbol{\kappa}^{*}$, the dimensionless parameters in the model are b, h^{*}, z^{*} and d^{*}. The rationale behind the choices of values for these parameters is discussed briefly below.

Although it is currently possible to simulate chains with much larger numbers of beads, recent studies indicate that chains with $N \sim 20$ are able to capture all qualitative features of longer chains [Hsieh *et al.*, 2003; Jendrejack *et al.*, 2000; Knudsen *et al.*, 1996; Kröger *et al.*, 2000; Li and Larson, 2000a,b]. As stated before in Chapter 2, the FENE parameter b is related to the number of Kuhn segments per spring, as through $b = 3N_{\mathrm{K,\,s}} - 5$. Since the FENE spring-force law (which is an approximation to the inverse Langevin force) is valid when $N_{\mathrm{K,\,s}} > O(10)$, simulations are typically performed with $b \geq 50$. Therefore, a value of $b = 50$ is chosen to study the effect of FE on the nature of the coupling between the nonlinear phenomena. The typical range of the HI parameter h^{*} used to examine the influence of this parameter on predictions of the bead-spring model is $0.1 \lesssim h^{*} \lesssim 0.3$ [Öttinger, 1987c]. For $N \geq 20$, it is well known that chains with $h^{*} = 0.25$ are able to reproduce

experimental results for the linear viscoelastic properties of solutions at the θ-state. The reason for this has been analyzed by several workers [Kröger *et al.*, 2000; Osaki, 1972; Zimm, 1956] and is discussed later in Chapter 8. This value is chosen for h^* in simulations of chains with HI.

As is well known, the excluded volume parameter z^* is related to another parameter z which measures the quality of the solvent, and [Kumar and Prakash, 2003; Öttinger, 1989b; Schäfer, 1999; Yamakawa, 1971]

$$z \equiv z^* N^{1/2} \,. \tag{4.19}$$

Theories for excluded volume effects in dilute polymer solutions show that for very long chains, the dependence of ratios such as $\alpha^2_{\mathrm{e,\,eq}}$ and α^3_{η} on the excluded volume parameter z^* always occurs through the combination $z^*\sqrt{N}$. For instance, predictions obtained for $\alpha^2_{\mathrm{e,\,eq}}$ for different (large) values of N and different values of z^*, can be nearly collapsed on to master curves when $\alpha^2_{\mathrm{e,\,eq}}$ is plotted against the parameter z defined in Eq. (4.19) above. Theories also suggest that z^* depends on temperature as $z^* \sim (1 - T_\theta/T)$, where T_θ is the theta temperature of the polymer-solvent system. This is corroborated by experiments, where it is observed that measurements of ratios such as $\alpha^2_{\mathrm{G,\,eq}} \equiv R_{\mathrm{G,\,eq}}/R^{\theta}_{\mathrm{G,\,eq}}$ for different polymer-solvent systems, molecular weights and temperatures can be collapsed on to master curves by plotting $\alpha^2_{\mathrm{G,\,eq}}$ against $v_0(1-T_\theta/T)M^{1/2}$, where v_0 is an empirically determined constant that depends solely on the polymer-solvent system [Berry, 1966; Graessley *et al.*, 1999; Miyaki and Fujita, 1981].

Asymptotic predictions of the variation of $\alpha^2_{\mathrm{e,\,eq}}$ or $\alpha^2_{\mathrm{G,\,eq}}$ with z can be obtained by taking the limits $z^* \to 0$ and $N \to \infty$ while keeping z constant. Although this behaviour is quite well known and has been studied extensively analytically [Schäfer, 1999; Yamakawa, 1971], Kumar and Prakash [2003] recently obtained predictions for universal master curves for equilibrium swelling ratios by extrapolating the data obtained in BD simulations using different chain lengths to the infinite chain limit. These authors further showed that the $\alpha^2_{\mathrm{G,\,eq}}$-versus-$z$ behaviour thus obtained is in excellent agreement with the experimental master plot obtained using the data of Miyaki and Fujita [1981].

Returning to the choice of the value of z^* in this section, it is observed that for

the range of polymer molecular weights currently available, values of z lie between 0 (the value for the theta state) and 10 for most experimental systems [Miyaki and Fujita, 1981; Schäfer, 1999; Yamakawa, 1971]. Here, a value of $z^* = 1/\sqrt{20} = 0.2236$ corresponding to $z = 1$ is chosen. Although this appears to be a small value, as will be shown shortly, the effect of EV interactions is significant even with this choice. The parameter d^* is set to unity, since it has been observed that for chains with $N = 20$, a choice of $d^* \approx 1$ results in the maximum influence of EV when $z = 1$ [Kumar and Prakash, 2003].

4.2.2 Modulation ratios

Keeping in mind the earlier observations of the simple nature of the coupling between the nonlinear phenomena in the case of the dumbbell model, it is useful to define the following ratios. For a given $\boldsymbol{\kappa}^*$ and at any instant t^*, it is expected that any property π predicted by a bead-spring chain model of with known N and with $d^* = 1$, would in general depend on the parameters h^*, z^*, and b, and therefore $\pi = \pi(h^*, z^*, b)$.

The ratio, σ_π, quantifies the value of the property π due to the inclusion of EV and HI, relative to its value in a model in which both effects are absent *i.e* $z^* = 0$ and $h^* = 0$. Using the notation π^{FE} to represent $\pi(0, 0, b)$,

$$\sigma_\pi(z^*, h^*, b) \equiv \frac{\pi(z^*, h^*, b)}{\pi^{\mathrm{FE}}} \,. \tag{4.20}$$

As $b \to \infty$, π^{FE} approaches the value of π predicted by the Rouse model, which is denoted as $\pi^{\mathrm{R}} = \pi(0, 0, \infty)$. The value of σ_π for models using Hookean springs is therefore independent of b, and $\sigma_{\pi,\infty}(z^*, h^*) \equiv \pi(z^*, h^*, \infty)/\pi^{\mathrm{R}}$. Similar ratios may be defined for models featuring either EV or HI, but not both. For a free-draining model ($h^* = 0$) in a good solvent ($z^* \neq 0$), the σ_π ratio is independent of h^* and is represented as ξ_π, where

$$\xi_\pi(z^*, b) \equiv \frac{\pi(z^*, 0, b)}{\pi^{\mathrm{FE}}} \,. \tag{4.21}$$

For a model for the θ-state ($z^* = 0$) but incorporating HI,

$$\chi_\pi(h^*, b) \equiv \frac{\pi(0, h^*, b)}{\pi^{\mathrm{FE}}}\,. \tag{4.22}$$

The ratios $\xi_{\pi,\infty}(z^*)$ and $\chi_{\pi,\infty}(h^*)$ may be correspondingly defined for models with Hookean springs, and are independent of b.

In the subsequent discussion, the subscripts π and ∞ will be dropped while describing qualitative features that are generally valid. In addition, since the ratios defined above appear to "modulate" the prediction of a plain FENE model to give the result of a model incorporating long-range interactions, the ratios σ, ξ and χ will be referred to as "modulation ratios".

4.2.3 Multiplicative decoupling of nonlinear phenomena

Figure 4.7 shows the dependence of the modulation ratios for the steady-state mean-squared end-to-end distance, *i.e.* $\pi = R_{\mathrm{e}}^{*\,2}$, with the dimensionless shear-rate, $\dot{\gamma}^*$. The modulation ratios for this property are identified with an "R" in subscript. From Fig. 4.7, it is evident that the values of z^* and h^* chosen here cause significant changes in property values of the properties, demonstrating that these parameter values are representative of strong EV and HI effects.

As expected, the ξ ratios are greater than unity, reflecting the fact that EV causes a swelling the overall chain dimensions. On the other hand, the χ ratios are close to unity at small shear-rates (since HI has no influence on the equilibrium $R_{\mathrm{e}}^{*\,2}$), but decrease rapidly at moderate shear-rates ($\beta \sim 1$). This is explained by the reduction in the drag forces experienced by the beads in the interior of a polymer coil as a consequence of the partial screening of the solvent velocity field caused by HI. Hence, a chain with HI deforms to a lesser extent than a free-draining chain in a shear flow. As shear-rate increases further, however, and the chain expands, the influences of both EV and HI diminish, and the ratios approach unity. Interestingly, it is seen that to a good extent, $\xi_R \approx \xi_{R,\infty}$, and $\chi_R \approx \chi_{R,\infty}$, indicating that FE has no significant influence on the ratios, for values of b in the range $50 \leq b < \infty$.

In Fig. 4.7 (c), the modulation ratio σ_R (solid circles), which measures the combined influence of EV and HI in a finitely extensible chain, has a value greater than

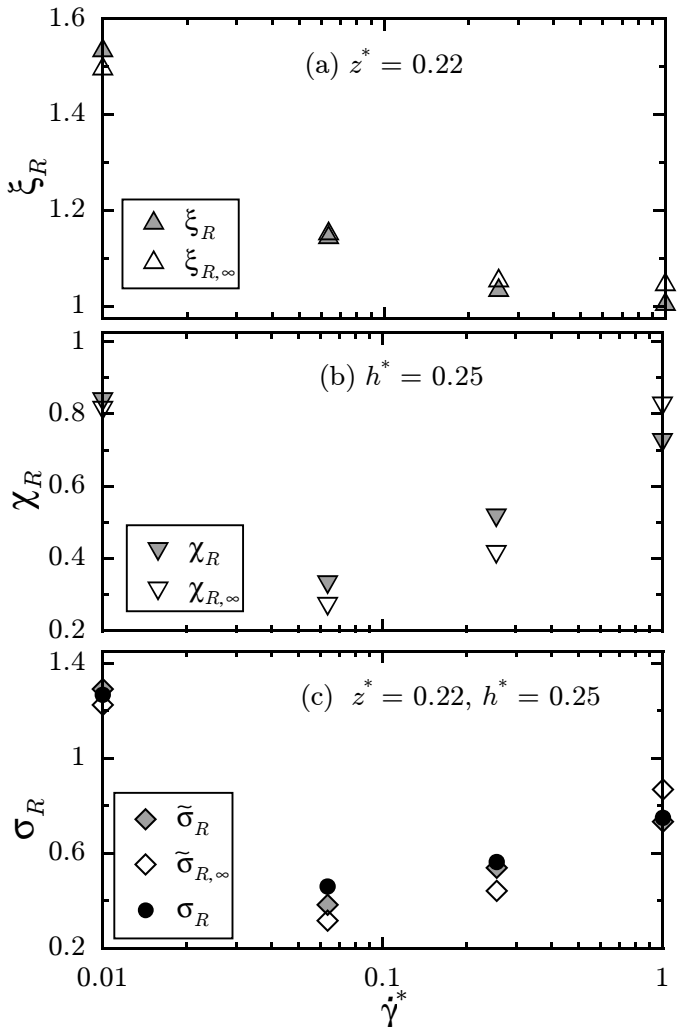

Figure 4.7: steady-state modulation ratios for the mean-squared end-to-end distance, versus the dimensionless shear-rate, $\dot{\gamma}^*$. In (c), $\widetilde{\sigma}_R = \xi_R \chi_R$ and $\widetilde{\sigma}_{R,\infty} = \xi_{R,\infty} \chi_{R,\infty}$.

1 at low shear-rates, but quickly decreases below unity, indicating that the influence of HI dominates with increasing shear-rate. This shows that, although EV and HI have opposing influences on the overall behaviour of the chain [De Gennes, 1979], they may not always cancel out each other. What is noticeable, however, is that the values of $\widetilde{\sigma}_R = \xi_R \chi_R$ calculated using the ratios shown in Figs. 4.7 (a) and (b) are quite close to σ_R for the entire range of shear-rates considered. Further, recalling the earlier observation that b has little influence on ξ_R and χ_R, plotting $\widetilde{\sigma}_{R,\infty} = \xi_{R,\infty} \chi_{R,\infty}$ on the same Figure shows that, to a reasonable extent, this

product is also reasonably close to σ_R for all shear-rates.

Based on these observations for $R_e^{*\,2}$, one could conjecture that an exact property $\pi \equiv \sigma_\pi \, \pi^{\mathrm{FE}}$ [Eq. (4.20)] predicted by a model incorporating EV, HI and FE, can be approximated as follows:

$$\pi(z^*, h^*, b) \;=\; \xi_\pi(z^*, b)\, \chi_\pi(h^*, b)\, \pi^{\mathrm{FE}}(b). \tag{4.23}$$

This equation indicates that the combined influence of EV and HI is separable into the independent factors ξ_π and χ_π. These functions are, however, dependent on b. Thus, this approximation achieves partial separation of the three nonlinearities, and will be referred to as the "PS" approximation in the rest of this article. An even stronger statement can be made in light of the results Figs. 4.7 (a) and (b) by replacing ξ_π and χ_π by $\xi_{\pi,\infty}$ and $\chi_{\pi,\infty}$ in the equation above, whereby

$$\pi(z^*, h^*, b) \;=\; \xi_{\pi,\infty}(z^*)\, \chi_{\pi,\infty}(h^*)\, \pi^{\mathrm{FE}}(b). \tag{4.24}$$

This approximation assumes that the influences of EV, HI and FE are fully separable ("FS"), with the contribution due to FE being the prediction of the plain FENE model. Figure (4.8) compares the predictions of the two approximations above for $R_e^{*\,2}$, and it is seen that the deviations from the exact results are small relative to the overall scale of the plot.

An advantage of relations such as those above is that one can use simpler models as "building blocks" to approximate the complete model. For example, in Eq. (4.24), ξ_∞ and χ_∞ can be evaluated using Rouse chains with EV and HI, respectively, while π^{FE} is the property predicted by a plain FENE model. Although this may offer no significant improvement from a simulation perspective, since it entails the simulation of three separate models in the place of one, this feature can nevertheless be exploited in the development of approximation schemes: it is sufficient to develop good approximations for each of the simpler individual cases, and then combine their predictions to approximate the complete model. Exact results from Brownian dynamics simulations are used to further examine the efficacy of the approximations above.

Considering the predictions for the steady-state rheological properties, η_p^* and

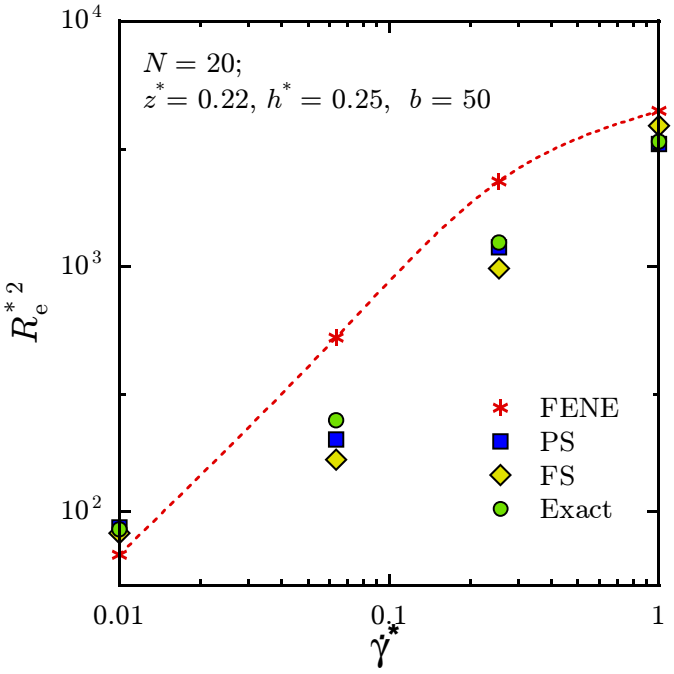

Figure 4.8: Comparison of the predictions of the approximations, with exact results for steady-state dimensionless mean-squared end-to-end distance versus the dimensionless shear-rate, $\dot{\gamma}^*$. The "$*$" symbols represent exact simulation results for a FENE chain with no interactions and the curve has been drawn to guide the eye. The "PS" in the legend refers to the approximation introduced in Eq. (4.23), while "FS" corresponds to Eq. (4.24). The rest of the notation used in the legend has been introduced in Fig. 4.7.

Ψ_1^* in Figs. 4.9 and 4.10 respectively, it is seen that both the approximations perform well. Predictions using the PS approximation (grey diamonds) are in closer agreement with the exact results (black circles), than those of the FS approximation (open diamonds). In the case of the second normal-stress difference coefficient Ψ_2^*, however, the modulation ratios are undefined, since $\Psi_2^* = 0$ at the steady-state, in any model with $h^* = 0$. Since this property is relatively small and difficult to measure experimentally, it is not considered any further in this Chapter.

Since the FS approximation is obtained by replacing $\widetilde{\sigma}$ with $\widetilde{\sigma}_\infty$, the deviation of this approximation indicates the extent to which FE modifies the ratios ξ and χ. For instance, Figs. 4.9 and 4.10 show that at the high shear-rate of $\dot{\gamma}^* = 1$, the results obtained using the FS approximation are practically the same as the plain FENE results. This results from the fact that ξ_∞ and χ_∞ are very close to unity at

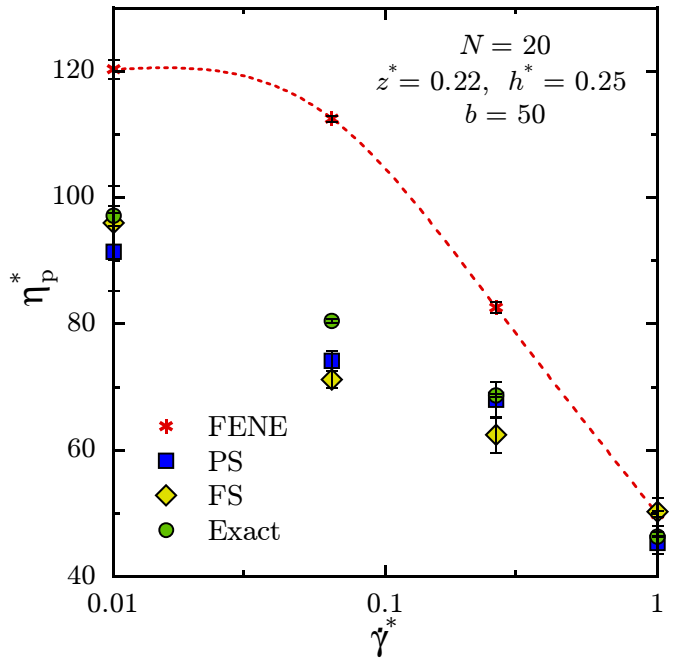

Figure 4.9: Comparison of the predictions of the approximations, with exact results for the dimensionless viscosity. The curves through the plain FENE results have been drawn to guide the eye.

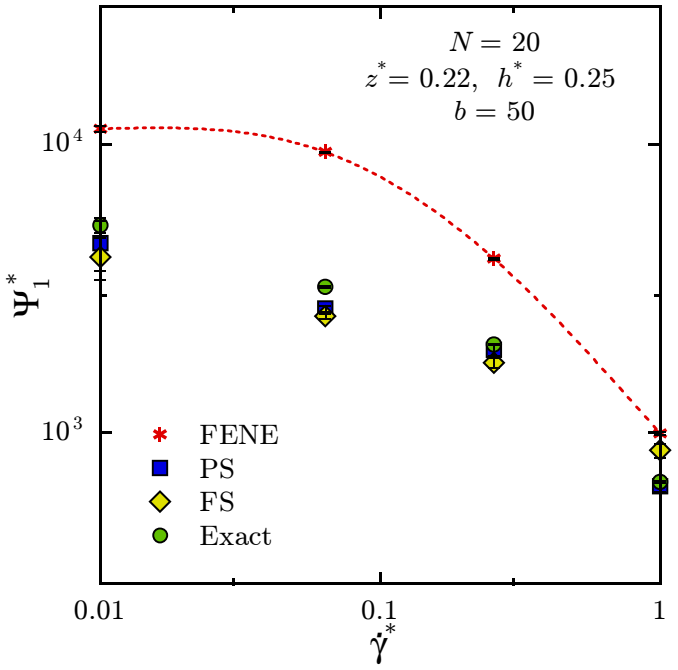

Figure 4.10: Comparison of the predictions of the approximations, with exact results for the dimensionless first normal-stress difference coefficient. The curves through the plain FENE results have been drawn to guide the eye.

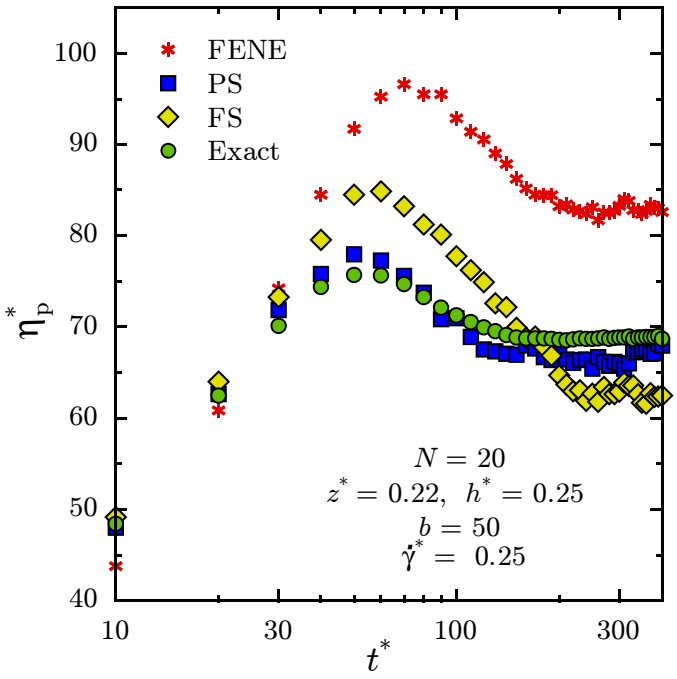

Figure 4.11: Comparison of the predictions of the approximations with exact results for transient growth of dimensionless shear viscosity on the sudden imposition of a constant shear-rate. The error bars are roughly of the same size, or smaller than the symbols used, and have been omitted for clarity.

very high shear-rates. On the other hand, the prediction of the PS approximation is below that of the FS approximation in both Fig. 4.9 and 4.10, indicating that $\xi\,\chi < \xi_\infty\,\chi_\infty$ for η_p^* and Ψ_1^*.

Figure 4.11 shows results for the transient behaviour of the viscosity on the sudden imposition of a constant value of the shear-rate in the nonlinear regime. The growth in the viscosity is characterized by a large overshoot in the plain FENE model [Doyle and Shaqfeh, 1998; Herrchen and Öttinger, 1997; van den Brule, 1993]. Inclusion of EV in the model tends to increase this overshoot, whereas HI attenuates it strongly (not shown). For the parameter values considered in Fig. 4.11, HI is the dominant effect, resulting in a smaller overshoot than the plain FENE model. The PS approximation does well in predicting this strong attenuation of the overshoot and is in good agreement with the exact results, whereas the FS approximation is only moderately successful. The influence of HI on the overshoot in η_p^* and Ψ_1^* is examined in greater detail in Chapter 6.

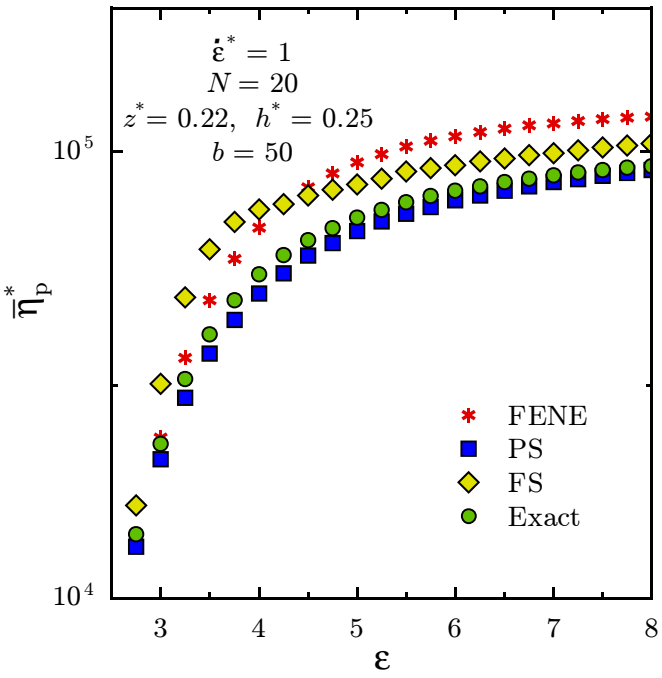

Figure 4.12: Comparison of the predictions of the approximations with exact results, for transient growth of dimensionless elongational viscosity, versus the Hencky strain $\epsilon = \dot{\epsilon}^* t^*$.

In elongational flows, it is well known that chains with Hookean springs do not reach a steady-state when the Weissenberg number Wi is greater than the critical value at which the coil-stretch transition occurs, Wi_c. For such values of Wi, an alternative definition of the ratios $\sigma_{\pi,\infty}$, $\xi_{\pi,\infty}$ and $\chi_{\pi,\infty}$ is used where a reasonably large value of b is taken to be a "reference" value, and the following assignment is made: $\sigma_{\pi,\infty} = \sigma_\pi(z^*, h^*, b_{\rm ref})$. The ratios $\xi_{\pi,\infty}$ and $\chi_{\pi,\infty}$ are analogously defined. To avoid introducing any new notation, the subscript "∞" here implies a model with $b = b_{\rm ref}$. The results shown below have been obtained with $b_{\rm ref} = 500$.

For the transient growth of the elongational viscosity on sudden imposition of uniaxial extensional flow at a dimensionless elongation rate $\dot{\varepsilon}^* = 1$, it is observed in Fig. 4.12 that although the agreement of the PS approximation with the exact results is excellent, the FS approximation does rather poorly, and is in fact worse than the plain FENE model for a large portion of the initial growth. These qualitative features are not expected to change significantly at higher elongation rates, since all the transient elongational viscosity curves begin to collapse on to a unique envelope

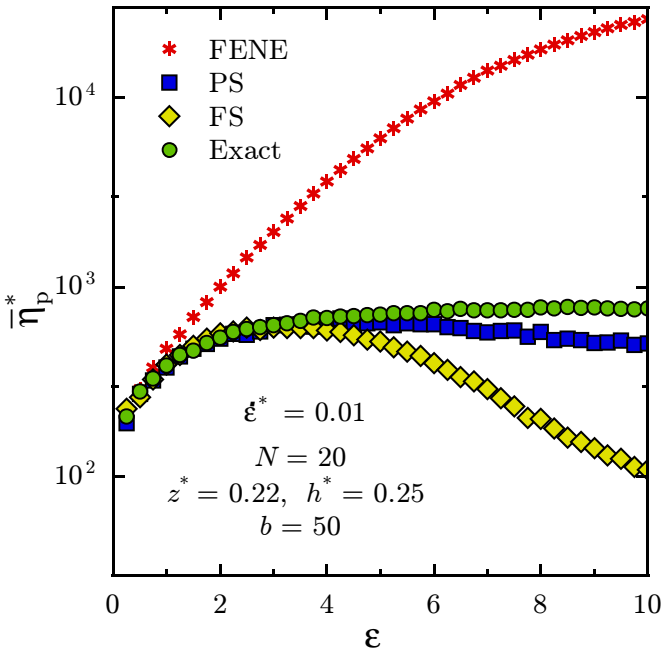

Figure 4.13: Comparison of the predictions of the approximations with exact results, for transient growth of dimensionless elongational viscosity, at $\dot{\varepsilon}^* = 0.01$.

as the elongation rate increases, and for $N = 20$ the curve for $\dot{\varepsilon}^* = 1$ is already close to this envelope (not shown). At a low strain rate (Fig. 4.13), however, even the PS approximation begins to break down at large values of the Hencky strain. This is unexpected, because in the case of shear flows, it was observed that both the approximations performed well at low shear-rates, closer to linear viscoelastic regime.

These differences are further highlighted when the modulation ratios are examined (Fig. 4.14). A significant difference between this case and all the other situations examined earlier, is that the modulation ratios decrease to much smaller values with increasing strain than before. This stems from the fact that the viscosity of the plain FENE chain grows to much higher values than that predicted by models with HI, at this elongation rate, as shown in Fig. 4.14.

An insight into this behaviour is gained by noting that the critical elongation rate $\dot{\epsilon}_c$ for the coil-stretch transition transition depends on whether or not a model includes HI [Magda *et al.*, 1988]. Hernandez Cifre and Garcia de la Torre [1999]

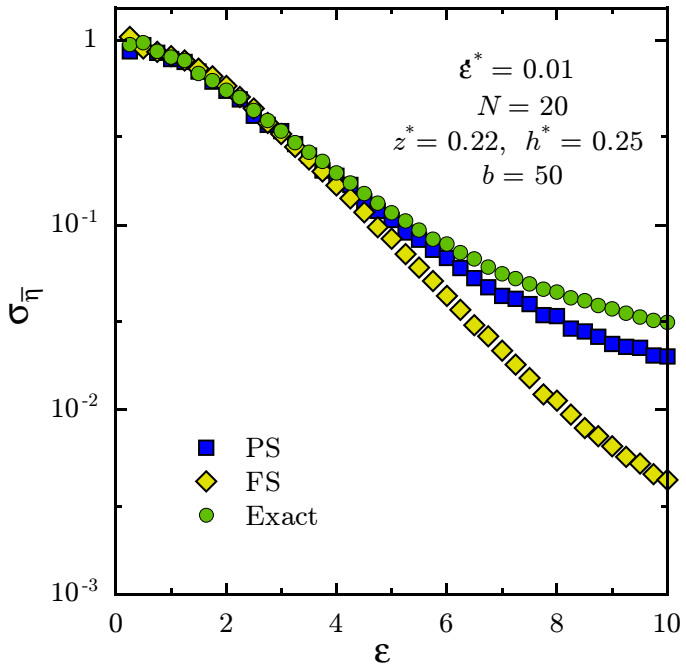

Figure 4.14: Comparison of the predictions of the approximations with exact results, for transient behaviour of the modulation ratio for elongational viscosity, at $\dot{\varepsilon}^* = 0.01$.

showed that EV has little effect on the value of $\dot{\varepsilon}_c^*$. However, HI plays a more dominant role in determining $\dot{\varepsilon}_c^*$. Hernandez Cifre and Garcia de la Torre found using simulations of FEBS chains with fluctuating HI that, with or without EV,

$$\dot{\varepsilon}_c^{*\,\mathrm{HI}} = 1.175 N^{-1.5}\,, \tag{4.25}$$

whereas, without HI,

$$\dot{\varepsilon}_c^{*\,\mathrm{no\ HI}} = 2.383 N^{-2}. \tag{4.26}$$

As is well known [Bird *et al.*, 1987b], the Rouse model predicts

$$\dot{\varepsilon}_c^{*\,\mathrm{Rouse}} = \sin^2(\pi/2N) \approx \frac{\pi^2}{4} N^{-2} = 2.467\, N^{-2}\,,\ \text{for large } N, \tag{4.27}$$

Using Eqs. (4.25) and (4.26) with $N = 20$, one obtains $\dot{\epsilon}_c^{*\,\mathrm{HI}} = 0.013$ and $\dot{\epsilon}_c^{*\,\mathrm{no\ HI}} = 7.075 \times 10^{-3}$. Therefore, the results shown in the Figs. 6 and 7 correspond to a case

where $\dot{\epsilon}_c^{*\,\mathrm{no\ HI}} < \dot{\varepsilon}^* < \dot{\epsilon}_c^{*\,\mathrm{HI}}$. As a result, the elongational viscosity for the plain FENE model grows to much larger values than those predicted by models with HI. The modulation ratios σ and χ then decrease to very small values, whereas the ξ's are close to unity since a model with EV alone has the same $\dot{\varepsilon}_c^*$ as a plain FENE model. The behaviour above also suggests that it may be more effective to determine the modulation ratios and the predictions of the FEBS model without HI and EV at the same Weissenberg number Wi (Eq. (2.108)), rather than at fixed dimensionless strain rates.

It was observed in simulations of dumbbells and 6-bead chains that both the approximations were quite accurate, in shear and extensional flows. In fact, it was found that for these small values of N, EV and HI appeared to couple additively [Prabhakar and Prakash, 2002]. This is a result of the fact that the ratios ξ and χ for low values of N deviate only marginally from unity. Therefore, if $\xi = 1 + \delta_{\mathrm{EV}}$ and $\chi = 1+\delta_{\mathrm{HI}}$, then $\widetilde{\sigma} = \xi\,\chi \approx 1+\delta_{\mathrm{EV}}+\delta_{\mathrm{HI}} = \xi+\chi-1$. Thus, it is reasonable to conclude that these approximations can be used for $N \sim O(10)$, for all shear-rates, and for elongation rates that are above Wi_c^{HI}.

The accuracy of the FS approximation as N increases may be estimated by considering analytical predictions of the asymptotic behaviour of long chains in the limit $N \to \infty$. Firstly, as pointed out already above, it may be necessary to calculate the obtain the predictions of the different models at the same Weissenberg number and strain, rather than the dimensionless strain rate and time. Secondly, Öttinger [1987b] showed using an approximate model incorporating FE and HI (but no EV) that at any fixed Weissenberg number and strain, the predictions of FEBS chain models approach those obtained with Rouse chains as N becomes very large. In other words, as N becomes large, the modulation ratios χ, ξ and σ approach predictions with Hookean springs, χ_∞, ξ_∞ and σ_∞.

Furthermore, a Renormalization Group (RG) analysis of Rouse chains with HI and/ or EV show that at any fixed Weissenberg number, the steady-state rheological properties in shear flows approach power-law behaviour with respect to N, as $N \to \infty$ [Öttinger, 1989b; Zylka and Öttinger, 1991], and $\eta_{\mathrm{p}}^* \sim N^{3\nu}$. The exponent ν is found to be a function of the solvent quality parameter z introduced previously in Eq. (4.19) in this Chapter, and a "draining parameter", $h \equiv h^*\sqrt{N}$, which is

discussed later in Chapter 7. As pointed out earlier, in the absence of EV effects, $z = 0$. When $z^* \neq 0$, $z \to \infty$ as $N \to \infty$ at a fixed z^*. This limit is commonly referred to as the "excluded volume limit" [Kumar and Prakash, 2003]. In the absence of HI, $h = 0$ for free-draining chains. The limit $h \to \infty$ is attained as $N \to \infty$ with h^* kept constant, and is referred to "non-draining" limit. The limiting values for ν calculated from the results of Öttinger [1989b] are shown in Table 4.1.

Table 4.1: The scaling exponent ν predicted by the RG calculations of Öttinger [1989b]. Viscosity η_{p}^* scales with N as $N^{3\nu}$. Here, $z \equiv z^*\sqrt{N_{\mathrm{s}}}$ as in Eq. (4.19) and $h \equiv h^*\sqrt{N_{\mathrm{s}}}$ is the draining parameter.

Model	z	h	ν
Rouse model	0	0	$\frac{2}{3}$
Theta chains, non-draining limit	0	$\to \infty$	$\frac{1}{2}$
EV limit, free-draining chains	$\to \infty$	0	$\frac{1}{2} + \frac{5}{32}$
EV limit, non-draining chains	$\to \infty$	$\to \infty$	$\frac{1}{2} + \frac{1}{16}$

Combining the observation stated above that the influence of the FE parameter b vanishes for large N, with the exponents in Table 4.1, one obtains the following asymptotic scaling relationships as $N \to \infty$:

$$\sigma_\eta \to \sigma_{\eta,\infty} \to N^{-5/16}, \tag{4.28}$$

$$\chi_\eta \to \chi_{\eta,\infty} \to N^{-1/2}, \tag{4.29}$$

$$\xi_\eta \to \xi_{\eta,\infty} \to N^{-1/32}, \tag{4.30}$$

$$\widetilde{\sigma}_\eta \to \widetilde{\sigma}_{\eta,\infty} = \chi_{\eta,\infty}\,\xi_{\eta,\infty} \to N^{-17/32}\,. \tag{4.31}$$

In the FS approximation for chains with Hookean springs, the ratio $\sigma_{\eta,\infty}$ is replaced by $\widetilde{\sigma}_{\eta,\infty}$. The relations above indicate that the ratio of $\widetilde{\sigma}_{\eta,\infty}$ to $\sigma_{\eta,\infty}$ decreases slowly as $N^{-3/32}$. In other words, at a fixed Weissenberg number the FS approximations predictions are estimated to deviate from the exact results for the viscosity roughly as $N^{-1/10}$. Since for $N = 20$ the FS approximation seems to do reasonably well,

it may be possible to use these approximations even for much larger N. However, since $\Psi_1^* \sim N^{6\,\nu}$, the deviations will grow faster as $N^{-1/5}$ for the first normal stress difference coefficient.

Chapter 5

Closure approximations: Governing equations

The Fokker-Planck equation for the configurational distribution function presented in Chapter 2 is the master equation governing the dynamics of the bead-spring model. The equivalent Itô stochastic differential equations can be integrated to directly calculate ensemble averages of interest without formally solving the Fokker-Planck equation for the distribution function. Although such BD simulations are computationally intense, exact analytical solutions for the distribution function are in general unavailable. The crux of the analytical intractability of the Fokker-Planck equation lies in the nonlinearities due to the spring force, excluded volume and/or hydrodynamic interactions. This is seen by considering the *exact* equation [Eq. (2.104)] for the evolution of the dimensionless second moment $\langle \boldsymbol{Q}_i^* \boldsymbol{Q}_j^* \rangle$ for a bead-spring model in which all three nonlinear phenomena of FE, EV and HI are represented:

$$\begin{aligned}
\langle \boldsymbol{Q}_i^* \boldsymbol{Q}_j^* \rangle_{(1)} &= \frac{d\langle \boldsymbol{Q}_i^* \boldsymbol{Q}_j^* \rangle}{dt^*} - \boldsymbol{\kappa}^* \cdot \langle \boldsymbol{Q}_i^* \boldsymbol{Q}_j^* \rangle - \langle \boldsymbol{Q}_i^* \boldsymbol{Q}_j^* \rangle \cdot \boldsymbol{\kappa}^{*\mathrm{T}} \\
&= -\frac{H^*}{4} \sum_{m=1}^{N_\mathrm{S}} \langle \boldsymbol{Q}_i^* \boldsymbol{Q}_m^* \xi_m \cdot \widetilde{\boldsymbol{A}}_{mj} + \widetilde{\boldsymbol{A}}_{im} \cdot \xi_m \boldsymbol{Q}_m^* \boldsymbol{Q}_j^* \rangle \\
&\quad + \frac{1}{4} \sum_{m,n=1}^{N_\mathrm{S}} \langle \boldsymbol{Q}_i^* \boldsymbol{Q}_n^* w_{nm}^* \cdot \widetilde{\boldsymbol{A}}_{mj} + \widetilde{\boldsymbol{A}}_{im} \cdot w_{mn}^* \boldsymbol{Q}_n^* \boldsymbol{Q}_j^* \rangle + \frac{1}{2} \langle \widetilde{\boldsymbol{A}}_{ij} \rangle \,.
\end{aligned} \tag{5.1}$$

It must be noted here that in this Chapter and for the rest of this thesis, the notation reverts back to using $\ell_s = R_s/\sqrt{3}$ [Eq. (2.49)] as the basic length scale. As a result of the nonlinearities in the functions ξ, E and $\boldsymbol{\Omega}$ introduced by the spring force law, EV, and HI respectively, the equation above for $\langle \boldsymbol{Q}_i^* \boldsymbol{Q}_j^* \rangle$ involves averages of complicated functions of the connector vectors on the right-hand side. These averages cannot be expressed as functions of the $\langle \boldsymbol{Q}_i^* \boldsymbol{Q}_j^* \rangle$ tensors, and require additional evolution equations of their own, which in turn involve more complicated averages, and so on. In other words, the evolution equations for the second moments, and for most other macroscopic averages including the polymer stress tensor $\boldsymbol{\tau}_p^*$, are not closed with respect to the averages in question.

One approach to generating approximate solutions is to make modifications to Eq. (5.1) above which lead to a set of closed equations for the second moments $\langle \boldsymbol{Q}_i^* \boldsymbol{Q}_j^* \rangle$. To be useful, the modifications should also consistently lead to expressions of all properties of interest, such as those occurring in the Kramer's expression for the stress,

$$\boldsymbol{\tau}_p^* = N_s \boldsymbol{\delta} - H^* \sum_{i=1}^{N_s} \langle \xi_i \boldsymbol{Q}_i^* \boldsymbol{Q}_i^* \rangle + \sum_{i,j=1}^{N_s} \langle w_{ij}^* \boldsymbol{Q}_i^* \boldsymbol{Q}_j^* \rangle \,, \tag{2.78}$$

in terms of the approximate second moments $\langle \boldsymbol{Q}_i^* \boldsymbol{Q}_j^* \rangle$, so that approximate predictions of the time evolution of macroscopic properties can be obtained. Since the quality of "closure approximations" cannot be ascertained *a priori* for arbitrary flows, it is necessary to test these approximations for a variety of flow situations and strengths by comparing their predictions with exact results obtained using other methods, such as BD simulations.

In this Chapter, the governing equations of some closure approximations for bead-spring models with HI, EV and/or FE are presented. Approximations for Rouse chains with HI are first discussed in Section 5.2. These approximations are well known, and the basic aim of this section is to show how the influence of fluctuations in HI are modeled with the well known Gaussian closure approximation. Approximate treatments of nonlinear forces in the absence of HI are next considered in Section 5.3. The Gaussian approximation for excluded volume interactions is first reviewed, and it is shown that the use of this approximation—which accounts

for the effect of fluctuations in EV interactions—can be interpreted in terms of a mean-field excluded volume potential. With this insight, a new closure approximation to handle the FENE nonlinearity is proposed. The resulting "FENE-PG" approximation is shown to be more general than the widely used FENE-P approximation. Following this, approximate models combining HI with nonlinear forces are taken up for discussion in Section 5.4. This is first attempted using a Hookean dumbbell model with EV and HI, and it is shown that the Gaussian approximation approach needs to be modified in order to ensure that the equilibrium solution is independent of hydrodynamic interactions. With this modification, an approximate model is derived that simultaneously incorporates the influence of fluctuations in all the three nonlinear phenomena of HI, EV and FE. In Section 5.5, some additional approximations for speeding up calculations are discussed, before concluding with a brief look in Section 5.6 at the numerical methods used to obtain solutions with the approximate models.

Before proceeding further, however, it is useful to first consider a few features that are common to all the closure approximations considered in the present work.

5.1 Common features

In what follows, the dimensionless second moments predicted by the approximations are denoted as $\boldsymbol{\sigma}^*_{ij}$ to distinguish them from the exact second moments $\langle\, \boldsymbol{Q}^*_i \boldsymbol{Q}^*_j \,\rangle$. In all the approximations considered in this work, the evolution equation for the second moments has the form

$$\boldsymbol{\sigma}^*_{ij,(1)} = -\frac{1}{4}\sum_{m=1}^{N_\mathrm{S}} [\boldsymbol{\sigma}^*_{im}\cdot\overline{\boldsymbol{M}}_{mj} + \overline{\boldsymbol{M}}^{\mathrm{T}}_{mi}\cdot\boldsymbol{\sigma}^*_{mj}] + \frac{1}{2}\overline{\boldsymbol{D}}_{ij}\,. \tag{5.2}$$

The various approximations studied here differ in their expressions for the dimensionless tensors $\overline{\boldsymbol{M}}_{ij}$ and $\overline{\boldsymbol{D}}_{ij}$. These tensors contain expectations involving the nonlinearities ξ_i, $\widetilde{\boldsymbol{A}}_{ij}$ and w^*_{ij}. However, all these expectations are themselves nonlinear functions of the second moments $\boldsymbol{\sigma}^*_{ij}$. The equations above thus constitute a set of N_S^2 coupled, nonlinear ordinary differential equations (ODE's) for the approximate second moments $\boldsymbol{\sigma}^*_{ij}$. By comparing Eq. (5.2) with Eq. (5.1), it is possible to

see that the tensors $\overline{\boldsymbol{D}}_{ij}$ are related to the average $\langle \widetilde{\boldsymbol{A}}_{ij} \rangle$. These tensors thus share the symmetry of the diffusion tensors and $\overline{\boldsymbol{D}}_{ij} = \overline{\boldsymbol{D}}^{\mathrm{T}}_{ji} = \overline{\boldsymbol{D}}^{\mathrm{T}}_{ij} = \overline{\boldsymbol{D}}_{ji}$.

It is straightforward to show that the following Fokker-Planck equation,

$$\frac{\partial \hat{\psi}}{\partial t^*} = -\sum_{i=1}^{N_\mathrm{s}} \frac{\partial}{\partial \boldsymbol{Q}^*_i} \cdot \left\{ \boldsymbol{\kappa}^* \cdot \boldsymbol{Q}^*_i - \frac{1}{4} \sum_{j=1}^{N_\mathrm{s}} \overline{\boldsymbol{M}}^{\mathrm{T}}_{ji} \cdot \boldsymbol{Q}^*_j \right\} \hat{\psi} + \frac{1}{4} \sum_{i,\,j=1}^{N_\mathrm{s}} \overline{\boldsymbol{D}}_{ij} : \frac{\partial^2 \hat{\psi}}{\partial \boldsymbol{Q}^*_i \partial \boldsymbol{Q}^*_j} \,, \quad (5.3)$$

leads to the same governing equation for the second moments as in Eq. (5.2). In other words, the tensors $\boldsymbol{\sigma}^*_{ij}$ are the second moments of the distribution function $\hat{\psi}$ governed by the Fokker-Planck equation in Eq. (5.3). In kinetic theory, approximations governed by equations of the form above are usually referred to as "mean-field" approximations [Hütter *et al.*, 2003; Hütter and Öttinger, 1996; Öttinger, 1996a]. An important feature of a mean-field approximation such as those considered here, is that unlike the Fokker-Planck equation for the original model, the equation above for the approximations is now nonlinear in $\hat{\psi}$ through its dependence on its expectations, but is linear with respect the connector vectors $\boldsymbol{Q}^*_i$.

It is well known that if the $3N_\mathrm{s} \times 3N_\mathrm{s}$ block-matrix whose 3×3 blocks comprise the tensors $\overline{\boldsymbol{D}}_{ij}$ is positive-definite, the solution to a Fokker-Planck equation of the form shown above is a multi-variate Gaussian [Öttinger, 1987b],

$$\hat{\psi} = \mathcal{N} \exp \left[-\frac{1}{2} \sum_{i,j=1}^{N_\mathrm{s}} \boldsymbol{Q}^*_i \cdot \boldsymbol{\rho}^*_{ij} \cdot \boldsymbol{Q}^*_j \right] , \quad (5.4)$$

where $\mathcal{N}$ is a normalization factor, and the tensors $\boldsymbol{\rho}^*_{ij}$ are related to the second moments $\boldsymbol{\sigma}^*_{ij}$ of the Gaussian distribution $\hat{\psi}$ through the following set of equations

$$\sum_{m=1}^{N_\mathrm{s}} \boldsymbol{\sigma}^*_{im} \cdot \boldsymbol{\rho}^*_{mj} = \delta_{ij} \boldsymbol{\delta} \,. \quad (5.5)$$

Since Eq. (5.2) is completely expressed in terms of the tensors $\boldsymbol{\sigma}^*_{ij}$ alone, on obtaining these tensors at time t^* after integrating Eq. (5.2), Eq. (5.5) can be treated as a set of N_s^2 linear algebraic equations for the tensors $\boldsymbol{\rho}^*_{ij}$, and therefore, as is well known, the Gaussian distribution $\hat{\psi}$ is completely specified once its second moments $\boldsymbol{\sigma}^*_{ij}$ are known. It is usually not required to explicitly calculate the tensors $\boldsymbol{\rho}^*_{ij}$, and Eq. (5.5)

above is used in algebraic manipulations to eliminate the $\boldsymbol{\rho}^*_{ij}$ tensors in favour of the $\boldsymbol{\sigma}^*_{ij}$ tensors.

The Gaussian nature of the approximate probability distribution is the key to achieving closure of Eq. (5.1), since the known form of the distribution and its well studied properties can be used to reduce some of the complicated expectations occurring in the original equation for the second moments, and in the equation for the stress [Eq. (2.78)], to algebraic functions of the second moments $\boldsymbol{\sigma}^*_{ij}$. An important property of Gaussian distributions is Wick's decomposition rule. For any Gaussian random variable $\boldsymbol{x}$ with mean $\langle \boldsymbol{x} \rangle = 0$, given a function $f(\boldsymbol{x})$,

$$\langle \boldsymbol{x} f(\boldsymbol{x}) \rangle = \langle \boldsymbol{x}\boldsymbol{x} \rangle \cdot \langle \frac{\partial f}{\partial \boldsymbol{x}} \rangle = \langle \frac{\partial f}{\partial \boldsymbol{x}} \rangle \cdot \langle \boldsymbol{x}\boldsymbol{x} \rangle \,, \tag{5.6}$$

provided the expectation $\langle \partial f / \partial \boldsymbol{x} \rangle$ exists for the Gaussian distribution, $\hat{\psi}$.

While developing closure approximations, it is desirable to retain the independence of the exact solution at equilibrium from the HI parameter h^*. The equilibrium solution of Eq. (5.2) is obtained by setting the convected derivative on the left-hand side of that equation to $\mathbf{0}$. The isotropic conditions at equilibrium imply that $\boldsymbol{\sigma}^*_{ij,\,\mathrm{eq}} = \sigma^*_{ij,\,\mathrm{eq}}\boldsymbol{\delta}$, $\overline{\boldsymbol{M}}_{ij,\,\mathrm{eq}} = \overline{M}_{ij,\,\mathrm{eq}}\boldsymbol{\delta} = \overline{M}_{ji,\,\mathrm{eq}}\boldsymbol{\delta}$, and $\overline{\boldsymbol{D}}_{ij,\,\mathrm{eq}} = \overline{D}_{ij,\,\mathrm{eq}}\boldsymbol{\delta}$. Using these results, Eq. (5.2) can be reduced to

$$0 = -\frac{1}{4}\sum_{m=1}^{N_\mathrm{s}} [\sigma^*_{im,\,\mathrm{eq}}\overline{M}_{mj,\,\mathrm{eq}} + \overline{M}_{im,\,\mathrm{eq}}\sigma^*_{mj,\,\mathrm{eq}}] + \frac{1}{2}\overline{D}_{ij,\,\mathrm{eq}} \,. \tag{5.7}$$

As stated earlier, the quantities $\overline{D}_{ij,\,\mathrm{eq}}$ are obtained by averaging the diffusion tensors. In the approximations considered in this work, the $N_\mathrm{s} \times N_\mathrm{s}$ matrix whose elements are $\overline{D}_{ij,\,\mathrm{eq}}$ is symmetric and positive definite. Denoting the (i,j)-th element of the inverse of the matrix consisting of the $\overline{D}_{ij,\,\mathrm{eq}}$'s as $\overline{D}^{-1}_{ij,\,\mathrm{eq}}$, Eq. (5.7) above can be written as

$$0 = \sum_{m=1}^{N_\mathrm{s}} [U_{im}\,\overline{D}_{mj,\,\mathrm{eq}} + \overline{D}_{im,\,\mathrm{eq}}\,U_{mj}] \,, \tag{5.8}$$

where,

$$U_{ij} \equiv \sum_{k,l=1}^{N_\mathrm{s}} \sigma^*_{ik,\,\mathrm{eq}}\, \overline{M}_{kl,\,\mathrm{eq}} \overline{D}^{-1}_{lj,\,\mathrm{eq}} - \delta_{ij}\,. \tag{5.9}$$

Equation (5.8) is a homogeneous linear equation for the quantities U_{ij}, whose unique solution for all $i,\, j = 1, \ldots, N_\mathrm{s}$ is,

$$U_{ij} = 0\,. \tag{5.10}$$

Therefore, using Eq. (5.9), one obtains

$$\sum_{k,l=1}^{N_\mathrm{s}} \sigma^*_{ik,\,\mathrm{eq}}\, \overline{M}_{kl,\,\mathrm{eq}} \overline{D}^{-1}_{lj,\,\mathrm{eq}} = \delta_{ij}\,, \tag{5.11}$$

or,

$$\sum_{m=1}^{N_\mathrm{s}} \overline{M}_{im,\,\mathrm{eq}}\, \overline{D}^{-1}_{mj,\,\mathrm{eq}} = \rho^*_{ij,\,\mathrm{eq}}\,. \tag{5.12}$$

Thus, it is evident that $\sigma^*_{ij,\,\mathrm{eq}}$, and hence the Gaussian distribution at equilibrium in the closure approximations, will be independent of the parameter h^* only if the left-hand side of Eq. (5.12) above is independent of that parameter. As shall be shown in this Chapter, not all closure approximations lead to h^*-independent second moments.

With this background in mind, the details of the closure approximations used in this study are presented below. Section 5.2 reviews some well known approximations for treating HI. The approximations in Section 5.2 are outlined for Rouse chains, in the absence of complexities arising from FE and EV effects. In Section 5.3, approximations for free-draining chains without HI are considered. The approximations for HI, EV and FE are then brought together in Section 5.4. In spite of the gains in computational efficiency with the closure approximations, it is still not possible to explore the behaviour of very long chains. Further improvements in speed can

be achieved by reducing the number of equations to be integrated by employing additional diagonalization assumptions. The equations for these approximations are derived for chains without EV interactions in Section 5.5. Finally, the numerical methods used in the calculations performed in this study are briefly discussed in Section 5.6.

5.2 Rouse chains with hydrodynamic interactions

As discussed in Chapter 2, with $\ell_{\mathrm{s}} = R_{\mathrm{s}}/\sqrt{3}$, $H^* = H\,\ell_{\mathrm{s}}^2/k_{\mathrm{B}}T = 1$ for Rouse chains. In the absence of EV interactions Eqs. (5.1) and Eq. (2.78) above reduce respectively to

$$\langle\, \boldsymbol{Q}_i^* \boldsymbol{Q}_j^* \,\rangle_{(1)} = -\frac{1}{4}\sum_{m=1}^{N_{\mathrm{s}}} \langle \boldsymbol{Q}_i^* \boldsymbol{Q}_m^* \cdot \widetilde{\boldsymbol{A}}_{mj} + \widetilde{\boldsymbol{A}}_{im} \cdot \boldsymbol{Q}_m^* \boldsymbol{Q}_j^* \rangle + \frac{1}{2}\langle \widetilde{\boldsymbol{A}}_{ij} \rangle\,, \tag{5.13}$$

and

$$\boldsymbol{\tau}_{\mathrm{p}}^* = N_{\mathrm{s}}\boldsymbol{\delta} - \sum_{i=1}^{N_{\mathrm{s}}} \boldsymbol{\sigma}_{ii}^*\,. \tag{5.14}$$

Thus, for Rouse chains, the polymer stress is directly related to the second moments of the distribution. A good starting point for discussing closure approximations for bead-spring models in general, and for chains with HI in particular, is the Zimm model.

5.2.1 Equilibrium Averaging: The Zimm model

Following Kirkwood and Riseman's [1948] treatment of hydrodynamic interactions in bead-rod chains, Zimm introduced "equilibrium-averaging" [1] of hydrodynamic interactions, which involves replacing the tensor $\boldsymbol{\Omega}_{\nu\mu}$ with its equilibrium average

[1] In much of the earlier literature on closure approximations, the word "preaveraging" is generally used. In this thesis, this term is avoided, and the kind of averaging used is explicitly stated. The replacement of fluctuating nonlinearities by averages of any kind are generally referred to as "mean-field" approximations.

$\langle \boldsymbol{\Omega}_{\nu\mu} \rangle_{\rm eq} = \int \boldsymbol{\Omega}_{\nu\mu} P_{\rm eq}(\boldsymbol{r}_{\mu\nu})\, d\boldsymbol{r}_{\mu\nu}$, where $P_{\rm eq}(\boldsymbol{r}_{\mu\nu})$ is the equilibrium probability distribution for the displacement $\boldsymbol{r}_{\mu\nu} = \boldsymbol{r}_\nu - \boldsymbol{r}_\mu$ between the ν-th and μ-th beads. In the absence of EV interactions, the equilibrium distribution for chains with Hookean springs is a Gaussian distribution for which (in dimensional terms)

$$\boldsymbol{\sigma}_{ij,\,\rm eq} = \delta_{ij}\, \ell_{\rm S}^2 \boldsymbol{\delta}\,, \tag{5.15}$$

where $\ell_{\rm S} = \ell_{\rm H} = \sqrt{k_{\rm B}T/H}$ for Hookean springs. The displacement $\boldsymbol{r}_{\mu\nu}$ is related to the connector vectors through [Eq. (2.26)],

$$\boldsymbol{r}_{\mu\nu} = \sum_{i=1}^{N_{\rm S}} \Delta\Theta^i_{\mu\nu} \boldsymbol{Q}_i\,. \tag{5.16}$$

Since $\boldsymbol{r}_{\mu\nu}$ is a linear combinations of the connector vectors, $P_{\rm eq}(\boldsymbol{r}_{\mu\nu})$ is also a Gaussian distribution whose variance

$$\boldsymbol{S}_{\mu\nu,\,\rm eq} \equiv \langle \boldsymbol{r}_{\mu\nu} \boldsymbol{r}_{\mu\nu} \rangle_{\rm eq} = \sum_{i,j=1}^{N_{\rm S}} \Delta\Theta^{ij}_{\mu\nu} \boldsymbol{\sigma}_{ij,\,\rm eq} = |\nu - \mu|\, \ell_{\rm S}^2 \boldsymbol{\delta}\,. \tag{5.17}$$

Although the Oseen-Burgers description of HI is known to be inaccurate when the pair-wise separation of beads is comparable to the size of the beads, in the development of closure approximations for chains with HI, it is especially advantageous to use the Oseen-Burgers definition of the HI tensor. A deeper reason for this choice is that the hydrodynamic behaviour of long polymer chains is dominated by the interactions between non-adjacent beads. On an average, for large values of N, the separation between most non-adjacent bead pairs is much larger than their sizes. Since the strength of HI decreases slowly as the reciprocal of the inter-bead separation, it is the long (spatial) range nature of the interaction that is important to the accuracy of approximations. Therefore, the short-range inaccuracy of the Oseen-Burgers description is relatively unimportant [Öttinger, 1987a; Zimm, 1980].

The Oseen-Burgers form of the HI tensor can be derived as the Greens function of the linearized Navier-Stokes equation, and can hence be represented as [Doi and

Edwards, 1986]

$$\boldsymbol{\Omega}(\boldsymbol{r}) = \frac{1}{(2\pi)^3 \eta_\mathrm{s}} \int \frac{1}{k^2} \left(\boldsymbol{\delta} - \frac{\boldsymbol{k}\boldsymbol{k}}{k^2} \right) e^{i\boldsymbol{k}\cdot\boldsymbol{r}} \, d\boldsymbol{k} \,, \tag{5.18}$$

where, in the context of polymer molecules, $\boldsymbol{r}$ is the displacement between a pair of hydrodynamically interacting points on the chain. Using this in conjunction with the Gaussian equilibrium probability distribution function P_eq leads to [Bird *et al.*, 1987b]

$$\langle \boldsymbol{\Omega}_{\mu\nu} \rangle_\mathrm{eq} = \frac{2}{3(2\pi)^{3/2} \eta_\mathrm{s}} \frac{1}{\ell_\mathrm{s}^2 \sqrt{|\nu - \mu|}} \boldsymbol{\delta} \,. \tag{5.19}$$

Substituting this result in the definition of the diffusion tensors leads to a modified diffusion tensor given by

$$\langle \widetilde{\boldsymbol{A}} \rangle_{ij,\,\mathrm{eq}} = \widetilde{A}_{ij} \boldsymbol{\delta} = \left[A_{ij} + \frac{2\,\zeta}{3(2\pi)^{3/2} \eta_\mathrm{s}} \frac{1}{\ell_\mathrm{s}} \left(\frac{2}{\sqrt{|i-j|}} - \frac{1}{\sqrt{|i-j+1|}} - \frac{1}{\sqrt{|i-j-1|}} \right) \right] \boldsymbol{\delta}, \tag{5.20}$$

where the convention $1/\sqrt{0} = 0$ is used. The $N_\mathrm{s} \times N_\mathrm{s}$ matrix formed by $\widetilde{A}_{ij}$ is known as the modified Rouse matrix [Bird *et al.*, 1987b]. This result also points naturally to the definition of a dimensionless hydrodynamic interaction parameter h^* as

$$h^* = \frac{\zeta}{6\pi^{3/2} \eta_\mathrm{s} \, \ell_\mathrm{s}} = \frac{a}{\sqrt{\pi} \, \ell_\mathrm{s}}. \tag{5.21}$$

where, in this context, $\ell_\mathrm{s}^2 = \ell_\mathrm{H}^2$. With this definition, Eq. (5.20) can be recast as

$$\langle \widetilde{\boldsymbol{A}} \rangle_{ij,\,\mathrm{eq}} = \widetilde{A}_{ij} \boldsymbol{\delta} = \left[A_{ij} + \sqrt{2} h^* \left(\frac{2}{\sqrt{|i-j|}} - \frac{1}{\sqrt{|i-j+1|}} - \frac{1}{\sqrt{|i-j-1|}} \right) \right] \boldsymbol{\delta}. \tag{5.22}$$

The following governing equation for the Zimm model is the obtained by replacing $\widetilde{\boldsymbol{A}}_{ij}$ with $\widetilde{A}_{ij}\boldsymbol{\delta}$ for all $i, j = 1, \ldots, N_\mathrm{s}$ in Eq. (5.13):

$$\boldsymbol{\sigma}^*_{ij,(1)} = -\frac{1}{4}\sum_{m=1}^{N_\mathrm{s}}[\boldsymbol{\sigma}^*_{im}\widetilde{A}_{mj} + \widetilde{A}_{im}\boldsymbol{\sigma}^*_{mj}] + \frac{1}{2}\widetilde{A}_{ij}\boldsymbol{\delta}\,. \tag{5.23}$$

Since the elements of the modified Rouse matrix $\widetilde{A}_{im}$ are constants, the right-hand side of the equation above depends solely on the second moments $\boldsymbol{\sigma}^*_{ij}$, and closure is thus achieved. Comparing Eq. (5.23) with Eq. (5.2), it is clear that for the Zimm model, $\overline{\boldsymbol{M}}_{ij} = \overline{\boldsymbol{D}}_{ij} = \widetilde{A}_{ij}\boldsymbol{\delta}$. Moreover, this equality immediately leads to $\boldsymbol{\rho}^*_{ij,\,\mathrm{eq}} = \delta_{ij}\boldsymbol{\delta}$ at equilibrium [Eq. (5.12)], from which one trivially obtains the equilibrium second moments $\boldsymbol{\sigma}^*_{ij,\,\mathrm{eq}} = \delta_{ij}\boldsymbol{\delta}$, which are in fact the exact second moments of the equilibrium distribution for Rouse chains. Starting with these equilibrium initial conditions, the evolution of the stress in unsteady flows can be computed after integrating the set of ODE's in Eq. (5.23) above.

The predictions of linear viscoelastic properties of dilute solutions under theta conditions with the Zimm model are in good agreement with experimental data [Johnson *et al.*, 1970; Sahouani and Lodge, 1992; Yamakawa, 1971]. This model successfully reproduces the experimentally observed molecular weight scaling of linear viscoelastic properties in theta solutions, and clearly establishes HI as a key phenomenon in the dynamics of dilute polymer solutions. However, the equilibrium-averaging of HI in the Zimm model results in predictions of shear-rate independent steady-state viscosity, η_p, and first normal stress difference coefficient, Ψ_1. This contrasts with experiment in which η_p, [Noda *et al.*, 1968] and Ψ_1 [Gupta *et al.*, 2000; Hsieh and Larson, 2004] are observed to depend on shear-rate.

5.2.2 Consistent-averaging of HI

Fixman [1966b] showed that shear-rate dependent material functions could be obtained by using *non-equilibrium* averages of the hydrodynamic interaction tensors, instead of the equilibrium averages. Fixman used a "boson-operator" formalism along with additional approximations (discussed in greater detail in Section 5.5)

to directly solve the modified Fokker-Planck equation for the approximate probability distribution, and obtained numerical results using an iterative technique [Magda *et al.*, 1988]. Öttinger [1987a] used the same idea of non-equilibrium averaged HI tensors, but avoided the additional approximations and the complexities of the boson-operator technique by considering evolution equations for the second moments. Öttinger's treatment of "consistently-averaged" HI is followed in this study due to its conceptual simplicity, and is reproduced below.

Öttinger pointed out that the replacement of the configuration dependent diffusion tensors $\widetilde{\boldsymbol{A}}_{ij}$ in Eq. (5.13) with their averages $\overline{\boldsymbol{A}}_{ij} \equiv \langle \widetilde{\boldsymbol{A}}_{ij} \rangle$ calculated consistently using the non-equilibrium distribution function leads to the following equation for the second moments

$$\boldsymbol{\sigma}^*_{ij,(1)} = -\frac{1}{4} \sum_{m=1}^{N_\mathrm{S}} [\boldsymbol{\sigma}^*_{im} \cdot \overline{\boldsymbol{A}}_{mj} + \overline{\boldsymbol{A}}_{im} \cdot \boldsymbol{\sigma}^*_{mj}] + \frac{1}{2} \overline{\boldsymbol{A}}_{ij} \,. \tag{5.24}$$

In the equation above, the averages $\overline{\boldsymbol{A}}_{ij}$ are assumed to be calculated "consistently", that is, with respect to the approximate distribution $\hat{\psi}$. Thus, in this approximation, $\overline{\boldsymbol{M}}_{ij} = \overline{\boldsymbol{D}}_{ij} = \overline{\boldsymbol{A}}_{ij}$ [Eq. (5.2)].

The definition of $\widetilde{\boldsymbol{A}}_{ij}$ in Eq. (2.8) shows that any averaged version of the diffusion tensors requires averaging of the HI tensors. Since the modified distribution $\hat{\psi}$ for the connector vectors is a Gaussian, the corresponding distribution $\hat{P}(\boldsymbol{r}_{\mu\nu})$ for the (dimensional) displacement $\boldsymbol{r}_{\mu\nu}$ is also a Gaussian of the form:

$$\hat{P}(\boldsymbol{r}_{\mu\nu}) = \frac{1}{\sqrt{(2\pi)^3 \det[\boldsymbol{S}_{\mu\nu}]}} \exp\left[-\frac{1}{2} \boldsymbol{S}^{-1}_{\mu\nu} : \boldsymbol{r}_{\mu\nu} \boldsymbol{r}_{\mu\nu} \right] , \tag{5.25}$$

where $\boldsymbol{S}_{\mu\nu} \equiv \langle \boldsymbol{r}_{\mu\nu} \boldsymbol{r}_{\mu\nu} \rangle$ is the variance of the non-equilibrium Gaussian probability distribution $\hat{P}$.

At this juncture, it is useful to introduce the following second-rank function of a second-rank tensor $\mathbf{s}$ [Öttinger, 1987a; Zylka and Öttinger, 1991]

$$\boldsymbol{H}(\mathbf{s}) \equiv \frac{3}{2(2\pi)^{3/2}} \int \frac{1}{k^2} \left(\boldsymbol{\delta} - \frac{\boldsymbol{k}\boldsymbol{k}}{k^2} \right) \exp(-\frac{1}{2} \boldsymbol{k}\boldsymbol{k} : \mathbf{s}) \, d\boldsymbol{k} \,. \tag{5.26}$$

The function $\boldsymbol{H}$ has the following important properties:

$$\boldsymbol{H} = \boldsymbol{H}^{\mathrm{T}}\,, \tag{5.27}$$

$$\boldsymbol{H}(\boldsymbol{\delta}) = \boldsymbol{\delta}\,, \tag{5.28}$$

and,

$$\boldsymbol{H}(\lambda \mathbf{s}) = \lambda^{-1/2}\boldsymbol{H}(\mathbf{s})\,. \tag{5.29}$$

The average of the HI tensor $\boldsymbol{\Omega}(\boldsymbol{r}_{\mu\nu})$ evaluated with $\hat{P}$ can be expressed in terms of the $\boldsymbol{H}$ function:

$$\begin{aligned}\langle \zeta \boldsymbol{\Omega}\rangle &= \frac{2\,\zeta}{3(2\pi)^{3/2}\eta_{\mathrm{s}}}\boldsymbol{H}(\boldsymbol{S}_{\mu\nu})\,,\\ &= \sqrt{2}h^{*}\boldsymbol{H}(\boldsymbol{S}^{*}_{\mu\nu})\,,\end{aligned} \tag{5.30}$$

where $\boldsymbol{S}^{*}_{\mu\nu} \equiv (1/\,\ell_{\mathrm{s}}^{2})\boldsymbol{S}_{\mu\nu}$ is the dimensionless variance of the Gaussian distribution $\hat{P}$.

Using the equations above, the diffusion tensors $\overline{\boldsymbol{A}}_{ij}$ in the model with consistently averaged HI can be expressed as

$$\overline{\boldsymbol{A}}_{ij} \equiv \langle \widetilde{\boldsymbol{A}}_{ij}\rangle = A_{ij}\boldsymbol{\delta} + \sqrt{2}h^{*}\left[\boldsymbol{H}_{ij} + \boldsymbol{H}_{i+1,\,j+1} - \boldsymbol{H}_{i+1,\,j} - \boldsymbol{H}_{i,\,j+1}\right]\,, \tag{5.31}$$

where $\boldsymbol{H}_{\mu\nu}$ denotes $\boldsymbol{H}(\boldsymbol{S}^{*}_{\mu\nu})$. As in Eq. (5.17), the dimensionless variances $\boldsymbol{S}^{*}_{\mu\nu}$ can be written as linear combinations of the second moment tensors $\boldsymbol{\sigma}^{*}_{ij}$,

$$\boldsymbol{S}^{*}_{\mu\nu} = \sum_{i,j=1}^{N_{\mathrm{s}}} \Delta\Theta^{ij}_{\mu\nu}\boldsymbol{\sigma}^{*}_{ij}\,, \tag{5.32}$$

and hence the consistently-averaged diffusion tensors $\overline{\boldsymbol{A}}_{ij}$ are all functions of the second moment tensors alone. At equilibrium, for bead-spring chains without EV interactions, $\boldsymbol{S}^{*}_{\mu\nu,\,\mathrm{eq}} = |\nu-\mu|\boldsymbol{\delta}$. Therefore, exploiting the properties of the HI function in Eqs. (5.28) and (5.29), one obtains $\boldsymbol{H}(\boldsymbol{S}^{*}_{\nu\mu,\,\mathrm{eq}}) = |\nu-\mu|^{-1/2}\boldsymbol{\delta}$. Substituting this result in Eq. (5.31) recovers the equilibrium-averaged result in Eq. (5.22). The

equilibrium distribution obtained with consistently-averaged approximation is the same as that obtained in the Zimm model.

The predictions of this model (also called the "Generalized-Zimm" model) have been extensively analyzed by Öttinger [1987a]. It is straightforward to show that, for Rouse chains, the second moment equations with the consistent-averaging approximation are identical with those obtained with equilibrium-averaging up to first order in the velocity gradient (see Appendix A). Therefore, the values of the zero-shear-rate viscosity predicted with both the approximations are the same. In addition, Öttinger has also shown that the predictions of $\Psi^*_{1,0}$ are equal. However, a non-zero positive value of $\Psi^*_{2,0}$ is predicted with the consistent-averaging approximation, whereas the Zimm model predicts $\Psi^*_2 = 0$ at all shear-rates. As remarked earlier, consistent-averaging of HI leads to shear-rate dependent predictions for the steady-state properties $\eta^*_{\rm p}$, Ψ^*_1, and Ψ^*_2. Thus, the approximation represents an improvement over the original Zimm model.

An interesting prediction of this model is that the steady-state predictions for $\eta_{\rm p}$ and Ψ_1 in shear are *non-monotonic* functions of the shear-rate. For chains with finite N, these properties decrease ("shear-thinning") from their linear viscoelastic plateau values at moderate shear-rates, before reaching a minimum followed by an upturn ("shear-thickening") and an eventual levelling-off at large shear-rates. With larger values of N, the predicted shear-thickening becomes increasingly prominent. This behaviour is discussed in greater detail in the following Chapter. Zylka [1991] showed however that predictions for $\eta^*_{\rm p}$ and Ψ^*_1 for steady shear flows using consistently-averaged HI are only in qualitative agreement with the results of BD simulations, whereas the "Gaussian approximation" describd below is much more accurate at high shear-rates.

5.2.3 Gaussian approximation for HI

Noting that the replacement of the diffusion tensors $\widetilde{\boldsymbol{A}}_{ij}$ with their averages $\overline{\boldsymbol{A}}_{ij}$ in the consistent-averaging approximation ignores the influence of fluctuations in HI, Öttinger [1989a] and Wedgewood [1989] suggested the "Gaussian approximation" to study the effect of fluctuations in HI. This approximation has recently been shown [Ilg *et al.*, 2002] to be a special case of a more general approach.

In this latter approach, the macroscopic behaviour of the dilute polymer solution is sought to be completely described in terms of a set of n macroscopic "state variables", which are in general linear functionals of the original distribution function. A typical choice for the state variables is the second- and/or higher-order moments of the original distribution function. Using some criteria, a distribution function of known form having n unknown parameters is used to approximate the original distribution function. Equations relating the parameters in this approximate *canonical distribution function* (CDF) to the state variables are then obtained by formally requiring that the predictions of the state variables using the CDF be equal in value to those obtained with the original distribution. As a consequence of this, the original n parameters in the CDF are expressible in terms of the n state variables. Finally, the specific mathematical properties of the CDF are exploited to simplify the complicated averages on the right-hand sides of the evolution equations for the state variables. The choice of the CDF is thus guided by the simplifications that can be made through its use. The resulting evolution equations so obtained are closed with respect to the n parameters of the CDF. The formal connection between the state variables and the parameters of the CDF then implies that the evolution equations are also closed with respect to the state variables. All other ensemble averages, such as the stress tensor, are evaluated using the CDF, and are hence expressible as functions entirely of the parameters of the CDF, and therefore the state variables. Therefore, after integrating the evolution equations for the state variables, the time variation of the other macroscopic properties of the system can be calculated. A simple introduction to the idea of using CDF's for developing closure approximations for polymer kinetic theory models is given by Lielens *et al.* [1998].

Choosing the N_s^2 second moments of the distribution as the state variables and a Gaussian distribution as the CDF leads to the Gaussian approximation of Öttinger and Wedgewood. This choice permits the use of Eq. (5.6) to decompose the complicated averages occurring in the equation for the second moment into functions of the second moments, thus enabling closure. The central motivation for the Gaussian approximation however goes beyond algebraic simplification. In Eq. (5.13), (and its more general version Eq. (5.1)), one encounters averages of the form $\langle \boldsymbol{x}\boldsymbol{x}f(\boldsymbol{x})\rangle$,

where $\boldsymbol{x}$ is the random variable of interest, and f is a nonlinear function of $\boldsymbol{x}$. The consistent-averaging replacement of f with its average $\langle f\rangle$, neglects fluctuations in f, and gives

$$\langle \boldsymbol{x}\boldsymbol{x}f\rangle = \langle \boldsymbol{x}\boldsymbol{x}\rangle\langle f\rangle. \tag{5.33}$$

If the true distribution had indeed been a Gaussian, applying the Wick's decomposition rule [Eq. (5.6)] leads to

$$\langle \boldsymbol{x}\boldsymbol{x}f\rangle = \langle \boldsymbol{x}\boldsymbol{x}\rangle\langle f\rangle + \langle \boldsymbol{x}\boldsymbol{x}\rangle \cdot \langle \frac{\partial f}{\partial \boldsymbol{x}}\boldsymbol{x}\rangle\,. \tag{5.34}$$

Thus, for a true distribution that is Gaussian, it is seen that fluctuations in f are accounted for by the second term on the right-hand side of the equation above. Therefore, replacing all averages of the form $\langle \boldsymbol{x}\boldsymbol{x}f\rangle$ occurring in Eq. (5.13) with the terms on the right-hand side of the equation above, will result in an exact solution for the second moments if the true distribution is a Gaussian. The exact non-equilibrium solution of the original Fokker-Planck equation for Rouse chains with HI is in fact non-Gaussian. Nevertheless, the Gaussian approximation accounts for fluctuations in the nonlinearity introduced by HI in an approximate sense.

Turning to the details of the approximation for Rouse chains with HI and no EV, the decomposition of the average $\langle \boldsymbol{Q}_i^*\boldsymbol{Q}_m^* \cdot \widetilde{\boldsymbol{A}}_{mj}\rangle$ in Eq. (5.13) can be obtained be considering the general (dimensional) average $\langle \boldsymbol{Q}_i\zeta\boldsymbol{\Omega}_{\nu\mu}\boldsymbol{Q}_j\rangle$, which is resolved using the Wick's theorem as follows [Öttinger, 1989a]:

$$\begin{aligned}
\langle \boldsymbol{Q}_i\zeta\boldsymbol{\Omega}_{\nu\mu}\boldsymbol{Q}_j\rangle &= \sum_{l=1}^{N_\mathrm{s}} \langle\, \boldsymbol{Q}_i\boldsymbol{Q}_l\,\rangle \cdot \langle \frac{\partial}{\partial \boldsymbol{Q}_l}(\zeta\boldsymbol{\Omega}_{\nu\mu}\boldsymbol{Q}_j)\rangle,\\
&= \langle \boldsymbol{Q}_i\langle\zeta\boldsymbol{\Omega}_{\nu\mu}\rangle\boldsymbol{Q}_j\rangle + \sum_{l=1}^{N_\mathrm{s}} \langle\, \boldsymbol{Q}_i\boldsymbol{Q}_l\,\rangle \cdot \langle \frac{\partial(\zeta\boldsymbol{\Omega}_{\nu\mu})}{\partial \boldsymbol{Q}_l}\boldsymbol{Q}_j\rangle,\\
&= \langle \boldsymbol{Q}_i\langle\zeta\boldsymbol{\Omega}_{\nu\mu}\rangle\boldsymbol{Q}_j\rangle + \langle \boldsymbol{Q}_i\boldsymbol{r}_{\mu\nu}\rangle \cdot \langle \frac{\partial(\zeta\boldsymbol{\Omega}_{\nu\mu})}{\partial \boldsymbol{r}_{\mu\nu}}\boldsymbol{r}_{\mu\nu}\rangle \cdot \boldsymbol{S}_{\mu\nu}^{-1} \cdot \langle \boldsymbol{r}_{\mu\nu}\boldsymbol{Q}_j\rangle\,.
\end{aligned} \tag{5.35}$$

Introducing the fourth-rank function of a second-rank tensor $\mathbf{s}$ [Zylka, 1991]

$$\boldsymbol{K}(\mathbf{s}) \equiv \frac{-2}{(2\pi)^{3/2}} \int \frac{1}{k^2} \boldsymbol{k} \left(\boldsymbol{\delta} - \frac{\boldsymbol{kk}}{k^2} \right) \boldsymbol{k} \, \exp(-\frac{1}{2} \, \boldsymbol{kk} : \mathbf{s}) \, d\boldsymbol{k} \,, \tag{5.36}$$

it is possible to show that using Eq. (5.18) that

$$\langle \frac{\partial(\zeta \boldsymbol{\Omega}_{\nu\mu})}{\partial \boldsymbol{r}_{\mu\nu}} \rangle = \frac{\zeta}{2(2\pi)^{3/2} \eta_{\mathrm{s}}} \boldsymbol{K}(\boldsymbol{S}_{\mu\nu}) \cdot \boldsymbol{S}_{\mu\nu} \,. \tag{5.37}$$

Like the $\boldsymbol{H}$ function introduced earlier in Eq. (5.26), the $\boldsymbol{K}$ function is also a homogeneous function, and

$$\boldsymbol{K}(\lambda \mathbf{s}) = \lambda^{-3/2} \boldsymbol{K}(\mathbf{s}) \,. \tag{5.38}$$

The result derived in Eq. (5.35) can be expressed in the following dimensionless form in terms of the $\boldsymbol{H}$ and $\boldsymbol{K}$ functions:

$$\langle \boldsymbol{Q}_i^* \zeta \boldsymbol{\Omega}_{\nu\mu} \boldsymbol{Q}_j^* \rangle = \sqrt{2} h^* \langle \boldsymbol{Q}_i^* \boldsymbol{H}(\boldsymbol{S}_{\mu\nu}^*) \boldsymbol{Q}_i^* \rangle + \frac{3\sqrt{2} h^*}{4} \langle \boldsymbol{Q}_i^* \boldsymbol{r}_{\mu\nu}^* \rangle \cdot \boldsymbol{K}(\boldsymbol{S}_{\mu\nu}^*) \cdot \langle \boldsymbol{r}_{\mu\nu}^* \boldsymbol{Q}_j^* \rangle \,. \tag{5.39}$$

The first term on the right-hand side of the last line of Eq. (5.39) above containing the $\boldsymbol{H}$ function arises from the average of the HI tensor, while the term containing the $\boldsymbol{K}$ function accounts for the influence of the fluctuations in the HI tensor.

Using these results, the governing equation for the dimensionless second moments in the Gaussian approximation for Rouse chains with HI can be obtained as

$$\boldsymbol{\sigma}_{ij,(1)}^* = -\frac{1}{4} \sum_{m=1}^{N_{\mathrm{s}}} \left[\boldsymbol{\sigma}_{im}^* \cdot (\overline{\boldsymbol{A}}_{mj} + \boldsymbol{\Delta}_{mj}) + (\overline{\boldsymbol{A}}_{im} + \boldsymbol{\Delta}_{mi}^{\mathrm{T}}) \cdot \boldsymbol{\sigma}_{mj}^* \right] + \frac{1}{2} \overline{\boldsymbol{A}}_{ij} \,, \tag{5.40}$$

where the dimensionless tensors

$$\boldsymbol{\Delta}_{pq} \equiv \sum_{r,s=1}^{N_{\mathrm{s}}} \boldsymbol{\Gamma}_{rq}^{ps} : \boldsymbol{\sigma}_{sr}^* ,$$

and,

$$\boldsymbol{\Delta}_{pq}^{\mathrm{T}} = \sum_{r,s=1}^{N_{\mathrm{S}}} \boldsymbol{\sigma}_{rs}^{*} : \boldsymbol{\Gamma}_{qr}^{sp} \,, \tag{5.41}$$

with

$$\boldsymbol{\Gamma}_{rq}^{ps} \equiv \frac{3\sqrt{2}h^{*}}{4}[\Delta\Theta_{rq}^{ps}\boldsymbol{K}_{rq} + \Delta\Theta_{r+1,\,q+1}^{ps}\boldsymbol{K}_{r+1,\,q+1} - \Delta\Theta_{r+1,\,q}^{ps}\boldsymbol{K}_{r+1,\,q} - \Delta\Theta_{r,\,q+1}^{ps}\boldsymbol{K}_{r,\,q+1}] \,, \tag{5.42}$$

where $\boldsymbol{K}_{\mu\nu}$ denotes the dimensionless function $\boldsymbol{K}(\boldsymbol{S}_{\mu\nu}^{*})$. The inner product of $\boldsymbol{K}$ with a second-rank tensor $\mathbf{a}$ is defined in component form as

$$(\boldsymbol{K} : \mathbf{a})_{\alpha\beta} = \sum_{\gamma,\delta=1}^{3} K_{\alpha\beta\gamma\delta}\, a_{\delta\gamma}, \tag{5.43}$$

and,

$$(\mathbf{a} : \boldsymbol{K})_{\alpha\beta} = \sum_{\gamma,\delta=1}^{3} a_{\delta\gamma}\, K_{\gamma\delta\alpha\beta} \;\text{ for } \alpha,\, \beta = 1,2,3 \,. \tag{5.44}$$

Comparing Eq. (5.40) with Eq. (5.24) for the consistent-averaging approximation, it is seen that the equations are identical except for the appearance of the tensors $\boldsymbol{\Delta}_{ij}$ in the governing equation for the Gaussian approximation, which represent the contribution of fluctuations in HI to the evolution of the second moments of the distribution. Further, comparing Eqs. (5.40) and Eq. (5.13) shows that

$$\overline{\boldsymbol{M}}_{ij} = \overline{\boldsymbol{A}}_{ij} + \boldsymbol{\Delta}_{ij} \,, \tag{5.45}$$

whereas,

$$\overline{\boldsymbol{D}}_{ij} = \overline{\boldsymbol{A}}_{ij} \,. \tag{5.46}$$

Thus, in contrast to the Zimm and consistent-averaging approximations, $\overline{\boldsymbol{M}}_{ij} \neq \overline{\boldsymbol{D}}_{ij}$

in the Gaussian approximation.

Interestingly however, this difference between the $\overline{\boldsymbol{M}}_{ij}$ and $\overline{\boldsymbol{D}}_{ij}$ vanishes at equilibrium. At equilibrium, all the variances $\boldsymbol{S}^*_{\mu\nu}$ are isotropic. As a consequence of the divergence-free nature of the Oseen-Burgers tensor, $(\partial/\partial\boldsymbol{r})\cdot\boldsymbol{\Omega}(\boldsymbol{r}) = \boldsymbol{0}$, it can be shown that using the definitions in Eqs. (5.36) and (5.37) that

$$\boldsymbol{K}:\boldsymbol{\delta} = \boldsymbol{\delta}:\boldsymbol{K} = \boldsymbol{0}\,. \tag{5.47}$$

Using Eqs. (5.47), (5.41) and (5.42) one can thus show that the fluctuation tensors vanish identically at equilibrium when $\boldsymbol{S}^*_{\mu\nu,\,\mathrm{eq}} = |\nu-\mu|\boldsymbol{\delta}$. Therefore, the equations for the second moments obtained at equilibrium with the equilibrium-averaging, consistent-averaging and Gaussian approximations are identical. It will be shown later in this Chapter that when EV and/or FE are also included, directly applying the Gaussian approximation leads to an unphysical dependence of the equilibrium distribution on h^*.

Although their equilibrium distributions are identical, the predictions of the linear viscoelastic properties $\eta_{\mathrm{p},0}$, $\Psi_{1,0}$ and $\Psi_{2,0}$ with the Gaussian approximation are found to be different from those obtained with the consistent-averaging approximation, with $\Psi_{2,0}$ being negative in comparison with the positive value predicted by consistent-averaging of HI. Predictions with this approximation for Rouse chains are compared with the exact results of BD simulations in the next Chapter.

Hütter and Öttinger [Hütter and Öttinger, 1996; Öttinger, 1996a] have shown that the Gaussian approximation violates the conventional forms of the fluctuation dissipation theorems. The origin of this violation is shown in Appendix A to lie in the inequality of the $\overline{\boldsymbol{M}}_{ij}$ and $\overline{\boldsymbol{D}}_{ij}$ tensors away from equilibrium, since the tensors $\boldsymbol{\Delta}_{ij}$ are non-zero even for marginal perturbations away from equilibrium. Hütter and Öttinger, however, suggest that the conventional forms of fluctuation-dissipation theorems cannot be used directly in models with mean-field interactions, and need to be suitably modified for such models. Interestingly, the Gaussian approximation has been shown to possess an important property. For the choice of the second moments as the state variables, and in all mean-field models in which the total

potential energy can be expressed as

$$\phi = \sum_{i=1}^{N_s} \left.\frac{dS}{d(Q^2)}\right|_{Q^2=\operatorname{tr}\boldsymbol{\sigma}_{ii}} Q_i^2 \,, \tag{5.48}$$

Ilg *et al.* [2002] have shown that the Gaussian distribution is the canonical distribution function that maximizes the non-equilibrium Gibbs entropy.

5.3 Free-draining chains with excluded volume interactions and/or finite extensibility

In this Section, approximations for handling nonlinearities originating from the intramolecular potential ϕ are discussed, in the absence of HI. For free-draining chains, $\widetilde{\boldsymbol{A}}_{ij} = A_{ij}\boldsymbol{\delta}$, and hence from Eq. (5.1), one obtains

$$\begin{aligned}\langle\, \boldsymbol{Q}_i^* \boldsymbol{Q}_j^* \,\rangle_{(1)} = &-\frac{H^*}{4}\sum_{m=1}^{N_s}\langle \boldsymbol{Q}_i^* \boldsymbol{Q}_m^* \xi_m\rangle A_{mj} + A_{im}\langle \xi_m \boldsymbol{Q}_m^* \boldsymbol{Q}_j^*\rangle \\ &+ \frac{1}{4}\sum_{m,n=1}^{N_s}\langle \boldsymbol{Q}_i^* \boldsymbol{Q}_n^* w_{nm}^*\rangle A_{mj} + A_{im}\langle w_{mn}^* \boldsymbol{Q}_n^* \boldsymbol{Q}_j^*\rangle + \frac{1}{2}A_{ij}\boldsymbol{\delta}\,.\end{aligned} \tag{5.49}$$

The equation for the polymer stress is the same as given in Eq. (2.78). To facilitate the discussion below, the terms contributed to Eq. (2.78) for the polymer stress by the nonlinear spring force and EV interactions are denoted as $\boldsymbol{\tau}_{\mathrm{p}}^{*\,,\mathrm{FE}}$ and $\boldsymbol{\tau}_{\mathrm{p}}^{*\,,\mathrm{EV}}$, respectively. Since the effects of FE and EV are represented by independent terms in Eq. (5.49) above, simplification of each of the terms is taken up separately.

5.3.1 Mean-field excluded volume interactions

Considering the term due to EV interactions first, it is useful to recall some of the definitions related to this term. The EV nonlinearity w_{ij}^* is related to the EV

connector force through

$$\boldsymbol{F}_j^{\mathrm{E},\,c\,*} = \frac{\partial(\phi^{\mathrm{E}}/k_{\mathrm{B}}T)}{\partial \boldsymbol{Q}_j^*} = -\sum_{m=1}^{N_{\mathrm{S}}} w_{jm}^* \boldsymbol{Q}_m^* \,. \tag{5.50}$$

Additionally,

$$w_{ij}^* = w_{ji}^* \equiv \sum_{\substack{\mu,\,\nu=1 \\ \mu\neq\nu}}^{N} \Delta\Theta_{\mu\nu}^{ij} \varrho_{\mu\nu}^* \,, \tag{5.51}$$

where

$$\varrho_{\mu\nu}^* \equiv \frac{\varrho_{\mu\nu}\,\ell_{\mathrm{S}}^2}{k_{\mathrm{B}}T} \equiv -\frac{dE_{\mu\nu}^*}{d(r_{\mu\nu}^{*\,2})} \tag{5.52}$$

and is related to the EV force exerted on the ν-th bead by the μ-th bead through

$$\boldsymbol{F}_{\mu\nu}^{\mathrm{E}\,*} = -\frac{\partial E_{\mu\nu}^*}{\partial \boldsymbol{r}_{\mu\nu}^*} = 2\varrho_{\mu\nu}^* \boldsymbol{r}_{\mu\nu}^* \,. \tag{5.53}$$

An extension of the consistent-averaging idea discussed earlier in the context of HI to handle the EV nonlinearity suggests the substitution of w_{jk}^* with its non-equilibrium average $\langle w_{jk}^* \rangle$. From Eq. (5.51) above, it is seen that the calculation of this average requires the average $\langle \varrho_{\mu\nu}^* \rangle$ evaluated with the approximate probability distribution $\hat{P}(\boldsymbol{r}_{\mu\nu}^*)$ which as observed earlier is a Gaussian in the case of models with mean-field interactions. In the case of the NGEV potential,

$$E_{\mu\nu}^* = \frac{z^*}{d^{*\,3}} \exp\left[-\frac{r_{\mu\nu}^{*\,2}}{2d^{*\,2}}\right] . \tag{5.54}$$

and hence

$$\varrho_{\mu\nu}^* = -\frac{z^*}{2d^{*\,5}} \exp\left[-\frac{r_{\mu\nu}^{*\,2}}{2d^{*\,2}}\right] = -\frac{E_{\mu\nu}^*}{2d^{*\,2}}, \tag{5.55}$$

for which it is straightforward to show that the Gaussian average

$$\langle \varrho^*_{\mu\nu} \rangle = -\frac{z^*}{2{d^*}^2} \frac{1}{\sqrt{\det\left[{d^*}^2 \boldsymbol{\delta} + \boldsymbol{S}^*_{\mu\nu}\right]}} \,. \tag{5.56}$$

As pointed out earlier, one of the motivations for using the NGEV potential is that it permits analysis of the predictions of the model as the EV potential approaches a δ-function. With the NGEV potential, this is achieved by considering predictions in the limit $d^* \to 0$. However, for finite $\boldsymbol{S}^*_{\mu\nu}$, the average in the equation above diverges as $d^* \to 0$, whereas as observed in the previous Chapter, results of BD simulations remain well defined as the parameter d^* approaches this limit.

Prakash and Öttinger [Prakash, 2001a,b, 2002; Prakash and Öttinger, 1999] avoided this difficulty and instead extended the idea of the Gaussian approximation to free-draining Rouse dumbbells and chains with NGEV interactions. As in the case of its application for chains with HI, the approximation involves assuming that the probability distribution function is Gaussian, and then using Wick's theorem to decompose the expectation $\langle \boldsymbol{Q}^*_i \boldsymbol{Q}^*_k w^*_{km} \rangle$ in Eq. (5.49). Using Eq. (5.51) above and Eq. (2.26) earlier, it is seen that

$$\begin{aligned} \sum_{k=1}^{N_\mathrm{S}} \langle \boldsymbol{Q}^*_i \boldsymbol{Q}^*_k w^*_{km} \rangle &= \sum_{\substack{\mu,\,\nu=1 \\ \mu \neq \nu}}^{N} \sum_{k=1}^{N_\mathrm{S}} \Delta\Theta^{km}_{\mu\nu} \langle \boldsymbol{Q}^*_i \boldsymbol{Q}^*_k \varrho^*_{\mu\nu} \rangle \,. \\ &= \sum_{\substack{\mu,\,\nu=1 \\ \mu \neq \nu}}^{N} \Delta\Theta^{m}_{\mu\nu} \langle \boldsymbol{Q}^*_i \boldsymbol{r}^*_{\mu\nu} \varrho^*_{\mu\nu} \rangle \,. \end{aligned} \tag{5.57}$$

Using Eq. (5.53), it is seen that the average on the right-hand side,

$$\langle \boldsymbol{Q}^*_i \boldsymbol{r}^*_{\mu\nu} \varrho^*_{\mu\nu} \rangle = -\frac{1}{2} \left\langle \boldsymbol{Q}^*_i \frac{\partial E^*_{\mu\nu}}{\partial \boldsymbol{r}^*_{\mu\nu}} \right\rangle = \frac{1}{2} \left\langle \boldsymbol{Q}^*_i \, \boldsymbol{F}^{\mathrm{E}\,*}_{\mu\nu} \right\rangle \,. \tag{5.58}$$

Invoking the Gaussian approximation, it is straightforward to apply Wick's decomposition theorem to show that,

$$\left\langle \boldsymbol{Q}^*_i \frac{\partial E^*_{\mu\nu}}{\partial \boldsymbol{r}^*_{\mu\nu}} \right\rangle = \langle \boldsymbol{Q}^*_i \boldsymbol{r}^*_{\mu\nu} \rangle \cdot \left\langle \frac{\partial^2 E^*_{\mu\nu}}{\partial \boldsymbol{r}^*_{\mu\nu} \boldsymbol{r}^*_{\mu\nu}} \right\rangle \,. \tag{5.59}$$

The expression on the right-hand side could have also been directly obtained if the following mean-field pair-wise bead EV potential,

$$\overline{E}^*_{\mu\nu} = \frac{1}{2}\left\langle \frac{\partial^2 E^*_{\mu\nu}}{\partial \boldsymbol{r}^*_{\mu\nu}\boldsymbol{r}^*_{\mu\nu}} \right\rangle : \boldsymbol{r}^*_{\mu\nu}\boldsymbol{r}^*_{\mu\nu}\,, \tag{5.60}$$

had been used in place of the exact EV potential $E^*_{\mu\nu}$. In other words, applying the Gaussian approximation as suggested by Prakash and Öttinger [1999] to simplify the average due to the EV effect in free-draining chains is equivalent to using the quadratic mean-field EV potential above, and one thus obtains

$$\left\langle \boldsymbol{Q}^*_i \frac{\partial E^*_{\mu\nu}}{\partial \boldsymbol{r}^*_{\mu\nu}} \right\rangle = \left\langle \boldsymbol{Q}^*_i \frac{\partial \overline{E}^*_{\mu\nu}}{\partial \boldsymbol{r}^*_{\mu\nu}} \right\rangle . \tag{5.61}$$

Furthermore, the mean-field EV force exerted on the ν-th bead by the μ-th bead is therefore

$$\overline{\boldsymbol{F}}^{\mathrm{E}\,*}_{\mu\nu} \equiv -\frac{\partial \overline{E}^*_{\mu\nu}}{\partial \boldsymbol{r}^*_{\mu\nu}}\,, \tag{5.62}$$

$$= -\left\langle \frac{\partial^2 E^*_{\mu\nu}}{\partial \boldsymbol{r}^*_{\mu\nu}\boldsymbol{r}^*_{\mu\nu}} \right\rangle \cdot \boldsymbol{r}^*_{\mu\nu}\,. \tag{5.63}$$

Prakash and Öttinger [1999] point out that Fixman's [1966a] original boson-operator approach for a model with δ-function EV interactions also yields a modified potential of the same form as in Eq. (5.60). Although the Gaussian approximation for EV has been studied in great detail, the interpretation of the approximation through the mean-field potential in Eq. (5.60) above has not received much attention before. This interpretation is shown shortly to be highly useful in constructing approximations for chains combining nonlinear intramolecular potentials with HI.

Noting that, for any scalar function f of the magnitude of a vector $\boldsymbol{x}$,

$$\frac{\partial f}{\partial \boldsymbol{x}} = 2\frac{df}{d(x^2)}\,\boldsymbol{x}\,, \tag{5.64}$$

and,

$$\frac{\partial^2 f}{\partial \boldsymbol{x}\partial \boldsymbol{x}} = 2\frac{df}{d(x^2)}\boldsymbol{\delta} + 4\frac{d^2 f}{d(x^2)^2}\boldsymbol{x}\boldsymbol{x}\,, \tag{5.65}$$

by comparing Eq. (5.53) with Eq. (5.64) above, the mean-field EV potential in Eq. (5.60) can be expressed in terms of $\varrho^*_{\mu\nu}$ as

$$\overline{E}^*_{\mu\nu} = -\left[\langle\varrho^*_{\mu\nu}\rangle\boldsymbol{\delta} + 2\left\langle\frac{d\varrho^*_{\mu\nu}}{d(r^{*\,2}_{\mu\nu})}\,\boldsymbol{r}^*_{\mu\nu}\boldsymbol{r}^*_{\mu\nu}\right\rangle\right] : \boldsymbol{r}^*_{\mu\nu}\boldsymbol{r}^*_{\mu\nu}\,, \tag{5.66}$$

The average $\langle\varrho^*_{\mu\nu}\rangle$ was encountered above in the discussion of consistently-averaging the EV nonlinearity. The second term within the brackets in the equation above thus represents the effect of fluctuations in the EV interactions.

Although the development thus far is valid for any EV potential, calculations are greatly simplified due the Gaussian nature of both the NGEV potential and the distribution $\hat{P}$. Thus, one obtains for the NGEV potential,

$$\overline{E}^*_{\mu\nu} = -\frac{z^*}{2}\boldsymbol{V}_{\mu\nu} : \boldsymbol{r}^*_{\mu\nu}\boldsymbol{r}^*_{\mu\nu}\,, \tag{5.67}$$

where,

$$\boldsymbol{V}_{\mu\nu} \equiv \boldsymbol{V}(\boldsymbol{S}^*_{\mu\nu}) \equiv \frac{1}{\sqrt{\det[d^{*\,2}\boldsymbol{\delta} + \boldsymbol{S}^*_{\mu\nu}]}}\,[d^{*\,2}\boldsymbol{\delta} + \boldsymbol{S}^*_{\mu\nu}]^{-1}\,. \tag{5.68}$$

The mean-field EV force derived using the NGEV potential is therefore

$$\overline{\boldsymbol{F}}^{\mathrm{E}\,*}_{\mu\nu} = -\frac{\partial\overline{E}^*_{\mu\nu}}{\partial\boldsymbol{r}^*_{\mu\nu}} = z^*\boldsymbol{V}_{\mu\nu}\cdot\boldsymbol{r}^*_{\mu\nu}\,. \tag{5.69}$$

Substituting the original pair-wise EV force $\boldsymbol{F}^{\mathrm{E}\,*}_{\mu\nu}$ in Eq. (5.58) with the mean-field force $\overline{\boldsymbol{F}}^{\mathrm{E}\,*}_{\mu\nu}$, leads to the following modification of the EV contribution to the

equation for second moments, Eq. (5.49):

$$\begin{aligned}\sum_{k=1}^{N_\mathrm{s}}\langle \boldsymbol{Q}_i^*\boldsymbol{Q}_k^* w_{km}^*\rangle &= \frac{1}{2}\sum_{\substack{\mu,\,\nu=1\\ \mu\neq\nu}}^{N}\Delta\Theta_{\mu\nu}^m\langle \boldsymbol{Q}_i^*\overline{\boldsymbol{F}}_{\mu\nu}^{\mathrm{E}\,*}\rangle\,,\\ &= \frac{z^*}{2}\sum_{\substack{\mu,\,\nu=1\\ \mu\neq\nu}}^{N}\Delta\Theta_{\mu\nu}^m\langle \boldsymbol{Q}_i^*\boldsymbol{r}_{\mu\nu}^*\rangle\cdot\boldsymbol{V}_{\mu\nu}\,,\\ &= z^*\sum_{k=1}^{N_\mathrm{s}}\boldsymbol{\sigma}_{ik}^*\cdot\boldsymbol{J}_{km}\,, \end{aligned} \tag{5.70}$$

where,

$$\boldsymbol{J}_{km} \equiv \frac{1}{2}\sum_{\substack{\mu,\,\nu=1\\ \mu\neq\nu}}^{N}\Delta\Theta_{\mu\nu}^{km}\boldsymbol{V}_{\mu\nu}. \tag{5.71}$$

Further, the mean-field EV connector force is

$$\overline{\boldsymbol{F}}_j^{\mathrm{E},c\,*} = -\frac{1}{2}\sum_{\substack{\mu,\,\nu=1\\ \mu\neq\nu}}^{N}\overline{\boldsymbol{F}}_{\mu\nu}^{\mathrm{E}\,*}\Delta\Theta_{\mu\nu}^j\,, \tag{5.72}$$

$$= -\frac{z^*}{2}\sum_{\substack{\mu,\,\nu=1\\ \mu\neq\nu}}^{N}\boldsymbol{V}_{\mu\nu}\cdot\boldsymbol{r}_{\mu\nu}^*\Delta\Theta_{\mu\nu}^j\,, \tag{5.73}$$

$$= -z^*\sum_{k=1}^{N_\mathrm{s}}\boldsymbol{J}_{jk}\cdot\boldsymbol{Q}_k^*\,. \tag{5.74}$$

Here, it may be pointed out that $\boldsymbol{J}_{ij} = \boldsymbol{J}_{ji} = \boldsymbol{J}_{ij}^{\mathrm{T}}$. Using these relations, the EV contribution to the polymer stress is obtained as

$$\boldsymbol{\tau}_\mathrm{p}^{*\,,\,\mathrm{EV}} = z^*\sum_{i,j\,=1}^{N_\mathrm{s}}\boldsymbol{\sigma}_{ij}^*\cdot\boldsymbol{J}_{ij} = \frac{z^*}{2}\sum_{\substack{\mu,\,\nu=1\\ \mu\neq\nu}}^{N}\boldsymbol{S}_{\mu\nu}^*\cdot\boldsymbol{V}_{\mu\nu}\,. \tag{5.75}$$

In contrast to the consistent averaging treatment of EV considered earlier, Eq. (5.68)

shows that in the $d^* \to 0$ limit,

$$\boldsymbol{V}_{\mu\nu} = \frac{1}{\sqrt{\det \boldsymbol{S}^*_{\mu\nu}}}\, \boldsymbol{S}^{*\,-1}_{\mu\nu}\,, \tag{5.76}$$

remains finite. Therefore, the inclusion of fluctuations in EV interactions is crucial in obtaining physically meaningful results as d^* becomes very small. Interestingly, the equation above shows that in the δ-function limit, the direct EV contribution to the polymer stress in Eq. (5.75) above becomes isotropic, and hence rheologically unimportant. Nevertheless, as shown by Prakash and Öttinger, EV exerts its influence through its contribution to the equations for the second moments in the Gaussian approximation, which does not vanish as $d^* \to 0$.

A thorough examination of the Gaussian approximation for free-draining Rouse chains with the NGEV potential has been carried out by Prakash and co-workers [Kumar and Prakash, 2003, 2004; Prakash, 2001b, 2002; Prakash and Öttinger, 1999]. Their analysis shows that a perturbation expansion of the governing equations of the Gaussian approximation in the z^* parameter yields equations that are identical to those obtained with a similar expansion constructed with the exact model. In other words, the Gaussian approximation for EV is exact to first order in z^*. This important property is also shared by the Gaussian approximation with HI, which is exact to first order in the HI parameter h^* [Öttinger and Rabin, 1989]. These studies have shown that the qualitative features predicted with the approximation for finite values of N, such as the expansion of the coil size at equilibrium and strong shear-thinning, mirror the behaviour observed with BD simulations. It is further found for finite chains that quantitative agreement with exact BD simulations' results is obtained only *beyond* a threshold value of d^*, which depends on the value of N chosen. Below this value of d^*, the results of BD simulations approach the Rouse model's predictions as $d^* \to 0$. However, predictions with the Gaussian approximation approach non-Rouse values in this limit.

Nevertheless, the approximation proposed by Prakash and Öttinger can serve as a useful starting point for closure approximations for bead-spring chain models with EV. Furthermore, the idea of using the Gaussian approximation to account for fluctuations in the EV forces can also be applied to other intramolecular potentials,

including nonlinear spring force laws as shown below.

5.3.2 Mean-field spring forces

Recognizing that in Eq. (5.49),

$$H^*\langle \boldsymbol{Q}_i^* \boldsymbol{Q}_m^* \xi_m \rangle = \left\langle \boldsymbol{Q}_i^* \frac{\partial S_m^*}{\partial \boldsymbol{Q}_m^*} \right\rangle , \tag{5.77}$$

where $S_m^* = S(\boldsymbol{Q}_m^*)$ is a general spring force potential, it is possible in principle to use the Gaussian approximation and proceed along the same lines as in Eq. (5.69) to obtain

$$\left\langle \boldsymbol{Q}_i^* \frac{\partial S_m^*}{\partial \boldsymbol{Q}_m^*} \right\rangle = \boldsymbol{\sigma}_{im}^* \cdot \left\langle \frac{\partial^2 S_m^*}{\partial \boldsymbol{Q}_m^* \partial \boldsymbol{Q}_m^*} \right\rangle , \tag{5.78}$$

$$= \left\langle \boldsymbol{Q}_i^* \frac{\partial \overline{S}_m^*}{\partial \boldsymbol{Q}_m^*} \right\rangle , \tag{5.79}$$

where the quadratic mean-field spring potential $\overline{S}_m^*$ is defined as follows:

$$\overline{S}_m^* \equiv \frac{1}{2} \left\langle \frac{\partial^2 S_m^*}{\partial \boldsymbol{Q}_m^* \partial \boldsymbol{Q}_m^*} \right\rangle : \boldsymbol{Q}_m^* \boldsymbol{Q}_m^* . \tag{5.80}$$

Further, using $\partial S_m^* / \partial \boldsymbol{Q}_m^* = H^* \xi_m \boldsymbol{Q}^*$, and the equation above, one obtains

$$\overline{S}_m^* = H^* \left[\langle \xi_m \rangle \boldsymbol{\delta} + \left\langle \frac{\partial \xi_m}{\partial \boldsymbol{Q}_m^*} \boldsymbol{Q}_m^* \right\rangle \right] . \tag{5.81}$$

Using Eq. (5.64), $\partial \xi_m / \partial \boldsymbol{Q}_m^* = 2\boldsymbol{Q}_m^* \, d\xi_m / d({Q_m^*}^2)$, and it is seen that the second term within the brackets on the right-hand side of the equation above has the same form as the term on the left hand-side of Eq. (5.77). Recursive application of Wick's decomposition rule then leads to a series expansion,

$$\overline{S}_m^* = H^* \left[\langle \xi_m \rangle \boldsymbol{\delta} + \sum_{s=1}^{\infty} 2^s \left\langle \frac{d^s \xi_m}{d({Q_m^*}^2)^s} \right\rangle \boldsymbol{\sigma}_{mm}^{*\,s} \right] , \tag{5.82}$$

where $\boldsymbol{\sigma}_{mm}^{*\,s}$ denotes the matrix product of s copies of $\boldsymbol{\sigma}_{mm}^*$.

As before the first term within the brackets on the right-hand side of the equation

above containing $\langle \xi_m \rangle$, the average of the spring force nonlinearity is recognized as that arising from a consistent-averaging treatment of that nonlinearity, while the remaining terms accounts for the influence of fluctuations in the spring force. The expansion above is valid provided the Gaussian averages $\langle \xi_m \rangle$ and $\langle d^s \xi_m / \, d(Q^{*\,2}_m)^s \rangle$, exist for all $s = 1, \ldots, \infty$

For FENE springs,

$$\xi_m = \frac{1}{(1 - Q^{*\,2}_m / b^*)} \,, \tag{5.83}$$

and,

$$\frac{d^s \xi_m}{d(Q^{*\,2}_m)^s} = \frac{s!}{b^{*\,s}} \frac{1}{(1 - Q^{*\,2}_m / b^*)^{s+1}} \,. \tag{5.84}$$

The Gaussian averages of these functions do not exist since all of them have non-integrable singularities at $Q^{*\,2}_m = b^*$, whereas the Gaussian distribution has an infinite range. To make analytical progress, further approximations are necessary and in this study,

$$\langle \xi_m \rangle \text{ is replaced with } \frac{1}{\langle (1 - Q^{*\,2}_m / b^*) \rangle} \tag{5.85}$$

and,

$$\left\langle \frac{d^s \xi_m}{d(Q^{*\,2}_m)^s} \right\rangle \text{ is replaced with } \frac{s!}{b^{*\,s}} \frac{1}{\langle (1 - Q^{*\,2}_m / b^*)^{s+1} \rangle} \,. \tag{5.86}$$

Although these replacements may result in each of the terms remaining bounded as long as $\langle Q^{*\,2}_m \rangle = \operatorname{tr} \boldsymbol{\sigma}^*_{mm} < b^*$, the convergence properties of the infinite series in Eq. (5.82) after making the replacements above need to be analyzed carefully before the full series is implemented. In this study, only the first term in the infinite series in Eq. (5.82) is retained to represent spring force fluctuations. Thus for FENE springs,

$$H^* \langle \boldsymbol{Q}^*_i \boldsymbol{Q}^*_m \xi_m \rangle = H^* \boldsymbol{\sigma}^*_{im} \cdot \boldsymbol{L}_m \,, \tag{5.87}$$

where,

$$\begin{aligned}\boldsymbol{L}_m &\equiv \frac{1}{\langle(1-Q_m^{*\,2}/b^*)\rangle}\boldsymbol{\delta} + \frac{2}{b^*}\frac{1}{\langle(1-Q_m^{*\,2}/b^*)^2\rangle}\boldsymbol{\sigma}_{mm}^*\,,\\ &= \frac{1}{1-\,\mathrm{tr}\,\boldsymbol{\sigma}_{mm}^*/b^*}\boldsymbol{\delta} + \frac{2/b^*}{1-2\,\mathrm{tr}\,\boldsymbol{\sigma}_{mm}^*/b^* + [(\,\mathrm{tr}\,\boldsymbol{\sigma}_{mm}^*)^2 + 2\boldsymbol{\sigma}_{mm}^*\colon\boldsymbol{\sigma}_{mm}^*]/b^{*\,2}}\boldsymbol{\sigma}_{mm}^*\,.\end{aligned} \tag{5.88}$$

The approximate expression above is also obtained by using a mean-field quadratic spring potential

$$\overline{S}_m^* = \frac{H^*}{2}\boldsymbol{L}_m\colon\boldsymbol{Q}_m^*\boldsymbol{Q}_m^*\,, \tag{5.89}$$

that leads to a mean-field spring force, force,

$$\overline{\boldsymbol{F}}_m^{\mathrm{S},\,c} = H^*\boldsymbol{L}_m\cdot\boldsymbol{Q}_m^*\,. \tag{5.90}$$

As mentioned above, neglecting the spring force fluctuation term in $\boldsymbol{L}_m$ is equivalent to a consistent-averaging treatment of the FENE nonlinearity, which leads to the well known FENE-P force law,

$$\overline{\boldsymbol{F}}_m^{\mathrm{S},\,c} = H^*\frac{1}{1-\,\mathrm{tr}\,\boldsymbol{\sigma}_{mm}^*/b^*}\boldsymbol{Q}_m^* \;= H^*\overline{\xi}_m\boldsymbol{Q}_m^* \tag{5.91}$$

proposed by Bird *et al.* [1980]. Incorporation of fluctuations through the Gaussian approximation leads to the spring force expression in Eq. (5.90) which will be henceforth be referred to as the "FENE-PG" spring force law.

It must be noted here that the derivation of the FENE-PG spring force makes three important assumptions, which can cause its predictions to deviate from the exact results obtained with FENE spring.

1. The probability distribution for the connector vectors is Gaussian.

2. Higher order terms in the infinite series representing spring force fluctuations are negligible.

3. Averages of the form $\langle(1-Q_m^{*\,2}/b^*)^{-p}\rangle$ are replaced by $\langle(1-Q_m^{*\,2}/b^*)^{p}\rangle^{-1}$. Such an approximation is referred to as a Peterlin replacement, or Peterlin closure.

Here, it must be pointed out that for finite $\boldsymbol{\sigma}^*_{mm}$, as $b^* \to \infty$, the fluctuation contribution in Eq. (5.88) becomes vanishingly small, $\boldsymbol{L}_m \to \boldsymbol{\delta}$ and the spring becomes more Hookean-like. On the other hand, as the bead-spring chain approaches its full extension, and

$$\boldsymbol{\sigma}^*_{mm} \to \begin{pmatrix} b^* & 0 & 0 \\ 0 & 0 & 0 \\ 0 & 0 & 0 \end{pmatrix}, \tag{5.92}$$

the scalar prefactor in the fluctuation term in Eq. (5.88) approaches $(1/b^*)$, which however becomes negligible compared to the FENE-P contribution, which diverges. Thus, as chains become highly stretched, predictions obtained with the FENE-P or FENE-PG approximations are expected to be nearly identical.

Using Eqs. 5.70 and 5.87 in Eq. (5.49), the evolution equation for the second moments in the Gaussian approximation for free-draining FEBS chains with EV interactions is

$$\boldsymbol{\sigma}^*_{ij,\,(1)} = -\frac{1}{4}\sum_{m,n=1}^{N_\mathrm{S}} \left(\boldsymbol{\sigma}^*_{in}\cdot\boldsymbol{T}_{nm}A_{mj} + A_{im}\boldsymbol{T}_{mn}\cdot\boldsymbol{\sigma}^*_{nj}\right) + \frac{1}{2}A_{ij}\boldsymbol{\delta}\,. \tag{5.93}$$

where,

$$\boldsymbol{T}_{ij} \equiv H^*\delta_{ij}\boldsymbol{L}_j\boldsymbol{\delta} - z^*\boldsymbol{J}_{ij}\,. \tag{5.94}$$

Comparing Eq. (5.93) with the general equation for second moments in Eq. (5.2), it is seen that for free-draining chains with EV and FE,

$$\overline{\boldsymbol{M}}_{ij} = \sum_{m=1}^{N_\mathrm{S}} \boldsymbol{T}_{im}A_{mj}; \quad \overline{\boldsymbol{D}}_{ij} = A_{ij}\boldsymbol{\delta}\,. \tag{5.95}$$

Further, the polymer stress predicted by the approximation is given by

$$\boldsymbol{\tau}^*_\mathrm{p} = N_\mathrm{S}\boldsymbol{\delta} - H^*\sum_{i=1}^{N_\mathrm{S}}\boldsymbol{\sigma}^*_{ii}\cdot\boldsymbol{L}_i + z^*\sum_{i,j=1}^{N_\mathrm{S}}\boldsymbol{\sigma}^*_{ij}\cdot\boldsymbol{J}_{ji} = N_\mathrm{S}\boldsymbol{\delta} - \sum_{i,j=1}^{N_\mathrm{S}}\boldsymbol{\sigma}^*_{ij}\cdot\boldsymbol{T}_{ji}\,. \tag{5.96}$$

Although the FENE-PG approximation is new and has been developed in this study, the FENE-P approximation has been studied in great detail by several workers [Ghosh *et al.*, 2001; Herrchen and Öttinger, 1997; Keunings, 1997; Öttinger, 1989b; van den Brule, 1993; Wedgewood and Bird, 1988; Wiest and Tanner, 1989; Wiest *et al.*, 1989]. As pointed out in many of these studies, perhaps the single most important difference between the exact FENE and the mean-field FENE-P and FENE-PG approximations lies in the nature of the configurational probability distribution function. The singularity in the non-averaged FENE spring force strictly restricts the lengths of the connector vectors to lie in the domain $[0, Q_0)$. However, with the Peterlin closure, the solution of the modified Fokker-Planck equation with FENE-P/PG springs is a Gaussian. Therefore, there is a non-zero probability that a spring has a length greater than Q_0. This has been clearly illustrated by Keunings [1997] who used Brownian dynamics simulations of dumbbells with FENE-P springs to show that in strong extensional flows, a significant proportion of the dumbbells had length greater than the "maximum allowed" dimensionless extension Q_0. However, in all the literature on the FENE-P model, the mean-squared lengths of the springs are observed to always be lesser than Q_0^2. In other words, the mean-field FENE-P model appears to satisfy the maximum extension constraint in an average sense.

It is observed in the studies cited above that predictions with the FENE-P approximation compare well with the FENE model for steady-state properties, in both shear and uniaxial extensional flows. At first sight, this agreement seems fortuitous since the probability distributions are so different in character. An explanation for the good agreement at steady-state in a strong extensional flow is however possible. This is based on the observation that the exact steady-state distribution function for the length of the spring in a dumbbell model is sharply peaked around $\sqrt{\langle Q^2 \rangle}$, and can be well approximated by a δ-function [Lielens *et al.*, 1998; Wiest and Tanner, 1989]. Lielens *et al.* showed that in a one-dimensional dumbbell model, assuming the following function as a CDF

$$\psi(Q) = \frac{1}{2}\delta(Q - \sqrt{\langle Q^2 \rangle}) + \frac{1}{2}\delta(Q + \sqrt{\langle Q^2 \rangle}) \tag{5.97}$$

and substituting it in the original equation for the second moment leads to a modified

equation that is identical to the one obtained with the FENE-P approximation. The FENE-P approximation does well at steady-state in strong extensional flows, where the true single-link distributions for the lengths of the springs are close to being δ-functions.

However, deviations between predictions obtained with free-draining FENE-P chains and the results of BD simulations of FENE chains, are considerably larger in unsteady flows [Herrchen and Öttinger, 1997; van den Brule, 1993]. For instance, Fig. 5.1 shows that prediction of the FENE-P model for the growth of the extensional viscosity $\overline{\eta}^*_{\rm p}$ agrees well with the results of BD simulations of FENE chains at small strains immediately after the imposition of a sudden uniaxial extensional flow. In this stage, chains are not stretched enough for the nonlinearity in the spring force to make an impact. However, as soon the spring force nonlinearity becomes important, deviations between the models begin to appear. In this regime of intermediate strains before steady-state is attained, the the stress is at first underpredicted by the FENE-P approximation, which is followed by a period of rapid stress growth in which the FENE-P prediction overtakes the exact results. Subsequent to this, a rapid levelling off to the steady-state value occurs in the prediction obtained with the FENE-P approximation. In comparison, the approach to steady-state of the $\overline{\eta}^*_{\rm p}$ results obtained with BD simulations is more gradual, although the steady-state value is nearly the same. Thus, in start-up of extensional flows, predictions with the FENE-P model for $\overline{\eta}^*_{\rm p}$ agree with BD simulations' results during the early stages, and at the steady-state, but display large deviations prior to the attainment of the steady-state.

The deviations of the FENE-P approximation from the exact results can be explained as follows. At intermediate strains in extensional flows, chains are still in the process of unravelling. Partially unravelled chains have several kinks which are regions of low local chain tension, and therefore are locally relatively un-stretched. Other parts of the chain, particularly those closer to the ends, are more stretched. Hence, the distribution of spring lengths is broad and nearly uniform. The FENE-P model cannot accurately capture the strong variation in spring lengths in this dynamic regime. This picture indicates that, as in the case of hydrodynamic interactions, the effect of fluctuations in the chain configuration on the spring force need

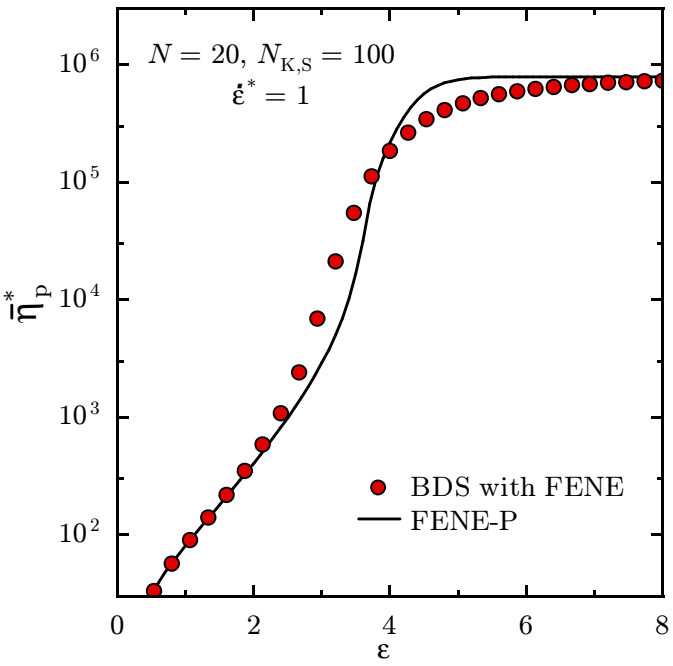

Figure 5.1: Comparison of the prediction of the free-draining FENE-P model with the results of BD simulations of FEBS chains with FENE springs, for the growth of the polymer contribution to the dimensionless extensional viscosity after the imposition of a steady uniaxial flow.

to be accounted for in order to develop accurate closure approximations for chains with nonlinear spring force laws.

The FENE-PG force law developed in this work is not the only way in which the FENE-P approximation can be improved upon. In conditions where springs can be highly stretched, the true spring length distribution is better approximated as the sum of a uniform distribution for smaller values of Q and a δ-function located at a large Q closer to (but less than) Q_0. This FENE-L approximation, and its three-dimensional counterpart, are shown to be more accurate than the FENE-P model, particularly in predicting the phenomenon of stress-conformational hysteresis [Lielens *et al.*, 1998, 1999; Sizaire *et al.*, 1999]. Gorban *et al.* [2001] show that an entropic argument can be used to improve upon the FENE-P approximation by first

expanding the exact FENE potential in a Taylor's series expansion about $\langle Q^2 \rangle$ as

$$\begin{aligned} S(Q^2) &= -\frac{1}{2} H Q_0^2 \ln[1 - (Q/Q_0)^2], \\ &= -\frac{1}{2} H Q_0^2 \sum_{m=0}^{\infty} \frac{1}{m!} \left. \frac{d^m S(x)}{dx^m} \right|_{x=\langle Q^2 \rangle} (Q^2 - \langle Q^2 \rangle)^m, \\ &= S(\langle Q^2 \rangle) + \frac{1}{2} H \frac{1}{1 - \langle Q^2 \rangle / Q_0^2} (Q^2 - \langle Q^2 \rangle) + \dots , \end{aligned} \tag{5.98}$$

and then systematically regrouping terms in the series before truncating it. This regrouping gives rise to a sequence of increasingly complex spring potentials, the simplest of which is shown to be the quadratic potential corresponding to the FENE-P force law. By using the next higher order potential (which is denoted as the "FENE-P+1" potential by Gorban *et al.* [2001]) in the sequence in a one-dimensional dumbbell model, these authors demonstrate that accuracy is significantly improved in an unsteady elongational flow.

At this juncture, it becomes necessary to consider the values of the parameters H^* amd b^* that should be used for the mean-field spring force laws described above. This presents a rather subtle question: does one regard a FENE-P or FENE-PG spring as an approximation to the original FENE spring, or as a model in their own right [Keunings, 1997]? If one were to decide in favour of the former, then the value of H^* and b^* should be the same as those used in the original FENE force. This choice however implies that the equilibrium mean-squared extension of the springs R_{S}^2 predicted by the approximations at the theta state would be different from that obtained with FENE springs. It may be recalled that, the value of H in the FENE force law is fixed in this work by equating the predicted R_{S}^2 to $b_{\mathrm{K}}^2 N_{\mathrm{K,\,S}}$ [Eq. (2.17)]. Hence, if the same value of H is used in the FENE-P expression, its prediction of R_{S}^2 will not equal $b_{\mathrm{K}}^2 N_{\mathrm{K,\,S}}$ (assuming that in either case $Q_0 = b_{\mathrm{K}} N_{\mathrm{K,\,S}}$). It is then natural to use $k_{\mathrm{B}}T/H$ and λ_{H} as the length and time scales for making quantities dimensionless, since these are the quantities that are being kept constant across the approximations. This has been case in the most of the literature on FENE-P springs, where the emphasis has been on understanding the consequences of the Peterlin approximation.

On the other hand, a mean-field approximation may be regarded as a model in

its own right. This would suggest that its parameters be obtained by consistently following the same procedure used for all other spring force models. That is, the parameter H in the FENE-P/ PG models must also be fixed so that $R_{\rm S}^2 = b_{\rm K}^2 N_{\rm K,\,S}$, when $Q_0 = b_{\rm K} N_{\rm K,\,S}$. This would ensure that the average equilibrium dimensions of the chains are identical across the different models. This study adopts this latter point of view, since numerical results obtained with the FENE-P model are compared directly with experiment (in Chapter 8) without any reference to the original FENE model. The idea here is that once the performance of a mean-field model is established by comparison against simulation and experiment, it can be used more regularly, in which case it is better to relate the parameters in the model to the molecular parameters directly. Hence, while comparing the different models, it is appropriate to use $\ell_{\rm S}^2 = R_{\rm S}^2/3 = b_{\rm K}^2 N_{\rm K,\,S}/3$ and the corresponding time scale $\lambda_{\rm S}$ as the basic scales for obtaining equations and properties in dimensionless form.

With this choice, $b^* = Q_0^2/\,\ell_{\rm S}^2 = 3N_{\rm K,\,S}$ as before. The dimensionless spring force constant H^* is determined by obtaining first the equilibrium predictions of the Gaussian approximation for free-draining FEBS chains in the absence of EV (that is, with $z^* = 0$ in Eq. (5.93) above). From Eq. (5.93), it is clear that the equilibrium second moments $\boldsymbol{\sigma}^*_{ij,\,\rm eq}$ are the solutions to the following set of algebraic equations in :

$$\mathbf{0} = -\frac{H^*}{4}\sum_{m=1}^{N_{\rm S}} \left(\boldsymbol{\sigma}^*_{im,\,\rm eq}\cdot \boldsymbol{L}_{m,\,\rm eq} A_{mj} + A_{im}\boldsymbol{L}_{m,\,\rm eq}\cdot \boldsymbol{\sigma}^*_{mj,\,\rm eq}\right) + \frac{1}{2}A_{ij}\boldsymbol{\delta}\,. \tag{5.99}$$

Due to the isotropic nature of the equilibrium state, $\boldsymbol{\sigma}^*_{ij,\,\rm eq} = \sigma^*_{ij,\,\rm eq}\boldsymbol{\delta}$ and $\boldsymbol{L}_{m,\,\rm eq} = L_{m,\,\rm eq}\boldsymbol{\delta}$. Hence, the equation above can be rearranged into the form shown in Eq. (5.8):

$$0 = \sum_{m=1}^{N_{\rm S}} \left(U_{im}A_{mj} + A_{im}U_{mj}\right)\,. \tag{5.100}$$

As pointed out at the beginning of this Chapter, the solution to the set of equations above is obtained by setting

$$U_{ij} = H^*\sigma^*_{ij,\,\rm eq}L_{j,\,\rm eq} - \delta_{ij} = 0\,. \tag{5.101}$$

The desired solution is $\boldsymbol{\sigma}^*_{ij,\,\mathrm{eq}} = \delta_{ij}\boldsymbol{\delta}$, and one thus obtains $H^*\boldsymbol{L}_{j,\,\mathrm{eq}} = \boldsymbol{\delta}$. Since all springs are identical and $\boldsymbol{L}_{j,\,\mathrm{eq}} = L_{\mathrm{eq}}\boldsymbol{\delta}$, and therefore

$$H^* L_{\mathrm{eq}} = 1\,. \tag{5.102}$$

Using $\mathrm{tr}\,\boldsymbol{\sigma}^*_{jj\,\mathrm{eq}} = 3$, $b^* = 3N_{\mathrm{K,\,s}}$, it can be shown using Eq. (5.88) that for FENE-PG springs,

$$H^* = \frac{3N^3_{\mathrm{K,\,s}} - 9N^2_{\mathrm{K,\,s}} + 13N_{\mathrm{K,\,s}} - 5}{3N^3_{\mathrm{K,\,s}} - 4N^2_{\mathrm{K,\,s}} + 5N_{\mathrm{K,\,s}}}\,. \tag{5.103}$$

For FENE-P springs, $L_{\mathrm{eq}} = \overline{\xi}_{\mathrm{eq}}$, where $\overline{\xi}_m$ was introduced in Eq. (5.91) earlier, and therefore

$$H^* = \frac{1}{\overline{\xi}_{\mathrm{eq}}} = 1 - \frac{1}{N_{\mathrm{K,\,s}}}\,. \tag{5.104}$$

When $z^* \neq 0$, $\boldsymbol{T}_{ij,\,\mathrm{eq}} = T_{ij,\,\mathrm{eq}}\boldsymbol{\delta}$ at equilibrium, and using Eq. (5.93)

$$0 = -\frac{1}{4}\sum_{m,n\,=\,1}^{N_{\mathrm{s}}} \left(\sigma^*_{im,\,\mathrm{eq}}\,T_{mn,\,\mathrm{eq}}A_{nj} + A_{im}T_{mn,\mathrm{eq}}\,\sigma^*_{nj,\mathrm{eq}}\right) + \frac{1}{2}A_{ij}\,. \tag{5.105}$$

Further, using the definition of $\boldsymbol{T}_{ij}$ in Eq. (5.94), it is seen that

$$U_{ij} = \sum_{m=1}^{N_{\mathrm{s}}} \sigma^*_{im,\,\mathrm{eq}}\left(H^*\delta_{mj}L_{j,\,\mathrm{eq}} - z^*J_{mj,\,\mathrm{eq}}\right) - \delta_{ij} = 0\,. \tag{5.106}$$

The equation above represents a set of nonlinear equations in $\sigma^*_{ij,\,\mathrm{eq}}$, and demonstrates the well known fact that EV interactions introduce cross-correlations, and $\sigma^*_{ij,\,\mathrm{eq}} \neq 0$, when $i \neq j$ [Yamakawa, 1971].

In the discussion above, the Gaussian approximation for EV interactions has been used to motivate the development of the FENE-PG spring force law to account for fluctuations in the spring force. In the next chapter, predictions of the FENE-P and FENE-PG approximations are compared with the results of BD simulations to understand the role of spring force fluctuations. As mentioned earlier, the Gaussian approximation for EV interactions in Rouse chains has been well studied

in literature. Except for some preliminary predictions for dumbbell models with HI, which will be discussed in the following section, no calculations have been performed with the Gaussian approximation for EV in this study. In the next section, equations are derived for a general mean-field model combining all the three phenomena of HI, EV and FE.

5.4 FEBS chains with excluded volume and hydrodynamic interactions

In the previous sections, the Gaussian approximation was individually applied to handle HI, EV and FE, and it was shown that this approximation accounts for fluctuations in each of these nonlinear phenomena. However, directly following the same procedure for models which simultaneously incorporate HI along with EV and/or FE has some undesirable consequences. This was demonstrated in a paper [Prabhakar and Prakash, 2002] published as a part of this study, in which the Gaussian closure was applied to a Hookean dumbbell model with EV and HI. In this section, the equations for this dumbbell model are first analyzed to identify the reason behind the problems encountered in that paper, and an alternative is suggested.

For a Hookean dumbbell model incorporating both EV and HI effects, Eq. (5.1) can be simplified using $N_s = 1$, $H^* = 1$, $\xi_1 = 1$, $\widetilde{\boldsymbol{A}}_{11} = \widetilde{\boldsymbol{A}} = 2[\boldsymbol{\delta} - \zeta\boldsymbol{\Omega}(\boldsymbol{Q})]$, and $w^*_{11} = w^* = (z^*/d^{*5})\exp[-Q^{*2}/2d^{*2}]$, to yield the following exact equation for the second moment $\langle\, \boldsymbol{Q}^*\boldsymbol{Q}^* \,\rangle$

$$\langle\, \boldsymbol{Q}^*\boldsymbol{Q}^* \,\rangle_{(1)} = -\frac{1}{4}\langle \boldsymbol{Q}^*\boldsymbol{Q}^* \cdot \widetilde{\boldsymbol{A}} + \widetilde{\boldsymbol{A}} \cdot \boldsymbol{Q}^*\boldsymbol{Q}^* \rangle + \frac{1}{4}\langle \boldsymbol{Q}^*\,\boldsymbol{Q}^* w^* \cdot \widetilde{\boldsymbol{A}} + \widetilde{\boldsymbol{A}} \cdot w^* \boldsymbol{Q}\,\boldsymbol{Q} \rangle + \frac{1}{2}\langle \widetilde{\boldsymbol{A}} \rangle. \tag{5.107}$$

The first average on the right-hand side involves HI alone and can be reduced using the results derived in Eq. (5.39) to give

$$\langle \boldsymbol{Q}^*\boldsymbol{Q}^* \cdot \widetilde{\boldsymbol{A}} \rangle = \boldsymbol{\sigma}^* \cdot [\overline{\boldsymbol{A}}(\boldsymbol{\sigma}^*) + \boldsymbol{\Delta}(\boldsymbol{\sigma}^*)]\,, \tag{5.108}$$

where,

$$\overline{\boldsymbol{A}} = \langle \widetilde{\boldsymbol{A}} \rangle = 2\boldsymbol{\delta} - 2\sqrt{2}h^* \boldsymbol{H}(\boldsymbol{\sigma}^*)\,, \tag{5.109}$$

and,

$$\boldsymbol{\Delta}(\boldsymbol{\sigma}^*) = -\frac{3\sqrt{2}h^*}{2}\boldsymbol{K}(\boldsymbol{\sigma}^*)\colon \boldsymbol{\sigma}^*\,. \tag{5.110}$$

Furthermore, $\boldsymbol{K}(\boldsymbol{\sigma}^*)\colon \boldsymbol{\sigma}^* = 4\boldsymbol{H}(\boldsymbol{\sigma}^*) - 4/3[\,\mathrm{tr}\,\boldsymbol{H}(\boldsymbol{\sigma}^*)]\boldsymbol{\delta}$ [Öttinger, 1989a], using which the right-hand side in Eq. (5.108) can be expressed in terms of the $\boldsymbol{H}$ function alone. However, the discussion below is presented using Eq. (5.108).

The second average on the right-hand side of Eq. (5.107) involves simultaneous contributions from both EV and HI, and has not been encountered before. The evaluation of this term becomes straightforward with the NGEV potential, since the Gaussian form of the potential can be combined with the Gaussian distribution to take advantage of the following result:

$$\begin{aligned}\langle \exp(-Q^{*2}/2d^{*2}) f(\boldsymbol{Q}^*)\rangle &= \frac{\langle \exp(-Q^{*2}/2d^{*2}) f(\boldsymbol{Q}^*)\rangle}{\langle \exp(-Q^{*2}/2d^{*2})\rangle}\,\langle \exp(-Q^{*2}/2d^{*2})\rangle, \\ &= \langle f(\boldsymbol{Q})\rangle' \,\frac{d^{*3}}{\sqrt{\det[d^{*2}\boldsymbol{\delta} + \boldsymbol{\sigma}^*]}}\end{aligned} \tag{5.111}$$

where $\langle \ldots \rangle'$ represents an average with a Gaussian distribution whose second moment is

$$\boldsymbol{\Pi} \equiv [(1/d^{*2})\boldsymbol{\delta} + \boldsymbol{\sigma}^{*-1}]^{-1} = d^{*2}\boldsymbol{\sigma}^* \cdot [d^{*2}\boldsymbol{\delta} + \boldsymbol{\sigma}^*]^{-1}\,. \tag{5.112}$$

Therefore, one obtains

$$\begin{aligned}\langle \boldsymbol{Q}^*\boldsymbol{Q}^* w^* \cdot \widetilde{\boldsymbol{A}}\rangle &= \frac{z^*}{d^{*5}}\langle \boldsymbol{Q}^*\boldsymbol{Q}^* \cdot \widetilde{\boldsymbol{A}} \exp[-Q^{*2}/2d^{*2}]\rangle\,, \\ &= \frac{z^*}{d^{*5}}\langle \boldsymbol{Q}^*\boldsymbol{Q}^* \cdot \widetilde{\boldsymbol{A}}\rangle' \frac{d^{*3}}{\sqrt{\det[d^{*2}\boldsymbol{\delta} + \boldsymbol{\sigma}^*]}}\,, \\ &= \frac{z^*}{d^{*2}\sqrt{\det[d^{*2}\boldsymbol{\delta} + \boldsymbol{\sigma}^*]}}\boldsymbol{\Pi} \cdot \{\overline{\boldsymbol{A}}(\boldsymbol{\Pi}) + \boldsymbol{\Delta}(\boldsymbol{\Pi})\}\,.\end{aligned} \tag{5.113}$$

Substituting from Eqs. (5.111) and (5.113) in Eq. (5.107) leads to

$$\begin{aligned}\boldsymbol{\sigma}^*_{(1)} = &-\frac{1}{2}\left[\boldsymbol{\sigma}^*\cdot\{\overline{\boldsymbol{A}}(\boldsymbol{\sigma}^*)+\boldsymbol{\Delta}(\boldsymbol{\sigma}^*)\}\right]\\ &+\frac{z^*}{2d^{*\,2}\sqrt{\det[d^{*\,2}\boldsymbol{\delta}+\boldsymbol{\sigma}^*]}}\left[\boldsymbol{\Pi}\cdot\{\overline{\boldsymbol{A}}(\boldsymbol{\Pi})+\boldsymbol{\Delta}(\boldsymbol{\Pi})\}\right]+\frac{1}{2}\overline{\boldsymbol{A}}(\boldsymbol{\sigma}^*)\,.\end{aligned} \tag{5.114}$$

The equation above shows that the direct application of the Gaussian approximation leads to a complex coupling of EV and HI through the functions $\overline{\boldsymbol{A}}(\boldsymbol{\Pi})$ and $\boldsymbol{\Delta}(\boldsymbol{\Pi})$.

At equilibrium, $\boldsymbol{\sigma}^*_{\rm eq}=\alpha^2_{\rm eq}\boldsymbol{\delta}$, where $\alpha^2_{\rm eq}$ is the EV swelling ratio introduced previously in Chapter 4. Therefore, $\boldsymbol{\Delta}(\boldsymbol{\sigma}^*_{\rm eq})\sim\boldsymbol{K}(\boldsymbol{\sigma}^*_{\rm eq})\colon\,\boldsymbol{\sigma}^*_{\rm eq}=\boldsymbol{0}$. Since $\boldsymbol{\Pi}_{\rm eq}$ is also isotropic, $\boldsymbol{\Delta}(\boldsymbol{\Pi}_{\rm eq})$ also vanishes. Thus, $\boldsymbol{\sigma}^*_{\rm eq}$ is obtained by solving

$$\begin{aligned}\boldsymbol{0} &= -\boldsymbol{\sigma}^*_{\rm eq}\cdot\overline{\boldsymbol{A}}(\boldsymbol{\sigma}^*_{\rm eq})+\frac{z^*}{d^{*\,2}\sqrt{\det[d^{*\,2}\boldsymbol{\delta}+\boldsymbol{\sigma}^*_{\rm eq}]}}\boldsymbol{\Pi}_{\rm eq}\cdot\overline{\boldsymbol{A}}(\boldsymbol{\Pi}_{\rm eq})+\overline{\boldsymbol{A}}(\boldsymbol{\sigma}^*_{\rm eq})\,,\\ &= -\boldsymbol{\sigma}^*_{\rm eq}+\frac{z^*}{d^{*\,2}\sqrt{\det[d^{*\,2}\boldsymbol{\delta}+\boldsymbol{\sigma}^*_{\rm eq}]}}\boldsymbol{\Pi}_{\rm eq}\cdot\overline{\boldsymbol{A}}(\boldsymbol{\Pi}_{\rm eq})\cdot\overline{\boldsymbol{A}}(\boldsymbol{\sigma}^*_{\rm eq})^{-1}+\boldsymbol{\delta}\,.\end{aligned} \tag{5.115}$$

Since $\overline{\boldsymbol{A}}(\boldsymbol{\Pi}_{\rm eq})\cdot\overline{\boldsymbol{A}}(\boldsymbol{\sigma}^*_{\rm eq})^{-1}\neq\boldsymbol{\delta}$ in the equation above, the equilibrium solution for $\boldsymbol{\sigma}^*_{\rm eq}$ depends on the hydrodynamic interaction parameter, h^*. Simplifying further, one obtains

$$0=-\alpha^2_{\rm eq}+\alpha^2_{\rm eq}\frac{z^*}{(d^{*\,2}+\alpha^2_{\rm eq})^{5/2}}\left(\frac{\alpha_{\rm eq}-\sqrt{2}h^*k}{\alpha_{\rm eq}-\sqrt{2}h^*}\right)+1, \tag{5.116}$$

where

$$k=\frac{\sqrt{d^{*\,2}+\alpha^2_{\rm eq}}}{d^*} \tag{5.117}$$

Figure 5.2 shows plots the physically valid root (real, >1) of the equation above for $\alpha^2_{\rm eq}$, against the parameter d^* for a fixed value of z^*. Although the variation of $\alpha^2_{\rm eq}$ with d^* appears to be qualitatively similar to the results of BD simulations, the predictions of the approximation differ from the exact results in two important respects. Firstly, the predictions of the approximation are seen to clearly depend on

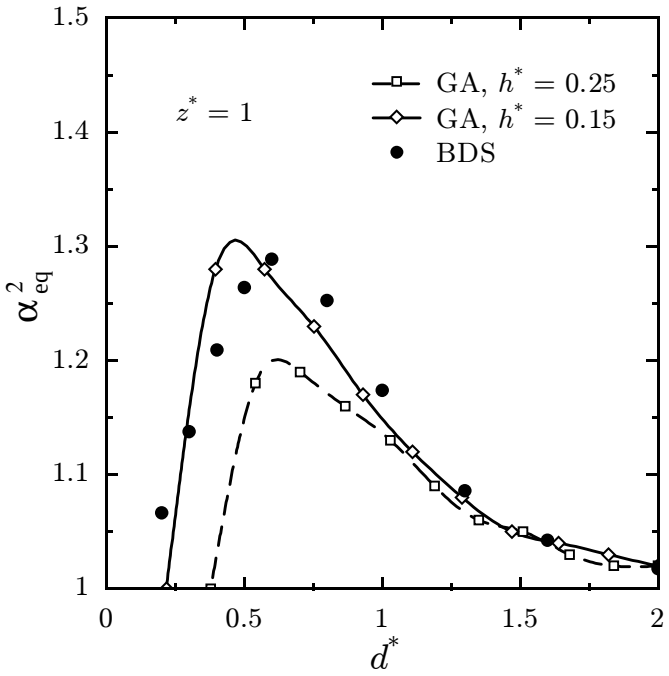

Figure 5.2: Equilibrium swelling ratio predicted with the direct application of the Gaussian approximation for Hookean dumbbells with EV and HI.

h^*. In addition, it is found that for $d^* < d^*_{\text{min}}$ where

$$d^*_{\text{min}} = h^* \sqrt{\frac{2}{1 - 2h^{*\,2}}}, \tag{5.118}$$

there is no root to Eq. (5.116) which is greater than unity.

The source of these problems with this model can be traced back to the terms $\overline{\boldsymbol{A}}(\boldsymbol{\Pi})$ and $\boldsymbol{\Delta}(\boldsymbol{\Pi})$ in the excluded volume contribution Eq. (5.114). The complex coupling of EV and HI in these terms is the consequence of using the Gaussian ansatz to simplify the term $\langle \boldsymbol{Q}^* \boldsymbol{Q}^* w^* \cdot \widetilde{\boldsymbol{A}} \rangle = -\langle \boldsymbol{Q}^* \boldsymbol{F}^{\text{E},c\,*} \cdot \widetilde{\boldsymbol{A}} \rangle$. It is clear that the same undesirable influence of HI at equilibrium will occur for any nonlinear connector force, including the FENE force.

One way in which the undesirable coupling of EV and HI can be removed is by first replacing the EV potential with its mean-field version derived previously in the context of free-draining chains, *before* attempting to simplify the EV term in the second moment equation. In other words, the average $-\langle \boldsymbol{Q}^* \boldsymbol{F}^{\text{E},c\,*} \cdot \widetilde{\boldsymbol{A}} \rangle$ is replaced first by $-\langle \boldsymbol{Q}^* \overline{\boldsymbol{F}}^{\text{E},c\,*} \cdot \widetilde{\boldsymbol{A}} \rangle = z^* \langle \boldsymbol{Q}^* \boldsymbol{Q}^* \cdot \boldsymbol{J} \cdot \widetilde{\boldsymbol{A}} \rangle$ [Eq. (5.74)] where, using Eqs. (5.68) and

(5.71),

$$\boldsymbol{J}(\boldsymbol{\sigma}^*) = \boldsymbol{V}_{12}(\boldsymbol{\sigma}^*) = \frac{1}{\sqrt{\det[d^{*\,2}\boldsymbol{\delta} + \boldsymbol{\sigma}^*]}}\,[d^{*\,2}\boldsymbol{\delta} + \boldsymbol{\sigma}^*]^{-1}\,. \tag{5.119}$$

Following this replacement, the Gaussian approximation can be applied to simplify further to yield,

$$\langle \boldsymbol{Q}^*\boldsymbol{Q}^* \cdot \boldsymbol{J} \cdot \widetilde{\boldsymbol{A}} \rangle = \boldsymbol{\sigma}^* \cdot \boldsymbol{J}(\boldsymbol{\sigma}^*) \cdot \overline{\boldsymbol{A}}(\boldsymbol{\sigma}^*) - \frac{3\sqrt{2}h^*}{2}\boldsymbol{\sigma}^* \cdot \boldsymbol{K}(\boldsymbol{\sigma}^*) \colon [\boldsymbol{\sigma}^* \cdot \boldsymbol{J}(\boldsymbol{\sigma}^*)]\,. \tag{5.120}$$

With this result, the equation for the second moment for Hookean dumbbells with EV and HI is

$$\boldsymbol{\sigma}^*_{(1)} = -\frac{1}{2}\boldsymbol{\sigma}^* \cdot \overline{\boldsymbol{M}} + \frac{1}{2}\overline{\boldsymbol{A}}(\boldsymbol{\sigma}^*)\,, \tag{5.121}$$

where,

$$\overline{\boldsymbol{M}} = \{\boldsymbol{\delta} - z^*\boldsymbol{J}(\boldsymbol{\sigma}^*)\} \cdot \overline{\boldsymbol{A}}(\boldsymbol{\sigma}^*) - \frac{3\sqrt{2}h^*}{2}\boldsymbol{K}(\boldsymbol{\sigma}^*) \colon [\boldsymbol{\sigma}^* \cdot \{\boldsymbol{\delta} - z^*\boldsymbol{J}(\boldsymbol{\sigma}^*)\}]\,. \tag{5.122}$$

At equilibrium, the term containing the $\boldsymbol{K}$ function in the expression for $\overline{\boldsymbol{M}}$ vanishes because both $\boldsymbol{\sigma}^*_{\mathrm{eq}}$ and $\boldsymbol{J}(\boldsymbol{\sigma}^*_{\mathrm{eq}})$ are isotropic. Hence, with $\overline{\boldsymbol{A}}_{\mathrm{eq}} = \overline{A}_{\mathrm{eq}}\boldsymbol{\delta}$ at equilibrium, the equation for the second moment reduces to

$$0 = -\frac{1}{2}\left[\sigma^*_{\mathrm{eq}}\{1 - z^*J(\sigma^*_{\mathrm{eq}})\} - 1\right]\overline{A}_{\mathrm{eq}}(\sigma^*_{\mathrm{eq}})\,, \tag{5.123}$$

from which it is evident that σ^*_{eq}, as the solution to

$$\sigma^*_{\mathrm{eq}}\{1 - z^*J(\sigma^*_{\mathrm{eq}})\} - 1 = 0\,, \tag{5.124}$$

must be independent of h^*. The same equation is obtained when Eq. (5.106) is used for free-draining Hookean dumbbells with EV.

The same approach can also be used for handling the FENE nonlinearity in dumbbells with HI. Moreover, extension of this approach to chains is straightforward. Thus, one finally obtains the following set of equations for the evolution of the second

moments for FEBS chains with EV and HI:

$$\boldsymbol{\sigma}^*_{ij} = -\frac{1}{4}\sum_{m=1}^{N_\mathrm{S}} \left[\boldsymbol{\sigma}^*_{im}\cdot\overline{\boldsymbol{M}}_{mj} + \overline{\boldsymbol{M}}^{\mathrm{T}}_{mi}\cdot\boldsymbol{\sigma}^*_{mj}\right] + \frac{1}{2}\overline{\boldsymbol{D}}_{ij}\,, \tag{5.125}$$

where,

$$\overline{\boldsymbol{D}}_{ij} = \overline{\boldsymbol{A}}_{ij}\,, \tag{5.126}$$

$$\overline{\boldsymbol{M}}_{ij} = \sum_{m=1}^{N_\mathrm{S}} \boldsymbol{T}_{im}\cdot\overline{\boldsymbol{A}}_{mj} + \sum_{m,p,q,=1}^{N_\mathrm{S}} \boldsymbol{\Gamma}^{mj}_{iq} : [\boldsymbol{\sigma}^*_{qp}\cdot\boldsymbol{T}_{pm}]\,. \tag{5.127}$$

The definitions of the auxiliary quantities are reproduced below for convenience,

$$\overline{\boldsymbol{A}}_{ij} \equiv A_{ij}\boldsymbol{\delta} + \sqrt{2}h^*(\boldsymbol{H}_{ij} + \boldsymbol{H}_{i+1,\,j+1} - \boldsymbol{H}_{i,\,j+1} - \boldsymbol{H}_{i+1,\,j})\,, \tag{5.31}$$

$$\boldsymbol{\Gamma}^{ps}_{rq} \equiv \frac{3\sqrt{2}h^*}{4}[\Delta\Theta^{ps}_{rq}\boldsymbol{K}_{rq} + \Delta\Theta^{ps}_{r+1,\,q+1}\boldsymbol{K}_{r+1,\,q+1} - \Delta\Theta^{ps}_{r+1,\,q}\boldsymbol{K}_{r+1,\,q} - \Delta\Theta^{ps}_{r,\,q+1}\boldsymbol{K}_{r,\,q+1}]\,, \tag{5.42}$$

$$\boldsymbol{T}_{ij} \equiv H^*\delta_{ij}\boldsymbol{L}_j - z^*\boldsymbol{J}_{ij}\,, \tag{5.94}$$

$$\boldsymbol{L}_m \equiv \frac{1}{1 - \operatorname{tr}\boldsymbol{\sigma}^*_{mm}/b^*}\boldsymbol{\delta} + \frac{2/b^*}{1 - 2\operatorname{tr}\boldsymbol{\sigma}^*_{mm}/b^* + [(\operatorname{tr}\boldsymbol{\sigma}^*_{mm})^2 + 2\boldsymbol{\sigma}^*_{mm} : \boldsymbol{\sigma}^*_{mm}]/b^{*\,2}}\boldsymbol{\sigma}^*_{mm}\,, \tag{5.88}$$

$$\boldsymbol{J}_{ij} \equiv \frac{1}{2}\sum_{\substack{\mu,\,\nu=1\\ \mu\neq\nu}}^{N} \Delta\Theta^{ij}_{\mu\nu}\boldsymbol{V}_{\mu\nu}\,, \tag{5.71}$$

$$\boldsymbol{V}_{\mu\nu} \equiv \frac{1}{\sqrt{\det[d^{*\,2}\boldsymbol{\delta} + \boldsymbol{S}^*_{\mu\nu}]}}[d^{*\,2}\boldsymbol{\delta} + \boldsymbol{S}^*_{\mu\nu}]^{-1}\,. \tag{5.68}$$

(5.128)

The polymer stress predicted by this model is

$$\boldsymbol{\tau}^*_\mathrm{p} = N_\mathrm{S}\boldsymbol{\delta} - \sum_{i,j=1}^{N_\mathrm{S}} \boldsymbol{\sigma}^*_{ij}\cdot\boldsymbol{T}_{ji}\,. \tag{5.129}$$

When $z^* \neq 0$, using $\overline{\boldsymbol{A}}_{ij,\,\mathrm{eq}} = \overline{A}_{ij,\,\mathrm{eq}}\boldsymbol{\delta}$ at equilibrium, and the fact that the

contributions due to the $\boldsymbol{K}$ tensors vanish at equilibrium, it can be shown that the values of $\sigma^*_{ij,\,\mathrm{eq}}$ are determined as the solutions to the following set of equations:

$$0 = -\frac{1}{4}\sum_{m,n=1}^{N_\mathrm{s}} \left(\sigma^*_{im,\,\mathrm{eq}}\, T_{mn,\,\mathrm{eq}} \overline{A}_{nj,\,\mathrm{eq}} + \overline{A}_{im,\,\mathrm{eq}} T_{mn,\mathrm{eq}}\, \sigma^*_{nj,\mathrm{eq}}\right) + \frac{1}{2}\overline{A}_{ij,\,\mathrm{eq}}\,. \tag{5.130}$$

Rearranging, one obtains an equation that is identical to Eq. (5.106) derived earlier for free-draining FEBS chains with EV:

$$U_{ij} = \sum_{m=1}^{N_\mathrm{s}} \sigma^*_{im,\,\mathrm{eq}} \left(H^* \delta_{mj} L_{j,\,\mathrm{eq}} - z^* J_{mj,\,\mathrm{eq}}\right) - \delta_{ij} = 0\,, \tag{5.106}$$

Thus, the equilibrium second moments are free of the HI parameter h^*.

The set of equations above can be interpreted as a new constitutive model for the polymer stress in dilute polymer solutions that is based on a molecular model incorporating the phenomena of HI, EV and FE. Although the derivation of this approximate mean-field Gaussian model above is based on heuristic arguments, its accuracy can be tested against results of BD simulations. In this study, no calculations have been performed using the approximation above for chains with EV. In the next Chapter, however, the mean-field Gaussian model is tested in the absence of EV interactions, by setting $z^* = 0$ in Eq. (5.125) above. In the resulting set of equations,

$$\overline{\boldsymbol{D}}_{ij} = \overline{\boldsymbol{A}}_{ij}\,, \tag{5.131}$$

as before, but

$$\overline{\boldsymbol{M}}_{ij} = H^* \boldsymbol{L}_i \cdot \overline{\boldsymbol{A}}_{ij} + H^* \sum_{m,q,\,=1}^{N_\mathrm{s}} \boldsymbol{\Gamma}^{mj}_{iq} : \left[\boldsymbol{\sigma}^*_{qm} \cdot \boldsymbol{L}_m\right], \tag{5.132}$$

while the polymer stress is given by

$$\boldsymbol{\tau}^*_\mathrm{p} = N_\mathrm{s}\boldsymbol{\delta} - H^* \sum_{i=1}^{N_\mathrm{s}} \boldsymbol{\sigma}^*_{ii} \cdot \boldsymbol{L}_i\,. \tag{5.133}$$

Besides being many times faster than BD simulations, the model above can be used to explore the effect of fluctuations in HI and the spring forces which are described in an approximate, and as mentioned before, heuristic sense. This is achieved by deriving several subsidiary models by turning on or off different terms in the model equations. These modifications can be separated into two classes: those that change the terms responsible for describing the effect of HI, and those controlling the influence of FE. Each subsidiary model is referred to with an acronym. The first two letters refer to the approximation used for HI, and the last letter refers to that used for FE. Table 5.1 shows the letter codes used. For example, the full Gaussian model is referred to as the GA-PG model. The Rouse model, on the other hand, is denoted as the FD-H model, whereas the Zimm model is denoted as EA-H.

5.5 Diagonalization approximations

In this section, some additional approximations are discussed for speeding up the calculations in the absence of EV interactions. These additional approximations have only been applied to chains with Hookean and FENE-P springs.

In all the cases discussed so far, the governing equations for the second moments consist of a set of N_{S}^2 coupled ODE's. These ODE's are also nonlinear in the second moments, the notable exception being the Zimm model [Eq. (5.23)]. The linear character of the Zimm model lends itself to a major simplification of its governing equations.

In the Zimm model, the set of the physical connector vectors $\{\boldsymbol{Q}_i | i = 1, \ldots, N_{\mathrm{S}}\}$ can be mapped onto a set of normal modes $\{\boldsymbol{Q}'_p | p = 1, \ldots, N_{\mathrm{S}}\}$ using the following transformation,

$$\boldsymbol{Q}'_p = \sum_{i=1}^{N_{\mathrm{S}}} \Pi^{\mathrm{Z}}_{ip} \boldsymbol{Q}^*_i \,, \tag{5.134}$$

where Π^{Z}_{ip} are the elements of the orthogonal matrix whose columns are formed by

Table 5.1: Nomenclature used for referring to subsidiary models, and modifications made to the Gaussian model.

	Acronym	Modification
Treatment of HI		
Free-draining	FD	$\overline{\boldsymbol{A}}_{ij} = A_{ij}\boldsymbol{\delta}$; $\boldsymbol{\Gamma}^{pq}_{rs} = \mathbf{0}$
Equilibrium-averaging	EA	$\overline{\boldsymbol{A}}_{ij} = \widetilde{A}_{ij}\boldsymbol{\delta}$; $\boldsymbol{\Gamma}^{pq}_{rs} = \mathbf{0}$
Consistent-averaging	CA	$\boldsymbol{\Gamma}^{pq}_{rs} = \mathbf{0}$
Gaussian approximation	GA	–
Treatment of FE		
Hookean springs	H	$\boldsymbol{L}_m = \boldsymbol{\delta}$
FENE-P	P	$\boldsymbol{L}_m = \dfrac{1}{1 - \operatorname{tr} \boldsymbol{\sigma}^*_{mm}/b^*}\boldsymbol{\delta}$
FENE-PG	PG	–

the eigenvectors of the modified Rouse matrix. That is,

$$\sum_{i,j=1}^{N_\mathrm{s}} \Pi^{\mathrm{z}}_{ip} \widetilde{A}_{ij} \Pi^{\mathrm{z}}_{jq} = \delta_{pq}\, \widetilde{a}_p \,, \tag{5.135}$$

where $\widetilde{a}_p$ is an eigenvalue of the modified Rouse matrix. These eigenvalues are usually referred to as the Zimm eigenvalues. By multiplying both sides of Eq. (5.23) by $\Pi^{\mathrm{z}}_{ip}\, \Pi^{\mathrm{z}}_{jq}$, summing over all i and j, and using the orthogonality relation

$$\sum_{k=1}^{N_\mathrm{s}} \Pi^{\mathrm{z}}_{mk} \Pi^{\mathrm{z}}_{nk} = \delta_{mn} = \sum_{k=1}^{N_\mathrm{s}} \Pi^{\mathrm{z}}_{km} \Pi^{\mathrm{z}}_{kn} \,, \tag{5.136}$$

the evolution equations for the covariances in the normal modes $\boldsymbol{\sigma}'_{pq}$ defined as

$$\boldsymbol{\sigma}'_{pq} = \sum_{i,j=1}^{N_\mathrm{s}} \Pi^{\mathrm{z}}_{ip} \boldsymbol{\sigma}^*_{ij} \Pi^{\mathrm{z}}_{jq} \,, \tag{5.137}$$

can be obtained as

$$\boldsymbol{\sigma}'_{pq,\,(1)} = -\frac{1}{4} \boldsymbol{\sigma}'_{pq} (\widetilde{a}_p + \widetilde{a}_q) + \frac{1}{2} \widetilde{a}_p \delta_{pq} \boldsymbol{\delta} \,. \tag{5.138}$$

At equilibrium, since $\boldsymbol{\sigma}^*_{ij,\,\mathrm{eq}} = \delta_{ij} \boldsymbol{\delta}$, $\boldsymbol{\sigma}'_{pq,\,\mathrm{eq}} = \delta_{pq} \boldsymbol{\delta}$. Consequently, for all flows starting with an equilibrium initial condition, the off-diagonal components remain unchanged and $\boldsymbol{\sigma}'_{pq} = \mathbf{0}$ if $p \neq q$. Hence, the covariance block-matrix is diagonal in the Zimm model, and one only needs to integrate the following N_s equations for the diagonal components,

$$\boldsymbol{\sigma}'_{p,(1)} = -\frac{1}{2} \widetilde{a}_p \boldsymbol{\sigma}'_p + \frac{1}{2} \widetilde{a}_p \boldsymbol{\delta} \,, \tag{5.139}$$

where the notation $(\dots)_p = (\dots)_{pp}$ is used, and

$$\boldsymbol{\sigma}'_{pq} = \delta_{pq} \boldsymbol{\sigma}_p \,. \tag{5.140}$$

The macroscopic properties of interest can then be obtained by the covariances in

physical space using

$$\boldsymbol{\sigma}^*_{ij} = \sum_{p=1}^{N_s} \Pi^z_{ip} \boldsymbol{\sigma}'_p \Pi^z_{jp} \,. \tag{5.141}$$

Although Eq. (5.139) above can be solved analytically to obtained closed form expressions for the $\boldsymbol{\sigma}'_p$ [Bird *et al.*, 1987a], if one wishes to solve problems numerically, then integrating the set of N_s equations for the normal mode covariances in Eq. (5.139) is computationally much more efficient than directly integrating the original set of N_s^2 equations in Eq. (5.23). The CPU-time required per time-step for Eq. (5.139) is proportional to N_s whereas the summation over m for each pair of i and j in Eq. (5.23) means that the computational cost per time step scales as N_s^3 for that equation. This massive overall gain is due not just to the reduction in the number of equations because of the diagonalization in Eq. (5.140), but also to the fact that these equations in Eq. (5.139) are decoupled and independent. The decoupling of the equations in Eq. (5.139) is the result of the fact that the eigenvalues $\widetilde{a}_p$ are constants which need be calculated only once and stored at the start of the integration. Interestingly, the CPU-time for the conversion of the $\boldsymbol{\sigma}'_p$ tensors back to the $\boldsymbol{\sigma}^*_{ij}$ tensors is proportional to N_s^3. If this conversion is performed after every time-step in the integration, the scaling of the total computational cost would approach N_s^3 as N_s becomes large. Of course, one is typically not interested in obtaining all the second moments $\boldsymbol{\sigma}^*_{ij}$ at every time-step.

It would be advantageous if a similar reduction in computational cost could be effected for the other closure approximations as well. However, for all the other approximations presented so far in this Chapter, the governing equations are nonlinear in $\boldsymbol{\sigma}^*_{ij}$ tensors, due to the appearance of the $\boldsymbol{H}$, $\boldsymbol{K}$ functions, and/or the FENE-P function

$$\overline{\xi}_m \equiv \frac{1}{1 - \text{ tr } \boldsymbol{\sigma}^*_{mm}/b^*} \,. \tag{5.142}$$

Furthermore, the functions $\overline{\boldsymbol{A}}_{ij}$ and Δ_{ij} are not constant and transforming to normal modes will involve the calculation of the eigenvalues and eigenvectors of the diffusion super-matrix at every time-step in the integration. Wiest and Tanner [1989] showed

with a free-draining FENE-P chain model that such a procedure is complicated, and Kisbaugh and McHugh [1990] point out that it is computationally more efficient to directly solve the N_s^2 equations for the second moments.

Instead, several workers have used additional assumptions to reduce the number of equations from N_s^2 to N_s. For instance, for free-draining chains with FENE-P springs, Eq. (5.125) represents a set of N_s^2 coupled, nonlinear ODE's. Wedgewood *et al.* [1991] introduced a further approximation—referred to in the literature as the "FENE-PM" approximation—in which $\overline{\xi}_m$ is replaced with the following function:

$$\widetilde{\xi} \equiv \frac{1}{1 - \sum_{k=1}^{N_\mathrm{s}} \operatorname{tr} \boldsymbol{\sigma}^*_{kk}/b^*} \,. \tag{5.143}$$

Since this function is independent of the index m, the resulting equations for the second moments,

$$\boldsymbol{\sigma}^*_{ij,(1)} = -\frac{H^*}{4}\,\widetilde{\xi} \sum_{m=1}^{N_\mathrm{s}} [\boldsymbol{\sigma}^*_{im} A_{mj} + A_{im} \boldsymbol{\sigma}^*_{mj}] + \frac{1}{2} A_{ij} \boldsymbol{\delta} \,, \tag{5.144}$$

can be diagonalized by a transformation to normal modes as in the Zimm model above, by using the orthogonal matrix that diagonalizes the Rouse matrix whose elements are A_{ij}. In this case, one again obtains a set of N_s equations for the normal mode variances $\boldsymbol{\sigma}'_p$,

$$\boldsymbol{\sigma}'_{p,(1)} = -\frac{H^*}{2} \widetilde{\xi} a_p \boldsymbol{\sigma}'_p + \frac{1}{2} a_p \boldsymbol{\delta} \,, \tag{5.145}$$

where a_p are the eigenvalues of the Rouse matrix. In contrast to Eq. (5.139) earlier, however, the presence of $\widetilde{\xi}$ in the equation above means that the N_s equations in this model are coupled, since

$$\widetilde{\xi} = \frac{1}{1 - \sum_{l=1}^{N_\mathrm{s}} (\sum_{k=1}^{N_\mathrm{s}} \Pi^{\mathrm{R}\,2}_{kl}) \operatorname{tr} \boldsymbol{\sigma}'_l / b^*} \,. \tag{5.146}$$

Here, Π^R_{kp} are elements of the Rouse orthogonal matrix. The values $g_p = \sum_{k=1}^{N_\mathrm{s}} \Pi^{\mathrm{R}\,2}_{kp}$ can be calculated and stored at the start of the integration, and the summation Eq. (5.146) is performed once every time step. Therefore, the overall computational

effort per time step in the free-draining FENE-PM model scales as N_s, which is a significant improvement over the N_s^3 scaling computational cost of original set of equations. However, the improvement in computational efficiency has been obtained at the cost of an additional approximation. Although Wedgewood *et al.* [1991] show that the loss in accuracy for a free-draining FENE-PM model is not great in steady and unsteady shear and extensional flows, this approximation does not offer the same advantage when applied to chains with HI, and is therefore not employed in the rest of this work.

A diagonalization approximation for Rouse chains with HI was suggested by Fixman [1966b] in his treatment of consistently-averaged HI. Fixman also proposed an iterative solution scheme for the resulting equations, and carried out the calculations for two iterations (the first iteration giving the results of the Zimm approximation). Magda *et al.* [1988] later refined the calculations by carrying out the iterative process to convergence and showed that the resulting predictions for steady shear η_p, Ψ_1 and Ψ_2 for chains with $N = 25$ were quite close to the results of Öttinger [1987a], which had been obtained by directly integrating Eq. (5.24) without the additional diagonalization approximation. Magda *et al.* were able to explore the steady-state behaviour in shear and extensional flows with N as large as 500. While Magda *et al.* used the boson-operator formalism of Fixman, Kisbaugh and McHugh [1990] used the framework introduced by Öttinger and confirmed that predictions with the additional diagonalization approximations deviated negligibly from those obtained with the original un-diagonalized approximation. They also extended this scheme to the CA-P model with FENE-P springs and consistently-averaged HI (Table 5.1). The equation for the second moments in the CA-P model is

$$\boldsymbol{\sigma}^*_{ij,(1)} = -\frac{H^*}{4}\sum_{m=1}^{N_s}\overline{\xi}_m[\boldsymbol{\sigma}^*_{im}\cdot\overline{\boldsymbol{A}}_{mj} + \overline{\boldsymbol{A}}_{im}\cdot\boldsymbol{\sigma}^*_{mj}] + \frac{1}{2}\overline{\boldsymbol{A}}_{ij}\,, \tag{5.147}$$

and the polymer stress is given by,

$$\boldsymbol{\tau}^*_p = N_s\boldsymbol{\delta} - H^*\sum_{i=1}^{N_s}\overline{\xi}_i\,\boldsymbol{\sigma}^*_{ii}\,. \tag{5.148}$$

The starting point for the treatment of Kisbaugh and McHugh is the same as

in Eq. (5.134): the transformation of the N_s physical connector vectors $\boldsymbol{Q}_i^*$ to the N_s normal modes $\boldsymbol{Q}'_p$. As in the Zimm model, Eq. (5.147) above is multiplied by the product of the elements of an orthogonal matrix $\Pi_{ip}\,\Pi_{jq}$ and summed over all i and j to obtain the following set of equations for the evolution of the dimensionless normal mode covariances $\boldsymbol{\sigma}'_{pq}$:

$$\boldsymbol{\sigma}'_{pq,\,(1)} = -\frac{H^*}{4}\sum_{u=1}^{N_\mathrm{s}}\left[\boldsymbol{\sigma}'_{pu}\cdot\boldsymbol{X}_{uq} + \boldsymbol{X}_{up}\cdot\boldsymbol{\sigma}'_{uq}\right] + \frac{1}{2}\boldsymbol{Z}_{pq}\,. \tag{5.149}$$

where the auxiliary tensors

$$\boldsymbol{Z}_{pq} \equiv \sum_{i,j=1}^{N_\mathrm{s}} \Pi^{\mathrm{Z}}_{ip}\overline{\boldsymbol{A}}_{ij}\Pi^{\mathrm{Z}}_{jq}\,, \tag{5.150}$$

$$\boldsymbol{X}_{pq} \equiv \sum_{i,j=1}^{N_\mathrm{s}} \Pi^{\mathrm{Z}}_{ip}\bar{\xi}_i\overline{\boldsymbol{A}}_{ij}\Pi^{\mathrm{Z}}_{jq}\,, \tag{5.151}$$

Thus far, the development has proceeded without additional approximations of any kind. At this stage, Kisbaugh and McHugh set

$$\Pi_{pq} = \Pi^{\mathrm{Z}}_{pq}\,, \tag{5.152}$$

and further *assume* that the off-diagonal blocks of the super-matrices comprising of $\boldsymbol{Z}_{pq}$ and $\boldsymbol{X}_{pq}$ are negligible:

$$\boldsymbol{Z}_{pq} \approx \boldsymbol{Z}_p\delta_{pq}; \quad \boldsymbol{X}_{pq} \approx \boldsymbol{X}_p\delta_{pq}\,. \tag{5.153}$$

Strictly speaking, the set of $\boldsymbol{Q}'_p$ vectors obtained with the assumption in Eq. (5.152) cannot be the normal modes of the system under arbitrary conditions of flow. However, for the sake of convenience, the tensors $\boldsymbol{\sigma}'_{pq}$ will be referred to as the "normal-mode" covariances.

With these assumptions, one obtains the following set of equations for the normal-mode variances:

$$\boldsymbol{\sigma}'_{p,\,(1)} = -\frac{H^*}{4}\left[\boldsymbol{\sigma}'_p\cdot\boldsymbol{X}_p + \boldsymbol{X}_p\cdot\boldsymbol{\sigma}'_q\right] + \frac{1}{2}\boldsymbol{Z}_p\,. \tag{5.154}$$

The equations above are the governing equations for the diagonalized CA-P model, which will be referred to as the DCA-P model. Equation (5.154) represents a set of $N_{\rm S}$ ODE's that are coupled and nonlinear. The coupling comes about because the auxiliary tensors $\boldsymbol{Z}_p$ and $\boldsymbol{X}_p$ depend, through the $\overline{\boldsymbol{A}}_{ij}$ tensors, on the tensors $\boldsymbol{H}_{\mu\nu}$, which in turn require the variances

$$\boldsymbol{S}^*_{\mu\nu} = \sum_{i,j=1}^{N_{\rm S}} \Delta\Theta^{ij}_{\mu\nu} \left(\sum_{k=1}^{N_{\rm S}} \Pi^{\rm Z}_{ik} \boldsymbol{\sigma}'_k \Pi^{\rm Z}_{jk}. \right) = \sum_{i,j=1}^{N_{\rm S}} \Delta\Theta^{ij}_{\mu\nu} \boldsymbol{\sigma}^*_{ij} \,. \tag{5.155}$$

The initial condition for the time integration of the ODE's for $\boldsymbol{\sigma}'_p$ is

$$\boldsymbol{\sigma}'_{p,\,\rm eq} = \sum_{i,j=1}^{N_{\rm S}} \Pi^{\rm Z}_{ip} \boldsymbol{\sigma}^*_{ij,\,\rm eq} \Pi^{\rm Z}_{jp} = \sum_{i,j=1}^{N_{\rm S}} \Pi^{\rm Z}_{ip} (\delta_{ij}\boldsymbol{\delta}) \Pi^{\rm Z}_{jp} = \boldsymbol{\delta} \,. \tag{5.156}$$

Furthermore, at equilibrium, $\overline{\boldsymbol{A}}_{ij,\,\rm eq} = \widetilde{A}_{ij}\boldsymbol{\delta}$, and therefore from Eq. (5.150), $\boldsymbol{Z}_{p,\,\rm eq} = \widetilde{a}_p\boldsymbol{\delta}$. As pointed out earlier in Eq. (5.104), with the FENE-P approximation, $H^*\overline{\xi}_{m,\,\rm eq} = H^*\overline{\xi}_{\rm eq} = 1$, which when used in Eq. (5.151) leads to $\boldsymbol{X}_{p,\,\rm eq} = \widetilde{a}_p\boldsymbol{\delta}$. Therefore, at equilibrium, Eq. (5.154) is consistent with the initial condition $\boldsymbol{\sigma}'_{p,\,\rm eq}$. Following the imposition of a velocity gradient $\boldsymbol{\kappa}^*$ at $t^* = 0$ and starting from the equilibrium initial condition, the tensors $\boldsymbol{\sigma}'_p$ at the end of the first time step in the integration of the ODE's are calculated first. The functions $\overline{\xi}_m$ can then be evaluated using Eqs. (5.141) and (5.142) as

$$\overline{\xi}_m = \frac{1}{1 - \left[\sum_{p=1}^{N_{\rm S}} \Pi^{{\rm Z}\,2}_{mp} \ {\rm tr}\,(\boldsymbol{\sigma}'_p) \right] / b^*} \,. \tag{5.157}$$

Using Eq. (5.155), the $\boldsymbol{S}^*_{\mu\nu}$ tensors can then be calculated for all pairs of beads. Hence, the $\boldsymbol{H}_{\mu\nu}$ tensors, and therefore $\overline{\boldsymbol{A}}_{ij}$ tensors, at that time-step can also be calculated. The definitions in Eq. (5.150) and (5.151) then lead to the $\boldsymbol{Z}_p$ and $\boldsymbol{X}_p$ tensors, respectively. Once these quantities are calculated, the integration can proceed to the next time-step.

It is possible to use these equations to generate simpler models. For instance, if equilibrium-averaged HI were to be used instead of consistent-averaging, the $\overline{\boldsymbol{A}}_{ij}$

tensors Eq. (5.151) are replaced with $\widetilde{A}_{ij}\boldsymbol{\delta}$ [Eq. (5.22)], and one obtains

$$\boldsymbol{\sigma}'_{p,\,(1)} = -\frac{H^*}{2}\boldsymbol{\sigma}'_p\widetilde{x}_p + \frac{1}{2}\widetilde{a}_p\,, \tag{5.158}$$

where

$$\widetilde{x}_p = \sum_{i,j=1}^{N_\mathrm{s}} \Pi^{\mathrm{Z}}_{ip}\overline{\xi}_i\widetilde{A}_{ij}\Pi^{\mathrm{Z}}_{jp}\,. \tag{5.159}$$

Equation (5.158) is a variation of "multi-mode" FENE-P constitutive models that are sometimes used to describe experimental data, in which the spectrum of relaxation times is based on the Zimm eigenvalues [Anna and McKinley, 2001; Entov and Hinch, 1997]. If $\widetilde{A}_{ij}$ in Eq. (5.159) above is replaced with the elements of the Rouse matrix A_{ij}, and the Rouse orthogonal matrix components Π^{R}_{ij} are used instead of Π^{Z}_{ij}, one obtains the diagonalized version of the free-draining model with FENE-P springs (the FD-P) model, which is referred to in this thesis as the DFD-P model.

With the DCA-P model, Kisbaugh and McHugh were able to explore the behaviour of FEBS chains with HI for large values of N, and showed for that the combination of FE and HI causes shear-thinning-thickening-thinning behaviour in solutions of high molecular weight polymers. Subsequently, Prakash and Öttinger [1997] also used the diagonalization assumption in conjunction with the Gaussian approximation for Rouse chains with HI. Since this combination was carried out with two different assumptions of "normality"–a Normal distribution, and transformation to normal modes–it was dubbed the "Two-Fold Normal" (TFN) approximation. In the present work, the TFN approximation is extended to chains with FENE-P springs.

The full set of equations for the normal-mode covariances in the TFN approximation is

$$\boldsymbol{\sigma}'_{pq,\,(1)} = -\frac{1}{4}\sum_{u=1}^{N_\mathrm{s}}\left[\boldsymbol{\sigma}'_{pu}\cdot(\boldsymbol{X}_{uq}+\boldsymbol{Y}_{uq}) + (\boldsymbol{X}_{up}+\boldsymbol{Y}^{\mathrm{T}}_{up})\cdot\boldsymbol{\sigma}'_{uq}\right] + \frac{1}{2}\boldsymbol{Z}_{pq}\,, \tag{5.160}$$

where the tensors $\boldsymbol{Z}_{pq}$ and $\boldsymbol{X}_{pq}$ are defined as in Eqs. (5.150) and (5.151), while the

tensors $\boldsymbol{Y}_{pq}$ are due to the fluctuation tensors:

$$\boldsymbol{Y}_{pq} = H^* \sum_{i,j=1}^{N_\mathrm{S}} \Pi^\mathrm{Z}_{ip} \bar{\xi}_i \boldsymbol{\Delta}_{ij} \Pi^\mathrm{Z}_{jq} \,. \tag{5.161}$$

Instead of the diagonalization assumptions in Eq. (5.153) along with

$$\boldsymbol{Y}_{pq} \approx \boldsymbol{Y}_p \delta_{pq} \,, \tag{5.162}$$

Prakash and Öttinger use

$$\boldsymbol{\sigma}'_{pq} \approx \delta_{pq} \boldsymbol{\sigma}'_p \,, \tag{5.163}$$

to derive

$$\boldsymbol{\sigma}'_{p,\,(1)} = -\frac{1}{4} \left[\boldsymbol{\sigma}'_p \cdot (\boldsymbol{X}_p + \boldsymbol{Y}_p) + (\boldsymbol{X}_p + \boldsymbol{Y}_p^\mathrm{T}) \cdot \boldsymbol{\sigma}'_q \right] + \frac{1}{2} \boldsymbol{Z}_p \,, \tag{5.164}$$

by considering only the equations for the normal-mode variances. Since the assumption in Eq. (5.163) alone is sufficient to produce Eq. (5.164), Prakash and Öttinger argue that the diagonalization assumption on the auxiliary tensors made by Kisbaugh and McHugh is not necessary. However, Eq. (5.160) shows that for the time derivatives of the off-diagonal components of the normal-mode covariances to remain negligible, it is necessary for both Eq. (5.163) and Eqs. (5.153) and (5.162) to be true. For equilibrium initial conditions, the off-diagonal covariances are initially negligible, and will stay small until the off-diagonal blocks of the auxiliary super-matrices are also negligible. The predictions of the diagonalized approximations will begin to deviate from those of the original approximations when the off-diagonal covariances become large. On the other hand, if it can be shown in both steady and unsteady shear and extensional flows that the diagonalization approximations for chains with HI give reasonably accurate predictions, then the equations of these approximations can be used as improved differential constitutive models for the polymer stress.

Using the TFN approximation for Rouse chains with HI, Prakash and Öttinger clearly established the accuracy of the additional diagonalization assumption by showing close quantitative agreement with the predictions of the un-diagonalized

Gaussian approximation. This was first done for the linear dynamic modulii G' and G'', and for $\eta_{\mathrm{p},0}$, $\Psi_{1,0}$ and $\Psi_{2,0}$. The agreement for the linear viscoelastic properties was found to remain close for the entire range of N in which comparisons were made ($N \leq 30$). With the gain in processing speed, predictions for chains up to $N \leq 150$ were obtained. Using these results, predictions for universal values of the ratios were obtained by extrapolating their values for finite N to the $N \to \infty$ limit. The values of the universal ratios thus obtained were found to be quite close to those obtained with the original Gaussian approximation. In addition, the predictions of the steady-state shear viscometric functions η_{p}, Ψ_1 and Ψ_2 were also found to be in excellent agreement with those of the Gaussian approximation, for a reasonably large values of $N = 45$, and for a wide range of values of the shear Weissenberg number, β. These results strongly suggest that the diagonalization approximation does not lead to a significant loss in accuracy across a wide range of N, in steady shear flows. Having established its accuracy, Prakash and Öttinger used the TFN approximation to collect the predictions the shear viscometric functions for several values of $N \leq 100$, and then extrapolate the values for the relative viscometric functions, $\eta_{\mathrm{p}}/\eta_{\mathrm{p},0}$, $\Psi_1/\Psi_{1,0}$ and $\Psi_2/\Psi_{2,0}$ to the $N \to \infty$ limit. In this limit, they showed that the predictions for the ratios become independent of the parameter h^*, and are functions of β alone. Since the TFN approximation is close to the Gaussian approximation, which in turn has been shown to be accurate in comparison with BD simulations results, it is reasonable to expect that the predictions obtained in this study should be quite close to the exact results for the universal viscometric functions in shear. In comparison, the predictions of the Renormalization Group theory [Zylka and Öttinger, 1991] are observed to deviate from the TFN approximation's predictions at high shear-rates.

As a result of the coupling of the equations due to Eq. (5.155) in the diagonalized approximations for chains with HI, the CPU-time per time step scales as N_{s}^3, even though the number of equations is only N_{s}. For every p in Eq. (5.154), each calculation of $\boldsymbol{Z}_p$ and $\boldsymbol{X}_p$ individually involves a double summation over all i and j in Eqs. (5.150) and (5.151), and hence the calculation of the auxiliary tensors $\boldsymbol{Z}_p$ and $\boldsymbol{X}_p$ scales as N_{s}^3. In the calculation of the variances $\boldsymbol{S}^*_{\mu\nu}$ using Eq. (5.155), each of the $\boldsymbol{\sigma}^*_{ij}$ requires a summation over all k. Since the values of $\boldsymbol{\sigma}^*_{ij}$ can be stored

Table 5.3: Sample comparison of CPU-time requirements for BD simulations, un-diagonalized and diagonalized approximations. The value reported for BD simulations is for 10^4 trajectories. For $N = 160$, the reported value has been calculated from the CPU-time required for 200 trajectories. The CPU-times reported for the CA-P and GA-P approximations for $N = 160$ have been projected from the CPU-time–versus–N scaling observed for $20 \leq N \leq 100$. All calculations using single 2.66 GHz, Pentium 4 (Dell Precision 250) processors.

N	CPU-time in hrs.			
	BDS	CA-P	GA-P	TFN-P
60	220	10	51	0.9
160	10012	2073	3131	32

at the beginning of each time-step, the total cost of generating the super-matrix containing the $\boldsymbol{\sigma}^*_{ij}$ tensors scales as N_s^3. The cost of the calculation of $\boldsymbol{S}^*_{\mu\nu}$ using

$$\boldsymbol{S}^*_{\mu\nu} = \boldsymbol{S}_{\mu,\nu-1} + \sum_{i=\mu}^{\nu-1} (\boldsymbol{\sigma}^*_{i,\nu-1} + \boldsymbol{\sigma}^*_{\nu-1,1}), \quad \mu < \nu, \tag{5.165}$$

can be shown to also scale as N_s^3. This CPU-time scaling remains the same even when the diagonalization approximation is extended to the Gaussian approximation.

Thus, as far as the CPU-time scaling is concerned, the diagonalization assumption does not offer an advantage over the original approximations in the calculation of properties in unsteady flows using bead-spring models with HI. However, the reduction in the number of equations to be integrated greatly reduces the prefactor in the CPU-time's power-law dependence on N_s.

The numerical methods used to integrate the differential equations for unsteady problems and for obtaining direct steady-state solutions are briefly discussed below.

5.6 Numerical methods

Numerical calculations are considerably simplified and made efficient by exploiting the following well known features of the equations described in this chapter.

1. In the un-diagonalized approximations, the total number of second moments,

and therefore the number of equations, is equal to $9N_s^2$. However, $\boldsymbol{\sigma}^*_{ij} = \boldsymbol{\sigma}^{*\mathrm{T}}_{ji}$. Further, the second moments must not change if the bead numbering is reversed. Thus, $\boldsymbol{\sigma}^*_{ij} = \boldsymbol{\sigma}^*_{N_s-i,N_s-j}$. Therefore, the number of independent second moments reduces by a factor of nearly 1/4 [Öttinger, 1989a]. In the diagonalized approximations, the number of normal mode variances is always N_s.

2. The symmetry of the imposed flow field can be used to reduce the number of components for all the tensorial quantities in the equations. In the undiagonalized approximations, the second moment tensors take the following form in shear flows:

$$\boldsymbol{\sigma} = \begin{pmatrix} \sigma_1 & \sigma_4 & 0 \\ \sigma_5 & \sigma_2 & 0 \\ 0 & 0 & \sigma_3 \end{pmatrix} . \tag{5.166}$$

In the diagonalized approximations, the normal mode variances are always symmetric, and hence $\sigma_4 = \sigma_5$ for these tensors. In uniaxial extensional flows, in both stress growth and relaxation phases, all tensorial quantities in the approximations have the form,

$$\boldsymbol{\sigma} = \begin{pmatrix} \sigma_1 & 0 & 0 \\ 0 & \sigma_2 & 0 \\ 0 & 0 & \sigma_2 \end{pmatrix} . \tag{5.167}$$

3. The exploitation of the symmetries to reduce the computation of the fourth rank tensorial function $\boldsymbol{K}(\mathbf{s})$ has been discussed thoroughly by Zylka [1991]. In general, for any symmetric tensor $\mathbf{s}$, only 21 of the 81 components of the $\boldsymbol{K}$ function are non-zero in a transformed coordinate system C in which the tensor $\mathbf{s}$ has a diagonal representation. Out of these 21 components, only 9 require independent numerical evaluation. The components K_{1111}, K_{2222} and K_{3333} can be used to calculate the remaining 12 non-zero components. Furthermore, the function $\boldsymbol{K}$ always appears in the equations as $\boldsymbol{K} : \boldsymbol{\sigma}$. In shear flows, this means that only 14 components of the $\boldsymbol{K}$ function in the

laboratory fixed coordinate system are required to be evaluated. In uniaxial extensional flows, it can be shown that only K_{xxxx} (where x is the direction of stretching) is required.

4. As shown by Zylka [1991], components of the $\boldsymbol{H}(\mathbf{s})$ and $\boldsymbol{K}(\mathbf{s})$ functions in the coordinate system C are efficiently evaluated using elliptic integrals.

Since predictions are obtained only for shear and uniaxial extensional flows in this study, separate computer codes were written for the two different flows, to take advantage of the reduction in the components due to their individual flow symmetries. A variable-step Adams method (the D02CJF routine in the NAG library) was used in this study for the integration of the ODE's. The steady-state solutions were obtained by setting the time derivatives in the ODE's to zero, and then using a Wegstein successive substitution algorithm to solve the set of nonlinear equations. Solutions were typically obtained for several values of the (shear or extensional) strain rate. The converged solution for the set of $\boldsymbol{\sigma}^*_{ij}$ or $\boldsymbol{\sigma}'_p$ at any strain rate was used as the initial guess for the next higher (or lower) strain rate for which a solution was desired. It was found that large steps in the strain rates could lead to unphysical, non-positive-definite solutions for the second moments, as reported earlier by Kisbaugh and McHugh [1990]; Wedgewood and Öttinger [1988]. Such behaviour was avoided by (manually) controlling the size of the steps in strain rate.

Chapter 6

Closure approximations: Predictions in shear and extensional flows

In the previous Chapter, the governing equations for several closure approximations for a FEBS chain model with HI were presented. The quality of the closure approximations in homogeneous shear and extensional flows is studied in this Chapter by comparing their predictions with the exact results obtained with Brownian dynamics simulations, for chains with $N = 20$. Moreover, the differences between the predictions of the approximations reveal the roles played by the different aspects of HI and FE. Firstly, results for steady-state properties in shear are presented below.

It may be noted here that this Chapter uses $\ell_{\mathrm{S}} = R_{\mathrm{S}}/\sqrt{3}$ and $\lambda_{\mathrm{S}} = \zeta\,\ell_{\mathrm{S}}^2/(4k_{\mathrm{B}}T)$ as the basic length and time scales, respectively. The somewhat odd choice of parameter values in many of the figures is because BD simulations' results shown in those figures were obtained by choosing values for dimensionless parameters defined using $\ell_{\mathrm{H}} = k_{\mathrm{B}}T/H$ and $\lambda_{\mathrm{S}} = \zeta\,\ell_{\mathrm{H}}^2/(4k_{\mathrm{B}}T)$ as the basic length and time scales.

6.1 Steady-state properties in shear flow

The methods used to obtain predictions for steady-state properties in shear flows has been described in the previous Chapter, in Section 5.6. Before considering results for

FEBS chains with HI, it is useful to first study the effects of the approximations for HI, and for FENE springs separately. Most of the results shown in this Section for steady-state properties in shear flow for Rouse chains with HI, and for free-draining FENE-P chains are well known and are reproduced below for aiding the discussion.

Figure 6.1 shows the predictions obtained for the steady-state shear viscosity using the consistent-averaging and Gaussian approximations for Rouse chains with HI, and compares these predictions with the results of BD simulations of chains with $N = 20$. The clear failure of the Zimm model in comparison with BD simulations shows that it is important to account for the dependence of HI on the configurational anisotropy caused by the flow. Furthermore, Fig. 6.1 also shows that it is necessary to incorporate configuration dependence (in either an exact sense, or through a mean-field description) to observe shear-rate dependent steady-state material functions.

It is seen in Fig. 6.1 that the incorporation of HI results in a reduction of viscosity at low to moderate shear-rates when compared to the plain Rouse model. The reduction in the viscosity is usually explained in terms of a reduction in the drag force experienced on an average by a polymer coil as a whole. The perturbations in the solvent velocity field *within* the polymer coil caused by the motion of the different parts of the chain lead to a net reduction in the average solvent velocity gradient within the polymeric coil [Larson, 1988; Öttinger, 1996b; Yamakawa, 1971]. Hence, the relative velocity of the solvent in the vicinity a bead within the polymer coil is smaller when hydrodynamic interactions are present, and the total drag force on the polymer coil is thus predicted to be smaller when a model with HI is used. The fact that the predictions of the Gaussian approximation and BD simulations are lower than those obtained with the Zimm and consistent-averaging approximations near equilibrium and at moderate shear-rates, indicates that under these conditions, fluctuations in configurations at equilibrium result in a more effective screening of the velocity field within the coil.

As the shear-rate increases, the steady-state viscosity (Fig. 6.1) and the first normal stress difference coefficient (Fig. 6.2) first decrease in models with HI, other than the Zimm model. This shear-thinning, although not very strong, is a distinctive feature of configuration-dependent HI. The initial shear-thinning is observed to be

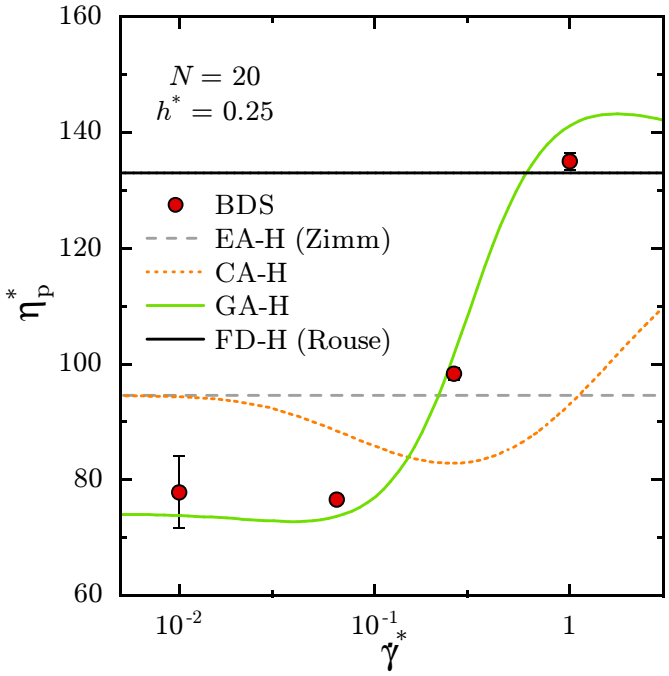

Figure 6.1: The influence of HI on the variation of the steady-state polymer viscosity with dimensionless shear-rate, for Rouse chains.

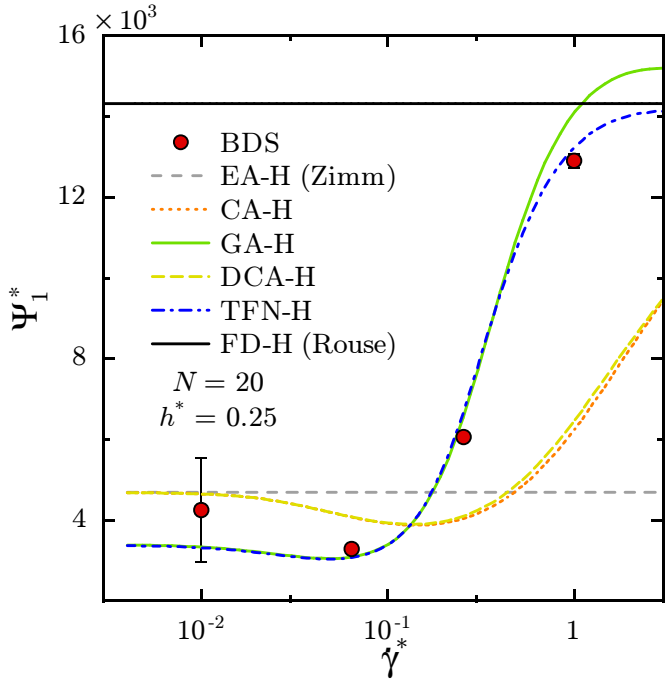

Figure 6.2: Variation of the steady-state first normal stress difference coefficient with shear-rate, for Rouse chains with HI.

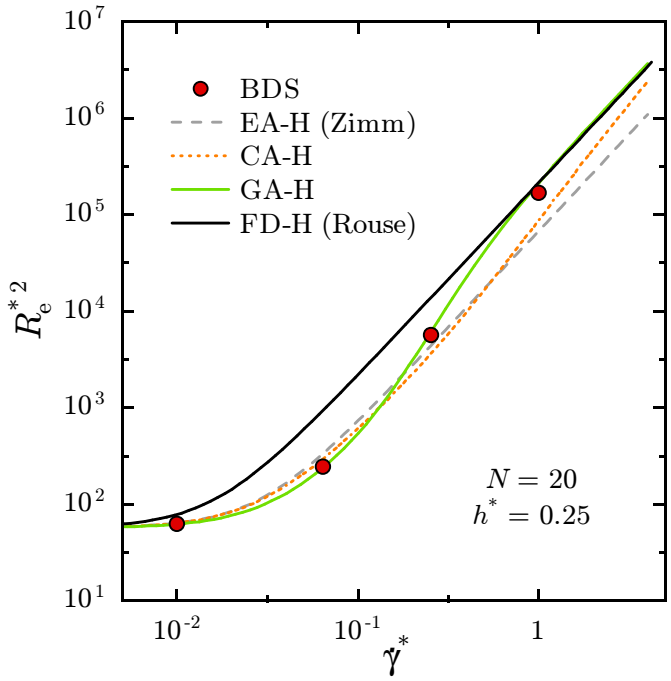

Figure 6.3: The influence of HI on the variation of the steady-state mean-squared end-to-end distance with shear-rate, for Rouse chains.

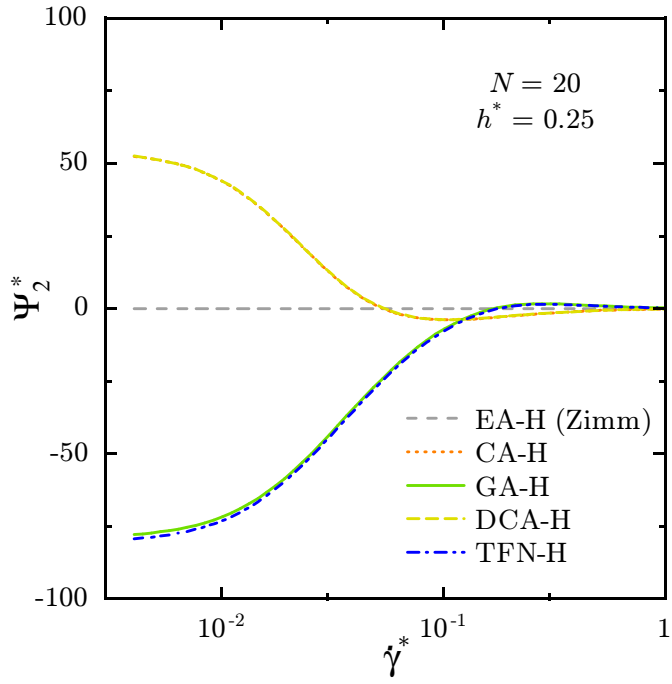

Figure 6.4: Variation of the steady-state second normal stress difference coefficient with shear-rate, for Rouse chains with HI.

more prominent with consistently-averaging than with the Gaussian approximation for HI. As the shear-rate increases, the predictions of η_{p}^{*} and Ψ_{1}^{*} obtained with BD simulations, and the CA-H and GA-H models, reach a minimum with respect to $\dot{\gamma}^{*}$. With a further increase in the shear-rate, shear-thickening is observed in these models, wherein η_{p}^{*} and Ψ_{1}^{*} begin to increase towards the constant value predicted by the Rouse model in which HI is absent. In this range of shear-rates, $R_{\mathrm{e}}^{*\,2}$ is much larger than $R_{\mathrm{e,\,eq}}^{*\,2}$ (Fig. 6.3), and the increase in η_{p}^{*} and Ψ_{1}^{*} towards the Rouse model's predictions is understood to be the consequence of the decreasing influence of HI as the average separation between the beads in the chains increases.

Interestingly, in Figs. 6.1 and 6.2, the predictions of the GA-H model and the BD simulations' results lie above the curve predicted by the CA-H model beyond a threshold shear-rate, and closer to the free-draining Rouse model's prediction. This behaviour is contrary to that observed near equilibrium. From this it appears that at higher shear-rates, fluctuations in HI increase the penetration of the solvent velocity field into the polymer coil. At even higher shear-rates, the Gaussian approximation and BD simulations predict values of the viscosity that are greater than the prediction of the free-draining Rouse model (Fig. 6.1). The curves predicted with consistently-averaged HI on the other hand, approaches the Rouse model's predictions asymptotically from below (not shown).

For chains with Hookean springs, the additional diagonalization assumptions in the DCA-H and TFN-H approximations lead to predictions that are not considerably different from the respective un-diagonalized original approximations. This is demonstrated in Figs. 6.2 and 6.4, which show the predictions for Ψ_{1}^{*} and Ψ_{2}^{*}, respectively. At larger shear-rates, the TFN-H approximation's predictions for η_{p}^{*} (not shown) and Ψ_{1}^{*} (Fig. 6.2) are larger than those obtained using the Gaussian approximation by about 5 to 10%. Deviations of similar relative magnitude were also observed by Prakash and Öttinger [1997] for chains with $N = 15$ and $N = 45$ at higher shear Weissenberg numbers. This suggests that for the predictions of steady-state shear material functions, the TFN-H approximation may remain relatively accurate in comparison with the Gaussian approximation at a fixed high Weissenberg number.

The qualitative features of the results for the steady-state Ψ_{1}^{*} are the same as

those observed in Fig. 6.1. Figure 6.4 shows that both the consistent-averaging and Gaussian approximations lead to shear-rate dependent predictions for Ψ_2^*, which are opposite in sign for a large range of shear-rates. This was first shown by Zylka [1991], thus demonstrating that fluctuations in HI lead to a change in the sign of Ψ_2^* at low to moderate shear-rates for Rouse chains. Although the large size of the standard error in the simulations' results obtained in this study for Ψ_2^* do not permit the evaluation of the approximations' accuracy in the prediction of this property, as will be shown below, the results for unsteady shear flow clearly demonstrate the strong influence of configurational fluctuations on this property.

Considering next the influence of using closure approximations for handling the FENE nonlinearity, it is seen in Fig. 6.5 that the steady-state shear viscosity predicted by both the FENE-P and FENE-PG approximations are in quantitative agreement with the values obtained with BD simulations of free-draining FENE chains. The good agreement in the case of FENE-P chains has also been observed in earlier studies with smaller values of N [Herrchen and Öttinger, 1997; van den Brule, 1993].

Although the free-draining model with FENE-P springs (FD-P model) has been used extensively in the literature on modeling dilute polymer solutions, only a few studies have compared the predictions of the approximate model with the results of BD simulations performed using FENE springs [Herrchen and Öttinger, 1997; Keunings, 1997; van den Brule, 1993]. Close to equilibrium, when the springs in the chain are not significantly stretched and the influence of FE is itself marginal, it is expected that the Peterlin approximation will have little influence on the predicted macroscopic behaviour, and the results with both FENE and FENE-P springs will be close to those calculated using the simple Rouse model. For instance, the zero-shear-rate viscosity with free-draining chains for arbitrary spring (and/or EV) potentials can be analytically shown to be [Bird *et al.*, 1987b; Prakash, 2001b]

$$\eta_{\mathrm{p},0} = \frac{n_{\mathrm{p}}\zeta}{6} N R^2_{\mathrm{G,\,eq}}\,. \tag{6.1}$$

As explained in Chapters 2 and 5 earlier, the spring constant H in all FEBS models is chosen such that the predicted (dimensional) values of $R^2_{\mathrm{e,\,eq}}$ are identical across the different models. This automatically ensures that the predictions of $R^2_{\mathrm{G,\,eq}}$ are also the same for all the FEBS models. By using $\ell_{\mathrm{s}} = R_{\mathrm{s}}/\sqrt{3}$ to express predictions

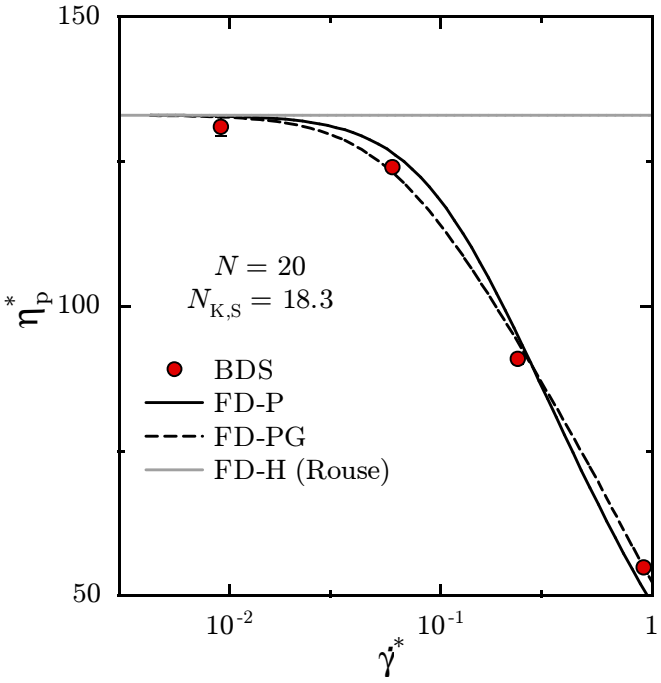

Figure 6.5: Variation of the steady-state polymer viscosity with shear-rate, for free-draining FEBS chains.

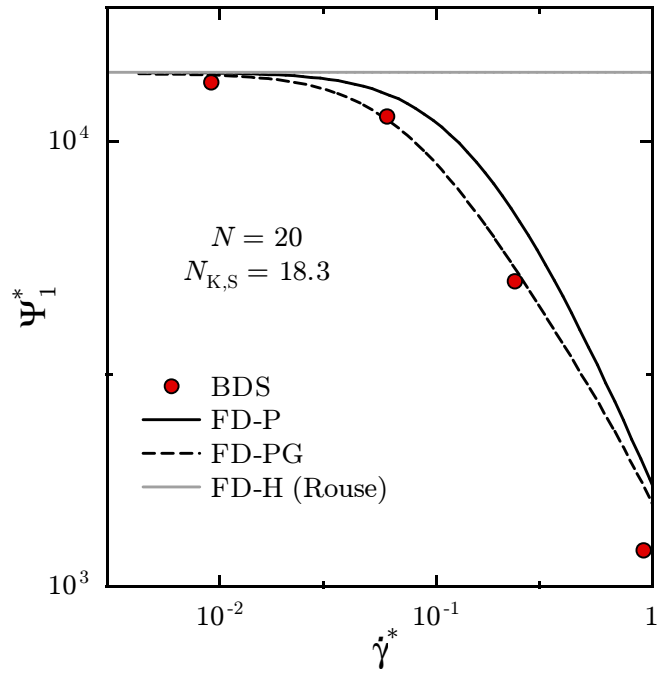

Figure 6.6: Variation of the steady-state first normal-stress difference coefficient with shear-rate, for free-draining FEBS chains.

in dimensionless terms, one thus also ensures that the predicted steady-state zero-shear-rate viscosities are identical.

The decrease in η_{p}^* with increasing shear-rates is a characteristic feature of free-draining FEBS models. As the shear-rate increases, and the polymer coil deforms, the average shape of a polymeric coil in flow is well represented as an ellipsoid whose principal axes are oriented in the directions specified by the eigenvectors of the gyration tensor $\boldsymbol{G}$. The angle subtended by the major axis of the ellipsoid and the x-axis (the principal flow direction in the shear flow) measures the degree to which coils are oriented towards the flow direction, and is denoted as χ_{G}. The angle χ_{G} is related to the components of $\boldsymbol{G}$ through

$$\tan(2\chi_{\mathrm{G}}) = \frac{2G_{yx}}{G_{xx} - G_{yy}}\,. \tag{6.2}$$

As shown in Fig. 6.8, polymer coils are forced by higher shear-rates into closer alignment with the principal direction of the flow. On the other hand, the second effect of the shear flow is to stretch the polymer molecule along the principal axis of the gyration ellipsoid. While the reduction of the orientation angle χ_{G} tends to reduce the total drag force on the coil, larger coil size in general leads to an increase in the drag force. In the free-draining Rouse model, these two opposing effects are always in balance and the viscosity remains a constant. In comparison with the Rouse model, FEBS chains show greater resistance to both orientation (Fig. 6.8) and stretching (Fig. 6.7). However, the finite extensibility of the chains in the FEBS models causes the coil size to saturate, whereas the orientation angle continues to decrease with increasing shear-rate. Consequently, the average drag force on a polymer molecule, and hence the steady-state polymer contribution to the viscosity, decreases as the shear-rate increases.

In Figs. 6.5 to 6.7, it is seen that the FENE-PG approximation for the FENE force law does better than the FENE-P approximation. Although the FENE-P approximation is accurate in its prediction of the viscosity in Fig. 6.5, Fig. 6.7 shows that the steady-state $R_{\mathrm{e}}^{*\,2}$ is overpredicted. Moreover, the prediction of Ψ_1^* with FENE-P springs also deteriorates with increasing shear-rate (Fig. 6.6). Using the FENE-PG approximation improves the predictions of $R_{\mathrm{e}}^{*\,2}$ and Ψ_1^* at moderate shear-rates. At $\dot{\gamma}^* \approx 1$, the predictions of $R_{\mathrm{e}}^{*\,2}$ and Ψ_1^* with FENE-PG springs also

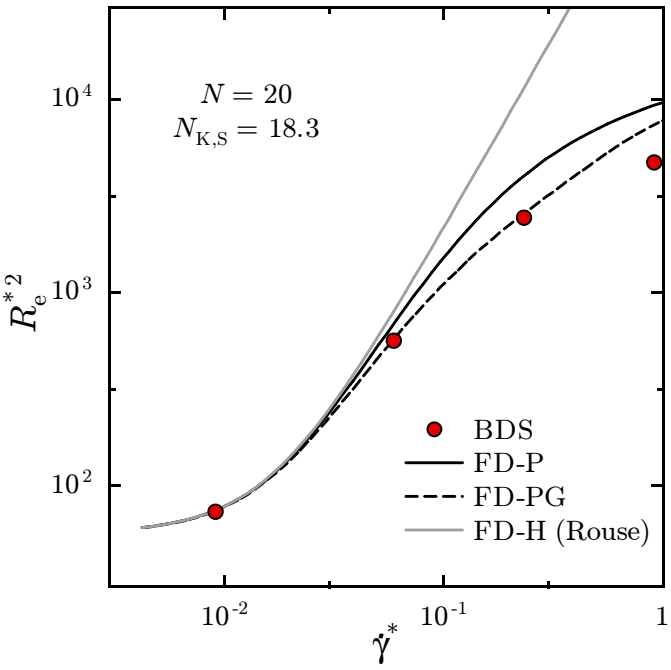

Figure 6.7: Variation of the steady-state mean-squared end-to-end distance with shear-rate, for free-draining FEBS chains.

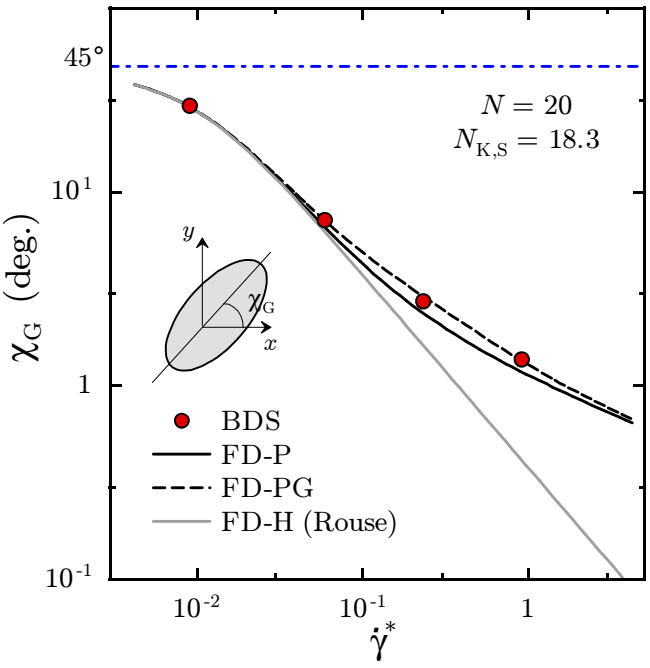

Figure 6.8: Variation of the steady-state orientation angle χ_G with shear-rate, for free-draining FEBS chains.

begin to deviate from the exact results, although the prediction of $\eta_{\rm p}^*$ is still in good agreement.

As pointed out in Chapter 5, there are three reasons why the FENE-PG approximation can deviate from exact results. Firstly, the use of a mean-field spring potential of the form shown in Eq. (5.82) itself may be inadequate. Secondly, the FENE-PG approximation used in this study results from the truncation of an infinite series at the second term. The contributions of the higher order terms may become important at higher shear-rates. Finally, the specific form of the Peterlin closure itself may lead to larger deviations at higher shear-rates. A more complete exploration of these interesting aspects of the closure approximations for the FENE nonlinearity are beyond the scope of the present work.

The results above can now be used to understand the behaviour of the closure approximations for FEBS chains with HI. To the present author's best knowledge, papers systematically exploring the implications of closure approximations for this combined case are relatively rare in the literature. Wedgewood and Öttinger [1988] presented a detailed study of the steady and unsteady predictions of the CA-P model for simple shear flow. Later, the steady-state results of the diagonalized version of this model (the DCA-P model) in shear flow were examined by Kisbaugh and McHugh [1990]. Although Ahn *et al.* [1993] studied an approximate model for FEBS chains with HI and EV using the boson-operator formalism of Fixman [1966a], as discussed earlier in Chapter 5 the treatment of HI with this formalism is essentially equivalent to the consistent-averaging approach of Öttinger [1987a].

Figures 6.9 and 6.10 show the results for the steady-state $\eta_{\rm p}^*$ and Ψ_1^* obtained by combining the consistent-averaging and Gaussian approximations for HI with the FENE-P and FENE-PG approximations for FENE springs. These figures show that the model combining the Gaussian approximation with FENE-PG springs compares well with the BD simulations across the range of shear-rates examined. As one would expect, at low shear-rates where the influence of FE is negligible, the observed behaviour is close to that observed for Rouse chains with HI for which the Gaussian approximation for HI was shown earlier (Figs. 6.1 and 6.2) to perform better than the consistent-averaging approximation. At moderate shear-rates when FE begins to exert its influence, it is seen that the Gaussian approximation is not as accurate

when used with FENE-P springs as it is with FENE-PG springs. This suggests that the fluctuations in the spring forces also become important at moderately large shear-rates.

Interestingly, spring force fluctuations seem to have a negligible effect on Ψ_2^*, since the curves in Fig. 6.12 for the approximations with the FENE-PG force expression are nearly the same as those employing the FENE-P approximation. As the shear-rate increases further, the differences between the consistent-averaging and Gaussian approximations reduce for the same choice of the spring force law. Figure 6.13 further shows that, as in the case of Rouse chains with HI, the additional normal-mode diagonalization assumptions in the DCA-P and TFN-P approximations cause negligible deviations in the predictions of the steady-state properties in shear.

As $\dot{\gamma}^*$ approaches unity, the GA-PG model is seen to deteriorate in Figs. 6.9 and 6.10. The prediction of $R_{\mathrm{e}}^{*\,2}$ by the GA-PG model in Fig. 6.11 is also significantly larger than the value calculated with BD simulations. In fact, at these high shear-rates the CA-PG model seems to perform better than the GA-PG model. On closer examination, however, this apparent agreement of the CA-PG model's predictions with BD results is seen to be the result of a fortuitous cancellation of errors. As discussed above, when $\dot{\gamma}^* \approx 1$, the predictions of the GA-PG model are nearly the same as the FD-PG model. As shown in Figs. 6.5, 6.6 and 6.7, for free-draining chains the FENE-PG force law leads to an overprediction of the stresses and $R_{\mathrm{e}}^{*\,2}$ at high shear-rates. On the other hand, the use of consistently-averaged HI leads to an underprediction of these properties. When both these approximations are combined together, the opposing tendencies seem to work in the CA-PG model's favour.

The weakening of the influence of HI when chains stretch at high shear-rates causes the predictions of the models with HI to approach those obtained with their corresponding free-draining versions (Figs. 6.5 and 6.6). This is more clearly illustrated in Figs. 6.14 and 6.15 which compare results obtained with FEBS models with HI with their free-draining versions. It is observed that at high shear-rates, the curves for the models using the Gaussian approximation for HI are closer to their free-draining counterparts. Thus, as in the case of Rouse chains, configurational fluctuations at high shear-rates aid in the weakening of the screening of the beads from the solvent's velocity field. In the case of Rouse chains, it was observed that

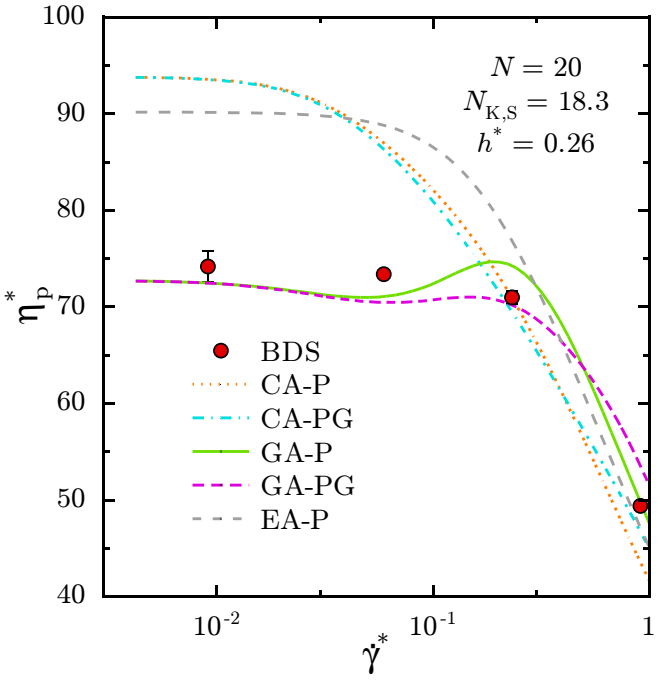

Figure 6.9: Variation of the steady-state polymer viscosity with shear-rate, for FEBS chains with HI.

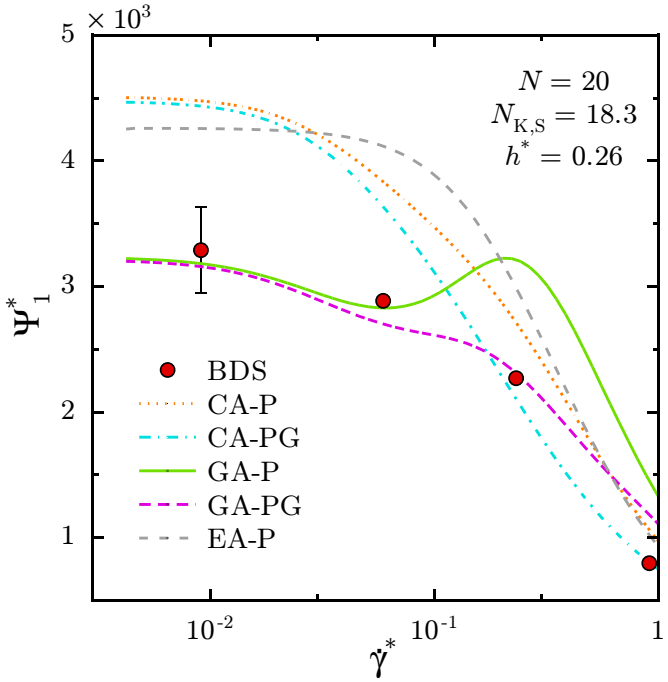

Figure 6.10: Variation of the steady-state first normal-stress difference coefficient with shear-rate, for FEBS chains with HI.

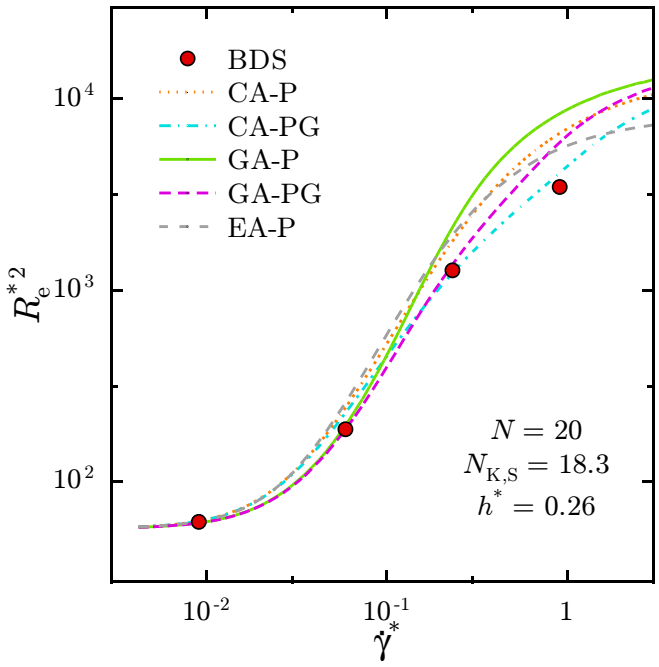

Figure 6.11: Variation of the steady-state mean-square end-to-end distance with shear-rate, for FEBS chains with HI.

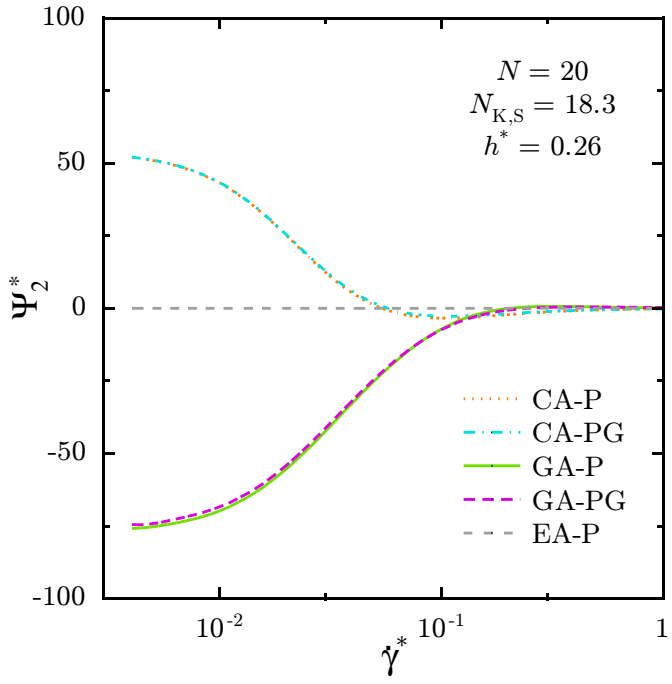

Figure 6.12: Variation of the steady-state second normal-stress difference coefficient with shear-rate, for FEBS chains with HI.

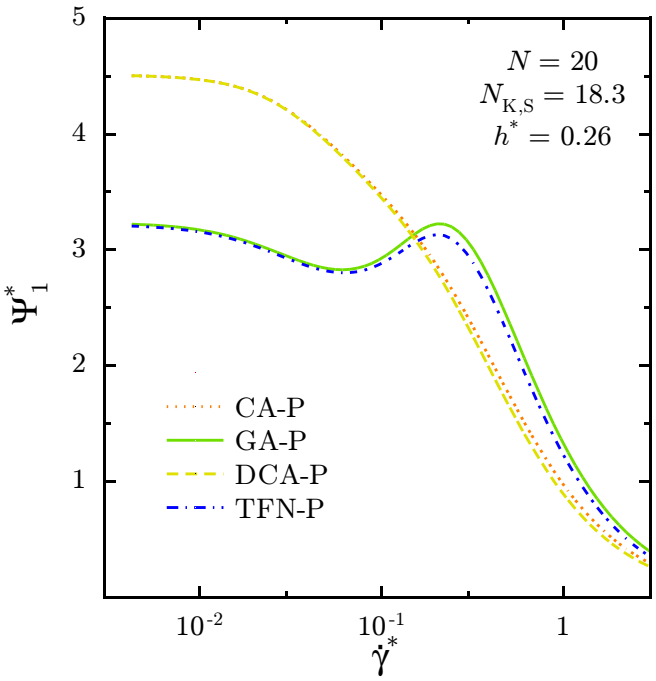

Figure 6.13: Effect of the diagonalization approximations on the prediction of the steady-state first normal-stress difference coefficient for FENE-P chains with HI.

the Gaussian approximation lead to predictions of η_p^* and Ψ_1^* greater than the values calculated with the free-draining Rouse model. Although this is not the case in Fig. 6.14, for a different set of parameters ($N_s = 25$ and $N_{K,\,s} = 400$) in Fig. 6.15, the Gaussian approximation for a FEBS model again predicts larger values of η_p^* at high shear-rates than the corresponding free-draining model. Thus, this feature of the approximation depends on the parameters used.

Although at high shear-rates Rouse chains with HI predict shear-thickening, FEBS models with HI predict shear-thinning. In fact, Kisbaugh and McHugh [1990] showed using the DCA-P model that more complicated behaviour can occur as a result of the interplay between the emergence of FE and the fading of HI. Figure 6.16 shows the predictions of η_p^* obtained with the CA-PG and GA-PG models for chains with 25 springs, and $N_{K,\,s} = 400$. The curve for the GA-PG model is observed to follow the curve for the GA-H model, showing the slight shear-thinning at low shear-rates followed by shear-thickening at moderate shear-rates. As the shear-rate is increased further, the GA-PG curve departs from the GA-H curve and goes through

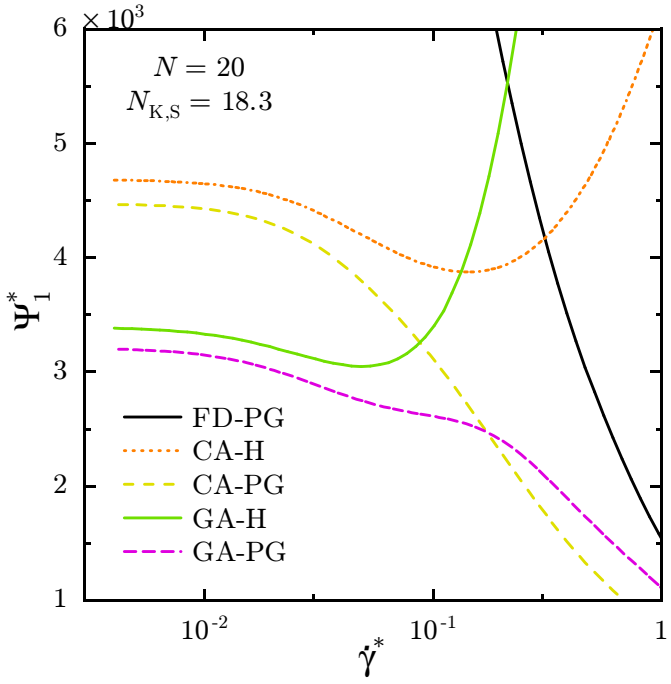

Figure 6.14: Variation of the steady-state first normal-stress difference coefficient with shear-rate, for FENE-PG chains with and without HI. For models with Hookean springs, $h^* = 0.25$, while for FEBS chains models, $h^* = 0.26$.

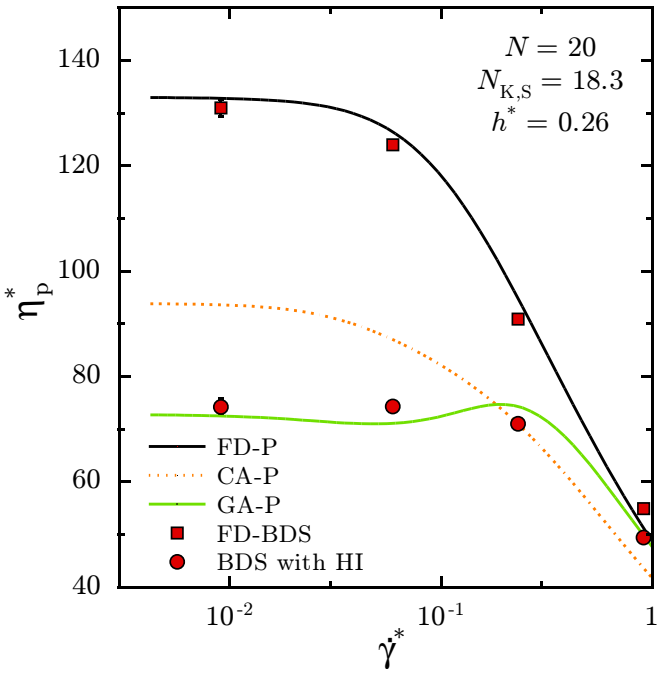

Figure 6.15: Variation of the steady-state polymer viscosity with shear-rate, for FENE-P chains with and without HI.

a maximum, before beginning to approach the terminal shear-thinning portion of the curve predicted by the free-draining model with FENE-PG springs. The departure of the GA-PG curve from the predictions of the GA-H model shows that FE begins to become important.

The behaviour in Fig. 6.16 suggests that the curve for the steady-state η_{p}^{*} predicted by a model combining an approximation "A" for HI and an approximation "F" for the nonlinear force in general is close to but below the curve predicted with the approximation "A" for Rouse chains at low to moderate shear-rates. At high shear-rates, the combined model switches over to being close to the terminal shear-thinning part of prediction of the free-draining model with the "F" approximation for the spring-force nonlinearity. The intersection of the curves for η_{p}^{*} predicted by the "A"-H and FD-"F" models can be regarded as a critical shear-rate $\dot{\gamma}_{\mathrm{c}}^{*}$. At shear-rates smaller than $\dot{\gamma}_{\mathrm{c}}^{*}$, the overall behaviour of the polymer chains is dominated by HI, whereas FE is the dominant phenomenon when $\dot{\gamma}^{*} > \dot{\gamma}_{\mathrm{c}}^{*}$. A similar demarcation of shear-rates was also suggested by Kisbaugh and McHugh [1990].

The results of Kisbaugh and McHugh also show that FE begins to dominate at smaller shear-rate in shorter chains. In addition, Figs. 6.16 and 6.17 also show that for any given choice of N and $N_{\mathrm{K,\,s}}$, the change in behaviour from shear-thickening to shear-thinning close to $\dot{\gamma}_{\mathrm{c}}^{*}$ is sharper with the Gaussian approximation for HI, than with consistent-averaging, although the value of $\dot{\gamma}_{\mathrm{c}}^{*}$ at which FE becomes dominant (determined as suggested above) is greater with the latter approximation.

Summarizing the discussion above, it appears that combining the Gaussian approximation with FENE-PG approximation leads to steady-state predictions in shear flows that compare reasonably well with the exact results of BD simulations of FENE chains with HI. This agreement is excellent at low to moderate shear-rates, but begins to deteriorate as $\dot{\gamma}^{*}$ approaches unity. The poorer quality of the combined approximation at high shear-rates may be attributed to the inaccuracy in the mean-field representation of the FENE nonlinearity. The results presented above point strongly to the important role that fluctuations—in HI and in the spring forces—play at all shear-rates. The following section further explores the predictions of the closure approximations for start-up of steady shear flows.

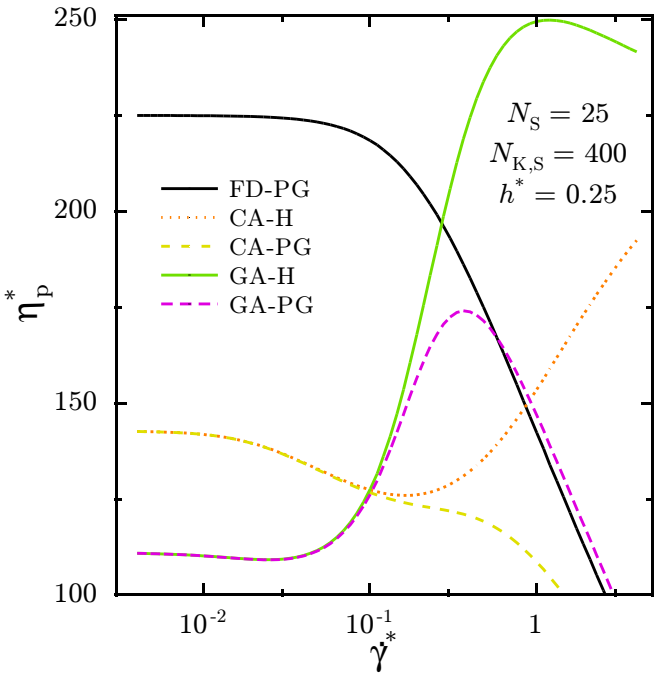

Figure 6.16: Prediction of shear-thinning-thickening-thinning of the steady-state shear viscosity by models with HI, for $N_K = N_S N_{K,\,S} = 10^4$.

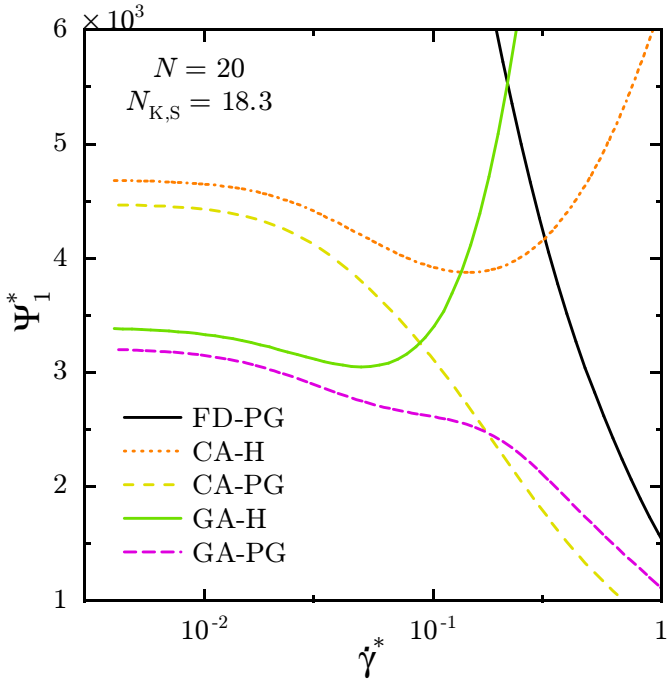

Figure 6.17: Prediction of shear-thinning-thickening-thinning of the steady-state first normal stress difference coefficient by models with HI, for $N_K = N_S N_{K,\,S} = 348.3$. For Rouse chains, $h^* = 0.25$, while for FEBS chains, $h^* = 0.26$.

6.2 Start-up of steady shear flow

The time variation in the properties predicted by the different approximations was obtained by integrating the ODE's for the approximations starting from equilibrium initial conditions. As before, the features of the approximations for HI and FE are first examined independently before considering the combined models. For Rouse chains with HI, use of equilibrium averaging in the Zimm models results in a fixed time dependence of properties that is independent of the shear-rate. This behaviour parallels the shear-rate independence of the material functions predicted at steady-state by the Zimm model. In contrast, the predictions of the consistent-averaging and Gaussian approximations, and the exact results of the simulations for the growth of the shear material functions η_{p}^* and Ψ_1^* depend on the imposed shear-rate. This is shown in Figs. 6.18 and 6.19. It is also seen that the Gaussian approximation for HI results in predictions that are much better agreement with the simulations' results, than are those predicted with just consistent-averaging of HI. The importance of including a description of the fluctuations in approximate models accounting for HI is further underlined by the clear superiority of the Gaussian approximation in predicting the variation of Ψ_2^* at a high shear-rate in Fig. 6.20. This Figure, and Fig. 6.21, also show that, as in the case of the behaviour at steady-state (Figs. 6.2 and 6.4), predictions of the DCA-H and TFN-H models closely follow the curves predicted by their original un-diagonalized counterparts. These figures further reinforce the fact that the Zimm model, although simple to use, is clearly deficient in fully describing the behaviour of dilute polymer solutions in unsteady shear flows.

In Fig. 6.18, the curves predicted with the Gaussian approximation initially lie below those predicted with consistently averaged HI, for both the shear-rates considered. At larger values of t^*, as steady-state is approached, the prediction of the Gaussian approximation at the higher shear-rate is seen to overtake the CA-H curve, whereas at the lower shear-rate, the GA-H prediction is always below that predicted by the CA-H model. This behaviour once again suggests that close to isotropic conditions, fluctuations in HI lead to a lowering of the effective drag felt by the polymer chain. Far away from equilibrium, fluctuations in HI in a highly deformed polymer chain effectively increase the overall drag felt by the molecule.

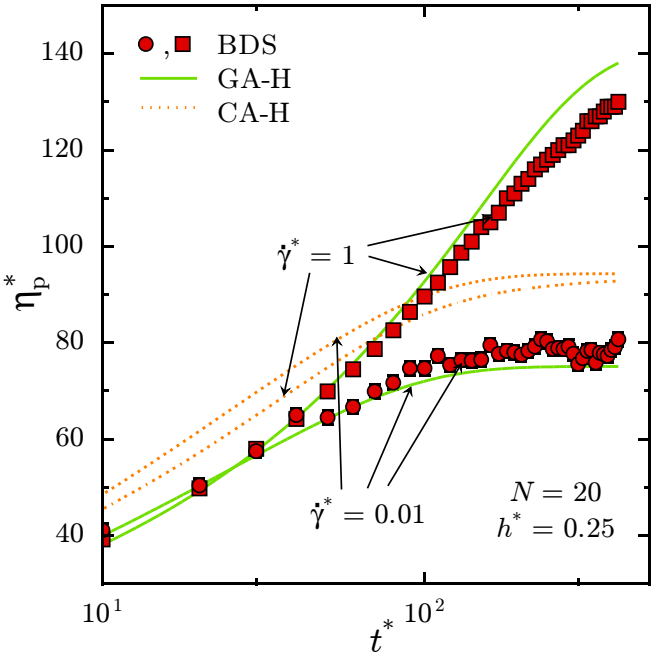

Figure 6.18: Growth of viscosity for Rouse chains with HI during start-up of steady shear flow.

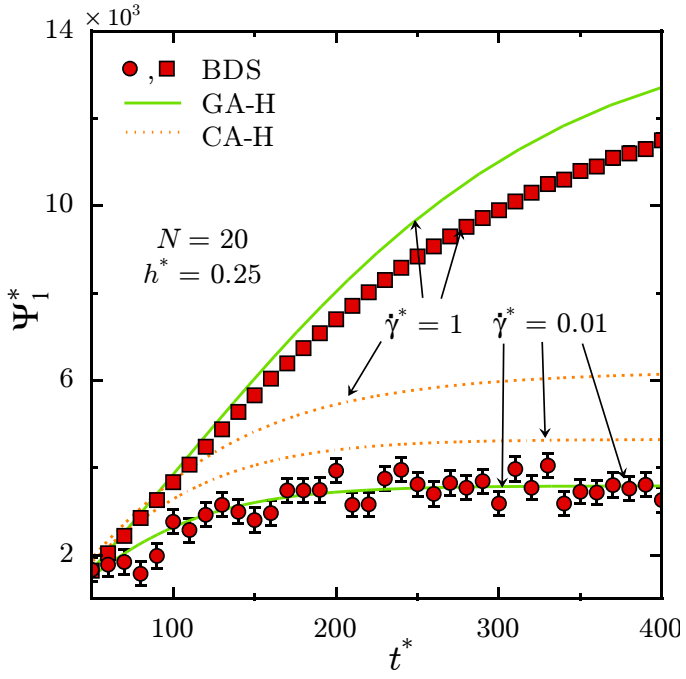

Figure 6.19: Growth of first normal-stress difference coefficient for Rouse chains with HI during start-up of steady shear flow.

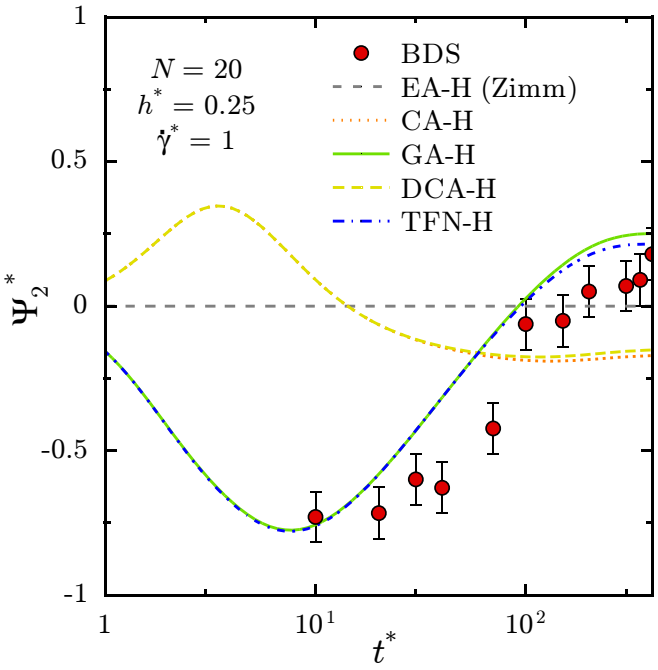

Figure 6.20: Growth of second normal-stress difference coefficient for Rouse chains with HI during start-up of a steady shear with $\dot{\gamma}^* = 1$.

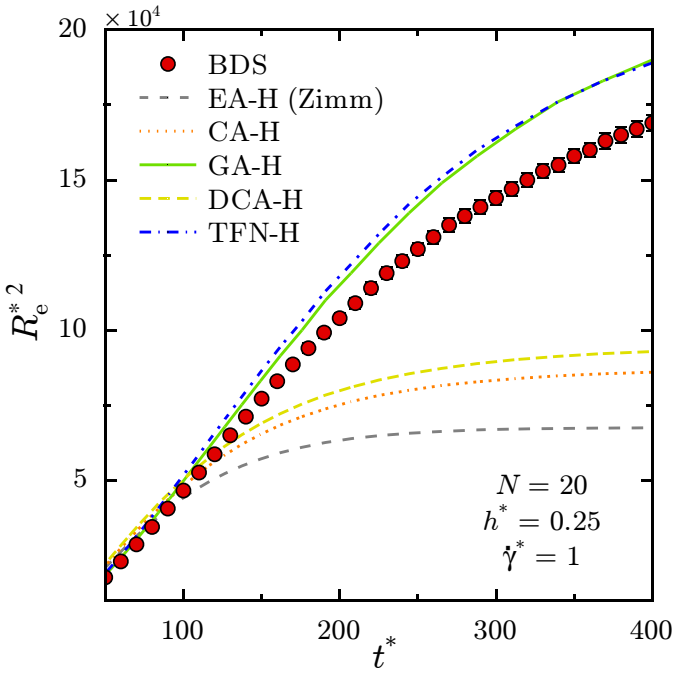

Figure 6.21: Growth of mean-squared end-to-end distance for Rouse chains with HI during start-up of a steady shear flow with $\dot{\gamma}^* = 1$.

Considering next the performance of the FENE-P and FENE-PG approximations for free-draining FEBS chains, it must be noted that at low shear-rates close to equilibrium, finite chain extensibility has little influence on the dynamic behaviour predicted by the models. Therefore, the predictions of the free-draining FEBS models are close to those predicted with the Rouse model (not shown). At higher shear-rates, earlier studies with FENE-P dumbbells [Herrchen and Öttinger, 1997] and chains with $N = 10$ [van den Brule, 1993] show that this approximation leads to predictions for unsteady shear properties that agree only qualitatively with the exact results obtained using FENE springs. Figures 6.22 to 6.25 show that this trend is continued for 20-bead chains. The incorporation of fluctuations in the spring force with the use of the FENE-PG approximation leads to a clear improvement in the quality of the predictions for all properties at moderate shear-rates (represented by the curves for $\dot{\gamma}^* = 0.23$ in Figs. 6.22 to 6.25). In particular, it is seen that the FENE-PG force law leads to the prediction of a transient non-zero positive second-normal stress difference coefficient which approaches zero at steady-state, in good (within errors in the simulations' results) agreement with the results of simulations . As observed earlier in the predictions at steady-state, the FENE-PG approximation also begins to deviate as the dimensionless shear-rate approaches unity.

As observed earlier in Chapter 4, large overshoots are observed in Figs. 6.22 and 6.23 in the results of all the models for η_{p}^* and Ψ_1^*. This feature is not observed at any shear-rate for Rouse chains with HI, and neither is it observed at low shear-rates for FEBS chains. The overshoots in the material functions are accompanied by a corresponding overshoot in the mean-squared end-to-end distance of the coils (Fig. 6.24). The overshoot in the transient η_{p}^*, Ψ_1^* and ${R_{\mathrm{e}}^*}^2$ during start-up of shear flows is known to be a signature of the influence of FE [Doyle and Shaqfeh, 1998; Herrchen and Öttinger, 1997; Hur *et al.*, 2001; van den Brule, 1993]. Hur *et al.* have obtained experimental evidence of such overshoots using dilute (and semi-dilute) solutions of DNA, and showed using simulations of bead-rod and bead-spring chains that the overshoot is caused by the rapid stretching of the molecules by the flow, before the orientation of the chains towards the flow direction reduces the total solvent drag sufficiently to reduce the stretching. Herrchen and Öttinger [1997] observed that the overshoot predicted with FENE-P springs is larger than that

obtained with FENE springs in the case of dumbbells. Interestingly, comparing Figs. 6.22 and 6.24, it is observed that at the higher shear-rate ($\dot{\gamma}^* \approx 1$), deviations between the predictions for $\eta_{\rm p}^*$ obtained with different spring force models appear before deviations in $R_{\rm e}^{*\,2}$ become significant.

For a model incorporating both FE and HI, the unsteady behaviour during start-up of weak shear flows is nearly the same as that predicted with Rouse chains for the same shear-rate, with HI being treated in the same manner as in the combined model. As the shear-rate increases, predictions for $\eta_{\rm p}^*$ and Ψ_1^* with the combined models begin to show overshoots that are characteristic of the influence of FE. Such behaviour has been observed earlier by Wedgewood and Öttinger [1988] in their detailed study of the behaviour of the CA-P model in shear flows. However, fluctuations in HI appear to delay the onset of the influence of FE. This is illustrated in Fig. 6.26 and 6.27, in which the $\eta_{\rm p}^*$- and Ψ_1^*-versus-t^* curves predicted by both the CA-P and CA-PG approximations at $\dot{\gamma}^* = 0.23$ show overshoots, but those obtained using the Gaussian approximation for HI, and the BD simulations' data do not.

The better overall agreement of the predictions of the GA-PG model with the exact results for the shear (Fig. 6.26), normal stresses (Figs. 6.27 and 6.30) and $R_{\rm e}^{*\,2}$ (Fig. 6.31) at $\dot{\gamma}^* = 0.23$ once again confirms the importance of fluctuations in HI and the spring forces. At the higher shear-rate of $\dot{\gamma}^* \approx 1$, however the predictions of the GA-PG approximation are only in qualitative agreement with the simulations' results (Figs. 6.28, 6.29, 6.32 and 6.33). At these high shear-rates, the CA-PG is seen to perform better. As pointed out earlier, the agreement may be due to a cancellation of the errors due to the inaccuracy of the FENE-PG force law at high shear-rates and those due to the neglect of fluctuations in HI.

As noted in Chapter 4, HI leads to an attenuation of the overshoot. This is shown in Fig. 6.34 where the ratio of the time-dependent $\eta_{\rm p}^*$ to its steady-state value is plotted as a function of time. The maximum in the curve predicted by the GA-PG model at $\dot{\gamma}^* \approx 1$ is smaller than that observed with the FD-PG model. At the lower shear-rate of $\dot{\gamma}^* = 0.23$, the curve predicted by the model with HI has no overshoot, unlike that obtained with the free-draining model. Earlier, it was seen in Fig. 6.17 that the predictions of the steady-state Ψ_1^* at $gdots = 0.23$ by the GA-H and GA-PG models at are quite different, indicating that at this shear-rate

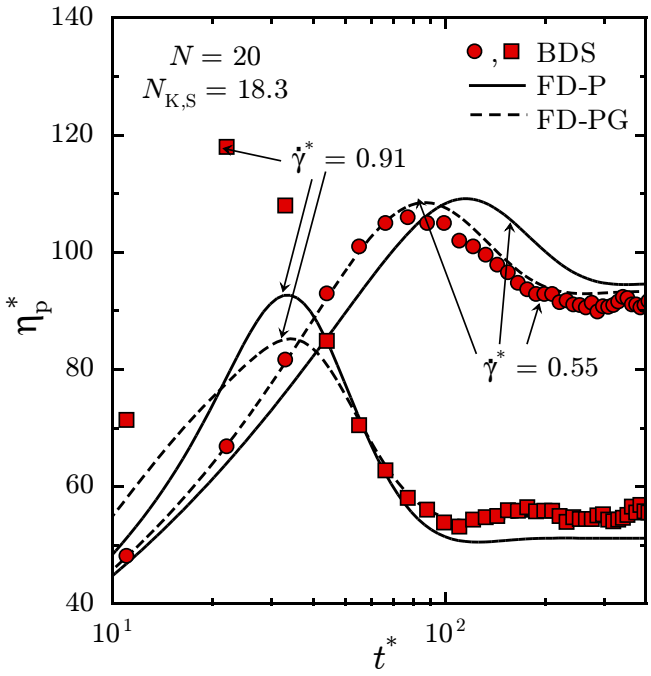

Figure 6.22: Growth of viscosity for free-draining FEBS chains during start-up of steady shear flow.

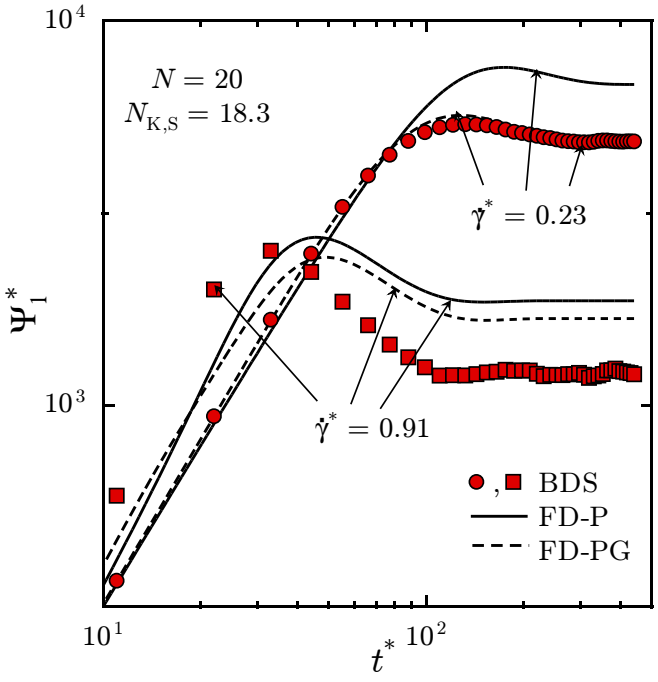

Figure 6.23: Growth of first normal-stress difference coefficient for free-draining FEBS chains during start-up of steady shear flow.

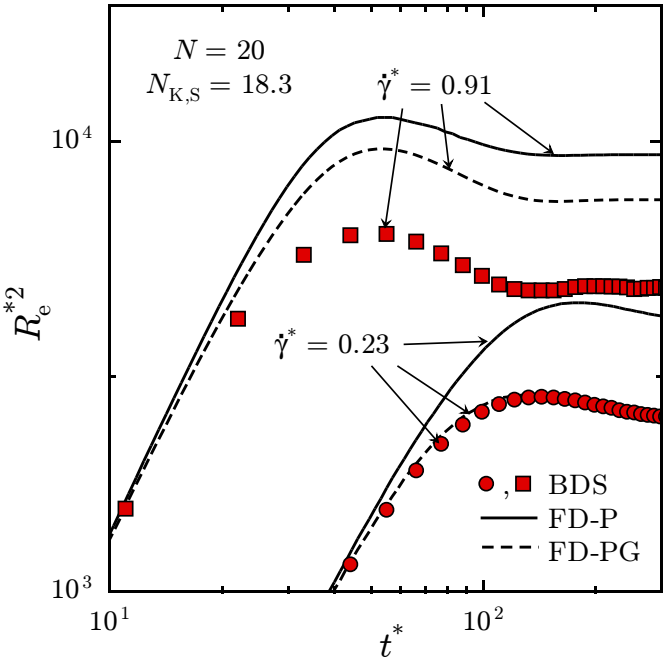

Figure 6.24: Growth of mean-squared end-to-end distance for free-draining FEBS chains during start-up of steady shear flow.

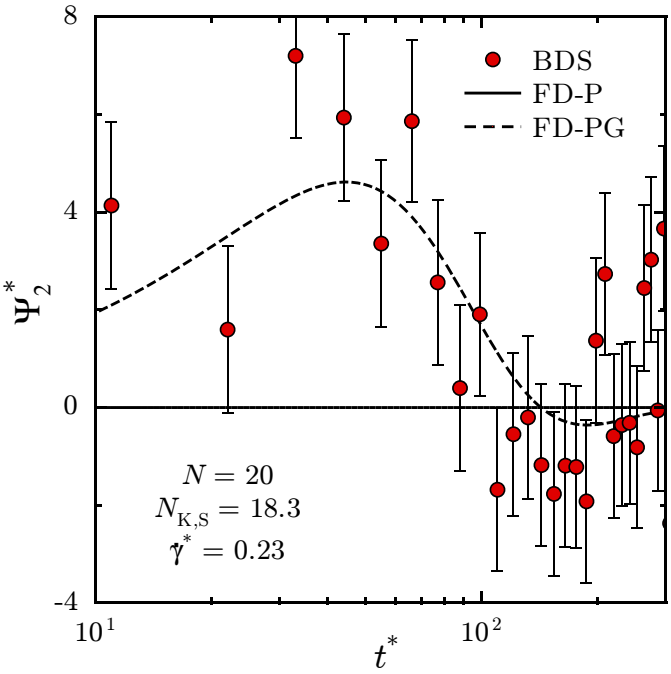

Figure 6.25: Growth of second normal-stress difference coefficient for free-draining FEBS chains during start-up of a steady shear with $\dot{\gamma}^* = 0.55$.

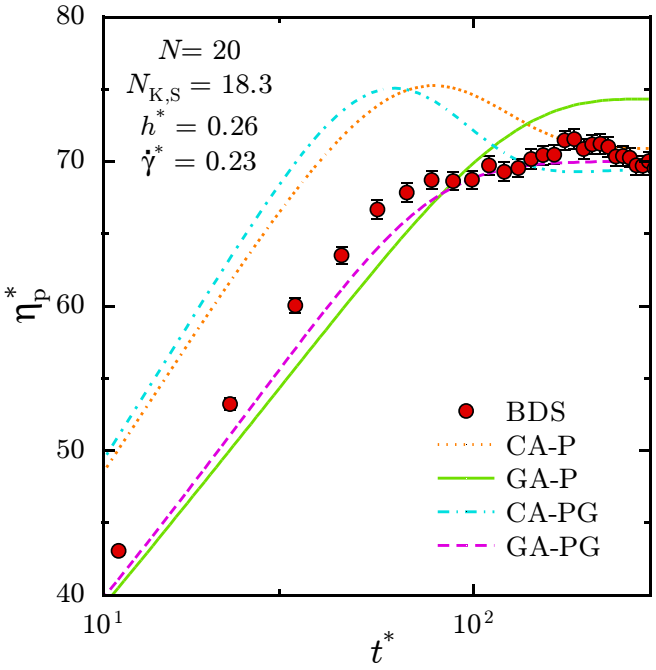

Figure 6.26: Growth of viscosity for FEBS chains with HI during start-up of a steady shear flow with $\dot{\gamma}^* = 0.23$.

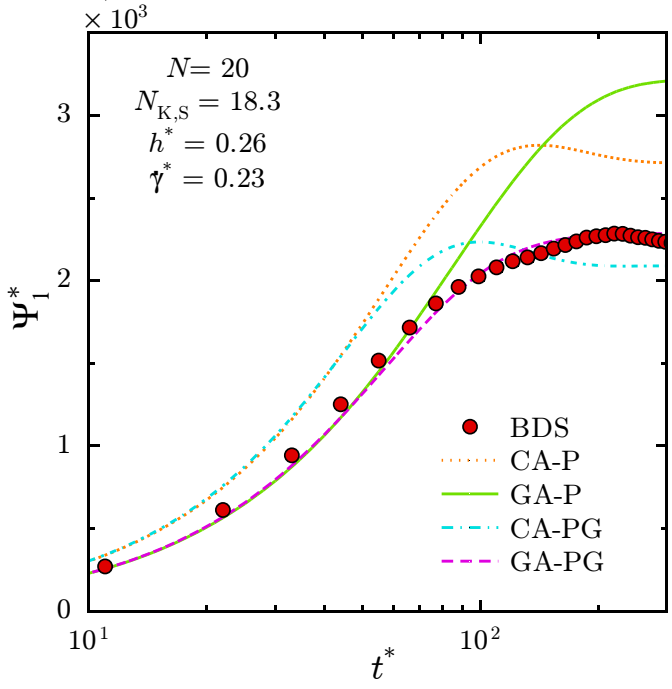

Figure 6.27: Growth of first normal-stress difference coefficient for FEBS chains with HI during start-up of steady shear flow with $\dot{\gamma}^* = 0.23$.

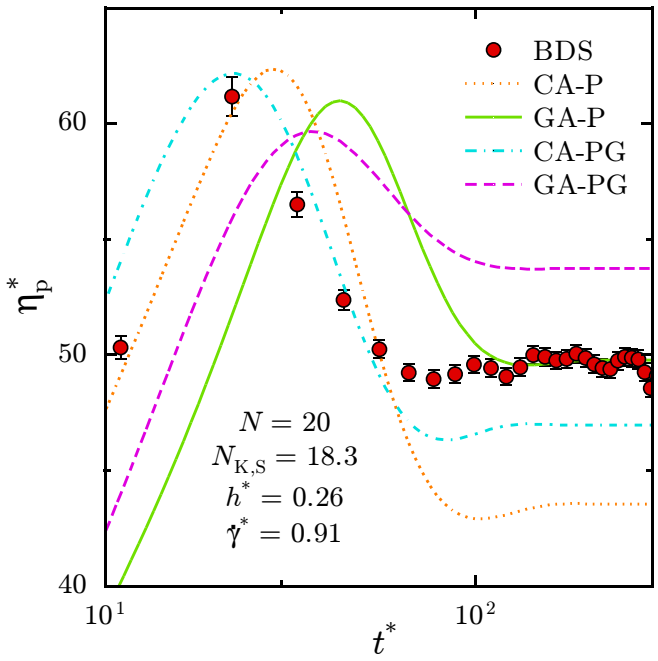

Figure 6.28: Growth of viscosity for FEBS chains with HI during start-up of a steady shear flow with $\dot{\gamma}^* = 0.91$.

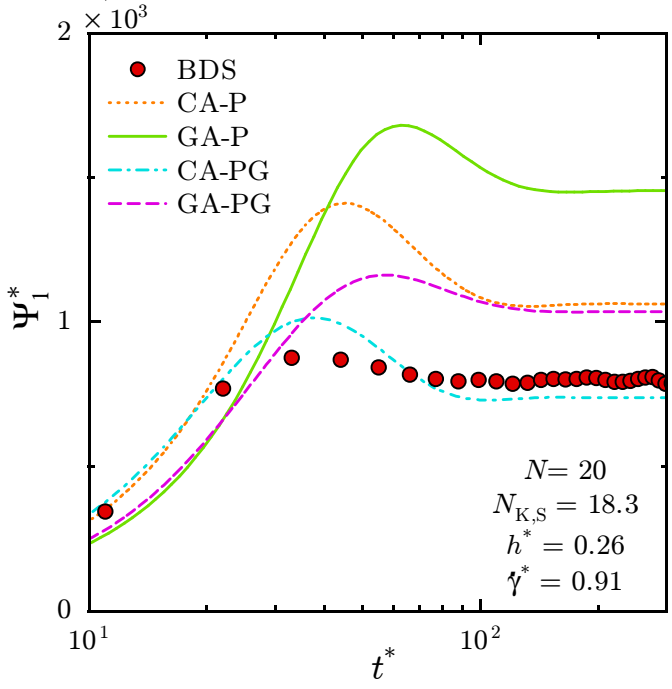

Figure 6.29: Growth of first normal-stress difference coefficient for FEBS chains with HI during start-up of steady shear flow with $\dot{\gamma}^* = 0.91$.

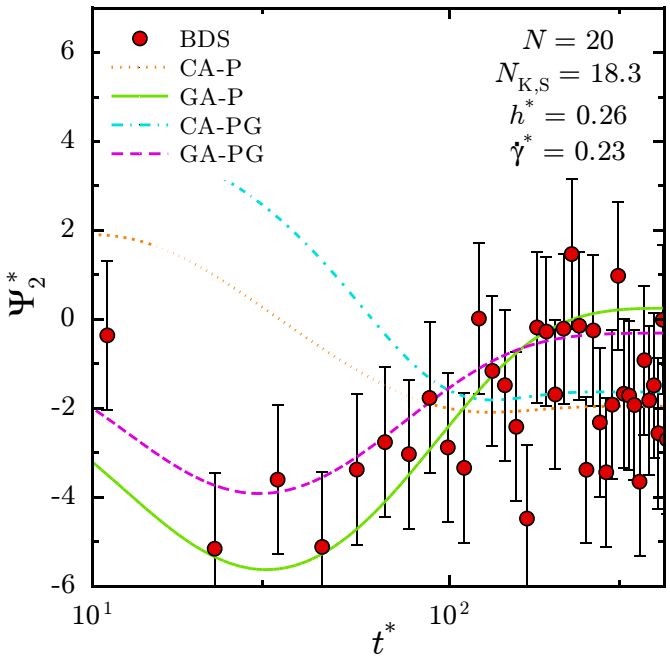

Figure 6.30: Growth of second normal-stress difference coefficient for FEBS chains with HI during start-up of steady shear flow with $\dot{\gamma}^* = 0.23$.

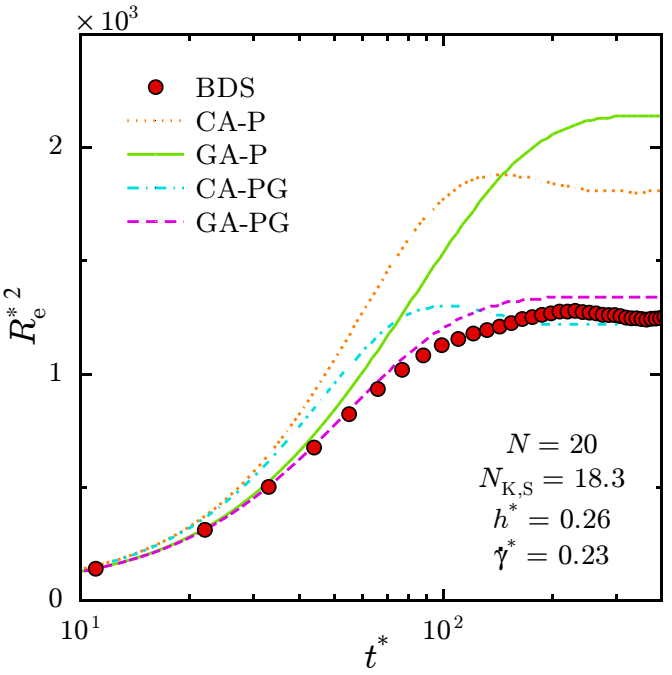

Figure 6.31: Growth of mean-squared end-to-end distance of FEBS chains with HI during start-up of steady shear flow with $\dot{\gamma}^* = 0.23$.

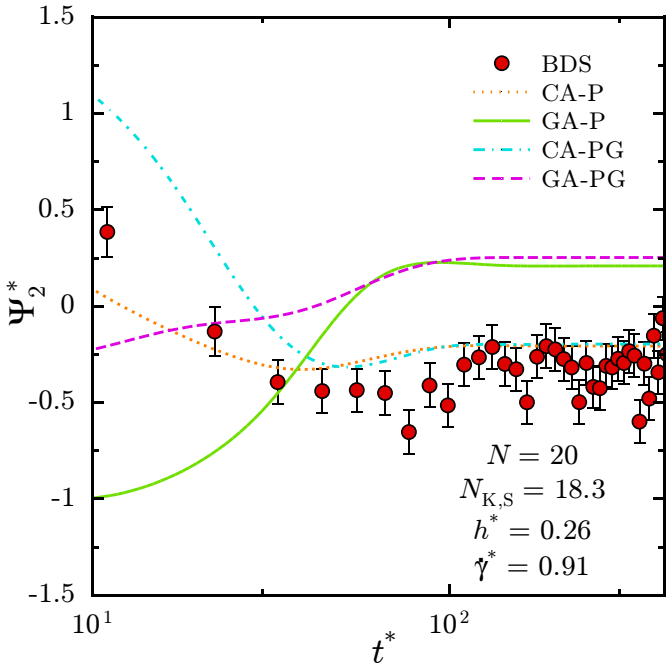

Figure 6.32: Growth of second normal-stress difference coefficient for FEBS chains with HI during start-up of steady shear flow with $\dot{\gamma}^* = 0.91$.

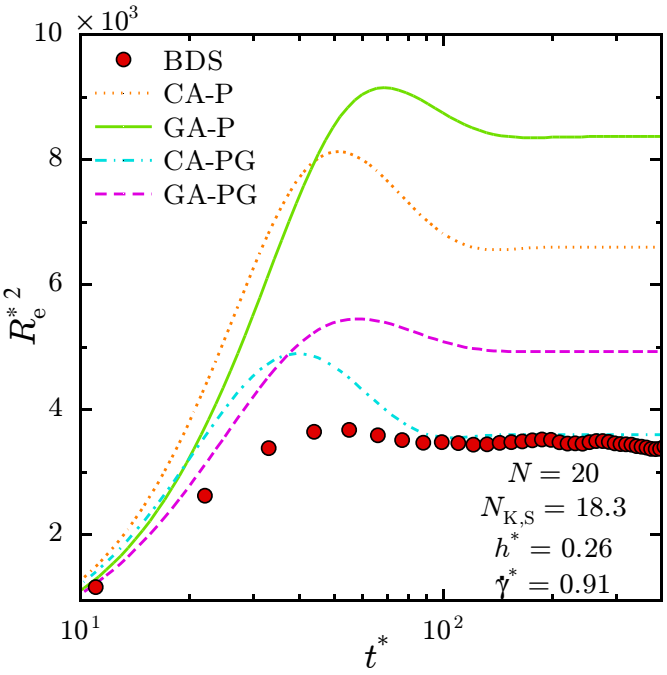

Figure 6.33: Growth of mean-squared end-to-end distance of FEBS chains with HI during start-up of steady shear flow with $\dot{\gamma}^* = 0.91$.

FE does exert a significant influence. However, the presence of HI is strong enough to completely eliminate the overshoot in the viscosity during start-up of shear at this shear-rate. Another interesting aspect of the influence of HI is that the data for both $\eta_{\rm p}^*$ (Fig. 6.35) and Ψ_1^* (not shown) at the lowest shear-rate almost form an envelope bounding the predictions at all other shear-rates. This is observed with the BD simulations as well as for all the approximate models for FEBS chains with HI. Such behaviour has earlier been observed experimentally for the growth of shear and normal stresses of melts and concentrated solutions [Huppler *et al.*, 1967; Wagner and Meissner, 1980], but has not been studied in dilute solutions. In contrast, the peak in the overshoot predicted at a high shear-rate by free-draining FEBS models is seen to lie well above the data for the lowest shear-rate (Fig. 6.22 and 6.23).

Figures 6.36 and 6.37 compare the predictions of the DCA-P and TFN-P approximations for Ψ_1^* and $R_{\rm e}^{*\,2}$ at $\dot\gamma^* \approx 1$ with those of the CA-P and GA-P approximations. Although none of the approximations are accurate at such high strain rates, it is seen that making the additional diagonalization assumption on the normal modes leads to larger deviations, particulary in $R_{\rm e}^{*\,2}$. The influence of the additional diagonalization assumption is examined by calculating the relative deviation between the predictions of a property π obtained with an approximation A and its diagonalized version DA:

$$\delta\pi_{\rm A} \equiv \frac{\pi_{\rm DA} - \pi_{\rm A}}{\pi_{\rm A}}\,. \tag{6.3}$$

It is observed in Fig. 6.38 that the relative deviation between the diagonalized and un-diagonalized approximations is quite small at a moderate shear-rate of $\dot\gamma^* = 0.23$. However, both the DCA-P and TFN-P approximations deteriorate as the shear-rate is increased, and may deviate by as much as 25% in their predictions of $R_{\rm e}^{*\,2}$ (Fig. 6.39), although the deviations are smaller in the case of Ψ_1^* (Fig. 6.38) and $\eta_{\rm p}^*$ (not shown). In contrast, the diagonalization assumption is much more accurate for Rouse chains with HI, for which the largest relative deviation does not exceed 10% even at the highest shear-rate studied (Figs. 6.40 and 6.41). Moreover, it is observed that the manner in which the deviations change with time is also quite different in the absence of FE. To understand the influence of FE on the quality of the diagonalization assumption, predictions were obtained with a diagonalized

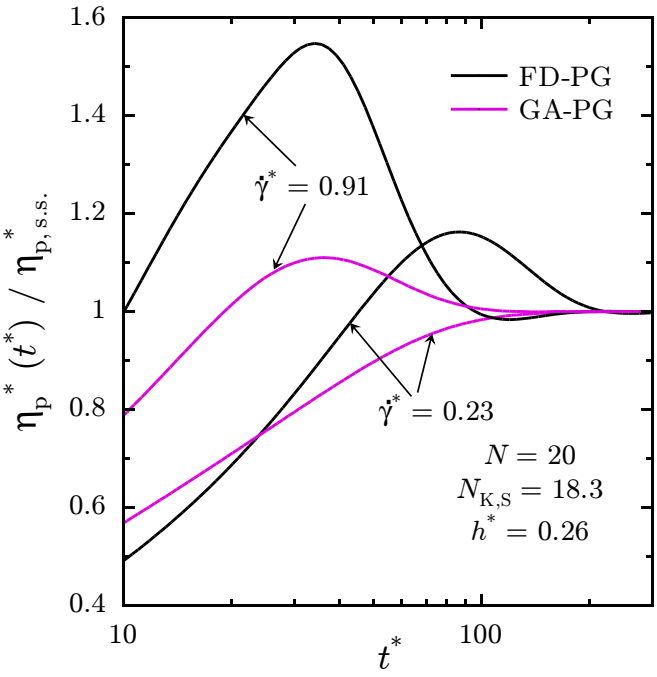

Figure 6.34: Growth of the ratio of the unsteady viscosity to its steady-state value for FENE-PG chains with and without HI during start-up of steady shear flows.

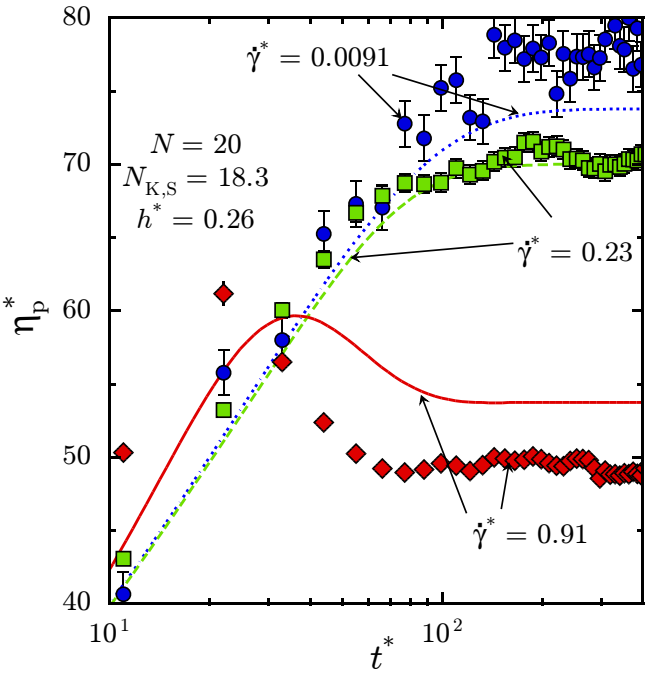

Figure 6.35: Effect of shear-rate on the growth of shear viscosity for FEBS chains with HI during start-up of steady shear flow. The smooth curves are the predictions of the GA-PG while symbols are the results of BD simulations.

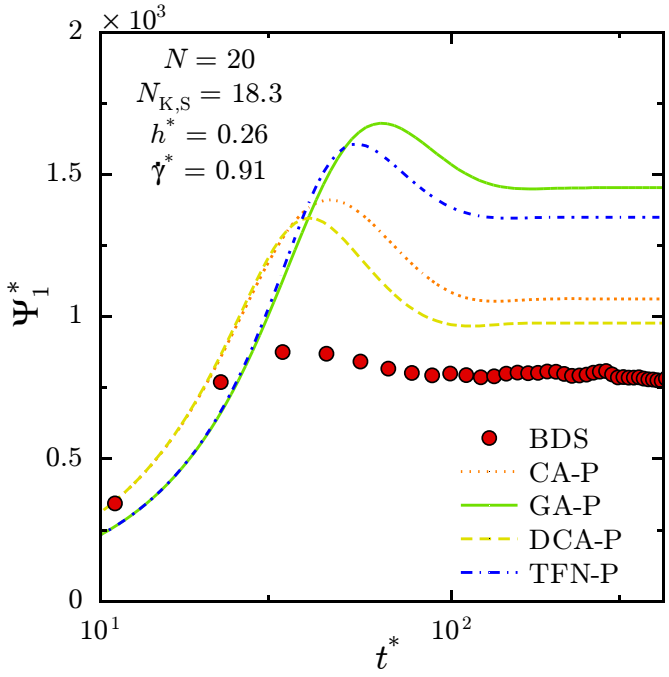

Figure 6.36: Effect of the diagonalization approximation in on the growth of the first normal-stress difference coefficient during start-up of steady shear flow with $\dot{\gamma}^* = 0.91$.

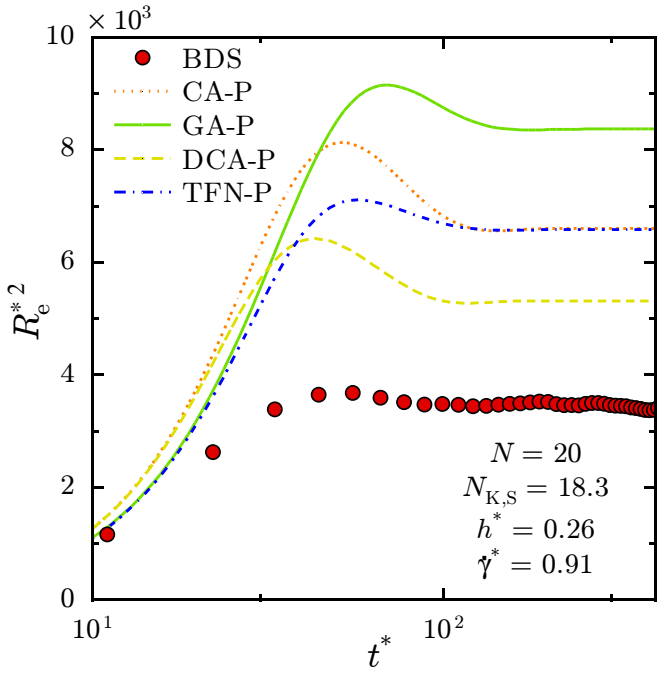

Figure 6.37: Effect of the diagonalization approximation in FEBS chains with HI on the mean-squared end-to-end distance during start-up of steady shear flow with $\dot{\gamma}^* = 0.91$.

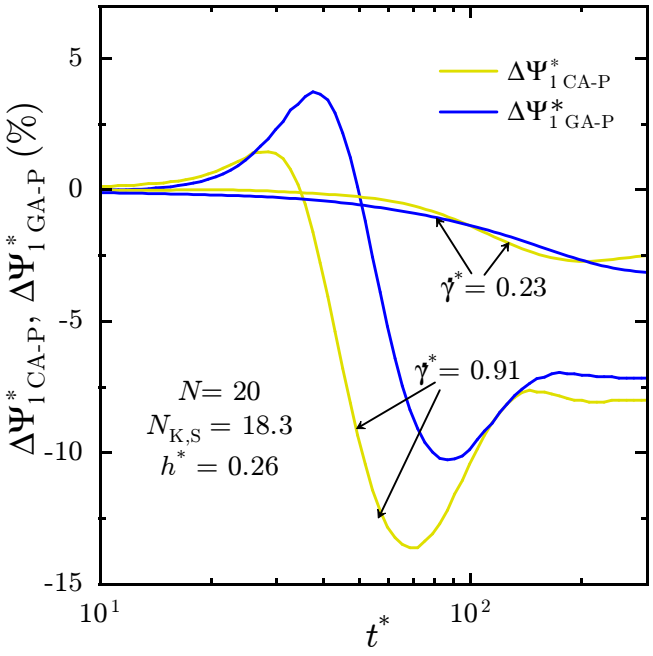

Figure 6.38: Deviations caused by diagonalization approximations in the prediction of first normal-stress difference coefficient in FEBS chains with HI.

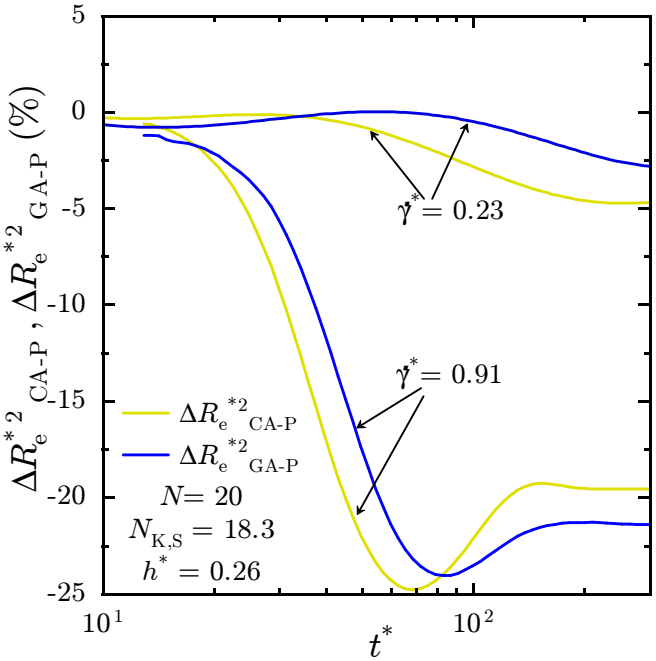

Figure 6.39: Deviations caused by diagonalization approximations in the prediction of mean-squared end-to-end distance in FEBS chains with HI.

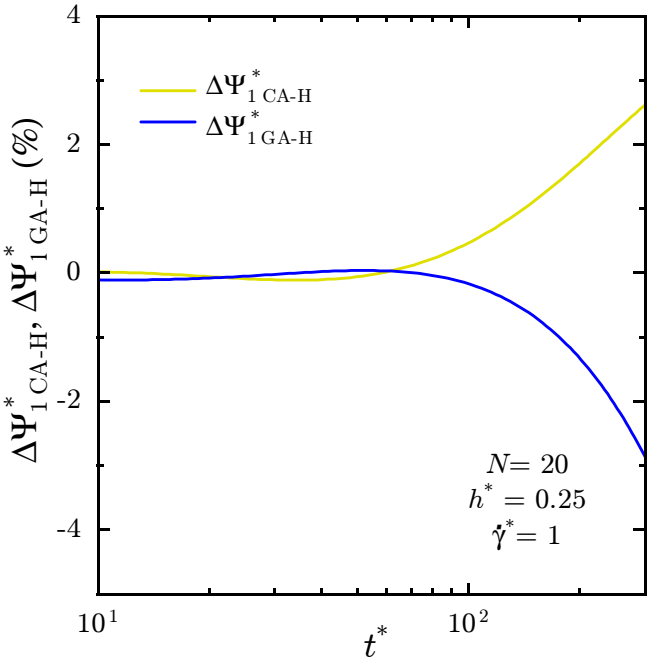

Figure 6.40: Deviations caused by diagonalization approximations in the prediction of first normal-stress difference coefficient in Rouse chains with HI.

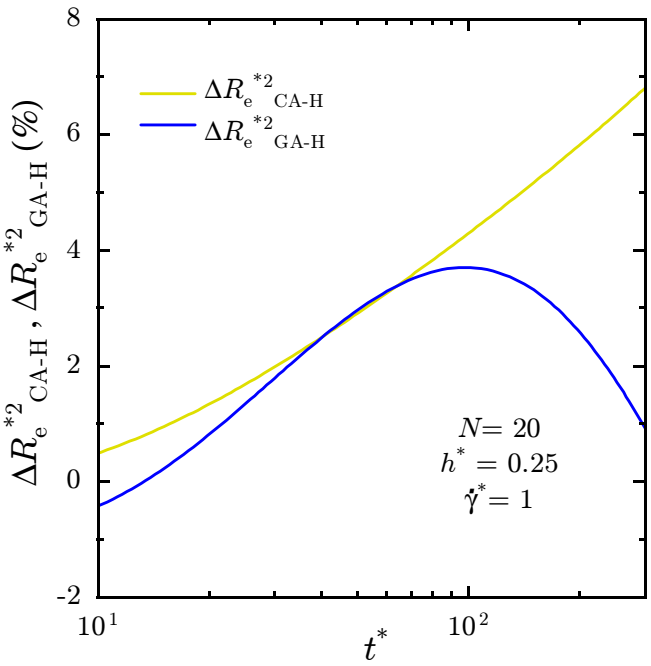

Figure 6.41: Deviations caused by diagonalization approximations in the prediction of mean-squared end-to-end distance in Rouse chains with HI.

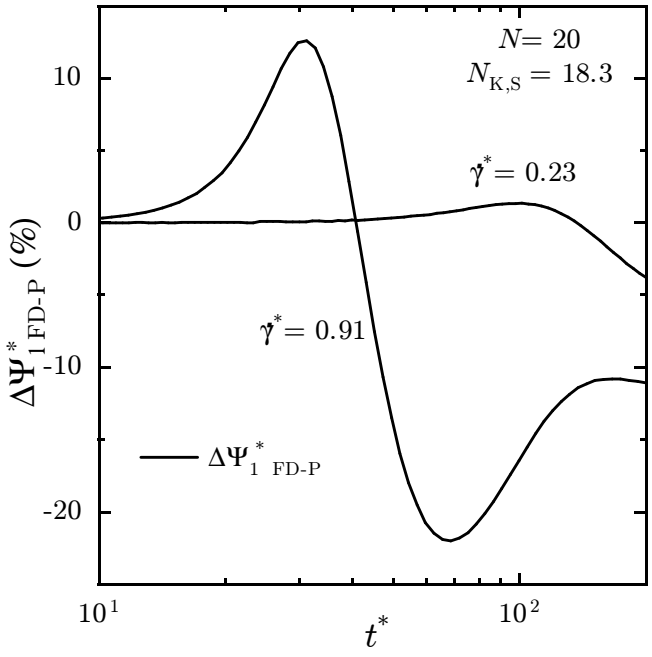

Figure 6.42: Deviations caused by diagonalization approximations in the prediction of first normal-stress difference coefficient in free-draining FEBS chains.

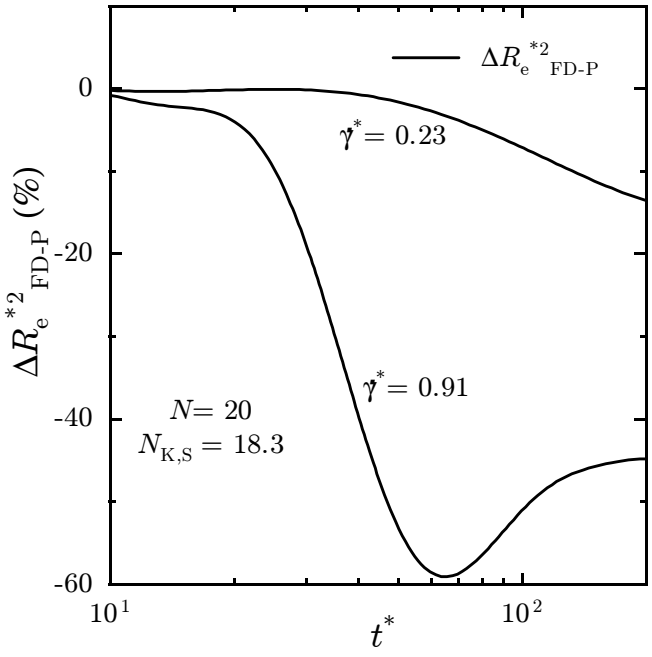

Figure 6.43: Deviations caused by diagonalization approximations in the prediction of mean-squared end-to-end distance in free-draining FEBS chains.

version of the FD-P model. In this case, the Rouse orthogonal matrix was used to transform to normal modes. The deviations between the diagonalized FD-P (DFD-P) model and the FD-P model are observed in Figs. 6.42 and 6.43 to be much larger at $\dot{\gamma}^* = 0.91$ than those seen in Figs. 6.38 and 6.39 at the same shear-rate, but the overall time variation is similar. Judging from these results, it appears that for free-draining FEBS chains, the off-diagonal components of the normal-mode covariances are not negligible at high shear-rates when the chains are highly stretched. However, on the inclusion of HI, the contribution of the off-diagonal components is relatively smaller, and the diagonalization assumption is more successful.

The results above for the unsteady evolution of properties during start-up of shear flows essentially reinforce the conclusions at the end of the discussion of the steady-state behaviour in shear flows. The Gaussian approximation, when combined with the FENE-PG force law, is seen to lead to predictions that are in quantitative agreement with the exact results until the breakdown of the FENE-PG approximation causes the combined model to deviate at high shear-rates. In addition, the diagonalization-of-normal modes assumption is also observed to hold for low to moderate shear-rates. At high shear-rates, where FE is the dominant effect, the diagonalization assumption becomes inaccurate, although the presence of HI appears to reduce the extent of the inaccuracies for the parameter values considered in the discussion above. The quality of the approximations in extensional flows is examined next.

6.3 Steady-state extensional viscosity

Exact results for the viscosity at steady-state in uniaxial extensional flows have not been obtained with BD simulations in this work. The accuracy of the approximations in their predictions for extensional flow *vis-a-vis* BD simulations is examined later in the subsequent section in the context of unsteady extensional flows.

Figure 6.44 compares the predictions of the extensional viscosity by free-draining models, and captures the essential features of the steady rheological behaviour of dilute polymer solutions in uniaxial extensional flows. The most important characteristic of the curves for the steady-state extensional viscosity is the occurrence of

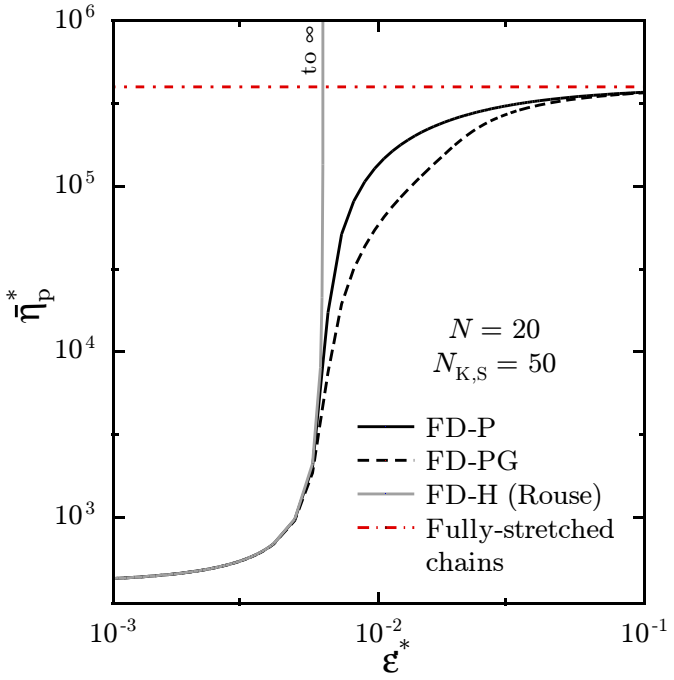

Figure 6.44: Variation of the steady-state polymer extensional viscosity with extension-rate, for free-draining FEBS chains.

a sudden rapid increase in its value within a narrow range of strain rates around a critical elongation rate $\dot{\varepsilon}^*_c$. As mentioned in Chapter 4, the value of $\dot{\varepsilon}^*_c$ can be calculated analytically in the Rouse model to be $\dot{\varepsilon}^*_c = \sin^2(\pi/2N)$ [Bird *et al.*, 1987b]. At this value of the extensional strain rate, the analytical solution for the contribution of the largest normal mode to the steady-state xx-component of the stress tensor becomes singular in the Rouse model, and the steady-state $\overline{\eta}^*_p$ predicted by the model diverges. This is understood to be the direct consequence of using Hookean springs which can be extended without limit. For $\dot{\varepsilon}^* \geq \dot{\varepsilon}^*_c$, the drag forces extending the Rouse chain in the direction of stretching in the uniaxial extensional flow grow faster with chain extension than the spring forces resisting the extension, and no steady-state is achieved with Rouse chains. This unrealistic behaviour is remedied with the use of finitely extensible springs, in which the steep increase in the spring forces as chains approach full extension means that a balance between the solvent drag forces and the spring forces is always achieved. However, as observed earlier in shear flows, the steady-state $\overline{\eta}^*_p$-versus-$\dot{\varepsilon}^*$ curves predicted by models with

FEBS chains are indistinguishable from the prediction of the Rouse model until FE becomes important.

As the extensional strain rate is increased beyond $\dot{\varepsilon}^*_c$, the predictions of the FEBS models for $\overline{\eta}^*_p$ in Fig. 6.44 approach the limit predicted for fully-stretched chains completely aligned in the flow direction [Hassager, 1974],

$$\overline{\eta}^*_p = N_{K,\,S} N_S (N_S + 1)(N_S + 2)\,. \tag{6.4}$$

It is observed the predictions with the FENE-PG and FENE-P approximations are significantly different at strain rates close to $\dot{\varepsilon}^*_c$, indicating that force fluctuations play an important role in determining the behaviour close to the critical strain rate. Moreover, the curve predicted by the FD-PG model is below that obtained with the FD-P model, indicating that force fluctuations effectively increase the stiffness of the springs leading to lower extensions, and hence lower values of $\overline{\eta}^*_p$. At higher strain rates, as the fractional stretch increases and the fully-stretched chain limit is approached, the difference between the two models diminishes. It was shown Chapter 5 that as the dimensionless mean-squared end-to-end distance of any spring approaches b^*, the additional term in the FENE-PG nonlinearity becomes negligible in comparison with the FENE-P contribution. At high extensional strain rates, the FENE-P model is known to be quite accurate in its prediction of the steady-state extensional viscosity [van den Brule, 1993]. The reason for the accuracy of the FENE-P approximation at high extension-rates, when the true spring-length distributions become narrow and δ-function-like, has been previously elaborated in Chapter 5.

In contrast to the behaviour observed in steady shear flow, the inclusion of HI does not change the qualitative features of the predictions for the variation of $\overline{\eta}^*_p$ with $\dot{\varepsilon}^*$ observed with free-draining chains. As in Fig. 6.44, a critical extension-rate exists at which predictions with Rouse chains diverge, irrespective of the approximation used for handling HI. On incorporating FE, finite steady-state viscosities are predicted for all $\dot{\varepsilon}^* \geq \dot{\varepsilon}^*_c$. As the extension-rate increases, the greater stretching of the chains causes a progressive decrease in the importance of HI, and the predictions of the models appear to approach the limit for fully-stretched chains with HI, which however is close to the limiting value for fully-stretched free-draining chains. The

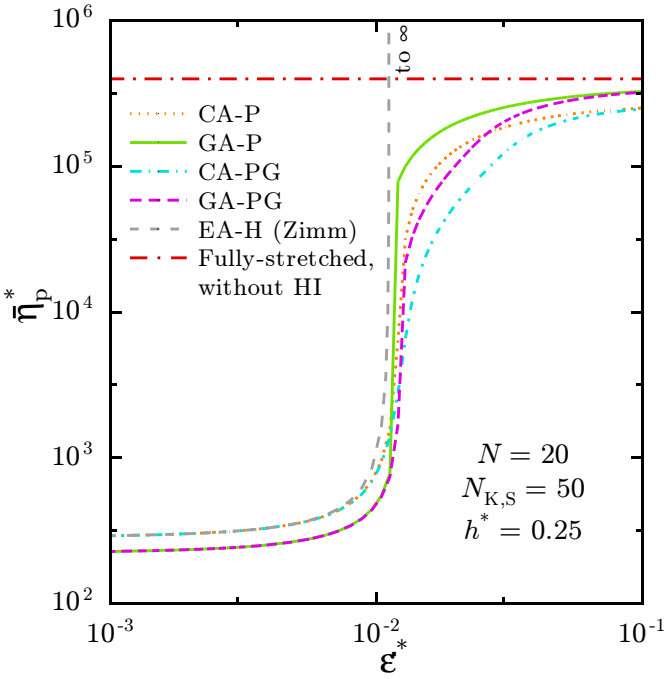

Figure 6.45: Variation of the steady-state polymer extensional viscosity with extension-rate, for FEBS chains with HI.

derivation of the exact limiting value of the steady-state $\overline{\eta}_p^*$ for fully-stretched chains is given in Appendix B.

For strain rates not much larger than $\dot{\varepsilon}_c^*$, the large differences between models employing the consistent-averaging and Gaussian approximations indicates the importance of fluctuations in HI. These fluctuations are found to hasten the weakening of the influence of HI, since the predictions with the Gaussian approximation lie closer to the curves predicted with the free-draining models. Such behaviour was also observed at high shear-rates. At the same time, fluctuations in the spring forces are also observed to be important. As in the case of shear flows, fluctuations in HI and in spring forces have opposing influences on the prediction of the extensional viscosity.

Figure 6.46 shows that the assumption of a diagonal normal-modes covariance block matrix becomes inaccurate beyond the critical strain rate. The deviation between the diagonalized and the corresponding un-diagonalized approximations is observed to be greater in the absence of HI, and seems to arise primarily due to

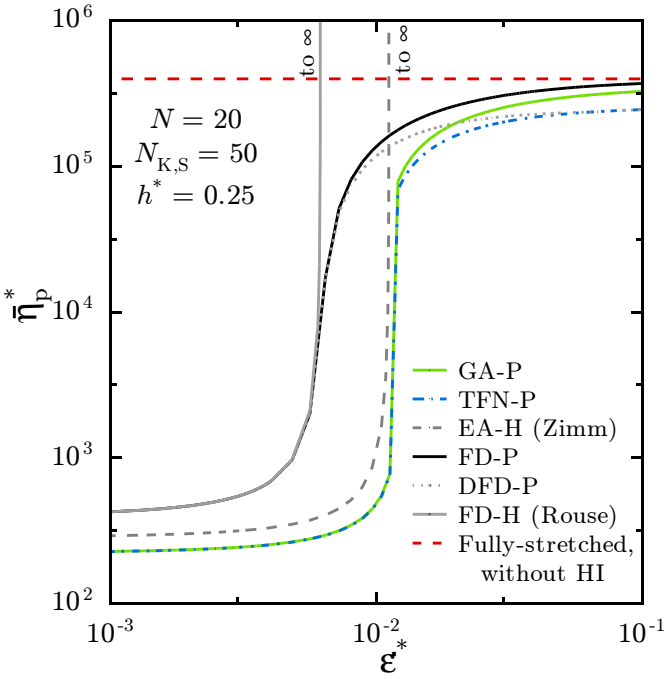

Figure 6.46: Effect of the diagonalization approximations on the variation of the steady-state polymer extensional viscosity with extension-rate, for FEBS chains with HI.

the influence of the spring force nonlinearity. This behaviour is consistent with that observed earlier at high shear-rates.

In shear flows, it was observed that increasing N_K lead to the appearance of a moderate shear-rate regime in which HI, although weakening, played a dominant role and shear-thickening was observed. In extensional flows, however, such a regime is not immediately evident. As observed before in the prediction of the steady shear viscosity, the prediction of a model combining both HI and FE is bounded by the curve predicted with Rouse chains with the same approximation for HI when $\dot{\varepsilon}^* < \dot{\varepsilon}_c^*$, and by the prediction obtained with free-draining chains using the same force law when $\dot{\varepsilon}^* > \dot{\varepsilon}_c^*$. Figure 6.46 provides an illustration of this behaviour, which is seen to be determined by the relative values of the critical strain rates for chains with and without HI. Increasing N_K by keeping N_S fixed and changing $N_{K,\,S}$ will therefore not result in any change in the difference between the respective values of $\dot{\varepsilon}_c^*$ predicted by Rouse chains with and without HI. On the other hand, an increase in N_S for the same value of $N_{K,\,S}$ will lead to a smaller value of $\dot{\varepsilon}_c^*$ with the free-draining Rouse

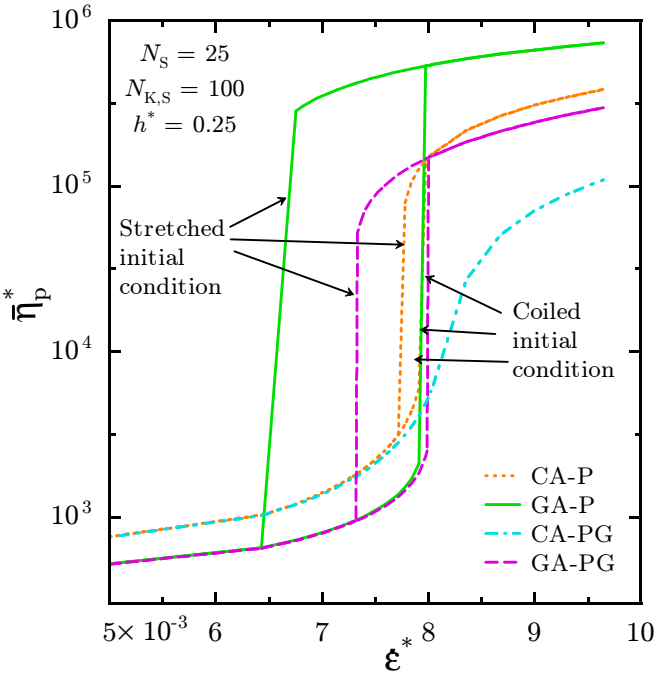

Figure 6.47: Prediction of coil-stretch hysteresis in the steady-state extensional viscosity by closure approximations for FEBS chains with HI.

model. As discussed previously in Chapter 4 and earlier in this Chapter, this is a consequence of the scaling of $\dot{\varepsilon}_c^*$ as N^{-2} for free-draining chains, in contrast to the slower decrease for chains with HI as $N^{-3/2}$. On a plot of $\overline{\eta}_p^*$ against $\dot{\varepsilon}^*$, an increase in N_s for the same value of $N_{K,\,s}$ shifts the free-draining curves leftward (and upward) relative to the curves obtained using models with HI. As a result, no new regime of moderate extension-rates is created.

Interestingly, the approximations for FEBS chains with HI can predict multiple steady-state values for the extensional viscosity for the same value of $\dot{\varepsilon}^*$. Figure 6.47 illustrates this behaviour, showing that for the parameter values in the shown in the figure, all models other than the CA-PG model, predict two very different sets of steady-state values for $\overline{\eta}_p^*$ for a range of strain rates whose upper bound is the critical strain rate, $\dot{\varepsilon}_c^*$. Similar predictions are obtained even with the DCA-P and TFN-P approximations (not shown).

The variation of the steady-state extensional viscosity with extension-rate is obtained as follows. Starting with the equilibrium second moments ($\boldsymbol{\sigma}_{ij,\,\mathrm{eq}}^* = \delta_{ij}\boldsymbol{\delta}$)

as the initial guess, the set of coupled, nonlinear equations for the steady-state second moments are first iteratively solved at a small value ($\ll \dot{\varepsilon}^*_c$) of the extension-rate (Section 5.6). After calculating the extensional viscosity with the converged solution for the equilibrium second moments, this solution is used as the guess for obtaining the solution numerically at a slightly larger value of $\dot{\varepsilon}^*$. This process is continued until $\dot{\varepsilon}^*$ is well beyond the value of '$\dot{\varepsilon}^*_c$ for the coil-to-stretch transition. The $\overline{\eta}^*_p$-versus-$\dot{\varepsilon}^*$ curve obtained thus is indicated as having been obtained with a "coiled initial condition" in Fig. 6.47. The process is then continued next by lowering the extension-rate. With the CA-PG approximation, and or the parameter values used in Fig. 6.47, the steady-state extensional viscosities obtained by decreasing $\dot{\varepsilon}^*$ results in the same set of values as obtained while increasing $\dot{\varepsilon}^*$. However, with all the other approximations for chains with HI, the $\overline{\eta}^*_p$-versus-$\dot{\varepsilon}^*$ curve follows a different route as $\dot{\varepsilon}^*$ is decreased. Since this steady-state solution branch is obtained starting from a highly "stretched initial condition", it is indicated as such in Fig. 6.47.

The existence of such multiple steady-states was first shown with a dumbbell model by De Gennes [1974] and was earlier obtained with the CA-H model by Magda *et al.* [1988]. This phenomenon is widely known as coil-stretch hysteresis. However, Fan *et al.* [1978] pointed out that the exact Fokker-Planck equation, being linear in the probability distribution, must have a unique solution at steady-state. The expectations of the exact distribution, and hence all properties such as $\overline{\eta}^*_p$, determined at steady-state must therefore be unique functions of the strain rate. Fan *et al.* hence concluded that the results obtained by De Gennes were artifices due to the use of mean-field approximations in his dumbbell model. The reasons behind this intriguing aspect of mean-field approximations are explored further in Section 6.5.2.

It is interesting to note that the size of the window of strain rates where multiple steady-states are obtained, depends strongly on the approximation used. On closer examination, it appears that the window size depends on the difference between the extensional viscosities in the coiled state (the lower branch of the hysteresis curve) and the stretched state (the upper branch of the hysteresis curve). Fluctuations in HI lead to a widening of the window because these fluctuations decrease the coiled state viscosity, but increase the viscosity when the chains are highly stretched. As

pointed out earlier, spring force fluctuations decrease the viscosity at the stretched states, thus leading to a smaller coil-stretch hysteresis window. In fact, in the absence of fluctuations in HI, spring fluctuations completely eliminate the hysteresis in the CA-PG model for the parameter values in Fig. 6.47.

From the discussion above, it appears that in models combining both HI and FE, the critical elongation rate separates the low strain-rate linear response regime–where HI is completely dominant and the influence of FE is negligible–from the regime of strong extensional flows where FE is important. Unlike shear flows, there appears to be no sizeable range of extension-rates where the viscoelastic behaviour is nonlinear with respect to the extension-rate and controlled largely by HI. Thus, a detailed study of the nonlinear viscoelastic behaviour of dilute polymer solutions in extensional flows seems meaningful only when FE is included in the model. The qualitative features of the closure approximations in strong unsteady extensional flows is considered below.

6.4 Start-up and cessation of steady uniaxial extensional flow

Models using Hookean springs predict unbounded extension is strong extensional flows. As a result of this unrealistic behaviour, the predictions of approximations for HI in Rouse chains have not until recently [Sunthar and Prakash, 2005] been examined in strong and unsteady extensional flows. However, at any finite time following the imposition of the flow, the values of the stresses and other properties obtained with Rouse chains are still finite. Therefore, comparing the predictions of the approximations and the results of BD simulations for Rouse chains may throw some light on the influence of HI in strong extensional flows. Figure 6.48 show results the growth of the polymer's contribution to $N^*_{1,\mathrm{p}}$ the dimensionless first normal stress difference upon the imposition of a steady extensional flow of $\dot{\varepsilon}^*_0 = 0.04$, which is well beyond $\dot{\varepsilon}^*_\mathrm{c}$ for the same set parameters (Fig. 6.45). Also shown in Fig. 6.48 are the predictions for the relaxation of $N^*_{1,\mathrm{p}}$ after the cessation of the extensional flow at different values of the Hencky strain. Predictions of properties in the stress

relaxation phase were obtained by setting the strain rate to zero at a predetermined $\varepsilon_{\max} = \dot{\varepsilon}_0^* t_{\max}^*$ [Eq. (2.74)], and then proceeding with the time integration in both BD simulations, and with the closure approximations. Figure 6.49 shows the corresponding evolution in the mean-squared end-to-end distance.

The results in Figs. 6.48 and 6.49 show several fascinating features. Firstly, the agreement of the approximations other than the Zimm model with the exact results of BD simulations is remarkable. Clearly, the use of equilibrium averaging in estimating the influence of HI can lead to considerable error in strong extensional flows. Moreover, the error grows larger during relaxation in the absence of the flow. Taking into account the influence of configurational anisotropy on HI through the use of consistent averaging leads to a dramatic improvement in the quality of the approximation. Furthermore, the use of the diagonalization assumption in the normal-modes is seen to have a negligible effect on the predictions of both the stress and the mean extension of the chains. The differences between the predictions of the consistent-averaging and Gaussian approximations do not appear to be large in Figs. 6.48 and 6.49. Figure 6.50 plots the relative difference between the predictions of $N_{1,\mathrm{p}}^*$ of the two approximations,

$$\Delta_{\text{GA-CA}} = \frac{N_{1,\mathrm{p}_{\text{GA}}}^* - N_{1,\mathrm{p}_{\text{CA}}}^*}{N_{1,\mathrm{p}_{\text{GA}}}^*}\,, \tag{6.5}$$

and shows that the difference between the two approximations in their predictions of $N_{1,\mathrm{p}}^*$ can be sizeable.

Predictions of free-draining FEBS models employing the FENE-P and FENE-PG approximations are compared with exact results of the simulations for the growth and relaxation of $N_{1,\mathrm{p}}^*$ and $R_{\mathrm{e}}^{*\,2}$ in Figs. 6.51 and 6.52. Also shown for comparison are the predictions of the simple Rouse model. The strain-rate for which the data are shown in these Figures is seen in Fig. 6.44 to be much larger than the critical strain rate for chains with $N = 20$. At this relatively high strain rate, the Rouse model predicts an exponential increase in both $N_{1,\mathrm{p}}^*$ and $R_{\mathrm{e}}^{*\,2}$ during extension. At small values of the Hencky strain during start-up of the extensional flow at this strain rate, all the data for the different models are essentially identical, since the springs are not stretched sufficiently for the spring-force nonlinearities to have any significant

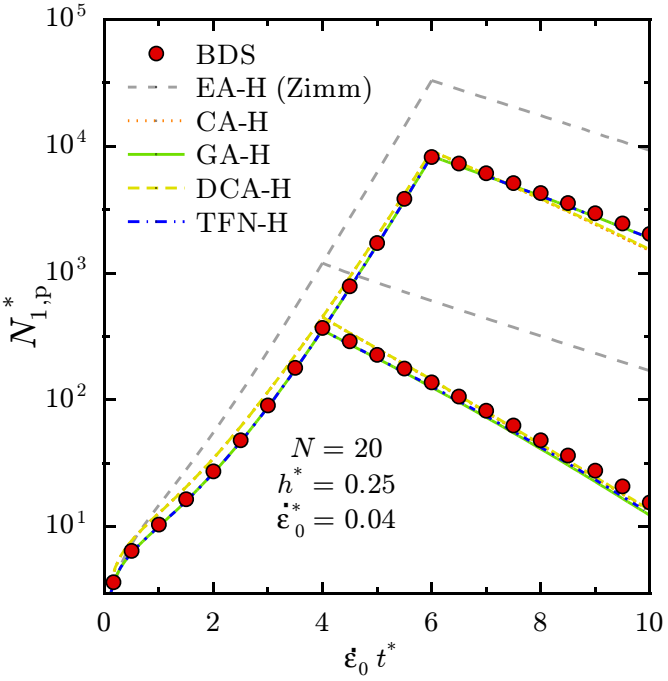

Figure 6.48: Growth and decay of the polymer contribution to the first normal-stress difference for Rouse chains with HI, during start-up and following cessation of steady extensional flow, respectively.

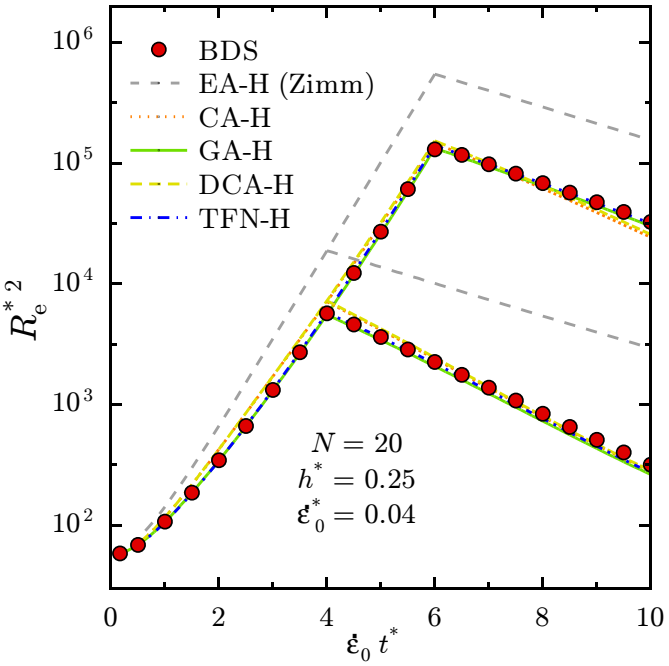

Figure 6.49: Growth and decay of the mean-squared end-to-end distance of Rouse chains with HI during start-up and following cessation of steady extensional flow, respectively.

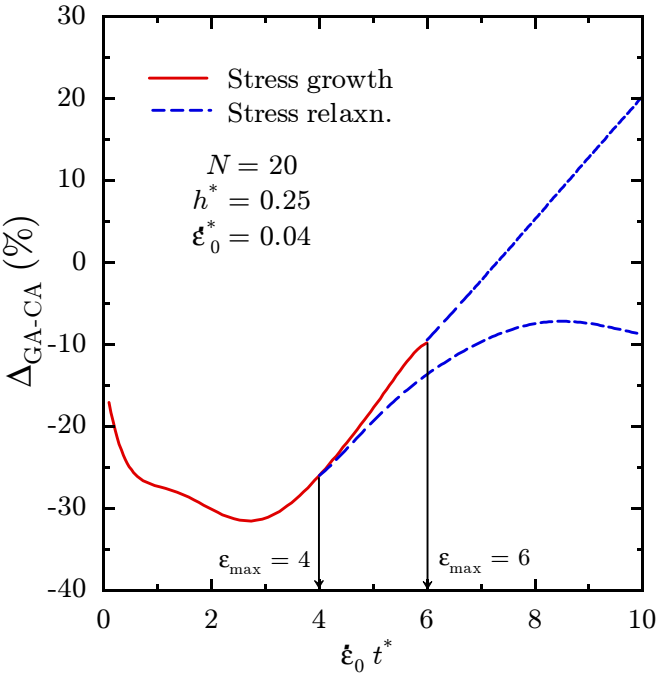

Figure 6.50: Effect of fluctuations in HI on the growth and decay of the polymer contribution to the first normal-stress difference for Rouse chains with HI, during start-up and following cessation of steady extensional flow, respectively.

effects. The influence of FE is first discerned in the growth of the stress when the curves for the FEBS chains separate from the prediction of the Rouse model. At this stage when FE begins to become important, the FENE-PG approximation is observed to be closer to the simulations' results. At higher strains, the deviations between the approximations and the exact results for $N^*_{1,\mathrm{p}}$ become more marked and reach a maximum when the approximate results level off sharply towards their eventual steady-states. The approach of the BD simulations' data to steady-state is more gradual. Even in this phase of the stress growth, the FENE-PG approximation is seen to do better.

On comparing Figs. 6.51 and 6.52, it is evident that the influence of FE on the development of stresses begins at an earlier strain than on the extension of the chains. The manner in which results with FEBS chains deviate from the Rouse model's predictions is interesting. For the normal stresses, the deviation is first positive before the FEBS models' results turn towards their respective steady-state values and intersect the ever-growing curve predicted by the Rouse model. On the

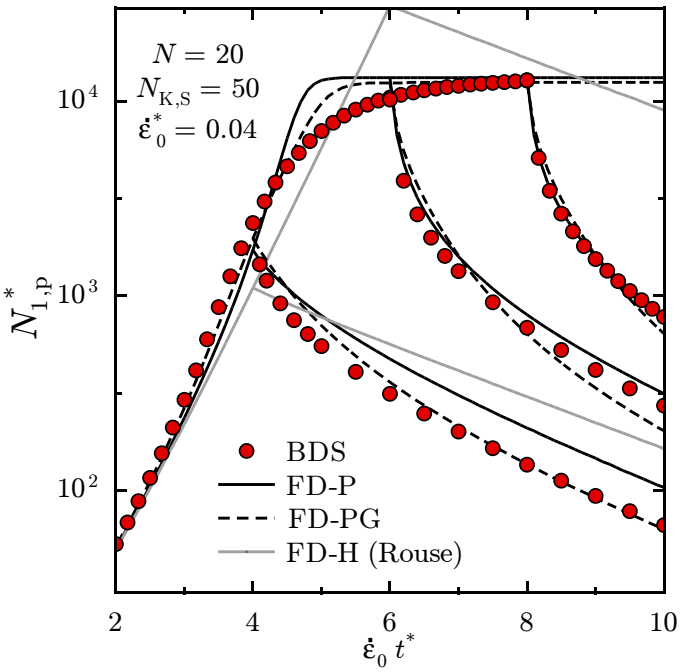

Figure 6.51: Growth of the polymer contribution to the first normal-stress difference for free-draining FEBS chains, during start-up, and following cessation, of steady extensional flow.

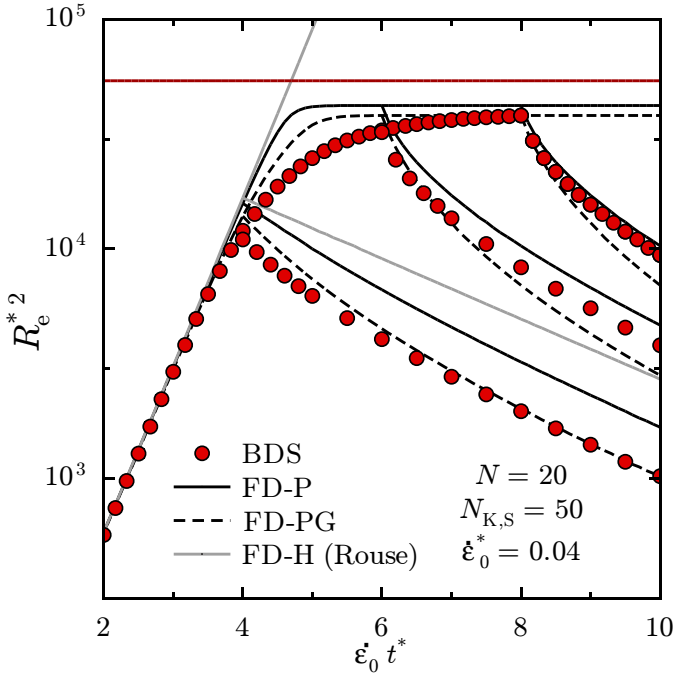

Figure 6.52: Growth of the mean-squared end-to-end distance of free-draining FEBS chains, during start-up, and following cessation, of steady extensional flow. The horizontal red line indicates the maximum possible value of $R_e^{*2} = 3N_{K,S}N_S^2$.

other hand, the curves for R_e^{*2} predicted by the FEBS models "peel off" from the Rouse model's curve to approach their steady-states. The deviations between the predictions of the approximate FEBS models and the exact BD results for $N_{1,p}^*$ also follow a characteristic pattern. Initially, the normal stresses are underpredicted by the approximate model. Thereafter, the predictions of $N_{1,p}^*$ with the approximations grow much more rapidly than the exact results, and lead to the large overprediction mentioned above.

The relaxation behaviour of free-draining FEBS chains following the cessation of extensional flow has been studied earlier by Doyle *et al.* [1998] and Wiest [1999b]. While Doyle *et al.* compared the predictions of the FENE-PM approximation (discussed earlier in Chapter 5) with BD simulations of FENE dumbbells and also bead-rod chains, Wiest [1999b] examined some interesting qualitative features in the stress-relaxation phase using the FENE-P model.

In the stress-relaxation phase after cessation of flow, the predictions of the Rouse model are observed to be vastly different from those obtained with the FEBS models, with both the stress and R_e^{*2} decaying exponentially with time, as evidenced by the nearly straight lines on the semi-logarithmic plot in Figs. 6.51 and 6.52. In contrast, BD simulations of FENE chains show a rapid decrease in the stress for a short period of time immediately after the cessation of the flow. The size of the drop in the stress during the initial relaxation increases significantly with the strain at which the extensional flow is stopped. The initial rapid decrease in stress is generally understood to be a consequence of the steepness of the entropic singularity in the spring force law. If the relaxation begins after a large strain is imposed and the springs are highly stretched, even a small decrease in the chain extension can result in a large decrease in the spring forces, and in the total polymer stress. Shaqfeh *et al.* [2004] observed that the initial rate of decrease is characteristic of the spring force law used in the model. These authors also show that the slower decrease in $N_{1,p}^*$ observed in Fig. 6.51 after the initial sharp fall follows a power law in time. Larson and co-workers [Li and Larson, 2000b; Li *et al.*, 2000] have further shown that the predictions obtained with BD simulations of free-draining FENE chains for stress relaxation are qualitatively similar to the measurements of stress relaxation in experiments.

The FENE-PG approximation is seen to lead to more accurate description of both the stress and extension in the relaxation phase when the strain at flow stoppage is not much larger than the strain at which FE begins to exerts its influence, whereas the FENE-P approximation leads to an overprediction of both properties. When the Hencky strain at flow stoppage is larger, the FENE-PG force law is seen to be in fact less trustworthy. This loss in accuracy when chains are highly stretched is consistent with the behaviour observed earlier in steady and unsteady shear flow.

The qualitative features of the relative behaviour of the different combined approximations are similar to that observed earlier in shear and at the steady-state in extensional flows. In Figs. 6.53 and 6.54, the initial growth in $N^*_{1,\mathrm{p}}$ and $R^{*\,2}_{\mathrm{e}}$ with strain is very nearly the same as that observed for Rouse chains with HI, with the Gaussian approximation predicting lower stresses and extension than the consistent-averaging approximation. The differences between the different approximations grow larger at intermediate strains during extension. At these strains and above, the curves predicted by the combined models are qualitatively similar to the predictions obtained with the approximations for free-draining FEBS chains. In particular, the nature of deviations between the BD simulations' results and the approximations' predictions appear to be decided largely by the approximation used for the FENE nonlinearity. Incorporating fluctuations in HI through the Gaussian approximation make the curves of the combined models resemble the predictions of the corresponding free-draining model. Predictions of the relaxation behaviour are observed to be better with the FENE-PG force law when the strain at flow stoppage is low. The largest deviations in the approximations' predictions of the relaxation behaviour occur when flow is stopped at a strain in the "knee" region just prior to steady-state.

6.5 Hysteretic phenomena in extensional flows

6.5.1 Stress-conformation hysteresis

The phenomenon of stress-conformational hysteresis in dilute polymer solutions has been studied in experiments [Orr and Sridhar, 1999; Spiegelberg and McKinley, 1996] and theoretically [Doyle *et al.*, 1998; Ghosh *et al.*, 2001; Li and Larson, 2000b;

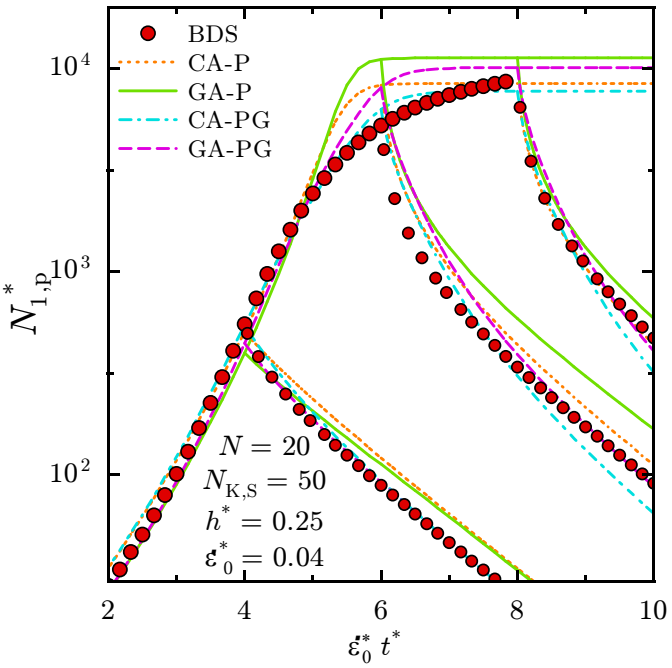

Figure 6.53: Growth and decay of the polymer contribution to the dimensionless first normal-stress difference for FEBS chains with HI, during start-up and following cessation, of steady extensional flow, respectively.

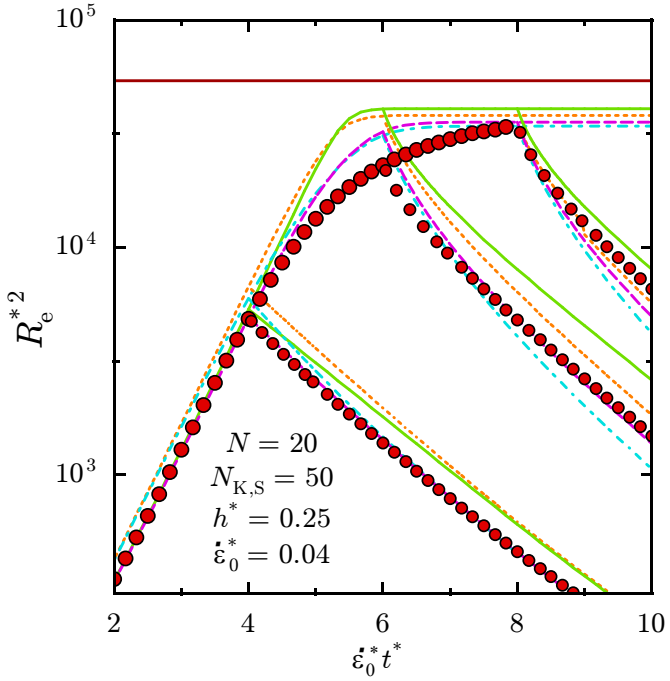

Figure 6.54: Growth and decay of the polymer contribution to the mean-squared end-to-end distance of FEBS chains with HI, during start-up and following cessation of steady extensional flow, respectively. The horizontal red line indicates the maximum possible value of $R^{*\,2}_{\mathrm{e}} = 3N_{\mathrm{K,\,S}}N^2_{\mathrm{S}}$.

Lielens *et al.*, 1998; Wiest, 1999a]. In extensional flows experiments, it is observed that when the normal stress is plotted against the birefringence of the solution, the curves described by the data points during the stress-growth and stress-relaxation phases are very different. In particular, at any fixed value of the birefringence, the stress during extension is larger than that measured during relaxation. Conversely, at a fixed stress, the birefringence during relaxation is larger.

Birefringence quantifies the degree of optical anisotropy in a material. Under the action of an imposed velocity gradient, deformation of polymer coils in a polymer solution induces anisotropy in its optical properties. Thus, the refractive index of the polymer solution–which is characterized by a single scalar quantity under isotropic equilibrium conditions–takes on a tensorial form in flow, denoted here as $\mathbf{n}$. The total flow birefringence of a polymer solution is the sum of two contributions *viz.* intrinsic birefringence $\mathbf{n}^{\mathrm{I}}$ and form birefringence $\mathbf{n}^{\mathrm{F}}$ [Bossart and Öttinger, 1997; Doi and Edwards, 1986]. The latter contribution vanishes if the refractive indices of the pure solvent and polymeric solute are equal. Since form birefringence is more difficult to predict, the solvent is usually chosen to keep the contribution of form birefringence low.

Intrinsic birefringence in polymer solutions is a consequence of the local alignment of the Kuhn segments of the polymer chains. The extents to which an individual Kuhn segment can polarize an incident beam of light in a direction along its length, and in a direction perpendicular to itself are different. The alignment of a majority of polymer segments in any single direction increases the total polarization of light in that direction, making the solution optically anisotropic. Thus, intrinsic birefringence measures the degree of local alignment of polymer chains.

It may be recalled that a spring in a bead-spring chain represents a sub-molecule consisting of $N_{\mathrm{K,\,s}}$ Kuhn segments. Further, when $\dot{\varepsilon}^* \lesssim 1$, each sub-molecule has sufficient time to sample the configuration space consistent with the corresponding spring's connector vector. Since the local segmental *equilibrium* distribution for a given end-to-end vector is unique (depending solely on $N_{\mathrm{K,\,s}}$), the total mean alignment of the segments, and hence the mean polarizability of a sub-molecule represented by a spring is uniquely related to its end-to-end vector. The intrinsic birefringence predicted with bead-spring chains can thus be derived to be [Doi and

Edwards, 1986; Wiest, 1999a]

$$\mathbf{n}^{\mathrm{I}} = n_{\mathrm{eq}}\boldsymbol{\delta} + \frac{A}{Q_0^2}\sum_{i=1}^{N_{\mathrm{S}}}\left[\langle\, \boldsymbol{Q}_i\boldsymbol{Q}_i \,\rangle - \frac{1}{3}\langle Q_i^2\rangle\boldsymbol{\delta}\right] , \tag{6.6}$$

where n_{eq} is the isotropic refractive index of the solution at equilibrium, and A is a constant that is proportional to the polymer concentration n_{p} besides depending on the chemical structure of the polymer and the solvent. In extensional flows, it is possible to define a dimensionless quantity, which for the sake of convenience will be referred to as the birefringence in this Section:

$$\Delta n^* \equiv \frac{n^{\mathrm{I}}_{xx} - n^{\mathrm{I}}_{yy}}{A} . \tag{6.7}$$

In dimensionless terms, therefore, the prediction of the bead-spring model for the birefringence in extensional flows is

$$\Delta n^* = \frac{1}{b^*}\sum_{i=1}^{N_{\mathrm{S}}}\langle Q^{*2}_{i,\,xx}\rangle - \langle Q^{*2}_{i,\,yy}\rangle . \tag{6.8}$$

In the absence of EV interactions, the expression for polymer stress given in Eq. (2.78) can be combined with with the definition of the dimensionless polymer contribution to the first normal stress difference in extensional flows in Eq. (2.89), to obtain

$$N^*_{1,\mathrm{p}} = H^*\sum_{i=1}^{N_{\mathrm{S}}}\langle \xi_i Q^{*2}_{i,\,xx}\rangle - \langle \xi_i Q^{*2}_{i,\,yy}\rangle . \tag{6.9}$$

Comparing Eqs. (6.8) and (6.9) it is clear that when the influence of FE is negligible,

$$\Delta n^* \approx \frac{1}{H^* b^*} N^*_{1,\mathrm{p}} . \tag{6.10}$$

The equation above is an expression of the well known stress-optic law, which permits the extraction of rheological information by a measurement of the optical properties of the polymer solution. However, the equations above also show that the stress-optic law is not valid at extension-rates (and high shear-rates) when polymer chains can be stretched significantly. Therefore, one would anticipate that a plot of $N^*_{1,\mathrm{p}}$

against Δn^* would in the very least be nonlinear in unsteady extensional flows, when $\dot{\varepsilon}^* > \dot{\varepsilon}^*_{\rm c}$. However, the observation of completely different curves for the stress-growth and relaxation phases by Spiegelberg and McKinley [1996] was at first unexpected.

The mean polarizability of a sub-molecule is uniquely related to its end-to-end vector. However, the spring force corresponding a given end-to-end vector is also unique. How, then, can one explain the observation that the stress-birefringence curves are not unique? Using BD simulations of FENE dumbbells, Lielens *et al.* [1998] showed that the explanation lies in the very different distributions of the end-to-end distance observed in extension and relaxation. In essence, two distributions for the end-to-end vector that have the same second moment $\langle\, \boldsymbol{QQ} \,\rangle$ can have completely different expectations of the dyadic product $\boldsymbol{QF}^{\rm s,\,c}$ occurring in the Kramer's expression for the polymer stress. Further, it is also essential that the spring force be nonlinear in order for the difference in the paths taken by the distributions (in function space) to be reflected in plots of stress against birefringence. Thus, the phenomenon of stress-birefringence hysteresis is a manifestation of the influence of FE, and consequently cannot be predicted with models using Hookean springs.

Although the study of this hysteretic phenomenon is interesting in its own right, the interest in this Section is to examine the extent to which closure approximations for bead-spring models capture this aspect of the results obtained with the exact model. Figure 6.55 compares the $N^*_{1,{\rm p}}$-versus-Δn^* behaviour predicted by BD simulations of free-draining FENE chains and the FD-P and FD-PG approximations. Also shown for reference is the prediction of the Rouse model. It is clear that both the approximations fail to reproduce the size of the hysteresis loop observed in the simulations. Besides predicting a smaller hysteresis loop, the FD-P model also predicts a larger birefringence than the exact simulations at any level of the stress. On the other hand, with fluctuations accounted for in the spring forces, the size of the hysteresis loop becomes even smaller with the FENE-PG approximation. Nevertheless, the curve predicted with the FD-PG lies within the loop predicted by the BD simulations.

While measurements of the intrinsic birefringence give an idea of the extent to which polymeric segments are oriented by the flow, to obtain a fuller description of

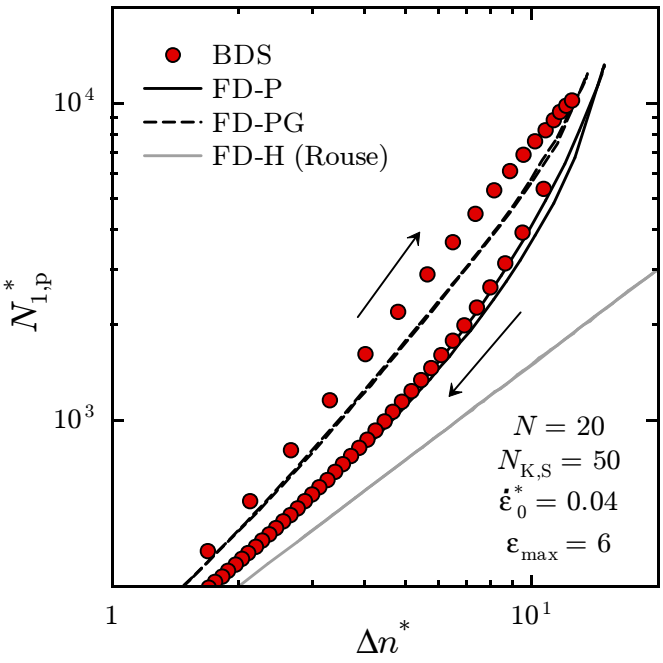

Figure 6.55: Stress-birefringence hysteresis for free-draining FEBS chains.

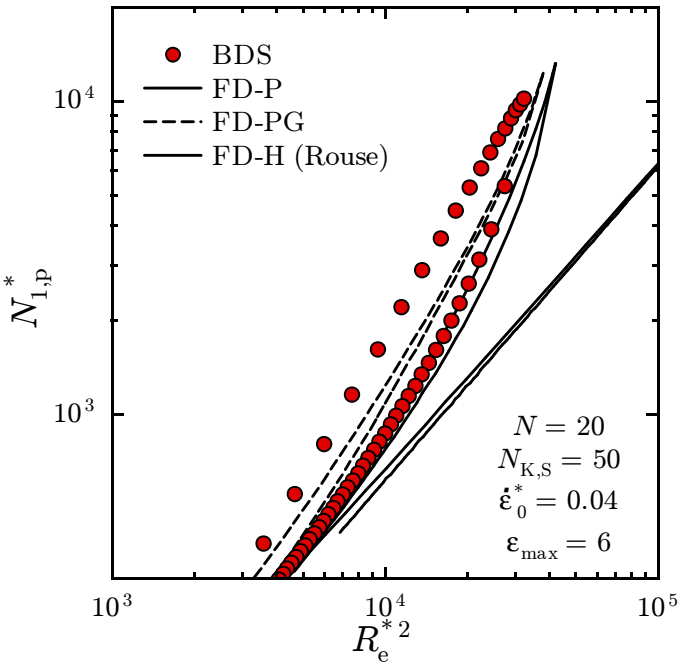

Figure 6.56: Stress-configuration hysteresis for free-draining FEBS chains.

the average chain configurations, it is necessary to complement birefringence data with estimates of the average dimensions of polymer chains in flow. Bossart and Öttinger [1995] have pointed out that birefringence and light scattering experiments measure fundamentally different aspects of polymer conformations. Ghosh *et al.* [2001] found that plotting the stress predicted in BD simulations of free-draining bead-rod chains and FENE dumbbells against their mean-squared end-to-end distance also resulted in a pronounced hysteresis loop. These authors distinguished stress-birefringence from the $N^*_{1,\mathrm{p}}$–$R^{*\,2}_{\mathrm{e}}$ hysteresis, and referred to the later as "stress-configuration" hysteresis, arguing that the latter is the result of differences in the physical shapes observed in the bead-rod simulations during extension and relaxation (such as "yo-yo's" and "stem-flowers", respectively).

Predictions for the $N^*_{1,\mathrm{p}}$-$R^{*\,2}_{\mathrm{e}}$ hysteresis obtained with the different free-draining models is shown in Fig. 6.56. The key difference between this Figure and Fig. 6.55 is the prediction of slightly different curves for extension and relaxation even by the Rouse model. In this case, the hysteresis is a simply a consequence of the different evolutions of the second moments of the Gaussian distribution during the stress-growth and relaxation phases. While the closeness of the final expressions for the stress and birefringence shows that the spring force nonlinearity is essential to observe stress-birefringence hysteresis, $N^*_{1,\mathrm{p}}$-$R^{*\,2}_{\mathrm{e}}$ hysteresis is the result of the differences in the evolution of the configurational probability distribution under different conditions. The incorporation of FE amplifies the distributional hysteresis, resulting in larger differences between the upper and lower curves. The relative behaviour of the exact and approximate models in Fig. 6.56 is quite similar to that observed in Fig. 6.55, showing that the both the approximations for the FENE nonlinearity are deficient in accurately describing stress-distribution hysteresis.

The prediction of distribution hysteresis in extension and relaxation even for simple Rouse chains in Fig. 6.56 suggests that it may be possible to observe similar behaviour when HI is included in Rouse chains. This is confirmed in Fig. 6.57, which shows the $N^*_{1,\mathrm{p}}$-versus-$R^{*\,2}_{\mathrm{e}}$ behaviour predicted by the BD simulations and different approximations for HI in Rouse chains. While Fig. 6.57 reproduces the close agreement with the BD simulations observed earlier in Figs. 6.48 and 6.49 of the curves predicted by the CA-H and GA-H approximations, and their diagonalized

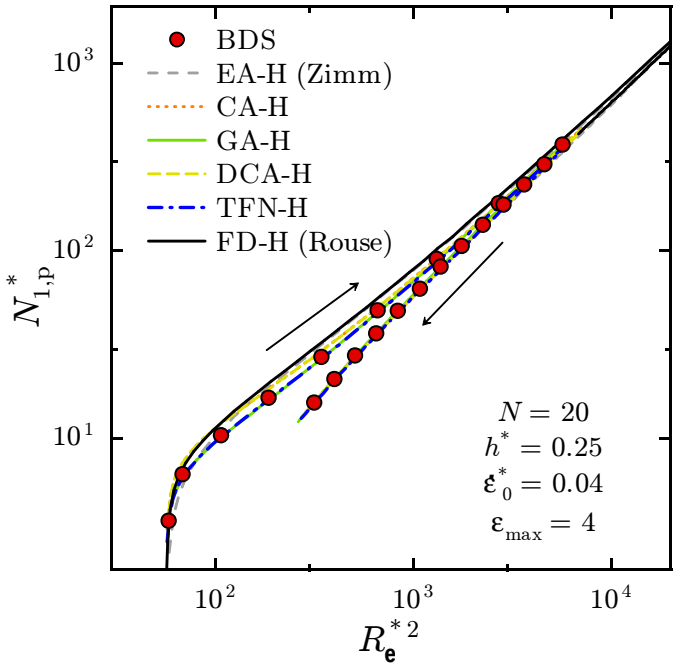

Figure 6.57: Stress-configuration hysteresis for Rouse chains with and without HI.

versions, the collapse of the $N_{1,p}^*$-versus-R_e^{*2} curves predicted by the Zimm and the Rouse models on the same data is quite unexpected, since the time evolution of these properties with equilibrium-averaged HI is observed to be considerably different from the other models. In Figs. 6.48 and 6.49, the time evolutions of $N_{1,p}^*$ and R_e^{*2} predicted by all the models are nearly exponential, during both extension and relaxation. Similar behaviour is predicted with the free-draining Rouse model in Fig. 6.56. Since $N_{1,p}^* \sim e^{Ct}$ and $R_e^{*2} \sim e^{Dt}$, double-logarithmic plots of $N_{1,p}^*$ against R_e^{*2} are straight lines with slopes of C/D. Therefore, it appears that the $N_{1,p}^*$-R_e^{*2} hysteresis in extension and subsequent relaxation is not very sensitive to whether or not HI is included in the model. The same conclusion is reached when the predictions of the models combining HI and FE for $N_{1,p}^*$-Δn^* and $N_{1,p}^*$-R_e^{*2} hysteresis are juxtaposed in Figs. 6.59 and 6.58 with the predictions of the free-draining models. The reason behind this insensitivity to HI is not understood.

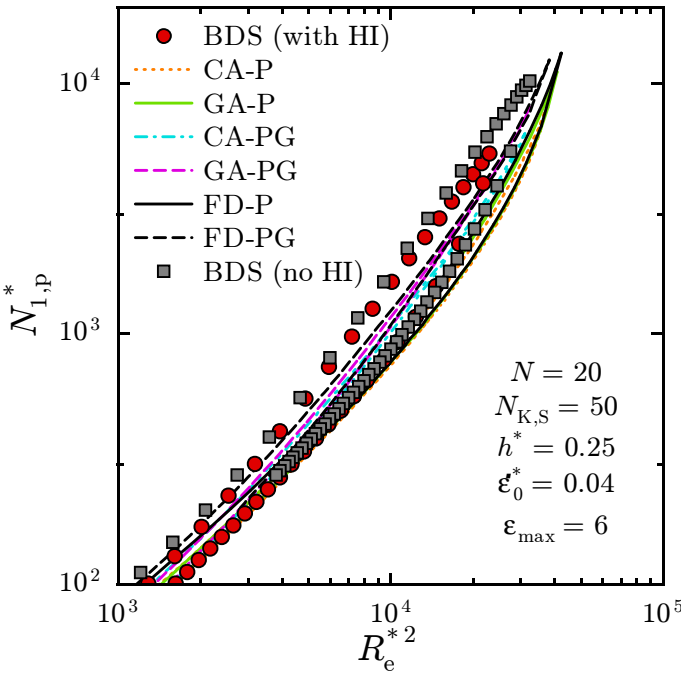

Figure 6.58: Stress-birefringence hysteresis for FEBS chains with and without HI.

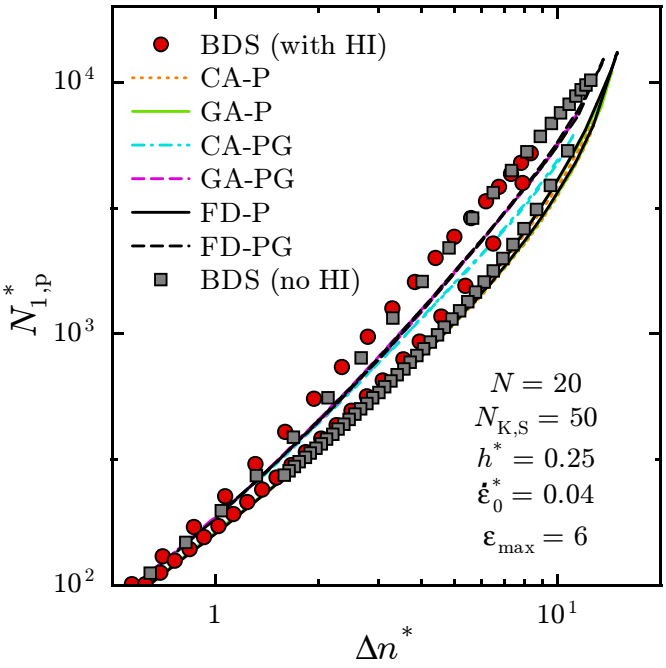

Figure 6.59: Stress-configuration hysteresis for FEBS chains with and without HI.

6.5.2 Coil-stretch hysteresis

In the discussion earlier in Section 6.3, it was shown that the mean-field approximations combining HI and FE predict multiple steady-states in the extensional viscosity over a range of extension-rates below the critical strain rate $\dot{\varepsilon}^*$. As mentioned there, De Gennes [1974] first obtained such multiple steady-states using a mean-field approximations in a simple dumbbell model. Later, Fan *et al.* [1978] solved the equations for the same dumbbell model numerically without using any approximations and found that single-valued predictions for the steady-state properties were obtained when plotted against the extensional strain rate. They argued that De Gennes' prediction of a coil-stretch hysteresis must therefore be an artifice of the mean-field approximations used in his model. The results of Fan *et al.* then prompts the question: are mean-field closure approximations then fundamentally flawed? An answer to this question is attempted in this Section. To this end, it is useful to revisit De Gennes' original dumbbell model.

De Gennes pointed out that one of the consequences of the existence of HI is that the effective drag coefficient of predominantly coiled molecules close to equilibrium is significantly different in value from predominantly stretched molecules in strong extensional flows. It is possible to calculate an effective drag coefficient of an average molecule in a steady extensional flow from the polymer contribution to the steady-state extensional viscosity as

$$\zeta \equiv \frac{\overline{\eta}_{\mathrm{p}}}{n_{\mathrm{p}} R_{\mathrm{e}}^2} \,. \tag{6.11}$$

Near equilibrium, polymer molecules are in a coil like state, and the mean drag coefficient ζ_{coil} can be calculated from the zero-strain-rate extensional viscosity which, as will shown in Chapter 8, is well described by an expression of the following form for large values of N_{K}:

$$\overline{\eta}_{\mathrm{p},\,0} = 3\eta_{\mathrm{p},0} = 3U_{\eta,\,0}^{\infty} n_{\mathrm{p}} \eta_{\mathrm{s}} R_{\mathrm{e,\,eq}}^3 \,, \tag{6.12}$$

where $U_{\eta,\,0}^{\infty}$ is a universal constant with a value of around 0.4. Substituting this

result in the definition of ζ in Eq. (6.11) above, one obtains

$$\zeta_{\text{coil}} = 3U^{\infty}_{\eta,\,0}\eta_{\text{s}}b_{\text{K}}\sqrt{N_{\text{K}}}\,, \tag{6.13}$$

On the other hand, the asymptotic value of extensional viscosity of a solution of fully stretched chains can be calculated as [Doi and Edwards, 1986; also see Appendix B]

$$\overline{\eta}_{\text{p}} = \frac{\pi}{6}n_{\text{p}}\eta_{\text{s}}b^3_{\text{K}}\frac{N^3_{\text{K}}}{\ln(N_{\text{K}}/2)}. \tag{6.14}$$

Since for fully stretched chains, $R^2_{\text{e}} = L^2 = b^2_{\text{K}}N^2_{\text{K}}$, the effective drag coefficient is

$$\zeta_{\text{stretch}} = \frac{\pi}{6}\eta_{\text{s}}b_{\text{K}}\frac{N_{\text{K}}}{\ln(N_{\text{K}}/2)}. \tag{6.15}$$

Therefore, the average drag coefficient of a long polymer molecule changes from $\zeta_{\text{coil}} \sim \sqrt{N_{\text{K}}}$ to $\zeta_{\text{stretch}} \sim N_{\text{K}}/\ln(N_{\text{K}})$ as the extension-rate is increased past the critical strain rate $\dot{\varepsilon}^*_{\text{c}}$.

For large values of N_{K}, this change can be considerable, and is essentially the result of the weakening of HI as the molecule stretches out. It is possible to construct a simple dumbbell toy model in which the effect of configuration dependent HI is represented by a variable drag coefficient that is a function of the dumbbell's end-to-end distance, Q, changing from ζ_{coil} when $Q = 0$, to ζ_{stretch} when $Q = Q_0 = L$. Using a FENE force law to describe the resistance of the molecule to stretching, one obtains the Fokker-Planck equation for the configurational probability distribution of the toy dumbbell,

$$\frac{\partial\psi}{\partial t} = -\frac{\partial}{\partial\boldsymbol{Q}}\cdot\left[\left\{\boldsymbol{Q}\cdot\boldsymbol{\kappa} - 2H\frac{\xi(Q)}{\zeta(Q)}\boldsymbol{Q}\right\}\psi - \frac{2k_{\text{B}}T}{\zeta(Q)}\frac{\partial\psi}{\partial\boldsymbol{Q}}\right], \tag{6.16}$$

where $\xi(Q)$ is the usual FENE nonlinearity. As mentioned above, the variable drag coefficient $\zeta(Q)$ represents the configuration dependence of HI in a more realistic chain model. The goal of this section is to understand the effect that the replacing the fluctuating nonlinearities ξ and ζ in the toy model above with mean-field quantities, $\overline{\xi}(\langle Q^2\rangle)$ and $\overline{\zeta}(\langle Q^2\rangle)$. Such replacements are analogous to the more complex mean-field approximations described in the previous and in this Chapter.

The original *ad hoc* mean-field form of the drag coefficient used by De Gennes was

$$\frac{1}{\overline{\overline{\zeta}}} = \frac{1}{N_{\mathrm{K}}\zeta_{\mathrm{stretch}}}\left(1 + \frac{\sqrt{N_{\mathrm{K}}}\,\zeta_{\mathrm{stretch}}/\zeta_{\mathrm{coil}}}{q}\right), \tag{6.17}$$

where $q = \sqrt{\langle Q^2\rangle}/Q_0 = \sqrt{\langle Q^2\rangle}/L$. Although a fluctuating version of the mean-field expression may be postulated by replacing $\sqrt{\langle Q^2\rangle}$ with $|Q|$, the expression becomes singular when $Q = 0$. Schroeder *et al.* [2004] recently used BD simulations of FEBS chains with HI to calculate the mean drag coefficient from the force required in a steady extensional flow to keep a chain's ends apart at a fixed fraction of the fully extended length. The ζ calculated in this manner is found to depend linearly on the fractional extension. The linear dependence of the drag coefficient observed by Schroeder *et al.* can be expressed as

$$\zeta = \zeta_{\mathrm{coil}}\left(1 + \alpha\frac{|Q|}{L}\right), \tag{6.18}$$

where $\alpha = \zeta_{\mathrm{stretch}}/\zeta_{\mathrm{coil}} - 1$. Although the equations above for ζ_{stretch} and ζ_{coil} mean that strictly $\zeta_{\mathrm{stretch}}/\zeta_{\mathrm{coil}} = (\pi/\,18U^{\infty}_{\eta,0})(\sqrt{N_{\mathrm{K}}}/\ln(N_{\mathrm{K}}/2))$, in keeping with the qualitative nature of the analysis in this section, order unity numerical constants are ignored, and $\alpha = \sqrt{N_{\mathrm{K}}}/\ln(N_{\mathrm{K}}/2) - 1$ is used. It is also found that assuming a quadratic dependence,

$$\zeta = \zeta_{\mathrm{coil}}\left(1 + \alpha\frac{Q^2}{L^2}\right), \tag{6.19}$$

leads to a simplification of the algebra involved, but does not change the qualitative features of the results.

As a result of the functions ξ and ζ, the equation above–which is identical in form to that studied by Fan *et al.* [1978]–is nonlinear in $\boldsymbol{Q}$, but is linear in the probability density ψ. Fan *et al.* pointed out that, given a flow field, the solution to such linear partial differential equations for ψ is always unique, irrespective of the nature of the coefficient functions. Therefore, in steady flows, the steady-state expectations with respect to ψ must be single-valued functions of the velocity gradient. Using the linear expression for the drag coefficient, Fan *et al.* substantiated this argument

by numerically solving the partial differential equation for ψ for steady extensional flows.

To explore the qualitative features of the predictions of this dumbbell model in strong extensional flows, it is further simplified by considering its one-dimensional equivalent, for which one obtains

$$\frac{\partial \psi}{\partial t} = -\frac{\partial}{\partial Q}\left[\left\{\dot{\varepsilon}\, Q - 2H\frac{\xi}{\zeta}\, Q\right\}\psi - \frac{2k_{\mathrm{B}}T}{\zeta}\frac{\partial \psi}{\partial Q}\right], \tag{6.20}$$

where $\dot{\varepsilon}$ is the strain rate of the one-dimensional extensional flow. At equilibrium, the model predicts

$$R^2_{\mathrm{e,\,eq}} = \frac{L^2}{\dfrac{L^2 H}{k_{\mathrm{B}}T} + 5}\,. \tag{6.21}$$

The spring constant H is chosen such that the $R^2_{\mathrm{e,\,eq}}$ predicted above matches the well known result for a one-dimensional random walk, $R^2_{\mathrm{e,\,eq}} = b^2_{\mathrm{K}} N_{\mathrm{K}}$. Thus, one obtains $HR^2_{\mathrm{e,\,eq}}/(k_{\mathrm{B}}T) = 1 - 5/N_{\mathrm{K}}$. Using $R_{\mathrm{e,\,eq}}$ as the characteristic length, and $\zeta_{\mathrm{coil}} R^2_{\mathrm{e,\,eq}}/4k_{\mathrm{B}}T$ as the characteristic time to convert to dimensionless form leads, at steady-state to

$$0 = -\frac{d}{dQ^*}\left[\left\{Wi - \frac{1}{2}\frac{\xi^*}{\zeta^*}\right\} Q^*\psi - \frac{1}{2\zeta^*}\frac{d\psi}{dQ^*}\right],$$

from which, one obtains for $Q^* \in [-\sqrt{N_{\mathrm{K}}}, \sqrt{N_{\mathrm{K}}}]$,

$$\frac{d\ln\psi}{dQ^*} - 2\left(Wi - \frac{1}{2}\frac{\xi^*}{\zeta^*}\right) Q^*\zeta^* = 0\,. \tag{6.22}$$

Here, the Weissenberg number $Wi = \dot{\varepsilon}\zeta_{\mathrm{coil}} R^2_{\mathrm{e,\,eq}}/4k_{\mathrm{B}}T$, $\xi^* = H^*\xi = (1 - 5/N_{\mathrm{K}})/(1 - Q^{*2}/N_{\mathrm{K}})$, and $\zeta^* = \zeta/\zeta_{\mathrm{coil}}$. The solution of the equation above for the steady-state distribution is

$$\psi(Q^*) = \frac{1}{J}\exp\left[-\int_0^{Q^*}\left\{\xi^*(s) - 2Wi\,\zeta^*(s)\right\} s\, ds\right], \tag{6.23}$$

where,

$$J = 2\int_0^{\sqrt{N_K}} \exp\left[-\int_0^{Q^*} \{\xi^*(s) - 2\,Wi\,\zeta^*(s)\}\,s\,ds\right] dQ^*\,, \tag{6.24}$$

is the normalization constant. An identical result has been obtained by Schroeder *et al.* [2004].

The argument above was in fact first used by De Gennes [1974] in his discussion of the reasons behind coil-stretch hysteresis. Although De Gennes did not use any specific expression for ζ during the course of the discussion, he pointed out that

$$\mathcal{F}(Q^*) = \int_0^{Q^*} \{\xi^*(s) - 2Wi\zeta^*(s)\}\,s\,ds\,, \tag{6.25}$$

could be regarded as an effective non-equilibrium free energy, whose maxima and minima in the domain of Q^* correspond to the locations of valleys and the peaks in the probability distribution. The locations of the maxima and minima in the probability distribution are obtained by equating $d\ln\psi/dQ^*$ to zero. From Eq. (6.22) above, these occur at $Q^* = 0$, and

$$\frac{1}{2}\frac{\xi^*}{\zeta^*} - Wi = 0\,. \tag{6.26}$$

At this juncture, it is worthwhile to digress briefly to consider the implication of the simple result derived above for more general bead-spring chain models. For any model in which the chain configuration can be represented as a d-dimensional vector $\mathbf{R}$, the steady-state Fokker-Planck equation is of the form

$$\mathbf{0} = -\boldsymbol{\nabla}\cdot\mathbf{J}\,, \tag{6.27}$$

where $\boldsymbol{\nabla} = \partial/\partial\mathbf{R}$ is the gradient operator in d-dimensional configuration space, and $\mathbf{J}$ is the probability current. For models with fluctuating HI, $\mathbf{J}$ takes the form

$$\mathbf{J} = -\mathbf{D}\cdot\boldsymbol{\nabla}\psi + \mathbf{A}\psi\,, \tag{6.28}$$

where $\mathbf{D}(\mathbf{R})$ is the fluctuating diffusion super-matrix, and $\mathbf{A}$ is the advection or drift

term. For homogeneous potential flows, the steady-state solution to the Fokker-Planck equation is obtained by setting the probability current $\mathbf{J} = \mathbf{0}$ [De Gennes, 1974; Risken, 1989]. Since $\mathbf{D}$ is always positive-definite, the solution must satisfy

$$\boldsymbol{\nabla} \ln \psi = \mathbf{F} \,, \tag{6.29}$$

where $\mathbf{D} \cdot \mathbf{F} = \mathbf{A}$. The locations of the maxima and minima in ψ, which are calculated by simultaneously requiring $\boldsymbol{\nabla}\psi = \mathbf{0}$, are then seen to be the zeros of $\mathbf{F}$, or equivalently the solutions of

$$\mathbf{D} \cdot \mathbf{F} = \mathbf{A} = \mathbf{0} \,. \tag{6.30}$$

Returning to Eq. (6.26) for the magnitude Q^*, which is the one-dimensional equivalent of Eq. (6.30) above, it can be recognized that the zeros of the drift term are controlled by the parameter Wi. The equation also suggests that the location of the maxima and minima of $\psi(Q^*)$ can be graphically obtained as the points of intersection of a plot of the ratio $\rho = \xi^*/\zeta^*$ as a function of Q^*, and horizontal lines located at a height of Wi above the $\rho = 0$ line.

Figure 6.60 plots the function $\rho(Q^*)$ for the quadratic drag given by Eq. (6.19), for $N_{\mathrm{K}} = 5000$. The non-monotonic nature of the curve is the result of the combination of the monotonic decrease in $1/\zeta^*$ and monotonic increase ξ^*, respectively. The curve obtained with the Eq. (6.18) has a similar shape (not shown). The shape of the ρ-versus-Q^* in Fig. 6.60 has three important consequences.

1. There exists a critical Weissenberg above which there exists only one point of intersection of any horizontal with the curve for ρ, for all $Q^* > 0$. This critical value will be referred to as the "upper" critical Weissenberg number, and denoted as Wi_{uc}. Figure 6.60 shows that the value of Wi_{uc} in the present toy model is determined by the line that is tangential to the ρ curve at $Q^* = 0$. Hence,

$$Wi_{\mathrm{uc}} = \rho(Q^* = 0) = \frac{1}{2}\left(1 - \frac{5}{N_{\mathrm{K}}}\right) . \tag{6.31}$$

2. There is a second critical Weissenberg number below which no intersection of

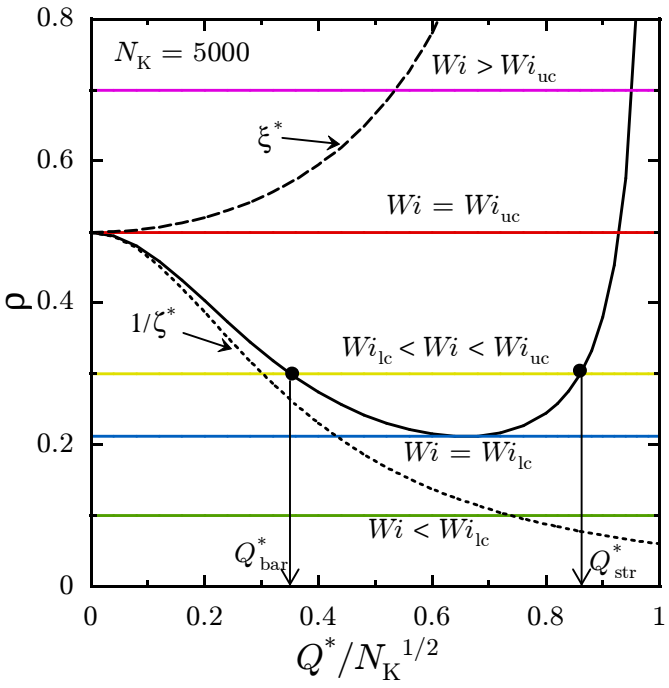

Figure 6.60: Graphical location of maxima and minima in the effective non-equilibrium free-energy for a one-dimensional finitely-extensible dumbbell with configuration-dependent drag.

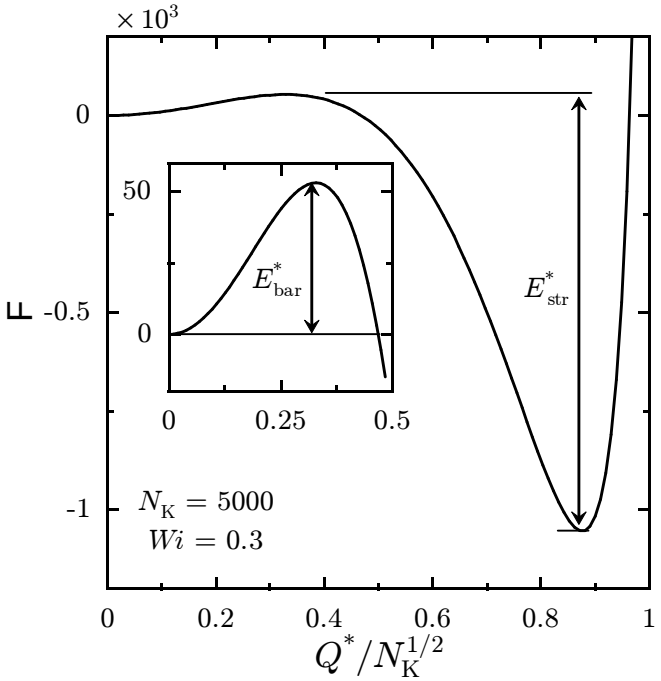

Figure 6.61: Variation in the effective non-equilibrium free-energy with the end-to-end distance of a one-dimensional finitely-extensible dumbbell with configuration-dependent drag.

any horizontal line with ρ exists. It will be shown later that, for the expressions for the drag coefficient considered here, the roots of Eq. (6.26) are imaginary for all values of Wi below this "lower" critical Weissenberg number $Wi_{\rm lc}$. For a quadratically varying drag coefficient,

$$Wi_{\rm lc} = \frac{1}{2}\left(1 - \frac{5}{N_{\rm K}}\right)\left(\frac{4\alpha}{4\alpha + (\alpha - 1)^2}\right) . \tag{6.32}$$

3. For all $Wi_{\rm lc} < Wi < Wi_{\rm uc}$, there exist two values of Q^* for which intersection is obtained. For reasons that will be made clear shortly, the value of Q^* at the intersection of the decreasing portion of ρ is denoted as $Q^*_{\rm bar}$, while $Q^*_{\rm str}$ denotes the value of the intersection on the steeply increasing part of ρ.

It can be shown that at $Q^* = Q^*_{\rm str}$, which is close to the fully stretched condition $Q^*/\sqrt{N_{\rm K}} = 1$, $d^2 \ln \psi / dQ^{*\,2} < 0$ for any positive functions ξ and ζ. This point therefore corresponds to a maximum in the probability, and a valley in the free energy curve. At $Q^* = Q^*_{\rm bar}$, $d^2 \ln \psi / dQ^{*\,2} > 0$, and a peak occurs at this value of Q^* in $\mathcal{F}$. These features are illustrated in Fig. 6.61, which shows the variation in the effective free-energy $\mathcal{F}$ with Q^*. It is seen that $E^*_{\rm bar}$, the height of the free-energy maximum above the datum at $Q^* = 0$, is much larger than unity. Since the free-energy has been made dimensionless by $k_{\rm B}T$, the large peak in $\mathcal{F}$ at $Q^*_{\rm bar}$ means that Brownian thermal fluctuations have little chance of causing any dumbbell with $Q^* < Q^*_{\rm bar}$ to "hop" over to the deep valley at $Q^*_{\rm str}$. In other words, $E^*_{\rm bar}$ quantifies the kinetic barrier to a random switch from the coiled ($Q^* \approx 1$) to a stretched ($Q^* \leq \sqrt{N_{\rm K}}$) state. The subscript "bar" denotes quantities associated with this free-energy barrier. In spite of the rather deep free-energy valley at $Q^* = 0$, the valley at $Q^* = Q^*_{\rm str}$ is even deeper, for the Wi and $N_{\rm K}$ values considered in Fig. 6.61. A highly stretched dumbbell trapped in this energy valley has an even larger mountain to climb before it can switch to the coiled state. The subscript "str" thus signifies the stable stretched state.

Figure 6.62 shows how the magnitudes of $E^*_{\rm bar}$ and $E^*_{\rm str}$ vary with Wi. For $Wi < Wi_{\rm lc}$, there is no local minimum in $\mathcal{F}$ close to the fully stretched state. However, $E^*_{\rm str}$ grows rapidly beyond $Wi_{\rm lc}$, and overtakes the decreasing curve for $E^*_{\rm bar}$ at a value of Wi which is designated as $Wi_{\rm c}$. For $N_{\rm K} = 5000$, $Wi_{\rm c} \approx 0.22$ in the dumbbell

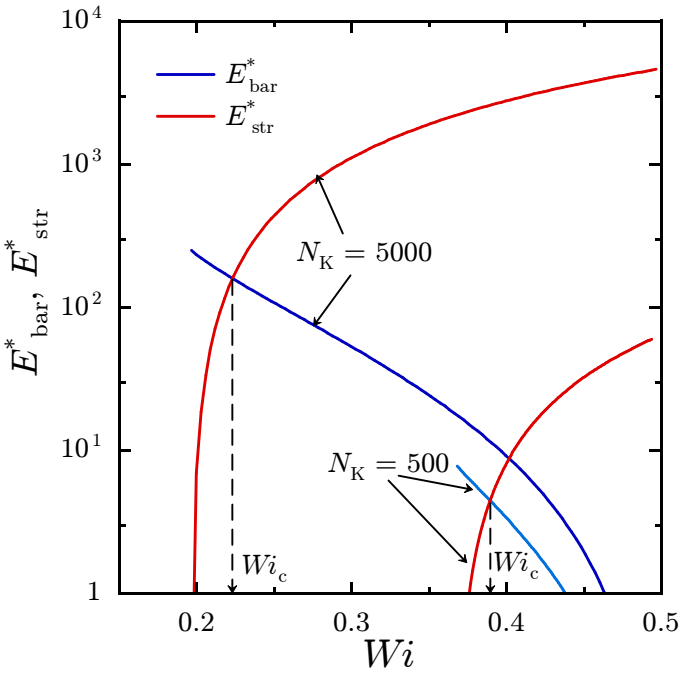

Figure 6.62: Variation of the free-energy barriers to coil-to-stretch, and stretch-to-coil transitions, with Weissenberg number. The vertical arrows indicate the value of $Wi = Wi_{\rm c}$ at which $E^*_{\rm bar} = E^*_{\rm str}$.

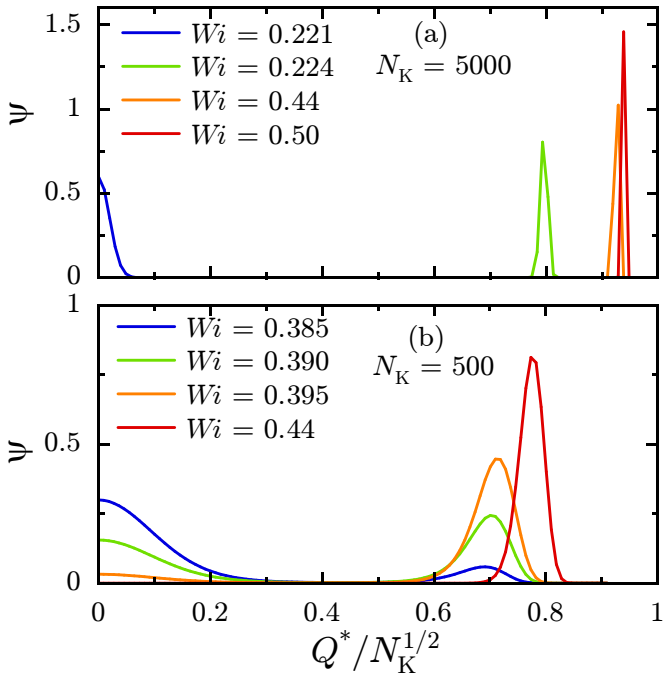

Figure 6.63: Probability distribution for the magnitude of the end-to-end distance of a one-dimensional dumbbell with variable drag coefficient.

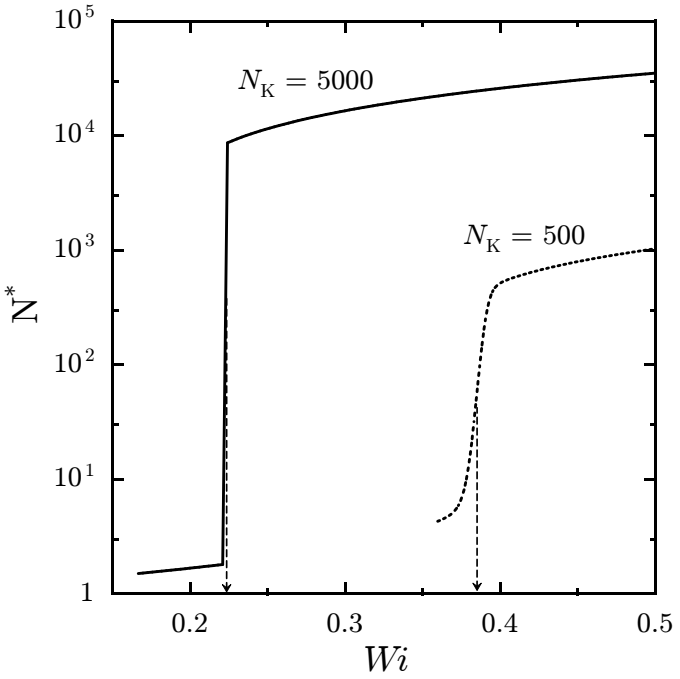

Figure 6.64: Variation of the stress in a one-dimensional dumbbell model with variable drag coefficient. The stress is calculated with the exact probability distribution for the end-to-end distance. The vertical arrows indicate the location of Wi_c.

model with quadratic drag. Figure 6.63 (a) plots the exact probability distribution for the magnitude of Q^* for different values of Wi around Wi_c, for $N_K = 5000$. It is seen the overall probability distribution of dumbbells changes character from being coil-dominated to stretch dominated within a narrow range of Wi values. The shape of the free energy curve in this range of Wi values does indicate that there must be two peaks in the probability distributions, one at $Q^* = 0$ and another at $Q^* = Q^*_{str}$, separated by a minimum at $Q^* = Q^*_{bar}$. However, the ratio of the height of the peak at Q^*_{str} to the one at $Q^* = 0$ is given by $p = \exp[-(E^*_{str} - E^*_{bar})]$. The magnitudes of E^*_{str} and E^*_{bar} are so large that p goes from being extremely small for a Wi slightly below Wi_c to extremely large when Wi is only marginally larger than Wi_c. In Fig. 6.63 (a), for instance, p changes from e^{-24} to e^{10}, as Wi goes from 0.221 to 0.224. Macroscopic properties, such as the dimensional stress $N^* = \langle \xi^* Q^{*2} \rangle$, calculated using this exact probability distribution are single valued functions of Wi, but show a dramatic change around Wi_c.

While the use of the full probability distribution to calculate macroscopic properties is formally correct, and can be achieved once the steady-state ψ is completely known, this situation is not practically realizable, both in experiments and in simulations of models more sophisticated than the dumbbell model used here. The presence of the massive kinetic barriers such as E^*_{bar} and E^*_{str} means that chains cannot ergodically explore the entire configuration space consistent with the true steady-state probability distribution. In other words, imposition of an extensional flow with $Wi_{\mathrm{lc}} < Wi < Wi_{\mathrm{uc}}$ on dilute solutions of large polymer molecules leads to, borrowing terminology from the theory of spin-glasses [Bouchad, 1992], "ergodicity breaking". Under these conditions, the finally measured "steady-states" are in fact not true steady-states, but represent kinetically trapped states. Further, these states depend strongly on the initial conditions used in the experiment or simulation. If the flow is imposed on a solution initially at equilibrium, the molecules are trapped in the coiled state by the presence of the barrier E^*_{bar}. On the other hand, if an experiment is performed wherein molecules are initially stretched at a flow whose $Wi > Wi_{\mathrm{uc}}$, and then the strain rate is reduced to a value in the range $[Wi_{\mathrm{lc}}, Wi_{\mathrm{uc}}]$, the stretched molecules are trapped in the well at Q^*_{str}. Such behaviour has recently been confirmed in both experiments with DNA molecules and simulations of FEBS chains with HI by Shaqfeh and co-workers [Schroeder *et al.*, 2003, 2004]. As suggested by De Gennes [1974], an estimate of the time scale for a random dumbbell to hop from the coil state over the barrier at Q^*_{bar} is $t^*_{\mathrm{C}\to\mathrm{S}} = (1/Wi_{\mathrm{c}}) \exp(E^*_{\mathrm{bar}})$. In terms of the Hencky strain, this simple estimate is $\varepsilon_{\mathrm{C}\to\mathrm{S}} = t^*_{\mathrm{C}\to\mathrm{S}} Wi_{\mathrm{c}} = \exp(E^*_{\mathrm{bar}})$. For the example used in Fig. 6.63 (a), the value of the $\varepsilon_{\mathrm{C}\to\mathrm{S}}$ is e^{165} at $Wi = 0.221$. Similarly, at the same Wi, at which no sizeable peak in the probability distribution is present close to the stretched state in Fig. 6.63 (a), the likely Hencky strain required to see a stretch-to-coil transition is $\varepsilon_{\mathrm{S}\to\mathrm{C}} = \exp(E^*_{\mathrm{str}}) = e^{140}$.

For smaller values of N_{K}, however, the situation is less drastic. As shown in Fig. 6.62, the sizes of the kinetic barriers are significantly reduced for $N_{\mathrm{K}} = 500$, and the bi-modality of the probability distribution predicted by the dumbbell model for this choice of N_{K} is clearly visible in Fig. 6.63 (b). Furthermore, the relative size of the range of Wi values in which such bi-modality is observed is also smaller. From

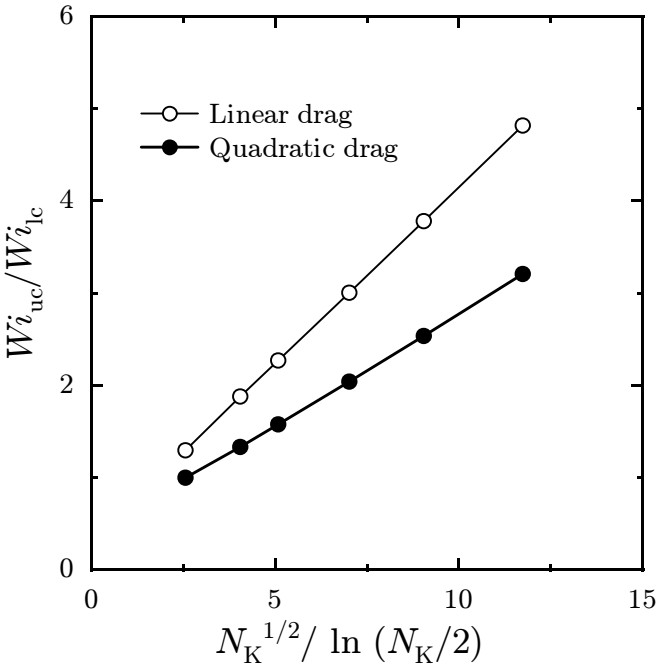

Figure 6.65: Variation of the ratio $Wi_{\rm uc}/Wi_{\rm lc}$ with respect to the ratio of drag coefficient in the fully-stretched state to that in the coiled state.

Eqs. (6.32) and (6.31), it is seen that using Eq. (6.19) for ζ leads to

$$\frac{Wi_{\rm uc}}{Wi_{\rm lc}} = 1 + \frac{(\alpha-1)^2}{4\alpha}\,. \tag{6.33}$$

For large values of $N_{\rm K}$, $\alpha >> 1$, and the ratio above grows linearly with respect to α. This is also observed in Fig. 6.65 for the case where a linear expression is used for ζ.

Summarizing the discussion so far, it appears from the results of the toy dumbbell model that although the steady-state probability distribution of a model with fluctuating nonlinearities due to HI and FENE is unique, the very same nonlinearities may lead to the emergence of deep local minima in the non-equilibrium free-energy landscape. The large kinetic barriers to ergodicity surrounding the local free-energy minima can lead to the emergence of long lived states which may, for all practical purposes, be interpreted as steady-states. These multiple quasi-steady-states arise even without the use of any mean-field approximations. With this picture in mind, it is now possible to introduce mean-field approximations to study their effect on

the qualitative features of the predictions.

Replacing Q^{*2} in the expression for ζ n Eq. (6.19) with $\langle Q^{*2}\rangle$,

$$\overline{\zeta}^{*} = \left(1 + \alpha \frac{\langle Q^{*2}\rangle}{N_{\mathrm{K}}}\right). \tag{6.34}$$

This replacement is equivalent in spirit to the consistent-averaging and Gaussian approximations for bead-spring chains with HI. The advantage of the simple one-dimensional toy model is that it is possible to use this approximation along with the un-approximated FENE force law. With this partial approximation, the steady-state probability distribution becomes

$$\begin{aligned}\psi(Q^{*}) &= \frac{1}{J}\exp\left[-\int_{0}^{Q^{*}} \xi^{*}(s)s\,ds + 2Wi\,\overline{\zeta}^{*}\,Q^{*2}\right], \\ &= \frac{J_{\mathrm{eq}}}{J}\psi_{\mathrm{eq}}\exp\left(2Wi\,\overline{\zeta}^{*}\,Q^{*2}\right),\end{aligned} \tag{6.35}$$

where ψ_{eq} is the equilibrium distribution with a FENE dumbbell, and J_{eq} is the corresponding normalization constant. In this case, calculation of the probability distribution requires a consistent estimation of its second moment, since $\overline{\zeta}$ on the right-hand side of the equation above depends on $\langle Q^{*2}\rangle$. The numerical evaluation of ψ in the equation above was preformed iteratively for any given value of Wi, by first starting with a guess of $\langle Q^{*2}\rangle$, followed by the calculation of the function $\psi(Q^{*})$ using the equation above, and then calculating the value of $\langle Q^{*2}\rangle$ which is used for the next iteration. The converged value of $\langle Q^{*2}\rangle$ was used as the starting guess for the next higher value of Wi. Calculations were repeated at every Wi starting with a large value of $\langle Q^{*2}\rangle \approx N_{\mathrm{K}}$ as an initial guess. For a range of Wi values, it was observed that the iterations performed with the two different initial guesses for $\langle Q^{*2}\rangle$ converged to different distribution functions $\psi(Q^{*})$.

As in the case of the original dumbbell model, the location of the maxima in the probability distribution are determined as solutions to the equation

$$\frac{1}{2}\frac{\xi^{*}}{\overline{\zeta}^{*}} - Wi = 0. \tag{6.36}$$

Since $\overline{\zeta}^{*}$ is a constant in the equation, the plot of $\rho = \xi^{*}/\overline{\zeta}^{*}$ against Q^{*} is the same as

that for the FENE nonlinearity ξ^*, but multiplied by a constant. This immediately implies that the probability distribution can have only one peak. If the horizontal line controlled by Wi (the Wi-line) lies completely below the monotonically increasing curve for ρ, the probability distribution is peaked at $Q^* = 0$. Otherwise, the ρ curve can intersect the Wi-line at a single value of Q^*, at which a single peak in ψ appears.

At low values of Wi, $\overline{\zeta}^* \approx 1$, and the horizontal Wi-line lies below the ρ-versus-Q^* curve. The distribution in this case resembles the equilibrium distribution, with a peak at $Q^* = 0$. As the value of Wi increases, a stage is reached when for a given value of Wi, as mentioned above, *two* different values of $\langle Q^{*2} \rangle$ are observed to be consistent with Eq. (6.35). Figure 6.66 shows a typical ρ-versus-Q^* plot for this situation. In the plot, for a single horizontal Wi-line, there are two ρ-versus-Q^* curves. The blue curve, obtained with the lower coil-like value of $\langle Q^{*2} \rangle$, lies completely above the Wi-line. The red curve corresponds to the ρ curve calculated with the larger value of $\langle Q^{*2} \rangle$, and intersects the Wi-line at a large value of Q^*. The two different steady-state probability distributions corresponding to the example in Fig. 6.66 are shown in Fig. 6.67.

The introduction of a mean-field approximation, by removing one of the two nonlinearities in the model, destroys the multi-modal nature of the original probability distribution. However, the approximation also results in making the Fokker-Planck equation nonlinear in ψ. While the original Fokker-Planck equation could have only one solution, the exchange in nonlinearities allows the modified Fokker-Planck equation to have multiple solutions. As Fig. 6.68 plotting the variation of $\langle Q^{*2} \rangle$ with Wi shows, the existence of two stable steady-states is remarkably restricted only to nearly the same range of Wi values in which multi-modal distributions were obtained for the "exact" dumbbell model. Above and below this range of Wi values, predictions of properties are single-valued functions of the strain rate.

If, instead of the drag coefficient, the mean-field approximation is made on the FENE nonlinearity, by replacing ξ with the FENE-P function $\overline{\xi}$, the original model once again loses its multi-modal character, but also loses stability in the bargain. It can be shown that in this model, dumbbells extend infinitely without limit beyond a certain Wi. A more interesting case is the model with both ξ and ζ replaced with

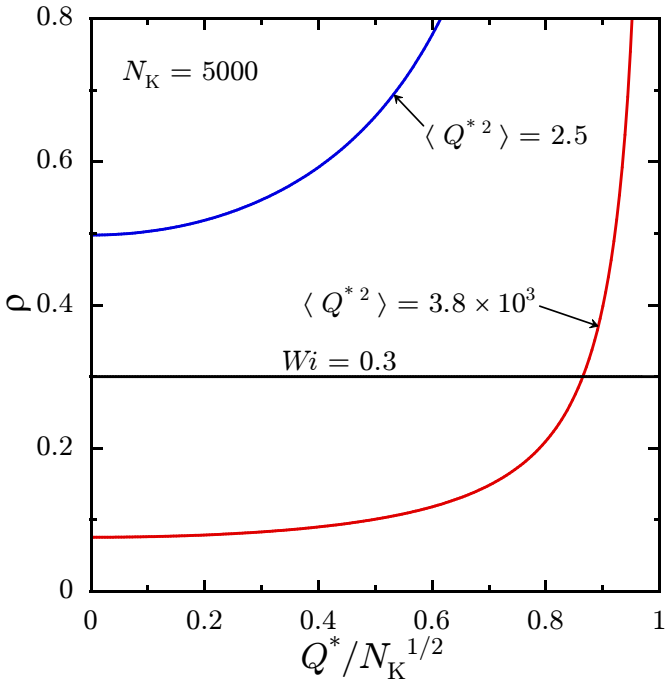

Figure 6.66: Variation of the ratio of the FENE nonlinearity to the mean-field drag coefficient with the end-to-end distance in a one-dimensional FENE dumbbell model with mean-field drag.

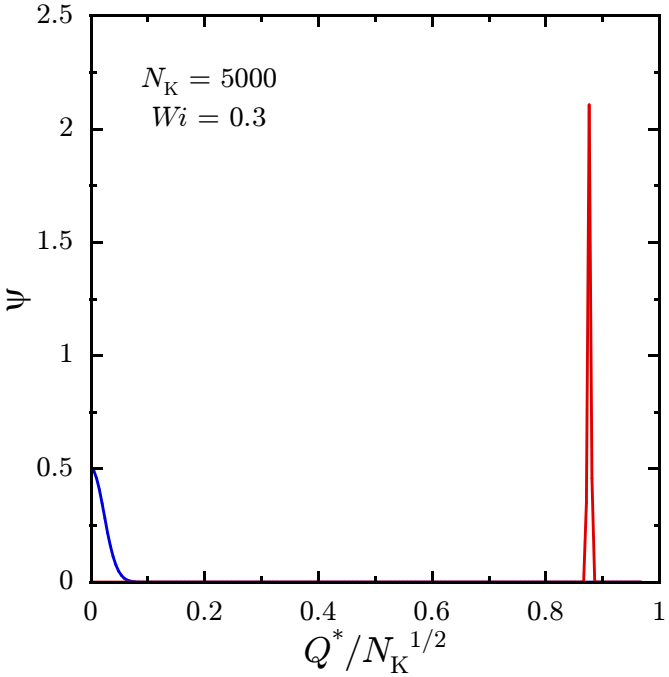

Figure 6.67: Multiple steady-state uni-modal probability distributions predicted with a one-dimensional FENE dumbbell model with a mean-field drag coefficient.

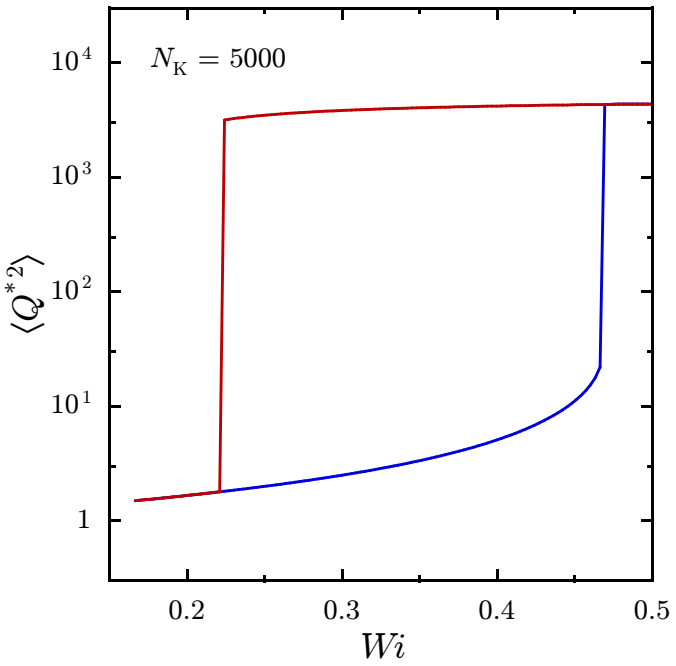

Figure 6.68: Multiple steady-states in the steady-state mean-squared end-to-end distance predicted with a one-dimensional FENE dumbbell model with a mean-field drag coefficient.

their mean-field equivalents, which leads to an approximate model similar to the one used by De Gennes [1974] to obtain his numerical results with multiple steady-states. In this case, the distribution function is a Gaussian, whose steady-state variance $\sigma = \langle Q^{*2} \rangle$ is the solution to the following equation:

$$0 = 2Wi\,\sigma - \frac{\overline{\xi}^*(\sigma)}{\overline{\zeta}^*(\sigma)}\sigma + \frac{1}{\overline{\zeta}^*(\sigma)}. \tag{6.37}$$

With the approximation in Eq. (6.34) for $\overline{\zeta}^*$, the equation above is a cubic in σ. The roots of this equation display an interesting bifurcation behaviour with respect to Wi that is shown in Fig. 6.69, in which the ratio of the magnitude of the roots $|\boldsymbol{\sigma}|$ to N_K is plotted against Wi.

At low values of Wi, one of the roots is positive, and the other two are complex conjugate roots. The positive root has a value close to unity, and is the prediction for the coiled state. The magnitude of the conjugate roots, on the other hand,

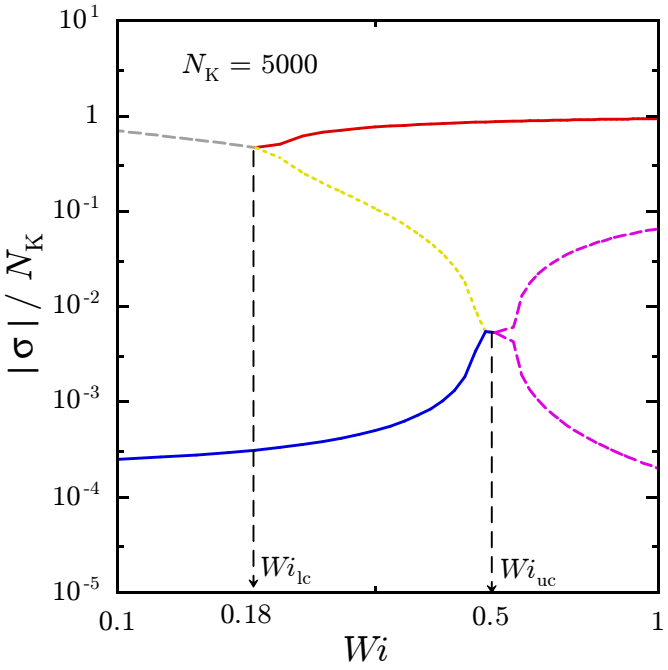

Figure 6.69: Bifurcation diagram for the roots of the equation for the steady-state variance of the Gaussian probability distribution in a one-dimensional FENE-P dumbbell model with a mean-field drag coefficient. The gray dashed line represents the absolute value of two complex, conjugate roots. The solid blue and red curves represent predictions for the coiled and stretched states, while the dashed yellow curve is an intermediate state. The dashed purple curves are the absolute values of two negative roots. The vertical arrows point to the location of $Wi_{\rm lc}$ and $Wi_{\rm uc}$.

is large and much closer to the fully stretched state value of $\sigma/N_{\rm K} = 1$. As the value of Wi is increased, the value of the coiled state's positive root increases slowly. The magnitude of the complex conjugate roots decreases until at a critical value of $Wi = 0.18$, the complex conjugate roots change character and split into two positive real roots. It is noted that the value of Wi at which this bifurcation occurs is close to the original $Wi_{\rm lc} = 0.196$. One of these new positive roots is a large value for $\langle Q^{*2} \rangle$, close to the fully stretched state value of $N_{\rm K}$, whereas the other is intermediate in value between the new large root and the original positive coiled-state root, which is still relatively much smaller than either of the new positive roots. As Wi is increased further, the stretched state root edges closer in value to $N_{\rm K}$, but the intermediate root decreases rapidly. The existence of these physically meaningful multiple steady-states continues until at $Wi = 0.5$, the intermediate and the coiled state roots merge.

Beyond this critical value, which is again very near in value to the original Wi_{uc}, the two merged roots change character, and become negative. Therefore, for all $Wi > 0.5$, only the stretched state positive root is physically valid as the variance of a Gaussian distribution.

The results above indicate that, although the uni-modal character of the probability distributions predicted with mean-field closure approximations are fundamentally different from the multi-modal distribution obtained with the original model, the predictions of multiple steady-states obtained with the approximations appear to closely follow the long-lived kinetically trapped states in the original model. Therefore, closure approximations for FEBS chains with HI may prove to be useful in a detailed exploration of hysteretic phenomena caused by ergodicity-breaking in dilute polymer solutions.

Chapter 7

Theory vs. experiment at the theta state: A brief review

Thus far in this thesis, the emphasis has been on understanding how FE modifies the influence of HI and EV on the rheological properties of dilute polymer solutions. The purpose of the present Chapter is to set the stage for the comparison of the predictions of models with HI and FE with experimental data on extensional flows under theta conditions, that will be carried out in the next Chapter.

As mentioned earlier, predictions obtained with bead-spring models with EV and HI are in good agreement with experiments near equilibrium, where the influence of FE is negligible. The first part of this Chapter describes the paradigm within which the theory for solutions of long polymer molecules is compared with experiments near equilibrium.

Before proceeding further, it is useful to define the following ratios for shear flows:

$$U_\eta \equiv \frac{[\eta]M}{N_{\rm A}R^3_{\rm e,eq}} = \frac{\eta_{\rm p}}{n_{\rm p}\eta_{\rm s}R^3_{\rm e,eq}}\,. \tag{7.1}$$

For extensional flows, the ratio $U_{\overline{\eta}}$ is equivalently defined in terms of the intrinsic extensional viscosity, $[\overline{\eta}]$, or the extensional viscosity $\overline{\eta}_{\rm p}$. Since for a dilute solution $\eta_{\rm p} = [\eta]c\eta_{\rm s} = [\eta]n_{\rm p}M\eta_{\rm s}/N_{\rm A}$, and $R^2_{\rm e,eq} = 3\,\ell^2_{\rm s}N_{\rm s}$, using $\eta^*_{\rm p} = \eta_{\rm p}/(n_{\rm p}k_{\rm B}T\lambda_{\rm s})$, and

$\lambda_{\rm S} = \zeta\,\ell_{\rm S}^2/4k_{\rm B}T = (3\pi^{3/2}/2)h^*(\eta_{\rm s}\,\ell_{\rm S}^3/k_{\rm B}T)$, one also obtains

$$U_\eta = \frac{\pi^{3/2}}{\sqrt{12}}\frac{h^*\eta_{\rm p}^*}{N_{\rm S}^{3/2}}\,. \tag{7.2}$$

Equation (7.1) defines U_η in terms of experimentally accessible quantities, while Eq. (7.2) expresses the same ratio in terms of dimensionless quantities that are more commonly encountered in literature on modeling of dilute polymer solutions. In what follows, experimental observations of this ratio are distinguished from its theoretical estimates by denoting the former as $U_\eta^{\rm ex}$. In the limit of vanishingly small shear-rates, $[\eta] = [\eta]_0$, the zero-shear-rate intrinsic viscosity, and the ratio U_η calculated using $[\eta]_0$ is denoted as $U_{\eta,\,0}$, which is related to the Flory constant, Φ, through $\Phi = U_{\eta,\,0}/N_{\rm A}$. In the absence of EV interactions, $6R_{\rm G,\,eq}^2 = R_{\rm e,\,eq}^2$ for large chains, and the ratio U_η defined above is related to the ratio

$$U_{\eta\,{\rm R}} = \frac{\eta}{n_{\rm p}(4\pi/3)R_{\rm G,\,eq}^3}\,, \tag{7.3}$$

(also denoted as $U_{\eta/\,S}$) defined by Öttinger and others [Kröger *et al.*, 2000; Öttinger, 1989b; Öttinger and Rabin, 1989; Prakash and Öttinger, 1999; Sunthar and Prakash, 2005] as $U_\eta = (8\pi/6^{5/2})\,U_{\eta\,{\rm R}}$.

Confirmation of the importance of the phenomenon of HI comes from the excellent comparison of theoretical predictions with rheological measurements in the linear viscoelastic regime. In experiments, the most well-studied polymers are perhaps polystyrene, poly(α-methylstyrene), polyisobutylene, 1,4-polybutadiene, and 1,4-polyisoprene [Fetters *et al.*, 1994]. In experiments with solutions of these polymers at the theta state, it is observed that $U_{\eta,\,0}^{\rm ex}$, is nearly independent of the polymer-solvent combination or the molecular weight of the polymer. Miyaki *et al.* [1980] report this constant to be 0.42 ± 0.02. From the definition of $U_{\eta,\,0}$, the observed constancy of this ratio implies that at the theta state $[\eta]_0 \sim M^{1/2}$, since $R_{\rm e,eq}^2 \sim M$ at the theta temperature.

As discussed earlier in Chapter 5, the theoretical treatment of HI which is currently prevalent in bead-rod and bead-spring models of dilute polymer solutions has its origins in the seminal papers by Kirkwood and Riseman [1948] and Zimm

[1956]. While Kirkwood and Riseman introduced equilibrium-averaged HI in the context of a bead-rod model, Zimm incorporated equilibrium-averaged HI between the beads of Rouse chains. Instead of calculating the $\eta^*_{\mathrm{p},\,0}$ individually for different small values of N_{S}, both Kirkwood and Riseman, and Zimm, looked for asymptotic behaviour in the limit of large N_{K} and N_{S}, respectively. For large values of N_{K} and N_{S}, summations over bead indices occurring in the governing equations for models with equilibrium-averaged HI are replaced by integrals, and the resulting integro-differential equations are solved numerically [Yamakawa, 1971; Zimm *et al.*, 1956]. Since the replacement of summations by integrals is exact only in the limit of N_{S} (or N_{K}) $\to \infty$, the results for ratios such U_η obtained with the procedure outlined above are interpreted as the asymptotic limits obtained as N_{S} (or N_{K}) $\to \infty$. The infinite chain prediction for U_η is denoted as U^∞_η.

In the infinite chain limit, it is observed that the dimensionless integro-differential equations governing the Zimm model in the infinite chain limit are parameterized by a single parameter $h \equiv h^*\sqrt{N_{\mathrm{S}}}$, which Zimm called the "draining" parameter. That is, predictions for U^∞_η can be obtained by simultaneously taking the limits $N_{\mathrm{S}} \to \infty$ and $h^* \to 0$, while keeping $h = h^*\sqrt{N_{\mathrm{S}}}$ constant. Thus, the ratio $U^\infty_{\eta,\,0}$ is obtained as a function solely of h.

Since h^* is a dimensionless hydrodynamic radius of a sub-molecule represented by a single spring, keeping h^* constant and taking the $N_{\mathrm{S}} \to \infty$ limit, while keeping ℓ_{S} constant is equivalent to keeping the size of a sub-molecule constant and increasing the number of sub-molecules, or equivalently, the molecular weight of the polymer chain, indefinitely. In this limit, the draining parameter $h = h^*\sqrt{N_{\mathrm{S}}} \to \infty$, and it has been shown [Auer and Gardner, 1955; Öttinger, 1987a] with the Zimm model that

$$\lim_{h\to\infty} U^\infty_{\eta,\,0}(h) \;=\; \lim_{\substack{N_{\mathrm{S}}\to\infty \\ h^* \text{ constant}}} U_{\eta,\,0} = \frac{\sqrt{3}\pi^2}{24[\Gamma(\frac{3}{4})]^2} = 0.47433103\,. \tag{7.4}$$

Zimm also showed that in the "free-draining" limit, as $h \to 0$, the scalings of properties with respect to N_{S} are the same as obtained with the Rouse model without HI. For free draining chains, $\eta^*_{\mathrm{p},\,0} \sim N_{\mathrm{S}}^2$. From Eq. (7.2), $U_\eta \sim h^* N_{\mathrm{S}}^2/N_{\mathrm{S}}^{3/2} \sim h$ for free-draining chains, which shows that as $h \to 0$, $U^\infty_{\eta,\,0}(h) \to 0$.

The Zimm model's prediction of $U^{\infty}_{\eta,0}(\infty)$ shown in Eq. (7.4) above is observed to be reasonably close to the experimentally observed $U^{\rm ex}_{\eta,0} = 0.42 \pm 0.02$. Further, the results of the Zimm model imply that, as $N_{\rm s}$ becomes very large while h^* is constant, $\eta^*_{{\rm p},0} \sim N_{\rm s}^{3/2}$ [Eq. (7.2)]. Associating $N_{\rm s}$ with the molecular weight, the Zimm model thus correctly predicts $[\eta]_0 \sim M^{1/2}$.

There is, however, an important difference between experimental measurements and the theoretical predictions. Experimental data are obtained with large, but *finite* molecules, but the measured $U^{\rm ex}_{\eta,0}$ show a remarkable constancy with molecular weight. On the other hand, as will be shown shortly, $U_{\eta,0}$ is not in general constant with respect to $N_{\rm s}$ for all values of h^*. The prediction of $[\eta]_0 \sim M^{1/2}$ in the Zimm model is strictly valid only in the asymptotic limit of infinitely long chains.

Following Zimm's work, results have also been obtained for equilibrium-averaged HI by keeping h fixed, and letting $h^* \to 0$ and $N_{\rm s} \to \infty$ simultaneously [Yamakawa, 1971]. In this "partial-draining" regime the limiting values of ratios such as $U_{\eta,0}$ are functions of h, which are observed to crossover smoothly from the free- to the non-draining limit as h increases from 0: for instance, $U^{\infty}_{\eta,0}(h)$ increases monotonically from 0 to 0.47. This limiting behaviour is also obtained with more refined treatments of HI than the Zimm model, including those using renormalization-group methods [Douglas and Freed, 1984; Freed *et al.*, 1988]. However, as mentioned before, since no significant (within experimental errors) change is observed in experiments in $U^{\rm ex}_{\eta,0}$ with increasing molecular weight which corresponds to increasing $h = h^*\sqrt{N_{\rm s}}$, experiments seem to be at variance with theory, leading Fujita [1988] to conclude that "no unquestionable theoretical evaluation of the hydrodynamic factors is as yet achieved".

As first pointed by Osaki [1972], this is perhaps explained by making the distinction between results (theoretical or experimental) for *finite* chains, and those obtained in the theoretical limit of infinite chains. Figure 7.1 plots the predictions of the Zimm model for $U_{\eta,0}$ for finite bead-spring chains against $1/\sqrt{N_{\rm s}}$. This choice is made because application of the Euler-Maclaurin formula [Osaki, 1972] shows that the leading corrections to the approximation of summations by integrals scales as $1/\sqrt{N_{\rm s}}$ in the Zimm model and that for finite values of $N_{\rm s}$, and for any given value

of h^*, the predictions of $U_{\eta,\,0}$ vary with $N_{\rm s}$ as

$$U_{\eta,\,0}(h^*, N_{\rm s}) = U^{\infty}_{\eta,\,0}(h=\infty) + c_{\eta,0}\left(\frac{1}{h^*_{\rm f}} - \frac{1}{h^*}\right)\frac{1}{\sqrt{N_{\rm s}}} + O(\frac{1}{N_{\rm s}})\,, \qquad (7.5)$$

where $c_{\eta,0}$ and $h^*_{\rm f}$ are constants. Henceforth, $U^{\infty}_{\eta,\,0}$ will be used to denote the non-draining limit $U^{\infty}_{\eta,\,0}(\infty)$. Wherever necessary, the partial draining limit $U^{\infty}_{\eta,\,0}(h)$ will be indicated explicitly. While the values of $U^{\infty}_{\eta,\,0}$, $c_{\eta,0}$ and $h^*_{\rm f}$ are model dependent, the nature of the approach of corrections in $U_{\eta,\,0}$ due to finite size effects is the same for all models with HI for the theta state [Kröger *et al.*, 2000; Öttinger, 1987a; Sunthar and Prakash, 2005].

In principle, the "fixed point" $h^*_{\rm f}$ is a unique constant fixed by the choice of the model, and identical for all ratios such as U_η (for which the infinite chain limits exist). In the Zimm model, $h^*_{\rm f}$ is analytically determined to be $6\sqrt{2}/35 = 0.2424...$ [Osaki, 1972]. However, when polynomials are fitted through the predictions for several finite chains, and for different values of h^*, it is found that different properties can have slightly different values of $h^*_{\rm f}$. For $U_{\eta,\,0}$, $h^*_{\rm f} = 0.256$ [Öttinger, 1987a]. As stated above, the value of $h^*_{\rm f}$ is also sensitive to the model used. It is observed, for instance, for FENE chains with equilibrium-averaged HI, the fixed point depends on the parameter $b^* = 3N_{\rm K,\,s}$ [Sunthar and Prakash, 2005]. This behaviour is also observed for a bead-rod model with HI, in which case the number of Kuhn segments $N_{\rm K}$, the HI parameter for a single Kuhn segment $h^*_{\rm K}$ and $h^*_{\rm K,\,f}$ (Appendix D) take the place of $N_{\rm s}$, h^* and $h^*_{\rm f}$ in Eq. (7.5) respectively. In Appendix D, it is shown that for a bead-rod model with equilibrium-averaged HI the value of $h^*_{\rm f}$ estimated is 0.19, which is significantly different from 0.2424.

Equation (7.5), and Fig. 7.1 show that it is possible to predict the value of $U^{\infty}_{\eta,\,0}$ with moderately large but finite $N_{\rm s}$, provided h^* is chosen to be equal to the value of the "fixed point", $h^*_{\rm f}$. Furthermore, Eq. (7.5) can be rearranged to read

$$U_{\eta,\,0}(h^*, N_{\rm s}) = U^{\infty}_{\eta,\,0} - \frac{c_{\eta,0}}{h} + \frac{c_{\eta,0}}{h^*_{\rm f}\sqrt{N_{\rm s}}} + O(\frac{1}{N_{\rm s}})+\,, \qquad (7.6)$$

The equation above shows that for a finite value of $N_{\rm s}$, the overall deviation of $U_{\eta,\,0}$ from the non-draining limit $U^{\infty}_{\eta,\,0}$ is the net result of the effect of partial-draining (*i.e.* finite $h = h^*\sqrt{N_{\rm s}}$) and that due to the finite $N_{\rm s}$. At the special value of $h^* = h^*_{\rm f}$,

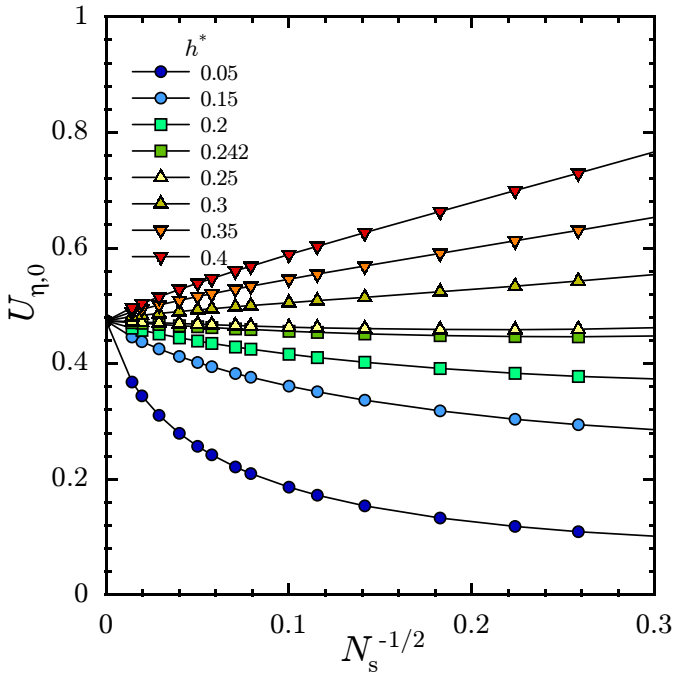

Figure 7.1: Predictions of U_η for finite chains obtained using the Zimm model, versus $1/\sqrt{N_\mathrm{s}}$, $15 \leq N_\mathrm{s} \leq 5000$, for various values of the HI parameter, h^*. The Zimm eigenvalues required for $U_{\eta,0}$ were calculated using standard routines from LAPACK. The value of the limit as $N_\mathrm{s} \to \infty$, $U^\infty_{\eta,0} = 0.47$ shown in the plot is taken from literature [Kröger *et al.*, 2000; Osaki, 1972; Yamakawa, 1971]. The smooth lines through the data points for finite N_s and the limit $U^\infty_{\eta,0}$ have been drawn to guide the eye.

the effect due to partial-draining is balanced (to order N_s^{-1}) by the correction due to finite size.

The existence of the fixed point can explain why experimental measurements of $U_{\eta,0}$ do not show any significant variation with increasing M. If it is accepted that a long but finite polymer molecule in a theta solvent is well described by a bead-rod chain with HI, then the constancy of $U^\mathrm{ex}_{\eta,0}$ suggests that the value of

$$h^*_\mathrm{K} \equiv \sqrt{\frac{3}{\pi}}\frac{a_\mathrm{K}}{b_\mathrm{K}}\,, \tag{2.66}$$

for the bead-rod representation is close to its fixed-point $h^*_{\mathrm{K,f}}$, whose value seems to be around 0.2. This could be so because in highly flexible polymers such as polyisobutylene or polystyrene in which such observations have been made, the true

hydrodynamic radius $a_{\rm K}$ of the Kuhn segment may of the same order of magnitude as $b_{\rm K}$. On the other hand, there may exist polymer molecules for which $h^*_{\rm K}$ is quite different from $h^*_{\rm K,\,f}$, and for such molecules $U^{\rm ex}_{\eta,\,0}$ may be measurably different from the value of 0.42 obtained with highly flexible molecules, even for fairly large molecular weights. Evidence of this behaviour may be obtained by careful measurements of dynamic properties in theta solutions near equilibrium for long ($N_{\rm K} \gg 1$), but stiff polymers. In stiff molecules, such as DNA, the length of a Kuhn segment $b_{\rm K}$ is much larger than the transverse dimensions of the molecule. In other words, each Kuhn segment can be pictured as a long thin rod of diameter d, whose translational drag coefficient is $\zeta_{\rm K} = 2\pi\eta_{\rm s}b_{\rm K}/\ln[b_{\rm K}/d]$ [Doi and Edwards, 1986]. Therefore, $a_{\rm K} = (1/3)b_{\rm K}/\ln(b_{\rm K}/d)$ and $h^*_{\rm K} = 1/[\sqrt{3\pi}\ln(b_{\rm K}/d)]$. For DNA, $d \approx 3$ nm and $b_{\rm K} \approx 130$ nm [Hsieh *et al.*, 2003; Larson *et al.*, 1999], using which one obtains $h^*_{\rm K} \approx 0.09$, which is much lower than $h^*_{\rm K,\,f} = 0.19$ estimated in Appendix D for the bead-rod model with equilibrium-averaged HI. If, on the other hand, it is observed that even with stiff molecules, no significant variation in $U^{\rm ex}_{\eta,\,0}$ occurs with respect to molecular weight, one may conclude that there exist other mechanisms even at the theta state which need to be taken into account while modeling.

Perhaps the most important feature of the asymptotic behaviour observed in Fig. 7.1 is that as chains become longer, the predictions of $U_{\eta,\,0}$ become insensitive to the choice made for h^*: in the limit of infinitely long chains, predictions of $U^{\infty}_{\eta,\,0}$ becomes *universal*, and independent of the parameter, h^*. In the years after the Zimm-model, insights gained from the study of critical phenomena and the development of renormalization-group (RG) methods have formed the basis for understanding such parameter-free universal behaviour. This insensitivity of the large-scale dynamics of long polymer chains to parameters that describe the local structure of the chain arises as the result of the union between the nearly self-similar (fractal) structure of very long chains, and the scale-invariance of the interactions such as HI and EV [De Gennes, 1979; des Cloizeaux and Jannink, 1990; Doi and Edwards, 1986; Schäfer, 1999].

For experiments, the significance of the emergence of universal behaviour in the theory is that, if correct, it implies that for molecules of sufficiently large $N_{\rm K}$, measurements of ratios such as $U_{\eta,\,0}$ must become insensitive to the chemical nature

of the polymer species. For example, if h^*_{K} for a stiff molecule such as DNA is 0.1, and $h^*_{\mathrm{K,f}}$ is 0.2, using the bead-rod equivalent of Eq. (7.5) for a molecule with $N_{\mathrm{K}} = 10^4$, assuming that $c_{\eta,0} \sim O(1)$, one calculates a deviation of about 10% from the infinite chain limit (taken to be 0.42). The data for more flexible molecules for the same value of N_{K} can be expected to lie within 10% of the infinite chain limit. Experimental error (due to errors in measurements of $[\eta]_0$ and $R_{\mathrm{e,eq}}$, control of temperature, and other solvent conditions, polydispersity in the sample, etc.) is typically of the same order. Thus, for very long molecules, ${U_{\eta,0}}^{\mathrm{ex}}$ becomes nearly universal, and independent of polymer-solvent chemistry.

Universal features of macroscopic observables are invaluable since they can serve as parameter-free tests of the validity of the phenomenology included in the models. For instance, Kröger *et al.* [2000] used Brownian dynamics simulations to compile exact results for $U_{\eta,0}$ (and other ratios) for a large range of N_{S} values and several values of h^*. Using the insight gained from the approach to universality shown in approximate models, they find that when $U_{\eta,0}$ is plotted against $1/\sqrt{N}$, the behaviour is similar to that observed in Fig. 7.1. Extrapolating the data for fixed h^* values on this plot gives the value of the non-draining limit $U^{\infty}_{\eta,0}$ predicted by the exact theory as 0.44 ± 0.02. In Chapter 5, it was observed that the Gaussian approximation predicts a lower value of the zero-shear-rate viscosity than the Zimm model. The results of Prakash and Öttinger [1997] show that $U^{\infty}_{\eta,0} = 0.3457 \pm 8 \times 10^{-4}$ for the Gaussian approximation. As mentioned in Chapter 5, the Gaussian approximation is exact to first order in the parameter h^*. An RG analysis based on refining results of a first order perturbation expansion in h^* yields $U^{\infty}_{\eta,0} = 0.3924 \pm 2 \times 10^{-4}$ [Öttinger and Rabin, 1989]. The agreement of the experimental value of 0.42 ± 0.02 with the theoretical values presented above strongly suggests that HI is the dominant physical mechanism governing the dynamics of theta-solutions near equilibrium.

In experiments, the establishment of the existence of a fixed point means that it is not necessary to study the behaviour of very long molecules for several polymer-solvent combinations to obtain measurements of the universal ratios. Measurements only need to made with a small set of highly flexible polymers. The same happy situation holds for simulations as well, and the universal results close to equilibrium

can be economically predicted for theta solutions using the results of finite ($N_\mathrm{s} \gtrsim 20$) bead-spring chains by choosing $h^* = h^*_\mathrm{f}$.

After the success of the theory with HI in describing the near-equilibrium dynamic behaviour of theta solutions, the question naturally arises whether this success can be replicated in the nonlinear regime, and if not, what other physical mechanisms need to be incorporated in models to achieve agreement with experiment. In recent years, the development of highly efficient simulation algorithms and the tremendous growth in computational resources have led to the emergence of BD simulations as an indispensable tool in the study of dilute polymer solutions. These simulations offer the possibility of directly comparing exact results of nonlinear models with experiment. Kumar and Prakash [2003] and Kröger *et al.* [2000] have successfully predicted experimentally observed static properties in good solvents and dynamic properties in theta solvents, respectively. Motivated by their remarkable success, it was decided to use BD simulations in this study to understand the role of HI away from equilibrium.

In steady shear flows, it is observed empirically in some studies [Kotaka *et al.*, 1966; Suzuki *et al.*, 1969] that data for different polymer-solvent combinations and molecular weights can be collapsed on to universal master curves when $\eta_\mathrm{p}/\eta_{\mathrm{p},0}$ is plotted against the shear Weissenberg number β. Early theoretical work [Fixman, 1966b; Peterlin, 1966a] also suggested that the ratio $\eta_\mathrm{p}/\eta_{\mathrm{p},0}$ for theta solutions is a universal function of β. This has been established more formally in the context of bead-spring models by Öttinger [1987b], who used the equations of the CA-P model (see Table 5.1) to analyze the predictions of FEBS chains with HI for *arbitrary* flows in the infinite chain limit. In particular, this analysis shows that for unsteady shear flows, as $h = h^*\sqrt{N_\mathrm{s}} \to \infty$, the ratio U_η defined in Eq. (7.2) approaches a limit U_η^∞, which is a universal function of the strain γ and a generalized Weissenberg number,

$$Wi_\circ \equiv \dot{\gamma}\,(\text{ or } \dot{\varepsilon}\,)\,\Lambda_\circ\,, \tag{7.7}$$

where the time constant,

$$\Lambda_\circ \equiv \frac{\eta_\mathrm{s} R^3_\mathrm{e,eq}}{k_\mathrm{B}T}\,. \tag{7.8}$$

In the infinite chain limit, it is further shown that the well known shear Weissenberg number $\beta = U^{\infty}_{\eta,0} Wi_{\circ}$. An important consequence of the existence of a well defined U^{∞}_{η} is that, for long chains, at *any* fixed Weissenberg number and strain, η^{*}_{p} or $\overline{\eta}^{*}_{\mathrm{p}}$ must asymptotically scale as $N_{\mathrm{s}}^{3/2}$ for chains with HI at the theta state.

Another significant outcome of this analysis is that the governing equations (in the approximate model considered by Öttinger) in the limit of infinite chains are identical for chains with Hookean or finitely-extensible springs. In the infinite chain limit, the it is shown that at a fixed Weissenberg number and strain, the FENE nonlinearity [Eq. (2.15)] $\xi \to 1$, as $N_{\mathrm{s}} \to \infty$ Furthermore, an RG analysis of the results of a perturbation expansion in the HI parameter h^{*} shows that the value of the fixed point remains unaffected by the flow [Zylka and Öttinger, 1991]. Therefore, universal predictions can be obtained by extrapolating the results of finite *Rouse* chains with $h^{*} = h^{*}_{\mathrm{f}}$, to the infinite chain limit, exactly as shown in Fig. 7.1. There is no need to use FEBS chains to obtain, for instance, $U^{\infty}_{\eta}(\gamma, \beta)$ in shear flows.

Using this procedure with the Gaussian approximation for HI, Prakash and Öttinger [1997] obtained at steady-state, the variation of the ratios $\eta_{\mathrm{p}}/\eta_{\mathrm{p},0}$, $\Psi_1/\Psi_{1,0}$ and Ψ_2/Ψ_1 with β in the infinite-chain limit, and showed that the extrapolated values obtained in this limit are independent of the choice of h^{*}. Their results show that the steady-state $U^{\infty}_{\eta}(\beta)$ has the following variation with respect to β. The ratio begins with a plateau at $U^{\infty}_{\eta,0}$ in the linear viscoelastic regime $\beta \ll 1$, and then decreases slightly (shear-thinning), attaining a minimum at $\beta = \beta_{\mathrm{min}} \approx 3$ before beginning to increase indefinitely as $\beta \to \infty$ (shear-thickening). These results are observed to differ significantly with the analytical results obtained by Zylka and Öttinger [1991] using RG methods, which do not show an initial shear-thinning, and a slower increase in U^{∞}_{η} with increasing β.

As shown in the previous section, it is perfectly valid to compare theoretical results for $U^{\infty}_{\eta,0}$ obtained in the infinite chain limit with experimental data obtained with dilute solutions of finite, but highly flexible molecules. Can a similar validation of the theory be achieved by comparing predictions for, say $U^{\infty}_{\eta}(\beta)$ in steady shear flows, with experimental measurements obtained with the same set of finite molecules?

Theoretical predictions of steady-state U^{∞}_{η} are functions solely of β, and by their

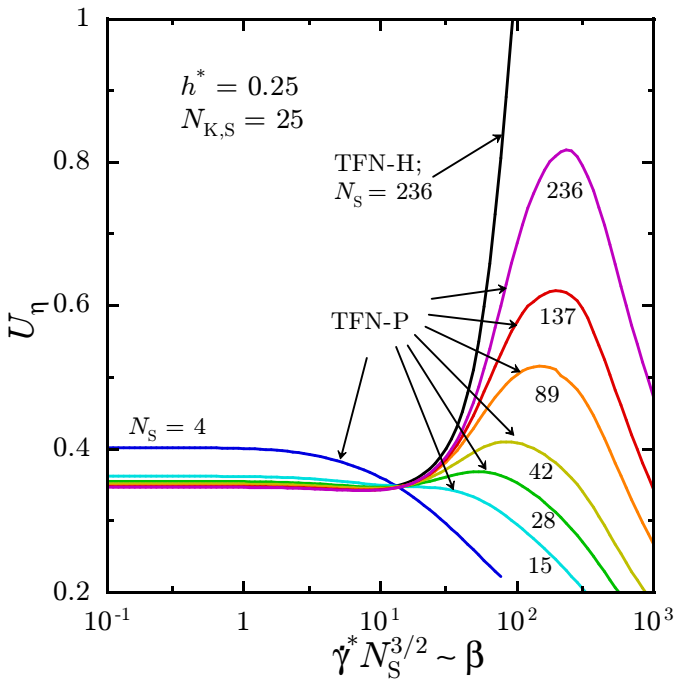

Figure 7.2: Effect of chain length on the onset of finite extensibility effects in steady shear flows.

very nature, have no additional parametric dependence on the chain length L or the molecular weight M. Noda *et al.* [1968], however, observed that when experimental data for $\eta_p/\eta_{p,0} = U_\eta^{ex}/U_{\eta,0}^{ex}$ are plotted against β, the curves obtained with different molecular weights are different. Moreover, the solutions are observed to be strongly shear-thinning, which, as observed in the previous Chapter, is a signature of the influence of finite chain extensibility.[1] As observed in Section 6.1 in the previous Chapter, FE leads to strong shear-thinning at high shear-rates, in contrast to the shear-thickening behaviour observed with Rouse chains. In Chapter 6, it was shown in Figs. 6.16 and 6.17 that the terminal shear-thinning regime due to FE effects sets in at a critical shear-rate $\dot{\gamma}_c^*$, which was shown to depend on the chain length,

[1]The data of Noda *et al.* [1968] where the molecular weight dependent shear-thinning is observed was obtained in good solvents. It is well known that excluded volume effects also cause strong shear-thinning [Fixman, 1966b; Kumar and Prakash, 2004; Prabhakar and Prakash, 2002; Prakash, 2002]. However, the onset (in terms of β) of shear-thinning is observed to be delayed with increasing molecular weight. This, as shown in Fig. 7.2, is characteristic of FE dominated shear-thinning. While excluded volume dominated shear-thinning becomes more prominent with increasing molecular weight (*i.e.* increasing $z \sim v\sqrt{M}$; Kumar and Prakash, 2004), the value of β at which the shear-thinning sets in does not depend strongly on M.

$N_K = N_{K,\,S} N_S$. The same qualitative behaviour is also observed in Fig. 7.2, which plots predictions of U_η obtained with the TFN-P model against $\dot{\gamma}^* N_S^{3/2}$ which is proportional to the shear Weissenberg number, β. Also shown is the prediction obtained with Hookean springs for a large value of $N_S = 236$, which can be regarded as a good estimate of the theoretical U_η^∞ curve.

It was shown earlier that the advantage of comparing experimental data with universal predictions is that it offers parameter-free validation of the physical phenomena postulated by the theory. The predictions shown in Fig. 7.2 suggest that, in order for experimental data to show a large enough shear-thickening portion so that the theory with HI can be validated at large values of Wi, N_K has to be of the order of 5000 or greater, since for $N_S \lesssim 200$, the influence of FE is strong enough to cause deviations from the U_η^∞ curve (represented by the prediction of the TFN-H model) in the nonlinear viscoelastic regime.

As mentioned above, the critical Weissenberg number β_c beyond which FE dominates in shear appears to increase with the chain length. The situation is more drastic in extensional flows, for which $Wi_c \approx 0.5$, beyond which predictions obtained with Rouse chains are clearly very different from those obtained with FEBS chains, as shown in the previous Chapter. It thus appears that theoretical predictions for universal behaviour obtained with Rouse chains cannot be directly compared with experimental data in strong shear and extensional flows. The validation of HI (and EV), and detailed analysis of their roles in determining the dynamic behaviour of polymer solutions in strong flows must therefore come in the presence of FE.

In this context, the observations of Gupta *et al.* [2000] are particularly interesting. These authors used a filament-stretching rheometer to measure the growth of the extensional viscosity after the imposition of a steady, homogeneous extensional flow on dilute solutions of high molecular weight polystyrenes (HMPS) in a mixed near-theta solvent consisting of dioctyl phthalate (DOP) and low molecular weight polystyrene (LMPS). It is found that the transient extensional viscosity of solutions of different molecular weights and concentrations can be collapsed onto (dimensional) master plots of the form $\overline{\eta}_p / cM = f(\varepsilon, Wi)$.

The central question is whether a model that accounts for the effects of HI and FE can adequately describe all the experimentally observed behaviour in strong shear

and extensional flows, such as the observations of Noda *et al.* [1968] and Gupta *et al.* [2000]? Further, is the behaviour of solutions of large polymer chains in such flows still insensitive to the local hydrodynamic details of the molecules, so that the establishment of the validity of these mechanisms be made in a parameter-free sense, as was possible near equilibrium? Answers to these questions are attempted in the next Chapter.

Chapter 8

Prediction of theta solution properties in using Successive Fine-Graining

Measurements in simple shear flows have been the mainstay of experimental rheology for a long time. Unfortunately, obtaining a clear resolution of the polymer's contribution to the total shear stress developed in these flows is difficult in dilute solutions, particulary with Boger-fluids made with high viscosity oligomeric solvents. This problem is further compounded by the fact that in the strong flow regime where finite size effects are dominant, the relative contribution of the dissolved polymers to the total shear stress becomes smaller with increasing shear-rate, due to shear-thinning. In strong elongational flows ($Wi > Wi_{\mathrm{c}}$), however, the polymer's contribution to the tensile stress can be larger than the solvent's contribution by several orders of magnitude, and can hence be clearly measured. In a remarkable breakthrough, the development of the filament-stretching rheometer [McKinley and Sridhar, 2002; Sridhar *et al.*, 1991; Tirtaatmadja and Sridhar, 1993] surmounted the technical hurdles that had earlier confounded the practical realization of homogeneous uniaxial extensional flows [Sridhar, 1990]. Using this device, Gupta *et al.* [2000] studied the transient growth of the elongational viscosity after the sudden imposition of uniaxial extensional flow on dilute solutions of high-molecular-weight

polystyrene in a mixed, near-theta solvent. Earlier, Orr and Sridhar [Orr and Sridhar, 1996, 1999] had studied stress relaxation following the cessation of uniaxial extensional flow in a filament stretching rheometer (FSR). The primary goal of this Chapter is compare predictions of BD simulations and closure approximations with experimental observations in extensional flows. The techniques used in this Chapter and some of the results obtained with BD simulations have been published [Prabhakar *et al.*, 2004].

At this stage it is necessary to consider an appropriate dimensionless representation of the experimental data for properties such as the viscosity. As pointed out in Chapter 2, the definition of the dimensionless viscosities $\eta_{\rm p}^*$ or $\overline{\eta}_{\rm p}^*$ involves the use of the model parameters h^* and $N_{\rm K,\,s}$, since

$$\eta_{\rm p}^* = \frac{\eta_{\rm p}}{n_{\rm p} k_{\rm B} T \lambda_{\rm s}} = \left(\frac{2}{3\pi^{3/2}}\right) \frac{\eta_{\rm p}}{n_{\rm p}\eta_{\rm s}\,\ell_{\rm s}^3 h^*} = \underline{\left[\frac{\sqrt{12}}{\pi^{3/2} h^* N_{\rm K,\,s}^{3/2}}\right] \frac{\eta_{\rm p}}{n_{\rm p}\eta_{\rm s} b_{\rm K}^3}}\,. \tag{8.1}$$

While examining the influence of the parameters h^* and $N_{\rm K,\,s}$ on the model's predictions, it is preferable to express the experimental data in a dimensionless form that is also free of these parameters. In the equation above, it is observed that the underlined term is dimensionless, and depends solely on experimentally accessible quantities. It is thus possible to introduce

$$\eta_{\rm p}^\dagger \equiv \frac{\eta_{\rm p}}{n_{\rm p}\eta_{\rm s} b_{\rm K}^3} = \frac{\pi^{3/2}}{\sqrt{12}} h^* N_{\rm K,\,s}^{3/2} \eta_{\rm p}^*\,. \tag{8.2}$$

For extensional flows, the dimensionless extensional viscosity $\overline{\eta}_{\rm p}^\dagger$ is defined similarly using $\overline{\eta}_{\rm p}$. Comparing the right-hand side with the definition of the ratio U_η in Eq. (7.2) in the previous Chapter, it is clear that

$$\eta_{\rm p}^\dagger = U_\eta N_{\rm K}^{3/2}\,. \tag{8.3}$$

Returning now to the problem at hand, in a first attempt at predicting the data of Gupta *et al.*, Li *et al.* [2000] used BD simulations of finitely extensible chains, but without HI. However, their predictions agreed only qualitatively with the data. Further, the drag-coefficient ζ had to be adjusted to ensure that their free-draining

model's prediction of the equilibrium relaxation time matched that predicted by the Zimm model, which incorporates HI. More recently, Larson and co-workers [Hsieh and Larson, 2004; Hsieh *et al.*, 2003] for the first time demonstrated that quantitative agreement can be obtained if HI is included in the model. However, even in this study, it was found that the drag coefficient had to be chosen carefully in order to describe the observed experimental behaviour well. Fitting the drag coefficient in a bead-spring model with spherical beads is equivalent to choosing the HI parameter, h^*. These studies show that for any fixed value of N_s, choosing $h^* = h_f^*$ does not give uniformly accurate predictions of the behaviour of solutions of long molecules in strong extensional flows.

As discussed earlier, the dynamic properties of long molecules close to equilibrium are well described by bead-spring chains models with relatively small N_s provided $h^* \approx h_f^*$. Subsequent to the imposition of a strong extensional flow on a polymer solution initially at equilibrium, molecules in the solution are forced by the solvent to unravel from their random coil conformations to a nearly fully-stretched state. In this state, a macromolecule looks like a long, slender rod. A simple derivation presented in Appendix B leads to the following approximate expression for the steady-state extensional viscosity of a solution of fully-stretched molecules modeled as bead-rod chains:

$$\overline{\eta}_p^\dagger = \frac{\pi}{6} \frac{N_K^3}{\ln(N_K/2) + 1/(\sqrt{3\pi} h_K^*)}, \tag{8.4}$$

where

$$h_K^* \equiv \sqrt{\frac{3}{\pi}} \frac{a_K}{b_K}, \tag{2.66}$$

is the HI parameter for a bead-rod chain with HI. In a fully-stretched bead-spring representation, however, the beads are each separated by a distance of $b_K N_{K,\,s}$, and the corresponding expression for fully-stretched bead-spring chains is

$$\overline{\eta}_p^\dagger = \frac{\pi}{6} \frac{N_K^3}{\sqrt{N_{K,\,s}}/\sqrt{3\pi} h^* + \ln(N_s/2)}. \tag{8.5}$$

It is clear that in a strong extensional flow when chains can be close to fully stretched,

a choice of $h^* = h_f^* \approx 0.25$ in the equation above for $N_s \ll N_K$ cannot reproduce the value of $\overline{\eta}_p^\dagger$ predicted with Eq. (8.4). For large values of N_K, the predictions of the bead-spring model with $h^* \approx 0.25$ for the steady-state extensional viscosity will be lower than that predicted by a bead-rod model by a factor that scales roughly as $\sqrt{N_{K,\,s}}$.

Hsieh *et al.* attempted to resolve this issue by choosing a value of h^* in the coarse bead-spring chain that leads to the same extensional viscosity of a solution of bead-rod chains in the fully-stretched state. However, with this approach, the near-equilibrium predictions of the bead-spring model no longer match experimental observations as $h^* \neq h_f^*$. In fact, equating Eqs. (8.4) and (8.5) shows that the value of h^* estimated with such a procedure,

$$h^* = \frac{\sqrt{N_{K,\,s}}}{h_K^{*-1} + \sqrt{3\pi}\ln(N_{K,\,s})}\,, \tag{8.6}$$

can be unrealistically large for large values of N_K and small values of N_s. Therefore one is forced to increase N_s to keep h^* within reasonable limits [Hsieh and Larson, 2004].

One is confronted with a dilemma when attempting to use a bead-spring model with small $N_s \approx 20$ in flow situations where considerable variation in the extent to which molecules are stretched is possible. If $h^* = h_f^*$, good agreement near equilibrium comes at the cost of inaccuracies when molecules are stretched. The opposite is true if h^* is chosen to match the drag characteristics of fully stretched molecules. This difficulty is in reality the result of using a fixed and relatively high degree of coarse-graining (that is, a fixed $N_s \ll N_K$) to represent a polymer chain. In a bead-spring model with a *constant* bead radius, a single choice of a relatively small number of springs cannot adequately describe the hydrodynamic properties of the underlying chain across the entire range of flow strengths with uniform accuracy.

The discussion above implies that for any large fixed value of N_K, predictions

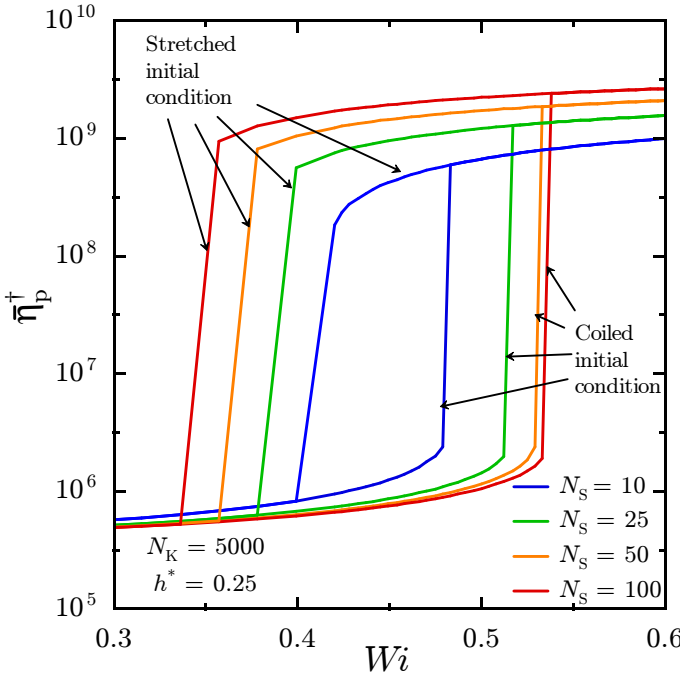

Figure 8.1: Effect of coarse-graining on predictionsof coil-stretch hysteresis in the dimensionless steady-state extensional viscosity obtained with the TFN-P model. Here, the Weissenberg number $Wi = U^{\infty}_{1,0} Wi_{\circ} = 0.2 Wi_{\circ}$ [Eq. (7.7)]. The universal ratio $U^{\infty}_{1,0}$ is defined in Section 8.0.3.

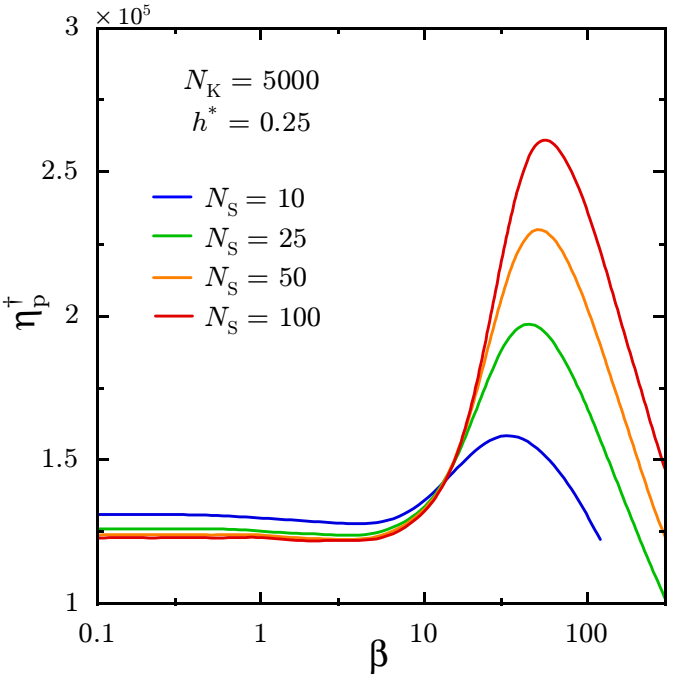

Figure 8.2: Effect of coarse-graining on predictions of the dimensionless steady-state shear viscosity obtained with the TFN-P model. Here, the shear Weissenberg number $\beta = U^{\infty}_{\eta,0} Wi_{\circ} = 0.42 Wi_{\circ}$ [Eq. (7.7)].

of models with finitely extensible springs become strongly dependent of the coarse-graining parameter $N_{\mathrm{K,\,s}}$ in situations where chains experience considerable stretching. In Fig. 8.1, the strong dependence on the degree of coarse graining is demonstrated with predictions of the TFN-P model for the steady-state extensional viscosity $\overline{\eta}^{\dagger}_{\mathrm{p}}$. It is observed that, $Wi_{\mathrm{uc}} - Wi_{\mathrm{lc}}$, the size of coil stretch window between the critical values for coil-to-stretch (Wi_{uc}) and stretch-to-coil (Wi_{lc}) depends on the value of N_{s}, and hence the degree of coarse graining $N_{\mathrm{K,\,s}}$, used for the calculations. (The method used to calculate the Weissenberg numbers in Fig. 8.1 and 8.2 is explained later in this Chapter.) Further, it is clear that at low values of $Wi < Wi_{\mathrm{lc}}$, predictions of $\overline{\eta}^{\dagger}_{\mathrm{p}}$ with a fixed value of N_{K} and for the value of $h^* = 0.25$ used, are not very sensitive to $N_{\mathrm{K,\,s}}$. However, above Wi_{uc}, when chains are highly stretched, the dependence of $\overline{\eta}^{\dagger}_{\mathrm{p}}$ on $N_{\mathrm{K,\,s}}$ is much stronger. In fact, the increase in the coil-stretch hysteresis window is the result of the strong sensitivity of the stretched-state viscosity to $N_{\mathrm{K,\,s}}$, since Wi_{uc} is observed to be less dependent on $N_{\mathrm{K,\,s}}$ than Wi_{lc}. The sensitivity of properties to $N_{\mathrm{K,\,s}}$ is not restricted to extensional flows, as seen in Fig. 8.2, where predictions for the steady-state shear viscosity $\eta^{\dagger}_{\mathrm{p}}$ in the FE dominated terminal shear-thinning regime are also observed to depend strongly on $N_{\mathrm{K,\,s}}$.

The most direct response to this difficulty would be to eliminate it altogether by modeling the polymer molecule as a bead-rod chain. When EV effects are neglected, $\overline{\eta}^{*}_{\mathrm{p}}$ in general depends on ε, Wi and the model parameters h^* and $N_{\mathrm{K,\,s}}$, besides also depending on the values chosen for N_{s}. Equation (8.2) shows therefore that for a bead-rod chain, ($N_{\mathrm{s}} = N_{\mathrm{K}}$, $h^* = h^*_{\mathrm{K}}$), predictions of the dimensionless extensional viscosity $\overline{\eta}^{\dagger}_{\mathrm{p}}$ in unsteady extensional flows, should in general depend on ε, Wi and must be parameterized by N_{K} and the HI parameter h^*_{K}, *i.e.* $\overline{\eta}^{\dagger}_{\mathrm{p}} = \overline{\eta}^{\dagger}_{\mathrm{p}}(\varepsilon, Wi, N_{\mathrm{K}}, h^*_{\mathrm{K}})$. Further, from Eq. (8.3), this means that $U_{\overline{\eta}} = U_{\overline{\eta}}(\varepsilon, Wi, N_{\mathrm{K}}, h^*_{\mathrm{K}})$ in general, where $U_{\overline{\eta}}$ is the extensional flow equivalent of the ratio U_{η} defined in Eq. (7.2) for shear flows. From the discussion in the previous Chapter, one expects that the dependence of $U_{\overline{\eta}}$ on h^*_{K} would be weak near equilibrium, for large values of N_{K}, and $U_{\overline{\eta}} \approx U^{\infty}_{\overline{\eta}}(\varepsilon, Wi)$, or $\overline{\eta}^{\dagger}_{\mathrm{p}} \approx U^{\infty}_{\overline{\eta}}(\varepsilon, Wi) N_{\mathrm{K}}^{3/2}$. As steady-state is approached in a strong extensional flow, $\overline{\eta}^{\dagger}_{\mathrm{p}}$ will be closer to the approximate expression in Eq. (8.4).

Equation (8.4) also indicates that for very long chains in the fully-stretched

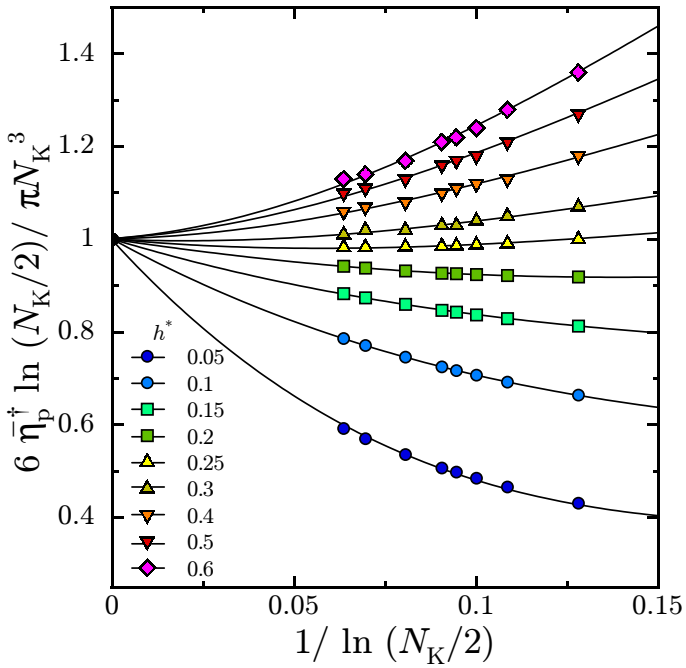

Figure 8.3: Exact predictions of the ratio $6\overline{\eta}^{\dagger}_{\rm p}\ln(N_{\rm K}/2)/(\pi N_{\rm K}^3)$ for finite fully-stretched bead-rod chains with HI, versus $1/\ln(N_{\rm K}/2)$, for values of $N_{\rm K}$ in the range $[10, 5252]$ and for various values of $h^*_{\rm K}$. Predictions were obtained for chains with RPY HI between the beads. The details of the calculations are given in Appendix B. The smooth lines shown have been drawn to guide the eye.

condition,

$$\begin{aligned}\overline{\eta}^{\dagger}_{\rm p} &= \frac{\pi}{6}\frac{N_{\rm K}^3}{\ln(N_{\rm K}/2)}\left(1+\frac{1}{\sqrt{3\pi}h^*_{\rm K}\ln(N_{\rm K}/2)}\right)^{-1}, \\ &= \frac{\pi}{6}\frac{N_{\rm K}^3}{\ln(N_{\rm K}/2)}\left(1-\frac{1}{\sqrt{3\pi}h^*_{\rm K}\ln(N_{\rm K}/2)}+O([\ln(N_{\rm K}/2)]^{-2})\right). \end{aligned} \tag{8.7}$$

For fully-stretched bead-rod chains, the equation above suggests that the ratio $6\overline{\eta}^{\dagger}_{\rm p}\ln(N_{\rm K}/2)/(\pi N_{\rm K}^3)$ converges to unity as $N_{\rm K}\to\infty$, irrespective of the value of $h^*_{\rm K}$ used. Figure 8.3 illustrates this convergence. The predictions in Fig. 8.3 were numerically calculated without approximations, for fully stretched bead-rod chains with pair-wise HI described using the RPY tensor. The details of this calculation are given in Appendix B.

For fully stretched chains, corrections to ratio plotted in Fig. 8.3 die out as

$1/\ln(N_K/2)$, which is much slower slower the $1/\sqrt{N_K}$ convergence of $U_{\eta,0}$ to $U^{\infty}_{\eta,0}$. It is interesting to note, however, that the infinite-chain limit for fully-stretched bead-rod chains seems to be approached nearly horizontally for a choice of $h^*_K \approx 0.25$. Combining this observation with the fact that the fixed-point for bead-rod chains is close to 0.2, one may conjecture that even in the transition between the coiled state to the stretched state, predictions of the bead-rod model for properties such as $\overline{\eta}^{\dagger}_p$ obtained using relatively small values of N_K and a value of h^*_K between 0.2 and 0.3 may be treated as being representative of the behaviour of much longer chains over a wider range of h^*_K values.

Direct BD simulations of bead-rod chains with HI for $N_K \gtrsim 100$ are prohibitively expensive, and a systematic exploration of the rheological behaviour of dilute polymer solutions using the bead-rod model is currently not possible. Such simulations may be avoided by noting that, although predictions of the FEBS model with a single choice of low N_S may not be accurate everywhere, a series of different simulations, each with the same value of N_K but a larger value of N_S than the one before may reveal a systematic trend in the predictions. Further, the HI parameter in the different bead-spring simulations can be held constant at some $h^* = h^*_K$. Then, if the macroscopic properties predicted by the FEBS model vary smoothly with respect to $N_{K,\,S}$, it may be possible to extrapolate the trends in rheological and other properties to the $N_S \to N_K$ limit to obtain an improved estimate of the prediction that would have been obtained in a bead-rod simulation with the same N_K and h^*_K, provided the strain-rate of the flow is such that $\dot{\varepsilon}\lambda_K \ll 1$, where Kuhn segment time constant λ_K has been introduced in Eq. (2.68). Thus, the dependence on the degree of coarse-graining $N_{K,\,S}$ caused by the use of spherical beads of fixed hydrodynamic radii, can be eliminated by extrapolating to the "bead-rod limit", $N_S \to N_K$.

The aim of this Chapter is to compare the results obtained using this "Successive Fine Graining" (SFG) procedure with some of the available rheological measurements for uniaxial extensional flows of dilute polymer solutions at the theta state. The key steps in effecting this comparison between theory and experiment are summarized below.

1. Collect the following data characterizing the experimental system: the polymer species, it molecular weight M, the number density n_p of polymer molecules

in the solution, the solvent viscosity η_s and the theta temperature at which measurements are made. For the given polymer, get the Kuhn segment length b_K and the number of Kuhn segments $N_K = M/m_K$, where m_K is the molecular weight of a single Kuhn step Appendix C lists the key formulae required for the calculation of m_K.

2. From the strain-rate $\dot{\varepsilon}^{ex}$ used in the experiment, calculate the experimental Weissenberg number, Wi^{ex}. The estimation of the experimental equilibrium relaxation time required for this calculation is described in Section 8.0.3 below.

3. Convert raw experimental $\overline{\eta}_p$-versus-t data into a plot of $\overline{\eta}_p\dagger$-versus-ε.

4. Choose a value of h_K^*, say 0.2.

5. Choose a small value of N_s, and calculate $N_{K,\,s} = N_K/N_s$, $\ell_s = b_K\sqrt{N_{K,\,s}/3}$, and $\lambda_s = (3\pi^{3/2}/2)\,h^*\,(\eta_s\,\ell_s^3/k_BT)$, with $h^* = h_K^*$.

6. Estimate (as shown Section 8.0.3) the dimensionless strain rate $\dot{\varepsilon}^*$ to be used in the BD simulation.

7. Perform a BD simulation with the parameters above, and express the resulting output for $\overline{\eta}_p^*$ in terms of $\overline{\eta}_p^\dagger$ using Eq. (8.2).

8. Choose a new larger value of N_s, and repeat from Step 5 above for several values of N_s.

9. At each ε, extrapolate the predicted $\overline{\eta}_p^\dagger$ data obtained with the different N_s values to the $N_s \to N_K$ limit. The details of the extrapolation procedure are given in Section 8.1. This yields the variation of the bead-rod limit of $\overline{\eta}_p^\dagger$ with ε for the chosen h_K^*.

10. Repeat from Step 5 with another value of h_K^*, say 0.3.

11. After obtaining the extrapolated $\overline{\eta}_p^\dagger$-versus- ε, examine sensitivity of predictions to h_K^*.

If HI is the dominant physical mechanism in dilute polymer solutions even in strong flows, one would expect to see experimental measurements of the transient

evolution of $\overline{\eta}_{\rm p}^{\dagger}$ for the same value of $N_{\rm K}$ in several polymer-solvent systems to be clustered around extrapolated predictions in the bead-rod limit. If the predictions for the different $h_{\rm K}^*$ values are not markedly different from each other for fairly large values of $N_{\rm K}$, and if significant and systematic deviations between these extrapolated predictions and experiment begin to appear, then the deviations from experiment can be ascribed to physical phenomena not accounted for in the model, rather than to the lack of detail in describing the local hydrodynamic characteristics of polymer molecules.

An important consideration in implementing the SFG procedure involves the calculation of the dimensionless strain rate that must be used in a BD simulation.

8.0.3 Choosing the strain-rate in the SFG procedure

Before proceeding further, it is necessary to first consider the definition of the "longest" relaxation time. In the approximate theories of HI described in Chapter 5, it is possible to obtain an expression for the relaxation modulus $G(t)$ of the general form

$$G(t) = \sum_{i=1}^{N_G} H_i \exp(-t/\lambda_i)\,. \tag{8.8}$$

The nature of the time constants λ_i and the relaxation weights H_i in the approximate models have been discussed thoroughly by Öttinger and Zylka [1992]. Conventionally, the largest of the time constants is denoted as λ_1, and is identified as the longest relaxation time $\Lambda_{1,0}$. The set of time constants is referred to as the relaxation spectrum. In BD simulations of chains with fluctuating HI, however, a discrete relaxation spectrum cannot be obtained. Instead, it is possible to identify $\Lambda_{1,0}$ as follows [Hsieh *et al.*, 2003; Perkins *et al.*, 1997; Sunthar and Prakash, 2005]. Under no-flow conditions, BD simulations are performed with an ensemble of FEBS chains that are initially all stretched to a certain large fraction (70% in this study) of their contour lengths. The time constant $\Lambda_{1,0}^* = \Lambda_{1,0}/\,\ell_{\rm s}$ is estimated by fitting a single exponential decay to the tail (after $R_{\rm e}^{*\,2}$ decreases below $2R_{\rm e,\,eq}^{*\,2}$ in this study) of the $R_{\rm e}^{*\,2}$-versus-t^* curve .

It is useful here to define a ratio similar to U_η for the longest relaxation time at

equilibrium, $\Lambda_{1,0}$, introduced in Section 2.5.5 of Chapter 2:

$$U_{1,0} \equiv \frac{\Lambda_{1,0} k_{\rm B} T}{\eta_{\rm s} R_{\rm e,eq}^3} = \frac{\pi^{3/2}}{\sqrt{12}} \frac{h^* \Lambda_{1,0}^*}{N_{\rm S}^{3/2}} \,. \tag{8.9}$$

Although $U_{1,0}^{\rm ex}$ is not typically measured in experiment (since direct visualization of synthetic polymer molecules such as polystyrene is currently not possible), this ratio is expected to be constant in solutions of long, flexible molecules, as observed in the case of $U_{\eta,0}^{\rm ex}$. Furthermore, the prediction of the universal constant $U_{\eta,0}^{\infty}$ obtained with BD simulations of bead-spring chains with HI is in excellent agreement with the experimentally measured value of $U_{\eta,0}^{\rm ex}$ [Kröger *et al.*, 2000]. Thus, it is reasonable to assume that $U_{1,0}^{\rm ex}$ is close to $U_{1,0}^{\infty}$, the infinite chain limit obtained theoretically.

In this study, the SFG procedure is used to obtain predictions to compare with the experimental $\overline{\eta}_{\rm p}^{\dagger}$-versus-$\varepsilon$ data. The experimentally imposed (dimensional) extension-rate is denoted as $\dot{\varepsilon}^{\rm ex}$. At first sight, using this value, or its dimensionless equivalent $\dot{\varepsilon}^{\rm ex}\lambda_{\rm S}$, seems to be an obvious input to simulations. It also seems equally reasonable to choose an $\dot{\varepsilon}$ in the simulations for any value of $N_{\rm s}$ such that the Weissenberg number in the model Wi equals that in the experiment, $Wi^{\rm ex} = \dot{\varepsilon}^{\rm ex}\Lambda_{1,0}^{\rm ex}$. This Section examines these two apparently unrelated choices further.

From the definitions above,

$$Wi^{\rm ex} = U_{1,0}^{\infty} \dot{\varepsilon}^{\rm ex} \frac{\eta_{\rm s} b_{\rm K}^3}{k_{\rm B} T} N_{\rm K}^{3/2} = U_{1,0}^{\infty} \dot{\varepsilon}^{\rm ex} \Lambda_{\circ} \,, \tag{8.10}$$

where the time constant $\Lambda_{\circ} = \eta_{\rm s} b_{\rm K}^3 N_{\rm K}^{3/2} / k_{\rm B} T$ has been introduced earlier in the previous Chapter [Eq. (7.8)]. For a bead-spring model with $N_{\rm s}$ springs for which the HI parameter is h^*, the Weissenberg number corresponding to some (dimensional) strain rate $\dot{\varepsilon}$ is

$$Wi = \dot{\varepsilon} \frac{\eta_{\rm s} b_{\rm K}^3}{k_{\rm B} T} U_{1,0}(h^*, N_{\rm S}, N_{\rm K,\,S}) N_{\rm K}^{3/2} \,, \tag{8.11}$$

where $U_{1,0}(h^*, N_{\rm S}, N_{\rm K,\,S})$ is the specific prediction of the ratio by the bead-spring model. If the rule $Wi = Wi^{\rm ex}$ is used to calculate the values of $\dot{\varepsilon}$ to be used in simulations, then using Eqs. (8.10) and (8.11) one obtains for the strain rate in the

bead-spring model,

$$\dot{\varepsilon} = \dot{\varepsilon}^{\mathrm{ex}} \frac{U^{\infty}_{1,0}}{U_{1,0}(h^*, N_{\mathrm{S}}, N_{\mathrm{K,\,S}})} \,. \tag{8.12}$$

In dimensionless terms, this implies

$$\dot{\varepsilon}^* = \dot{\varepsilon}\lambda_{\mathrm{S}} = \left(\dot{\varepsilon}^{\mathrm{ex}} \frac{3\pi^{3/2}}{2} \frac{\eta_{\mathrm{S}}}{k_{\mathrm{B}}T} h^* \, \ell_{\mathrm{S}}^3 \right) \frac{U^{\infty}_{1,0}}{U_{1,0}(h^*, N_{\mathrm{S}}, N_{\mathrm{K,\,S}})} \,. \tag{8.13}$$

Since $h^* = h^*_{\mathrm{K}}$ is a value that is chosen *a priori*, the value of $\dot{\varepsilon}^*$ to be used in the simulation can be calculated, once the ratio $U^{\infty}_{1,0}/U_{1,0}$ is known. Equation (8.12) above shows the extent to which the value of $\dot{\varepsilon}$ determined by the Weissenberg equality rule differs from a direct choice of $\dot{\varepsilon}^{\mathrm{ex}}$ as the simulations' input.

In this study, the ratio $U^{\infty}_{1,0}/U_{1,0}(h^*, N_{\mathrm{S}}, N_{\mathrm{K,\,S}})$ is obtained by estimating the relaxation time $\Lambda^*_{1,0}$ using the procedure described at the start of this Section. These simulations are performed for three different values of $h^* = 0.2$, 0.25, and 0.3, and using a single value of $N_{\mathrm{K}} = 2627$. The ratio $U_{1,0}$ is calculated using the definition in Eq. (8.9). Although the results are obtained with N_{K} kept constant at a large value, the relatively small values of N_{S} used ($25 \leq N \leq 50$) means that the springs behave as Hookean springs in the final stages of relaxation in which the estimate of $\Lambda^*_{1,0}$ is made. In other words, the results for $U_{1,0}$ are effectively independent of the value of $N_{\mathrm{K,\,S}}$ used, depending only on N_{S} and h^*. The data can be regarded as having been obtained using Hookean springs, and can thus be extrapolated to the limit $N_{\mathrm{S}} \to \infty$. Following the procedure of Kröger *et al.* [2000], data for finite chains is plotted against $1/\sqrt{N_{\mathrm{S}}}$ and straight-line fits through the data are extrapolated to the limit $N_{\mathrm{S}} \to \infty$ to obtain an estimate of $U^{\infty}_{1,0}$. The values of $U^{\infty}_{1,0}$ thus obtained are given in Table 8.1. It is seen that the resulting values $U^{\infty}_{1,0}$ for the three different h^* values are close, but not identical. Therefore, the mean of the three values ($= 0.21$) is taken to be $U^{\infty}_{1,0}$, and straight lines are fitted through the data sets for the different h^* values such that all have the same intercept and equal to the mean $U^{\infty}_{1,0}$. It may be noted that defining the largest equilibrium relaxation time in the Zimm model as $\Lambda_{1,0} = 2\lambda_{\mathrm{S}}/, \widetilde{a}^*_1$, where $\widetilde{a}^*_1$ is the smallest eigenvalue of the modified Rouse matrix [Eq. (5.20)] leads to $U^{\infty}_{1,0} = 0.20$ [Auer and Gardner, 1955; Kröger *et al.*, 2000].

The resulting straight line fits through the $U_{1,0}$-versus-$1/\sqrt{N_{\mathrm{S}}}$ data obtained in

Table 8.1: Values of the constants $U^{\infty}_{1,0}$ obtained by fitting straight lines of the form $U_{1,0} = U^{\infty}_{1,0}(1 + m/\sqrt{N_s})$ to the $U_{1,0}$-versus-$1/\sqrt{N_s}$ data obtained with BD simulations for h^* values of 0.2, 0.25 and 0.3.

h^*	$U^{\infty}_{1,0}$
0.2	0.215 ± 0.008
0.25	0.223 ± 0.007
0.3	0.206 ± 0.005
Average	0.21 ± 0.01

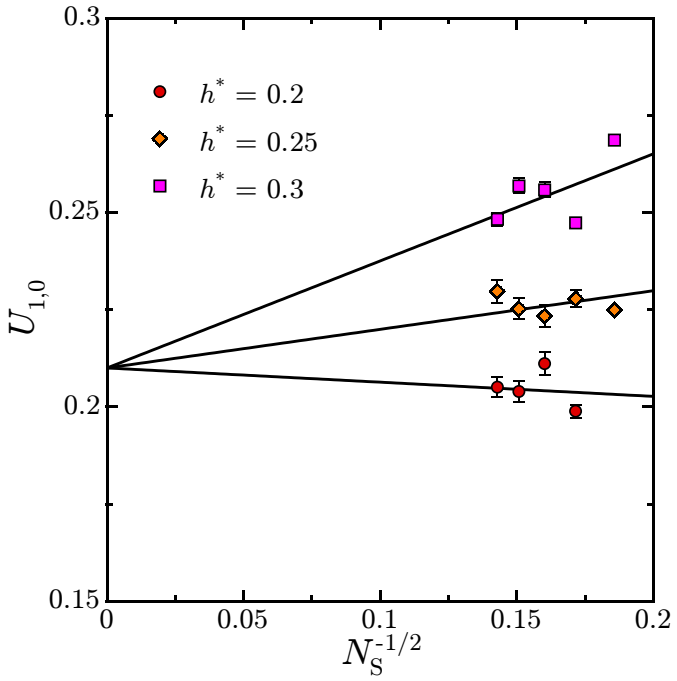

Figure 8.4: Exact results for the ratio $U_{1,0}$ from Brownian dynamics simulations, versus $1/\sqrt{N_s}$ for $25 \leq N_s \leq 50$. The equations of the lines of best-fit are as follows: for $h^* = 0.2$, $U_{1,0} = 0.21 - 0.048/\sqrt{N_s}$, for $h^* = 0.25$, $U_{1,0} = 0.21 + 0.090/\sqrt{N_s}$; for $h^* = 0.3$, $U_{1,0} = 0.21 + 0.260/\sqrt{N_s}$.

the simulations, and their equations for each h^*, are shown in Fig. 8.4. With these equations, the ratio $U^{\infty}_{1,0}/U_{1,0}$ in Eq. (8.13) can be calculated for any value of N_s for the three different h^* values in the range $[0.2, 0.3]$, using which the $\dot{\varepsilon}^*$ to be used in a simulation for any given values of N_s can be calculated.

8.1 SFG Extrapolations

Figure 8.5 plots the variation of $\overline{\eta}^{\dagger}_{\rm p}$ with respect to $1/\sqrt{N_{\rm s}}$ for the two different values of $h^* = h^*_{\rm K} = 0.2$ and 0.3, at different strains. It is found that the deviations due to coarse-graining can be as large as 40 to 50%, even though the values of $N_{\rm s}$ used are not small ($60 \leq N \leq 160$). However, as anticipated, the trend across with respect to $1/\sqrt{N_{\rm s}}$ appears to be reasonably smooth, permitting the use of curve fits through the data which can then be extrapolated to the $1/\sqrt{N_{\rm s}} \to 1/\sqrt{N_{\rm K}}$ limit.

For the smaller values of the Hencky strain ($\varepsilon \lesssim 3$ in Fig. 8.5), the predictions for $\overline{\eta}^{\dagger}_{\rm p}$ show a nearly linear (within simulation errors) dependence on $1/\sqrt{N_{\rm s}}$, which may be understood as follows. At low strains, the influence of FE has not yet begun to manifest itself, and one expects that at any fixed ε and Wi ,

$$\overline{\eta}^{\dagger}_{\rm p} = U_{\overline{\eta}} N_{\rm K}^{3/2} = \left[U^{\infty}_{\overline{\eta}} + c_{\overline{\eta}} \left(\frac{1}{h^*_{\rm f}} - \frac{1}{h^*} \right) \frac{1}{\sqrt{N_{\rm s}}} + \ldots \right] N_{\rm K}^{3/2} \,. \tag{8.14}$$

In the equation above, $U_{\overline{\eta}}$ is different from the ratio $U_{\overline{\eta},0}$ obtained for finite chains in the limit of vanishingly small extension-rates. However, although $Wi > Wi_{\rm c}$ polymer molecules are not highly stretched at low values of ε and the expansion of $U_{\overline{\eta}}$ can be expected to have the same form as shown in Eq. (7.5) for $U_{\eta,0}$. The form of the function $U_{\overline{\eta}}$ in the equation above is valid for chains with Hookean or finitely extensible springs. The parameter $h^*_{\rm f}$ is however dependent on $N_{\rm K,\,s}$. In other words, it is possible to construct plots such as the one shown for the Zimm model Fig. 7.1 in the previous Chapter but with FEBS chains, keeping $N_{\rm K,\,s}$ fixed and increasing $N_{\rm s}$. In such a case, Sunthar and Prakash [2005] have shown that $h^*_{\rm f}$, the value of h^* for which the infinite chain limit of $U_{\eta,0}$ (or $U_{\overline{\eta},0}$) is approached horizontally for large values of $N_{\rm s}$, depends on $N_{\rm K,\,s}$. In fact, as mentioned in Chapter 7, the value of $h^*_{\rm f}$ for the bead-rod model is 0.19, whereas for Rouse chains it is approximately 0.25 [Kröger *et al.*, 2000]. Hence, it is expected that $h^*_{\rm f}$ has only a weak dependence on $N_{\rm K,\,s}$. Further, for any fixed $N_{\rm K,\,s}$, the value of $h^*_{\rm f}$ is expected to be remain unaffected away from equilibrium [Zylka and Öttinger, 1991], as long as FE effects are not dominant. Since $h^*_{\rm f}$ is a weak function of $N_{\rm K,\,s}$, its reciprocal may be expanded in a Taylor's series in $\sqrt{N_{\rm K,\,s}}$ around $(h^*_{\rm K,\,f})^{-1}$, the value for the bead-rod model. Therefore, for a

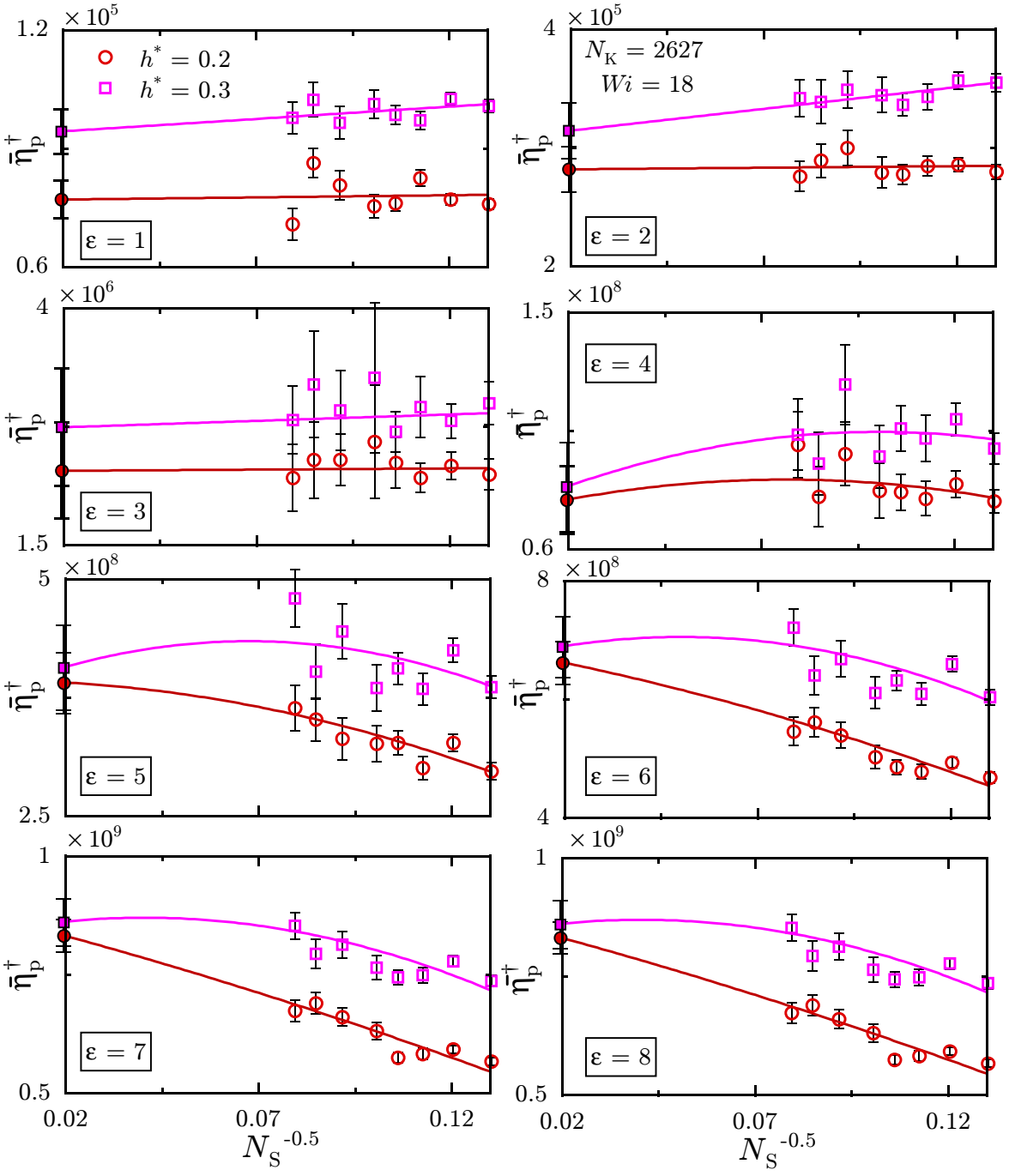

Figure 8.5: Extrapolations of the results of BD simulations for the dimensionless extensional viscosity $\overline{\eta}_p^+$ to the $N_S \to N_K$ limit. Symbols ($h^* = 0.2$, open red circles; $h^* = 0.3$ open cyan squares) are results of simulations, while continuous lines are curve fits through the data. The solid symbols ($h_K^* = 0.2$, red circles; $h_K^* = 0.3$, cyan squares) represent the extrapolated values.

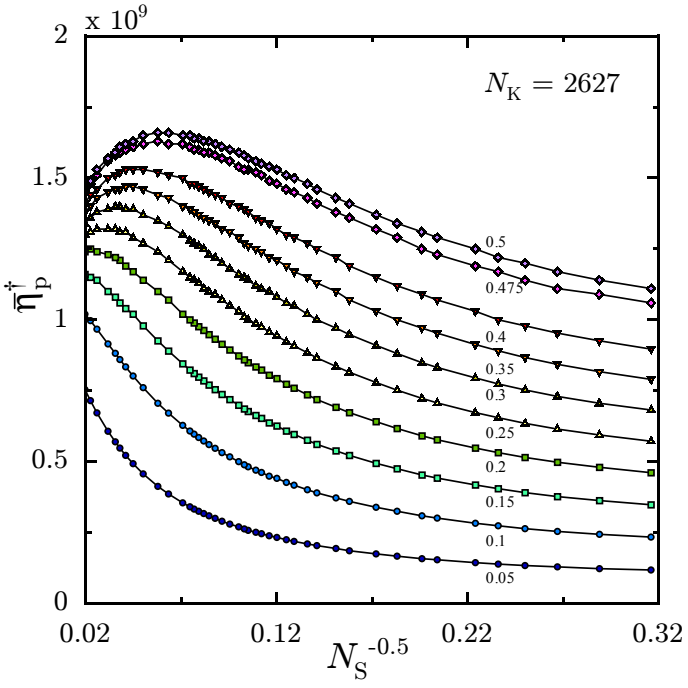

Figure 8.6: Exact predictions (Appendix B) of $\overline{\eta}^{\dagger}_{p}$ for different bead-"spring" discretizations (*i.e* N_S) of a fully-stretched bead-rod chain of $N_K = 2627$ ($1/\sqrt{N_K} = 0.0195$), for different values (indicated alongside curves) of $h^* = h^*_K$.

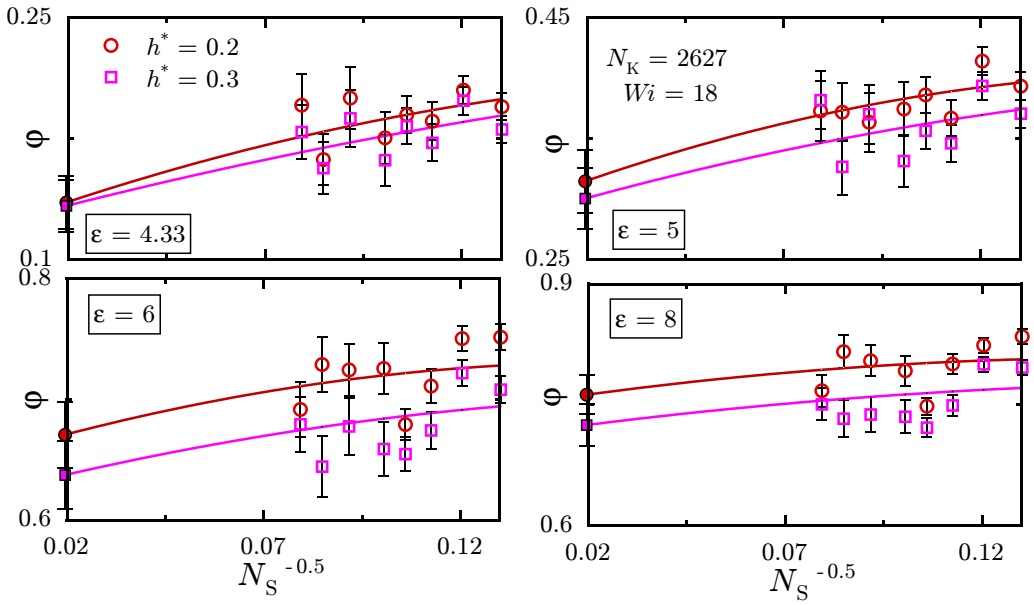

Figure 8.7: Extrapolations of the ratio φ defined in Eq. (8.16), to the $N_S \to N_K$ limit. Symbols ($h^* = 0.2$, open red circles; $h^* = 0.3$ open cyan squares) are results of simulations, while continuous lines are curve fits through the data. The solid symbols ($h^* = 0.2$, red circles; $h^* = 0.3$, cyan squares) represent the extrapolated values.

fixed value of N_{K}, it is possible to write

$$\overline{\eta}_{\mathrm{p}}^{\dagger} = U_{\overline{\eta}} N_{\mathrm{K}}^{3/2} = \left[U_{\overline{\eta}}^{\infty} + c_{\overline{\eta}} \left(\frac{1}{h^*_{\mathrm{K,f}}} - \frac{1}{h^*} \right) \frac{1}{\sqrt{N_{\mathrm{S}}}} + O(\frac{1}{N_{\mathrm{S}}}) \right] N_{\mathrm{K}}^{3/2} . \tag{8.15}$$

The equation above shows that, at low values of ε when FE is not a dominant effect, it is valid to fit low-order polynomials in $1/\sqrt{N_{\mathrm{S}}}$ through the BD simulations data obtained by keeping N_{K} fixed, and extrapolate them to obtain predictions in the bead-rod limit, $N_{\mathrm{S}} \to N_{\mathrm{K}}$.

As ε increases however, $\overline{\eta}_{\mathrm{p}}^{\dagger}$ becomes a stronger function of $1/\sqrt{N_{\mathrm{S}}}$. In addition, for intermediate values of the strain (for example, $\varepsilon = 6$ in Fig. 8.5), fluctuations in the simulations are large for all values of N_{S}. This is caused by the large variations in chain conformations that signal the onset of the coil-to-stretch transition [Larson *et al.*, 1999; Perkins *et al.*, 1997; Smith and Chu, 1998]. Fitting linear or higher-order polynomials directly to noisy data on $\overline{\eta}_{\mathrm{p}}^{\dagger}$ in this regime is problematic.

To understand the nature of the variation in $\overline{\eta}_{\mathrm{p}}^{\dagger}$ with respect to N_{S} (while keeping N_{K} fixed) when chains are highly stretched, analytical results for fully stretched chains are examined first in Fig. 8.6. The results in the Figure were obtained for for various bead-"spring" discretizations of a fully stretched bead-rod chain with $N_{\mathrm{K}} = 2627$. The details of the calculations are given in Appendix B. In Fig. 8.6, the predictions of $\overline{\eta}_{\mathrm{p}}^{\dagger}$ for fully-stretched bead-spring chains are plotted against $1/\sqrt{N_{\mathrm{S}}}$, and various values of h^*. The variation of $\overline{\eta}_{\mathrm{p}}^{\dagger}$ in Fig. 8.6 with respect to $1/\sqrt{N_{\mathrm{S}}}$ is qualitatively similar to that observed in the simulations' data at high Hencky strains ($\varepsilon \geq 5$ in Fig. 8.5), for the same values of h^* and $1/\sqrt{N_{\mathrm{S}}}$.

It is useful to define the following ratio

$$\varphi \equiv \frac{\overline{\eta}_{\mathrm{p}}^{\dagger}(\varepsilon, Wi; h^*, N_{\mathrm{S}}, N_{\mathrm{K}})}{\overline{\eta}_{\mathrm{p}}^{\dagger}(\infty, \infty, h^*, N_{\mathrm{S}}, N_{\mathrm{K}})} , \tag{8.16}$$

where $\overline{\eta}_{\mathrm{p}}^{\dagger}(\infty, \infty, h^*, N_{\mathrm{S}}, N_{\mathrm{K}})$ denotes the analytical calculation of $\overline{\eta}_{\mathrm{p}}^{\dagger}$ for fully-stretched chains. Due to the qualitative similarity in the $\overline{\eta}_{\mathrm{p}}^{\dagger}$-versus-$1/\sqrt{N_{\mathrm{S}}}$ behaviour in Figs. 8.5 and 8.6, the ratio φ is observed in Fig. 8.7 to be a weaker function of $1/\sqrt{N_{\mathrm{S}}}$ than $\overline{\eta}_{\mathrm{p}}^{\dagger}$ itself. Nevertheless, fitting polynomials or rational functions through the data expressed in terms of φ can sometimes lead to unphysical negative viscosities.

To avoid such problems, an approximate expression for $\overline{\eta}_{\rm p}^{\dagger}$ is developed using a one-dimensional model for partially stretched bead-spring chains, which is discussed in Appendix B. Although in reality the extent to which individual springs are stretched varies across the chain (springs in the middle of the chain are more stretched than those at the ends), assuming that all springs are stretched to the same extent leads to a simplified expression for $\overline{\eta}_{\rm p}^{\dagger}$ in which the mean fractional stretch $\overline{\alpha}$ enters as an unknown parameter:

$$\overline{\eta}_{\rm p}^{\dagger} = \frac{\pi^{3/2}}{\sqrt{12}} \frac{\overline{\alpha}^3 \, h^* \, N_{\rm K}^3}{\overline{\alpha} N_{\rm K,\,s}^{1/2} + \sqrt{3\pi} h^* \ln(N_{\rm s}/2)} \,, \tag{8.17}$$

and therefore, for the simple one-dimensional model,

$$\varphi = \overline{\alpha}^3 \frac{1 + \sqrt{3\pi/N_{\rm K,\,s}} h^* \ln(N_{\rm s}/2)}{\overline{\alpha} + \sqrt{3\pi/N_{\rm K,\,s}} h^* \ln(N_{\rm s}/2)} \,. \tag{8.18}$$

The expression above contains a single parameter $\overline{\alpha}$. Using standard non-linear least-squares regression techniques [Press *et al.*, 1992], a function of the form in the equation above is fitted through the actual data for φ-versus-$1/\sqrt{N_{\rm s}}$ data by treating $\overline{\alpha}$ as a tuneable parameter. To allow for the variation of mean stretch with $N_{\rm s}$, $\overline{\alpha}$ itself is considered to be linear with respect $1/\sqrt{N_{\rm s}}$, and the overall procedure involves fitting the two constants involved. The smooth curves shown in Figs. 8.5 and 8.7 through the simulations' data for $\varepsilon > 4$ have been obtained in this manner. At each value of the Hencky strain, the fitted curve is then extrapolated to obtain the prediction of φ at $1/\sqrt{N_{\rm s}} = 1/\sqrt{N_{\rm K}}$, which is then converted back to $\overline{\eta}_{\rm p}^{\dagger}$ by multiplying it with the exact value of $\overline{\eta}_{\rm p}^{\dagger}$ for the fully-stretched chain (Fig. 8.6).

Thus far, extrapolations of BD simulations' data for $\overline{\eta}_{\rm p}^{\dagger}$ have been discussed. Extrapolated results in the bead-rod limit are also obtained for properties related to average chain dimensions, such as $R_{\rm e}^2$ and components of the radius of gyration tensor $\boldsymbol{G}$. As in the case of the extensional viscosity, predictions for these quantities are first expressed in a dimensionless form by defining

$$R_{\rm e}^{\dagger\,2} \equiv \frac{R_{\rm e}^2}{b_{\rm K}^2} = \frac{N_{\rm K,\,s}}{3} R_{\rm e}^{*\,2} \,, \tag{8.19}$$

and similarly,

$$\boldsymbol{G}^{\dagger} = \frac{1}{b_{\mathrm{K}}^2}\boldsymbol{G} = \frac{N_{\mathrm{K,\,S}}}{3}\boldsymbol{G}^{*}\,. \tag{8.20}$$

When the results of simulations are expressed in terms of the dimensionless quantities above, the variation with respect to $\sqrt{N_{\mathrm{S}}}$ is found to be reasonably smooth, which allows the fitting of low-order polynomials in $\sqrt{N_{\mathrm{S}}}$ to perform extrapolations.

8.2 Comparison with experiment

Table 8.2 shows the properties characterizing the polymer solutions whose extensional flow data are compared with the results obtained in this work by using the SFG procedure, and Table 8.3 summarizes the parameters used for BD simulations. To examine the dependence of $\overline{\eta}_{\mathrm{p}}^{\dagger}$ on N_{K}, BD simulations were also performed for chains with N_{K} values in the range $2627/4 < N_{\mathrm{K}} < 2627$. These simulations were carried out for $Wi = 2.0$, and 18. The predictions obtained after SFG extrapolations are compared with experimental data in Figs. 8.8 to 8.11. While Figs. 8.8 (a) to (d) pertain to the growth of $\overline{\eta}_{\mathrm{p}}^{\dagger}$ during the startup of a uniaxial extensional flow, Fig. 8.11 presents data on the variation in dimensionless first normal stress difference [Eq. (2.89)] during start-up and following cessation of steady uniaxial extensional flow.

It is encouraging to observe that the predicted behaviour in all the Figures is observed to be generally in good agreement with experiment across the range of N_{K}, Wi and ε values studied. This confirms that models with HI can describe the dynamic behaviour of dilute polymer solutions reasonably well away from equilibrium provided the influence of coarse-graining are accounted for. On closer examination, however, it is possible to notice the following deviations.

1. In Figs. 8.8 (a) and (b), for either value of h_{K}^{*}, predictions are larger than experiment at higher strains. The deviation at $Wi = 2$ is observed to be larger than at $Wi = 3.8$. At the higher Weissenberg numbers, the agreement is excellent in Figs. 8.8 (c) and (d).

2. For the same polymer and solvent, Fig. 8.9 shows the experimental data for

Table 8.2: Details of experimental systems.

	Solution I	Solution II			Solution III
		A	B	C	
Polymer	Polystyrene	Polystyrene			Polyisobutylene
Solvent	DOP/LMPS	DOP/ LMPS			Kerosene/ Polybutene
b_{K} (nm)	1.8	1.8			1.2
M_{w} ($\times 10^6$)	1.95	10.2			2.4
$M_{\mathrm{w}}/M_{\mathrm{n}}$	1.1	1.1			1.73
N_{K}	2627	13747			8727
n_{p}^{*} [a] ($\times 10^{14}$ cm^{-3})	44.7	3.7			24
n_{p} ($\times 10^{14}$ cm^{-3})	2.4	0.049	0.23	0.44	4.2
T ($^\circ$ C)	21	21			21
η_{s} (Pa s)	30.1	30.7	30.0	28.1	26.7
$\Lambda_\circ$ (s) [b]	5.8	71[c]			9.8
$\Lambda_{\eta,0}$ [d] (s)	9.6	31			4.3
$\Lambda_{1,0}$ [e] (s)	1.2	15			2.1
Reference	Gupta *et al.* [2000]	Gupta *et al.* [2000]			Orr [1998]

[a] Critical number density: $n_{\mathrm{p}}^{*} = \left(\frac{4}{3}\pi\sqrt{\det[3\boldsymbol{G}_{\mathrm{eq}}]}\right)^{-1} = \left(\frac{4}{3}\pi R_{\mathrm{G,eq}}^3\right)^{-1}$

[b] $\Lambda_\circ = \eta_{\mathrm{s}} b_{\mathrm{K}}^3 N_{\mathrm{K}}^{3/2}/k_{\mathrm{B}}T$ [Eq. (7.8)]

[c] Calculated using $\eta_{\mathrm{s}} = 30.7$ Pa s.

[d] $\Lambda_{\eta,0} = U_{\eta,0}^{\infty}\Lambda_\circ = 0.44\Lambda_\circ$; $U_{\eta,0}^{\infty}$ estimated by Kröger *et al.* [2000] using BD simulations.

[e] $\Lambda_{1,0} = U_{1,0}^{\infty}\Lambda_\circ = 0.21\Lambda_\circ$; $U_{1,0}^{\infty}$ estimated in this study using BD simulations.

Table 8.3: Values of parameters used in the BD simulations for comparing with experimental data. N_{traj} indicates the number of chain trajectories used in the simulations. As the number of beads N is increased, N_{traj} is decreased to save CPU-time. The range of N_{traj} corresponds to the range of N used.

N_{K}	Wi	N	N_{traj}	h^*
13747	30, 75	20 – 100	1000 – 500	0.2
8727	4.2	20 – 100	1000 – 500	0.2
2627	2.0, 3.8, 9.9, 18	60 – 160	2000 – 200	0.2, 0.3
657, 1313, 1970	2.0, 18	25 – 80	1000 – 200	0.2, 0.3

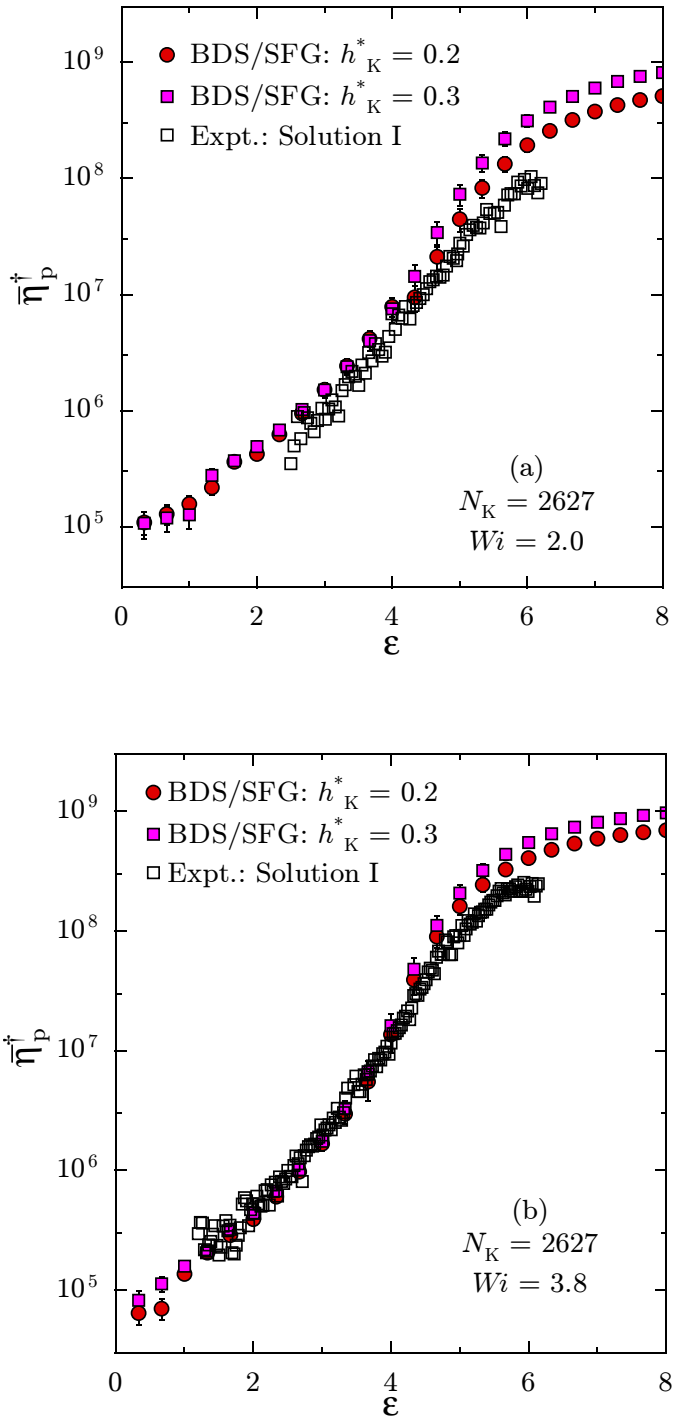

Figure 8.8: Comparison of extrapolated results obtained using BD simulations for the growth of the dimensionless extensional viscosity $\overline{\eta}^{\dagger}_p$, with experimental data obtained with Solution I in Table 8.2.

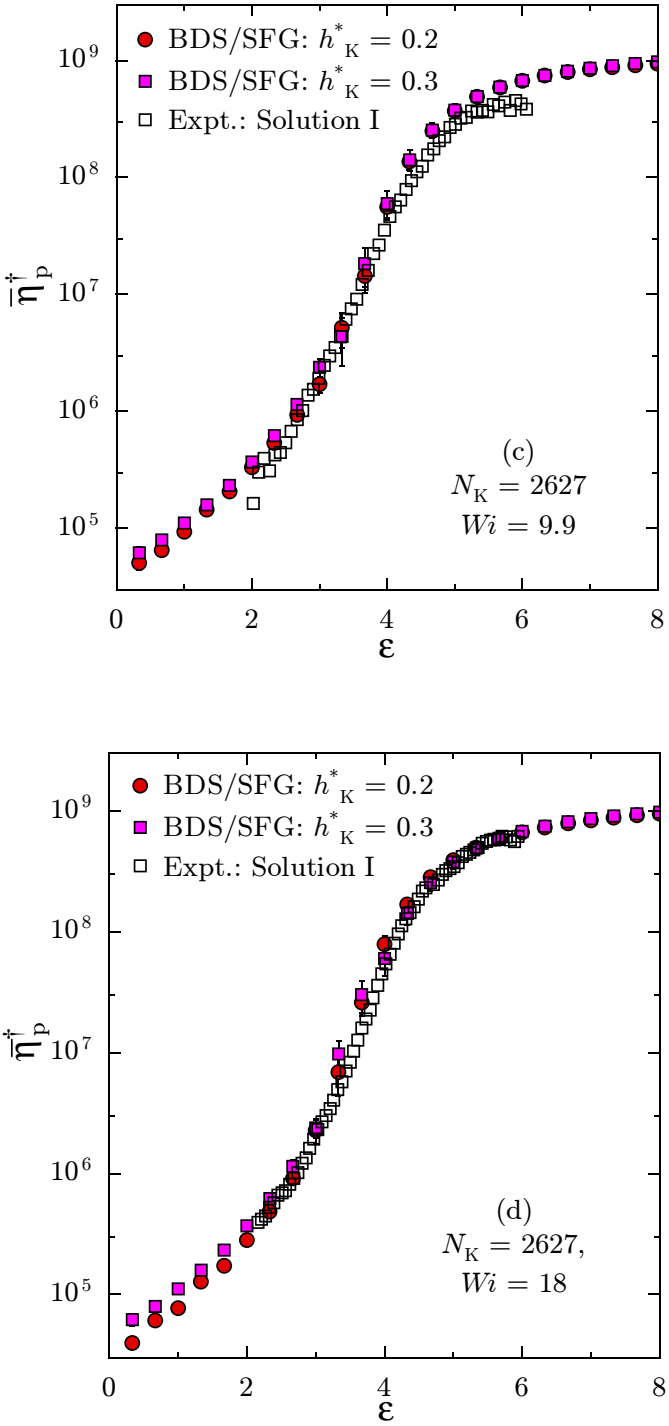
BDS/SFG: $h^*_K = 0.2$
BDS/SFG: $h^*_K = 0.3$
Expt.: Solution I
(c)
$N_K = 2627$
$Wi = 9.9$
$\bar{\eta}^{\dagger}_p$
ε
BDS/SFG: $h^*_K = 0.2$
BDS/SFG: $h^*_K = 0.3$
Expt.: Solution I
(d)
$N_K = 2627$,
$Wi = 18$
$\bar{\eta}^{\dagger}_p$
ε

Figure 8.8

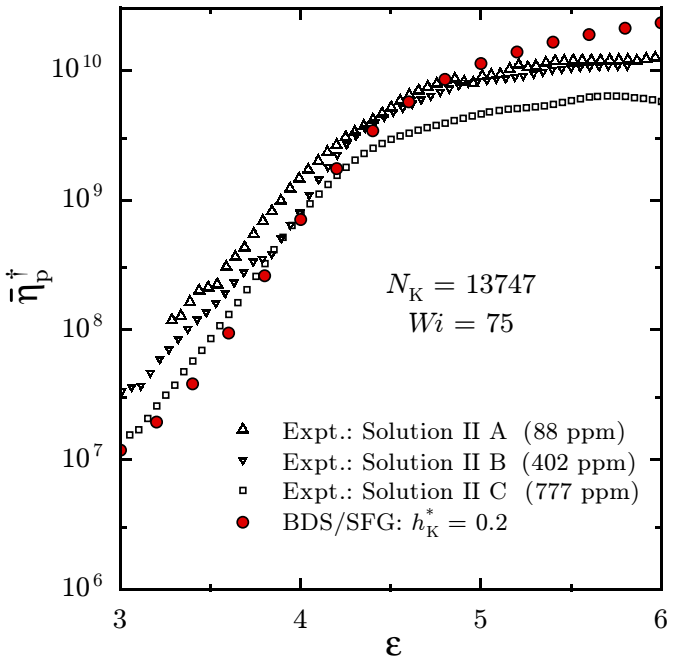

Figure 8.9: Comparison of extrapolated results for the growth of $\overline{\eta}_{\rm p}^{\dagger}$ for $h_{\rm K}^{*} = 0.2$ (red circles), with experimental data obtained with Solutions II A (open upright triangles), B (open inverted triangles) and C (open squares) in Table 8.2.

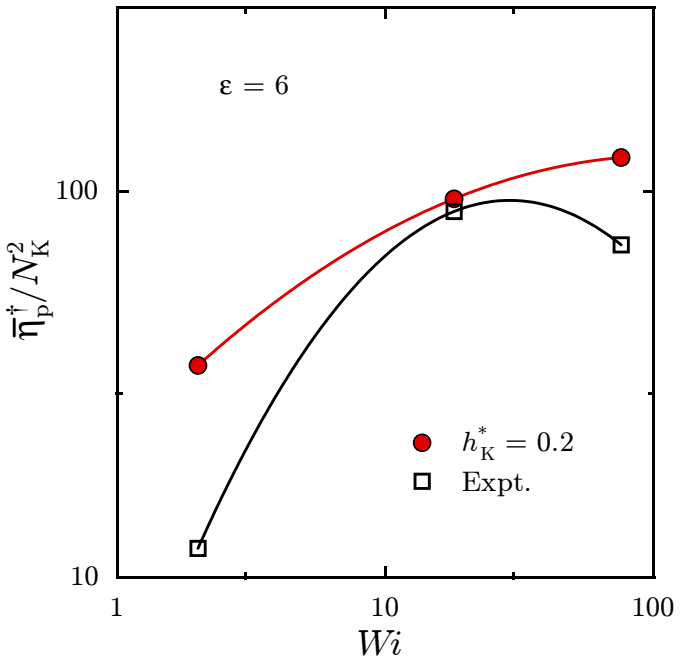

Figure 8.10: Extrapolated results for $h_{\rm K}^{*} = 0.2$ (red circles) for the variation of the ratio $\overline{\eta}_{\rm p}^{\dagger}/N_{\rm K}^{2}$ with Wi at a fixed Hencky strain $\varepsilon = 6$. The experimental data points (open squares) at the two lower values of Wi have been obtained with Solution I in Table 8.2, while the last point has been obtained with Solution II A.

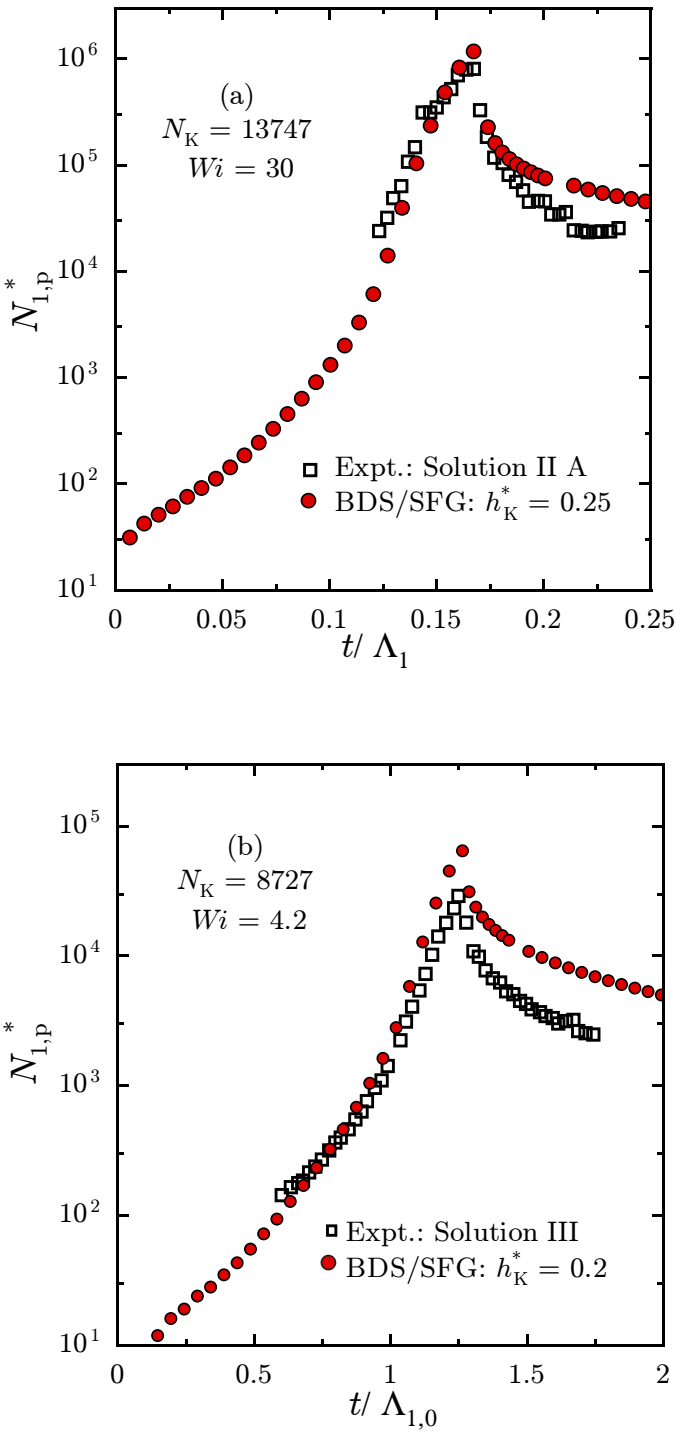

Figure 8.11: Comparison of extrapolated results of the growth and relaxation of the dimensionless first normal-stress difference $N^*_{1,p}$, with the experimental data for (a) Solution II A, and (b) Solution III in Table 8.2.

a larger value of N_{κ}, for three different concentrations. At moderate strains ($\varepsilon \sim 3$), the extrapolated predictions agree with the data obtained with for the solution of a higher concentration (Solution II C, Table 8.2). The measurements for the other two solutions of *lower* concentrations are much larger those of Solution II C. This concentration dependence is unexpected, since the ratio $\overline{\eta}_{\rm p}^{\dagger} \sim \overline{\eta}_{\rm p}/n_{\rm p}$ is expected to be independent of concentration for dilute solutions. Also surprising is the fact that the theoretical predictions valid in the dilute solution limit ($n_{\rm p} \to 0$) agree better with data obtained with a more concentrated solution. The measurements of the polymer stress at the lower strains shown in Fig. 8.9 were significantly larger ($> 100\%$) than the solvent contribution, and therefore the discrepancy at lower strains cannot be attributed to lack of instrument resolution.

3. At higher strains, it is the data for the two solutions of lower concentrations that are closer to the theoretical predictions in Fig. 8.9. But even these are significantly lower (by nearly 50% at $\varepsilon = 6$) than the extrapolated results.

4. This overprediction is also the reason why the simulations fail to predict the "extension-thinning" observed in experiment. Gupta *et al.* [2000] observed this intriguing phenomenon in their experiments, wherein at a fixed high value of ε, a plot of $\overline{\eta}_{\rm p}/cM$ versus Wi shows a maximum. Beyond a threshold value Wi, $\overline{\eta}_{\rm p}/cM$ *decreases* with increasing Wi. Remarkably, this decrease cannot be attributed to discrepancies due to molecular weight scaling of $\overline{\eta}_{\rm p}$, since it is observed to occur even for a single polymer solution. That is, above the threshold Wi, $\overline{\eta}_{\rm p}$ *decreases* with increasing extensional strain-rate. In a different study, Dubbelboer [2004] observed a similar decrease in the mean fractional stretch of stained DNA molecules beyond a threshold Wi in planar and uniaxial extensional flows. The lack of any extension-thinning in the simulations' results is illustrated in Fig. 8.10, where $\overline{\eta}_{\rm p}^{\dagger}/N_{\kappa}^2$ is plotted for two different values of N_{κ}. Interestingly, Li and Denn [2004] have predicted extension-thinning in the steady-state extensional viscosity, with Monte Carlo simulations of *free-draining* FENE chains. However, steady-state results obtained with the FD-P and FD-PG models in this study show no such decrease in the extensional

viscosity with increasing strain rate.

5. The prediction of N_1^* in Fig. 8.11 (a) following cessation of extensional flow for the same solution is observed to agree well with the experimental measurements during the initial stages of the relaxation. However, the experimental decay is faster and attains much lower values with the progress of time.

6. The disagreement is severe in the stress-relaxation phase in Fig. 8.11 (b), and this is preceded by a less marked but still significant deviation in the stress-growth stage.

8.3 Deviations between theory and experiment

There seem to be at least three possible sources for the deviations listed above.

8.3.1 Errors in extrapolations

Firstly, even after applying the extrapolation procedure described in Section 8.1, it may not be possible to completely eliminate the influence of coarse-graining. This is particularly true for the larger values of $N_{\mathrm{K}} = 13747$, and 8727, for which the largest value of N used was 100, which implies $N_{\mathrm{K,\,s}} \sim 100$. The effect of coarse-graining may be more severe for predictions of stress-relaxation where a rapid initial decay of the stress is observed in experiment. This rapid dissipation is understood to be caused by the fast rotational diffusive motion of the individual Kuhn segments [Doyle *et al.*, 1998], and an extrapolation based on the trends obtained with coarse bead-spring chains may not be reliable. To resolve this issue with absolute certainty, one would require in principle the firm establishment of the SFG extrapolation procedure by comparison with full bead-rod model simulations across a wide range of parameter values. Nevertheless, from the trends obtained in this study for the variation of $N_{1,\mathrm{p}}^*$ with respect to N_{s}—of which Fig. 8.12 is an example—the differences observed in the relaxation phase appear too large to be completely attributable to errors due to extrapolations. This is also true of the deviations observed in the stress-growth phase in Figs. 8.8 and 8.9.

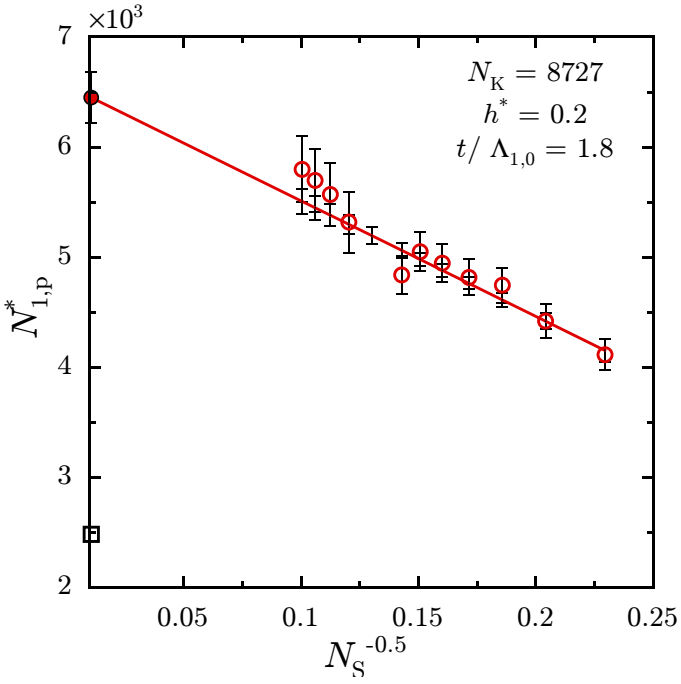

Figure 8.12: SFG extrapolation of predictions of the dimensionless normal stress difference $N^*_{1,\mathrm{p}}$ in the stress-relaxation phase of Fig 8.11 (b), to the $N_\mathrm{s} \rightarrow N_\mathrm{K}$ limit (solid red circle). The open red circles are results of simulations for $h^* = 0.2$, while the continuous line is a linear fit through the data. The open square symbol in the figure represents the experimentally measured value.

8.3.2 Lack of hydrodynamic detail in the model

The second possible cause for the deviations between predictions and experiment could be a consequence of the lack of detail in the model in describing local hydrodynamic characteristics of the real polymer. As explained in at the beginning of this Chapter, the importance of local hydrodynamic details can be gauged by looking at the sensitivity of the extrapolated results to the parameter h^*_K. Although a more quantitative analysis of the sensitivity of the extrapolated results to h^*_K can be in principle be carried out, this could not be done in this study as a result of the large size of the errors in the extrapolated results, obtained with both the simulations and approximations.

Visually, however, it appears from Figs. 8.8 (a) to (d) that the sensitivity of the predictions to h^*_K is small compared to the overall scale of variation in $\overline{\eta}^\dagger_\mathrm{p}$. Predictions at lower Wi values seem more sensitive to model parameters. For $Wi = 2$ and

3.8, this sensitivity of $\overline{\eta}_{\mathrm{p}}^{\dagger}$ to h_{K}^{*} appears to increase with strain. The increased at sensitivity at $\varepsilon \gtrsim 3$ for the two lower values of Wi [Figs. 8.8 (a) and (b)] suggests that local chemical details may exert a noticeable influence under these conditions. It is also under these conditions that deviations between theory and experiment are observed. At the two higher values of Wi considered in Figs. 8.8 (c) and (d), the sensitivity of the extrapolated results to h_{K}^{*} is smaller, and the agreement with experiment is also much improved.

8.3.3 Physical phenomena not accounted for in the model

As mentioned earlier, the third reason why deviations between theory and experiment can occur is the existence of phenomena that are not important at equilibrium, but come into play under the conditions examined.

For instance, an examination of the evolution of individual chains configurations using Brownian dynamics simulations reveals that chains are compressed strongly in the direction transverse to the principal flow direction in a uniaxial extensional flow. This causes different parts of the chain to approach each other quite closely, and in most cases, the existence of HI leads to a marked retardation of the unravelling process [Agarwal, 2000; Hsieh and Larson, 2004]. As is well known, however, modeling HI using the Oseen-Burgers tensor and its variants (such as the RPY tensor) cannot accurately describe the interactions between particles that are physically close [Kim and Karrila, 1990]. Under such conditions, more detailed modeling of the near-bead HI may become necessary.

Further, polymer molecules at the theta state are modeled in the current paradigm by setting the EV potential to zero. On the other hand, there have been studies which have used EV potentials (such as the Lennard-Jones 6-12 potential) in which the strengths of short-range repulsive and long-range attractive components are so adjusted to give the required molecular weight scaling of static equilibrium properties under theta conditions. Larson [2004] has pointed to the possibility that even in theta solutions, when beads are squeezed together in strong extensional flows, the existence of an attractive part in the EV potential may also contribute to the retardation of the unravelling process, leading to lower values of the $\overline{\eta}_{\mathrm{p}}^{\dagger}$ at high strains observed in experiments.

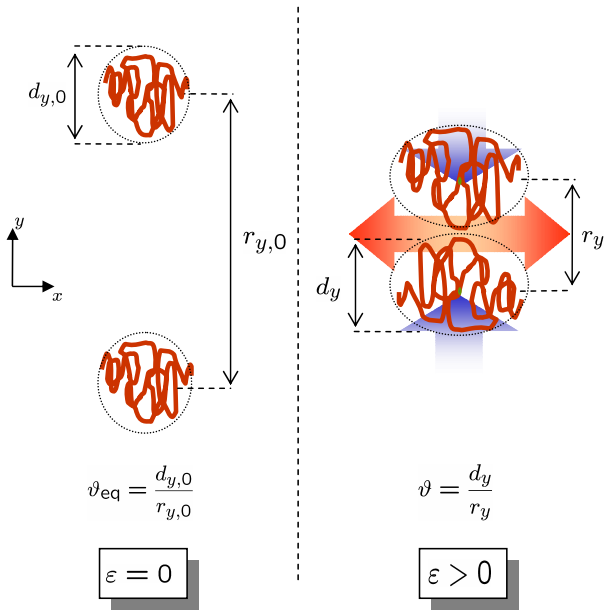

Figure 8.13: Schematic illustration of lateral overlap of polymer coils.

The results of the simulations performed in this work also reveal another intriguing possibility. In a uniaxial extensional flow, the compression in the direction transverse to the direction of stretching (the x-direction) could lead to a greater interaction between adjacent polymer molecules during flow than at equilibrium.

This possibility of "self-concentration" is first demonstrated for the highly idealized situation of two chains whose centres-of-masses at equilibrium have exactly the same x-component, but are separated by a distance of r_0 in the y-direction. This situation is schematically illustrated in Fig. 8.13. After the imposition of a strong steady uniaxial extensional flow, the centres-of-masses[1] are assumed to move affinely towards each other, that is $r(\varepsilon) = r_0 e^{-\varepsilon/2}$. The initial separation is calculated from the number density n_{p} using $r_0 = (6\eta_{\mathrm{HCP}}/\pi n_{\mathrm{p}})^{1/3}$, where $\eta_{\mathrm{HCP}} = \pi/3\sqrt{2}$ is the packing density for spheres arranged in a hexagonally-closest packing (HCP) lattice [Weisstein, 1999].

At any instant, one measure of the average tranverse dimensions of a polymer

[1] More accurately, it is the centres of resistance which have no mean relative motion with respect to the solvent in the absence of external forces [Bird *et al.*, 1987b]. As a first approximation, this difference is ignored here.

coil is given by

$$d_y = 2\sqrt{3G_{yy}}, \tag{8.21}$$

where G_{yy} is the yy-component of the gyration tensor $\boldsymbol{G}$ [Eq. (2.98)]. The expression above for d_y is based on an estimate of the coil volume derived in Appendix E. To check whether or not a physical overlap of coils transverse to the x-direction occurs, the following "lateral-overlap" ratio is defined:

$$\vartheta = \frac{d_y}{r}. \tag{8.22}$$

A value of ϑ that is larger than unity indicates that the two adjacent chains physically overlap. Since ϑ will remain at $\vartheta_0 = d_{y,0}/r_0$ if the shrinkage in the average lateral dimensions of coils is affine and $d_y = d_{y,0}e^{-\varepsilon/2}$, the lateral overlap ratio will increase only if the lateral shrinkage does not keep pace with the motion of the centre-of-mass.

Figure 8.14 shows the prediction of ϑ for different Wi and N_{K} values calculated using extrapolated values of $G^{\dagger}_{yy}$ for $h^*_{\mathrm{K}} = 0.2$, where $\boldsymbol{G}^{\dagger}$ has been defined in Eq. 8.20 earlier. For $N_{\mathrm{K}} = 2627$, n_{p} is assigned the value shown in Table 8.2 for Solution I. In this case, the ratio $n_{\mathrm{p}}/n^*_{\mathrm{p}}$ has a low value of 0.054, when the critical number density n^*_{p} is calculated using the mean dimensions of polymer coils at equilibrium. Recalling that lines of zero slope in this plot correspond to completely affine motion, the increase of ϑ with ε in Fig. 8.14 indicates that the lateral shrinkage does not keep pace with the centre-of-mass motion of the chain. Thus, for any fixed Wi and a given value of the number density n_{p}, there exists a value of ε beyond which $\vartheta > 1$. However, with increasing Wi, the slope of the curves decreases as the variation of d_y tends towards affine shrinkage. This indicates that as Wi increases, the strains at which lateral overlap can occur becomes larger. The deviations between experiment and theory in Fig. 8.8 also follow the same pattern.

However, the picture described in Fig. 8.13 is oversimplified. For instance, even if two adjacent coils start out at equilibrium as shown in Fig. 8.13, the kinematics of a uniaxial extensional flow is such that even a small perturbation in the x-component of the centre-of-mass will result in the coils separating exponentially in the x-direction. Instead, Fig. 8.15 plots the fraction ϕ of the total volume that is

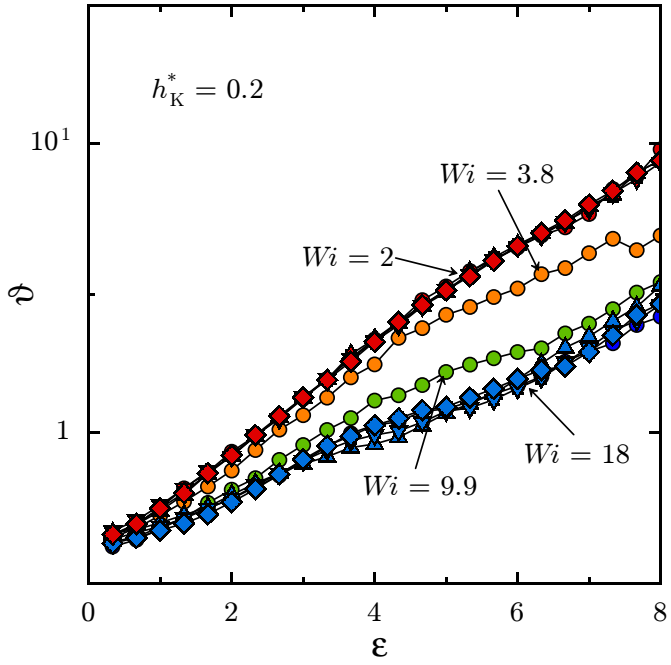

Figure 8.14: Prediction of the variation in lateral overlap ratio ϑ for different values of Wi (red symbols, $Wi = 2$; orange symbols, $Wi = 3.8$; green symbols, $Wi = 9.9$; blue symbols, $Wi = 18$), and N_K (upright triangles, $N_K = 657$; inverted triangles, $N_K = 1313$; diamonds, $N_K = 1970$; circles, $N_K = 2627$). The n_p values for $N_K < 2627$ are chosen such that the initial ϑ is identical for all chain lengths.

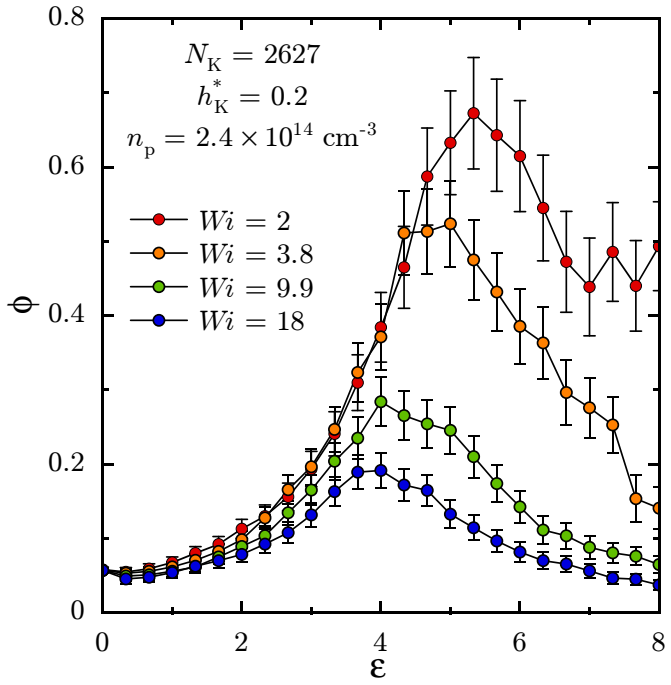

Figure 8.15: Prediction of the variation of the polymer volume fraction ϕ with respect to ε and Wi.

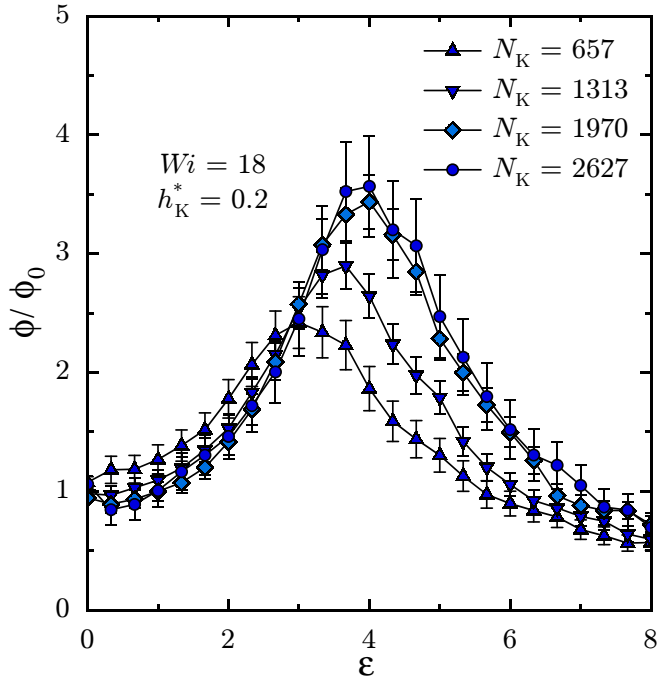

Figure 8.16: Prediction of the variation of the relative volume fraction ϕ/ϕ_0 with respect to ε for different values of N_K.

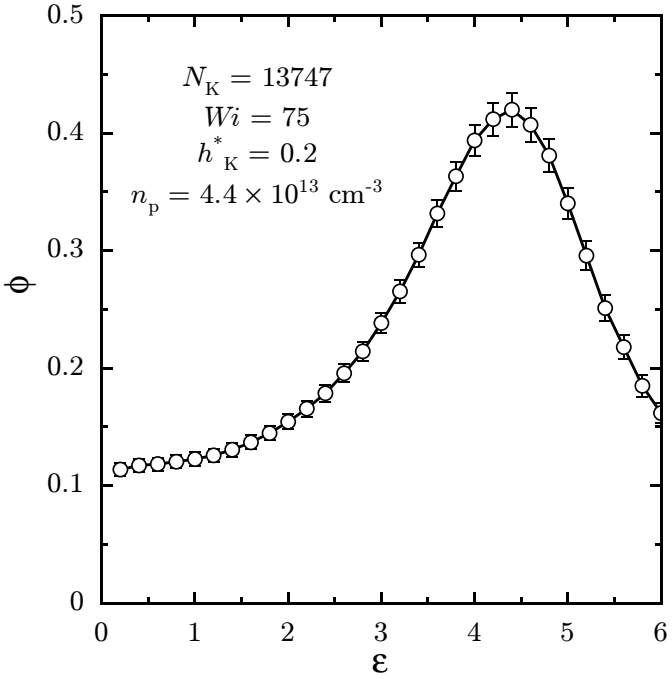

Figure 8.17: Prediction of the variation of the volume fraction ϕ with respect to ε for Solution II C.

occupied by the polymer molecules, where

$$\phi = \frac{4\pi n_{\mathrm{p}} b_{\mathrm{K}}^3}{3}\sqrt{\det[3\boldsymbol{G}^{\dagger}]}. \tag{8.23}$$

The equation above is based on an estimate derived in Appendix E for the average volume spanned by a polymer molecule, $V_{\mathrm{p}} = (4\pi/3)\sqrt{\det[3\boldsymbol{G}]}$. At equilibrium, $\boldsymbol{G}^{\dagger}_{\mathrm{eq}} = (R^2_{\mathrm{G,\,eq}}/3b^2_{\mathrm{K}})\,\boldsymbol{\delta}$, and $\phi_{\mathrm{eq}} = 4\pi n_{\mathrm{p}} R^3_{\mathrm{G,\,eq}}/3$. This is usually regarded in literature as the "c/c^*" ratio [Doi and Edwards, 1986].

Although ϕ goes through a maximum in Fig. 8.15 rather than increasing continuously like ϑ, the conclusion from the Figure is the same: there is a greater possibility for intermolecular interactions between adjacent molecules at lower Wi values. On the other hand, the influence of N_{K} on the coil overlap as predicted by ϕ is different from that predicted by ϑ: while chain length has little effect on the latter, ϕ is observed to increase with N_{K} in Fig. 8.16. This is to be expected, since the near-independence of ϑ on N_{K} behaviour in Fig. 8.14 suggests that $G_{yy} \sim N_{\mathrm{K}}$ at all strains, whereas at high strains when chains approach full stretch, $G_{xx} \sim N^2_{\mathrm{K}}$. Therefore, $\phi/\phi_0 \sim \sqrt{G_{xx}G^2_{yy}}/R^3_{\mathrm{G,eq}} \sim \sqrt{N_{\mathrm{K}}}$ at higher strains. Thus, for the same initial volume fraction ϕ_0, solutions of higher molecular weight samples are more likely to show the influence of direct intermolecular interactions.

In Fig. 8.15, it is seen that for the values of Wi considered, the maximum value of ϕ does not exceed 0.5. It was observed in Figs. 8.8 (a) to (d) that experimental data are well predicted for the two larger values of Wi considered for $N_{\mathrm{K}} = 2627$. For the lower Weissenberg numbers, on the other hand, the peak volume fractions predicted by the theoretical calculations are higher than 50 %. Under such conditions, the influence of fluctuating intermolecular HI becomes as important as intramolecular interactions. Although simulations predict that ϕ decreases at high strains, once intermolecular interactions become important, the theory used to obtain these predictions is no longer correct, and hence predictions must be ignored.

If intermolecular interactions are the reason why the theory deviates from experiment, then correlating the variation in ϕ shown in Fig. 8.15 with the results in Figs. 8.8 (a)-(d), it appears that the dilute solution theory is accurate as long as $\phi \lesssim 0.5$. This also seems to be supported by comparing the differences between extrapolated results in Fig. 8.9 and experimental data for Solution II C, with the

strain variation in ϕ presented in Fig. 8.17 for the same solution and flow conditions. For the more dilute solutions, Solutions II A and B, the maximum in the ϕ-versus-ε curve (proportional to the initial ϕ_0) will be even be further below 0.5 than the curve shown in Fig. 8.17. For these solutions, not only do experimental data at higher strains lie closer to the predicted behaviour, but the dependence of the experimental value of $\overline{\eta}_{\mathrm{p}}^{\dagger}$ on concentration is also negligible. However, even these data are clearly lower than model predictions, and in fact lie on the extension-thinning arm at $\varepsilon = 6$ [Fig. 8.10]. (Moreover, for these more dilute solutions, deviations are observed at the lower strains in Fig. 8.9.) Thus, the observation of extension-thinning in experiment may not be due to intermolecular interactions.

Interestingly, the results of the simulations indicate that the possibility of interactions between neighbouring molecules is enhanced in a stress-relaxation experiment after the cessation of flow. It is observed in simulations that the rate of decrease in G_{xx} in the stress-relaxation phase is smaller than the rate at which G_{yy}^2 increases [Fig. 8.18]. Since the coil volume depends on the product of these two quantities, the overall volume fraction does not decrease initially as rapidly as G_{xx}, but may in fact grow in the period following flow stoppage. Eventually, the volume fraction will relax back to its equilibrium value. This may however happen only at time-scales much larger than the rather brief post-cessation observation period for which most experimental data are typically collected. For instance, Fig. 8.19 shows that for the stress-relaxation experiment considered in Fig. 8.11 (b), the model predicts $\phi > 1$ even before commencement of the relaxation phase. This is essentially due to the adverse combination of a high value of N_{K} and a low Wi. Further, after relaxation begins, the volume fraction predicted by the dilute solution theory does not change significantly in the period for which experimental data is available. Thus, for Solution III, it may be possible to attribute the large differences observed between theory and experiment in Fig. 8.11 (b) to intermolecular interactions. On the other hand, in the case of the stress relaxation experiment shown in Fig. 8.11 (a) for Solution II A, Fig. 8.19 also shows that self-concentration effects may not be behind the deviations seen in the relaxation phase.

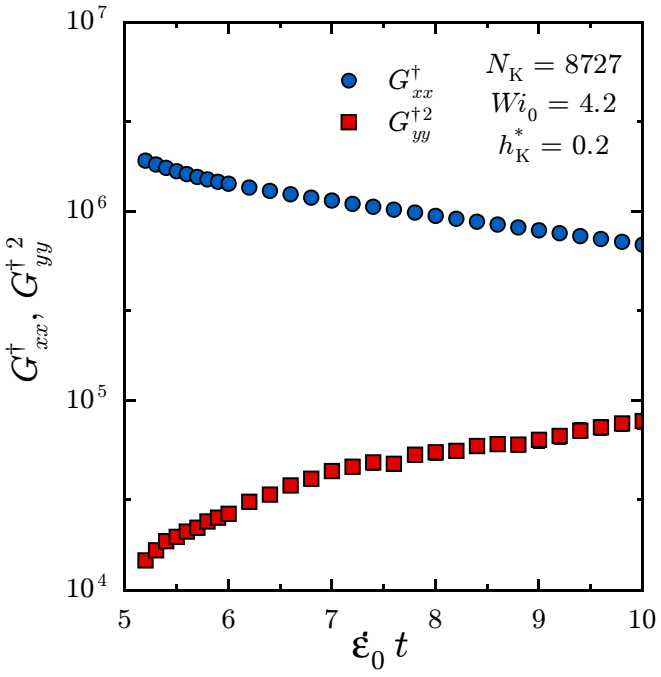

Figure 8.18: Prediction of the variation of $G^{\dagger}_{xx}$ and $G^{\dagger 2}_{yy}$ with respect to ε after cessation of extensional flow of $Wi_0 = 4.2$ at $\varepsilon_0 = 5.2$.

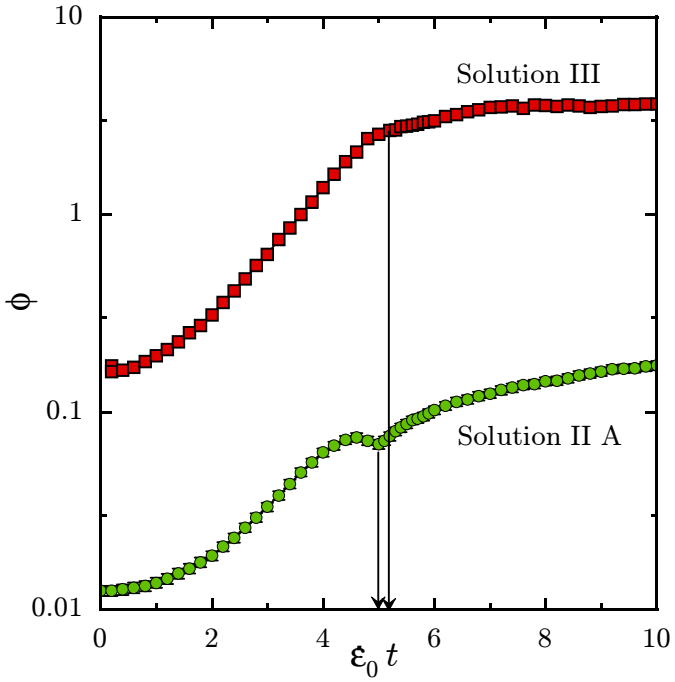

Figure 8.19: Prediction of the variation of the polymer volume fraction ϕ with respect to $\dot{\varepsilon}_0 t$ for Solutions II and III in Table 8.2 in stress-growth/relaxation experiments. The arrows mark the values of ε_0 at which flow is stopped.

8.4 Experimental comparison and closure approximations

The results for $\overline{\eta}^{\dagger}_{\rm p}$ obtained with closure approximations can also be extrapolated to obtain predictions in the $N_{\rm s} \rightarrow N_{\rm K}$ limit. Since the values obtained with the approximations are free of errors due to Brownian noise, it is possible to fit low order polynomials directly to the $\overline{\eta}^{\dagger}_{\rm p}$-versus-$1/\sqrt{N_{\rm s}}$ data and set $N_{\rm s} = N_{\rm K}$ in the fitted polynomial expressions to obtain the extrapolated value of $\overline{\eta}^{\dagger}_{\rm p}$. Figure 8.20 shows extrapolations for the CA-P, GA-P and TFN-P models, for $N_{\rm K} = 2627$, $h^* = h^*_{\rm K} = 0.2$ and $Wi = 18$, and compares these with the results of BD simulations for the same parameters (Fig. 8.5). The FENE-PG approximation was developed late in this study, and extrapolated results with this spring force approximation have not been obtained in this study. Table 8.4 shows the parameters used for carrying out the SFG procedure with the results of the closure approximations, for comparing with experiments, and the results obtained with the BD simulations discussed in the previous Section.

Figures 8.21 (a) to (d) compare the extrapolated results obtained with the CA-P, GA-P and TFN-P approximations with experimental data on Solution I. While Figs. 8.21 (a) and (b) present results for $Wi = 2$, for $h^*_{\rm K} = 0.2$ and 0.3, respectively, results for $Wi = 18$ for the same values of $h^*_{\rm K}$ are shown in Figs. 8.21 (c) and (d). As observed in Chapter 6, the predictions of the approximations agree closely with the results obtained with BD simulations at low strains, when the influence of FE is negligible. At these low strains, predictions of both simulations and approximations (coloured lines) for $N_{\rm K} = 2627$ are close to the universal $\overline{\eta}^{\dagger}_{\rm p}$-versus-$\varepsilon$ predictions obtained with the TFN-H approximation (black lines).

The universal predictions in Figures 8.21 (a) to (d) were obtained by following the same procedure used by Öttinger and co-workers [Prakash and Öttinger, 1997; Zylka and Öttinger, 1991] for steady-state rheological properties in shear, and discussed earlier in the previous Chapter. Predictions of the TFN-H approximation for the variation of the ratio $U_{\overline{\eta}}$ with ε for the two different values of $Wi = 2$ and 18 shown in Fig. 8.21, were collected for values of N ranging from 20 to 200, for $h^* = 0.2$, 0.25 and 0.3. These results were then extrapolated to the infinite chain limit, by

Table 8.4: Values of parameters used with closure approximation, for comparing with experimental data.

N_κ	Wi	N	h^*	Model
13747	30, 75	20 – 100	0.2	TFN-P
8727	4.2	20 – 100	0.2	TFN-P
2627	2.0, 3.8, 9.9, 18	20 – 100	0.2, 0.3	CA-P, GA-P, TFN-P

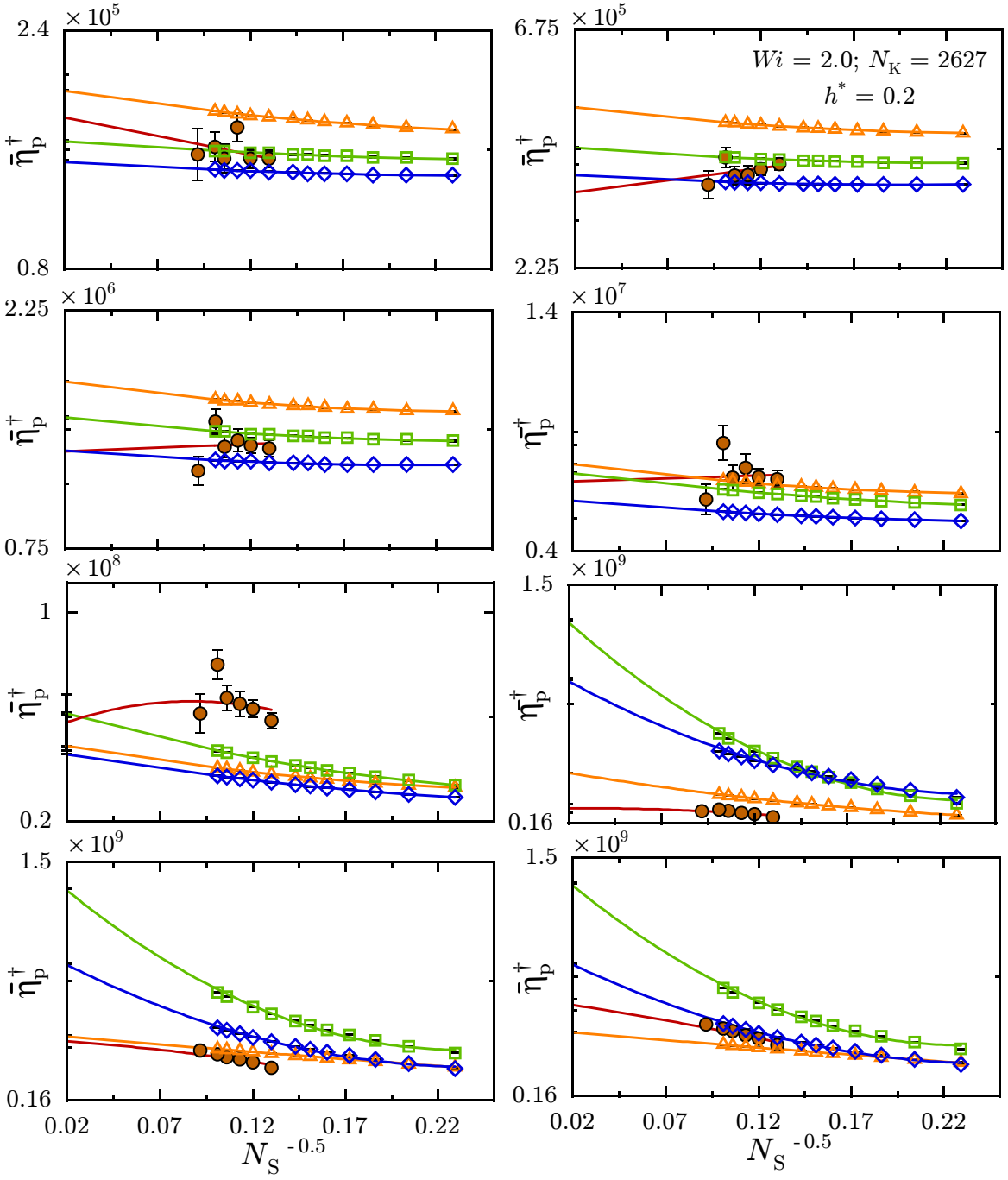

Figure 8.20: Extrapolations of the dimensionless extensional viscosity $\overline{\eta}_{\rm p}^{\dagger}$ predicted by closure approximations, to the $N_{\rm S} \to N_{\rm K}$ limit. Symbols (CA-P model, open orange squares; GA-P model open green squares, and TFN-P model, open blue squares) are results of the approximations, while continuous lines through the symbols are curve fits through the data. The solid red circles are the results of BD simulations for $h^* = 0.2$, shown earlier in Fig. 8.5.

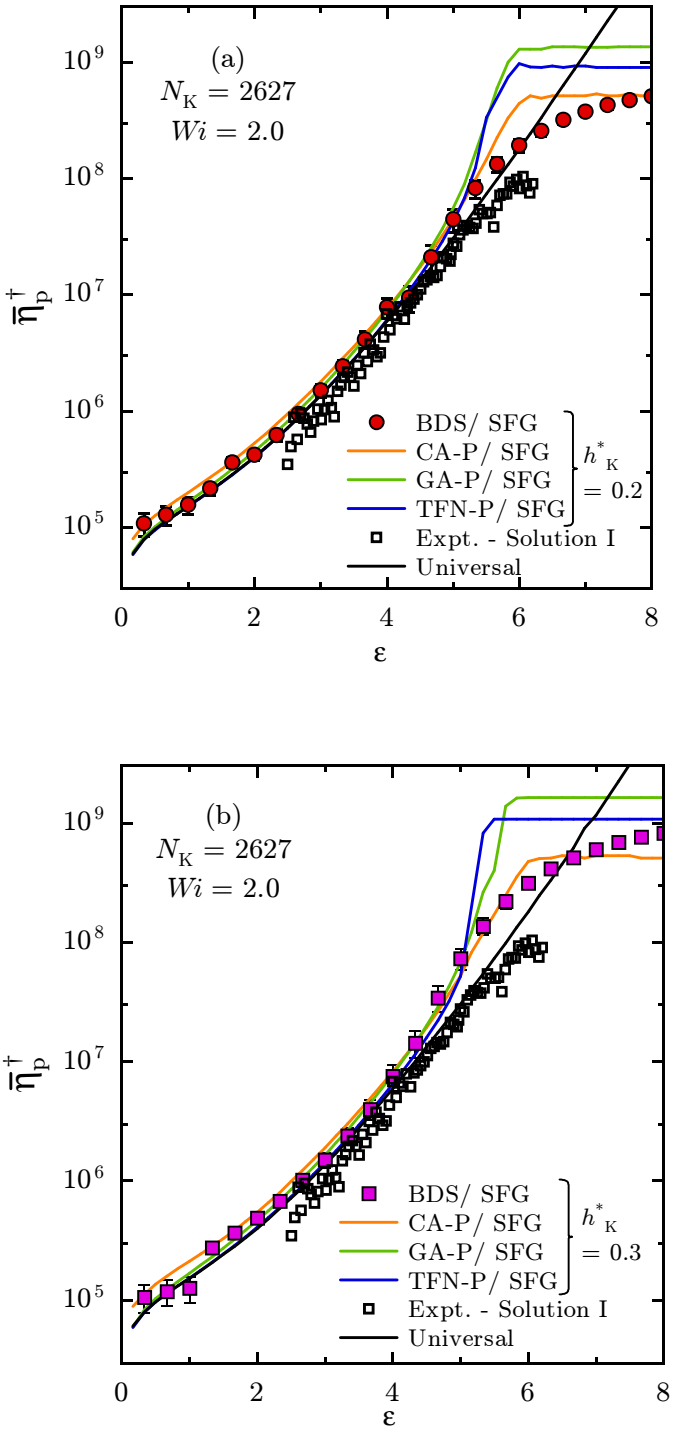

Figure 8.21: Comparison of extrapolated results obtained using closure approximations, for the growth of the dimensionless extensional viscosity $\overline{\eta}_p^+$, with experimental data (open squares) obtained with Solution I in Table 8.2, and extrapolated results obtained using BD simulations. The solid black line is the universal prediction $\overline{\eta}_p^+ = U_{\overline{\eta}}^{\infty} N_K^{3/2}$ obtained by extrapolating results of the TFN-H model obtained with finite values of N_S to the $N_S \to \infty$ limit.

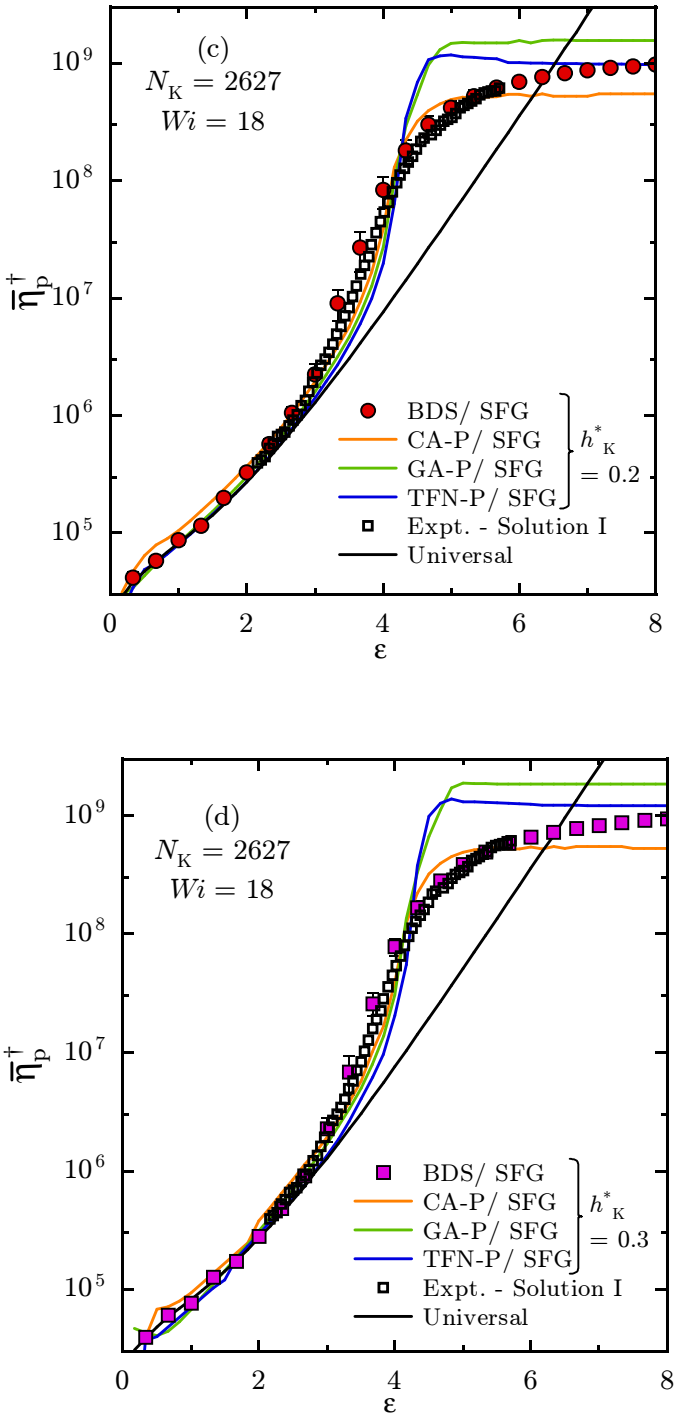
(c)
$N_K = 2627$
$Wi = 18$
10^9
10^8
10^7
10^6
10^5
$\bar{\eta}_p^+$
0
2
4
6
8
ε
BDS/ SFG
CA-P/ SFG
GA-P/ SFG
TFN-P/ SFG
$h^*_K = 0.2$
Expt. - Solution I
Universal
(d)
$N_K = 2627$
$Wi = 18$
10^9
10^8
10^7
10^6
10^5
$\bar{\eta}_p^+$
0
2
4
6
8
ε
BDS/ SFG
CA-P/ SFG
GA-P/ SFG
TFN-P/ SFG
$h^*_K = 0.3$
Expt. - Solution I
Universal

Figure 8.21

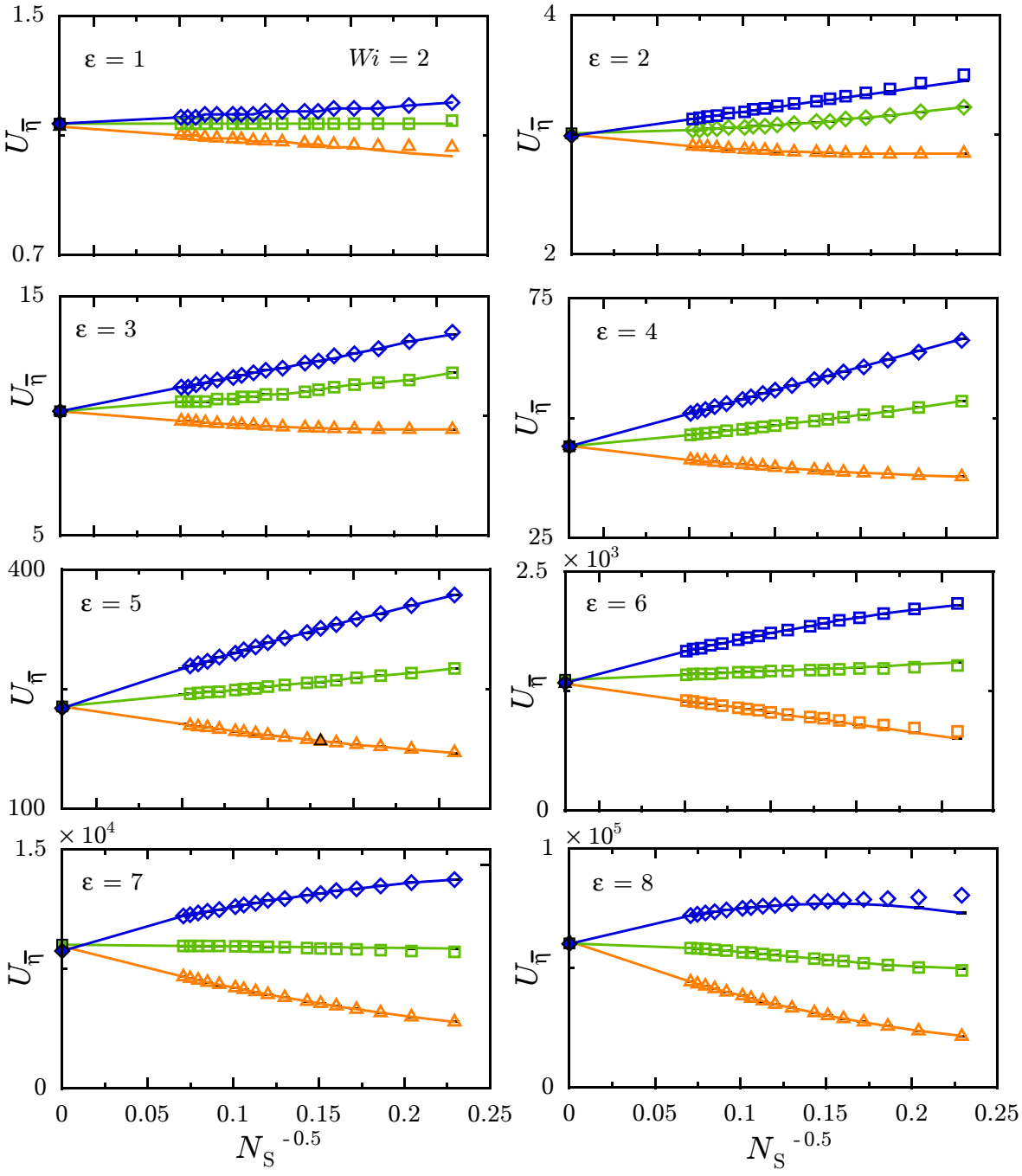

Figure 8.22: Extrapolations of the ratio $U_{\overline{\eta}}$ predicted by the TFN-H approximation, to the $N_s \to \infty$ limit. Symbols ($h^* = 0.2$, open orange triangles; $h^* = 0.25$, open green squares; $h^* = 0.3$, open blue diamonds) are predictions obtained with the approximation, while continuous lines through the symbols are curve fits through the data. The extrapolated values for $U_{\overline{\eta}}^{\infty}$, for each of the three different values of h^* is indicated by the solid symbols. The errors in the extrapolated values are smaller than the solid symbols.

fitting low-order polynomials through the data obtained at finite values of N_s. For each value of h^*, the choice of the polynomial fit through the data was optimized using the TEXTRA algorithm described by Öttinger [1996a]. The extrapolated values thus obtained at the different values of ε and Wi represent the prediction of the universal function $U_{\overline{\eta}}^{\infty}(\varepsilon, Wi)$ by the TFN-H approximation. Figure 8.22 shows the predictions of the approximation and the polynomial extrapolations for several values of ε, at $Wi = 2$.

It is seen in Fig. 8.22 that the extrapolated values obtained in the infinite chain limit are independent of h^*. From the Figure, it is apparent that the value of the fixed point for bead-spring chains lies between 0.2 and 0.25, since the data for $h^* = 0.2$ and $h^* = 0.25$ approach their infinite chain limits from below and above, respectively. The same behaviour is also observed at the higher value of $Wi = 18$ (not shown). The behaviour in Fig. 8.22 strongly suggests that the fixed point value is independent of the strain or the Weissenberg number, as shown analytically by Zylka and Öttinger [1991] using RG theory.

The universal $\overline{\eta}_p^{\dagger}$-versus-$\varepsilon$ prediction shown in Fig. 8.21 is calculated using Eq. (8.3) with the $U_{\overline{\eta}}^{\infty}(\varepsilon, Wi)$ function, so that $\overline{\eta}_p^{\dagger}(\varepsilon, Wi) = U_{\overline{\eta}}^{\infty}(\varepsilon, Wi)\, N_K^{3/2}$. For both the values of Wi considered in Figs. 8.21 (a) to (d) it is seen that experimental data at low strains are very close to the universal curves for $\overline{\eta}_p^{\dagger}$. Similar agreement has been obtained by Sunthar and Prakash [2005], who compared the universal results for transient extensional flows obtained by extrapolating the results of BD simulations, with the experimental measurements of DNA extension in planar extensional flows made by Smith and Chu [1998]. The results of Sunthar and Prakash also account for the effect of solvent quality, and along with the results shown in Fig. 8.21 (a) to (d), *constitute the first parameter-free experimental validation of the phenomena of HI and EV in the nonlinear viscoelastic regime, where FE is not dominant.*

At higher values of ε, the influence of FE becomes important, and deviations between approximations, simulations and experiments begin to grow. The behaviour of the approximations at these higher strains show the same qualitative features observed in Chapter 6 earlier, in Section 6.4. The deviations between BD simulations and the approximations are observed to be largest in the range of intermediate strains before the attainment of steady-state. The direction of the deviations of the

approximations' predictions—initial underprediction followed by overprediction—was shown to be be largely due to the mean-field approximation used for the FENE nonlinearity. Further, fluctuations in HI which are accounted for in the Gaussian approximation lead to higher extensional viscosities as the chains become stretched. Although the diagonalization assumption in the TFN-P approximation causes its predictions to differ from those of the un-diagonalized GA-P approximation, the TFN-P approximation is not bad in its predictions in the stress-growth phase.

In Figs. 8.23 (a) and (b), extrapolated results obtained with the TFN-P approximation for stress relaxation following the cessation of extensional flow are compared with experimental data on Solutions II A and III (Table 8.2), respectively. It is clear that the prediction of stress relaxation by the approximation is not very accurate, in comparison with both BD simulations' results and experimental data. The use of the diagonalization approximation was identified in Chapter 6 as the cause for the deterioration of the TFN-P approximation in the stress relaxation phase.

8.5 Molecular weight scaling

As mentioned earlier in the previous Chapter, Gupta *et al.* [2000] observed that the transient extensional viscosity of solutions of different molecular weights and concentrations can be collapsed onto master plots of the form $\overline{\eta}_{\rm p}/cM = f(\varepsilon, Wi)$. Since $c \sim n_{\rm p}M$, this suggests that any fixed Hencky strain and Wi, $\overline{\eta}_{\rm p}/n_{\rm p} \sim M^2 \sim N_{\rm K}^2$.

On the theoretical front, Öttinger [1987b] has shown using a FEBS model with consistently-averaged HI that for any arbitrary homogeneous flow, characterized by a constant strain-rate, in the limit of infinitely long chains, the dimensionless large-scale properties such as the viscosity indeed approach universal functions of a Weissenberg number and a strain measure defined as the product of the strain-rate and time. It is possible to show that the equations of Öttinger imply $\overline{\eta}_{\rm p}^{\dagger} \sim N_{\rm K}^{3/2}$ at any fixed Weissenberg number and strain. This was demonstrated in the previous Section, where the existence of the universal infinite-chain limit $U_{\overline{\eta}}^{\infty}(\varepsilon, Wi)$ meant that for long chains $\overline{\eta}_{\rm p}^{\dagger} \approx U_{\overline{\eta}}^{\infty}(\varepsilon, Wi) N_{\rm K}^{3/2}$ at small strains. As chains are stretched

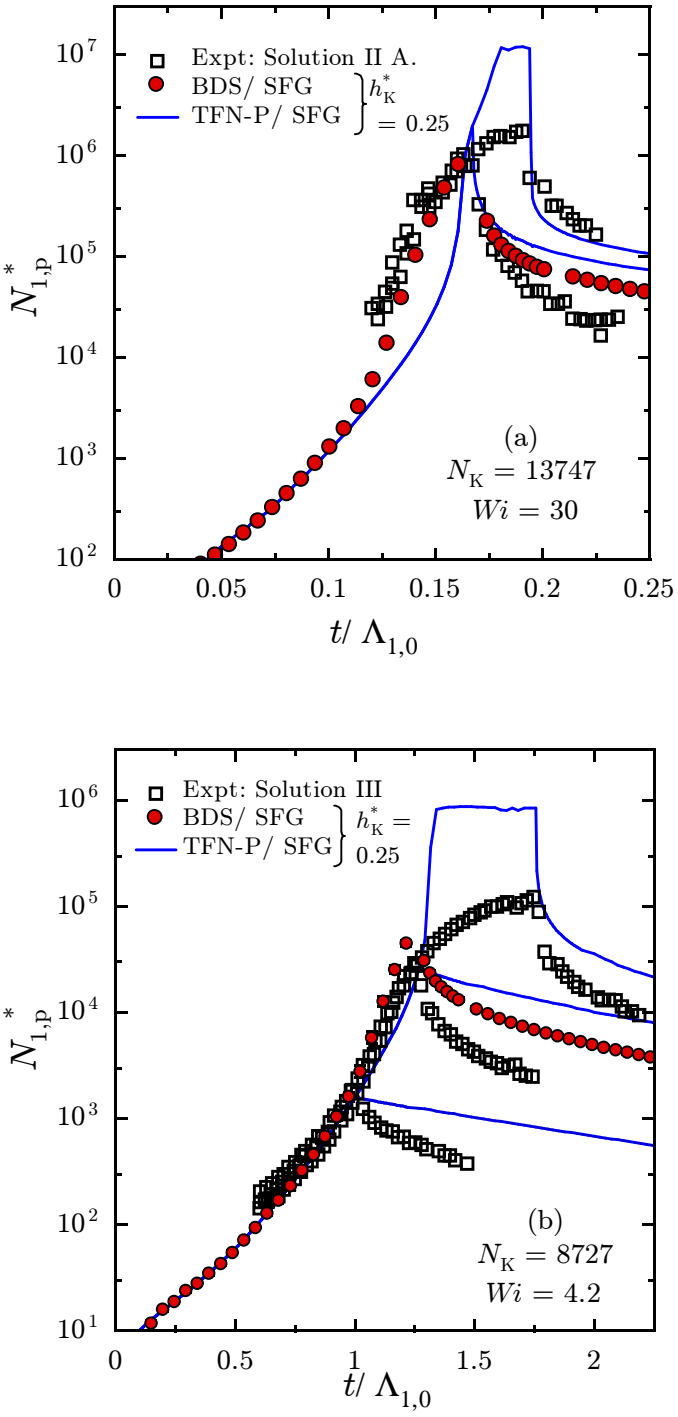

Figure 8.23: Comparison of extrapolated results of the growth and relaxation of the first normal-stress difference $N_{1,p}^*$ obtained with the TFN-P approximation, with the experimental data for (a) Solution II A, and (b) Solution III in Table 8.2.

out close to their full extension, Eq. (8.7) shows that for long chains

$$\overline{\eta}_{\mathrm{p}}^{\dagger} \approx \frac{\pi}{6} \frac{N_{\mathrm{K}}^3}{\ln(N_{\mathrm{K}}/2)}. \tag{8.24}$$

Therefore, it is expected that when Wi is greater that the critical value for the coil-to-stretch transition, polymer molecules will align, unravel and stretch out close to their full contour length. Therefore, as steady-state is approached, $\overline{\eta}_{\mathrm{p}}^{\dagger}$ will begin to scale roughly as N_{K}^3. The experimental observation of an exponent of 2 hence lies between the value of 3/2 predicted for low strains, and the value of 3 predicted at high strains.

Since the SFG procedure corrects for the influence of coarse-graining, it is possible to use the results of BD simulations to obtain a clearer picture of the scaling of the extensional viscosity with respect to molecular weight. Figure 8.24(a) shows the predictions obtained in this study using the SFG procedure for the growth of $\overline{\eta}_{\mathrm{p}}^{\dagger}$ for four different values of N_{K}, with fixed $Wi = 18$. In Fig. 8.24(b), the variation of the effective exponent μ with respect to ε is examined, where μ is obtained by fitting a power-law $\overline{\eta}_{\mathrm{p}}^{\dagger} = C N_{\mathrm{K}}^{\mu}$ through the data for the different N_{K} values, at each value of ε. It is observed that μ is not a constant, but is a function of both Wi and ε.

In Fig. 8.24 (b), it is observed that the effective exponent μ is close to 3/2 at low strains as expected, for both the values of Wi considered. At higher strains, the exponent approaches a value close to 3. One of the reasons for the master curves observed by Gupta *et al.* could be that the intermediate value of $\mu = 2$ acts as an apparent exponent in the range of ε for which the experimental data were obtained, since it is not possible to resolve the variable exponent more accurately in experiments.

Interestingly, the approach of the exponent $\mu(\varepsilon)$ to its steady-state value is non-monotonic. At higher Wi, the dip in the value of the exponent is more pronounced and occurs at a smaller ε. From Fig. 8.24 (a), it is apparent that this dip is caused by the crowding together of the $\overline{\eta}_{\mathrm{p}}^{\dagger}$ versus ε curves for the different N_{K} values, at values of $\varepsilon \approx 3$. The crowding together of the different curves can be understood by recalling the argument by Hinch [1994], who pointed out that long chains initially stretch nearly affinely when placed in a strong elongational flow. As the coils unravel,

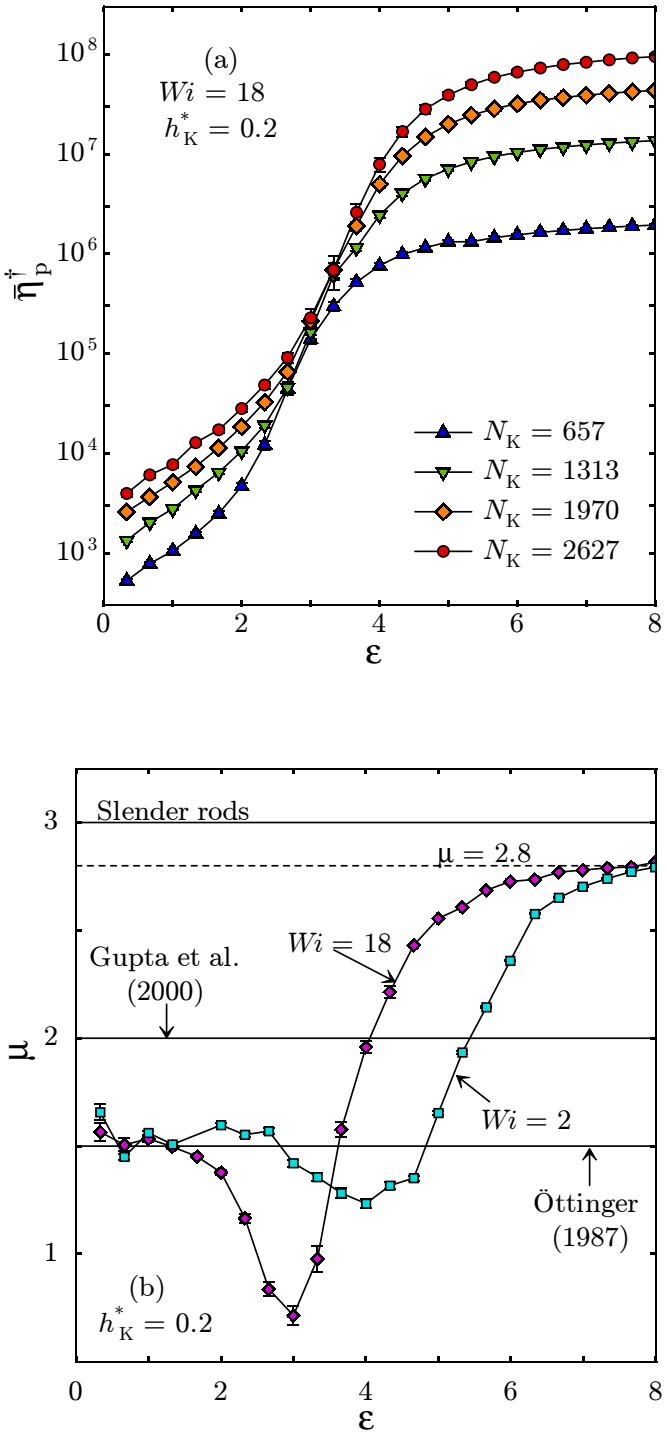

Figure 8.24: (a) Predictions of the dimensionless extensional viscosity $\overline{\eta}^\dagger_p$ versus ε for different values of N_K, at $Wi = 18$. (b) Variation of the effective scaling exponent μ in $\overline{\eta}^\dagger_p \sim N_K^\mu$, with ε. The horizontal lines in (b) correspond to the exponent predicted by Öttinger [1987b] ($\mu = 3/2$), the scaling reported by Gupta *et al.* [2000] ($\mu = 2$), and the asymptotic steady-state prediction for slender rods in strong extensional flows($\mu = 3$).

the chains begin to "feel" the effects of their finite extensibility when $e^{2\varepsilon} \approx L^2/R^2_{\mathrm{e,\,eq}}$, or when $\varepsilon = 0.5 \ln N_{\mathrm{K}}$. Although this argument was made originally in the context of free-draining chains, Fig. 8.25 shows that this is approximately true for chains with HI as well: the ratio of R^2_{e} predicted in flow by the simulations, to $R^2_{\mathrm{e,\,eq}} e^{2\varepsilon}$–the value expected if the coil deformation is affine–shows a brief plateau at lower values of ε, indicating that $R^2_{\mathrm{e}} \sim e^{2\varepsilon}$, and the chains undergo nearly affine stretching. Soon afterwards, finite extensibility causes chain stretching to slow down considerably. Additionally, the size of the affine-stretch plateau in Fig. 8.25 increases slowly with N_{K}. Therefore, the Hencky strain at which chains with HI begin to feel their finite length also increases as $0.5 \ln N_{\mathrm{K}}$. Hinch also found that the onset of FE dominated behaviour is accompanied by a sharp increase in the extensional stresses at $\varepsilon \approx 0.5 \ln N_{\mathrm{K}}$. In plots of $\overline{\eta}^{\dagger}_{\mathrm{p}}$ against ε for different values of N_{K}, the rightward shift for larger values of N_{K}, of the strain at which the rapid increase in $\overline{\eta}^{\dagger}_{\mathrm{p}}$ occurs, leads to a narrowing of the vertical separation between different curves in a small range of values of ε.

Hinch showed that the $\overline{\eta}^{\dagger}_{\mathrm{p}}$-versus-$\varepsilon$ curves, can be collapsed beyond $\varepsilon \gtrsim 1/2 \ln N_{\mathrm{K}}$ onto a master curve when $\overline{\eta}^{\dagger}_{\mathrm{p}}/N^3_{\mathrm{K}}$ is plotted against a modified Hencky strain $\varepsilon' = \varepsilon - 1/2 \ln N_{\mathrm{K}}$. The source of this behaviour may be understood in the light of the discussion above: the apparent rightward shift of the curves in Fig. 8.24(a) is eliminated when the data are plotted in terms of ε'. Furthermore, since the $\overline{\eta}_{\mathrm{p}}$ predicted for fully-stretched free-draining chains scales directly as N^3_{K}, normalizing by N^3_{K} leads to master curves at high Wi and strains. The exact results in Figure 8.24(b) suggest that for long chains with HI, with values of N_{K} in the range examined in this study, dividing the $\overline{\eta}^{\dagger}_{\mathrm{p}}$ data obtained at constant Wi by $N^{2.8}_{\mathrm{K}}$ will cause the curves to collapse at higher values of ε'. This is demonstrated in Fig. 8.26.

At lower values of strains ε', it is observed in Fig. 8.26 that the rescaled simulations' data do not collapse onto a unique master curve. This is to be expected, since $\overline{\eta}^{\dagger}_{\mathrm{p}} \sim N^{3/2}_{\mathrm{K}}$ for small strains, as shown in Fig. 8.24 (b). Thus, it appears that in transient extensional flows, the scaling exponent changes from an initial value of 3/2 to a value close to 3, as the finite extensibility of the chain begins to control the behaviour of the chain. Since this change is expected to occur at approximately $\varepsilon = 0.5 \ln N_{\mathrm{K}}$, it can be argued that for any *fixed* ε, as $N_{\mathrm{K}} \to \infty$, the influence

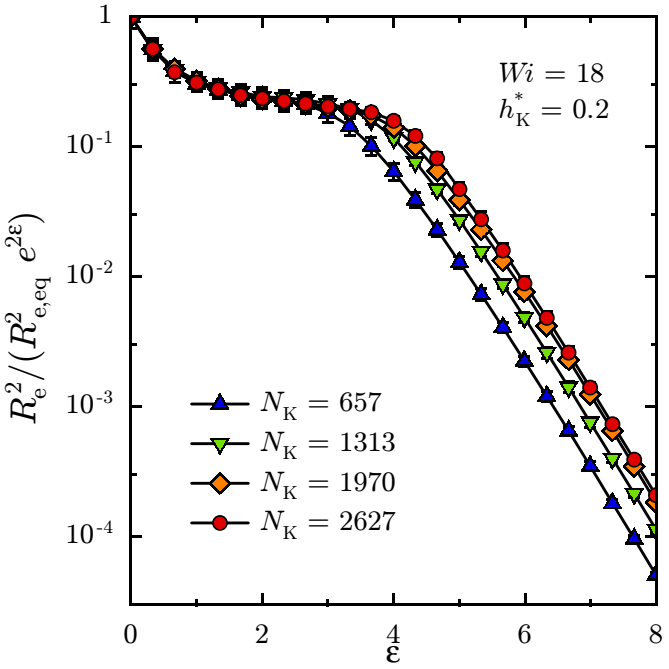

Figure 8.25: Predictions of the ratio of $R_e^2/(R_{e,eq}^2\, e^{2\varepsilon})$, versus the Hencky strain, ε. The error-bars are smaller than the size of the symbols. The slope of the curves shown at high ε values is greater than -2, the value expected if $R_e^2/R_{e,eq}^2$ attains a constant steady-state value.

of the molecules' finite contour length will diminish. At any fixed ε, therefore, for all $N_K \gg e^{2\varepsilon}$, $\overline{\eta}_p^\dagger$ will begin to scale as $N_K^{3/2}$, while for $N_K \lesssim e^{2\varepsilon}$, μ is an effective exponent that decreases from the value of 3 to its eventual asymptote of 3/2 as N_K increases.

8.6 Does neglect of HI cause a lag in the growth of the extensional viscosity?

Larson and co-workers [Li *et al.*, 2000] used Brownian dynamics simulations of FEBS chains ($N = 20$) without HI to predict the extensional flow behaviour of the experimental system of Gupta *et al.* [2000], and observed that growth of the Trouton

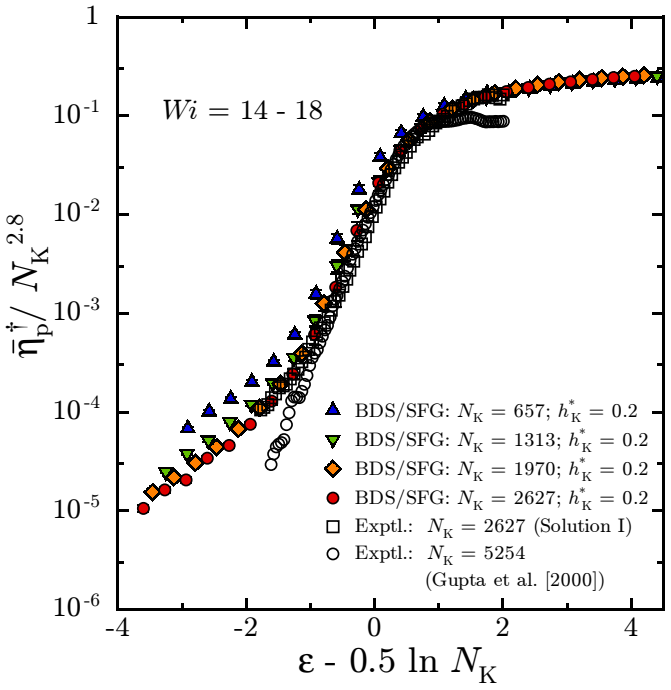

Figure 8.26: Rescaled dimensionless extensional viscosity $\overline{\eta}^{\dagger}_{\rm p}/N_{\rm K}^{2.8}$, versus the modified Hencky strain, $\varepsilon' = \varepsilon - 0.5 \ln N_{\rm K}$. The experimental data for $N_{\rm K} = 5254$ obtained by Gupta *et al.* [2000] (open circles) is at $Wi = 14$, and the rest of the data shown are at $Wi = 18$.

ratio,

$$Tr = \frac{\overline{\eta}_{\rm p} + 3\eta_{\rm s}}{\eta_0} \approx \frac{\overline{\eta}_{\rm p}}{\eta_{\rm s}} + 3, \tag{8.25}$$

(where the zero-shear-rate viscosity of the solution $\eta_0 \approx \eta_{\rm s}$ for the dilute solutions considered), lagged behind experiment considerably. This effect was more pronounced for chains of higher molecular weights. After incorporating HI in their simulations [Hsieh *et al.*, 2003], it was found that the predictions are in much better agreement with experiment. Therefore, these authors attribute the lag observed previously with free-draining chains to the neglect of HI in those simulations. This issue is reexamined here by applying the SFG procedure to simulations of free-draining chains without HI.

In their simulations of free-draining FEBS chains in extensional flows, Li *et al.* used the characteristic relaxation time $\Lambda_{\eta,0}$ to define a Weissenberg number, which

is denoted in this study as Wi_η (Section 2.5.5). To compare the behaviour of free-draining (FD) chains and chains with HI at the *same* Weissenberg number, it is necessary to use values of the strain-rates in these two models such that $\dot{\varepsilon}^{\mathrm{FD}}\Lambda^{\mathrm{FD}}_{\eta,0} = \dot{\varepsilon}^{\mathrm{HI}}\Lambda^{\mathrm{HI}}_{\eta,0}$. It can be shown that for $N_{\mathrm{s}} \gg 1$, any free-draining bead-spring chain model without EV interactions predicts [Prakash, 2001b],

$$\eta_{\mathrm{p},0} = \frac{n_{\mathrm{p}}\zeta}{36} N_{\mathrm{s}} R^2_{\mathrm{e,eq}}. \tag{8.26}$$

Therefore, one obtains for long chains

$$\Lambda^{\mathrm{FD}}_{\eta,0} = \frac{\zeta R^2_{\mathrm{e,eq}}}{36 k_{\mathrm{B}} T}\, N_{\mathrm{s}}. \tag{8.27}$$

Using $\Lambda^{\mathrm{FD}}_{\eta,0}$ and the chain's equilibrium root-mean-square length $R_{\mathrm{e,eq}}$ as the characteristic time and length-scales to non-dimensionalize the Fokker-Planck equation Eq. (2.3) for free-draining bead-spring chains (for which $\boldsymbol{\Upsilon}_{\nu\mu} = \delta_{\nu\mu}\boldsymbol{\delta}$), one obtains for arbitrary homogeneous flows,

$$Wi_\eta \left[\frac{\partial}{\partial \varepsilon} + \sum_{\nu=1}^{N} \frac{\partial}{\partial \hat{\boldsymbol{r}}_\nu} \cdot (\widetilde{\boldsymbol{\kappa}} \cdot \hat{\boldsymbol{r}}_\nu)\right] \Psi = -\frac{N_{\mathrm{s}}}{36} \sum_{\nu=1}^{N} \left[\frac{\partial}{\partial \hat{\boldsymbol{r}}_\nu} \cdot \hat{\boldsymbol{F}}^{\phi}_{\nu} + \frac{\partial}{\partial \hat{\boldsymbol{r}}_\nu} \cdot \frac{\partial}{\partial \hat{\boldsymbol{r}}^{\dagger}_\nu}\right] \Psi. \tag{8.28}$$

In this equation, $\hat{\boldsymbol{r}}_\nu = \boldsymbol{r}_\nu / R_{\mathrm{e,eq}}$ and $\hat{\boldsymbol{F}}^{\phi}_{\nu} = \boldsymbol{F}^{\phi}_{\nu} R_{\mathrm{e,eq}}/k_{\mathrm{B}}T$, and the tensor $\widetilde{\boldsymbol{\kappa}}$ has been defined earlier in Section 2.5.1. From the form of this master equation for the free-draining FEBS model, it is evident that all dimensionless predictions in extensional flows, such as

$$\hat{\overline{\eta}}_{\mathrm{p}}^{\ \mathrm{FD}} = \frac{\overline{\eta}^{\mathrm{FD}}_{\mathrm{p}}}{n_{\mathrm{p}} k_{\mathrm{B}} T \Lambda^{\mathrm{FD}}_{\eta,0}} = \frac{\overline{\eta}^{\mathrm{FD}}_{\mathrm{p}}}{\eta^{\mathrm{FD}}_{\mathrm{p},0}}, \tag{8.29}$$

are functions solely of the Weissenberg number Wi_η [Section. 2.5.5], ε, $N_{\mathrm{K,\,s}}$ and N_{s}.

Figure 8.27 plots the results of the SFG procedure for the evolution of the ratio φ introduced earlier in Section 8.1 [Eq. (8.18)] for chains with and without HI, at two different values of Wi_η. In calculating this ratio for free-draining chains, the following well known result for the extensional viscosity of dilute solutions of fully-stretched

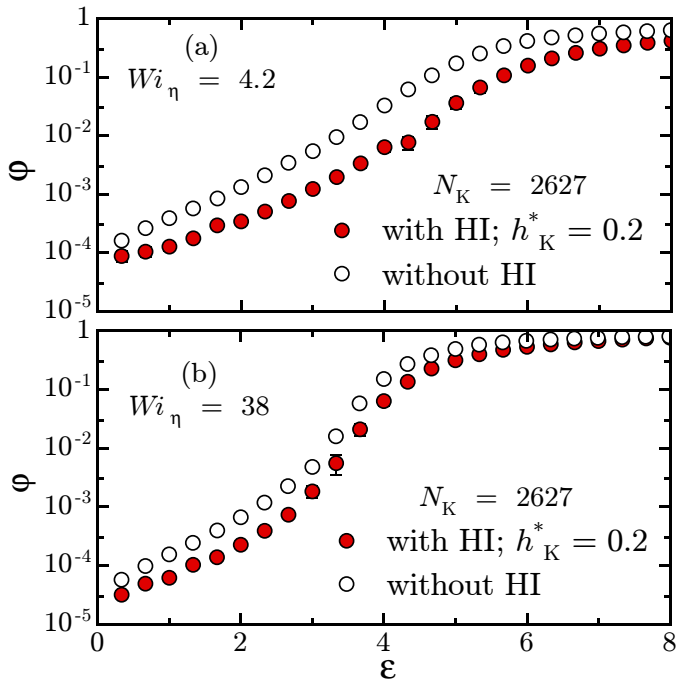

Figure 8.27: Comparison of the growth of the ratio φ predicted for chains with and without HI.

chains without HI has been used [Hassager, 1974]:

$$\overline{\eta}_p^{FD} = \frac{n_p \zeta_K b_K^2 N_K^3}{12}. \tag{8.30}$$

It is seen in Fig. 8.27 that the free-draining results for φ do not lag behind the non-draining predictions, but in fact grow faster. At the higher value of Wi_η, the two curves become almost identical, that is $\varphi^{FD} \approx \varphi^{HI}$.

Since

$$\varphi^{FD} = \frac{\overline{\eta}_p^{FD}}{n_p \zeta_K^{FD} b_K^2 N_K^3/12}, \tag{8.31}$$

and using Eq. (8.7) as a good approximation for the extensional viscosity for full-stretched bead-rod chains with HI,

$$\varphi^{HI} = \frac{\overline{\eta}_p^{HI}}{(\pi/6) n_p \eta_s b_K^3 N_K^3/\ln(N_K/2)}, \tag{8.32}$$

the approximate equality of φ at all ε for $Wi_\eta = 38$ in Fig. 8.27 implies that

$$\frac{\overline{\eta}_{\mathrm{p}}^{\mathrm{FD}}}{\overline{\eta}_{\mathrm{p}}^{\mathrm{HI}}} \approx \sqrt{3\pi} h_{\mathrm{K}}^{*\,\mathrm{FD}} \ln(N_{\mathrm{K}}/2). \tag{8.33}$$

As observed in Fig. 8.8 (d), the predicted value of $\overline{\eta}_{\mathrm{p}}^{\mathrm{HI}}$ for $Wi_\eta = 38$ ($Wi = 18$) is quite close to the values measured in experiment. The equation above therefore indicates that the ratio $\overline{\eta}_{\mathrm{p}}^{\mathrm{FD}} / \overline{\eta}_{\mathrm{p}}^{\mathrm{exp}}$ depends directly on the value of the HI parameter, or equivalently the bead friction coefficient, chosen in the free-draining model, and thus points to an explanation for the deviations observed between experimental data and predictions obtained by Li *et al.* using a free-draining model.

In their paper, Li *et al.* used the following expression for the time constant $\Lambda_{\eta,0}^{\mathrm{FD}}$ instead of the one shown in Eq. (8.34):

$$\Lambda_{\eta,0}^{\mathrm{FD}} = \frac{2.369}{6\pi^2} \frac{\zeta^{\mathrm{FD}} R_{\mathrm{e,eq}}^2}{k_{\mathrm{B}} T} N_{\mathrm{S}}, \tag{8.34}$$

By equating $\Lambda_{\eta,0}^{\mathrm{FD}}$ in the equation above to that predicted for non-draining chains,

$$\Lambda_{\eta,0}^{\mathrm{ND}} = U_{\eta,\,0}^{\infty} \frac{\eta_{\mathrm{s}} R_{\mathrm{e,eq}}^3}{k_{\mathrm{B}} T}\,, \tag{8.35}$$

the drag coefficient estimated by Li *et al.* in their free-draining model is,

$$\zeta^{\mathrm{FD}} = \frac{6\pi^2 U_{\eta,\,0}^{\infty}}{2.369} \frac{\eta_{\mathrm{s}} R_{\mathrm{e,\,eq}}}{N_{\mathrm{S}}}\,. \tag{8.36}$$

Since $h^* = \zeta/(6\pi^{3/2}\eta_{\mathrm{s}}\,\ell_{\mathrm{s}})$, and $\ell_{\mathrm{s}} = R_{\mathrm{e,\,eq}}/\sqrt{3\,N_{\mathrm{s}}}$, the value of $h^{*\mathrm{FD}}$ is estimated as,

$$h^{*\,\mathrm{FD}} = \frac{\sqrt{3\pi} U_{\eta,\,0}^{\infty}}{2.369} \frac{1}{\sqrt{N_{\mathrm{S}}}}. \tag{8.37}$$

Although Li *et al.* used $N = 20$ in their simulations, their argument can be extended to the bead-rod limit. Substituting the resulting $h_{\mathrm{K}}^{*\,\mathrm{FD}}$ obtained from the equation above in Eq. (8.33), one obtains

$$\frac{\overline{\eta}_{\mathrm{p}}^{\mathrm{FD}}}{\overline{\eta}_{\mathrm{p}}^{\mathrm{HI}}} \approx \frac{\overline{\eta}_{\mathrm{p}}^{\mathrm{FD}}}{\overline{\eta}_{\mathrm{p}}^{\mathrm{ex}}} \approx \frac{3\pi U_{\eta,\,0}^{\infty}}{2.369} \frac{\ln(N_{\mathrm{K}}/2)}{\sqrt{N_{\mathrm{K}}}} \approx 1.8 \frac{\ln(N_{\mathrm{K}}/2)}{\sqrt{N_{\mathrm{K}}}}. \tag{8.38}$$

Thus, when the predictions for the extensional viscosity obtained with chains with HI are compared with those obtained by Li *et al.* in terms the Trouton ratio defined in Eq. (8.25), the differences are small at small strains, where $\overline{\eta}_{\mathrm{p}}/\eta_{\mathrm{s}} \ll 3$. However, at larger values of the strain, Eq. (8.38) shows that the Tr-vs-ε curve for the free-draining model can lie below experimental data. The overall effect is that of a "lag" in the growth of Tr predicted by free-draining chains. This effect becomes more pronounced for larger molecular weights.

Chapter 9

Conclusions

The objective of this work has been to use bead-spring models of dilute solutions of long, flexible polymers to obtain a detailed predictive understanding of the influence of the nonlinear phenomena of intramolecular hydrodynamic interactions, and to a lesser extent, intramolecular excluded volume interactions in strong flows. In such conditions, the finite extensibility of polymer chains plays an important role in determining the macroscopic rheological behaviour of dilute polymer solutions. Predictions for the nonlinear viscoelastic and other related properties were obtained with exact Brownian dynamics simulations, and with closure approximations. The following methods were developed as a part of this work.

1. An unconditionally stable semi-implicit, predictor-corrector algorithm with adaptive time-stepping was developed for the integration of the nonlinear stochastic differential equations governing models with FENE springs, HI and EV.

2. A new closure approximation for the FENE nonlinearity—the "FENE-PG" approximation—was developed, which improves upon the well known FENE-P approximation by accounting for fluctuations in the spring force.

3. Direct application of the Gaussian approximation for Hookean dumbbells with EV and HI leads to an undesirable dependence of the predictions of equilibrium static properties on the hydrodynamic interaction parameter, h^*. Closer

analysis revealed that this problem is common to all bead-spring models seeking to combine HI with nonlinear non-hydrodynamic inter-bead forces. A method to overcome this problem was suggested, which was then applied to FENE chains with HI. This new approximate model accounts for the influence of fluctuations in both HI and the spring forces.

4. It was shown that when bead-spring chains are highly stretched, predictions obtained with FEBS chains are strongly dependent on the degree of coarse graining. To reduce this dependence, the Successive Fine-Graining procedure was introduced wherein predictions accumulated for several values of N_{S} are extrapolated to the $N_{\mathrm{S}} \to N_{\mathrm{K}}$ limit. When using this procedure to obtain predictions at the theta state for any given N_{K}, the value of the HI parameter h^* and the Weissenberg number Wi are kept constant for the different values of N_{S}. The extrapolated result may therefore be regarded as an improved estimate of the behaviour that would have been predicted with a bead-rod model of the same values of N_{K}, h^* and at the same Weissenberg number.

The principal findings of this work are summarized below.

1. The quantitative agreement of the extrapolated results obtained in this study with the SFG scheme, with experimental data obtained in strong unsteady extensional flows under theta conditions, underlines the importance of the phenomenon of hydrodynamic interactions even well away from equilibrium.

2. The results strongly suggest furthermore that, at the theta state, when properties are expressed in an appropriate dimensionless form, an accurate description of the behaviour of dilute polymer solutions of highly flexible polymer molecules in strong unsteady homogeneous flows requires only one parameter characterizing the polymer—the number of Kuhn segments, N_{K}. For flexible polymers with $N_{\mathrm{K}} \gg 1$, predictions do not seem to be highly sensitive to the hydrodynamic radius of a single Kuhn step, represented by the dimensionless parameter h^*_{K}, when $h^*_{\mathrm{K}} \approx h^*_{\mathrm{k,\,f}}$. The value of the fixed point $h^*_{\mathrm{k,\,f}}$ for bead-rod chains was found to be 0.19.

3. The results of the simulations show that for a fixed range of molecular weights, the molecular weight scaling exponent of the polymer's contribution to the

transient extensional viscosity is a function of the strain when Wi is above the critical value for the coil-stretch transition, varying from 3/2 at low strains to a value close to 3 as steady-state is approached. The constant value of 2 reported earlier by Gupta *et al.* [2000] is shown to be only approximately valid.

4. The results of the simulations reveal that the lateral compression in extensional flows can cause polymer chains to approach each other closely. Whether or not chains actually overlap depends on the initial number density, the Weissenberg number and the chain length. The tendency for "self-concentration" was found to increase during the stress-relaxation phase following cessation of extensional flow.

5. The qualitative features of the combined influence of EV, HI and FE were studied with BD simulations of 20-bead chains. The results of these simulations were used to probe the coupling of these nonlinear phenomena. It was found that most of the rheological properties of interest in shear and extensional flows could be approximately resolved as the product of independent contributions from each nonlinear effect.

6. Several closure approximations for FEBS chains with HI were tested by comparing their predictions with the results of BD simulations of 20-bead FENE chains with HI. The method of combining the Gaussian approximation for HI with the FENE-PG approximation for HI suggested in this study was found to lead to predictions that in general compare well with BD simulations. The good agreement of the GA-PG model in steady and unsteady shear and extensional flows confirms the importance of fluctuations in HI, and also highlights the role FENE spring force fluctuations play at moderate and high strain rates.

7. The predictions obtained with the Gaussian approximation for HI in steady and unsteady shear and extensional flows confirms previous observations on the role of fluctuations in HI on macroscopic behaviour. When chains are close to their equilibrium isotropic states, fluctuations in HI enhance the screening of the solvent velocity gradient caused by HI. In contrast, in situations where polymer chains experience significant stretching, fluctuations in HI are found

to weaken the screening of the velocity field. Consequently, the solvent is able to engage a firmer "grip" on the chains and this tends to deform an already anisotropic chain further. On the other hand, fluctuations in the FENE spring force are found to increase the chains' resistance to stretching.

8. The closure approximations for FEBS chains with HI were found to predict multiple steady-states in the steady-state extensional viscosity in a range of extension-rates immediately below the critical strain rate for the coil-to-stretch transition. A one-dimensional dumbbell model with configuration dependent drag was used to understand the origins of the phenomenon of coil-stretch hysteresis. The predictions of this toy model indicate that in the exact FEBS chain model with HI, the probability distribution becomes multi-modal with distinct peaks near the coiled state and close to the fully stretched state. Depending on the initial conditions, chains in simulations and experiments are kinetically trapped in either of these states by large barriers to ergodicity in the non-equilibrium free energy. Use of mean-field closure approximations substitutes the unique, multi-modal probability distribution in the original model with multiple, uni-modal distributions.

9. Surprisingly, HI was found to have a negligible influence on the phenomenon of stress-conformational hysteresis observed in extensional flows. When the stress predicted in BD simulations of FEBS chains during the start-up and following the cessation of a strong extensional flow is plotted against predictions of the mean-squared end-to-end distance of the chains, or against the intrinsic birefringence, large hysteresis loops were observed. The hysteresis loops predicted with closure approximations were much smaller than those predicted with the simulations. However, with both simulations and approximations, the stress-versus-conformation curves obtained with and without HI were nearly the same, for the same values of the initial extensional strain rate, and the maximum strain prior to cessation of flow.

Although results of the BD simulations have compared well with experiments in general, several deviations have also been observed, the reasons for which are currently not fully understood.

1. A small but significant deviation between simulations' results and experimental data was observed at high strains, and low Wi values. The deviation decreased with increasing extension-rate.

2. Even after correcting for the effects of coarse graining, the "extension-thinning" behaviour observed by Gupta *et al.* [2000] in experiments has not been observed with the simulations performed in this study.

3. The predictions obtained with the simulations for the transient extensional viscosity for a high molecular weight polystyrene ($M_{\rm w} = 10.4 \times 10^6$) disagree with the experimental data both at low and high strains. Similar observations have been reported by Hsieh *et al.* [2003].

These issues have been highlighted in a recent review by Larson [2004]. The results of the simulations in this study indicate that some of the differences mentioned above may be attributed to self-concentration effects in extensional flows. A proper theoretical description of such effects requires the incorporation of intermolecular hydrodynamic interactions in some form.

Although the methods developed in this study have proved to be of much use in modeling dilute polymer solutions, several further improvements are possible.

1. Variance reduction techniques can lead to significant improvements in the computational efficiency of BD simulations. Kumar and Prakash [2003; 2004] observed that the Rouse model could be used to generate the control variate in simulations of free-draining Rouse chains with EV in shear flows. The success of the closure approximations combining EV and HI suggests that the SDE's corresponding to these models could also be used as control variates to reduce the error in exact simulations.

2. As pointed out in Chapter 8, the conventional bead-spring model with $N \ll N_{\rm K}$ hydrodynamically interacting spherical beads of fixed radii cannot accurately represent the changes in the hydrodynamic characteristics of a long flexible molecule as it unravels and stretches in strong flows. The SFG procedure was proposed to correct for this defect in the bead-spring model. Although the

good agreement between the results obtained with the SFG procedure and experiment are encouraging, it is however necessary to validate the extrapolation procedure by comparing with results of simulations of bead-rod chains with HI.

3. The results obtained with the closure approximations show that the largest deviations occur at large strain rates, when FE is dominant. These deviations arise as a result of the approximations for the FENE nonlinearity. The development of the FENE-PG approximation in this study, and others such as the FENE-L approximation [Lielens *et al.*, 1998] shows that improvements are possible in the mean-field description of the FENE nonlinearity. The results of this study also indicate that combining the Gaussian approximation for HI with a good approximation for the FENE nonlinearity should lead to much closer agreement with simulations of FEBS chains with HI.

Appendix A

The Green-Kubo formula for the zero-shear-rate viscosity

Fluctuation-dissipation theorems of the first kind relate the near-equilibrium transport coefficients, which characterize dissipative processes close to the equilibrium state, directly to flux-flux time correlations in the equilibrium state, which are driven completely by thermal fluctuations at equilibrium in the absence of any externally imposed forces.

An example of a fluctuation-dissipation theorem of the first kind is the Green-Kubo formula in Eq. (2.95) for the relaxation modulus $G^*(t^*)$, using which the zero-shear-viscosity is calculated in Eq. (2.93). Fixman [1981] derived Eq. (2.95) for bead-spring models of dilute polymer solutions using linear operator theory. The discussion of the theory for linear viscoelastic properties by Doi and Edwards [1986] offers an alternative route to the derivation of the Green-Kubo formula for the relaxation modulus. Here, the derivation of the Green-Kubo formula for $G^*(t^*)$ is presented for a dumbbell model following Doi and Edwards.

The Kramer's expression for the dimensionless polymer stress [Eq. (2.76)] in a dumbbell model is

$$\boldsymbol{\tau}_{\mathrm{p}}^* = \boldsymbol{\delta} - \left\langle \boldsymbol{Q}^* \frac{\partial \phi^*}{\partial \boldsymbol{Q}^*} \right\rangle . \tag{A.1}$$

The value of $\boldsymbol{\tau}_{\mathrm{p}}^*$ predicted by this expression vanishes identically at equilibrium,

since

$$\left\langle \boldsymbol{Q}^* \frac{\partial \phi^*}{\partial \boldsymbol{Q}^*} \right\rangle_{\text{eq}} = \mathcal{N}_{\text{eq}} \int \boldsymbol{Q}^* \frac{\partial \phi^*}{\partial \boldsymbol{Q}^*} \exp(-\phi^*)\, d\boldsymbol{Q}^* = \boldsymbol{\delta}\,. \tag{A.2}$$

Therefore, Eq. (A.1) can be rewritten as

$$\boldsymbol{\tau}_{\text{p}}^* = \langle \boldsymbol{I} \rangle_{\text{eq}} - \langle \boldsymbol{I} \rangle\,, \tag{A.3}$$

where

$$\boldsymbol{I} \equiv \boldsymbol{Q}^* \frac{\partial \phi^*}{\partial \boldsymbol{Q}^*}\,. \tag{A.4}$$

If a small deformation described by the small strain tensor $\boldsymbol{\gamma}$ [Bird *et al.*, 1987a] is imposed instantaneously on the polymer solution at $t^* = 0$, the dimensionless work done on the material per molecule is given by

$$W^* = -\frac{1}{2} \boldsymbol{\gamma} : \boldsymbol{\tau}_{\text{p}}^* \big|_{t^*=0}\,, \tag{A.5}$$

Since the deformation is "instantaneous", there is no time for dissipation to occur, and all the work done by the external agency in creating the deformation is stored elastically. In other words, if a dumbbell's configuration in the ensemble just prior to the imposition of the strain at $t^* = 0^-$ is $\boldsymbol{Q}^{*-}$, and the imposed deformation causes a change in the configuration to $\boldsymbol{Q}^*$ at $t^* = 0$, then its potential energy before and after the deformation must be related through

$$\phi^* = \phi^{*-} + \Delta\phi^*\,, \tag{A.6}$$

where $\phi^* = \phi^*(Q^*)$, $\phi^{*-} = \phi^*(Q^{*-})$, and $\Delta\phi^*$ is the change in the potential energy of the dumbbell such that

$$\langle \Delta\phi^* \rangle = W^*\,. \tag{A.7}$$

Substituting from Eqs. (2.78), (A.4), and (A.5) in the equation above, and noting

that for an incompressible fluid, $\boldsymbol{\gamma} : \boldsymbol{\delta} = \mathbf{0}$, it is possible to identify

$$\Delta\phi^* = \frac{1}{2}\,\boldsymbol{I} \colon \boldsymbol{\gamma}\,. \tag{A.8}$$

Hence, for a dumbbell whose configuration at $t = 0$ is $\boldsymbol{Q}^*$, the potential energy at $t^* = 0^-$ is given by

$$\phi^{*-} = \phi^* - \Delta\phi^* = \phi^* - \frac{1}{2}\,\boldsymbol{I} \colon \boldsymbol{\gamma}\,. \tag{A.9}$$

As a consequence of the relation above, the configurational probability distributions before and after the imposition of the deformation, denoted as ψ and ψ^- respectively, must be related in a way such that

$$\psi\, d\boldsymbol{Q}^* = \psi^-\, d\boldsymbol{Q}^{*-}\,. \tag{A.10}$$

Since at $t^* = 0^-$, the polymer solution is at equilibrium, and

$$\psi^- = \psi_{\text{eq}} \sim \exp(-\phi^{*-})\,. \tag{A.11}$$

The mapping from $\boldsymbol{Q}^{*-}$ to $\boldsymbol{Q}^*$ must therefore satisfy Eq. (A.9) above, one obtains

$$\psi\, d\boldsymbol{Q}^* = \frac{\exp\left[-(\phi^* - \frac{1}{2}\,\boldsymbol{I} \colon \boldsymbol{\gamma})\right]\,\det(\mathbf{J})\, d\boldsymbol{Q}^*}{\int \exp\left[-(\phi^* - \frac{1}{2}\,\boldsymbol{I} \colon \boldsymbol{\gamma})\right] \det(\mathbf{J})\, d\boldsymbol{Q}^*}\,, \tag{A.12}$$

where $\mathbf{J} = \partial\boldsymbol{Q}^{*-}/\partial\boldsymbol{Q}^*$ is the Jacobian of the inverse mapping of $\boldsymbol{Q}^*$ to $\boldsymbol{Q}^{*-}$. The tensor $\mathbf{J}$ can be expanded as a perturbation series in the imposed deformation. Since $\mathbf{J}$ describes the change in the shape and size of the volume element in the configurational phase space, and must remain unchanged on a reversal of the coordinate axes, the perturbation expansion of $\mathbf{J}$ with respect to $\boldsymbol{\gamma}$ must contain only even powers of $\boldsymbol{\gamma}$. Therefore, it is possible to write for small imposed deformations

$$\psi = \frac{\exp[-\phi^*]\left(1 + \frac{1}{2}\,\boldsymbol{I} \colon \boldsymbol{\gamma} + \ldots\right) \det(\boldsymbol{\delta} + \ldots)}{\int \exp[-\phi^*]\left(1 + \frac{1}{2}\,\boldsymbol{I} \colon \boldsymbol{\gamma} + \ldots\right) \det(\boldsymbol{\delta} + \ldots)\, d\boldsymbol{Q}^*}\,. \tag{A.13}$$

Since, $\int \exp\left[-\phi^*\right] \boldsymbol{I} : \boldsymbol{\gamma}\, d\boldsymbol{Q}^* \sim \boldsymbol{\delta} : \boldsymbol{\gamma} = \boldsymbol{0}$, the probability distribution at $t^* = 0$ is given by

$$\psi(\boldsymbol{Q}^*) = \psi_{\mathrm{eq}}(\boldsymbol{Q}^*) \left(1 + \frac{1}{2}\, \boldsymbol{I} : \boldsymbol{\gamma} + \ldots\right) . \tag{A.14}$$

At any $t^* > 0$ after the imposition of the deformation, the polymer solution undergoes stress relaxation under quiescent conditions. During this phase, probability distribution is given by

$$\psi(\boldsymbol{Q}^*, t^*) = \int p(\boldsymbol{Q}^*, t^* | \boldsymbol{Q}^{*\prime}, 0) \psi(\boldsymbol{Q}^{*\prime}, 0)\, d\boldsymbol{Q}^{*\prime} , \tag{A.15}$$

where $p(\boldsymbol{Q}^*, t^* | \boldsymbol{Q}^{*\prime}, 0)$ is the conditional (transition) probability that a dumbbell having a configuration specified by $\boldsymbol{Q}^{*\prime}$ at $t^* = 0$, has a configuration $\boldsymbol{Q}^*$ at $t^* > 0$. From Eqs. (2.78) and (A.15), the polymer stress at any time $t^* > 0$ is given by

$$\boldsymbol{\tau}_{\mathrm{p}}^*(t^*) = \langle \boldsymbol{I} \rangle_{\mathrm{eq}} - \int \int \boldsymbol{I}(\boldsymbol{Q}^*)\, p\left(\boldsymbol{Q}^*, t^* | \, \boldsymbol{Q}^{*\prime}, 0\right) \psi(\boldsymbol{Q}^{*\prime}, 0)\, d\boldsymbol{Q}^*\, d\boldsymbol{Q}^{*\prime} . \tag{A.16}$$

Substituting for $\psi(\boldsymbol{Q}^{*\prime}, 0)$ in the equation above from Eq. (A.14), one obtains

$$\begin{aligned}
\boldsymbol{\tau}_{\mathrm{p}}^*(t^*) &= \langle \boldsymbol{I} \rangle_{\mathrm{eq}} - \int \int \boldsymbol{I}(\boldsymbol{Q}^*) \left[1 + \frac{1}{2}\, \boldsymbol{I}(\boldsymbol{Q}^{*\prime}) : \boldsymbol{\gamma}\right] p\left(\boldsymbol{Q}^*, t^* | \, \boldsymbol{Q}^{*\prime}, 0\right) \psi_{\mathrm{eq}}(\boldsymbol{Q}^{*\prime})\, d\boldsymbol{Q}^*\, d\boldsymbol{Q}^{*\prime}, \\
&= \left[\langle \boldsymbol{I} \rangle_{\mathrm{eq}} - \int \int \boldsymbol{I}(\boldsymbol{Q}^*)\, p\left(\boldsymbol{Q}^*, t^* | \, \boldsymbol{Q}^{*\prime}, 0\right) \psi_{\mathrm{eq}}\left(\boldsymbol{Q}^{*\prime}\right)\right] d\boldsymbol{Q}^*\, d\boldsymbol{Q}^{*\prime}\Bigg] \\
&\quad - \left[\frac{1}{2} \int \int \boldsymbol{I}(\boldsymbol{Q}^*)\, \boldsymbol{I}(\boldsymbol{Q}^*)\, p\left(\boldsymbol{Q}^*, t^* | \, \boldsymbol{Q}^{*\prime}, 0\right) \psi_{\mathrm{eq}}(\boldsymbol{Q}^{*\prime})\, d\boldsymbol{Q}^*\, d\boldsymbol{Q}^{*\prime}\right] : \boldsymbol{\gamma} .
\end{aligned} \tag{A.17}$$

An important assumption in the standard derivation of the Green-Kubo formulae is that the transition probability p during stress relaxation is obtained as the solution of the *equilibrium* Fokker-Planck equation, since p during the stress relaxation is obtained in the absence of any imposed flow. If this assumption is valid, then p satisfies the following stationarity condition,

$$\psi_{\mathrm{eq}}(\boldsymbol{Q}^*) = \int p\left(\boldsymbol{Q}^*, t^* | \, \boldsymbol{Q}^{*\prime}, 0\right) \psi_{\mathrm{eq}}(\boldsymbol{Q}^{*\prime})\, d\boldsymbol{Q}^{*\prime} . \tag{A.18}$$

Substituting the result above in Eq. (A.17), one obtains

$$\begin{aligned}\boldsymbol{\tau}_{\mathrm{p}}^{*}(t^{*}) &= -\frac{1}{2}\left\{\int\int \boldsymbol{I}(\boldsymbol{Q}^{*})\boldsymbol{I}(\boldsymbol{Q}^{*\prime})\, p\,(\boldsymbol{Q}^{*}, t^{*}|\, \boldsymbol{Q}^{*\prime}, 0)\, \psi_{\mathrm{eq}}(\boldsymbol{Q}^{*\prime})\, d\boldsymbol{Q}^{*}\, d\boldsymbol{Q}^{*\prime}\right\} : \boldsymbol{\gamma}\,, \\ &= -\frac{1}{2}\,\langle \boldsymbol{I}(t^{*})\boldsymbol{I}(0)\rangle_{\mathrm{eq}} : \boldsymbol{\gamma}\,. \end{aligned} \tag{A.19}$$

As will be shown shortly, this assumption is not always valid in when mean-field approximations are used. Here, $\langle\, f(t^{*})g(0)\,\rangle$ denotes the time correlation between f and g:

$$\langle\, f(t^{*})g(0)\,\rangle \equiv \int\int f(\boldsymbol{Q}^{*})g(\boldsymbol{Q}^{*\prime})\, p\,(\boldsymbol{Q}^{*}, t^{*}|\, \boldsymbol{Q}^{*\prime}, 0)\, \psi(\boldsymbol{Q}^{*\prime}, 0)\, d\boldsymbol{Q}^{*}\, d\boldsymbol{Q}^{*\prime}\,. \tag{A.20}$$

For a small shear strain [Bird *et al.*, 1987a],

$$\boldsymbol{\gamma} = \begin{pmatrix} 0 & \gamma_{yx} & 0 \\ \gamma_{yx} & 0 & 0 \\ 0 & 0 & 0 \end{pmatrix}\,, \tag{A.21}$$

and $\boldsymbol{I} : \boldsymbol{\gamma} = 2\, I_{yx}\gamma_{yx}$. At equilibrium, only the autocorrelation $\langle I_{yx}(t)I_{yx}(0)\rangle$ survives and all other cross-correlations with I_{yx} vanish. Hence,

$$\boldsymbol{\tau}_{\mathrm{p}}^{*} = -\begin{pmatrix} 0 & \langle I_{yx}(t^{*})I_{yx}(0)\rangle_{\mathrm{eq}}\gamma_{yx} & 0 \\ \langle I_{yx}(t^{*})I_{yx}(0)\rangle_{\mathrm{eq}}\gamma_{yx} & 0 & 0 \\ 0 & 0 & 0 \end{pmatrix}\,, \tag{A.22}$$

and from the definition of the shear relaxation modulus in Eq. (2.94),

$$G_{\mathrm{p}}^{*}(t^{*}) = -\frac{\tau_{\mathrm{p},yx}^{*}}{\gamma_{yx}} = \langle I_{yx}(t^{*})I_{yx}(0)\rangle_{\mathrm{eq}}\,. \tag{A.23}$$

Since

$$\eta_{\mathrm{p},\,0}^{*} = \int_{0}^{\infty} G_{\mathrm{p}}^{*}(t^{*})\, dt^{*}, \tag{A.24}$$

the Green-Kubo formula relating the near-equilibrium transport coefficient $\eta_{\mathrm{p},\,0}^{*}$ to

an equilibrium autocorrelation is obtained:

$$\lim_{\dot{\gamma}\to 0} \eta_{\mathrm{p}}^{*} = \eta_{\mathrm{p},\,0}^{*} = \int_{0}^{\infty} \langle\, I_{yx}(t^{*}) I_{yx}(0) \,\rangle_{\mathrm{eq}}\, dt^{*}\,. \tag{A.25}$$

Given any model, the left-hand and right-hand sides of the equation above can be calculated independently. The limit on the left-hand side can either be evaluated by explicitly extrapolating values obtained at several small values of the shear-rate to the zero shear-rate limit, or can be analytically calculated in the case of approximations using a perturbation expansion. The integral on the right-hand side can be evaluated by first calculating the equilibrium auto-correlation. This requires a calculation with the *equilibrium* Fokker-Planck equation for the given model.

As mentioned earlier, an important step in the derivation of the Green-Kubo formula in Eq.(A.25) is the assumption that the Fokker-Planck equation governing the transition probability p following the momentary imposition of a small strain is identical to the equilibrium Fokker-Planck equation for p. Although this is always true with the exact Fokker-Planck equation [Eq. (2.51)] with the fluctuating nonlinearities ξ, w^{*} and $\widetilde{\boldsymbol{A}}$, Hütter and Öttinger [1996] showed that this assumption does not always hold when mean-field closure approximations are used. In particular, it was found that the assumption is not valid when the Gaussian approximation is used for HI. Hence, the Green-Kubo relation in Eq. (A.25) is cannot be used directly with the Gaussian approximation for HI. Following Hütter and Öttinger, the source of this interesting aspect of mean-field approximations is examined below, in the context of a dumbbell model.

As pointed out in Chapter 5, the closure approximations studied in this work are used to obtain an equation of the following form for the time evolution of the dimensionless second moment [Eq. (5.2) applied to the dumbbell case]:

$$\boldsymbol{\sigma}_{(1)}^{*} = -\frac{1}{4}\left[\boldsymbol{\sigma}^{*}\cdot\overline{\boldsymbol{M}} + \overline{\boldsymbol{M}}^{\mathrm{T}}\cdot\boldsymbol{\sigma}^{*}\right] + \frac{1}{2}\overline{\boldsymbol{D}}\,. \tag{A.26}$$

The Fokker-Planck equation for the transition probability $\hat{p}\,(\boldsymbol{Q}^*, t^* | \, \boldsymbol{Q}^{*\prime}, 0)$ corresponding to the second moment equation above is [Eq. (5.3)],

$$\frac{\partial \hat{p}}{\partial t^*} = -\frac{\partial}{\partial \boldsymbol{Q}^*} \cdot \left\{ \boldsymbol{\kappa}^* \cdot \boldsymbol{Q}^* - \frac{1}{4} \overline{\boldsymbol{M}}^{\mathrm{T}} \cdot \boldsymbol{Q}^* \right\} \hat{p} + \frac{1}{4} \overline{\boldsymbol{D}} \colon \frac{\partial^2 \hat{p}}{\partial \boldsymbol{Q}^* \partial \boldsymbol{Q}^*} \,. \tag{A.27}$$

The sudden imposition of a strain $\boldsymbol{\gamma}$ at $t^* = 0$ can be formally described using a velocity gradient,

$$\boldsymbol{\kappa}^* = \gamma \, \delta(t^*) \, \widetilde{\boldsymbol{\kappa}}^* \,, \tag{A.28}$$

where $\gamma = \sqrt{\frac{1}{2} \boldsymbol{\gamma} \colon \boldsymbol{\gamma}}$, and $\widetilde{\boldsymbol{\kappa}}^*$ is the tensor specifying the structure of the imposed strain. For small values of γ, the second moment $\boldsymbol{\sigma}^*$ can be expanded to first order in γ about its equilibrium value $\boldsymbol{\sigma}^*_{\mathrm{eq}}$, and

$$\boldsymbol{\sigma}^* = \boldsymbol{\sigma}^*_{\mathrm{eq}} + \boldsymbol{\sigma}^{*(1)} + \ldots \tag{A.29}$$

Since $\overline{\boldsymbol{M}}$ and $\overline{\boldsymbol{D}}$ are functions of the second moment, their first order expansions in the strain can be represented as

$$\overline{\boldsymbol{M}} = \overline{\boldsymbol{M}}_{\mathrm{eq}} + \overline{\boldsymbol{M}}^{(1)} + \ldots, \tag{A.30}$$

and,

$$\overline{\boldsymbol{D}} = \overline{\boldsymbol{D}}_{\mathrm{eq}} + \overline{\boldsymbol{D}}^{(1)} + \ldots \tag{A.31}$$

$$\tag{A.32}$$

The tensors $\boldsymbol{\sigma}^*_{\mathrm{eq}}$, $\overline{\boldsymbol{M}}_{\mathrm{eq}}$ and $\overline{\boldsymbol{D}}_{\mathrm{eq}}$ are all evaluated using the equilibrium Boltzmann distribution in the mean-field model, $\hat{\psi}_{\mathrm{eq}} \sim \exp\left(-\overline{\phi}^*\right)$, where $\overline{\phi}^*$ is the total mean-field potential energy in the model [Eqs. (5.60) and (5.80)]. Substituting the expansions

above in Eq. (A.26) and collecting together the terms of like order in γ, one obtains

$$\mathbf{0} = -\frac{1}{4}\left[\boldsymbol{\sigma}^*_{\mathrm{eq}} \cdot \overline{\boldsymbol{M}}_{\mathrm{eq}} + \overline{\boldsymbol{M}}^{\mathrm{T}}_{\mathrm{eq}} \cdot \boldsymbol{\sigma}^*_{\mathrm{eq}}\right] + \frac{1}{2}\overline{\boldsymbol{D}}_{\mathrm{eq}}\,, \tag{A.33}$$

$$\begin{aligned}\frac{d\boldsymbol{\sigma}^{*(1)}}{dt^*} &= \gamma\left[\widetilde{\boldsymbol{\kappa}}^* \cdot \boldsymbol{\sigma}^*_{\mathrm{eq}} + \boldsymbol{\sigma}^*_{\mathrm{eq}} \cdot \widetilde{\boldsymbol{\kappa}}^{*\,\mathrm{T}}\right]\delta(t^*) \\ &\quad - \frac{1}{4}\left[\boldsymbol{\sigma}^{*(1)} \cdot \overline{\boldsymbol{M}}_{\mathrm{eq}} + \overline{\boldsymbol{M}}^{\mathrm{T}}_{\mathrm{eq}} \cdot \boldsymbol{\sigma}^{*(1)}\right] \underline{-\frac{1}{4}\left[\boldsymbol{\sigma}^*_{\mathrm{eq}} \cdot \overline{\boldsymbol{M}}^{(1)} + \overline{\boldsymbol{M}}^{(1),\,\mathrm{T}} \cdot \boldsymbol{\sigma}^*_{\mathrm{eq}}\right]} \\ &\quad \underline{+\frac{1}{2}\overline{\boldsymbol{D}}^{(1)}}\,.\end{aligned} \tag{A.34}$$

Equation (A.33) above is simply the equation for the second moment at equilibrium. As pointed out in Chapter 5, closure approximations need to be designed such that the solution $\boldsymbol{\sigma}^*_{\mathrm{eq}}$ is consistent with the Boltzmann distribution, $\hat{\psi}_{\mathrm{eq}} \sim \exp(-\overline{\phi}^*)$. If it happens that, for small values of γ, the sum of the underlined terms in the equation above vanishes, that is

$$-\frac{1}{4}\left[\boldsymbol{\sigma}^*_{\mathrm{eq}} \cdot \overline{\boldsymbol{M}}^{(1)} + \overline{\boldsymbol{M}}^{(1),\,\mathrm{T}} \cdot \boldsymbol{\sigma}^*_{\mathrm{eq}}\right] + \frac{1}{2}\overline{\boldsymbol{D}}^{(1)} = \mathbf{0}\,, \tag{A.35}$$

then the equation for the second moment $\boldsymbol{\sigma}^*$ for all $t^* > 0$, is given by

$$\frac{d\boldsymbol{\sigma}^*}{dt} = -\frac{1}{4}\left[\boldsymbol{\sigma}^* \cdot \overline{\boldsymbol{M}}_{\mathrm{eq}} + \overline{\boldsymbol{M}}^{\mathrm{T}}_{\mathrm{eq}} \cdot \boldsymbol{\sigma}^*\right] + \frac{1}{2}\overline{\boldsymbol{D}}_{\mathrm{eq}} + \ldots \tag{A.36}$$

Therefore, up to the first order in γ, the Fokker-Planck equation for the transition probability $\hat{p}$ in the mean-field model for $t^* > 0$ is,

$$\frac{\partial \hat{p}}{\partial t^*} = \frac{1}{4}\frac{\partial}{\partial \boldsymbol{Q}^*} \cdot \left\{\overline{\boldsymbol{M}}_{\mathrm{eq}} \cdot \boldsymbol{Q}^*\right\}\hat{p} + \frac{1}{4}\,\overline{\boldsymbol{D}}_{\mathrm{eq}} \colon \frac{\partial^2 \hat{p}}{\partial \boldsymbol{Q}^* \partial \boldsymbol{Q}^*}\,. \tag{A.37}$$

The transition probability $\hat{p}$ governed by the equation above satisfies the stationarity condition in Eq. (A.18), which is crucial to the derivation of a Green-Kubo formula, such as the one in Eq. (A.25). If, on the other hand, a mean-field approximation does not satisfy the condition in Eq. (A.35), then the conventional form of the Green-Kubo formula is not valid for that approximation.

For Hookean dumbbells with consistently-averaged HI and no EV [Eq. (5.24)], $\overline{\boldsymbol{M}} = \overline{\boldsymbol{D}} = \overline{\boldsymbol{A}}$. In addition, $\boldsymbol{\sigma}^*_{\mathrm{eq}} = \boldsymbol{\delta}$. Therefore, in this model, $\overline{\boldsymbol{M}}^{(1)} = \overline{\boldsymbol{D}}^{(1)} = \overline{\boldsymbol{A}}^{(1)}$, and the condition in Eq. (A.35) is satisfied. However, with the Gaussian

approximation for HI [Eq. (5.40)], $\overline{\boldsymbol{D}} = \overline{\boldsymbol{A}}$, but

$$\overline{\boldsymbol{M}}^{(1)} = \overline{\boldsymbol{A}}^{(1)} + \boldsymbol{\Delta}^{(1)}, \tag{A.38}$$

which, when combined with $\boldsymbol{\sigma}^*_{\mathrm{eq}} = \boldsymbol{\delta}$ for Hookean dumbbells without EV, clearly does not satisfy the condition in Eq. (A.35). Therefore, in the case of the Gaussian approximation, the appearance of the fluctuation tensors leads to the invalidation of the Green-Kubo formula for this approximation. This behaviour is not restricted to approximations for HI alone. For a free-draining FENE-P dumbbell with no EV, $\overline{\boldsymbol{M}} = 2H^*\overline{\xi}\boldsymbol{\delta}$, $\overline{\boldsymbol{D}} = 2\boldsymbol{\delta}$, and $\boldsymbol{\sigma}^*_{\mathrm{eq}} = \boldsymbol{\delta}$. Since for small values of γ, $\overline{\xi}^{(1)} \neq 1$, Eq. (A.35) is not satisfied. However, this deviation can be expected to be weak for moderately large values of $N_{\mathrm{K,\,s}}$, since the results for the model must approach those for the Hookean dumbbell as $N_{\mathrm{K,\,s}} \to \infty$. On the other hand, with the mean-field EV potential shown in Eq. (5.60), the appearance of the $\boldsymbol{J}$ tensor in [Eq. (5.71)] in the equation for the second moment means that a model with mean-field EV interactions does not satisfy the conventional form of the Green-Kubo formula.

Appendix B

The steady-state extensional viscosity of completely aligned, partially stretched bead-spring chains

In this Appendix, a one-dimensional model is considered in which a bead-spring chain is completely aligned in the principal direction of a uniaxial extensional flow. For the sake of convenience, it is assumed that the number of springs N_s is even. Figure B.1 provides a schematic illustration of this model.

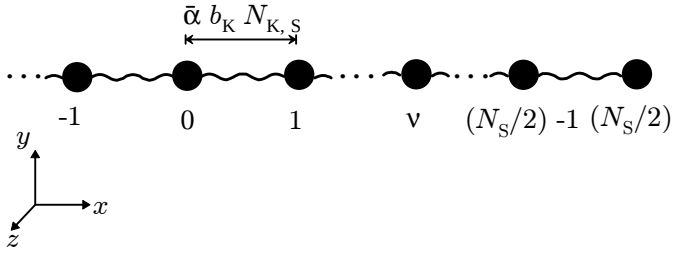

Figure B.1: Schematic illustration of a partially stretched bead-spring chain that is fully aligned in the stretching direction (the x-direction) of the uniaxial elongational flow.

From Eq. (2.42), the total hydrodynamic drag force, $\boldsymbol{F}_{\nu}^{\mathrm{h}}$, on the ν-th bead ($\nu = -N_{\mathrm{s}}/2, ..., 0, ..., N_{\mathrm{s}}/2$) is given by

$$\boldsymbol{F}_{\nu}^{\mathrm{h}} = -\zeta \left[[\![\, \dot{\boldsymbol{r}}_{\nu} \,]\!] - (\boldsymbol{v}_{\nu} + \Delta \boldsymbol{v}_{\nu}) \right] . \tag{B.1}$$

where the imposed velocity of the continuum solvent at the ν-th bead's position $\boldsymbol{r}_{\nu}$ is $\boldsymbol{v}_{\nu} = \boldsymbol{v}_0 + \boldsymbol{\kappa} \cdot \boldsymbol{r}_{\nu}$, and the total perturbation of the solvent's velocity at $\boldsymbol{r}_{\nu}$ is the sum of the individual perturbations caused by the motion of each of the other beads in the chain:

$$\Delta \boldsymbol{v}_{\nu} = \sum_{\substack{\mu=1 \\ \nu \neq \mu}}^{N} \Delta \boldsymbol{v}_{\nu\mu} \, . \tag{B.2}$$

The velocity perturbation at the ν-th bead's position due to the μ-th bead is expressed as

$$\Delta \boldsymbol{v}_{\nu\mu} = \boldsymbol{\Omega}_{\nu\mu} \cdot (-\boldsymbol{F}_{\mu}^{\mathrm{h}}) \, . \tag{B.3}$$

where the hydrodynamic interaction tensor $\boldsymbol{\Omega}_{\nu\mu}$ has been introduced earlier in Chapter 2.

Due to the symmetry in the model, the position of the centre of hydrodynamic resistance coincides with the centre of mass of the chain. Hence, the centre of mass of the chain located at bead "0", has the same velocity as that of the unperturbed solvent. Further, at steady-state in a uniaxial extensional flow, the fully-stretched chain configuration shown in Fig. B.1 is assumed to move rigidly and there is no relative motion between the beads. Therefore,

$$[\![\dot{\boldsymbol{r}}_{\nu}]\!] = [\![\dot{\boldsymbol{r}}_0]\!] = \boldsymbol{v}_0 + \boldsymbol{\kappa} \cdot \boldsymbol{r}_0 \, , \tag{B.4}$$

where $\boldsymbol{r}_0$ is the position-vector of bead "0". The unperturbed velocity of the solvent at the ν-th bead's position is however,

$$\boldsymbol{v}_{\nu} = \boldsymbol{v}_0 + \boldsymbol{\kappa} \cdot \boldsymbol{r}_{\nu} \tag{B.5}$$

Substituting from Eqs. (B.5), (B.4), (B.3), and (B.2), in Eq (B.1) and rearranging, one obtains

$$\sum_{\mu=-N_{\rm s}/2}^{N_{\rm s}/2} [\delta_{\nu\mu}\boldsymbol{\delta} + (1-\delta_{\nu\mu})\zeta\boldsymbol{\Omega}_{\nu\mu}] \cdot \boldsymbol{F}_{\mu}^{\rm h} = \zeta\, \boldsymbol{\kappa} \cdot (\boldsymbol{r}_{\nu} - \boldsymbol{r}_0) = \zeta\, \boldsymbol{\kappa} \cdot\, \boldsymbol{R}_{\nu}, \tag{B.6}$$

Concentrating on the x-component (in the stretching direction of the elongational flow) of the equation above, and respectively denoting the x-components of $\boldsymbol{F}_{\nu}^{\rm h}$ and $\boldsymbol{R}_{\nu}$ as $F_{\nu}^{\rm h}$ and R_{ν}, and denoting the xx-component of the HI tensor as $\Omega_{\nu\mu}$, in an extensional flow characterized by a strain rate $\dot{\epsilon}$,

$$\sum_{\mu=-N_{\rm s}/2}^{N_{\rm s}/2} [\delta_{\nu\mu} + (1-\delta_{\nu\mu})\zeta\Omega_{\nu\mu}]\, F_{\mu}^{\rm h} = \zeta\, \dot{\epsilon}\, R_{\nu}\,. \tag{B.7}$$

In Eq. (B.7) above, for a given strain rate $\dot{\epsilon}$, both the sets F_{ν}^{h} and R_{ν}, $\nu = -N_{\rm s}/2, \ldots, N_{\rm s}/2$ are unknown. The exact solution of this equation requires additionally a force balance for each bead, wherein the resultant of the hydrodynamic and the spring forces on either side of a bead is equated to zero. Since, in strong extensional flows, the springs are likely to nearly fully stretched, it is assumed that every spring in the chain is stretched to the same fraction $\overline{\alpha}$ of its maximum allowed length $b_{\rm K}N_{\rm K,\,s}$. This "mean-stretch" assumption implies that $R_{\nu} = \overline{\alpha}\,\nu\, b_{\rm K}N_{\rm K,\,s}$, and $r_{\nu\mu} = |\nu-\mu|\,\overline{\alpha}\, b_{\rm K}N_{\rm K,\,s}$, and as a result Eq. (B.6) can be written as

$$\boldsymbol{A} \cdot \boldsymbol{F}^{h} = \zeta\, \dot{\epsilon}\, \overline{\alpha}\, b_{\rm K}N_{\rm K,\,s}\boldsymbol{\rho}, \tag{B.8}$$

where $\boldsymbol{\rho}$ and $\boldsymbol{F}^{h}$ are $N_{\rm s}$+1-component column-vectors given by $[-N_{\rm s}/2, \ldots, 0, \ldots, N_{\rm s}/2]^{\rm T}$ and $[F^{h}_{-N_{\rm s}/2}, \ldots, F^{h}_{0}, \ldots, F^{h}_{N_{\rm s}/2}]^{\rm T}$, respectively. The (ν,μ)-th element in $\boldsymbol{A}$ is given by

$$A_{\nu\mu} = \delta_{\nu\mu} + (1-\delta_{\nu\mu})\zeta\Omega_{\nu\mu}\,, \tag{B.9}$$

where,

$$\Omega_{\nu\mu} = \frac{C_{\nu\mu}}{8\pi\eta_{\rm s}\,\overline{\alpha}\,|\nu-\mu|\,N_{\rm K,\,s}}\,. \tag{B.10}$$

Here, $C_{\nu\mu}$ depends on the choice of the hydrodynamic interaction tensor. For chains without HI, $C_{\nu\mu} = 0$. For chains with HI, $C_{\nu\mu} = 2$ if the Oseen-Burgers tensor is used, whereas with the RPY tensor, $C_{\nu\mu}$ is a simple function of $\overline{\alpha}\,|\nu-\mu|\,N_{\rm K,\,s}$ and h^*.

In the case of strong extensional flows where $|\tau_{{\rm p},xx} - \tau_{{\rm p},yy}| \gg 1$, the modified Kramer's expression [Bird *et al.*, 1987b] for the polymer contribution to the stress tensor gives

$$\tau_{{\rm p},xx} - \tau_{{\rm p},yy} \approx -n_{\rm p} \sum_{\nu=-N_{\rm s}/2}^{N_{\rm s}/2} R_\nu F_\nu^h = -n_{\rm p}\,\overline{\alpha}\,b_{\rm K} N_{\rm K,\,s}\,\boldsymbol{\rho}\cdot\boldsymbol{F}^h. \tag{B.11}$$

Substituting $\boldsymbol{F}^h = \zeta\,\dot{\epsilon}\,\overline{\alpha}\,b_{\rm K}N_{\rm K,\,s}\boldsymbol{A}^{-1}\cdot\boldsymbol{\rho}$ in the equation above, the dimensionless extensional viscosity predicted by this one-dimensional model is

$$\overline{\eta}_{\rm p} = n_{\rm p} b_{\rm K}^2 \zeta \overline{\alpha}^{\,2}\, N_{\rm K,\,s}^2\,\boldsymbol{\rho}\cdot\boldsymbol{A}^{-1}\cdot\boldsymbol{\rho}. \tag{B.12}$$

With the definition $\overline{\eta}_{\rm p}^{\dagger} = \overline{\eta}_{\rm p}/(n_{\rm p}\eta_{\rm s}b_{\rm K}^3)$ [Eq. (8.2)],

$$\overline{\eta}_{\rm p}^{\dagger} = \sqrt{12}\,\pi^{3/2}\,h^*\,\overline{\alpha}^{\,2}\,N_{\rm K,\,s}^{5/2}\,\boldsymbol{\rho}\cdot\boldsymbol{A}^{-1}\cdot\boldsymbol{\rho}\,. \tag{B.13}$$

The results shown in Fig. 8.6 for $N_{\rm K} = 2627$ have been obtained using the equation above with $\overline{\alpha} = 1$ for the "fully-stretched" condition.

Following Doi and Edwards [1986], it is possible to simplify further by assuming that the total velocity perturbation at the ν-th bead's position is proportional to the perturbations caused by the bead's closest neighbours:

$$\Delta v_\nu = \sum_{\substack{\mu=-N_{\rm S}/2\\ \mu\neq\nu}}^{N_{\rm s}/2} \Delta v_{\nu\mu} \approx \omega(\Delta v_{\nu\,\nu+1} + \Delta v_{\nu\,\nu-1}), \tag{B.14}$$

where ω is a constant whose estimation is discussed shortly. Setting $\omega = 0$ is

equivalent to switching off HI. For chains with HI, the approximation above implies that the second term on the left-hand side of Eq. (B.6) can be simplified as follows:

$$\sum_{\mu=-N_\mathrm{s}/2}^{N_\mathrm{s}/2}(1-\delta_{\nu\mu})\zeta\Omega_{\nu\mu}F_\mu^\mathrm{h} \;\approx\; \omega\,\zeta\left[\Omega_{\nu,\,\nu+1}F_{\nu+1}^\mathrm{h}+\Omega_{\nu,\,\nu-1}F_{\nu-1}^\mathrm{h}\right] \;\approx\; 2\,\omega\,\zeta\,\Omega_{\nu,\,\nu+1}F_\nu^\mathrm{h}. \tag{B.15}$$

Here, the symmetry condition $\Omega_{\nu,\,\nu-1}=\Omega_{\nu,\,\nu+1}$ has been used, and $F_{\nu+1}^\mathrm{h}+F_{\nu-1}^\mathrm{h}$ has been approximated as $2F_\nu^\mathrm{h}$. Using the Oseen-Burgers definition of the hydrodynamic interaction tensors, one thus obtains

$$F_\mu^\mathrm{h}=\frac{\zeta\,\dot{\epsilon}\,\overline{\alpha}\,b_\mathrm{K}N_{\mathrm{K},\,\mathrm{s}}\,\mu}{\left(1+\dfrac{\omega\,\zeta}{2\pi\eta_\mathrm{s}b_\mathrm{K}N_{\mathrm{K},\,\mathrm{s}}\,\overline{\alpha}}\right)}. \tag{B.16}$$

Hence, $F_\mu^\mathrm{h}\sim\mu$ in Eq. (B.16), while in Eq. (B.10), $\Omega_{\nu\mu}\sim|\,\nu-\mu\,|^{-1}$. The velocity perturbation caused by the μ-th bead at the ν-th bead's position in an aligned but partially stretched chain can thus be written as

$$\Delta v_{\nu\mu}=\Omega_{\nu\mu}F_\mu^\mathrm{h}=k\frac{\mu}{|\nu-\mu|}, \tag{B.17}$$

where k is a constant independent of the bead index. This expression for $\Delta v_{\nu\mu}$ can be substituted in Eq. (B.17). For long chains, the total velocity perturbation at the ν-th bead's position can be calculated by replacing the summation in Eq. (B.17) by an integral. Using the transformations $r=2\nu/N_\mathrm{s}$ and $s=2\mu/N_\mathrm{s}$, one has

$$\Delta v(r)=k\frac{N_\mathrm{s}}{2}\begin{cases}\displaystyle\int_{r+2/N_\mathrm{s}}^{1}\frac{s}{s-r}\,ds+\int_{-1}^{r-2/N_\mathrm{s}}\frac{s}{r-s}\,ds, & \\ \qquad\qquad\qquad\qquad |r|\le 1-2/N_\mathrm{s}, & \\ \mathrm{sgn}\,(r)\displaystyle\int_{-1}^{1-2/N_\mathrm{s}}\frac{s}{|r|-s}\,ds, |r|>1-2/N_\mathrm{s}. & \end{cases} \tag{B.18}$$

For all $|r| \leq 1 - 2/N_{\rm s}$, this leads to

$$\Delta v(r) = k\frac{N_{\rm s}}{2}\left[2\ln\frac{N_{\rm s}}{2} + 2\ln(1-r^2) - 2\right] \approx \omega k 2r(N_{\rm s}/2). \tag{B.19}$$

This gives $\omega = \ln(N_{\rm s}/2) + \ln(1-r^2) - 1$. At any fixed r, as $N_{\rm s} \to N_{\rm K} \to \infty$, $\omega \to \ln(N_{\rm s}/2)$. Therefore, for large values of $N_{\rm s}$, $\omega = \ln(N_{\rm s}/2)$ can be used as a first approximation.

Finally, substituting for $F_\nu^{\rm h}$ from Eq. (B.16) with $\omega = \ln(N_{\rm s}/2)$ in the modified Kramer's expression, Eq. (B.11) and converting the summation to an integral, we can obtain the extensional viscosity in dimensionless terms as

$$\overline{\eta}_{\rm p}^{\dagger} = \frac{\pi^{3/2}}{\sqrt{12}}\,\frac{\overline{\alpha}^2\, h^*\, N_{\rm K}^3\, N_{\rm K,\,s}^{-1/2}}{1+\gamma}, \tag{B.20}$$

where

$$\gamma = \begin{cases} 0 & \text{for chains without HI,} \\ \dfrac{\sqrt{3\pi}\, h^* \ln(N_{\rm s}/2)}{\overline{\alpha}\, N_{\rm K,\,s}^{1/2}} & \text{for chains with HI.} \end{cases} \tag{B.21}$$

As mentioned earlier, with $\overline{\alpha} = 1$, the prediction of $\overline{\eta}_{\rm p}^{\dagger}$ for the fully-stretched state is obtained.

From the equations above, it is recognized that for chains without HI, $\overline{\eta}_{\rm p}^{\dagger}$ is directly proportional to h^*. Therefore, in the limit $N_{\rm s} \to N_{\rm K}$ and $h^* \to h_{\rm K}^*$, the macroscopic properties of the solution are strongly influenced by the local hydrodynamic characteristics of the Kuhn segment. In particular, the (dimensional) extensional viscosity for fully-stretched free-draining bead-rod chains is obtained as

$$\overline{\eta}_{\rm p} = \frac{n_{\rm p}\zeta_{\rm K} b_{\rm K}^2 N_{\rm K}^3}{12} \tag{B.22}$$

which is the result derived by Hassager [1974]. For chains with HI, however, this dependence on local details is progressively weakened as $\ln N_{\rm K} \to \infty$, and for very

large chains, a parameter-free limit is obtained in the fully-stretched state,

$$\overline{\eta}_{\mathrm{p}}^{\dagger} = \frac{\pi}{6} \frac{N_{\mathrm{K}}^3}{\ln\left(N_{\mathrm{K}}/2\right)}. \tag{B.23}$$

A similar result (with $\ln N_{\mathrm{K}}$ in the denominator, instead of $\ln(N_{\mathrm{K}}/2)$ above) can be obtained using the expression derived by Doi and Edwards [1986] (and by Batchelor [1970] earlier) for the translational drag coefficient of a long slender rod in a direction parallel to its length.

Appendix C

Calculation of the length and molecular weight of a single Kuhn segment in some common vinyl polymers

This Appendix briefly presents some basic formulae for the calculation of the parameters characterizing the Kuhn segment of vinyl polymers for which experimental data are discussed in this work. The theory behind these formulae has been discussed thoroughly by Yamakawa [1971].

The "unperturbed" mean-squared end-to-end distance $R^2_{\mathrm{e,\,eq}}$ of a polymer chain in a theta solvent is related to n, the number of monomeric subunits in the homopolymer backbone, and their length l through the following equations:

$$R^2_{\mathrm{e,\,eq}} = \sigma^2 \left(\frac{1 - \cos\theta}{1 + \cos\theta} \right) nl^2 = C_\infty nl^2 = b_{\mathrm{K}}^2 N_{\mathrm{K}}. \tag{C.1}$$

Here, θ is the bond angle (= 109.5 ° for vinyl polymers), and σ quantifies the influence of steric hindrances on the local stiffness of the chain. Often, the effects of the bond-angle and steric hindrances are absorbed into a single constant C_∞ in experimental literature. The equation above also forms the first part of the definition of the constants b_{K}, the Kuhn segment length and N_{K}, the number of

Kuhn segments. The second part of the definition comes from the equation for the total contour length of the polymer chain,

$$L = \sin(\theta/2) n l = b_{\mathrm{K}} N_{\mathrm{K}}. \tag{C.2}$$

Combining these definitions above leads to

$$N_{\mathrm{K}} = n \left(\frac{1 + \cos\theta}{2\sigma^2} \right) = \frac{n}{\sigma^2 + C_\infty}, \tag{C.3}$$

$$b_{\mathrm{K}} = l \left(\frac{2\sigma^2 \sin(\theta/2)}{1 + \cos\theta} \right) = l \sqrt{C_\infty (\sigma^2 + C_\infty)}. \tag{C.4}$$

Since the number of monomeric units $n = M/m$, where M and m are the molecular weights of the polymer molecule and the monomer, respectively, one further obtains the following useful expression which permits the direct calculation of N_{K} as M/m_{K}:

$$m_{\mathrm{K}} = m \left(\frac{2\sigma^2}{1 + \cos\theta} \right) = m\,(\sigma^2 + C_\infty). \tag{C.5}$$

For vinyl polymers, $l = 0.153$ nm, $\sin(\theta/2) = 0.82$ [Yamakawa, 1971]. Table C.1 gathers together the key parameters in the estimation of b_{K} and N_{K} for two vinyl polymers for which experimental data are analyzed in this work.

Table C.1: Kuhn segment parameters for some vinyl polymers.

Polymer	Polystyrene	Polyisobutylene
Structure	$[(C_6H_5)CH_2–CH_2]_n$	$[(C_6H_5)_2C–CH_2]_n$
m	52	28
C_∞	9.6	6.6
b_{K} (nm)	1.8	1.2
m_{K}	742	275
Reference	Li *et al.* [2000]	Bandrup *et al.* [1999]

Appendix D

The value of the fixed-point for Kramer's chains with hydrodynamic interactions

For a bead-rod chain of N_{K} rods and $N = N_{\mathrm{K}} + 1$ beads, the Kirkwood-Riseman diffusivity is,

$$\mathcal{D}_0 = \frac{k_{\mathrm{B}}T}{N_{\mathrm{K}}\zeta_{\mathrm{K}}}\left[1 + \frac{2a_{\mathrm{K}}/b_{\mathrm{K}}}{N_{\mathrm{K}}}S_2\right], \tag{D.1}$$

where S_2 is defined as,

$$S_2 = b_{\mathrm{K}}\sum_{\nu=1}^{N}\sum_{\mu=\nu+1}^{N}\left\langle\frac{1}{r_{\nu\mu}}\right\rangle_{\mathrm{eq}}. \tag{D.2}$$

Defining the ratio U_{RD} as

$$U_{RD} = \frac{6\pi\eta_{\mathrm{s}}\mathcal{D}_0 R_{\mathrm{G,\,eq}}}{k_{\mathrm{B}}T} \tag{D.3}$$

where $R_{\mathrm{G,\,eq}} = (1/\sqrt{6})b_{\mathrm{K}}N_{\mathrm{K}}^{1/2}$ is the equilibrium root-mean-square radius of gyration for large N_{K} under theta conditions, one obtains using the equations above,

$$\begin{aligned} U_{RD} &= \frac{R_{\mathrm{G,\,eq}}/a_{\mathrm{K}}}{N_{\mathrm{K}}}\left[1+\frac{2a_{\mathrm{K}}/b_{\mathrm{K}}}{N_{\mathrm{K}}}S_2\right], \\ &= \frac{1}{\sqrt{2\pi}h_{\mathrm{K}}^{*}N_{\mathrm{K}}^{1/2}}+\frac{\sqrt{2/3}}{N_{\mathrm{K}}^{3/2}}S_2\,. \end{aligned} \tag{D.4}$$

Since it is known that for long chains the approach of U_{RD} to the universal value U_{RD}^{∞} takes the form [Kröger *et al.*, 2000; Öttinger, 1987a]

$$U_{RD} = U_{RD}^{\infty} + C\left(\frac{1}{h_{\mathrm{K}}^{*}}-\frac{1}{h_{\mathrm{f}}^{*}}\right)\frac{1}{\sqrt{N_{\mathrm{K}}}}+O(\frac{1}{N_{\mathrm{K}}})\,, \tag{D.5}$$

where U_{RD}^{∞} is the limit of U_{RD} as $N_{\mathrm{K}}\to\infty$, equating the two expressions for U_{RD} in Eqs. (D.4) and (D.5) above yields

$$\frac{\sqrt{2/3}}{N_{\mathrm{K}}^{3/2}}S_2 = U_{RD}^{\infty} + C\left(\frac{1}{h_{\mathrm{K}}^{*}}-\frac{1}{h_{\mathrm{f}}^{*}}\right)\frac{1}{\sqrt{N_{\mathrm{K}}}}-\frac{1}{\sqrt{2\pi}h_{\mathrm{K}}^{*}\sqrt{N_{\mathrm{K}}}}+O(\frac{1}{N_{\mathrm{K}}}) \tag{D.6}$$

Since S_2 is a static average at equilibrium, it is independent of the HI parameter h_{K}^{*}. As a result, all the dependence on h_{K}^{*} must vanish from the right-hand side. For the leading order term, this is achieved by setting $C = 1/\sqrt{2\pi}$, and therefore,

$$\frac{\sqrt{2/3}}{N_{\mathrm{K}}^{3/2}}S_2 = U_{RD}^{\infty} - \frac{1}{\sqrt{2\pi}h_{\mathrm{f}}^{*}}\frac{1}{\sqrt{N_{\mathrm{K}}}}+O(\frac{1}{N_{\mathrm{K}}})\,. \tag{D.7}$$

By examining the asymptotic behaviour of the ratio $\sqrt{2/3}\,S_2/N_{\mathrm{K}}^{3/2}$ as $1/\sqrt{N_{\mathrm{K}}}\to 0$, U_{RD}^{∞} and h_{f}^{*} can be obtained. Predictions of S_2 for several values of N_{K} in the range [25, 2000] were obtained by generating equilibrium configurations of freely-jointed Kramer's chains. Fitting a quadratic expression through the S_2-versus-$1/\sqrt{N_{\mathrm{K}}}$ data gives $h_{\mathrm{f}}^{*} = 0.1857 \pm 0.0003$, and a $U_{RD}^{\infty} = 1.5039 \pm 0.0004$. This prediction is close to the value of $8/(3\sqrt{\pi}) = 1.5045$ predicted [Sunthar and Prakash, 2005] for Rouse chains with equilibrium-averaged HI (the Zimm model), showing that this universal limit is independent of the representation used to describe the polymer chain. The value of the fixed point h_{f}^{*} however depends on the local stiffness in the model.

While the Zimm theory which uses equilibrium-averaged HI in Rouse chains leads to a $h_{\mathrm{f}}^{*} = 12/(35\sqrt{2}) = 0.2424$, the use of a equilibrium-averaged HI in bead-rod chains gives $h_{\mathrm{f}}^{*} = 0.19$ (rounded off to two decimal places), as calculated above.

Appendix E

An estimate for the average volume of a polymer coil

This aim of this Appendix is to propose a simple but general estimate for the average spatial volume spanned by a polymer coil.

The gyration tensor was introduced in Chapter 2 as

$$\boldsymbol{G} = \frac{1}{N}\sum_{\nu=1}^{N}\langle \boldsymbol{R}_\nu \boldsymbol{R}_\nu \rangle \,, \tag{E.1}$$

where $\boldsymbol{R}_\nu$ is the displacement vector of the ν-th bead from the centre-of-mass of the polymer chain, $\boldsymbol{R}_\nu = \boldsymbol{r}_\nu - (1/N)\sum_{\mu=1}^{N}\boldsymbol{r}_\mu$. If $\rho(\boldsymbol{R})d\boldsymbol{R}$ denotes the probability of finding a bead of the chain in the volume element $d\boldsymbol{R}$ around a point located at a displacement $\boldsymbol{R}$ from the centre-of-mass of the chain, then

$$\rho(\boldsymbol{R}) = \frac{1}{N}\sum_{\nu=1}^{N}\int \delta(\boldsymbol{R}-\boldsymbol{R}_\nu)\psi \, d\boldsymbol{R}_1 \ldots d\boldsymbol{R}_N \,, \tag{E.2}$$

where ψ is the configurational probability density. Hence, the second moment of the bead-density distribution ρ

$$\int \boldsymbol{R}\boldsymbol{R}\rho(\boldsymbol{R})\, d\boldsymbol{R} = \int\int \boldsymbol{R}\boldsymbol{R}\left[\frac{1}{N}\sum_{\nu=1}^{N}\delta(\boldsymbol{R}-\boldsymbol{R}_\nu)\psi\right] d\boldsymbol{R}_1 \ldots d\boldsymbol{R}_N \, d\boldsymbol{R} \,, \tag{E.3}$$

$$= \boldsymbol{G}. \tag{E.4}$$

Picturing the polymer as a collection of beads, the "average polymer" can be thought of as an ellipsoid whose principal axes are oriented along the eigenvectors of the variance of the bead density distribution, $\boldsymbol{G}$.

The volume spanned by any solid ellipsoid whose semi-axes are equal to the eigenvalues of $K\boldsymbol{G}$ is,

$$V_{\text{ellipsoid}} = \frac{4\pi}{3}\sqrt{\det[K\boldsymbol{G}]}\,, \tag{E.5}$$

where K is some constant. In order to use an expression of this form to calculate the volume spanned by a polymer coil, it is necessary to choose a reasonable value for K.

A commonly used expression for the average volume spanned by a polymer coil at equilibrium is

$$V_{\text{chain, eq}} = \frac{4\pi}{3}R^3_{\text{G, eq}}\,. \tag{E.6}$$

Since $\boldsymbol{G}_{\text{eq}} = (R^2_{\text{G, eq}}/3)\boldsymbol{\delta}$ for the average chain, and the volume of an arbitrary ellipsoid described by the tensor $K\boldsymbol{G}_{\text{eq}}$ is

$$V_{\text{ellipsoid, eq}} = \frac{4\pi}{3}\left(\frac{K}{3}\right)^{3/2}R^3_{\text{G, eq}}\,. \tag{E.7}$$

Matching the two expressions above leads to a choice of $K = 3$.

Therefore, if $\boldsymbol{G}$ is the gyration tensor, then the mean volume spanned by a polymer chain can be estimated as

$$V_{\text{chain}} = \frac{4\pi}{3}\sqrt{\det[3\boldsymbol{G}]} = 4\pi\sqrt{3\det[\boldsymbol{G}]}\,. \tag{E.8}$$

With this estimate, the fraction of the total volume of the polymer solution spanned by polymer coils is

$$\phi = n_{\text{p}}V_{\text{chain}} = 4\pi n_{\text{p}}\sqrt{3\det[\boldsymbol{G}]}\,. \tag{E.9}$$

At equilibrium, this corresponds exactly to the commonly defined c/c^* ratio. Hence, ϕ can be regarded as an indicator of whether of not polymer chains interpenetrate

under general flow situations.

Bibliography

Agarwal, U. S., "Effect of initial conformation, flow strength, and hydrodynamic interaction on polymer molecules in extensional flows," J. Chem. Phys. **113**, 3397–3403 (2000).

Ahn, K. H., J. L. Schrag and S. J. Lee, "Bead-spring chain model for the dynamics of dilute polymer solutions: Part 2. Comparisons with experimental data," J. Non-Newtonian Fluid Mech. **50**, 349–373 (1993).

Andrews, N. C., A. K. Doufas and A. J. McHugh, "Effect of solvent quality on the rheological and rheooptical properties of flexible polymer solutions," Macromolecules **31**, 3104–3108 (1998).

Anna, S. L. and G. H. McKinley, "Elasto-capillary thinning and breakup of model elastic liquids," J. Rheol. **45**, 115–138 (2001).

Auer, P. L. and C. S. Gardner, "Note on singular integral equations of the Kirkwood-Riseman type/ Solution of the Kirkwood-Riseman equation in the asymptotic limit," J. Chem. Phys. **33**, 1545–1547 (1955).

Bandrup, J., E. H. Immergut and E. A. Grulke, *Polymer Handbook*, Wiley Interscience, Hoboken, N.J., 4th edn. (1999).

Batchelor, G. K., "Slender-body theory for particles of arbitrary cross-section in Stokes flow," J. Fluid Mech. **44**, 419–440 (1970).

Berry, G. C., "Thermodynamic and conformational properties of polystyrene. I. Light-scattering studies on dilute solutions of linear polystyrenes," J. Chem. Phys. **44**, 4550–4564 (1966).

Bird, R. B., R. C. Armstrong and O. Hassager, *Dynamics of Polymeric Liquids - Volume 1: Fluid Mechanics*, John Wiley, New York, 2nd edn. (1987a).

Bird, R. B., C. F. Curtiss, R. C. Armstrong and O. Hassager, *Dynamics of Polymeric Liquids - Volume 2: Kinetic Theory*, John Wiley, New York, 2nd edn. (1987b).

Bird, R. B., P. J. Dotson and N. L. Johnson, "Polymer solution bheology based on a finitely extensible bead-spring chain model," J. Non-Newtonian Fluid Mech. **7**, 213–235 (1980).

Bossart, J. and H. C. Öttinger, "Orientation of polymer coils in dilute solutions undergoing shear flow: Birefringence and light scattering," Macromolecules **28**, 5852–5860 (1995).

Bossart, J. and H. C. Öttinger, "Orientation of polymer coils in dilute solutions undergoing shear flow: Birefringence experiments," Macromolecules **30**, 5527–5540 (1997).

Bouchad, J. P., "Weak ergodicity breaking and aging in disordered systems," J. de Physique I **2**, 1705–1713 (1992).

Cascales, J. L. and J. Garcia de la Torre, "shear-rate dependence of the intrinsic viscosity of bead and spring chains. Hydrodynamic interaction and excluded volume effects," Polymer **32**, 3359–3363 (1991).

De Gennes, P.-G., "Coil-stretch transition of dilute flexible polymers under ultrahigh velocity gradients," J. Chem. Phys. **60**, 5030–5042 (1974).

De Gennes, P.-G., *Scaling Concepts in Polymer Physics*, Cornell University Press (1979).

De Gennes, P.-G., "Relaxation anomalies in linear polymer melts," Macromolecules **35**, 3785–3786 (2002).

des Cloizeaux, J. and G. Jannink, *Polymers in Solution, Their Modeling and Structure*, Oxford Science Publishers (1990).

Doi, M. and S. F. Edwards, *The Theory of Polymer Dynamics*, Oxford University Press, New York (1986).

Douglas, J. F. and K. F. Freed, "Renormalization and the two-parameter theory," Macromolecules **17**, 2344–2354 (1984).

Doyle, P. S. and E. S. G. Shaqfeh, "Dynamic simulation of freely draining, flexible bead-rod chains: Start-up of extensional and shear flow," J. Non-Newtonian Fluid Mech. **76**, 43–78 (1998).

Doyle, P. S., E. S. G. Shaqfeh, G. H. McKinley and S. H. Spiegelberg, "Relaxation of dilute polymers solutions following extensional flow," J. Non-Newtonian Fluid Mech. **76**, 79–110 (1998).

Dubbelboer, R., *Extensional rheology of two model polyelectrolytes in dilute solution*, Ph.D. thesis, Monash University (2004).

Entov, V. M. and E. J. Hinch, "Effect of a spectrum of relaxation times on the capillary thinning of a filament of elastic liquid," J. Non-Newtonian Fluid Mech. **72**, 31–53 (1997).

Fan, X. J., R. B. Bird and M. Renardy, "A finitely extensible bead-spring chain model for dilute polymer solutions," J. Non-Newtonian Fluid Mech. **69**, 1352–1360 (1978).

Fetters, L. J., N. Hadjichristidis, J. S. Lindner and J. W. Mays, "Molecular weight dependence of hydrodynamic and thermodynamic properties for well-defined linear polymers in solution," J. Phys. Chem. Ref. Data **23**, 619–640 (1994).

Fixman, M., "Polymer dynamics: Boson representation and excluded volume forces," J. Chem. Phys. **45**, 785–792 (1966a).

Fixman, M., "Polymer dynamics: Non-Newtonian intrinsic viscosity," J. Chem. Phys. **45**, 793–803 (1966b).

Fixman, M., "Inclusion of hydrodynamic interaction in polymer dynamical simulations," Macromolecules **14**, 1710–1717 (1981).

Fixman, M., "Construction of Langevin forces in the simulation of hydrodynamic interaction," Macromolecules **19**, 1204–1207 (1986).

Flory, P. J., "The configuration of real polymer chains," J. Chem. Phys. **17**, 303–310 (1949).

Flory, P. J., *Principles of Polymer Chemistry*, Cornell University Press, Ithaca, New York (1953).

Freed, K. F., S.-Q. Wang, J. Roovers and J. F. Douglas, "Partial draining and universality of dilute solution polymer dynamics: Comparison of theory and experiment," Macromolecules **21**, 2219–2224 (1988).

Fujita, H., "Some unsolved uroblems on dilute polymer solutions," Macromolecules **21**, 179–185 (1988).

Ghosh, I., G. H. McKinley, R. A. Brown and R. C. Armstrong, "Deficiencies of FENE dumbbell models in describing rapid stretching of dilute polymer solutions," J. Rheol. **45**, 721–758 (2001).

Gorban, A. N., I. V. Karlin, P. Ilg and H. C. Öttinger, "Corrections and enhancements of quasi-equilibrium states," J. Non-Newtonian Fluid Mech. **96**, 203–219 (2001).

Graessley, W. W., R. C. Hayward and G. S. Grest, "Excluded-volume effects in polymer solutions: 2. Comparison of experimental results with numerical simulation data," Macromolecules **32**, 3510–3517 (1999).

Gupta, R. K., D. A. Nguyen and T. Sridhar, "Extensional viscosity of dilute polystyrene solutions: Effect of concentration and molecular weight," Phys. Fluids **12**, 1296–1318 (2000).

Hassager, O., "Kinetic theory and rheology of bead-rod models for macromolecular solutions I. Equilibrium and steady flow properties," J. Chem. Phys. **60**, 2111–2124 (1974).

Hernandez Cifre, J. G. and J. Garcia de la Torre, "Steady-state behaviour of dilute polymers in elongational flow. Dependence of the critical elongational rate on chain length, hydrodynamic interaction, and excluded volume," J. Rheol. **43**, 339–358 (1999).

Herrchen, M. and H. C. Öttinger, "A detailed comparison of various FENE models," J. Non-Newtonian Fluid Mech. **68**, 17–42 (1997).

Hinch, E. J., "Uncoiling a polymer molecule in a strong extensional flow," J. Non-Newtonian Fluid Mech. **54**, 209–230 (1994).

Hsieh, C.-C. and R. G. Larson, "Modeling hydrodynamic interaction in Brownian dynamics: Simulations of extensional and shear flows of dilute solutions of high molecular weight polystyrene," J. Rheol. **48**, 995–1021 (2004).

Hsieh, C.-C., L. Li and R. G. Larson, "Modeling hydrodynamic interaction in Brownian dynamics: Simulations of extensional flows of dilute solutions of DNA and polystyrene," J. Non-Newtonian Fluid Mech. **113**, 147–191 (2003).

Huppler, J. D., I. F. MacDonald, E. Ashare, T. W. Spriggs, R. B. Bird and L. A. Holmes, "Rheological properties of three solutions. Part II. Relaxation and growth of shear and normal stresses," Trans. Soc. Rheol. **11**, 181–204 (1967).

Hur, J. S., E. S. G. Shaqfeh, H. P. Babcock, D. E. Smith and S. Chu, "Dynamics of dilute and semidilute DNA solutions in the start-up of shear flow," J. Rheol. **45**, 421–450 (2001).

Hütter, M., I. V. Karlin and H. C. Öttinger, "Dynamic mean-field models from a nonequilibrium thermodynamics perspective," Phys. Rev. E **68**, Art. No. 016115 (2003).

Hütter, M. and H. C. Öttinger, "Modification of linear response theory for mean-field approximations," Phys. Rev. E **54**, 2526–2530 (1996).

Ilg, P., I. V. Karlin and H. C. Öttinger, "Canonical distribution functions in polymer dynamics. (I). Dilute solutions of flexible polymers," Physica A **315**, 367–385 (2002).

Jendrejack, R. M., J. J. de Pablo and M. D. Graham, "Stochastic simulations of DNA in flow: Dynamics and the effects of hydrodynamic interactions," J. Chem. Phys. **116**, 7752–7759 (2002).

Jendrejack, R. M., M. D. Graham and J. J. de Pablo, "Hydrodynamic interactions in long chain polymers: Application of the Chebyshev polynomial approximation in stochastic simulations," J. Chem. Phys. **113**, 2894–2900 (2000).

Johnson, R. M., J. L. Schrag and J. D. Ferry, "Infinite-dilution viscoelastic properties of polystyrene in θ-solvents and good solvents," Polymer Japanese **1**, 742–749 (1970).

Keunings, R., "On the Peterlin approximation for finitely extensible dumbbells," J. Non-Newtonian Fluid Mech. **68**, 85–100 (1997).

Kim, S. and S. J. Karrila, *Microhydrodynamics : Principles and Selected Applications*, Butterworth-Heinemann, Boston (1990).

Kirkwood, J. G. and J. Riseman, "The intrinsic viscosities and diffusion constants of flexible macromolecules in solution," J. Chem. Phys. **16**, 565–573 (1948).

Kisbaugh, A. J. and A. J. McHugh, "A discussion of shear-thickening in bead-spring models," J. Non-Newtonian Fluid Mech. **34**, 181–206 (1990).

Knudsen, K. D., J. G. de la Torre and A. Elgsaeter, "Gaussian chains with excluded volume and hydrodynamic interaction: Shear rate dependence of radius of gyration, intrinsic viscosity and flow birefringence," Polymer **37**, 1317–1322 (1996).

Kotaka, T., H. Suzuki and H. Inagaki, "Shear-rate dependence of the intrinsic viscosity of flexible linear macromolecules," J. Chem. Phys. **45**, 2770–2773 (1966).

Kramer, H. A., "Het gedrag van macromoleculen in een stroomende vloeistof," Physica **11**, 1–11 (1944).

Kröger, M., A. Alba-Pérez, M. Laso and H. C. Öttinger, "Variance reduced Brownian simulation of a bead-spring chain under steady shear flow considering hydrodynamic interaction effects," J. Chem. Phys. **113**, 4767–4773 (2000).

Kumar, K. S. and J. R. Prakash, "Equilibrium swelling and universal ratios in dilute polymer solutions: Exact Brownian dynamics simulations for a delta function excluded volume potential," Macromolecules **36**, 7842–7856 (2003).

Kumar, K. S. and J. R. Prakash, "Universal consequences of the presence of excluded volume interactions in dilute polymer solutions undergoing shear flow," J. Chem. Phys. **121**, 3886–3897 (2004).

Larson, R. G., *Constitutive Equations for Polymer Melts and Solutions*, Butterworths, Boston (1988).

Larson, R. G., "The rheology of dilute solutions of flexible polymers: Progress and problems," J. Rheol. **49**, 1–70 (2004).

Larson, R. G., H. Hu, D. E. Smith and S. Chu, "Brownian dynamics simulations of a DNA molecule in an extensional flow field," J. Rheol. **43**, 267–304 (1999).

Li, L. and R. G. Larson, "Comparison of Brownian dynamics simulations with microscopic light-scattering measurements of polymer deformation under flow," Macromolecules **33**, 1411–1415 (2000a).

Li, L. and R. G. Larson, "Excluded volume effects on the birefringence and stress of dilute polymer solutions in extensional flow," Rheol. Acta **39**, 419–427 (2000b).

Li, L., R. G. Larson and T. Sridhar, "Brownian dynamics simulations of dilute polystyrene solutions," J. Rheol. **44**, 291–322 (2000).

Li, X. and M. M. Denn, "Monte carlo simulation of steady extensional flows," J. Rheol. **48**, 805–821 (2004).

Lielens, G., P. Halin, I. Jaumin, R. Keunings and V. Legat, "New closure approximations for the kinetic theory of finitely extensible dumbbells," J. Non-Newtonian Fluid Mech. **76**, 249–279 (1998).

Lielens, G., R. Keunings and V. Legat, "The FENE-L and FENE-LS closure approximations to the kinetic theory of finitely extensible dumbbells," J. Non-Newtonian Fluid Mech. **87**, 279–296 (1999).

Magda, J. J., R. G. Larson and M. E. Mackay, "Deformation-dependent hydrodynamic interaction in flows of dilute polymer solutions," J. Chem. Phys. **89**, 2504–2513 (1988).

McKinley, G. H. and T. Sridhar, "Filament-stretching rheometry of complex fluids," Annu. Rev. Fluid Mech. **34**, 375–415 (2002).

Miyaki, Y., Y. Einaga, H. Fujita and M. Fukuda, "Flory's viscosity factor for the system polystyrene + cyclohexane at 34.5 ° C," Macromolecules **13**, 588–592 (1980).

Miyaki, Y. and H. Fujita, "Excluded-volume effects in dilute polymer solutions. 11. Tests of the two-parameter theory for radius of gyration and intrinsic viscosity," Macromolecules **14**, 742–746 (1981).

Noda, I., Y. Yamada and M. Nagasawa, "The rate of shear dependence of the intrinsic viscosity of monodisperse polymer," J. Phys. Chem. **72**, 2890–2898 (1968).

Orr, N. V., *Dynamics of polymer molecules in extensional flow*, Ph.D. thesis, Monash University (1998).

Orr, N. V. and T. Sridhar, "Stress relaxation in uniaxial extension," J. Non-Newtonian Fluid Mech. **67**, 77–103 (1996).

Orr, N. V. and T. Sridhar, "Probing the dynamics of polymer solutions in extensional flow using step strain rate experiments," J. Non-Newtonian Fluid Mech. **82**, 203–232 (1999).

Osaki, K., "A revised version of the integrodifferential equation in the Zimm theory for polymer solution dynamics," Macromolecules **5**, 141–144 (1972).

Öttinger, H. C., "Generalized Zimm model for dilute polymer solutions under theta conditions," J. Chem. Phys. **86**, 3731–3749 (1987a).

Öttinger, H. C., "A model of dilute polymer solutions with hydrodynamic interaction and finite extensibility. I. Basic equations and series expansions," J. Non-Newtonian Fluid Mech. **26**, 207–246 (1987b).

Öttinger, H. C., "Translational diffusivity from the Zimm model," J. Chem. Phys. **87**, 3156–3165 (1987c).

Öttinger, H. C., "Gaussian approximation for Rouse chains with hydrodynamic interaction," J. Chem. Phys. **90**, 463–473 (1989a).

Öttinger, H. C., "Renormalization-group calculation of excluded-volume effects on the viscometric functions of dilute polymer solutions," Phys. Rev. A **40**, 2664–2671 (1989b).

Öttinger, H. C., *Stochastic Processes in Polymeric Fluids*, Springer-Verlag (1996a).

Öttinger, H. C., "Velocity field in nondraining polymer chains," Rheol. Acta **35**, 134–138 (1996b).

Öttinger, H. C. and Y. Rabin, "Renormalization-group calculation of viscometric functions based on conventional polymer kinetic theory," J. Non-Newtonian Fluid Mech. **33**, 53–93 (1989).

Öttinger, H. C. and W. Zylka, "On the relaxation spectra for models of dilute polymer solutions," J. Rheol. **36**, 885–910 (1992).

Pamies, R., M. C. L. Martinez, J. G. Hernandez Cifre and J. Garcia de la Torre, "Non-Newtonian viscosity of dilute polymer solutions," Macromolecules **38**, 1371–1377 (2005).

Perkins, T. T., D. E. Smith and S. Chu, "Single polymer dynamics in an elongational flow," Science **276**, 2016–2021 (1997).

Peterlin, A., "Hydrodynamics of linear macromolecules," Pure Appl. Chemistry **12**, 563–586 (1966a).

Peterlin, A., "Hydrodynamics of macromolecules in a velocity field with longitudinal gradient," J. Poly. Sci. B, Poly. Lett. **4B**, 287–291 (1966b).

Phillies, G. D. J. and P. Peczak, "The ubiquity of stretched-exponential forms in polymer dynamics," Macromolecules **21**, 214–220 (1988).

Prabhakar, R. and J. R. Prakash, "Viscometric functions for Hookean dumbbells with excluded volume and hydrodynamic interaction," J. Rheol. **46**, 1191–1220 (2002).

Prabhakar, R. and J. R. Prakash, "Multiplicative separation of the influences of excluded volume, hydrodynamic interactions and finite extensibility on the rheological properties of dilute polymer solutions," J. Non-Newtonian Fluid Mech. **116**, 163–182 (2004).

Prabhakar, R., J. R. Prakash and T. Sridhar, "A successive fine-graining scheme for predicting the rheological properties of dilute polymer solution," J. Non-Newtonian Fluid Mech. **116**, 163–182 (2004).

Prakash, J. R., "The kinetic theory of dilute solutions of flexible polymers: Hydrodynamic interaction," in *Advances in flow and rheology of non-Newtonian fluids*, eds. D. A. Siginer, D. D. Kee and R. P. Chhabra, pp. 467–517, Rheology Series, Amsterdam, Elsevier Science (1999).

Prakash, J. R., "The influence of the range of excluded volume interactions on the linear viscoelastic properties of dilute polymer solutions," Chem. Eng. Sci. **56**, 5555–5564 (2001a).

Prakash, J. R., "Rouse chains with excluded volume interactions: Linear viscoelasticity," Macromolecules **34**, 3396–3411 (2001b).

Prakash, J. R., "Rouse chains with excluded volume interactions in steady simple shear flow," J. Rheol. **46**, 1353–1380 (2002).

Prakash, J. R. and H. C. Öttinger, "Universal viscometric functions for dilute polymer solutions," J. Non-Newtonian Fluid Mech. **71**, 245–272 (1997).

Prakash, J. R. and H. C. Öttinger, "Viscometric functions for a dilute solution of polymers in a good solvent," Macromolecules **32**, 2028–2043 (1999).

Press, W. H., S. A. Teukolsky, W. T. Vetterling and B. P. Flannery, *Numerical Recipes in Fortran*, Cambridge University Press, Cambridge, 2nd edn. (1992).

Press, W. H., S. A. Teukolsky, W. T. Vetterling and B. P. Flannery, *Numerical Recipes in Fortran 90: The Art of Parallel Scientific Computing*, Cambridge University Press, Cambridge, 2nd edn. (1996).

Risken, H., *The Fokker-Planck equation : Methods of Solution and Applications*, Springer-Verlag, Berlin, 2nd edn. (1989).

Rotne, J. and S. Prager, "Variational treatment of hydrodynamic interaction in polymers," J. Chem. Phys. **50**, 4831–4837 (1969).

Rouse, P. E., "A theory of the linear viscoelastic properties of dilute polymer solutions of coiling polymers," J. Chem. Phys. **21**, 1272–1280 (1953).

Sahouani, H. and T. Lodge, "Onset of excluded volume effects in chain dynamics," Macromolecules **25**, 5632–5642 (1992).

Schäfer, L., *Excluded Volume Effects in Polymer Solutions*, Springer-Verlag, Berlin (1999).

Schroeder, C. M., H. P. Babcock, E. S. G. Shaqfeh and S. Chu, "Observation of polymer conformation hysteresis in extensional flow," Science **301**, 1515–1519 (2003).

Schroeder, C. M., E. S. G. Shaqfeh and S. Chu, "Effect of hydrodynamic interactions on DNA dynamics in extensional flow: Simulation and single molecule experiments," Macromolecules **37**, 9242–9256 (2004).

Shaqfeh, E. S. G., G. H. McKinley, N. Woo, D. A. Ngyuen and T. Sridhar, "On the polymer entropic force singularity and its relation to extensional stress relaxation and filament recoil," J. Rheol. **48**, 209–221 (2004).

Sizaire, R., G. Lielens, I. Jaumain, R. Keunings and V. Legat, "On the hysteretic behaviour of dilute polymer solutions in relaxation following extensional flow," J. Non-Newtonian Fluid Mech. **82**, 233–253 (1999).

Smith, D. E. and S. Chu, "Response of flexible polymers to a sudden elongational flow," Science **281**, 1335–1340 (1998).

Somasi, M., B. Khomami, N. J. Woo, J. S. Hur and E. S. G. Shaqfeh, "Brownian dynamics simulations of bead-rod and bead-spring chains: Numerical algorithms and coarse graining issues," J. Non-Newtonian Fluid Mech. **108**, 227–255 (2002).

Spiegelberg, S. H. and G. H. McKinley, "Elastic and viscous contributions to stress in extensional rheometry of viscous polymer solutions," in *Proceedings of the XIth International Congress on Rheology*, p. 211 212, Quebec City (1996).

Sridhar, T., "An overview of the Project M1," J. Non-Newtonian Fluid Mech. **35**, 85–92 (1990).

Sridhar, T., V. Tirtaatmadja, D. A. Nguyen and R. K. Gupta, "Measurement of extensional viscosity of polymer solutions," J. Non-Newtonian Fluid Mech. **40**, 271–280 (1991).

Ströbl, G. R., *The Physics of Polymers*, Springer Verlag, Berlin (1996).

Sunthar, P. and J. R. Prakash, "Parameter-free prediction of DNA conformations in elongational flow by Successive Fine Graining," Macromolecules **38**, 617–640 (2005).

Suzuki, H., T. Kotaka and H. Inagaki, "Shear-rate dependence of the intrinsic viscosity of flexible linear macromolecules II. Solvent effect," J. Chem. Phys. **51**, 1279–1285 (1969).

Tirtaatmadja, V. and T. Sridhar, "A filament stretching device for measurement of extensional viscosity," J. Rheol. **37**, 1081–1102 (1993).

van den Brule, B. H. A. A., "Brownian dynamics simulation of finitely extensible bead-spring chains," J. Non-Newtonian Fluid Mech. **47**, 357–378 (1993).

Wagner, M. H. and J. Meissner, "Network disentanglement and time-dependent flow behaviour of polymer melts," Makromol. Chem. **181**, 1533–1550 (1980).

Wagner, N. J. and H. C. Öttinger, "Accurate simulation of linear viscoelastic properties by variance reduction through the use of control variates," J. Rheol. **41**, 757–768 (1997).

Warner, H. R., "Kinetic theory and rheology of dilute suspensions of finitely extensible dumbbells," Ind. Eng. Chem. Fundam. **11**, 379–387 (1972).

Wedgewood, L. E., "A Gaussian closure of the second-moment equation for a Hookean dumbbell with hydrodynamic interaction," J. Non-Newtonian Fluid Mech. **31**, 127–142 (1989).

Wedgewood, L. E. and R. B. Bird, "From molecular models to the solution of flow problems," Ind. Eng. Chem. Res. **27**, 1313–1320 (1988).

Wedgewood, L. E., D. N. Ostrov and R. B. Bird, "A finitely extensible bead-spring chain model for dilute polymer solutions," J. Non-Newtonian Fluid Mech. **40**, 119–139 (1991).

Wedgewood, L. E. and H. C. Öttinger, "A model of dilute polymer solutions with hydrodynamic interaction and finite extensibility. II. Shear flows," J. Non-Newtonian Fluid Mech. **27**, 245–264 (1988).

Weisstein, E. W., "Sphere packing," in *MathWorld–A Wolfram Web Resource*, p. http://mathworld.wolfram.com/SpherePacking.html, CRC Press (1999).

Wiest, J. M., "Birefringence in strong flows of polymer solutions," Polymer **40**, 1917–1922 (1999a).

Wiest, J. M., "Relaxation following uniaxial extension of dilute polymer solutions," J. Chem. Phys. **111**, 5205–5211 (1999b).

Wiest, J. M. and R. I. Tanner, "Rheology of bead-nonlinear spring chain molecules," J. Rheol. **33**, 281–316 (1989).

Wiest, J. M., L. E. Wedgewood and R. B. Bird, "On coil-stretch transitions in dilute polymer solutions," J. Chem. Phys. **90**, 587–594 (1989).

Yamakawa, H., "Transport properties of polymer chains in dilute solution: Hydrodynamic interactions," J. Chem. Phys. **53**, 436–443 (1970).

Yamakawa, H., *Modern Theory of Polymer Solutions*, Harper and Row, New York (1971).

Zimm, B. H., "Dynamics of polymer molecules in dilute solution: Viscoelasticity, flow birefringence and dielectric loss," J. Chem. Phys. **24**, 269–278 (1956).

Zimm, B. H., "Chain molecule hydrodynamics by the Monte-Carlo method and the validity of the Kirkwood-Riseman approximation," Macromolecules **13**, 592–602 (1980).

Zimm, B. H., G. M. Roe and L. F. Epstein, "Solution of a characteristic value problem from the theory of chain molecules," J. Chem. Phys. **24**, 279–281 (1956).

Zylka, W., "Gaussian approximation and Brownian dynamics simulations for Rouse chains with hydrodynamic interaction undergoing simple shear flow," J. Chem. Phys. **94**, 4628–4636 (1991).

Zylka, W. and H. C. Öttinger, "A comparison between simulations and various approximations for Hookean dumbbells with hydrodynamic interaction," J. Chem. Phys. **90**, 474–480 (1989).

Zylka, W. and H. C. Öttinger, "Calculation of various universal properties for dilute polymer solutions undergoing shear flow," Macromolecules **24**, 484–494 (1991).